UC Berkeley
UC Berkeley Electronic Theses and Dissertations

Title

Electrochemical Sensors for Molten Fluoride Salt Loop Operations, Redox Monitoring, and Corrosion Product Quantification

Permalink

https://escholarship.org/uc/item/00r435tz

ISBN

9798173787217

Author

Borrello, Michael Anthony

Publication Date

2026-08-10

Peer reviewed|Thesis/dissertation

eScholarship.org Powered by the California Digital Library
University of California

Electrochemical Sensors for Molten Fluoride Salt Loop Operations, Redox Monitoring, and Corrosion Product Quantification

By

Michael Anthony Borrello

A dissertation submitted in partial satisfaction of the
requirements for the degree of

Doctor of Philosophy
in
Nuclear Engineering

in the
Graduate Division
of the
University of California, Berkeley

Committee in charge:
Professor Raluca O. Scarlat, Chair
Professor Per F. Peterson
Professor Guanyu Su
Professor Neil Razdan

Summer 2026

Abstract

Electrochemical Sensors for Molten Fluoride Salt Loop Operations, Redox Monitoring, and Corrosion Product Quantification

Michael Anthony Borrello

Doctor of Philosophy in Nuclear Engineering

University of California, Berkeley

Professor Raluca O. Scarlat, Chair

Molten fluoride salts are enabling materials for advanced nuclear energy systems, high-temperature heat transport, and chemical processing because they can operate at temperatures and chemical conditions inaccessible to conventional aqueous systems. In molten salt reactors and related test systems, however, the salt chemistry continuously evolves as structural materials corrode, impurities are introduced, redox-active species change oxidation state, and thermal gradients create spatial variation in composition. Conventional analytical methods provide valuable compositional information but generally require *ex situ* sampling and therefore cannot continuously track an operating system. The goal of this dissertation is to develop and evaluate electrochemical sensing methodologies and deployment strategies capable of monitoring molten fluoride salt chemistry under increasingly representative operating conditions.

To connect electrochemical measurements to reactor-relevant deployment, this work first examines molten salt system design and operation. A FLiBe transfer system was designed and operated with the goal of partitioning salt in its molten state. Temperature and mass-transfer measurements were collected during operation. The process data provides both operational control and system diagnostics information using thermocouple signals, gravimetric sensors, and gas-flow measurements. These results informed the design of a NaF-BeF_2 natural circulation loop for corrosion, chemistry, and electrochemical sensing studies.

Electrochemical sensor hardware was developed for molten fluoride salt experiments with emphasis on implementing a reference electrode for redox potential and quantifying corrosion product concentrations. A replaceable wire-electrode probe and printed electrode chip were designed, fabricated, and tested in aqueous ferricyanide solution and molten salts. The probe produced interpretable open-circuit potential, cyclic voltammetry, and impedance measurements, demonstrating its use as a functional electrochemical platform while showing that surface-area calibration, reference stability, and ohmic-drop correction are necessary for quantitative interpretation. The electrode chip devices produced valid aqueous responses, but high-temperature and molten-salt tests revealed delamination, adhesion failure, and packaging limitations.

Redox measurements in FLiNaK and FLiBe were used to evaluate practical reference electrode concepts for high-temperature fluoride salts. Potassium dynamic reference measurements in FLiNaK-CrF_3 provided an internal potential scale at low chromium concentrations but became limited by material and operational failures at higher additions. In FLiBe, Ni/NiF_2, Ag/AgF, and Be/BeF_2 redox couples were evaluated in their usability and limitations. The Be dynamic reference electrode mechanistic insights are given with respect to relaxation behavior with a locally modified LiF-BeF_2 interfacial composition.

Finally, chronopotentiometry, cyclic voltammetry, and square-wave voltammetry were applied to dissolved corrosion product quantification. The FLiNaK-CrF_3 dataset demonstrated that chromium electrochemistry is quantitative but only with explicit treatment of ohmic drop, activity coefficients, well defined electroactive surface area, and identifying ranges of linearity with bulk concentration. Square-wave voltammetry in FLiBe detected changes in impurity chemistry after oxidant and material additions, but quantitative peak assignments require well controlled electrode surface areas, internal references, and post-test characterization. Collectively, this dissertation shows that electrochemical sensing can provide meaningful *in situ* information on molten salt redox state and corrosion-product chemistry when the sensor, reference electrode, and cell geometry are designed to account for the thermochemistry and transport regime found in a prototypical molten salt reactor environment.

“Find the board within the tree.” – Big Z

Contents

Electrochemical Sensors for Molten Fluoride Salt Loop Operations, Redox Monitoring, and Corrosion Product Quantification 1
Abstract 1
Contents ii
List of Figures vii
List of Tables xv
List of Acronyms xvi
List of Variables xviii
Acknowledgements xxv
1. Introduction 1
2. Design and Operation of Molten Salt Systems 4
2.1 High Level Design Process 5
2.2 Molten Salt System Design - Introduction 6
2.2.1 Static Crucible Systems 7
2.2.2 Flowing / “Seesaw” Salt Systems 9
2.2.3 Dynamic & Recirculating Salt Systems 11
2.2.4 Complex Salt Systems 14
2.3 Design and Operation of Salt Transfer System - Methods 15
2.3.1 Salt Transfer Piping & Instrumentation 15
2.3.2 Design Calculations 18
2.3.3 Configuring the Instrumentation & Controls 19
2.3.4 Assembly of Salt Transfer System 19
2.4 Temperature and Mass Transfer Data - Results 20
2.4.1 Heating and cooling data 23
2.4.2 Heating Zone Shakedown Tests 27
2.4.3 Salt Melting and Transfer Operation 28
2.5 Design Evolution and Operational Lessons - Discussion 33
2.5.1 Thermal Control as the Dominant Design Constraint 34
2.5.2 Insulation Performance and Heat Losses 34
2.6 Design of Molten Salt Loop - Methods 34
2.6.1 Functional Requirements of Natural Circulation Loop 35

2.6.2 Mass-Energy Balance 39
2.6.3 Pressure Losses & Pipe Sizing 39
2.6.4 Operating Parameters 41
2.6.5 Method of Calculating Flow 42
2.6.6 Heat Exchanger Sizing 43
2.7 Design Outcomes - Results 46
2.8 Lessons Learned - Conclusion 47
2.8.1 Salt Transfer Lessons Learned 47
2.8.2 Loop Design Lessons Learned 48
3. Electrochemical Sensor Design for Molten Salt Loops 51
3.1 Molten Salt Electrochemical Sensors - Introduction 52
3.1.1 Background on Molten Salt Electrochemical Sensors 53
3.1.2 Electroanalytical Techniques 53
3.2 Electrochemical Loop Probe Design - Methods 56
3.2.1 Functional Requirements of Echem Probe 57
3.2.2 Mechanical Design of the Echem Probe 71
3.2.3 Fabrication of Echem Probe 78
3.3 Testing of Echem Probe - Results 80
3.3.1 Aqueous testing 80
3.3.2 Salt testing 83
3.4 Echem Probe Design Review - Discussion 84
3.5 Printed Electrochemical Sensors -Introduction 85
3.6 Design of printed electrodes - Methods 87
3.7 Testing Printed Electrodes - Results 89
3.7.1 Aqueous Testing 89
3.7.2 Thermal Stress Testing 93
3.7.3 FLiBe Testing 95
3.7.4 FLiNaK Testing 99
3.7.5 OCP on Printed Electrode 100
3.7.6 CV on Printed Electrode 101
3.8 Printed Electrode Design Review - Discussion 104
3.8.1 Operational challenges 105

3.9 Molten Salt Electrochemical Cell Design Lessons - Conclusion 105
4. Redox Measurements in Molten Salts for System Health Monitoring 109
4.1 Understanding Molten Salt Redox Potential - Background 109
4.2 Methods of Probing Redox Potential - Introduction 110
4.3 Probing Redox in FLiNaK - Methods 112
4.3.1 Potassium Dynamic Reference Electrode (KDRE) 114
4.4 Chronopotentiometry of FLiNaK-CrF_3 - Results 115
4.4.1 Operational Failure in Chronopotentiometry 121
4.4.2 Material failure in Chronopotentiometry 123
4.5 Probing redox in FLiNaK - Discussion 124
4.6 Probing Redox in FLiBe – Methods & Results 125
4.6.1 Ni-NiF_2 Thermodynamic Reference Electrode (NiTRE) 125
4.6.2 Silver-Silver Fluoride Thermodynamic Reference Electrode (AgTRE) 140
4.6.3 Beryllium Dynamic Reference Electrode (BeDRE) 142
4.7 Probing Redox in FLiBe - Conclusion 151
5. Electroanalytical Corrosion Product Quantification in Molten Salt Systems 152
5.1 Electroanalytical Methods of Quantification - Introduction 152
5.1.1 CP in Molten FLiNaK 154
5.1.2 CV in Molten FLiNaK 155
5.1.3 SWV in Molten FLiNaK 156
5.2 Application of Electroanalytical Methods in FLiNaK-CrF_3 - Methods 156
5.2.1 Preparation of FLiNaK-CrF_3 salt 157
5.2.2 Chronopotentiometry of FLiNaK-CrF_3 157
5.2.3 Cyclic Voltammetry of FLiNaK-CrF_3 157
5.2.4 Square Wave Voltammetry of FLiNaK-CrF_3 158
5.3 Electroanalytical Data from FLiNaK-CrF_3 System – Results & Discussion 159
5.3.1 Chronopotentiometry Results 159
5.3.2 Cyclic Voltammetry Results 162
5.4 Quantification in FLiNaK-CrF_3 System - Conclusions 174
5.5 Application of Electroanalytical Methods in FLiBe with Impurities – Methods 175
5.6 Electroanalytical Data from FLiBe System – Results & Discussion 179
5.7 Quantification and Redox Peak Assignments - Conclusions 184

6. Conclusion 186
Research Funding Acknowledgements 191
Statement on AI Usage 191
References 192
Appendix A. General Calculations 1
A.1 Salt Transfer Operating Pressures 1
A.2 Transfer Line salt “Bleed-Off” Mass 3
A.3 Heating Time vs Power Input for TK01 4
A.4 Heat Loss from Transfer Line During Operation 5
A.5 Pressure stability with large volumes 7
A.6 Echem Probe Sensitivity to Cr^{2+} Temperature Dependence 8
A.7 Coulometry of the Diffusion Layer 9
A.8 Error Propagation of CrF_3 concentration in FLiNaK 10
A.9 Uncertainty of CrF3 concentration in Yoko and Bailey (1984) 11
A.10 Uncertainty of electrode surface area in Yoko and Bailey (1984) 12
A.11 Uncertainty in peak current density data in Yoko at Bailey (1984) 13
A.12 Surface concentration in Fatouros and Krulic Model 13
A.13 Natural-Convection Velocity and Boundary-Layer Estimate 14
Appendix B. Supplementary Data & Figures 1
B.1 Measured Current and Power Curves for Variac Controllers 1
B.2 Wiring Diagram for PID Controllers 2
B.3 Dynamic Pressure Losses through Fittings 2
B.4 Pseudo Code for Calculating the mass flow rate and inventory of the salt loop 3
B.5 EIS of Echem Probe in Aqueous Solution 5
B.6 Images of Echem Probe in Experiments 6
B.7 Wire Electrode vs Printed Electrode Cyclic Voltammogram 9
B.8 Printed Electrode CV in FLiNaK 11
B.9 CV of FLiBe with Impurities at Varying Potential Window 12
B.10 CV of FLiBe with Impurities at varying scan rate 13
B.11 Microscopy and LIBS of Printed Electrodes 14
B.12 Microscopy and LIBS of Wire Electrodes after FLiBe Testing 25
B.13 Cyclic Polarization of Ultramet NiTRE 29

B.14 Cyclic Voltammograms of FLiNaK-CrF_3 30
B.15 Temperature profile during FLiNaK-CrF_3 Additions 34
Appendix C. Supplementary Photos & Images 1
C.1 Images of Salt Transfer Equipment and Assembly 1
Appendix D. Supplementary Tables & Documents 1
D.1 Salt Transfer Operation Timeline 1
D.2 Salt Transfer System Functional Requirements 5
D.3 Salt Transfer System Design Constraints 7
D.4 Thermocouple Legend for Salt Transfer Operation 8
D.5 Power Controller Legend for Salt Transfer Operation 10
D.6 Pressure Indicator Legend for Salt Transfer Operation 12
D.7 Salt Transfer Operation Safety Review 13
D.8 Salt Transfer Step-by-Step Procedure 16
Power and temperature monitoring setup for transfer from TK01 to TK02 16
Heating System Shakedown 16
Heating System Shakedown (continued) 16
TK01 salt melting procedure 17
TK01 salt melting procedure (continued) 17
Salt transfer procedure from TK01 to TK02 18
Transferring salt from TK01 to TK03 19
Transferring salt from TK01 to TK04 (Glassy Carbon Crucible) 20
Salt Transfer Procedure - End of Life 21
D.9 MATLAB Script for LaF_3 Crystal Sizing Calculation 23
Appendix E. Data Archiving 1

List of Figures

Figure 1. Example schematic of static crucible system (not to scale)..... 8
Figure 2. Example schematic of a flowing/seesaw salt system. Solid arrow indicates direction of salt movement. Dotted arrows indicate direction of gas movement. Heater and controls information not shown in this schematic..... 10
Figure 3. A schematic of a dynamic & recirculation salt system with values from the UCB natural circulation loop design document. 13
Figure 4. P&ID for the Li-7 enriched salt transfer system..... 16
Figure 5. CAD model of TK01, the Li-7 enriched FLiBe salt vessel from UW. 17
Figure 6. CAD model of TK02, the salt transfer vessel fabricated by MIT. 18
Figure 7. Salt Transfer System front-view components in the beryllium glovebox train. Labeled parts of the image (a) old salt transfer line, (b) TK03, (c) TK02, and (d) TK01. 20
Figure 8. Temperature data from the thermocouple logging DAQ during heating tape shakedown test. Time t=0 started on 2025-03-13. 21
Figure 9. (left) Exposed wiring of the heating tape leads. (middle) burned heating element in heating tape. (right) Singe marks on the ceramic fiber insulation. 21
Figure 10. Temperature profile during heating tape test (recorded on TT11 in Figure 4) 22
Figure 11. Temperature data and forecasts from system shakedown tests (see Figure 4 for temperature locations)..... 25
Figure 12. Temperature data from the melting and transfer operations. (t=0 @ 2025-12-01 15:25)..... 29
Figure 13. Enlarged section of the temperature data in Figure 12. The salt transfer start time is at timestamp G..... 30
Figure 14. Measured mass transfer rate of Li-7 FLiBe from TK01 to TK02..... 31
Figure 15. Concept design for the natural circulation loop including some interfacing instrumentation and corrosion specimen (see Table 10 for legend)..... 38
Figure 16. Solidworks drawings of the natural circulation loop assembly. Dimensions given in inches and degrees. 42
Figure 17. Heat exchanger design (dimensions given in inches)..... 45
Figure 18. HX flow diagram for salt loop + glovebox interfaces 46
Figure 19. Chromium depletion from the hot leg in a thermal gradient loop operating at T_c = 454ºC, T_h = 621ºC, where redox buffer is set by the equilibrium defined in Eq.(3.26). Parameters used in the mass loss calculation are given in Table 6. 63
Figure 20. Cr concentration profile across non-isothermal loop with instantaneous local salt equilibrium and solid diffusion lag model assuming $\boldsymbol{aU4+/aU3+=50}$ redox buffer. 1-D model assumes fully mixed flow at every point in the normalized position. $\boldsymbol{klag}$ is an empirical parameter that describes the lumped effect of Cr solid state diffusion to the wall surface and Cr dissolution/deposition kinetics (assuming the kinetics of deposition are faster than dissolution). 68
Figure 21. Concentration and potential dependence with and without boundary layer mixing. input parameters: imposed current, $\boldsymbol{i = -7.72 \times 10 - 5}$ A/cm^2; limiting current, calculated from $\boldsymbol{iL = -nFDcb\delta = 9.65 \times 10 - 5}$ A/cm^2; diffusivity, $\boldsymbol{D = 10 - 5}$cm^2/s; electrons transferred, $\boldsymbol{n = 1}$; bulk concentration, $\boldsymbol{cb = 10 - 6}$mol/cm^3..... 70

Figure 22. Schematic of the reference electrode with boron nitride body, lanthanum fluoride wall, and FLiBe reference electrode salt. Key dimensions for the calculation are labeled as they appear in the MATLAB calculations script. 73
Figure 23. (left) Illustration of the probe placed in flowing loop system. Estimated physical dimensions are noted on the illustration. (right) CAD assembly of the first probe design. 74
Figure 24. CAD drawing of the probe with initial 4-electrode concept and flow conditioning shield. Dimensions are given in inches. 75
Figure 25. CAD assembly of the second iteration of the Echem probe. 76
Figure 26. Final drawing of the Echem probe being installed on the salt loop. Full size drawing in Appendix A. 77
Figure 27. (left) Electrochemical probe in hand; 19mm (0.75in) diameter tube. (center) Connection between the probe shaft and the flow shield with holes to allow for salt recirculation. (right) Top of the probe with four copper wire leads entering the boron nitride spacers and connecting to the electrodes at the bottom. Conax gas sealing fitting not shown. 78
Figure 28. The shaft collar latched around the electrochemical probe shaft controls the vertical position of the probe. 79
Figure 29. (left) Copper crimp connectors holding electrodes to conductive wire. (right) copper crimp connections are sprayed with electrically insulating boron nitride spray. 79
Figure 30. OCP data collected by the Echem probe in 0.01M $K_3[Fe(CN)_6]$ and 0.1 M KCl at 25°C. Pt WE, Pt CE, Pt qRE, Au AuxE. 80
Figure 31. CV data collected by the Echem probe in 0.01M $K_3[Fe(CN)_6]$ and 0.1 M KCl at 25°C. Pt WE, Pt CE, Pt qRE, Au AuxE. 81
Figure 32. Peak current versus square root of scan rate data from Figure 31. 82
Figure 33. Changes to OCP of FLiBe at 600°C measured with Echem Probe upon addition of Cr_2O_3 and stirring (Pt WE, GC CE, Ag/Ag^+ RE). 84
Figure 34. Reproduction of figure from Heinze[76]. Experimental cyclic voltammograms taken on microelectrodes. 86
Figure 35. Schematic of a printed electrode chip featuring a four-electrode system with conductive microchannel routed toward contact pads. Configuration 1 from Table 20 is shown. 87
Figure 36. Printed electrode chip layer configuration schematic. The designed layer thickness and material chosen is presented in this schematic. The chosen electrode material for the electrodes fabricated at UC Berkeley was platinum. Figure reproduced from A. Consiglio.[80] 88
Figure 37. Schematics of two separate printed electrode test apparatuses used in argon gloveboxes. Furnace dimensions have approximate height and inner diameter of 15.24cm (6.0in) and 7.62cm (3.0in), respectively. 89
Figure 38. CVs in 0.01 M $K_3[Fe(CN)_6]$ and 0.1 M KCl measured by a printed macroelectrode configuration 4 from Table 20. 90
Figure 39. Peak current versus square root of scan rate data from Figure 38. 91
Figure 40. CVs in 0.01 M $K_3[Fe(CN)_6]$ and 0.1 M KCl measured by a printed microelectrode 92
Figure 41. Reproduced from [83] showing the transition on microelectrode array from radial diffusion to linear diffusion as time evolves. 93

Figure 42. Images of two printed electrodes fabricated with microelectrode arrays after high temperature testing. (left) Microelectrode with breakage across the conductive channels. Clean material degradation along the edges of the chip. (right) Microelectrode with conductive channels still intact. Visible damage on the edge of the chip, but the damage does not interfere with the conductive channels. 94
Figure 43. Images of printed electrode with brakeage across conducting channels. (left) Electroactive area on printed electrode. (right) Printed electrode contact pads leading to conductive channels. 94
Figure 44. (top) Printed electrode before exposure to molten FLiBe. (bottom) Printed electrode after exposure to FLiBe with 1.0wt% Cr_2O_3 at 650°C for 1 hour. Delamination of the metal layer is visible.... 96
Figure 45. Printed electrode immediately after FLiBe exposure. Colored boxes are examined under magnification in Figure 46, Figure 47, and Figure 48. 97
Figure 46. Optical image of microelectrode contact pad showing the difference between before and after FLiBe exposure. This image is the red box enlarged from Figure 45. (left) electrode pre-FLiBe exposure. (right) electrode post-FLiBe exposure. 98
Figure 47. Optical image of microelectrode contact pad showing the difference between before and after FLiBe exposure. This image is the blue box enlarged from Figure 45. (left) Sample electrode pre-FLiBe exposure, but not the same electrode used in the FLiBe exposure. (right) Electrode post-FLiBe exposure. Frozen salt covers the electroactive surface area. 98
Figure 48. Optical image of microelectrode contact pad showing the difference between before and after FLiBe exposure. This image is the green box enlarged from Figure 45. (left) Electrode pre-FLiBe exposure. (right) Electrode post-FLiBe exposure. There is discontinuous contact along the conductive channels.... 99
Figure 49. Printed electrode configuration 1 in Table 20. (a) Image of the droplet beginning to melt. (b) Image of the droplet at 550°C. 100
Figure 50. FLiNaK droplet (~690 mg) with 5.0wt% FeF2 added in furnace at 550°C on printed electrode sensor chip. 100
Figure 51. OCP measurement of printed electrode wetted by FLiNaK at 550°C. FLiNaK data taken on configuration 3 and FLiNaK-FeF_2 taken on configuration 1 (see Table 20 for details). Time t=0 occurs approximately 10 minutes after signs of salt melting are visible for each curve. 101
Figure 52. CV on printed electrode configuration 3 (see Table 20 for details) in FLiNaK droplet at 550°C. 102
Figure 53. CV on printed electrode configuration 1 (see Table 20 for details) in FLiNaK+FeF_2 at 550°C. 103
Figure 54. CV on printed electrode configuration 1 (see Table 20 for details) in FLiNaK+FeF_2 at 550°C. 103
Figure 55. Printed electrode sensor chip after tests with FLiNaK with 5.0wt% FeF_2 added at 550°C for approximately 2 hours. (left) The electrode metal layer completely delaminated from the surface of the chip and stuck to the frozen salt. (right) The delaminated surface of the chip substrate showing a mark where the electroactive surface was removed from the chip. 104
Figure 56. Cell diagram of U^{3+}/U^{4+} reaction studied in ORNL-4396 110
Figure 57. Chronopotentiometry of FLiNaK with and without CrF3 addition at 800oC. The K/K^+ oxidation potential is measured from determining the transition time on the potentiogram. W WE; W CE; W qRE; polarized with 100mA for 10 second followed by open circuit relaxation transient. 117

Figure 58. Ellingham diagram of Cr/Cr^{2+} and Cr/Cr^{3+} on a KDRE potential scale in FLiNaK as functions of concentration. Blue "X"s are collected data points from CP. 118
Figure 59. Chronopotentiometry of FLiNaK at 800oC with W WE, W CE, W qRE. See Table 22 for run details. 119
Figure 60. Zoomed in region at the transition from imposed current to open circuit in Figure 59. Showing the effect present in Addition 1 (see Table 22 for details) as an example. 120
Figure 61. Chronopotentiometry data of FLiNaK-CrF_3 system; Addition 2 and Addition 3 details present in Table 22. 121
Figure 62. Image of frozen FLiNaK with 10.9wt% CrF_3 added. The red circle shows the tip of the W counter electrode consumed and sticking out of the melt. 123
Figure 63. Graphite foam disk (Sample# 40S01, see Table 23 for details) with BN coating added via CVD. The graphite disk measures 12.97 mm (0.51 in) in diameter. The caliper jaws are open to a gap of 10.00mm. 128
Figure 64. Stacked graphitic foam disks for control experiments. Sample names annotated in the image (see Table 23 for details) Image take prior to inserting them in furnace for high exposure. 129
Figure 65. Cross section of BN coated graphitic foam samples. (left) Sample#40S06 (see Table 23 for details) showing signs of salt infiltration of the pores. (right) Sample#40S05 (see Table 23 for details) showing little to no salt infiltration. 129
Figure 66. Sample#40S05 (see Table 23 for details) map of microscopy images. No obvious signs of graphitic foam or BN coating degradation. 130
Figure 67. Sample#40S06 (see Table 23 for details) map of microscopy images. No obvious signs of graphitic foam or BN coating degradation. 131
Figure 68. Microscopy at 5X magnification of Sample#40S05 (see Table 23 for details). Image location at 40S05_5x_02 shown in Figure 66. Graphitic foam seen in this image is dark network. BN coating is grey-white crystal layer on dark network. Red-brown dust is polishing compound. 132
Figure 69. Microscopy at 5X magnification of Sample#40S06. Image location at 40S06_5x_04 shown in Figure 67. Graphitic foam seen in this image is dark network. BN coating is shiny-yellow crystal layer on dark network. Large white region is frozen FLiBe salt in the BN covered pores. Red-brown dust is polishing compound. 133
Figure 70. Microscopy of Sample#40S06 at 50X magnification. Image location at 40S06_5X_04 shown on Figure 67. 134
Figure 71. LaF_3 crystal cast for BN coated graphitic foam TRE bodies. 135
Figure 72. (left) SEM image of LaF_3 crystal cast exterior. (right) EDS of "spectrum 4" from the SEM image. Data provided by Ultramet. 135
Figure 73. (left) SEM image of LaF_3 cast interior. (right) EDS of "spectrum 8" from the SEM image. Data provided by Ultramet. 136
Figure 74. OCP of BN coated graphitic foam NiTRE in FLiBe with 1mol% NiF_2 in the reference salt. Steady state potential was approximately $\mathbf{-1.0}$V vs. OCP. Cell configuration; Ni WE in FLiBe+1mol% NiF_2, Ni CE, Ni qRE. 137
Figure 75. OCP of BN coated graphitic foam NiTRE in FLiBe with 1mol% NiF_2 in the reference salt. t=0 starts with completely frozen FLiBe in crucible. Steady state potential was approximately $\mathbf{-0.9}$V vs. OCP. Cell configuration; Ni WE in FLiBe+1mol% NiF_2, Ni CE, Ni qRE. 138

Figure 76. BN coated Graphitic foam NiTRE body with BN cap. (left) NiTRE with the BN cap covering reference FLiBe+1mol% NiF_2 salt bath prior to thermal exposure. (right) Same NiTRE after thermal exposure with chunk of graphitic foam body broken off. 139
Figure 77. BN coated graphitic foam NiTRE body submerged in FLiBe. Frozen FLiBe is forming on the surface of the salt near the crucible walls and on the inside of the graphitic form body. The salt in the crucible appears slightly cloudy. 139
Figure 78. Schematic of the first AgF TRE construction (left) and AgF reactions with Residual Moisture (blue, short dashes) and Boron Nitride (red, long dashes) in Salt (AgF(s) used in lieu of AgF(l) HSC Data) (right) 141
Figure 79. (top left) AgF + BN before heating (top right) AgF + BN after heating. 141
Figure 80: (left) Schematic of electrochemical cell (top right) Images of AgF TRE and Be rod (bottom right) OCP vs Be^{2+}/Be of the constructed TRE over ~18 hours. 142
Figure 81. BeF_2 redox potential (left) and activity (right) as a function of composition in LiF-BeF_2 at 800°C. Blue shaded region indicates the composition range of Hitch and Baes[112] data. 143
Figure 82. Chronopotentiometry data from a BeDRE measurement in FLiBe at 550°C. Electrochemical cell configuration: molybdenum WE, glassy carbon CE, Ni/NiF_2 RE. 145
Figure 83. Apparent surface concentration on BeDRE during open circuit transient. $\boldsymbol{t = 0}$ starts at the beginning of the relaxation transient on Figure 82. 146
Figure 84. Apparent interdiffusion coefficient derived from the BeDRE relaxation at x_{BeF2}= 0.33 and $\boldsymbol{550 \circ C}$, compared with diffusion coefficients reported by Vallet et al. for LiF–BeF_2 mixtures. The measurement type is given by ED (electromigrational depletion), MD (molecular dynamics), or conductance. 147
Figure 85. Chronopotentiogram of the BeDRE relaxation transient using transformed time axis, where $\boldsymbol{\tau = 529\ s}$, measured from the point of inflection on Figure 82. 148
Figure 86. Cyclic voltammetry of FLiBe with trace oxidants at 600°C using a gold WE, gold CE, and silver qRE. Zoomed window shows the variation of zero-current crossing potential on anodic sweep after beryllium deposition. Temporal evolution of the data is depicted by darkening of the trace. The data has been iR corrected for a resistance of 0.3$\boldsymbol{\Omega}$. 149
Figure 87. Apparent Be oxidation potential measured in FLiBe at 600°C using CVs. Potentials chosen at zero-current crossing potential on anodic sweep after beryllium deposition. The grey region indicate +/-1$\boldsymbol{\sigma}$ of the total measured values. 150
Figure 88. CP data taken in FLiBe with trace oxidants at 600°C. Consecutive runs are plotted together (see Table 25 for run details) showing the behavior of the Be oxidation plateau with different test parameters. 151
Figure 89. Chronopotentiometry data in FLiNaK-CrF_3 system from Addition 1 (see Table 22) showing how $\boldsymbol{\tau}$ is measured using Kuwana's method[139]. 160
Figure 90. CVs on FLiNaK-CrF_3 system at 800°C with varying concentrations of CrF_3 added. Theoretical Cr/Cr^{2+} (blue vertical line) and Cr/Cr^{3+} (red vertical line) reaction potentials are shown. Potential scale is shifted to versus the KDRE, but only Blank and Addition 1 were able to measure the KDRE potential. Discrepancy in theoretical potentials versus the measured potential is attributed to qRE drift with added CrF_3 concentration and inability to measure the KDRE after Addition 1. 164
Figure 91. CV of FLiNaK Blank at 800°C and 1000 mV/s scan rate, 10 consecutive scans. 166

Figure 92. Peak current densities of each addition of CrF_3 (see Table 27 for details) in FLiNaK at 800°C. The peak current density is normalized by the square root of the scan rate, $\boldsymbol{v1/2}$. The reaction with the more linear fit is Cr^{3+}/Cr^{2+} while the reaction with the least linear fit is Cr^0/Cr^{2+}. 168
Figure 93. CV in FLiNaK-CrF_3 at 800°C at with x_{CrF3} = 1.7e-3 at varying scan rates..... 169
Figure 94. Apparent diffusivity as a function of added CrF_3 mole fraction in FLiNaK at 800°C (see Table 27 for details). Data are shown for scan rates of 100, 500, and 1000 mV s^{-1}. Error bars in $\boldsymbol{x}$ reflect the uncertainty in added CrF_3 mole fraction, while error bars in $\boldsymbol{y}$ reflect propagated uncertainty in apparent diffusivity including contributions from concentration, assumed electrode surface area, and temperature. 171
Figure 95. Half wave potential of the Cr^0/Cr^{2+} reaction (left, blue) and Cr^{2+}/Cr^{3+} reaction (right, red) in CVs measured at 500 mV/s. Y-error bars are from the uncertainty in peak locations identified in the CVs due to ohmic drop and poor peak resolution. X-error bars are calculated from uncertainty in CrF_3 titration mass. 172
Figure 96. Calculated activity coefficient of Cr^{3+} using ORNL-1816 data as baseline. 174
Figure 97. Wire-electrode electrochemical cell used for high-temperature FLiBe measurements. Electrochemical cell: Au WE, Ag qRE, Au CE, Au AuxE. The top image shows clean wire electrodes prior to salt exposure; the bottom image shows the electrodes frozen into the FLiBe puck after testing. 176
Figure 98. Redox-potential measurements of FLiBe at 600 °C before and after the NiWC3b tribology specimen was contacted with the melt. 177
Figure 99. CV of FLiBe blank at 600°C showing potential window down to beryllium reduction. The upper limit may be gold fluorination or oxyfluoride formation. 178
Figure 100. Square wave voltammogram of FLiBe after EuF_3 and NiWC3b additions, at 600°C with plausible peak assignments given in Table 33. 180
Figure 101. Time for TK01 to reach operating temperature as a function of heater load 5
Figure 102. Current curve as a function of voltage on variable power controller. The controller output follows Ohm's law within the range of tested outputs. 1
Figure 103. Power curve as a function of voltage on variable power controller. The controller output follows $\boldsymbol{P = V2/R}$ within the range of tested outputs 1
Figure 104. Wiring diagram of HTS Amptek PID Module installed in lab assembled controllers. 2
Figure 105. EIS data of Echem probe in 0.01M $K_3[Fe(CN)_6]$ and 0.1 M KCl at 25°C. Pt WE, Pt CE, Pt qRE, Au AuxE. R_u is approximately 20$\boldsymbol{\Omega}$ from the CPE with diffusion model fit (red dashed line). 5
Figure 106. (left) Ag^+/Ag TRE in BN crucible. (right) Ag^+/Ag TRE, Ni CE, and Pt WE tested in FLiNaK at 600°C in a Ni crucible 6
Figure 107. Electrochemical probe for FLiBe experiments installed in gas-tight cell in the beryllium glovebox-train. Echem probe is the central tube in the flange lid. 7
Figure 108. Electrochemical probe used for E-TDS experiments. Electrodes (graphite WE, GC CE, Ag, RE) are immersed in FLiBe at approximately 900°C. 8
Figure 109. Cyclic Voltammograms from two separate electrochemical sensors in an aqueous solution of 0.01 M K3[Fe(CN)6] and 0.1 M KCl. The [Fe(CN)6]4-/[Fe(CN)6]3- redox reaction being probed is previously characterized on printed electrodes by prior literature [3]. The position of the peak potential may shift due to the drift of the quasi-reference Pt electrode. Current is reported because effective surface area and surface roughness of the electrodes was not determined, since surface roughness of the electrodes was

not measured. (a) CV polarogram measured by the tradition wire electrodes. (b) CV polarogram measured by the printed electrodes. See Table 20 for printed electrode surface areas. 9
Figure 110. Peak oxidizing and reducing currents from CV scans with the printed electrode chip in in an aqueous solution of 0.01 M $K_3[Fe(CN)_6]$ and 0.1 M KCl. The slope of the line is proportional to the square root of the diffusivity of the ionic species given by the Randels-Sevcik equation.[33] 10
Figure 111. Cyclic voltammogram of FLiNaK droplet (~700 mg) at 550ºC on printed electrode sensor, configuration 6 in Table 20. Repeated cycles were conducted at 100 mV/s, and after each cycle the noise of the scan would increase. After 12 cycles, the scans failed in the window around -0.7V vs Ref and -2mA. Examining this electrode post experiment it became clear it was badly damaged and the electroactive area was not functioning properly. 11
Figure 112. Cyclic voltammograms of FLiBe with trace oxidants at 600ºC. The electrode used in this cell were Au WE, Au CE, Ag qRE. Scan rate for all four scans was 1 V/s. Each scan covers slightly different potential windows attempting to sandwich particular reactions. The text next to each vertical line indicated a proposed concentration of cation which would correspond to a given half-cell reaction in FLiBe. 12
Figure 113. Cyclic voltammograms of FLiBe with trace oxidants at 600ºC. The electrode used in this cell were Au WE, Au CE, Ag qRE. Scan rate for the plot of the left was 100 V/s. The scan rate for the plot on the right was 10 mV/s. The text next to each vertical line indicated a proposed concentration of cation which would correspond to a given half-cell reaction in FLiBe. 13
Figure 114. Pre- and post-exposure images of printed electrodes from FLiBe exposure test at 650ºC. 14
Figure 115. Printed electrode configuration 3 from Table 20. Evidence of a manufacturing defect in the printed electrode. The electrically insulating surface deposit of Si_3N_4 is removed, revealing a subsurface layer of possible SiO_2 or Ni. 15
Figure 116. Printed electrode configuration 3 from Table 20. LIBS analysis of different colored regions in the image is provided in the table above. 17
Figure 117. Printed electrode configuration 3 from Table 20. Elemental analysis bulk composition reported from LIBS. The “silicon” compound is likely SiO_2 from the subsurface adhesion layer. The “platinum” indicated by the arrow is surprising because Consiglio[80] did not indicate Pt would be present at that location. 18
Figure 118. Printed electrode configuration 3 from Table 20. Green “crack” shape in the electroactive layer shows excess deposit of Si_3N_4 bleeding into the electrode region. Green layers are indicative of Si_3N_4 overlapping with Pt. Dark regions are of unknown composition. 19
Figure 119. Printed electrode configuration 3 from Table 20. Close up of electroactive surfaces on the WE array. Cracks and delamination of the Si_3N_4 layer are visible. Small black dot near the bottom-right of the image is where the laser from LIBS analysis ablated material. Green layers are indicative of Si_3N_4 overlapping with Pt. 20
Figure 120. Printed electrode configuration 3 from Table 20Table 20. Close up of individual microelectrode on the WE array. Clear signs of delamination and cracking of the Si_3N_4 layer (pink) are present. Possible signs of Pt surface roughness is seen (grey aberrations in grey disk). Green layers are indicative of Si_3N_4 overlapping with Pt. 21
Figure 121. Printed electrode configuration 3 from Table 20. Green layers are indicative of Si_3N_4 overlapping with Pt. Grey disk is the Pt electroactive area. Small translucent bits in the grey disk may be remaining photoresist from fabrication and not indicative of Pt surface roughness. 22

Figure 122. Printed electrode configuration 3 from Table 20. Close up of a Pt contact pad which gets connected to an alligator clip in the test apparatus. The grey region is Pt. It is unclear what the difference is between the peach region and the purple region while they appear to have the same LIBS spectrum..... 23
Figure 123. Zone 1 of the Au WE from FLiBe electrochemical test for corrosion product detection. Zone 1 was wetted by the FLiBe and participated in electrochemical reactions. Large image showing the view at 0 drilling steps. Small figures to left of image show the surface after each ablation step. Subplot to the right shows approximate atomic composition of the surface after ablation steps 1 to 15. 25
Figure 124. Zone 1 of the Au WE from FLiBe electrochemical test for corrosion product detection. Zone 1 was wetted by the FLiBe and participated in electrochemical reactions. Large image showing the view at 15 drilling steps. Small figures to left of image show the surface after each ablation step. Subplot to the right shows approximate atomic composition of the surface after ablation steps 16 to 30..... 26
Figure 125. Zone 1 of the Au WE from FLiBe electrochemical test for corrosion product detection. Zone 1 was wetted by the FLiBe and participated in electrochemical reactions. Large image showing the view at 30 drilling steps. Small figures to left of image show the surface after each ablation step. Subplot to the right shows approximate atomic composition of the surface after ablation steps 31 to 45..... 27
Figure 126. Zone 2 of the Au WE from FLiBe electrochemical test for corrosion product detection. Zone 2 was wetted by the FLiBe and participated in electrochemical reactions. Large image showing the view at 0 drilling steps. Small figures to left of image show the surface after each ablation step. Subplot to the right shows approximate atomic composition of the surface after ablation steps 0 to 15. 28
Figure 127. Cyclic polarization curves of BN coated graphitic foam body NiTRE. Data was recorded after NiTRE body capsized in the melt and the melt concentration inside matched the melt concentration outside. 29
Figure 128. CV of FLiNaK-CrF_3 at 800°C and x_{CrF3} = 8.2e-4. W WE, W CE, W qRE. Peak locations and currents are identified. 30
Figure 129. CV of FLiNaK-CrF_3 at 800°C and x_{CrF3} = 1.7e-3. W WE, W CE, W qRE. Peak locations and currents are identified. 30
Figure 130. CV of FLiNaK-CrF_3 at 800°C and x_{CrF3} = 3.4e-3. W WE, W CE, W qRE. Peak locations and currents are identified. 31
Figure 131. CV of FLiNaK-CrF_3 at 800°C and x_{CrF3} = 1.0e-2. W WE, W CE, W qRE. Peak locations and currents are identified. 31
Figure 132. CV of FLiNaK-CrF_3 at 800°C and x_{CrF3} = 2.2e-2. W WE, W CE, W qRE. Peak locations and currents are identified. 32
Figure 133. CVs of FLiNaK-CrF_3 at 800°C with varying concentration of CrF_3. Potentials have been shifted such that the C1 (Cr^{2+}/Cr^0) peak potential is 0V. 32
Figure 134. CVs of FLiNaK-CrF_3 at 800°C at 500mV/s. C1/A1' correspond to Cr^0/Cr^{2+}; C2/A2 correspond to Cr^{2+}/Cr^{3+}. A1 peak may be characteristic of Cr-W dealloying. C1' peak appears to be characteristic of underpotential deposition (UPD) of Cr metal. 33
Figure 135. Temperature of the FLiNaK-CrF_3 system during electroanalytical testing. Temperature was measured by a K Type thermocouple in a Mo sheath placed in the salt. Dips and oscillations on the temperature trace are caused by opening and closing the furnace lid. 34
Figure 136. Image of TK01 Li-7 enriched FLiBe salt vessel (front) and natural enrichment FLiBe salt vessel (back) at UW-Madison. 1

Figure 137. TK01 salt vessel containing Li-7 enriched FLiBe. (left) Vessel wrapped with ceramic fiber insulation. (right) Vessel wrapped with insulation tape and loaded in the glovebox on top of furnace brick insulation. 2
Figure 138. (left) Assembled TK02A transfer vessel with Swagelok fittings, salt-facing thermocouple, and pressure gauge. (middle) Vessel with wrapped heating tape around the bottom half of the vessel. (right) Vessel with ceramic fiber insulation and insulation tape on the walls. 2
Figure 139. TK02B salt vessel assembled for heating tape preliminary testing. 3
Figure 140. Singed insulation caused by a thermocouple-induced short of a heating tape. (Left) Transfer line with heating tape and insulation replacement. (Right) 3
Figure 141. Salt transfer system side-view with redesigned salt transfer line. (a) new salt transfer line, (b) TK02, (c) TK03, and (d) TK01. 4
Figure 142. heat damage to the plexiglass window on the bottom-west panel of glovebox 4. 5

List of Tables

Table 1. Example of how to list functional requirements 6
Table 2. Prototypical Static Crucible Functional Requirements 8
Table 3. Prototypical Flowing Salt System Functional Requirements 10
Table 4. Prototypical Recirculating Salt System Functional Requirements 13
Table 5. Points of Failure in Attempt 1 23
Table 6. Parameters of the lumped thermal capacitance model 25
Table 7. Fitted parameters from the lumped thermal capacitance model 26
Table 8. Labeled Events in Figure 12 29
Table 9. Functional Requirements for UCB Natural Circulation Salt Loop 35
Table 10. Instrumentation and Equipment labeled in Figure 15 38
Table 11. Example calculation table for effect of flow rate on pressure losses and dT 40
Table 12. Fluid Properties used in Natural Circulation Calculation 40
Table 13. Pressure Losses from Geometry of Loop 41
Table 14. Operating parameters of the natural circulation salt loop 41
Table 15. Functional Requirements for Salt Loop HX 43
Table 16. Final Loop Design Parameters 46
Table 17. Electroanalytical Techniques 56
Table 18. Functional Requirements of Echem Probe 57
Table 19. Inputs used in the chromium depletion calculation 59
Table 20. Printed Electrode Chip Sensor Electroactive Area Configurations[80] 88
Table 21. Studies identified that used potassium redox potential as reference in FLiNaK 112
Table 22. Summary of CP results in FLiNaK-CrF_3 @ 800ºC 116
Table 23. Graphitic foam disk sample test matrix 127
Table 24. $\boldsymbol{xBeF2}$ are surface concentration values calculated from Figure 82 and Eq.(4.24) 146
Table 25. CP test parameters for scans depicted in Figure 88 150
Table 26. Electroanalytical quantification techniques 153
Table 27. Cyclic Voltammetry Test Matrix 158

Table 28. Square Wave Voltammetry Test Matrix 158
Table 29. Calculated diffusivities of Cr^{2+} and Cr^{3+} from 161
Table 30. Calculated diffusivities for Addition 2 (see Table 27 for details) 170
Table 31. Relative standard deviation of Diffusivities across scan rates and constant concentrations 170
Table 32. Calculated Activity Coefficients for Cr^{3+} in FLiNaK 173
Table 33. Figure 100 Peak Assignment Summary 180
Table 34. Number of Electrons Transferred in SWV with comparing Barker and Fatouros & Krulic model predictions 182
Table 35. In-salt Element Concentrations from ICP-OES 183
Table 36. Reaction Potentials in FLiBe 184
Table 37. Initial and Final calculations for velocity of fluid in transfer line 2
Table 38. Timeline of Major Events for the Salt Transfer Procedure 1
Table 39. Salt Transfer Attempt 3 Timeline 1
Table 40. Salt Transfer System Functional Requirements 5
Table 41. Salt Transfer System Design Constraints 7
Table 42. Thermocouple Legend for Figure 4 8
Table 43. Heating Zone and Power Controller Legend 10
Table 44. Heating Zone and Power Controller Legend for Second Attempt 10
Table 45. PID Controller Component Table 11
Table 46. Pressure Indicator Legend 12
Table 47. Design Basis Accidents (DBAs) 13

List of Acronyms

ACS	American Chemical Society
AgTRE	Silver-silver fluoride thermodynamic reference electrode
ARE	Aircraft Reactor Experiment
ASV	Anodic stripping voltammetry
AuxE	Auxiliary electrode
BeDRE	Beryllium dynamic reference electrode
CAD	Computer-aided design
CE	Counter electrode
CP	Chronopotentiometry
CPE	Constant phase element
CV	Cyclic voltammetry
CVD	Chemical vapor deposition
DAQ	Data acquisition
DBA	Design basis accident
DI	Deionized
DOE	U.S. Department of Energy
DOE-NE	U.S. Department of Energy, Office of Nuclear Energy

DRE	Dynamic reference electrode
E-TDS	Electrochemical thermal desorption spectroscopy
ECP	Electrochemical corrosion potential
EDS	Energy dispersive X-ray spectroscopy
EIS	Electrochemical impedance spectroscopy
EMF	Electromotive force
FI	Flow indicator
FLiBe	67LiF-33BeF_2 (mol%)
FLiNaK	46.5LiF-11.5NaF-42KF (mol%)
GB	Glovebox
GC	Glassy carbon
GFCI	Ground fault circuit interrupter
HSC	Branded metallurgical simulation software
HT	Heater
HX	Heat exchanger
HZ	Heating zone
ICP	Inductively coupled plasma
ICP-MS	Inductively coupled plasma mass spectroscopy
ICP-OES	Inductively coupled plasma optical emission spectroscopy
ID	Inner diameter
IHA	In house assembled
IRP	Integrated research project
KDRE	Potassium dynamic reference electrode
L/D	Length-to-diameter ratio
LIBS	Laser-induced breakdown spectroscopy
LKE	LiCl-KCl eutectic
LOD	Limit of detection
LWR	Light-water reactor
MD	Molecular dynamics
MI	Mineral insulated
MIT	Massachusetts Institute of Technology
MSR	Molten salt reactor
MSRE	Molten salt reactor experiment
NaFBe	57NaF-43BeF_2 (mol%)
NEMA	National Electrical Manufacturers Association
NEUP	Nuclear Energy University Program
NiTRE	Nickel-nickel fluoride thermodynamic reference electrode
NPS	Nominal pipe size
OCP	Open-circuit potential / open-circuit potentiometry
OD	Outer diameter
ORNL	Oak Ridge National Laboratory
OSHA	Occupational Safety and Health Administration

OTS	Off-the-shelf
P&ID	Piping and instrumentation diagram
PCV	Pressure control valve
PI	Pressure indicator
PID	Proportional-integral-derivative
ppb	Parts per billion
ppm	Parts per million
qRE	Quasi reference electrode
RE	Reference electrode
RSD	Relative standard deviation
RV	Relief valve
SCFM	Standard cubic feet per minute
SEM	Scanning electron microscopy/microscope
SS	Stainless steel
SS316H	Type 316H stainless steel
SS316L	Type 316L stainless steel
SSR	Solid state relay
SWV	Square wave voltammetry
TBD	To be determined
TC	Thermocouple
TDS	Thermal desorption spectroscopy
TI	Temperature indicator
TK	Tank / salt vessel
TPC	Temperature-power controller
TRE	Thermodynamic reference electrode
TS	Temperature sensor
TT	Temperature transducer
UCB	University of California, Berkeley
UPD	Underpotential deposition
WE	Working electrode

List of Variables

A	heat-transfer area; pipe flow area; electrode area; electroactive area; wetted surface area
A_{cold}	Cold-leg wetted surface area
A_{hot}	Hot-leg wetted surface area
A_1	nominal area
$A_{1,min/max}$	minimum/maximum area
A_{cyl}	cylindrical electrode area
A_e	electroactive area; calculated electroactive area
a_{KF}	activity of KF in solution; KF activity; activity of KF
a_{LiF}	activity of LiF

a_{ox}	activity of oxidized species
a_{red}	activity of reduced species
A_s	effective salt heat-transfer area
a_{U3+}	activity of U3+
a_{U4+}	activity of U4+
b	microdisk radius (as implied by microelectrode limiting-current form)
C	concentration; bulk concentration
$c(0,t)$	cation concentration at electrode surface; surface concentration
C_{atoms}	Approximate alloy atomic density
C_b	bulk reactant concentration; bulk concentration
c_b	bulk cation concentration; bulk concentration
C_{Cr3+}	concentration of Cr3+
C_{CrF3}	CrF3 concentration
c_i	concentration of species i
C_n	area/L-D constant
$C_{ox}*$	bulk oxidized-species concentration
$c_{p,h}$	heat capacity at hot/mean condition; heat capacity
$c_{p,ins}$	heat capacity of insulation
$c_{p,liquid}$	liquid heat capacity
$c_{p,s}$	heat capacity of salt
$c_{p,solid}$	solid heat capacity
$c_{p,w}$	heat capacity of vessel wall
C_s	surface concentration
D	geometric diameter; diffusivity
d	tube diameter
D_{Cr3+}	Cr3+ diffusivity
D_i	diffusivity of species i
D_{ox}	oxidized-species diffusivity
d_t	transfer-line inner diameter; transfer-line diameter
E	electrode potential
$E0$	standard potential
$E^0_{Be2+/Be}$	standard Be^{2+}/Be potential in FLiBe
$E^0_{Ni2+\|Ni}$	standard Ni redox potential in FLiBe
E_{cell}	cell potential
E_{CV}	applied cyclic-voltammetry potential
E_i	initial potential
E_{KDRE}	potassium dynamic-reference electrode potential
E_{meas}	measured potential
$E_{measured}$	measured potential
$E_{OCP,ss}$	steady-state open-circuit potential
E_{Pt}	platinum electrode potential difference
F	Faraday constant

f	Darcy friction factor or friction factor function
F'	grouped friction term
f_{dep}	surface depletion factor
f_D	Darcy friction factor
f_F	Fanning friction factor
g	gravitational constant
g'	reduced gravity/buoyancy acceleration
G_{F2}	Gibbs free energy/chemical potential expression for fluorine
G_{KF}^{0}	standard Gibbs free energy for KF formation; standard Gibbs free energy of KF formation
h	heat-transfer coefficient; immersed height
h_{RE}	reference-electrode salt height
h_w	wire/electrode immersion length or height; wire height/immersion length
I	total current
i	current density
i, n	summation indices as written
i_{CP}	imposed current during chronopotentiometry
i_{Cr3+}	current required to polarize/reduce Cr3+ inventory
i_f	forward sweep current density
i_L	limiting current
i_p	peak current density
i_r	reverse sweep current density
i_{SWV}	differential square-wave-voltammetry current density
K	equilibrium constant
k	pipe thermal conductivity
k_{ins}	insulation thermal conductivity
k_s	apparent/effective FLiBe thermal conductivity
k_w	wall thermal conductivity
L	total equivalent tube length; equivalent length; length; heated length; length scale
L_{ins}	insulation heat-transfer length
L_{nc}	natural-convection length scale
l_s	effective mean heat-transfer length in the salt
l_t	transfer-line length
L_w	wall heat-transfer length
M_{Ar}	molar mass of argon
M_{Cr}	chromium molar mass
M_{Cr2O3}	molar mass of chromium oxide
m_{Cr2O3}	chromium oxide mass
m_{Cr3+}	Cr3+ mass
$m_{D,cyl}$	diffusion-layer salt mass
m_{FLiBe}	FLiBe mass; mass of FLiBe reference salt
m_{gas}	net gas mass addition rate; gas mass addition rate
m_i	component/addition mass

m_{in}	gas mass flow rate into control volume
m_{ins}	insulation mass
$m_{LaF3,d}$	mass of LaF3 dissolved; calculated dissolved LaF3 mass in the worked example
m_{NC}	natural-circulation mass flow rate
$m_{NC,ss}$	steady-state natural-circulation mass flow rate
m_{out}	gas mass flow rate out
m_s	salt mass; salt mass retained in transfer line
M_{salt}	salt molar mass
m_{salt}	salt mass
m_w	wall mass
n	number of electrons; moles of reacting species; electrons; electrons transferred
n_1	electrons transferred in less-cathodic reaction
n_2	electrons transferred in more-cathodic reaction
n_{Cr2+}	moles of Cr2+
n_{Cr2O3}	moles of Cr2O3
n_{Cr3+}	moles of Cr3+
n_{CrF3}	moles of CrF3
$N_{Cu/H}$	surface molar amount
N_i	flux density of species i
n_i	component/addition moles
n_{salt}	moles of salt
P	argon pressure; gas pressure; pressure
p	static pressure
P_{end}	pressure at flow initiation/end of pressurization period
P_f	final pressure
p_{F2}	fluorine partial pressure
P_i	initial pressure
p_{O2}	oxygen partial pressure
P_{start}	initial pressure
Q	heat loss; charge
Q_{Cr}	charge needed for Cr3+ reaction
$Q_{Cu/H}$	charge
Q_h	heater power/thermal duty; heater power
Q_{lat}	latent heat
$Q_{sens,1/2}$	sensible heat before/after melting
Q_{tot}	total heat
R	gas constant; resistance; outer tube radius
r	reaction rate; electrode radius
R_{inner}	inner tube radius
R_{ins}	insulation thermal resistance
$r_{ins,in}$	inner insulation radius
$r_{ins,o}$	outer insulation radius

r_{RE}	reference-electrode radius
R_s	salt-side thermal resistance
R_u	uncompensated resistance
R_w	wall thermal resistance
$r_{w,in}$	inner wall radius
$r_{w,o}$	outer wall radius
Re	Reynolds number
$s_{LaF3,FLiBe}$	equilibrium solubility of LaF3 in FLiBe
T	fluid temperature; inlet-gas temperature; gas temperature; temperature; temperature in K
t	time; imposed-current time; experiment/reaction time; polarization time
T_0	reference-state temperature
T_a	ambient temperature
T_{amb}	ambient temperature
T_C	cold-leg loop temperature
T_f	fluid temperature
T_h	hot-leg loop temperature
T_{ins}	insulation temperature node
T_{melt}	melting temperature
T_{op}	operating temperature
t_p	polarization time; pulse/polarization time
T_s	salt temperature node
T_w	wall temperature node
U_{nc}	natural-convection velocity scale
V	volumetric flow rate; voltage/potential; oxide-layer volume
v	fluid velocity; velocity vector; velocity; minimum velocity for Re > 4000
$V_{covergas}$	cover-gas volume; calculated cover-gas volume for the worked example
$V_{D,cyl}$	cylindrical diffusion-layer volume
V_{dl}	diffusion-layer volume
V_f	final gas volume
V_{gas}	gas-space volume or volumetric gas flow, depending on local notation
V_i	initial gas volume
V_{LaF3}	LaF3 crystal volume as a function of dissolved thickness; dissolved LaF3 volume
v_{nc}	natural-convection velocity scale
V_{RE}	reference-electrode salt volume
V_{salt}	salt volumetric displacement/flow rate; salt volume
V_t	transfer-line volume
$W_{1/2}$	half-peak width for SWV model
W_2	dimensionless peak-width parameter
w_2	peak width in potential units
$wt\%$	mass percent
x_{BeF2}	mole fraction of BeF2 in FLiBe; surface mole fraction of BeF2
x_{Cr2+}	Cr2+ mole fraction

$x_{Cr3+,1}$	initial/first-state Cr3+ mole fraction; initial Cr3+ mole fraction
$x_{Cr3+,f}$	final Cr3+ mole fraction
$x_{Cr3+,i}$	initial Cr3+ mole fraction
x_{CrF3}	CrF3 mole fraction
x_{NiF2}	mole fraction of NiF2 in NiTRE
x_{U3+}	mole fraction of U3+ species
x_{U4+}	mole fraction of U4+ species
y	dissolved thickness/height; dissolved crystal thickness/height
y_{min}	minimum required LaF3 crystal thickness/height
z	fluid height/elevation; charge number/electron stoichiometry
z_{Cr3+}	Cr^{3+} charge/oxidation state
z_{NC}	natural-circulation elevation difference; elevation difference
β	thermal expansivity of the fluid; thermal expansivity
γ_{BeF2}	BeF_2 activity coefficient
$\gamma_{Cr3+,1}$	initial/first-state Cr^{3+} activity coefficient; initial Cr^{3+} activity coefficient
$\gamma_{Cr3+,f}$	final Cr^{3+} activity coefficient
Γ_1	surface coverage/deposited inventory parameter
Γ_{ML}	monolayer surface coverage
δ	boundary-layer thickness; oxide-layer thickness
δ_D	diffusion length
δ_c	concentration boundary-layer thickness
δ_{dl}	diffusion-layer thickness/mean one-dimensional diffusion length; diffusion-layer thickness
Δ	change/difference
ΔG^0	standard Gibbs free energy of reaction at 800 C
ΔG^0_{800C}	standard Gibbs free energy at 800 C
ΔG_{rxn}	Gibbs free energy of reaction
ΔH_f	heat of fusion
ΔP	pressure variation; available pressure difference after subtracting hydrostatic head
$\Delta \rho$	density difference between hot and cold fluid; density difference
Δt	time required to initiate flow; SWV time step
Δv	velocity change/estimated velocity from pressure difference
Δz	elevation change
η	heater efficiency; criterion for stationary microelectrode behavior
η_s	surface overpotential of the working electrode
κ	radius ratio R_inner/R
μ	dynamic viscosity
ν	potential scan rate; scan rate
π	mathematical constant
ρ	density; ratio of ohmic potential drop to Nernstian potential shift
ρ_0	density at T_0; reference density
ρ_{FLiBe}	FLiBe density
ρ_{FLiNaK}	FLiNaK density

ρ_{LaF3}	LaF3 density
ρ_{avg}	average density
ρ_{gas}	gas density; argon gas density
ρ_{salt}	salt density
ρ_t	salt density at transfer condition
ΣF	sum of frictional losses; frictional losses
τ	transition time; time elapsed since electrolysis begins
τ_1	transition time for n1 reaction; first measured transition time
τ_2	transition time for n2 reaction; second measured transition time
τ_w	wall shear stress
Φ	total supplied power
χ	dimensionless ratio of diffusion-layer dissolved inventory to surface deposited inventory
∂	partial derivative
∇	gradient operator
$\nabla\cdot$	divergence operator

Acknowledgements

From the first day I came to Berkeley, I have been supported and uplifted by the community of colleagues and scholars in the university, in the Bay area, and across the world. First, I must express my gratitude to my advisor, Dr. Raluca O. Scarlat. Under your tutelage, I learned to appreciate the power of asking the right questions, democratizing education, and maintaining an unyielding commitment to improving the world. You have broadened my understanding of what it means to be an engineer. I would also like to thank my Ph.D. dissertation committee: Dr. Per Peterson, Dr. Guanyu Su, and Dr. Neil Razdan. Your guidance and expertise have inspired me to appreciate the importance of scale, dimensional analysis, and systems-level problems. I am also grateful to the faculty members who accepted me as a graduate student instructor: Dr. Rebecca Abergel and Dr. Karl van Bibber. You have cultivated my teaching skills, and I am honored to have taught alongside you.

I am grateful to the colleagues and scholars that made every day bearable and, in some cases, even enjoyable. To the members of the SALT Research Group past, present, and future: You are a breed of researcher that the world is not prepared to contain. Be ambitious—be creative—be unbreakable! Lorenzo Vergari, Haley Williams, Sara Mastromarino, Sasha Kennedy, Christian M. Sclafani, Ryan Hayes, Nathanael Gardner, Alan Zenagui, Maksim Pecherskiy, Niv Moran, Maximilen Denis, Randall Chiu, Riccardo Chebac, Sondre Iveland, Sander Ratso, Qiye Hu, Tim Pickarski, Nicole Johnson, Sarah Heagy, Louis Pointreau, Pierre Boca, Agathe Moissy, David Park, Yusuf Shehata, Momoka Imoto, Jean Bassili, and Matei Ignuta: you are all superhuman and I hope you continue to use your powers for good. It's been my pleasure to break equipment with you and learn how to fix what we just broke.

Thank you to the undergraduate researchers that have joined me throughout my journey in graduate school. You have kept me honest, humble, and humored over the last five years. You may not believe it, but I have learned just as much from you as you have from me, if not more! Chris Forsyth, Magnus Gu, Jimmy Xu, Zach Falkowski, Daniel Chavez, Sean Noor, Isabel Caro, Howard Chen, Sebastian Barnes, Julia Gottlieb, Patricia Moon, Amaris Charton, Leiv Berg, Jenna Grant, and Dane Grunt—I expect at least one of you will be my future boss.

To the friends that stuck with me through this journey—why are you like this? Get some help. I could not have made it through the 1,813 days of this journey without you. Bradley Brown, Sahil Kumar, and Jean-Carlos Peña: you three have a 30-year mortgage in my mind-palace. This dissertation might as well be yours. Jacob, Trevor, and Malachi: the world may be a grim place, but sharing a living room with you three made it just that much worse. With love. Kinggatrie and InsomniacCat: discord is a home when you two are on. May there be many more hours of anime and unionized mining. Nathanael, Jacob, and Mahek: you all really push my buttons. Most of the time you push my self-destruct button, but sometimes we still get along pretty well. Art Gang: you are all unique beams of genius on this chaotic world. And to the Choice Money collective: you know what you've done. I wish you all a Boney Loafmas.

To my family—you believed in me before I knew I could even get this far. Mom and Dad, I'm glad you endured seeing me on Zoom once a week for the last five years. Hopefully you think it was worth it now! Joe and Stevie, I couldn't have asked for cooler siblings who are always succeeding and giving me someone to look up to. Papa, you keep me telling jokes every day and making people smile. I love you all for always reminding me that life is too important to be taken seriously.

To the person that has changed my life forever, Megan Schiferl. I've told you an uncountable number of times, my degree will only ever be the second-best thing to come from this program. You are my love and inspiration. There will never be another you.

And thank You God for walking this path with me.

1. INTRODUCTION

Molten fluoride salts have reemerged as enabling materials for advanced nuclear energy systems, high-temperature heat transport, electrochemical separations, and critical materials processing because of their favorable thermophysical properties, chemical stability, and compatibility with operation at temperatures exceeding those achievable by conventional aqueous systems. Among these applications, molten salt reactors (MSRs) present one of the most demanding environments for chemical process monitoring. During reactor operation, the salt continuously evolves as structural materials corrode, fission products dissolve, transmutation and activation of the coolant and structural materials evolve, impurities are introduced, and the oxidation state of the salt changes. These coupled chemical processes directly influence corrosion rates, fuel chemistry, tritium transport, and ultimately reactor safety and performance. Despite decades of research into molten salt chemistry, the ability to measure these chemical changes continuously and *in situ* remains one of the principal technological barriers to the deployment of molten salt reactor technology.

The chemistry of molten fluoride salts is inherently dynamic. Dissolved corrosion products, dissolved oxide species, redox-active impurities, and changing thermodynamic equilibria alter the electrochemical state of the salt throughout operation. Conventional analytical methods generally rely on removing salt samples for *ex situ* characterization using techniques such as inductively coupled plasma optical emission spectroscopy (ICP-OES), mass spectrometry (ICP-MS), or similar chromatographic chemical analysis. While these methods provide excellent compositional information, they interrupt system operation, provide only discrete measurements in time, and are often impractical for continuous monitoring of operating reactor systems. Consequently, there is considerable interest in developing electrochemical sensors capable of providing real-time measurements of molten salt chemistry directly within operating systems.

Electrochemical techniques offer several advantages for *in situ* monitoring because they provide direct access to thermodynamic, kinetic, and transport information while requiring relatively simple instrumentation. Measurements including open-circuit potentiometry, cyclic voltammetry, square-wave voltammetry, and chronopotentiometry can quantify redox potential, identify dissolved electroactive species, estimate corrosion product concentrations, and monitor changes in salt chemistry as they occur. However, successful deployment of these techniques depends on overcoming several fundamental challenges unique to molten fluoride salts. Reliable high-temperature reference electrodes remain difficult to construct, electrochemical measurements are influenced by mass transport and solution resistance, flowing salt environments introduce additional transport phenomena, and sensor behavior must remain stable over extended operation under chemically aggressive conditions.

For electrochemical sensing to become useful in molten salt reactor technology, sensors must ultimately be deployed not only in simplified laboratory cells but also in prototypical systems where the measured signal reflects the coupled behavior of the salt, structural materials, thermal gradients, and flow field. In this role, electrochemical sensors function as system-health-monitoring instruments: they provide real-time indicators of redox condition, corrosion product accumulation, impurity evolution, and changes in local salt chemistry that may signal degradation or off-normal operation. This deployment context introduces requirements beyond conventional electroanalytical measurement. Sensors must be mechanically integrated into heated vessels and flowing loops, maintain electrical isolation and chemical compatibility during long-

duration operation, provide interpretable measurements in non-isothermal and non-equilibrium environments, and produce data that can be connected to operational decisions. Therefore, the development of molten salt electrochemical diagnostics requires both electrochemical method validation and system-level engineering of probes, reference electrodes, instrumentation, and operating procedures suitable for reactor-relevant environments.

The central objective of this dissertation is therefore to develop and evaluate electrochemical sensing methodologies and deployment strategies capable of monitoring molten fluoride salt chemistry under increasingly representative operating conditions. Rather than focusing on a single electrochemical technique or sensor design, this work examines the broader problem of integrating electrochemical diagnostics into realistic molten salt systems. The research seeks to answer several fundamental questions:

1. How do we systematically design and develop operational knowledge for prototypical molten salt systems—in particular molten salt reactors? (Chapter 2)
2. What system design, instrumentation, and operational practices are necessary for long-duration health sensing in reactor-relevant molten salt systems? (Chapter 2 and Chapter 3)
3. How do flow, thermal gradients, and system geometry affect electrochemical measurements relative to static laboratory experiments? (Chapter 3, Chapter 4, and Chapter 5)
4. What practical reference electrode concepts enable accurate electrochemical measurements in high-temperature molten fluoride salts? (Chapter 4)
5. What is the sensitivity, reproducibility, and limitations of electrochemical methods for quantifying dissolved corrosion products and redox state in molten fluoride salts? (Chapter 5)

To address these questions, this dissertation combines system design, electrochemical sensor design, sensor viability and characterization testing, and electroanalytical studies. Experimental platforms ranging from static crucible experiments to natural circulation and recirculating molten salt loops were designed and constructed to investigate electrochemical sensor performance under progressively more realistic operating conditions. Electrochemical measurements included open-circuit potential (OCP) measurements, chronopotentiometry (CP), cyclic voltammetry (CV) , and square-wave voltammetry (SWV) techniques performed in molten fluoride salts including 2LiF-BeF_2 (FLiBe), 46.5LiF-11.5NaF-42KF (FLiNaK), and 57NaF-43BeF_2 (NaFBe)-based systems. Complementary analytical techniques, including inductively coupled plasma mass spectroscopy/optical emission spectroscopy (ICP-MS/OES), were used to quantify dissolved metal concentrations and validate electrochemical measurements where appropriate. Additional experiments investigated molten salt transfer operations, electrochemical probe deployment, and the practical engineering considerations required for operation of high-temperature molten salt facilities.

The results demonstrate that electrochemical sensing can provide quantitative and reproducible information regarding molten salt chemistry when measurements are interpreted within the context of the coupled thermodynamic and transport processes governing the system. The work establishes methods for monitoring dissolved corrosion products, evaluates the performance and limitations of several high-temperature reference electrode concepts, and provides new insight into the dynamic behavior of beryllium-based reference electrodes in fluoride salts. Furthermore, the research demonstrates that successful deployment of electrochemical sensors requires consideration of system-level phenomena—including salt

flow, thermal gradients, electrical resistance, and experimental architecture—in addition to traditional electrochemical theory. Beyond individual sensor development, the dissertation presents experimental platforms and operational methodologies that enable future long-duration studies of corrosion, redox chemistry, and molten salt process monitoring.

Collectively, this work advances the development of electrochemical diagnostics for molten fluoride salts by integrating sensor development, experimental infrastructure, and fundamental electrochemical analysis into a unified framework for *in situ* chemical monitoring. The results contribute to the broader goal of enabling continuous characterization and control of molten salt chemistry in advanced reactor systems and other high-temperature molten salt technologies, where reliable knowledge of the chemical state is essential for safe, efficient, and predictable operation.

2. DESIGN AND OPERATION OF MOLTEN SALT SYSTEMS

Molten salt technologies have re-emerged as a central focus in advanced nuclear energy systems, particularly in the context of high-temperature reactors, fuel cycle strategies, and fusion blanket concepts. Among candidate salts, fluoroberyllates such as $LiF\text{-}BeF_2$ and $NaF\text{-}BeF_2$ are of particular interest due to favorable neutronic, thermophysical, and chemical properties, including low neutron absorption cross section, high heat capacity, high boiling point, and chemical stability at elevated temperatures. Other fluoride salts, such as LiF-NaF-KF and $LiF\text{-}AlF_3$, are useful surrogates [1], [2], [3] for studying thermohydraulic and thermochemical phenomena to avoid introducing a beryllium hazard to the lab. The practical deployment of these salt systems introduces substantial engineering challenges, particularly in the handling, transport, and partitioning of molten salt under tightly constrained safety and reliability requirements.

A critical yet underdeveloped aspect of molten salt system engineering is the design of salt transfer infrastructure capable of supporting partitioning operations. Partitioning—the controlled separation and redirection of salt constituents or phases—plays a central role in applications such as tritium management, impurity control, and fuel processing. These processes require precise, repeatable movement of high-temperature, chemically reactive fluids through complex geometries while maintaining strict containment and minimizing contamination, corrosion, and operational transients. Consequently, the design of a salt transfer system is not merely a fluid transport problem, but an integrated challenge involving thermal hydraulics, materials compatibility, system controls, and fault tolerance.

The central engineering question considered in this work is therefore: how does one design a safe, reliable, and robust molten salt system? Designing such systems requires knowledge of the coupled thermophysical and chemical behavior of molten salts, including temperature-dependent viscosity, thermal expansion, phase stability, and sensitivity to oxygen and moisture impurities. At an applied level, molten salt systems must additionally be designed to accommodate challenges such as salt freezing, material incompatibility, galling of mechanical interfaces, and operation of instrumentation at temperatures frequently exceeding 600ºC.

The objective of this work is to establish a design framework for salt transfer systems that explicitly integrates safety, reliability, and operational robustness. Safety considerations include high-temperature hazards, electrical hazards, operational hazards such as salt freezing, mitigation of salt spillage, and control of hazardous chemical interactions, particularly involving beryllium-containing and fluorine-containing species. Reliability is addressed through component selection, redundancy strategies, and minimization of failure modes associated with high-temperature operation and corrosive environments. Robustness, in this context, refers to the system's ability to tolerate operational variability and disturbances—such as thermal gradients, power transients, or partial blockages—without loss of function or safety margin.

The broader design philosophy adopted throughout this work is that molten salt systems should be designed according to the dominant physical phenomena under investigation while maintaining safe operation under off-normal operating conditions. Experimental systems that isolate specific thermal, chemical, or transport mechanisms produce results that are more interpretable, reproducible, and generalizable. Accordingly, the

following sections develop a generalized methodology for molten salt system design based on functional requirements, operational constraints, and classification of system architectures according to their dominant transport behavior.

Building on this framework, the discussion examines representative molten salt system architectures, including static, flowing, recirculating, and coupled systems, and identifies the instrumentation and control strategies required for their safe operation. The design and operation of a FLiBe salt transfer system are then presented as a case study demonstrating how these principles can be implemented in practice. Remaining challenges and future research needs are also identified, particularly in the areas of instrumentation, autonomous control, and integrated system testing.

2.1 HIGH LEVEL DESIGN PROCESS

Design is one of the defining technical skills of engineering practice. Society relies on engineers to critically evaluate problems and develop safe, reliable, and repeatable solutions under real-world constraints. In molten salt engineering, this process is particularly challenging because thermal, chemical, mechanical, and operational phenomena are strongly coupled. Consequently, successful molten salt system design requires both physical understanding of the governing phenomena and a structured methodology for translating experimental objectives into practical hardware configurations. Dym et al.[4] define engineering design as:

> "the systematic, intelligent generation and evaluation of specifications for artifacts whose form and function achieve stated objectives and satisfy specified constraints."

This definition is particularly applicable to molten salt systems because the same functional objective can often be achieved through multiple valid hardware implementations. For example, a molten salt system may require operation above 600C for extended durations. This requirement defines the function of the system but does not uniquely determine how the temperature is achieved. Heating may instead be provided through radiant furnaces, conductive heating tape, mineral-insulated heaters, or inductive heating systems depending on the operational constraints and system requirements.

Dym and Brown further argue that engineering design requires the ability to represent a system in multiple forms, including functional requirements, analytical models, process flow diagrams, instrumentation schematics, fabrication drawings, and physical hardware [5]. In molten salt engineering, these representations are closely interconnected. Functional requirements define the design problem, while engineering drawings, control schemes, and fabricated assemblies represent physical realizations of those requirements.

The design philosophy adopted throughout this work is that molten salt systems should first be defined according to their required functions before selecting the hardware used to implement them. Premature selection of process equipment can unintentionally constrain the design space and obscure alternative solutions that may better satisfy safety, reliability, or operational objectives. Consequently, the design

process used in this work begins with identification of the dominant physical phenomena under investigation and proceeds through iterative development of functional requirements, system architectures, instrumentation strategies, and operational procedures. The design work in this chapter focuses specifically on systems developed for molten salt chemistry and electrochemical experimentation. As with most engineering problems, no single "correct" solution exists. Instead, successful system designs emerge through balancing competing operational constraints, safety considerations, experimental objectives, and practical limitations associated with high-temperature molten salt operation.

2.2 MOLTEN SALT SYSTEM DESIGN - INTRODUCTION

Molten salt systems can be defined by a unique set of functional requirements. Functional requirements, sometimes referred to as functional specifications, describe what a system must accomplish without prescribing how those objectives are achieved. In this sense, the functional requirements serve as the foundational definition of the engineering problem. For example, a common functional requirement for molten salt systems is the ability to maintain salt temperatures above the melting point for extended durations. This requirement defines a thermal function that the system must satisfy but does not uniquely determine the process equipment used to achieve it.

The design process used in this work assumes that a molten salt system is sufficiently defined once a comprehensive set of functional requirements can be established. These requirements provide the basis for evaluating competing design solutions and translating engineering objectives into physical hardware configurations. Table 1 provides an example methodology for defining functional requirements in terms of operational targets, engineering justification, and associated design considerations.

Table 1. Example of how to list functional requirements

Requirement	Specific Detail	Justification	Comments
Maintain operating temperature	$T_{salt} \geq 600^{o}C$	Experiments require salt to hold 600°C for 100-hour run	linked to system heat removal requirement

Establishing complete functional requirements is important for several reasons. First, incomplete requirements necessarily produce incomplete solutions because the system is not fully constrained by the engineering objectives. Second, functional requirements allow the design problem to be represented in multiple equivalent forms, including process flow diagrams, instrumentation schematics, analytical models, CAD assemblies, fabrication drawings, and operational procedures. These representations correspond to different realizations of the same underlying engineering problem and collectively form the system design.

Molten salt system design research questions are abundant. Formulating a research question [6] that creates reproducible results and is generalizable can be a large challenge when designing molten salt systems. The history of molten salt research potentially suffers from asking "Does the system work?" before asking "What questions about molten salt reactors are we trying to answer?" This is in part due to the societal and global circumstances where molten salt reactors were first considered for use. Though molten salts were studied as early as 1808 when Davy studied the decomposition [7] of alkaline earth metal fused salts,

engineering system design didn't begin until the 1950s during the Aircraft Reactor Experiment (ARE) at Oak Ridge National Laboratory (ORNL). The development of molten salt systems required "a cooperative effort of Chemistry, Experimental Engineering, and Metallurgy" [8, p. 3] to design test beds for corrosion experiments and developing instrumentation for salt operations.

During ARE, the corrosion test apparatuses were split into four separate categories: static, flowing (or "seesaw"), natural circulation, and forced circulation. These categories arose from trying to isolate different material degradation mechanisms. In static testing, the specific mechanism of chemical corrosion can be studied. In flowing systems, effects of cycling salt and gases through system piping can be studied. Under natural circulation, mass transfer of structural material can be studied under thermal gradients with fluid flow rates under 10 cm/s. And forced circulation systems are used to examine the mass transfer of structural materials at variable flow rates in turbulent regimes. ORNL continued to iterate on molten salt system experimental design as they pivoted to the Molten Salt Reactor Experiment (MSRE) in the late 1950s and throughout the 1960s. New natural circulation loop designs [9] were created and preconditioning methodologies [10] were developed to enhance the reproducibility of the results between separate apparatuses.

The molten salt system classifications and operational methodologies developed during ARE and MSRE demonstrate the value of categorizing molten salt systems according to the dominant physical mechanisms under investigation. By isolating specific phenomena such as chemical corrosion, thermal-gradient-driven mass transfer, or flow-assisted material degradation, experimental systems can be designed to produce more interpretable and generalizable results. Although modern molten salt systems may differ substantially from those developed during ARE, a generalized classification framework remains valuable for guiding system design, defining functional requirements, and identifying operational constraints relevant to a given research objective.

To organize the diverse architectures encountered in molten salt research, the systems considered in this work are classified into four categories: static, flowing, recirculating, and complex systems.

2.2.1 STATIC CRUCIBLE SYSTEMS

The majority of published molten salt literature falls into the category of *static tests*. A static crucible system is one which the molten salt remains contained in one crucible or tank and maintains roughly isothermal conditions. Notably, molten salt experiments even in static tests are rarely static in terms of fluid flow. The nature of these systems holding high temperatures, anywhere from 500°C to 1000°C, in contrast to the ambient temperatures in the cover gas or atmosphere surrounding the apparatus makes even small heat flux will promote natural convection within the salt. Electrochemical experiments were performed to validate simulations showing the effect of this natural convection [11] on the diffusion layer within their system.

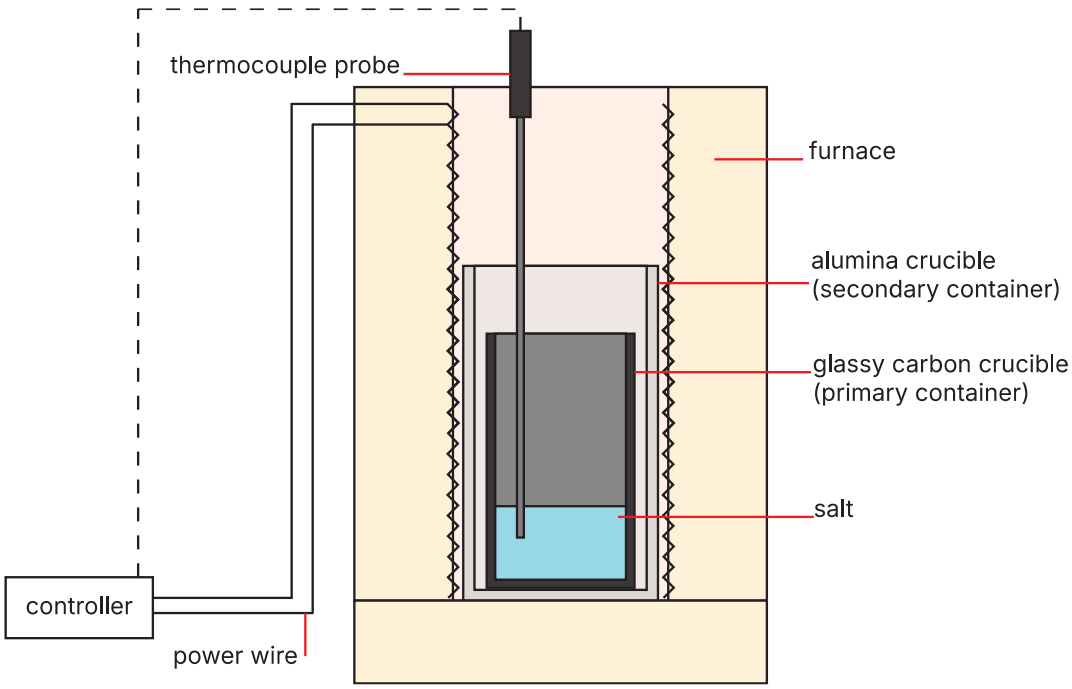


Figure 1. Example schematic of static crucible system (not to scale)

Some items present in Figure 1 are ubiquitous to all static crucible systems. In particular, a furnace, a crucible for salt containment, and a temperature sensing device, are in every static crucible system without fail. The complexity of these systems arise from the interfacing systems that are coupled with them, such as electrochemical sensing equipment. Static crucible apparatuses generally possess the fewest functional requirements among molten salt experimental architectures. See Table 2 for prototypical functional requirements in a static crucible system.

Table 2. Prototypical Static Crucible Functional Requirements

Requirement	Specific Detail	Justification	Comments
Maintain operating temperature	$T_{salt} \geq 600^{o}C$	Experiments require salt to hold 600°C for 100-hour run	linked to system heat removal requirement
Maintain near isothermal conditions	$\Delta T < 10^{o}C$ throughout the salt inventory	Assuming isothermal conditions in the entire crucible is often desired when performing experiments	Important for reproducibility of experimental results
Contain molten salt inventory	No measurable salt leakage during operation	Prevent hazardous material release	
Maintain inert atmosphere	$O_2 < 10ppm$ $H_2O < 10ppm$	Minimize salt exposure to impurities that will make the salt oxidizing	Typically achieved with inert glovebox or purge gas system

Enable temperature measurements	Minimum of two independent temperature measurements within vessel	Monitor thermal stability and record temperatures in the melt and cover gas	
Enable salt loading and removal	Vessel geometry must permit charging and draining of salt inventory	Support repeat experimental campaigns and sampling of salt inventory during experiments	May require removable lid or transfer interface

2.2.2 FLOWING / "SEESAW" SALT SYSTEMS

Flowing salt systems differ from static systems in that the molten salt inventory is intentionally displaced from one local volume to another. The term "seesaw" originates from early molten salt experiments [8] in which salt was periodically transferred back and forth between two vessels to simulate repeated flow and transport phenomena. Unlike static systems, flowing systems require active coupling between the molten salt inventory and a driving mechanism capable of producing controlled fluid motion.

A representative flowing salt system can be conceptualized as two vessels connected by a transfer line, where molten salt is displaced from one tank into another through application of a pressure differential or other external driving force. Although these systems may still approach thermal equilibrium globally, the introduction of active salt transfer significantly increases operational complexity relative to static systems. Flowing systems must additionally accommodate transient pressure behavior, changing hydrostatic conditions, freeze prevention within transfer pathways, and dynamic thermal-fluid interactions during transfer operations. Figure 2 shows a representative schematic of a flowing molten salt system including the direction of the salt flow as well as the direction of the cover gas flow.

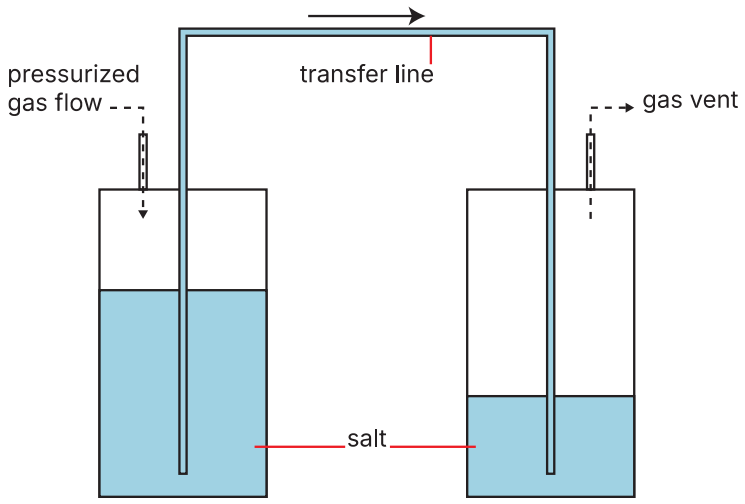


Figure 2. Example schematic of a flowing/seesaw salt system. Solid arrow indicates direction of salt movement. Dotted arrows indicate direction of gas movement. Heater and controls information not shown in this schematic.

Salt transfer systems fall in the flow salt category. The goal of performing a salt transfer is to partition a known volume of salt from one inventory into another. On the laboratory scale, this can range from decant molten salt from one crucible into another, pumping molten salt from a vessel into a crucible, pumping molten salt through tubes and tube fittings, or any combination of the former. On the industrial scale, this can also include dumping salt into drain tanks and adding/removing salt into the reactor volume. Several general functional requirements of a prototypical flowing salt system are given in Table 3. Note that some functional requirements of a static crucible system are also applicable to flowing salt systems.

Table 3. Prototypical Flowing Salt System Functional Requirements

Requirement	Specific Detail	Justification	Comments
Maintain salt above liquidus temperature	$T_{salt} \geq 600^{o}C$ throughout vessels and transfer line	Prevent salt freezing during transfer operations	Critical in transfer tubing and fittings
Maintain trace heating along pathway	All wetted transfer components maintained above liquidus temperature	Avoid freeze blockage	Small diameter regions and exterior regions are typically highest freeze-risk
Enable controlled salt transfer	Transfer rate can be measured and set to a specified/measure flow rate	Allow predictable partitioning operations	

Pressure-driven flow capability	Vessels containing salt inventory can be pressurized up to the required head	Allows salt to be driven above the system head	
Maintain inert cover gas atmosphere	$O_2 < 10\text{ppm}$ $H_2O < 10\text{ppm}$	Minimize salt exposure to impurities that will make the salt oxidizing	Typically achieved with inert glovebox or purge gas system
Prevent vessel over pressurization	Pressure relief or vent path required	Protect vessel integrity and meet safety requirements for operation	
Support transient thermal expansion	Accommodate thermal growth of piping and fittings	Reduce mechanical stress during heating	Important for long heated transfer lines or rigid connection points
Maintain leak-tight salt containment	No measurable salt leakage during operation	Prevent hazardous material release	Tube fittings are prone to leaks when not properly installed and over high temperature gradients
Enable transfer line drainage	Transfer geometry permits post-transfer salt drainage and avoids horizontal sections and tube dips that cannot drain under gravity	Reduces residual salt freezing in the system and improves recovery of salt inventory	
Maintain compatible structural materials	Wetted materials compatible with fluoride salt chemistry	Minimize corrosion and contamination	
Support distributed temperature monitoring	Thermocouples located on vessels and transfer lines	Detect freeze-prone regions and monitor transfer progression	Thermal transients useful for operational diagnostics

2.2.3 DYNAMIC & RECIRCULATING SALT SYSTEMS

Dynamic and recirculating salt systems differ from static and flowing systems in that the salt inventory continuously circulates through a closed system volume. Unlike static systems, which may approach global

thermodynamic equilibrium, or flowing systems, which primarily transfer salt between discrete volumes, recirculating systems are characterized by persistent transport of heat, mass, or both throughout the system.

In practice, recirculating systems typically contain one or more regions where thermal gradients, concentration gradients, or both are intentionally maintained. As a result, the entire salt inventory rarely achieves a single thermodynamic equilibrium state. Instead, local thermodynamic equilibrium is often assumed within small regions of the system, allowing the overall behavior of the loop to be analyzed as a series of coupled equilibrium conditions linked by fluid transport.

This distinction is particularly important because many phenomena relevant to molten salt reactors emerge only in recirculating systems. Thermal gradients can drive dissolution of structural materials in hotter regions and deposition in colder regions through thermally driven mass transfer. Similarly, concentration gradients may arise through corrosion, chemical reactions, or electrochemical processes, producing spatial variations in salt chemistry that evolve with time. The resulting system behavior is governed not only by thermodynamics, but also by transport kinetics and fluid motion.

Figure 3 shows a representative schematic of a dynamic and recirculation molten salt loop. The flow in this salt loop is driven by natural circulation. This phenomenon occurs when a temperature gradient exists across the flow circuit such that the fluid near the bottom of the loop is heater to a temperature greater than the fluid at the top of the loop. Assuming the fluid is Boussinesq, the density of the fluid can be modeled as a function of temperature given by Eq.(2.1):

$$\rho(T) = \rho_0[1 - \beta(T - T_0)] \tag{2.1}$$

ρ is the density of the fluid at temperature T, ρ_0 is the density of the fluid at the reference state T_0, and β is the thermal expansivity of the fluid. Fluid at the bottom of the loop passes through heated section, becomes less dense, and rises through the circuit. Conversely, fluid at the top of the loop rejects heat by passing through a heat exchanger, becomes denser, and falls through the circuit. The equations for determining flow as a function of temperature and heat exchange are described in Section 2.6.

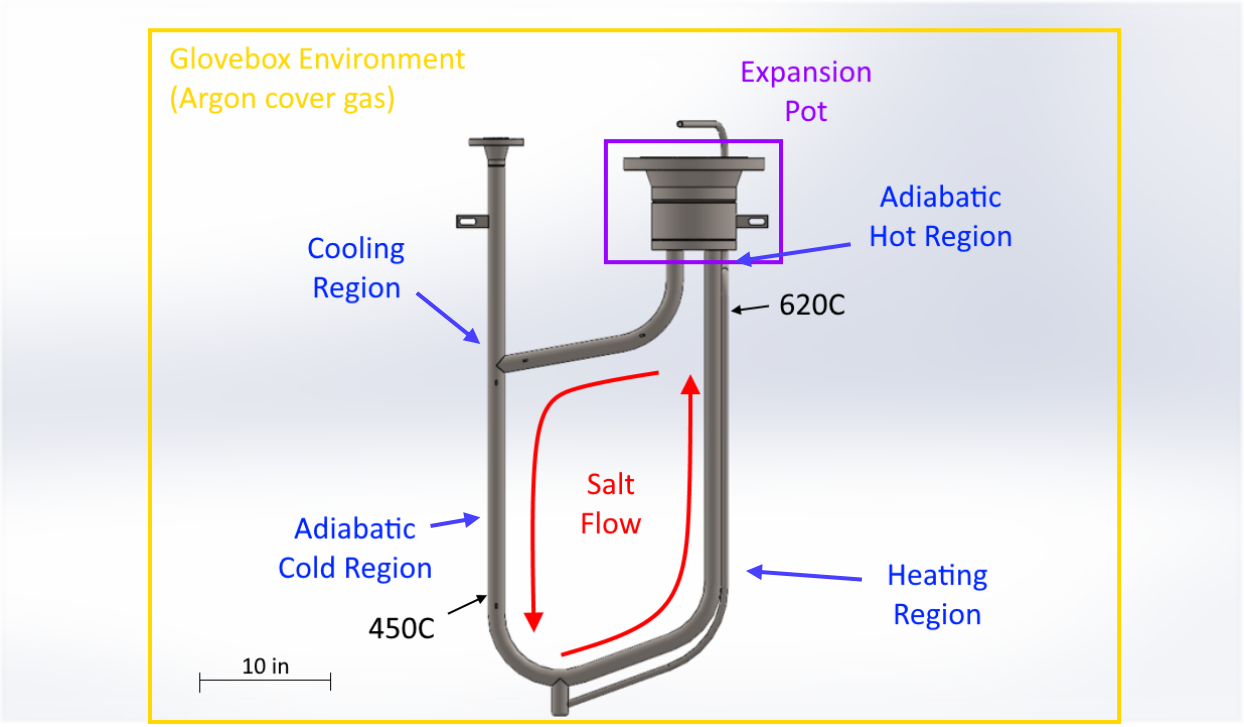


Figure 3. A schematic of a dynamic & recirculation salt system with values from the UCB natural circulation loop design document.

The defining feature of recirculating systems is the coupling between flow, heat transfer, and chemistry. Thermal gradients can drive natural circulation, alter local solubility limits, and promote thermal-gradient-driven mass transfer of structural materials. Concentration gradients can develop as corrosion products, impurities, or electroactive species are produced in one region and transported to another. Consequently, these systems are particularly valuable for studying degradation mechanisms and chemical evolution under conditions that more closely resemble reactor-relevant operation than static crucible tests.

Natural circulation loops represent a particularly important subset of recirculating molten salt systems because the flow is driven by density differences generated by imposed thermal gradients rather than by mechanical pumping. In these systems, the circulation rate depends on the balance between buoyancy forces and hydraulic resistance. This makes natural circulation loops useful for studying passive heat transport, thermal stratification, and corrosion or mass transfer under low-flow conditions.

Table 4. Prototypical Recirculating Salt System Functional Requirements

Requirement	Specific Detail	Justification	Comments
Maintain salt above liquidus temperature	$T_{salt} \geq T_{melt}$ throughout all wetted regions	Prevent salt freezing and flow blockage	
Sustain fluid flow	Molten salt must be driven by a means of convection	Driver of recirculation is necessary for the flow to exist	Can be natural convection or forced convection

Control heater input	Q_{in} must be manipulable	Heat input will affect the temperatures and flow achieved	
Control heat rejection	Q_{out} must be manipulable	Heat rejection will affect the temperatures and flow achieved	
Maintain structural integrity	No material failure during thermal cycling and operation	Ensures safe operations over thermal transients	
Maintain inert cover gas atmosphere	$O_2 < 10\text{ppm}$ $H_2O < 10\text{ppm}$	Minimize salt exposure to impurities that will make the salt oxidizing	Typically achieved with inert glovebox or purge gas system
Support corrosion monitoring	Provide locations for corrosion coupons or probes	Quantify material degradation mechanisms	Enables mass-transfer studies
Support chemical monitoring	Measure salt chemistry during operation	Monitor salt redox potential and change in chemical inventory over time	
Support temperature monitoring	Thermocouples located throughout loop	Provide temperature feedback for control and safety systems	
Accommodate salt thermal expansion	Allow expansion of salt and cover gas volumes under thermal transients	Prevent strain on the system by allowing the free liquid salt surface to expand	
Enable salt recovery	Recover ≥95% of salt inventory following operation	Minimize material losses, support post-test characterization, and facilitate reuse or disposal of salt. Also allow safe shutdown, maintenance, emergency recovery, and post-test processing	Often linked to freeze valves, drain tanks, or transfer systems

2.2.4 COMPLEX SALT SYSTEMS

Complex salt systems are reserved for systems that are coupled with auxiliary systems, such as the primary and secondary loops of an MSR. These systems are complex because changes in the input of one system can result in changes in the output of another system. A useful heuristic is that complex systems are composed of multiple subsystems, each of which could independently be classified as a static, flowing, or recirculating system. The engineering challenge arises not from the individual subsystems themselves, but from the interactions between them.

During operation of the MSRE, reactor power was strongly coupled to heat removal in the secondary loop through the negative temperature coefficient of reactivity. Changes in heat rejection altered fuel-salt

temperature, which in turn affected reactor reactivity and power generation. Because reactor power determines the rate of fissions, long-term changes in heat removal also influence fuel depletion and the evolution of fuel-salt composition [12]. These are the types of systems one might expect to design for industrial applications and could have their own independent thesis written on any one specific subsystem design. For the scope of this thesis, we will not discuss complex salt systems in any further detail.

2.3 Design and Operation of Salt Transfer System - Methods

The design methodology developed in the previous sections was applied to the development of a laboratory-scale FLiBe transfer system intended to support molten salt chemistry and electrochemical experimentation. The primary objective of the system was to enable controlled partitioning of molten FLiBe between separate vessels while maintaining safe operation and minimizing contamination of the salt inventory. The goal of this section is to prepare the novice molten salt engineers and scientists of the world for the problems and solutions faced with developing these systems. We hope to answer the question—**how do you design a safe, reliable, and robust salt transfer system?**

As part of the NEUP Integrated Research Project (IRP) Molten Salt Reactor Test Bed with Neutron Irradiation, the University of California, Berkeley was tasked with partitioning and transferring approximately 25 kg of Li-7 enriched FLiBe for shipment to the Massachusetts Institute of Technology. The salt was intended for use in a neutron-irradiated FLiBe loop designed to study tritium generation, transport, and electrochemical behavior under reactor-relevant conditions. The use of Li-7 enriched material was necessary to reduce tritium production from the Li-6(n,α)T reaction and thereby limit the radiological source term while preserving the ability to study tritium behavior in the molten salt.

The transfer operation required moving molten FLiBe from a source vessel into two receiving vessels while maintaining salt purity, minimizing operator exposure, and preventing solidification within the transfer system. Unlike many conventional fluid transfer operations, molten salt transfer must be conducted while maintaining all wetted surfaces above the salt liquidus temperature. Failure to do so can result in formation of frozen salt plugs that obstruct flow and may require extensive recovery operations. Consequently, thermal management represented the primary engineering challenge governing system design and operation.

Although the transfer campaign ultimately succeeded, multiple transfer attempts and system modifications were required before reliable operation was achieved. These development efforts provided an opportunity to identify the dominant engineering constraints governing molten salt transfer operations and evaluate practical strategies for improving system robustness. The discussion presented here focuses on the lessons learned during system development and the engineering conclusions obtained from the transfer campaign.

2.3.1 Salt Transfer Piping & Instrumentation

The design of the FLiBe transfer system followed the methodology established in Section 2.1 and Section 2.2, beginning with the identification of functional requirements and design constraints before selecting process equipment. These requirements are documented in the internal documentation for the salt transfer procedure titled “UCBS44EG01 Salt Transfer System Design” and can also be found in Appendix D.2,

Table 40. The piping and instrumentation diagram (P&ID) for the final system assembly is given in Figure 4. The P&ID shows:

- Heating zone assignments and locations (HZ01-HZ04)
- Salt transfer vessel assignments and locations (TK01, TK02A)
- Temperature and pressure sensors (TT01-TT12, PI01-PI04)
- Direction of pressurized gas flow and salt flow (solid arrows)
- Temperature and power communication (long-dashed colored lines)
- Temperature logging communication (short-dashed black lines)

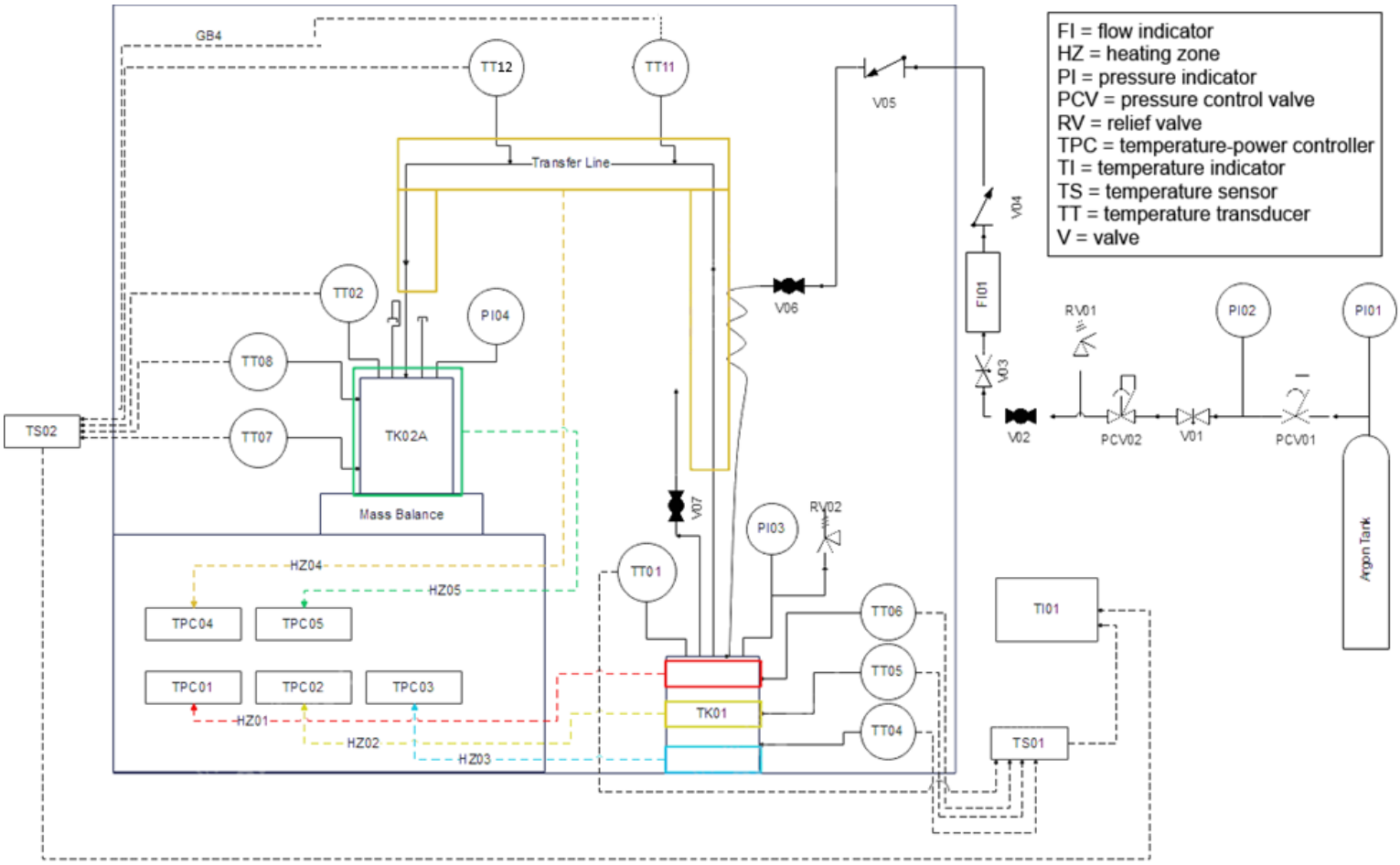


Figure 4. P&ID for the Li-7 enriched salt transfer system

Figure 5 shows the 3D CAD model of TK01 found in Figure 4. TK01 includes five welded tube ports on the top of the tank and a "X" shaped fin configuration at the base of the tank. All tube ports are fitted with Swagelok compression fittings. The central tube port is reserved for moving salt out of the tank. A dip tube is inserted through the central port and salt travels up the tube into connective transfer lines. The remaining tube ports are reserved for (i) a gas inlet line, (ii) a gas bypass valve, (iii) a thermocouple port, and (iv) a mechanical relief valve. The fins at the base of the tank provide stability to the vessel.

Figure 6 shows the 3D CAD model of TK01 found in Figure 4. The features of TK02A are similar to those of TK01. The difference in the design of TK02 is that the base is fitted with a “skirt” instead of a “X” fin geometry. This redesign reduced the welding difficulty by removing the need to center “X” fins on a rounded tank surface.

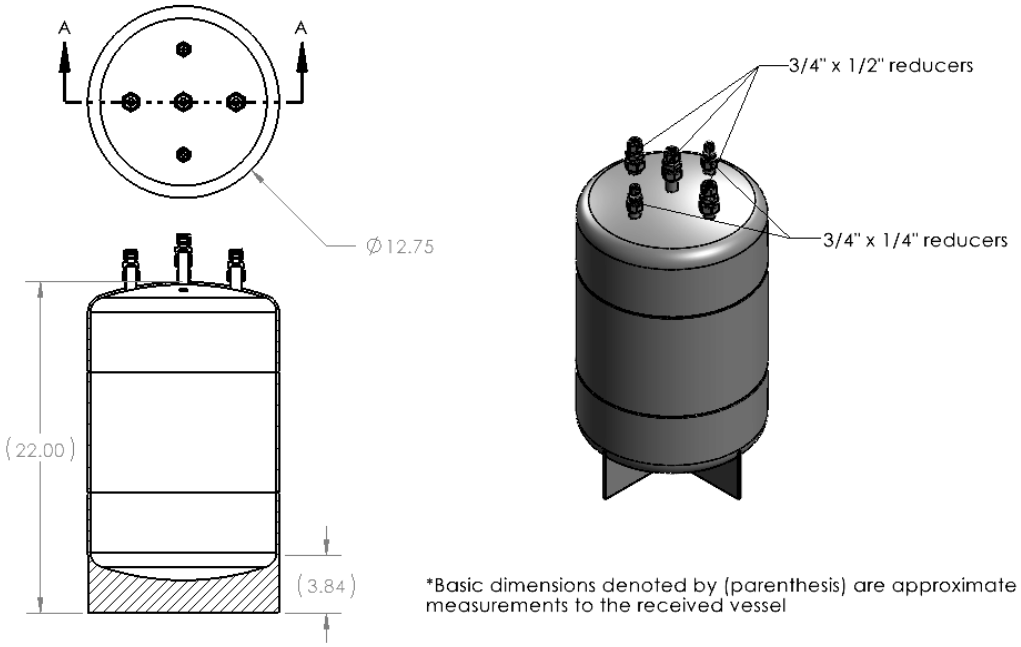


Figure 5. CAD model of TK01, the Li-7 enriched FLiBe salt vessel from UW.

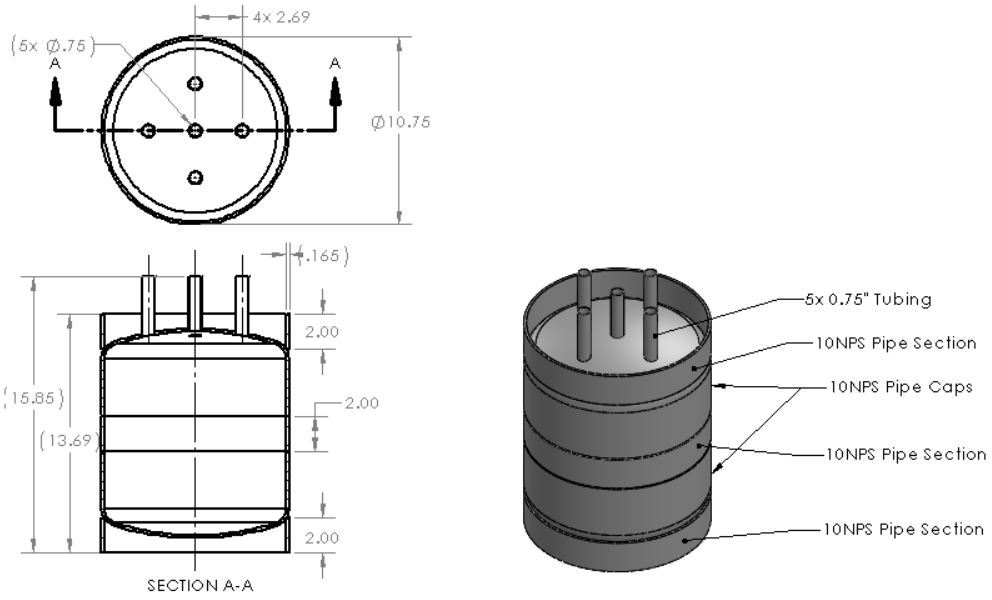


Figure 6. CAD model of TK02, the salt transfer vessel fabricated by MIT.

2.3.2 DESIGN CALCULATIONS

Transferring any fluid through any length of pipe requires work on the fluid. We need to satisfy the mechanical energy requirements to push the salt from one tank into another. Levenspiel [13] discusses these systems with great clarity and provides the framework for this analysis. The mechanical energy balance for the salt transfer system is given by:

$$g\Delta z + \frac{\Delta v^2}{2} + \int_1^2 \frac{dp}{\rho} + \Sigma F = 0 \tag{2.2}$$

g is the gravitational constant, Δz is the difference in height of the fluid from the entrance to the exit, Δv is the change in velocity of the fluid from the entrance to the exit, Δp is the difference in static pressure of the fluid from the entrance to the exit, ρ is the average density of the fluid, and ΣF are the sum of all frictional forces. We account for the energy losses around tube bends, tube fittings, and cross-sectional area changes by equating the loss to friction in an equivalent length of straight pipe, L_{equiv}, and add this length to the actual length of straight tube of the system, L_{actual}. We calculate the total losses by the term,

$$\Sigma F = \frac{2 f_F L v^2}{g d} \tag{2.3}$$

where L is the length of tube equal to the sum of L_{equiv} and L_{actual}, d is the diameter of the pipe the fluid is traveling through, and the Fanning friction factor, f_F, is defined by,

$$f_F = \frac{\tau_w}{\rho \frac{v^2}{g}} \tag{2.4}$$

For laminar flows, a useful relationship for determining f_F is given below:

$$f_F = \frac{16}{\mathrm{Re}} \tag{2.5}$$

For turbulent flow where $Re < 100{,}000$, the Blasius correlation is useful as well:

$$f_F = 0.079 Re^{-\frac{1}{4}} \tag{2.6}$$

Where Re is given by,

$$Re = \frac{\rho v D}{\mu} \tag{2.7}$$

It is an operating heuristic to prevent the salt from flowing in the laminar regime in transfer lines during the operation. Laminar flow can lead to thermal stratification in the radial direction in small diameter tube resulting in freezing at the wall and choking the flow [14]. We can stimulate turbulent flow in the transfer line by forcing the fluid to move at a minimum velocity. The calculation is shown in Appendix A.1 which solves the minimum pressure required to push salt through the transfer line while remaining turbulent.

A critical feature of the salt transfer is the ability to partition an accurate quantity of salt. This means we need to account for salt transferred into the tank *after* the pressurize line has been closed. The total amount of salt expected to "bleed" off of the transfer line was calculated to be around 50g. This calculation is given in Appendix 0.

2.3.3 Configuring the Instrumentation & Controls

Temperature control PID controllers were used to supply power to the heating tapes and ceramic insulated heating blocks for salt vessel heating and trace heating. Each heating zone was designed to supply a maximum load of 600W while the heating tapes and bands are designed for a load of 624W and 600W, respectively. The heating zones were each controlled independently by PID controllers listed in Appendix D.5.

2.3.4 Assembly of Salt Transfer System

To assemble the salt transfer system, we performed a beryllium glovebox opening procedure. These procedures can be intense for researchers and requires training and coordination for all researchers that perform the procedure. Beryllium hygiene protocol was followed in accordance with the SALT Research Group's Beryllium Exposure Control Plan. This plan is found in the internal research group folders with document number "UCBS-SF-BE-001 Be Hygiene Plan."

Figure 7 shows the assembled salt transfer system and some of the power wire and thermocouple wire routing inside the glovebox. This image shows the small spatial budget this system had to be assembled

compared to open-floor systems. The spatial constraint was well managed by creating a 3D CAD assembly model and following the placement of each item before assembling the system.

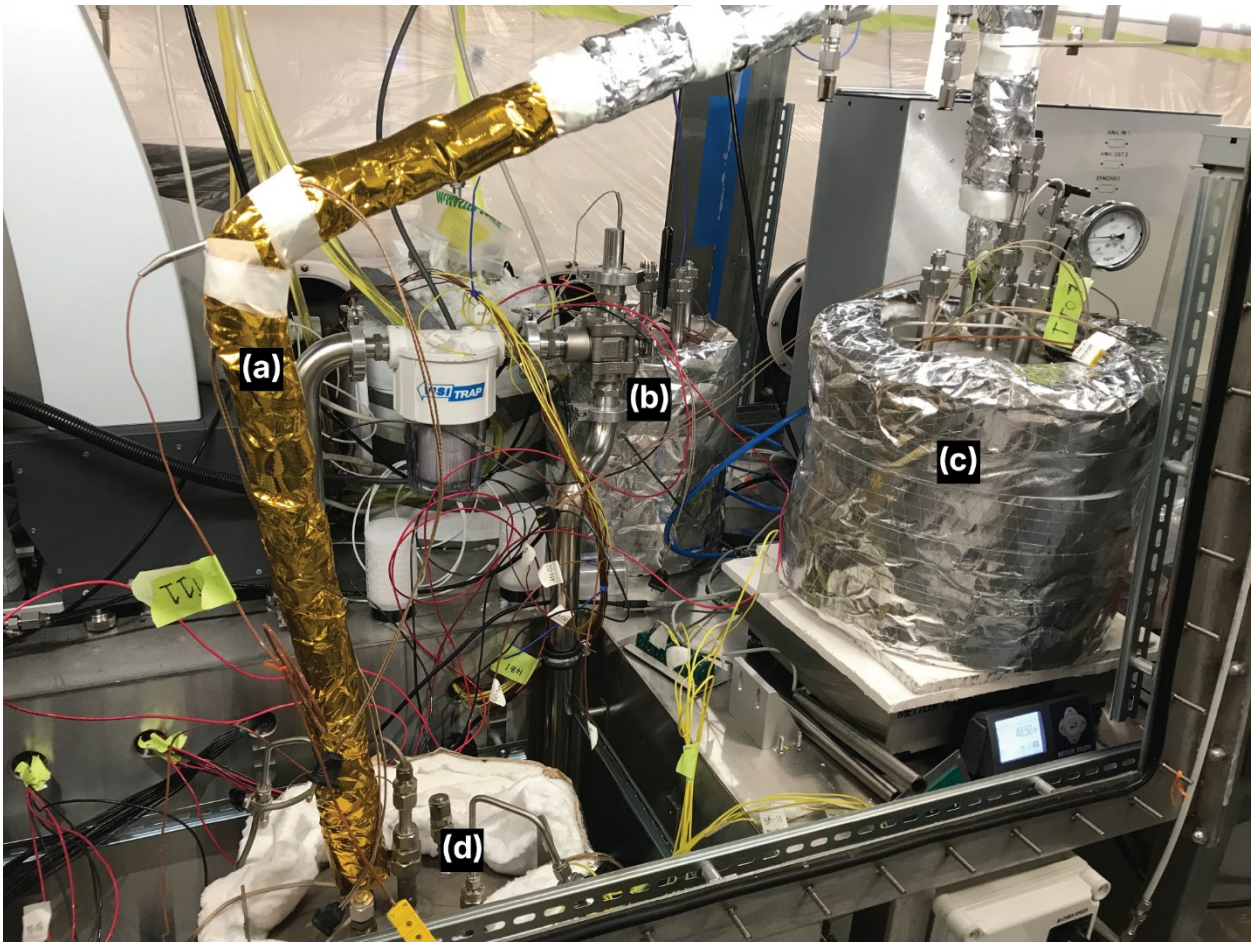


Figure 7. Salt Transfer System front-view components in the beryllium glovebox train. Labeled parts of the image (a) old salt transfer line, (b) TK03, (c) TK02, and (d) TK01.

2.4 TEMPERATURE AND MASS TRANSFER DATA - RESULTS

The data collected during the salt transfer consists of temperature data and power output data both digitally and manually recorded. The continuously logged temperature data was used during the procedure to enable remote monitoring of the system overnight and identify system "off-normal" behavior, such as heating tape failure or setpoint overshooting. We can see transients in temperature upon startup and during shakedown tests. Importantly, we can identify signs that indicate system failure which upon inspection revealed the heating tapes were burning out. Figure 8 is annotated with several key failures and actions taken during the procedure. The sharp declines in temperature are indicative of heating tape failures. We verify the heating tape failures by opening the insulation on the part of the system which has suspected failure and then observing the tape for signs of fraying, burning, or breaking like what is shown in Figure 9. At the first and second heating tape failure annotated on Figure 8, we opened the insulation, confirmed the heating tapes failed, and replaced them with new tapes. We decided to postpone the first salt transfer attempt after a third heating tape failure occurred at a part of the system which was impossible to reach without opening the

gloveboxes. This decision prompted a root cause analysis of the failures we experienced during the first attempt. The root cause analysis is provided briefly in Table 5.

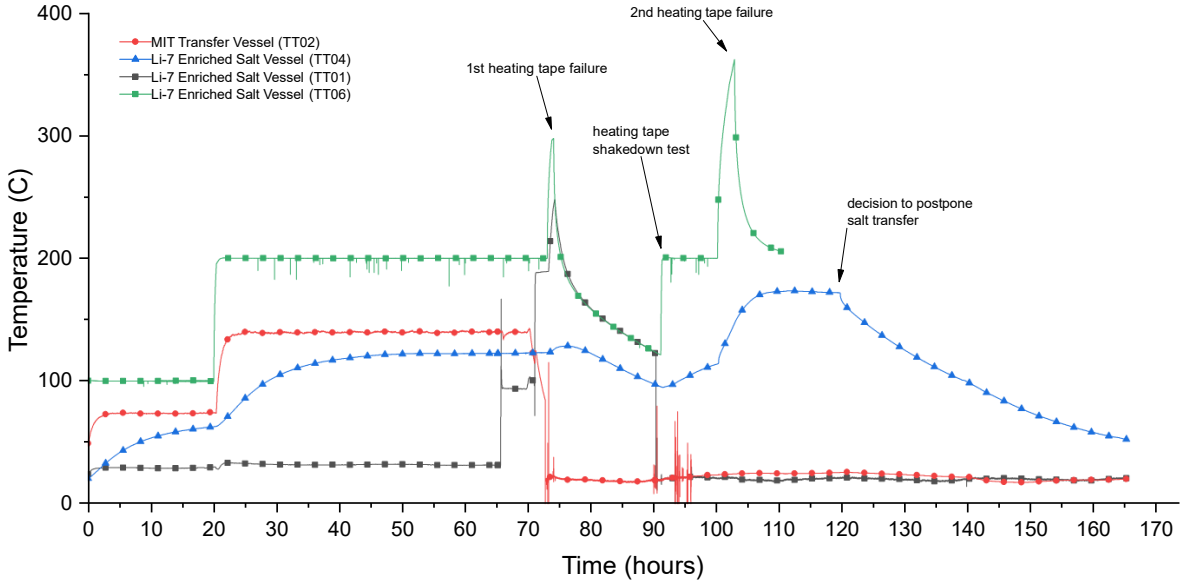


Figure 8. Temperature data from the thermocouple logging DAQ during heating tape shakedown test. Time t=0 started on 2025-03-13.

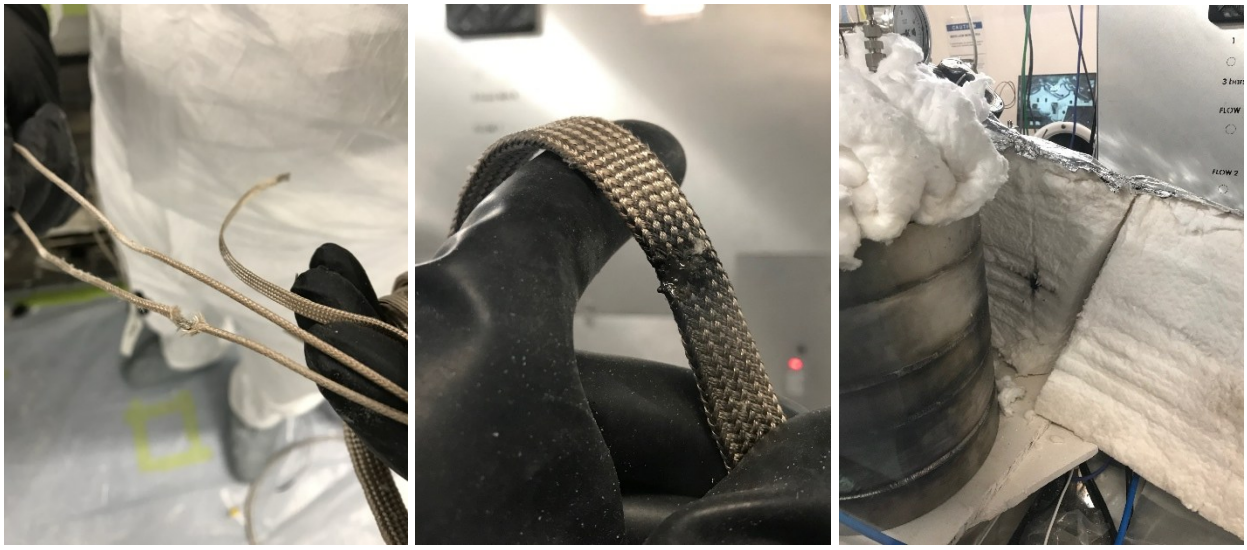


Figure 9. (left) Exposed wiring of the heating tape leads. (middle) burned heating element in heating tape. (right) Singe marks on the ceramic fiber insulation.

Heating tape burnout posed a high frequency occurrence in the salt transfer system, so we collected data that would help predict when heating tapes were about to fail. In Figure 10, temperature data is presented during a heating tape failure test. Manual power steps are seen in Figure 10 as indicated by sharp increases in the derivative of temperature. We can see this signature around hour 3.6 in Figure 10, where the derivative of the temperature began to increase again without any manual power step. We hypothesize this signal is indicative of the onset of heating tape failure. The proposed mechanism for heating failure accounts for the

increase in ductility of the heating elements as temperature increase. More ductile heating elements are thinned out with thermal stresses imposed by the system on the heating tape, and thinner section of heating elements have higher electrical resistance causing them to heat faster than the rest of the tape. This is a positive feedback loop which would result in specific sections of heating tape under high mechanical stress breaking faster than the other sections.

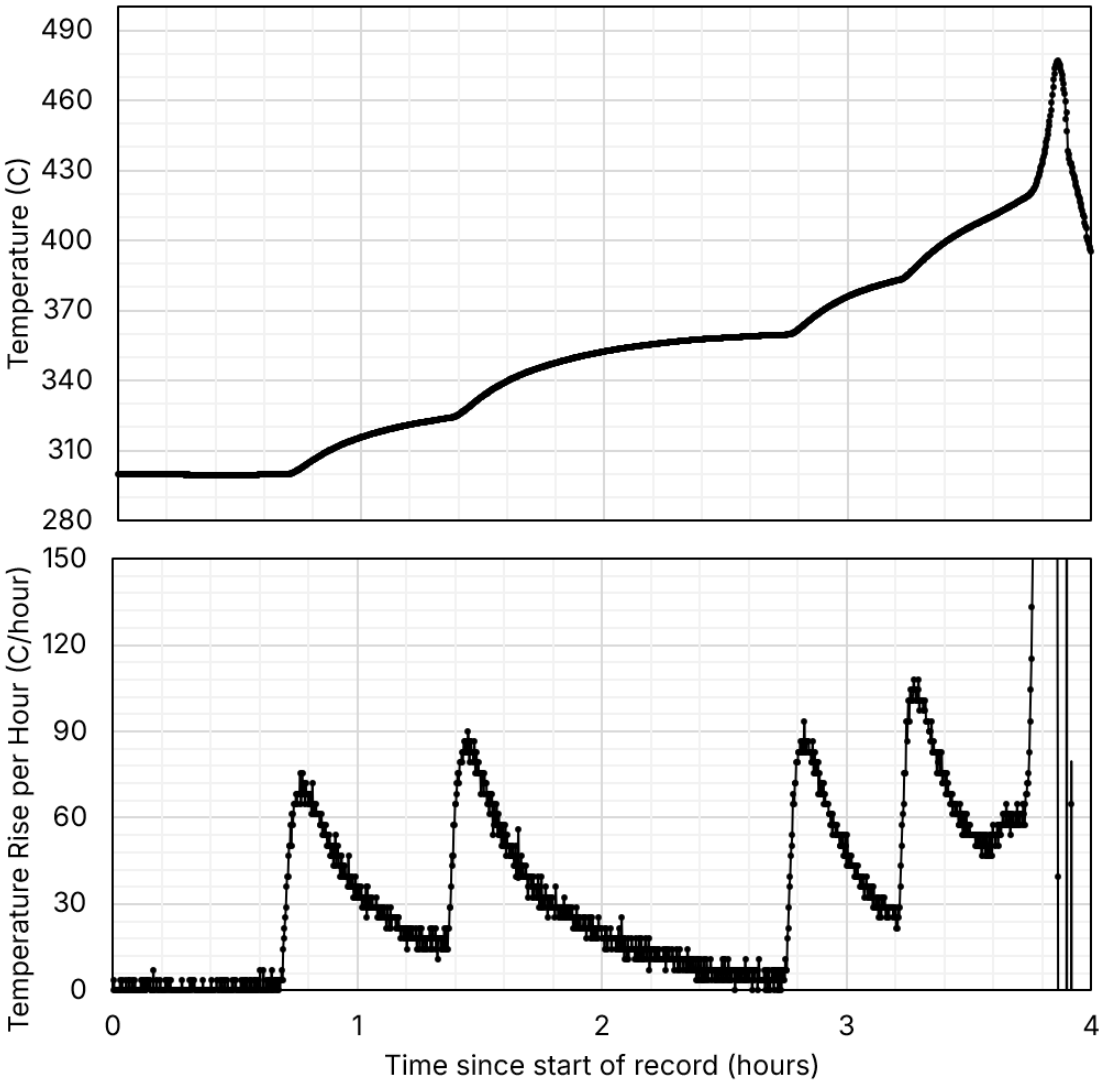


Figure 10. Temperature profile during heating tape test (recorded on TT11 in Figure 4)

The second attempt began with root cause analysis of the first attempt failure. The failure analysis from salt transfer attempt 1 led to a redesign of the heating system and power delivery systems. Heating tapes around TK01 were replaced with two clamshell ceramic heating clamps (MPI Morheat Ceramic Band 600W, 120V). The heating bands have heating elements embedded in ceramic blocks and lead wires braided in stainless steel. Both the embedded heating elements and braided leads help avoid the possibility of exposing wires that could short circuit.

Table 5. Points of Failure in Attempt 1

Failure Observed	Possible Root Cause	Justification
Heating tape burnout	Transfer line tube diameter size was too small	Twisting heating tape on small diameter tubing can strain the internal wires and cause overheating on sections that overlap. Tightly wrapped heating tapes experience more strain than loosely wrapped tapes, leading to faster burnout.
	Overpowering the heating zone	The heating load on each zone was rated to a maximum of 624W, and the power supply was capable of pushing 1000VA at the source. Therefore, pushing the power supply above 62% of its total output would fry the heating tapes in the respective heating zone.
Exposed conductive power wire	Poorly routed heating tape and power wires in the glovebox	The power wire and heating tape lead wires were not carefully routed through the system and would lead to points of tugging and pinching. Excess cable length and strain relief on the wires would prevent them from tugging and fraying their insulating sheaths in the glovebox.

2.4.1 HEATING AND COOLING DATA

System temperatures were consistently monitored from the heater testing phase through the attempted melt. Figure 6 shows the heating and cooling curves for the preliminary test heating of the Li-7 vessel with the new clamshell heating bands. This testing indicated the stability of the system and provided data for calculations on the projected thermal response under different operating conditions.

The data in Figure 11 shows typical data that were collected for temperature forecasting of the system. We used a transient lumped capacitance thermal resistance model to fit the temperature profile measured from

each thermocouple. The model considers three temperature regions: the solid FLiBe, s, the stainless steel wall, w, and the insulation, ins.

$$m_w c_{p,w} \frac{dT_w}{dt} = \eta\Phi - \frac{T_w - T_s}{R_w + R_s} - \frac{T_w - T_{ins}}{R_{ins}} \tag{2.8}$$

$$m_s c_{p,s} \frac{dT_s}{dt} = \frac{T_w - T_s}{R_w + R_s} \tag{2.9}$$

$$m_{ins} c_{p,ins} \frac{dT_{ins}}{dt} = \frac{T_w - T_{ins}}{R_{ins}} - hA(T_{ins} - T_{amb}) \tag{2.10}$$

where m_i is the approximate total mass of phase i, $c_{p,i}$ is the heat capacity of phase i, T_i is the temperature measured at the interphase of phase i, R_i is the thermal resistance of phase i, Φ is the total power supplied to the system, and η is the efficiency of the heater. Each of the thermal resistances are given below:

$$R_w = \frac{\ln\left(\frac{r_{w,o}}{r_{w,in}}\right)}{2\pi k_w L_w} \tag{2.11}$$

$$R_s = \frac{l_s}{k_s A_s} \tag{2.12}$$

$$R_{ins} = \frac{\ln\left(\frac{r_{ins,in}}{r_{ins,o}}\right)}{2\pi k_{ins} L_{ins}} \tag{2.13}$$

where $r_{i,o}$ is the outer radius of phase i, $r_{i,in}$ is the inner radius of phase i, k_i is the thermal conductivity of phase i, L_i is the total length of the region orthogonal to the direction of heat flow in phase i, l_s is the effective mean length of heat transfer in the salt (taken to be approximately the radius of TK01), and A_s is the effective surface area conducting heat to the salt (taken to be the surface area of the heated regions on TK01). The input parameters for the model are given in Table 6. The script fits each thermocouple independently using a lumped thermal resistance network. The model represents heat input from the heater, heat transfer into the internal vessel region, conductive losses through insulation, and convective losses to the glovebox atmosphere. The fitted parameters should be interpreted as apparent thermal parameters, because the simplified model absorbs three-dimensional conduction, imperfect heater contact, insulation gaps, thermal bridges, and local geometry into effective conductances and capacitances. Considering the R^2 >0.99 for all fit curves, it is possible this model is overfitting the data.

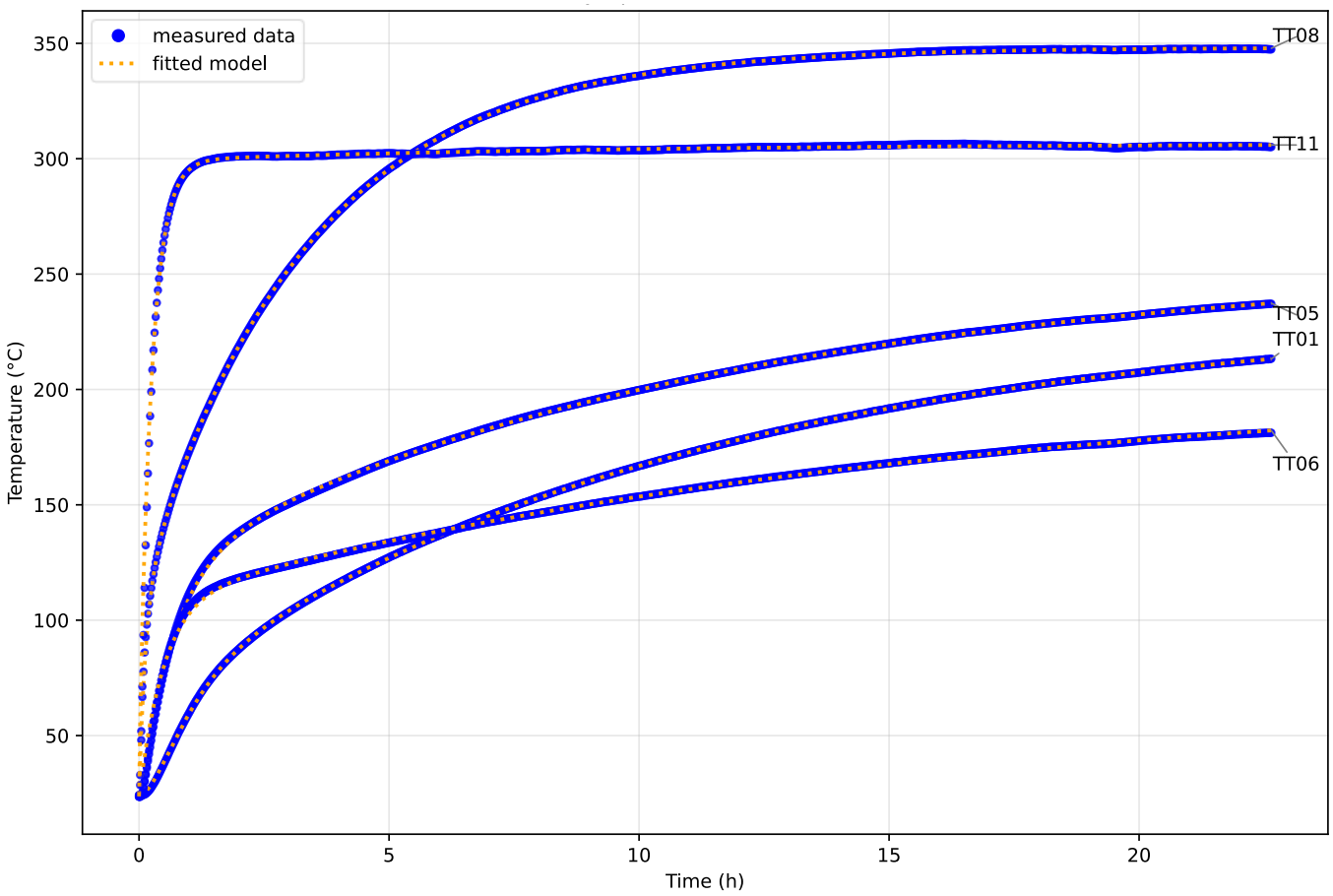


Figure 11. Temperature data and forecasts from system shakedown tests (see Figure 4 for temperature locations)

Table 6. Parameters of the lumped thermal capacitance model

Parameter	Value	Units	Source / basis
Input power, Φ	300	W	Experimental input power per measured region
Stainless steel thermal conductivity, k_w	16.3	W m^{-1} K^{-1}	Literature value for SS316/316L; typical range ~13–17 W m^{-1} K^{-1}
Insulation thermal conductivity, k_{ins}	0.0846	W m^{-1} K^{-1}	Literature value for calcium silicate insulation near 300 K
Thickness of insulation, Δt_{ins}	0.0762	m	Assumed insulation thickness, 3 in
Heating tape surface area, A_{TT11}	0.04645	m^2	1 in wide × 6 ft long heating tape
Diameter of transfer line, D_{TT11}	0.00635	m	1/4 in tube outer diameter
Thickness of wall, Δt_w	0.000889	m	0.035 in tube wall thickness

Axial length of transfer line, l_{TT11}	1.524	m	Approx. 60 in tube length
Cover gas volume, V_{TT01}	0.00144	m^3	Estimated TK01 cover-gas volume, 1.44 L
Length of heated section of TK01, L_{TK01}	0.3048	m	12 in heated vessel length for TT05, TT06, TT08
Diameter of heated section of TK01, D_{TK01}	0.32385	m	12.75 in vessel diameter
Surface area of heating load on salt in TK01, A_s	$\pi DL \approx 0.310$	m^2	Calculated heat-transfer area for TT05, TT06, TT08
Ambient temperature, T_{amb}	25	°C	Taken from each thermocouple trace as ambient/reference temperature
Heat transfer coefficient in argon, h_{ag}	fitted	W m^{-2} K^{-1}	Apparent exterior convection coefficient
Apparent thermal conductivity of FLiBe, k_s	fitted	W m^{-1} K^{-1}	Apparent FLiBe conduction parameter
Heater efficiency, η	fitted	dimensionless	Apparent heater efficiency / effective power fraction

The fitted parameters from the lumped thermal capacitance model are given in Table 7. The apparent FLiBe thermal conductivity was 0.04–0.19 W m^{-1} K^{-1}, approximately an order of magnitude below literature values for solid Li_2BeF_4 [15]. This discrepancy indicates that the fitted parameter should be interpreted as an effective heat-transfer parameter for the vessel/salt assembly rather than as a direct material property. In particular, low apparent conductivity likely reflects incomplete thermal contact between the solid salt and vessel wall, geometric spreading resistance, and uncertainty in the effective salt volume participating in the transient heat-up. By allowing the model to calculate the "apparent FLiBe conductivity," it is clear that the model is overfitting the data by not defining this physical property.

Table 7. Fitted parameters from the lumped thermal capacitance model

Thermocouple	**Model interpretation**	**Apparent argon heat-transfer coefficient, h (W m^{-2} K^{-1})**	**Apparent FLiBe thermal conductivity $k_{FLiBe,app}$ (W m^{-1} K^{-1})**	**Heater efficiency η**
TT01	Argon cover-gas node	0.01	—	0.09

TT05	Vessel wall + solid FLiBe node	—	0.188	0.299
TT06	Vessel wall + solid FLiBe node	—	0.137	0.205
TT08	Vessel wall + solid FLiBe node	—	0.0367	0.168
TT11	Argon-filled transfer line	22.29	—	0.231

To make sense of the low apparent conductivity of FLiBe, we determined there were air gaps in the insulation around the system. These gaps were acting as extra "node" in our heat transfer model causing an increase in lumped capacitance and decreasing heater efficiency. The corrective action was to rewrap the system insulation and ensure the fiber insulation was securely tightened with no room for air gaps.

Along with heat losses, we were experiencing frequent loss of power events due to heater shorting. The corrective action was to include inline ground fault circuit interrupters (GFCIs) with each HZ. With the knowledge that heating tape short-circuits are somewhat frequent, it was prudent to include GFCI protection on each HZ. We also realized that the GFCIs could potentially prevent further heating tape failures in the first place by breaking the circuit at the moment small leakage current was detected. We tested if the system was electrically grounded by performing an electrical continuity test with a multimeter. It was confirmed that every distinct surface of the salt transfer system was electrically grounded without any further alteration of its assembly. However, we included an additional grounding clip on TK01 that was rated for grounding a 120V, 30A circuit break to ensure proper electrical protections with the addition of another 600W heating zone.

2.4.2 Heating Zone Shakedown Tests

Before bringing the salt in TK01 to melting temperature, we performed heating shakedown tests to verify the reconfigured system functioned as intended. Specifically, we run shakedown tests to:

1. determine whether the equipment is capable of sustaining long-term heat transfer,
2. determine if the temperature of the system can hold its setpoint(s),
3. find any problems that should be fixed before continuing with the operation,
4. determine process relationships between the power output in heating zones and the temperature measured in the heating zones, and
5. train operators on how to use the equipment before running the full operation.

We recalled there were several incidents of heating tape failure from the last salt transfer attempt. For this shakedown test, we wanted to verify all of the controllers being used to run the system were functioning correctly and record the current and power output for the controllers before ramping the system to operating

conditions. There were two types of controllers being used for the procedure – a manual variable power controller (typically called a "variac," not necessarily referring to the specific brand) and a solid state relay (SSR) proportional-integral-derivative (PID) temperature controller. An important distinction between the two controllers is that the variac controller adjusts the voltage output to control the power whereas the PID controller adjusts the duty cycle to control the power output. This seemed to matter for our applications as the heating tapes in the transfer line heating zone (HZ4) had a maximum current limit which was exceeded by some of the PID controller's output. For example, the heating tape in HZ4 were sized for a total heating load of 468W and a max current of 3.9A. The PID controller would send 468W of power to the heating tape by sending 4.5A to the tape for 85% of the time (for a 1 second duty cycle, the circuit would be closed for 0.85 seconds). Since we had issues with heating tape burnout previously and it was inconclusive if this was due to the controller itself, we opted to avoid this potential problem during this attempt. Therefore, to control the heating tapes we relied only on using the manual variac controllers. The potential-current and the potential-power curves are shown in Figure 102 and Figure 103, respectively.

2.4.3 SALT MELTING AND TRANSFER OPERATION

The salt melting procedure initiated by raising the output power of HZ1-3 to 100% output (1800W total) and allow the temperature of the system to reach the FLiBe melting point, approximately 459ºC. Figure 12 shows the rising temperature of the system during the melting procedure. The thermocouple names from Figure 4 are labeled next to their trace in Figure 12. Events of interest are labeled along the top of Figure 12 with letters. Each labeled event is described in Table 8.

During the temperature ramp, several GFCI breaker trips occurred which limited the temperature rise achieved over the course of the melting procedure. Several GFCI trip events are mentioned in Table 8 and the effect of temperature rise is observed in Figure 12. The characteristic GFCI breaker trip signal results in a temperature drop around specific HZ. Power would be restored as soon as an operator noticed the temperature drop and the melting procedure would continue.

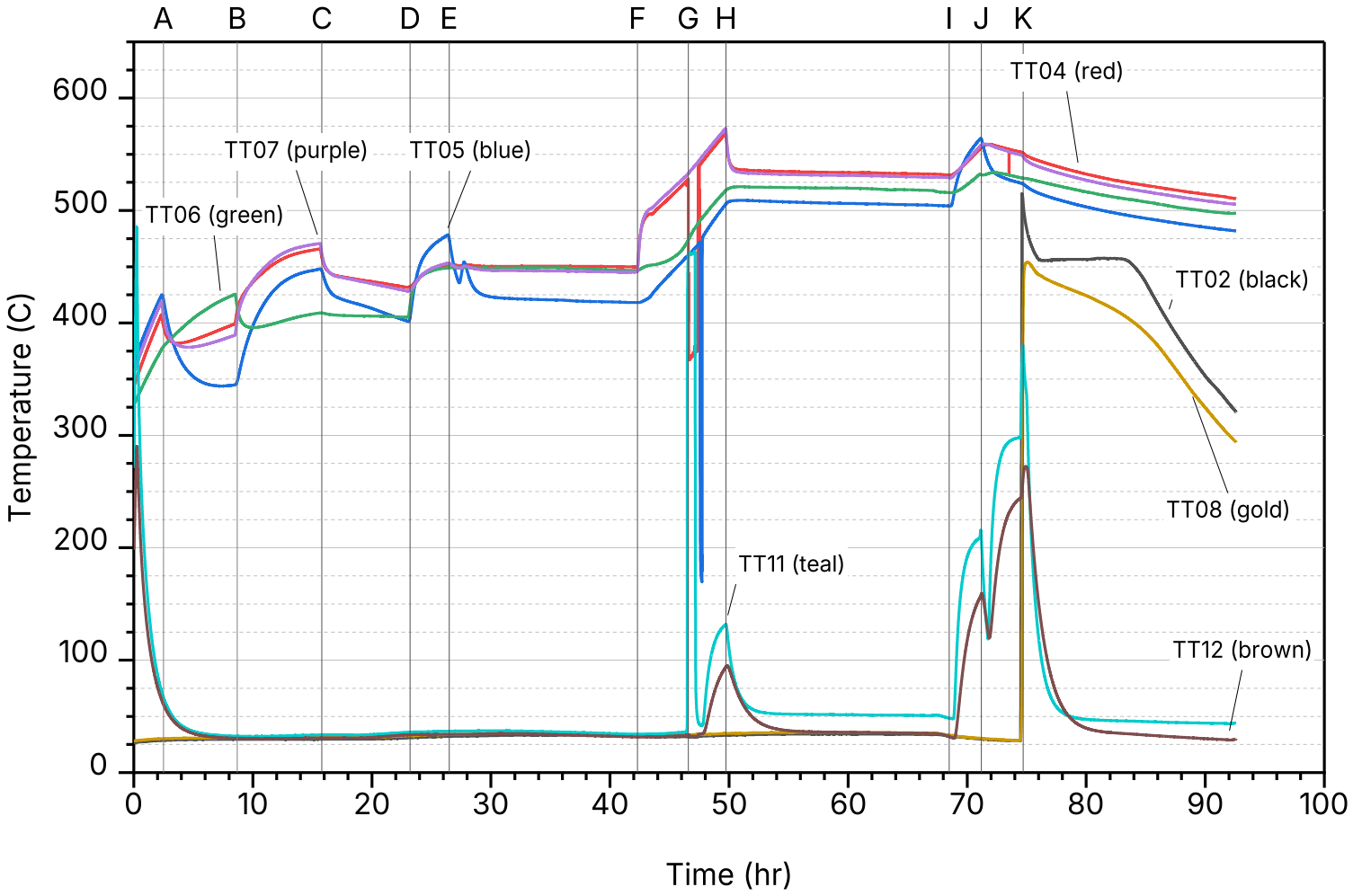


Figure 12. Temperature data from the melting and transfer operations. (t=0 @ 2025-12-01 15:25)

Table 8. Labeled Events in Figure 12

Event Label	Event Description
A	GFCI trip – HZ1 and HZ2 lost power overnight.
B	GFCI breaker reset – Power restored.
C	GFCI trip – HZ1 and HZ2 lost power. Attempts to find system fault during day.
D	Power restored to HZ1, but not HZ2. Likely heater shorting occurring on HZ2.
E	GFCI trip – HZ1 lost power overnight.
F	Power restored to HZ1 and HZ2 but only to max 60% power output.
G	Salt transfer operation occurs when TK01 temperatures are >550°C
H	GFCI trip – HZ2 complete failure and cannot be turned on without system trip.
I	Replaced heating tape on HZ4 and turned on to 30% power.
J	GFCI trip – HZ1 and HZ4 lost power
K	HZ4 heating tape burnout observed. System allowed to cool and stop procedure.

At $t = 46.5$ hr, event G in Figure 12, we began the salt transfer operation. This decision was made after determining that the linear temperature increase was characteristic of liquid heat transfer at the inner wall of TK01. We followed the procedure outline in Appendix D.1, and we successfully measured mass transfer from TK01 into TK02. The temperature data from the salt transfer operation is shown in greater time resolution in Figure 13. This data shows the exact moment salt flow entered the transfer line from the sharp temperature spike from TT11 in Figure 13. We can also see the effect of adding cold, pressurized argon gas into TK01 from the temperature drop from TT04 in Figure 13. The drop in temperature of the transfer occurs shortly after the transfer procedure concluded, indicative that the salt drained from the line near the TC. The temperature in HZ1 sharply increased after the procedure concluded when we sealed the gas bypass valve (V07 in Figure 4) and stopped gas flow through the vapor space of TK01. This confirms that the gas flow through the vessel vapor space was the cause of the temperature drop.

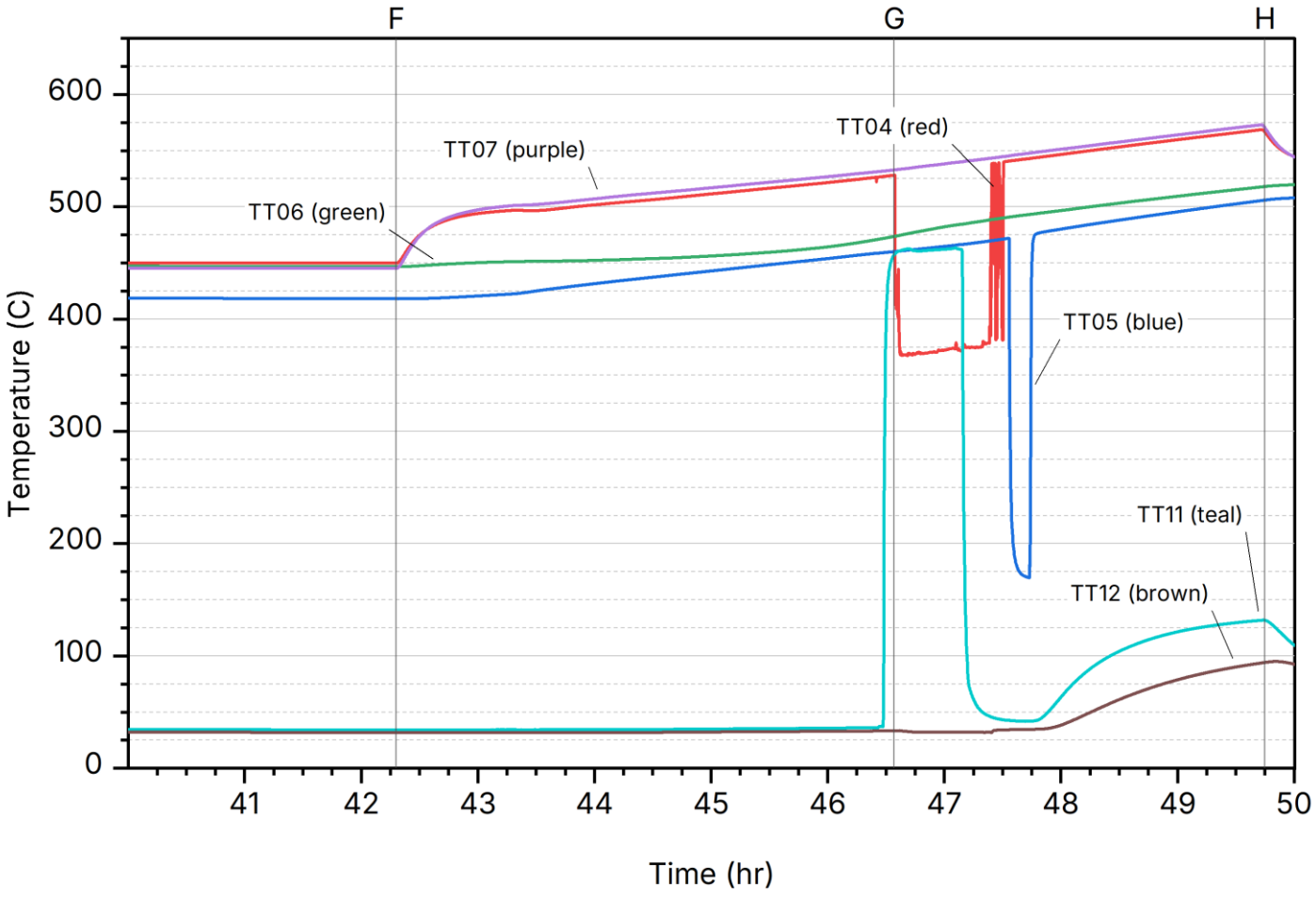


Figure 13. Enlarged section of the temperature data in Figure 12. The salt transfer start time is at timestamp G.

The mass transfer rate was recorded manually by noting the elapsed time of the procedure as set weight intervals. The transfer operation required partitioning 20kg of FLiBe into TK02A. The mass transfer data is presented in Figure 14. The starting mass and target mass of TK02A is marked with a dashed horizontal line. Data points of measured masses at specified times are given by black squares. The linear regression

that fits the data is given by a dotted black line. The predicted slope given by a red solid line is based on an assumed volumetric flow rate equivalence between the inlet argon stream and the outlet salt stream. The error bars on the predicted flow rate come from the uncertainty in the measured volumetric flow rate of argon (relative error of 10% of the measured flow rate, representing 2σ of uncertainty) from the flow indicator (FI01 in Figure 4).

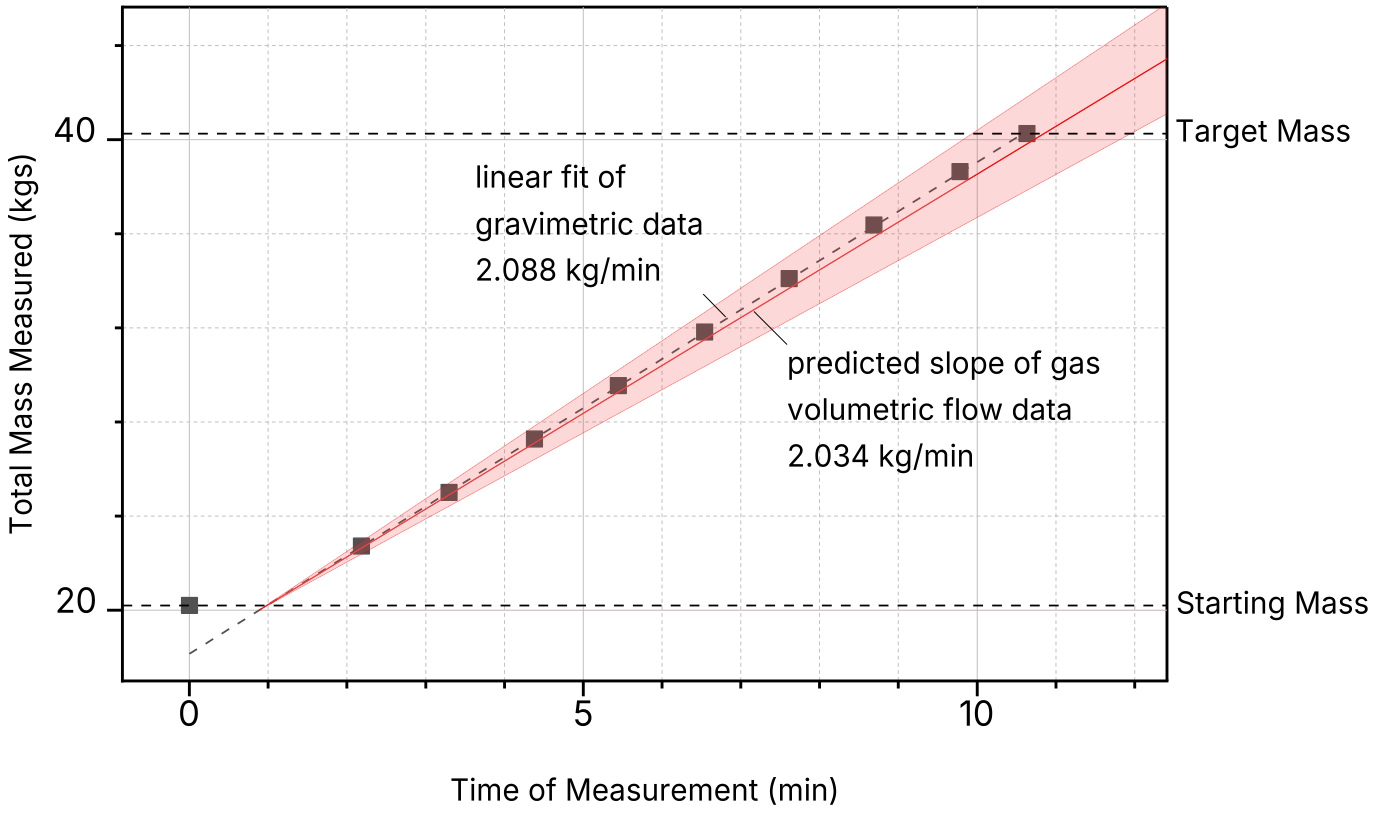


Figure 14. Measured mass transfer rate of Li-7 FLiBe from TK01 to TK02.

We predicted mass transfer from TK01 to TK02 at steady state would balance the volumetric flow of argon into the system with the volumetric flow of salt out of the system,

$$\dot{V}_{gas} = \dot{V}_{salt} \tag{2.14}$$

This prediction is a perfect model as it does not consider the compressibility of the argon gas. However, this prediction is likely passable for our system for two reasons. The first reason is that the volumetric flow rate of gas was slow enough to prevent the gas space of TK01 from varying more than 1% of the initial pressure setpoint to drive salt flow. The second reason is that the change in salt volume in TK01 did not cause a large change in gas space volume per unit time. We can show this by the equation of continuity.

$$\frac{d}{dt}\left(\rho_{gas} V_{gas}\right) = \dot{m}_{in} - \dot{m}_{out} \tag{2.15}$$

During the salt transfer, argon is supplied to TK01,

$$\frac{d}{dt}\left(\rho_{gas}V_{gas}\right) = \dot{m}_{gas} \tag{2.16}$$

The density of the gas is expressed,

$$\rho_{gas} = \frac{P\mathcal{M}_{Ar}}{RT} \tag{2.17}$$

P is the pressure of the argon inlet, $\mathcal{M}_{Ar}$ is the molar mass of argon, R is the gas constant, and T is the temperature of the inlet gas. If we assume the gas added to the vessel is approximately constant temperature (since there is no heating on the inlet line),

$$\frac{d}{dt}\left(\rho_{gas}\right) = \frac{\mathcal{M}_{Ar}}{RT}\frac{dP}{dt} \tag{2.18}$$

Substitute this value back into Eq.(2.16) and expand the derivative by the product rule,

$$V_{gas}\frac{\mathcal{M}_{Ar}}{RT}\frac{dP}{dt} + \rho_{gas}\frac{dV_{gas}}{dt} = \dot{m}_{gas} \tag{2.19}$$

The first term on the left-hand side represents compressibility effects associated with transient pressure variation, while the second term represents volumetric displacement caused by the salt leaving TK01. For sufficiently small gas flow rates under pressure regulator control, the pressure variation in the gas space remains small relative to the operating pressure, i.e.

$$\frac{\Delta P}{P} \ll 1 \tag{2.20}$$

This relation is true over time, so we simplify the first term of Eq.(2.19) and reduce to the new form,

$$V_{gas}\frac{\mathcal{M}_{Ar}}{RT}\frac{dP}{dt} \approx 0 \tag{2.21}$$

$$\rho_{gas}\frac{dV_{gas}}{dt} \approx \dot{m}_{gas} \tag{2.22}$$

$$\frac{dV_{gas}}{dt} \approx \frac{\dot{m}_{gas}}{\rho_{gas}} = \dot{V}_{gas} \tag{2.23}$$

Since the increase in volume corresponds directly to the decrease in salt volume of TK01,

$$\frac{dV_{gas}}{dt} = \dot{V}_{salt} \tag{2.24}$$

We have thus proved our assumption in Eq.(2.14). We can generalize this result and realize that any transfer of incompressible fluid driven by a compressible fluid stream have approximately the same volumetric flow rate in and out of the system if the compressibility of the flow is negligible which is the case under small flow rates.

From the linear regression in Figure 14, we can also calculate the volume of the gas space in TK01. Given the initial pressure of TK01, the pressure required to initiate salt flow out of TK01, the volumetric flow rate of the argon gas into TK01, and the time at which the regression intercepts the starting mass, we can solve for total volume of the system. Integrating the ideal gas law during the pressurization period yields:

$$V_{covergas} = \dot{V}\Delta t \ln\left(\frac{P_{start}}{P_{end}}\right) \tag{2.25}$$

Where $V_{covergas}$ is the volume of the gas space in TK01, $\dot{V}$ is the volumetric flow rate, Δt is the time it takes to initiate flow in the system, P_{start} is the initial TK01 gas pressure, and P_{end} is the pressure to initiate flow out of TK01. For our system we calculate:

$$V_{covergas} = \left(1\frac{L}{min}\right)(1\ min)\ln\left(\frac{2\ bar}{1\ bar}\right) \approx 1.44\ L \tag{2.26}$$

Thermocouple data identified heater failures during shakedown and were subsequently analyzed using a lumped thermal-resistance/capacitance model representing heat input from the heating tape, transient heat storage in the vessel wall or transfer line, heat transfer to the internal salt or argon volume, and heat loss through insulation to the glovebox environment. The model reproduced the measured heat-up behavior at multiple thermocouple locations, with fitted parameters interpreted as apparent heat-transfer quantities rather than intrinsic material properties. This analysis provided a physics-based interpretation of the thermal transients and helped distinguish local heating behavior, insulation performance, and internal heat transfer limitations. During the transfer, the same thermocouple network captured transfer-specific signatures: the TT11 temperature spike marked salt entering the transfer line, while the TT04 temperature drop indicated cooling from the incoming argon cover gas. A 20 kg transfer into TK02A was measured gravimetrically with a slope of 2.088 kg/min, while the predicted transfer rate from argon volumetric displacement was 2.034 kg/min using FI01 and a 10% flow-meter uncertainty. The approximately 2.7% difference between the measured and predicted rates is smaller than the flow-indicator uncertainty, supporting the assumption that, under leak-tight and low-compressibility conditions, inlet gas volume can be used as a practical estimate of displaced molten salt volume. Conversely, when both gravimetric and gas-volumetric measurements are available, disagreement between the two becomes a leak, blockage, or inventory-drift diagnostic that could be implemented in supervisory controls for safety, operations, or safeguards-related inventory verification. The same pressure-flow logic also inferred a TK01 cover-gas volume of approximately 1.44 L, illustrating how transfer transients can be used to estimate liquid level or remaining salt inventory inside opaque vessels.

2.5 Design Evolution and Operational Lessons - Discussion

The transfer campaign consisted of multiple transfer attempts separated by periods of system modification and troubleshooting. While the initial objective was simply to transfer salt inventory, the development process revealed several important engineering principles that governed system behavior.

2.5.1 THERMAL CONTROL AS THE DOMINANT DESIGN CONSTRAINT

The first and second transfer attempts were unsuccessful because repeated heater failures prevented complete melting of the FLiBe inventory. Portions of the system remained below the required operating temperature. The third attempt was initially successful but ended with failure to partition the salt multiple times. Holcomb and Cetiner[16] state the operating temperature required should be approximately 100°C about the liquidous line. Sohal et al.[17] add the heuristic to always maintain a small amount of flow in the lines to prevent freezing. Our data shows when within 50°C of the liquidous temperature, even with constant flow of salt, freezing still occurred. It is maintained that both heating above the liquidous temperature and constant flow of salt are required to prevent freezing. In small diameter tubing (1/4" and less), thawing the salt was not a feasible option without taking extreme measures, such as using a torch to melt specific areas of the tube.

2.5.2 INSULATION PERFORMANCE AND HEAT LOSSES

Following the initial transfer attempt, significant effort was devoted to evaluating system heat losses and heater performance. During subsequent operation it became apparent that actual thermal losses were substantially greater than anticipated during the design phase. Gaps between insulation sections, complex geometries around vessel penetrations, and exposed hardware produced localized heat loss pathways that were not adequately represented by simplified thermal calculations. Thermal performance of the insulation was significantly lower than theoretical predictions. Our result agrees with Kearney et al.[18] showing the importance of having well-modeled heat loss data of lab scale equipment as well as pilot scale systems. The effective loss of heat due to small gaps between insulation and metal surfaces is shown by Robb[19]. Our result agrees as were able to reach liquidous temperature ins TK01 after we tightened the insulation around the system to avoid gaps between insulation and metal walls. This reinforces the importance of including discretized gaps between insulation and metal surfaces in modeling system heat losses. The importance of thermal continuity throughout the entire transfer pathway is corroborated by Yoder et al.[20], who observed persistent cold spots in the ORNL fluoride salt loop at the heat exchanger and externally mounted flowmeter, demonstrating that localized cold regions were the limiting factor and not overall heating power.

2.6 DESIGN OF MOLTEN SALT LOOP - METHODS

In the 1950s, Oak Ridge National Lab (ORNL) made a significant effort to study thermally driven corrosion and mass transfer from hot to cold legs of natural circulation loops as a part of the Aircraft Reactor Experiment (ARE). . In flowing salt systems, we see a separate corrosion phenomenon which occurs due to the bulk fluid temperature drop across the loop circuit. The complete mechanism for this corrosion phenomenon is complicated and requires further investigation. In MSRs and FHRs, large bulk fluid temperature drops occur over the core and heat exchanger systems and therefore are prone to experiencing loop corrosion.

There is growing interest in establishing a common method of designing molten salt loops so that test facilities can perform their own salt loop tests. Natural circulation molten salt loop design for corrosion and mass transport experiments[21], [22] allows facilities to operate scalable flowing experiments without the

expense of designing and procuring pumps[23] and turbomachinery to drive circulation. That is not to say design and operation of natural circulation loops is trivial, but it is comparatively straightforward.

Historically, facilities that operate molten salt loops have done so on a case-by-case basis, where each loop is uniquely designed and operates differently. Having a common method of design will enable more test facilities to build their own salt loop from standard research in literature. The design of natural circulation molten salt loops is slightly more restricted since desired flow rate and desired fluid temperature are coupled[24], unlike in pump driven systems which can set flow rates independent of temperature. For the purposes of establishing common design methodology, it is beneficial to have these natural circulation restrictions.

A natural circulation molten salt loop was designed by the SALT Research Group at UC Berkeley for the study of long-term corrosion behavior of SS316H in NaF-BeF_2 salt. Unique to the UC Berkeley salt loop design, the molten salt loop hot leg and cold leg section are designed to normally operate with a bulk fluid temperature difference of 170°C, with temperatures in the hot and cold leg of 620°C and 450°C, respectively. The loop is designed for up to 3kWth heat input and heat rejection within a closed Beryllium glove box under an Argon atmosphere. This is the first reported loop to be designed within the constraints of a glove box environment. Predicted flow rates are comparable to flow rates which were produced on similar natural circulation loops.

2.6.1 FUNCTIONAL REQUIREMENTS OF NATURAL CIRCULATION LOOP

Unlike natural circulation loops which are used for thermal hydraulic studies, this loop was intended for corrosion studies and thus had to meet different functional requirements compared to other loops found in literature. The conceptual design is shown in Figure 15. A key feature in this loop design is the ability to access a free liquid surface in both the hot and cold leg. The full list of functional requirements for this loop were previously discussed by Sclafani[25], but we include them in this work to benefit the reader's understanding of the differences between a loop designed for corrosion and electrochemical studies rather than thermal hydraulic studies.

Table 9. Functional Requirements for UCB Natural Circulation Salt Loop

Requirement	Specific Detail	Justification	Comments
Salt composition	The loop will run purified NaF-BeF_2 in a 57-43 mol% composition	This is a prototypical secondary salt composition for fluoroberyllate systems	
Hot leg temperature	The bulk fluid temperature in the hot leg must reach $T = 621$°C	This is a representative temperature of the hot side of a secondary heat exchanger design	

Cold leg temperature	The bulk fluid temperature in the cold leg must reach $T = 454$°C	This is a representative temperature of the cold side of a secondary heat exchanger design	
Fluid temperature gradient	The temperature gradient of the bulk fluid across the loop must be controlled $\Delta T = 167$°C for planned long-term corrosion test	Thermal gradient corrosion is the phenomenon of interest and is a control variable for corrosion studies in the loop	Achieving the hot and cold leg temperature requirements will be sufficient to meet the "as designed" configuration that ThorCon will care to study
Surface area to volume ratio (Φ)	The surface area to volume of the salt-facing material chosen from prototypical system designs $\Phi_{\text{hotleg}} = 450\ m^{-1}$ $\Phi_{\text{coldleg}} = 560\ m^{-1}$	Defining a scaled surface area to volume of pilot sized system	The "as-built" configuration is $\Phi_{\text{hotleg}} = 300\ m^{-1}$ $\Phi_{\text{coldleg}} = \text{TBD}$ (Cold leg Φ is TBD because there may be more/less corrosion specimen in the salt at startup)
Volume ratios of hot and cold legs	The volume of the salt in the hot and cold leg chosen from prototypical system designs $\text{V}_{\text{hotleg}}/\text{V}_{\text{coldleg}} = 2.5$	Defining a scaled volume ratio of pilot sized system	Isothermal piping parameters are not known. "As built" volume ratio is given from $\text{V}_{\text{hotleg}} \approx 3.5\ m^3$ $\text{V}_{\text{coldleg}} \approx 1.4\ m^3$ $\frac{\text{V}_{\text{hotleg}}}{\text{V}_{\text{coldleg}}} \approx 2.5$
Long-term Operation	The system will operate in flow conditions for 6 months with possibility of extending it to 24 months.	Interest to study long term ΔT corrosion should allow for flexible length of operation	

Materials	316H for all components in contact with the salt	Avoid corrosion driven by dissimilar materials in contact with the salt.	Small surface area interactions between 316L SS are permissible (e.g. TC probe tips, electrodes)
Redox probes	Electrochem probes will measure redox potential on the cold leg and the hot leg.		
Temperature probes	Measure $T_{b,hot}$ and $T_{b,cold}$ Temperature at the location of the redox probes. Temperature at the location of the corrosion coupons.		Probes must be placed where temperature change can be read axially and radially in the loop.
Corrosion Coupon Placement	Coupons are placed in four separate regions Heating region Isothermal hot region Cooling region Isothermal cold region	Aim to have coupon in all distinct heating and cooling regions in the loop	
Clearance from the glovebox walls	Maintain 6 inches of clearance between the system piping and the glovebox dimension	Allow for enough clearance in order to install and repair insulation	

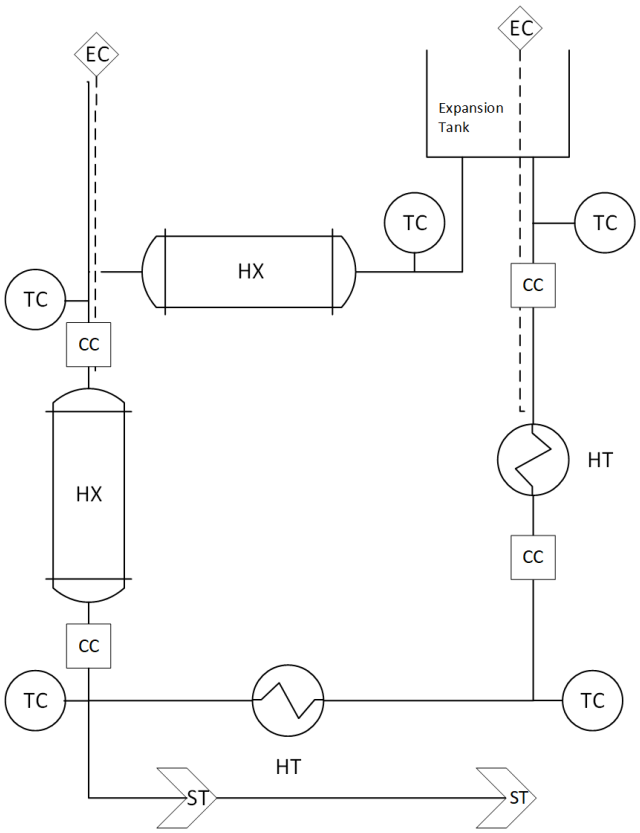


Figure 15. Concept design for the natural circulation loop including some interfacing instrumentation and corrosion specimen (see Table 10 for legend).

Table 10. Instrumentation and Equipment labeled in Figure 15

Instrument/Equipment	Symbol	Purpose
Thermocouples	TC	Measuring temperature at distinct regions of hot and cold legs
Redox Sensors	EC	Measuring redox potential of the salt at varying temperatures
Corrosion Specimen	CC	Samples to be removed from the loop during operation for corrosion characterization of welds
Transfer Lines	ST	Remove/add salt from the system depending on the operating mode of the loop
Heat Exchanger	HX	Reject heat from the loop to control recirculation rate
Heater	HT	Add heat to the loop to drive natural circulation

2.6.2 *MASS-ENERGY BALANCE*

This section estimates the heater power required to produce the target temperature drop across the natural circulation loop while maintaining a self-consistent salt mass flow rate. The calculation uses the natural-circulation momentum and energy balance relationships to related buoyancy driving force, pressure losses, loop geometry, and heat removal. By equating the mass flow rate predicted from the mechanical energy balance with the mass flow rate required to remove a specified heater power over a prescribed temperature difference, the required thermal duty of the loop can be determined. This provides a first-order design basis for selecting heater power, estimating circulation rate, and evaluating whether the proposed loop geometry can support the intended $\Delta T_h \approx 170\ ^\circ\mathrm{C}$ operating condition. Using the relationship derived in [24]:

$$m_{NC}^2 = 2\rho_0^2 g\beta \frac{\Delta z_{NC}\Delta T_h}{F'(Re)} \tag{2.27}$$

$$m_{NC,ss}^3 = \frac{2\rho_0^2 g\beta}{c_{p,h}} \frac{\Delta z_{NC} Q_h}{F'(Re)} \tag{2.28}$$

We can solve for the heater power, Q_h, as a function of temperature drop, ΔT_h, by setting the mass flow rate in each express to be equivalent.

$$m_{NC} = \sqrt{2\rho_0^2 g\beta \frac{\Delta z_{NC}\Delta T_h}{F'(Re)}} = \sqrt[3]{\frac{2\rho_0^2 g\beta}{c_{p,h}} \frac{\Delta z_{NC} Q_h}{F'(Re)}} \tag{2.29}$$

We assume $\Delta T \approx 170K$ by the design specifications. Other constituent equations for the frictional losses, F', and Fanning friction factor, f_F, are given in Eq.(2.30) and Eq.(2.31).

$$F'(Re) = C_n f(Re) = \left(\frac{1}{A^2}\frac{L}{D}\right) f(Re) \tag{2.30}$$

$$f_F \approx \frac{16}{Re} \text{ for } Re < 2100 \tag{2.31}$$

Pressure losses from bends, fittings, and cross-sectional expansion are captured by a length over diameter, L/D, which are inserted into Eq.(2.30) for each respective feature. The total pressure losses are summed before being used to calculate the mass flow rate in Eq.(2.29). The calculation is solved iteratively because the pressure losses are a function of the mass flow rate which is briefly discussed in Section 2.6.3. However, when the system is restricted to the laminar regime, we can solve the linearly independent system.

2.6.3 *PRESSURE LOSSES & PIPE SIZING*

Preliminary design calculations are performed by assuming an initial mass flow rate and choosing some pipe dimensions and lengths based on the functional requirements and design constraints of the system. Table 11 gives examples of the inputs to the equations listed in the method as well as their outputs, specifically the outputs m_{soln}, v, and ΔT.

Table 11. Example calculation table for effect of flow rate on pressure losses and dT

	Variable	First Iteration	Intermediate Iteration	Last Iteration
Physical properties	$m_{guess}\left(\frac{\text{kg}}{\text{s}}\right)$	0.1	0.1	0.1
	$\rho\left(\frac{\text{kg}}{\text{m}^3}\right)$	2071.1	2071.1	2071.1
	$\rho\beta\left(\frac{\text{kg}}{\text{m}^3 K}\right)$	0.37	0.37	0.37
	$C_{p,h}\left(\frac{\text{J}}{\text{kgK}}\right)$	2176	2176	2176
	μ (Pa s)	0.01765	0.01765	0.01765
Design parameters	pipe ID (m)	0.0158	0.0158	0.0158
	straight pipe Length (m)	1.524	1.524	1.524
	Δz (m)	0.305	0.305	0.305
	Q_h (kW)	1.6	3.0	8.0
Dependent variables	$m_{soln}\left(\frac{\text{kg}}{\text{s}}\right)$	0.00978	0.0134	0.0219
	$v\left(\frac{\text{cm}}{\text{s}}\right)$	2.41	3.30	5.39
	ΔT (K)	75	103	168

In the final iteration column, we find a Q_h value of 8 kW which gives a $\Delta T = 168K$ which is the target specification for this loop. This result is about 4 times larger than we expect to be easily manageable within the design constraints for the loop. However, we need to also account for parts of the circuit which are contributing to pressure losses. For example, including corrosion coupons, pipe bends, and expansion/contraction regions in the flow-through expansion tank all introduce frictional losses unaccounted for in Table 11. The fluid friction variables and geometric L/D losses are capture in Table 12 and Table 13. The data for the L/D values are given in Appendix B.1.

Table 12. Fluid Properties used in Natural Circulation Calculation

Variable	Units	Value	Formula/Correlation	Valid Ranges
Reynolds Number (Re)	--	11.27	Eq.(2.7)	always
friction factor (f_F)	--	5.6781	Eq.(2.31)	Re < 2100
Area L/D constant (C_n)	$\frac{1}{m^4}$	6.32E+09	Eq.(2.30)	always
friction coeff. (F')	$\frac{1}{m^4}$	3.59E+10	Eq.(2.30)	always
flow velocity (v)	$\frac{m}{s}$	0.00361	$\frac{m}{\rho A}$	always
vol. flow rate (V)	$\frac{m^3}{s}$	2.01E-06	vA	always

Table 13. Pressure Losses from Geometry of Loop

Variable	Units	Value	Formula/Correlation	Valid Ranges
type of fitting 1	-	90 deg Elbow: Regular Flanged	$\frac{L}{D}$	always
number of fitting 1	-	2		always
Eq Length fitting 1	m	2.40	$\left(\frac{L}{D}\right)nD$	always
type of fitting 2	-	Tee: Branch Flow Screwed	$\frac{L}{D}$	always
number of fitting 2	-	2		always
Eq Length fitting 2	m	3.46	$\left(\frac{L}{D}\right)nD$	always
Coupon frictional loses (L/D)	-	1500	$\frac{L}{D}$	always
Eq. Length Coupon Sections	m	39.97	$\left(\frac{L}{D}\right)D$	always
Total Equivalent Length	m	49.074	$\Sigma\left(\frac{L}{D_i}\right)D_i$	always

2.6.4 OPERATING PARAMETERS

As we narrowed in on a final mechanical design of the salt loop, we were able to solidify the calculation of predicted salt flow rate as a function of heater input with the restriction of $\Delta T = 167$°C. Table 14 shows the final operating parameters of the system.

Table 14. Operating parameters of the natural circulation salt loop

Variable	Units	Value
mass flow rate (actual)	kg/s	0.00420
average flow velocity (actual)	cm/s	0.4
closed loop salt inventory at T_{cold}	kg	3.804
total salt inventory (loop+tank)	kg	7.126
Δz	m	0.25
High Temp (T_{hot})	C	621
Low Temp (T_{cold})	C	454
Average Temp (T_{avg})	C	537.5
Temp Drop (ΔT)	C	167
Heater power (Q_h)	kW	1.5

Notably, there are interfacing systems with the salt loop which also have their own operating parameters. In particular, the heat exchangers for the cold leg of the loop will be operated independently from the heating system on the salt loop, but their performance and operation will impact the targeted performance of the

salt loop. To simplify the design of the loop, we include a separate section for the design of the heat exchangers and the heat rejection system from the glovebox.

2.6.5 METHOD OF CALCULATING FLOW

As we alluded to earlier, calculating the mass flow of the natural circulation loop at steady state can be a dynamic problem. The fluid friction terms are dependent on the velocity term which is dependent on the fluid friction. Additionally, the fluid friction terms are dependent on the viscosity which is dependent on the temperature which is dependent on the heater power which will affect the velocity, and this impacts the fluid friction term again. There are several ways the system can show non-linear behavior just by the dependencies of fluid friction and velocity. It is worth noting that with the restriction that the fluid is always laminar in flow and the fluid mass flow can be modeled in a 1-dimensional circuit, $m(x,t)$, then this system has a closed solution. However, it has proven to be helpful for rapid development to solve for the mass flow rate non-linearly through iterative "guess-and-check" calculations. The iterative method used for calculating the mass flow is given in more detail in Appendix B.4.and how we used the mass flow rate calculation to change the loop geometry in the design phase.

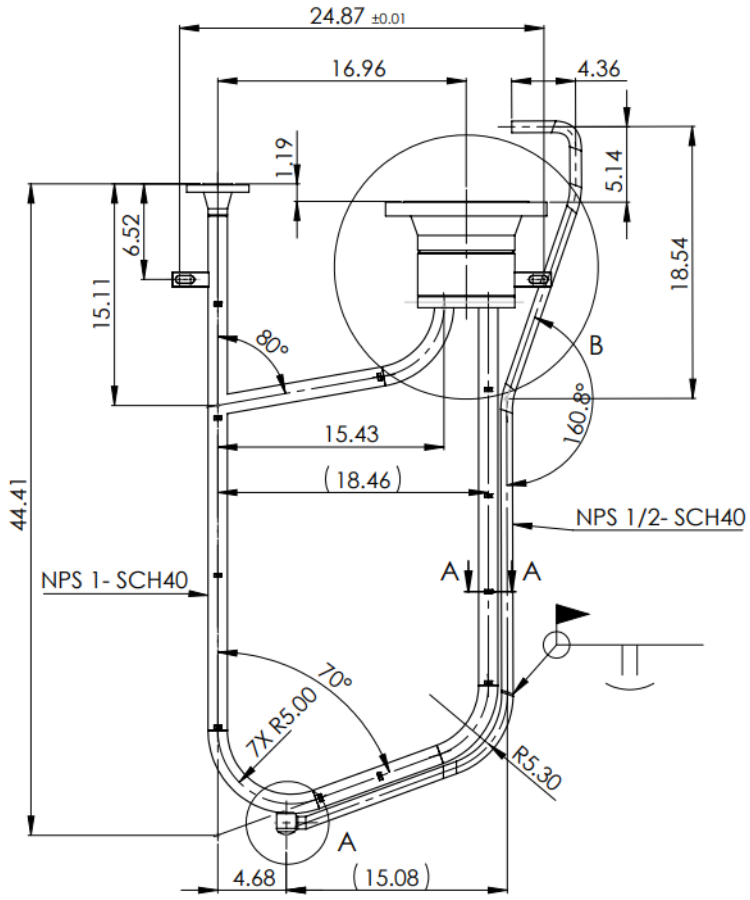


Figure 16. Solidworks drawings of the natural circulation loop assembly. Dimensions given in inches and degrees.

The final drawing of the salt transfer loop is given in Figure 16. The document with functional calculator is found at the group internal link: 28EG007v3 Natural Circulation Salt Loop Design Calculation.

2.6.6 HEAT EXCHANGER SIZING

Table 15. Functional Requirements for Salt Loop HX

Requirement	Specific Detail	Justification	Comments
Heat Removal	3kW steady-state cooling	Maintain the target hot-leg/cold-leg temperature difference	
Tube-side fluid temperatures	620oC salt inlet; 450oC salt outlet; $\Delta T_{b,loop}$ = 170oC	Specified in the salt loop functional requirements	
Shell-side cooling fluid	Argon cover gas to be used as coolant	Maintains compatibility with glovebox operation and avoids introducing additional fluids near the salt loop	Cooling performance depends on argon flow rate and glovebox heat rejection capacity
Tube-side OD	1” pipe OD (tube OD)	Matches the selected loop pipe geometry and defines available heat transfer area	Heat exchanger module must mechanically interface with the loop pipe
Location on salt loop	Placement on top cross-over bar and vertical cold leg (during operation at 3kW)	Removes heat from the cold region of the loop and supports the desired natural-circulation driving force	Cooling location affects both ΔT and effective elevation difference

Variable Cooling Load	Ability to change cooling load during operation, max cooling of 3.5kW	Allows adjustment of loop temperature difference and circulation rate during operation	May be achieved by changing argon flow rate, bypassing modules, or changing active cooling length
Variable Cooling Elevation	Ability to change cooling elevation (to change effective dz)	Natural circulation flow depends on the relative elevation of heat addition and heat rejection	
Shell-side coolant max temperature	Max air outlet temperature compatible with heat sink or lowest temperature rated component in flow	Protects glovebox components, blower, seals, filters, and heat exchanger interfaces from overheating	
Provide trace heating to sections of loop	HX must be removable or contain heating elements to allow for cold leg sections of pipe to be heating during filling/draining operations	Prevents salt freezing in cooled regions during startup, shutdown, and recovery operations	
Measure temperature tube-side and shell-side	Allow for internal and surface temperature measurements, both shell and tube side Total heat removal measurement from the shell-side and tube-side fluids	Enables calculation of heat removal and characterization of axial/radial temperature gradients	Temperature measurements must be taken at varying locations along the loop. Collect temperature data in the axial and radial dimensions $T = T(x,r)$

The heat exchanger is designed to be a shell which attaches on top of the salt loop by bolting the axial flanges together. The effective cooling length is 18in and it covers a 1NPS pipe, for a total of 74.3in^2 (0.0479m^2) effective cooling area per module. The salt loop can a maximum of one 18in and one 24in module. A schematic of the 18in module is shown in Figure 17. The inlet and outlet to each module are offset from perpendicular to the axis to spin the flow and allow for baffles to be introduced into future design revisions. The ends of each module will be filled with ceramic fiber insulation and fiberglass tape to

reduce gas passage. The axial flanges will be filled with the same insulation and tightened to reduce gas passage as well.

The salt loop HX uses Argon cover gas as coolant. The salt loop coolant gas loop is driven by an external recirculating blower for the glovebox ambient cover gas. The coolant gas is pulled from the ambient glovebox cover gas through the salt loop HX module inlet, through the length of the HX. The outlet of the salt loop HX modules go to the glovebox water-cooled HX to be cooled down to the controlled ambient glovebox temperature. The cooled gas is pulled back into the glovebox ambient by a variable speed blower. The maximum glovebox ambient temperature is 40ºC, and the loop is designed to return cover gas at 25ºC. Any excess hot cover gas is cooled by a second recirculating blower/glovebox HX not connected to the salt loop HX loop. The complete block flow diagram for the salt loop HX is shown in Figure 18.

The total salt loop HX is sized to cool 3kW thermal with 45SCFM of Argon gas flow and 42in of effective cooling length. The variable speed blower can easily provide 60SCFM of Argon gas flow which will allow for less effective cooling length and allow for modules to be varied to fit the desired experimental needs.

The glovebox HX is sized to cool 5kW thermal with cooling water. The specification sheet for this HX is provided in the reference files. If the outlet of the glovebox HX is hotter than expected, the optional chiller can be turned on to provide a sufficiently large ΔT for the HX.

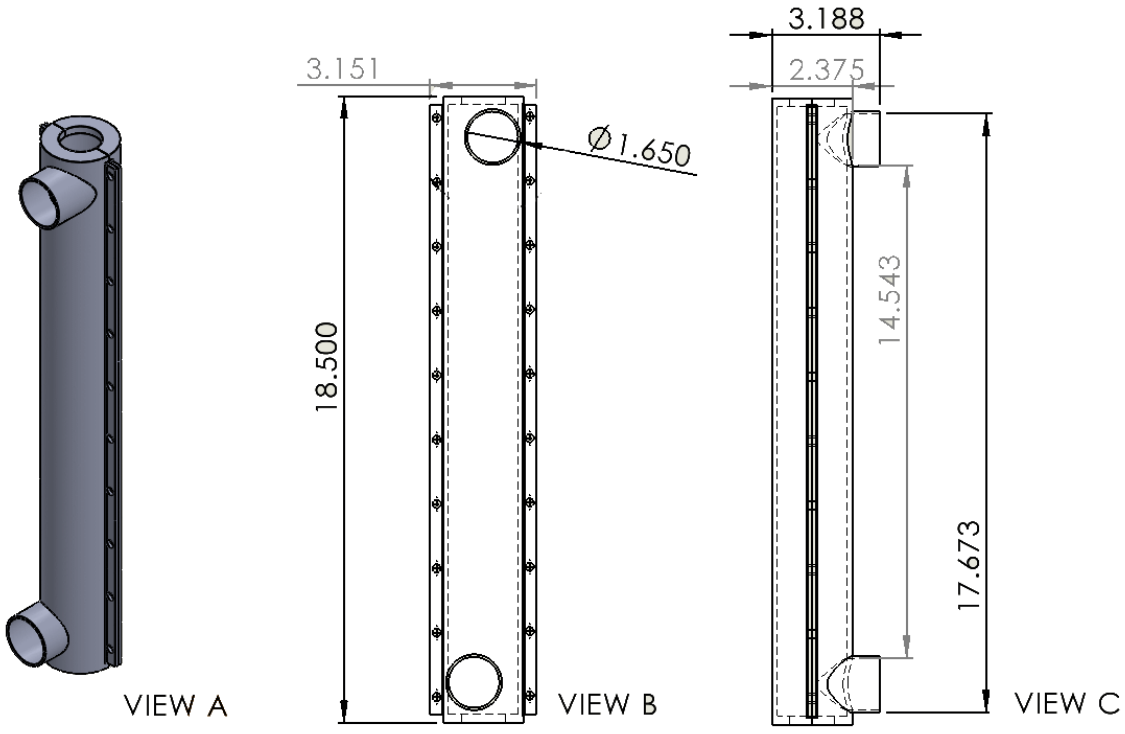


Figure 17. Heat exchanger design (dimensions given in inches)

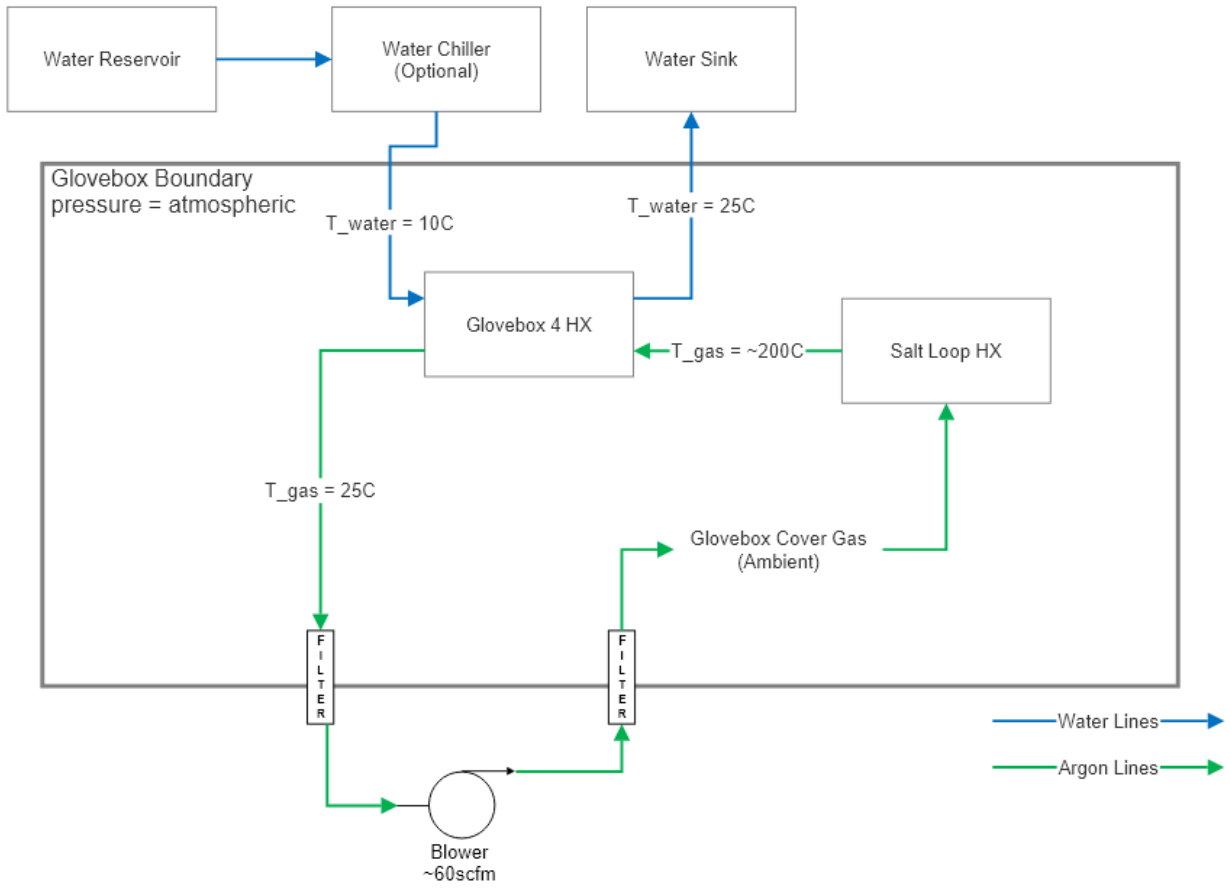


Figure 18. HX flow diagram for salt loop + glovebox interfaces

2.7 DESIGN OUTCOMES - RESULTS

The final design parameters were chosen after several iterations of running flow calculations, updating CAD drawings, and selecting system instrumentation and controls. Table 16 shows some of the final design choices that are present on our loop.

Table 16. Final Loop Design Parameters

Loop Parameter	Specifics	Notes
Dry mass of the loop	26 kg	The entire loop is made of SS316H where possible, and SS316L where not possible
Loop Circuit Pipe Selection	1NPS Sch.40	ID: 1.049 in. OD: 1.315 in. SS316H
Drain Straw Pipe Selection	1/2NPS Sch.40	ID: 0.622 in.

		OD: 0.840 in. SS316H
Salt Inventory	7.1 kg	Salt inventory accounts for salt in the loop circuit, the expansion tank, and the drain straw
Loop Internal Surface Area	0.30 m^{-1}	Calculated by taking the average surface area exposed to salt
Flow Rate at Steady State	0.4 cm/s	Very slow flow rate, will possibly be difficult for startup
Power Input	3 kW_{th}	Heating is provided by insulated heating tape or clamshell heaters

The complete fabrication documentation and control system design is covered by Sclafani[25]. Molten salt natural circulation has yet to be demonstrated in this loop. The final loop design represents a compromise between reactor-relevant corrosion conditions and the practical constraints of glovebox operation. The selected configuration uses a 26 kg dry SS316H/SS316L loop assembly, 1 NPS Schedule 40 loop piping, a 1/2 NPS Schedule 40 drain straw, approximately 7.1 kg of salt inventory, 3 kW thermal input, and a predicted steady-state flow velocity of approximately 0.4 cm/s. These parameters make the loop suitable for low-flow, thermally driven corrosion and redox-sensing studies, but they also identify the operating risks that must be managed before long-duration testing: low circulation velocity may complicate startup, heat rejection must be actively adjustable, and the system must remain recoverable during filling, draining, and off-normal cooling. Because natural circulation has not yet been demonstrated in this loop, the design outcome should be presented as a validated engineering design basis rather than as an experimentally proven operating envelope. The next experimental milestone is therefore to verify circulation, heat rejection, and salt recovery under molten conditions before using the loop for corrosion-product quantification or redox monitoring.

2.8 LESSONS LEARNED - CONCLUSION

This chapter presented a framework for the design of molten salt systems based on functional requirements, operational constraints, and the dominant physical phenomena under investigation. Molten salt systems were categorized as static, flowing, recirculating, and complex systems to provide a basis for relating experimental objectives to system architecture. The framework was applied to the design of a FLiBe salt transfer system and a natural circulation molten salt loop intended for corrosion, chemistry, and electrochemical sensing experiments.

2.8.1 SALT TRANSFER LESSONS LEARNED

Operation of the FLiBe transfer system provided several insights into the practical engineering challenges associated with molten salt handling. The transfer campaign demonstrated that first-order predictions of salt movement based on pressure-driven volumetric displacement were sufficient to describe system behavior during nominal operation. Throughout the transfer campaign, successful operation depended on

the ability to continuously maintain a molten pathway between vessels. Once the bulk salt inventory was molten, transfer reliability became governed by local thermal conditions within the transfer line, heater performance, electrical protection behavior, and the ability to recover from off-normal conditions.

As discussed in Section 2.4, the salt-transfer data show that inexpensive process measurements can provide both operational control and system diagnostics when they are interpreted together. Thermocouple data identified heater failures during shakedown, forecasted thermal response within 1% of the eventual steady temperature depending on location, and captured transfer-specific signatures. The lumped thermal capacitance model fit an apparent FLiBe thermal conductivity in the range of 0.04-0.19 W m^{-1} K^{-1}, which is an order of magnitude below the literature value. This indicates our system was experiences more thermal losses and resistance at the interfaces than we expected, ultimately lowering the efficiency of the heaters to be lower than 20%.

The TT11 temperature spike marked salt entering the transfer line, while the TT04 temperature drop indicated cooling from the incoming argon cover gas. The mass-transfer result is particularly important. A 20 kg transfer into TK02A was measured gravimetrically with a slope of 2.088 kg/min, while the predicted transfer rate from argon volumetric displacement was 2.034 kg/min using FI01 and a 10% flow-meter uncertainty. The approximately 2.7% difference between the measured and predicted rates is smaller than the flow-indicator uncertainty, supporting the assumption that, under leak-tight and low-compressibility conditions, inlet gas volume can be used as a practical estimate of displaced molten salt volume. Conversely, when both gravimetric and gas-volumetric measurements are available, disagreement between the two becomes a leak, blockage, or inventory-drift diagnostic that could be implemented in supervisory controls for safety, operations, or safeguards-related inventory verification. The same pressure-flow logic also inferred a TK01 cover-gas volume of approximately 1.44 L, illustrating how transfer transients can be used to estimate liquid level or remaining salt inventory inside opaque vessels.

2.8.2 Loop Design Lessons Learned

With the salt transfer experience, there are several operational challenges that may prove insurmountable with the current configuration of the salt loop. These challenges are numbered below.

1. Heating equipment failure
2. Electrical protection on heating load
3. Power distribution infrastructure
4. Planned loss of glovebox cover gas
5. Disassembly and end of life

During the salt transfer procedure, we noted the numerous heating tape failures that occurred during the shakedown tests and melting procedure. The source of the heating tape failures was never fully understood. There are two hypotheses for high frequency heating tape failure:

(i) Heating failure is a result of increased ductility of the heating elements as temperature increases. More ductile heating elements are thinned out with thermal stresses imposed by the system on the heating tape, and thinner section of heating elements have higher electrical

resistance causing them to heat faster than the rest of the tape. This is a positive feedback loop which would result in specific sections of heating tape under high mechanical stress breaking faster than the other sections.

(ii) While operating in an inert atmosphere, heating tapes never built up an oxide layer on the heating wire as temperatures increased. Then, as power was ramped and the system shifted under thermal expansion, heating wires came within a short enough distance for electrical current to jump the gap between each other or the metal surface of the system and short circuited the tapes.

Theory (i) is supported by the data provided in Figure 10 because the power delivered to the heating tape in this experiment was constant and only temperature was ramping. Because the temperature rapidly increased with a constant power transient, we suspect the heating tape resistance increased due to mechanical deformation. This data doesn't disprove theory (ii) but may suggest both theory (i) and (ii) occur concurrently.

To run a natural circulation molten salt loop continuously without heating equipment failure, it is non-negotiable that the heating tape infrastructure must be replaced with more robust heating solutions. These heating solutions can include mineral-insulated (MI) heating cable, MI heating bands, and radiative furnaces. Implementing these systems would require further structural design of the supports required to hoist the heaters and shakedown testing to determine the lifespan of the equipment. This work will be carried out in a glovebox, so replacement of equipment is long, arduous, and demoralizing for researchers.

Electrical protection on the heating load is already considered in the salt loop design. However, the problem that arises with the advent of electrical protection on the salt loop heaters is the leakage of current causing frequent GFCI breaker trips. The experience during the salt transfer revealed that small current leakage, even when there was no short circuiting of the heating load, would yield the GFCI breakers to trip. These are not new problems to the field of electronics and should reinforce the need for professional consulting and installation of electrical protection for the salt loop systems. There are standard practices to reduce the frequency of GFCI trips[26]. Some of the practices that will improve the system design are: 1) minimize the number of heaters connected to a single GFCI breaker, 2) reduce the ground cabling between the GFCI breaker and the heating load, and 3) avoid excessive moisture in the environment (such as liquid cooling or water spills).

Along with a redesign of the electrical protection on the salt loop heaters, the power distribution system for the salt loop needs to be reconfigured for sustainable operations. During the salt transfer procedure, power was distributed in the glovebox through 14AWG wire runs in feedthroughs made from KF-40 quick-clamp vacuum fittings. When inside the glovebox, the 14AWG power wire is installed in a DIN rail power brick with a standard 5-15 NEMA socket. Two operational hazards that become evident during the salt transfer shakedown tests were the unfastening of power wire from the DIN rail power bricks and the yanking of power cables from the NEMA sockets. Loosening the power wires and power cables presents an electrical hazard to the operators where they risk touching exposed leads that are energized. This hazard is already considered by professional engineering societies and a standard[27] exists for employing "strain relief" on electrical cabling. To improve the power distributing systems, power wires and cabling must be assembled

in the final configuration with appropriate strain relief to mitigate the risk of operators touching loose energized leads.

3. ELECTROCHEMICAL SENSOR DESIGN FOR MOLTEN SALT LOOPS

Electrochemical systems exist at the intersection of simultaneously complex phenomena. Effects from chemical thermodynamics, reaction kinetics, and transport phenomena must all be deconvolved when probing electrochemical reactions in a cell. Engineering procedures for electrochemical system and sensor design are still new to development[28], as compared to say mass-transfer operations like distillation. With the combination of molten salt thermochemistry and electrochemical engineering, refining and separation processes are made possible, such as the Hall-Héroult process used in aluminum production [29] and pyroprocessing of spent nuclear fuel [30], [31], [32]. Beyond chemical processing and separations, electrochemical systems also provide a powerful basis for *in situ* sensing and diagnostics. Electrochemical sensors exploit relationships between electrical response and chemical state to measure quantities such as species concentration, redox potential, impurity content, corrosion activity, and mass transport behavior [28], [33], [34].

In the modern fleet of nuclear power plants, electrochemical measurements have become a practical method of system health monitoring. Light-water reactors (LWRs) implement electrochemical sensors to quantify coolant chemistry, monitor corrosion-driving forces, and assess the susceptibility of structural materials to degradation mechanisms [35], [36], [37], [38], [39]. Measurements of electrochemical corrosion potential (ECP), dissolved oxidants and reductants, conductivity, and polarization resistance provide real-time indicators of the thermodynamic and kinetic conditions that govern material performance. These measurements establish a direct link between coolant chemistry and component integrity, enabling operators to manage corrosion risks through chemistry control and operational adjustments. As a result, electrochemical monitoring has positioned itself as a critical element of plant chemistry programs and safety management strategies.

The deployment of electrochemical monitoring in LWRs was driven by the need to predict and mitigate corrosion-related failures. Electrochemical corrosion potential emerged as a particularly important parameter because it provides a mechanistic connection between reactor water chemistry and environmentally assisted cracking [35]. The development of robust high-temperature reference electrodes and electrochemical probes [37], [39] enabled continuous measurements in reactor environments, allowing electrochemical data to be incorporated into predictive models of corrosion and component lifetime.

Molten salt reactors and other molten-salt-based nuclear technologies face many of the same challenges that motivate electrochemical monitoring in water-cooled reactors. MSR instrumentation frameworks emphasize (i) tracking evolving fuel salt composition for process history and control, (ii) monitoring dissolved structural alloy constituents as corrosion indicators, and (iii) measuring salt redox state because it is directly linked to corrosion risk and can evolve over time[40]. However, electrochemical monitoring of molten salt systems proves to still be difficult to implement often times owing to the design and implementation of the electrochemical sensors themselves. We seek to expand the knowledge and methodology for developing and characterizing electrochemical sensors for molten salt systems.

In designing electrochemical sensors, we must apply design constraints by considering:

1. Material compatibility with the process environment

2. Electrochemical regime (either neglect ohmic drop or neglect concentration gradients)
3. Physical dimensions of the electrodes and sensor components

Materials compatibility, as it was discussed in Chapter 0, presents difficult challenges again in the physical design of electrochemical sensors for molten fluoride salts. Following Newman's dichotomy of electrochemical systems, we constrain our electrochemical system to either study *convective-transport problems* or *potential-theory problems*[41]. When probing system of dilute electroactive analyte – systems that are discussed in Chapter 5 – we can neglect ohmic drop and ion migration and thusly design sensors which are more sensitive to convective transport. When probing systems which are well below the limiting current and therefore concentration gradient from the electrode to the bulk is negligible – systems that are discussed in Chapter 4 – we can design electrodes which are sensitive to the potential windows of concern. It is also possible to have a system where both convective transport effects and ohmic drop effects are occurring simultaneously, but the design of sensors to study such systems is predicated on understanding first how to design sensors which can operate in one regime or the other. Once the material selection is narrowed and the electrochemical regime is determined, physical dimensioning constraints can be applied.

The goal of this chapter is to show how one can apply the principles of design discussed in Chapter 0 to molten salt electrochemical sensors. Specifically, we want to design sensors which will be functional on prototypical molten salt system. We have a question – **how do we design an electrochemical sensor that will function in a molten salt loop?** And implicit to that question is the assumption we understand how to interpret the signals from our sensors. So also – **how do we interpret the electroanalytical response to recirculating salt?** The results from this chapter will build into research questions of Chapter 4 and Chapter 5 which focus on the application of the designed sensors.

3.1 Molten Salt Electrochemical Sensors - Introduction

Electrochemical sensors have been deployed in light water reactors (LWRs) for the purpose of monitoring and controlling the water chemistry. Several measurements made by electrochemical sensors in aqueous systems include in-situ measurements of boron concentration, dissolved gas concentration, redox potential, corrosion product concentration, hydrogen concentration, electrical conductivity, and corrosion rates of system components[42]. Due to the range of detection capabilities and ability to monitor in-situ, deploying electrochemical sensors in molten fluoride salt systems is one of the promising methods of continuous chemistry monitoring and control. In addition to monitoring and controlling redox chemistry, electrochemical sensors are being developed to detect early signs of material degradation from salt-wetted components. The design of an electrochemical sensor is specific to the desired functionality of the sensor. We consider the design of electrochemical sensors made for the following applications:

1. Redox potential control
2. Chemical quantification
3. Material health monitoring

Redox potential control systems are critical for the operation of MSRs and molten salt systems with a thermochemical gradient[43], [44], [45]. An integral part of a redox control system is the ability to take frequent, accurate, and reliable measurement of the redox potential of the melt. Chapter 4 is dedicated to

the techniques for electrochemical measurement of redox potential and the analysis of electrochemical redox potential sensing devices. The mechanical design work and validation of the data collected from electrochemical sensors is presented within this chapter.

Chemical quantification of major, minor, and trace constituents in the melt can be performed with electrochemical sensors. The methods of quantification may change depending on the concentration regime of the species of interest. For example, the quantification techniques in the weight percent concentration range will differ from those in the ppm concentration range, and both techniques may differ from the techniques applied in the sub ppb concentration range. The development of an electroanalytical quantification methodology is explored in greater detail in Chapter 5.

Material health monitoring performed by electrochemical sensors may occur directly (i.e. probing the degrading material) or indirectly (i.e. probing the salt interfacing with the material). The electrochemical sensing we will consider is that of indirect probing. Two designs of electrochemical sensors were considered for this work. Design 1 feature inert metal wire electrodes inserted in the melt as a probe. Design 2 featured printed inert metal electrodes on a silicon wafer inserted in the melt as chip sensors. Both designs feature inert metal directly exposed to the salt melt, but each offer particular benefits depending on the functional requirements of the system. Wire electrode sensors are discussed in Section 3.2. Printed electrode sensors are discussed in Section 3.5.

The electroanalytical techniques which will be used for redox monitoring and corrosion product quantification are discussed in Section 3.1.2. These techniques have been analyzed for static systems where flow is absent or negligible. In flowing systems however, the electrochemical response in the melt will not be diffusion limited, and more robust analysis is required to interpret the signal. While it is possible to solve the convection-diffusion problem with numerical methods, we indicate a parameter that shows in some cases the fluid flow analysis is ancillary. Additionally, we consider the design choice of conditioning the fluid flow around the electrodes. The development of predictable flow regimes would improve the repeatability of signal interpretation from our electrochemical sensor in flow.

3.1.1 Background on Molten Salt Electrochemical Sensors

3.1.2 Electroanalytical Techniques

The electrochemical sensor must support multiple electroanalytical techniques capable of quantifying different aspects of molten salt chemistry. No single electrochemical method can independently characterize redox state, corrosion products, impurity concentrations, and thermodynamic reference potentials. Consequently, the probe was designed to perform open-circuit potentiometry (OCP), chronopotentiometry (CP), cyclic voltammetry (CV), and square-wave voltammetry (SWV). These techniques provide complementary information regarding equilibrium thermodynamics, transient electrode behavior, reaction kinetics, and trace-species concentrations. In the following discussion of techniques, the functional forms of transient techniques describing potential or current originate from the solution to the diffusion equation in the absence of convective and electromotive transport,

$$\frac{\partial C}{dt} = D\frac{\partial^2 C}{\partial x^2} \tag{3.1}$$

Subsequent analysis of this equation in systems where convection or electromigrational transport are not negligible will yield different functional forms than what is described in the following section.

3.1.2.1 OPEN CIRCUIT POTENTIOMETRY

Open circuit potentiometry measures the equilibrium potential difference between a working electrode and a reference electrode in the absence of externally applied current. Therefore, the defining current of open circuit potentiometry is,

$$i_{OCP} = 0 \tag{3.2}$$

Under these conditions, the measured potential reflects the balance of oxidation and reduction reactions occurring at the electrode surface and can often be related to the chemical state of the melt through the Nernst equation, given in Eq.(3.3),

$$E = E^o + \frac{RT}{nF}\ln\left(\frac{a_{ox}}{a_{red}}\right) \tag{3.3}$$

OCP measurements can be used to monitor salt redox potential, changes in oxidation state, and deviations from system equilibrium following perturbations.

3.1.2.2 CHRONOPOTENTIOMETRY

Chronopotentiometry measures the potential response of an electrode subjected to an imposed current step. Therefore, the defining current of chronopotentiometry is,

$$i_{CP} = \text{constant} \tag{3.4}$$

The potential is thus a function of time, and we can use the trace of the potential curve to calculate a transition time for specific redox reactions. The functional form of the potential as a function of time for reversible reactions is,

$$E(t) = E_{\tau/4} + \frac{RT}{nF}\ln\left(\frac{\tau^{1/2} - t^{1/2}}{\tau^{1/2}}\right) \tag{3.5}$$

where τ is the transition time. Sand evaluated the transition time of reaction in terms of the diffusivity of reactants, bulk concentration, and current step [46] to solve in terms of transport parameters.

$$\tau = \pi D\left(\frac{nFC_b}{2i}\right)^2 \tag{3.6}$$

Eq.(3.6) is referred to as the Sand equation, D is the diffusivity of reacting species, n is the number of electrons in reaction, F is Faraday's constant, C_b is the bulk concentration of reactant in the solution, and i is the current density. CP is a technique which is useful for studying the mechanisms of electrodeposition

and dissolution. This will be discussed in greater detail when we examine the dynamic reference electrode (DRE) technique in Chapter 4.

3.1.2.3 CYCLIC VOLTAMMETRY

CV measures current while sweeping the electrode potential at a controlled scan rate. Therefore, CVs are defined by the potential as a function of time:

$$E_{CV}(t) = E_i + \nu t \tag{3.7}$$

For the work in this chapter, we will consider the current response for a Nernstian, or reversible, system without complicated kinetics. Importantly, the current response for reversible, quasi-reversible, and irreversible systems is always proportional to the concentration of reactant,

$$i(t) \propto C \tag{3.8}$$

where the proportionality is dependent on the kinetics of the system being studied. Sevcik[47] found a useful result for reversible systems which was able to equate peak current density in the potential wave to the diffusivity of reactant, bulk concentration of reactant, and scan rate of the potential wave.

$$i_p = 0.4463 C_b \sqrt{\frac{(nF)^3 D\nu}{RT}} \tag{3.9}$$

Eq.(3.9) is the Randles-Sevcik equation. It's modern derivation is provided by Bard and Faulkner [33] where i_p is the peak current density, ν is the potential scan rate, and all other variable take their previous meaning. The technique of CV provides a powerful and fast way of identifying potential windows of redox reactions, calculating diffusivities for a reactant, and measuring concentration of reactants. Many electrochemists adopt the CV as the primary tool of analysis, and this makes the technique suitable to be used as a benchmark in electrochemical studies for Echem Probe design.

3.1.2.4 SQUARE WAVE VOLTAMMETRY

Similar to CV, SWV measured current response with potential. SWV is unique in that the potential signal being generated is a superimposed square wave with a step wave, creating a discrete potential sweep which has the functional form,

$$E(t) = E_i + \Delta E_s \lfloor ft \rfloor + \Delta E_a \,\mathrm{sgn}(\sin(2\pi f t)) \tag{3.10}$$

where E_i is the initial potential, ΔE_s is the step potential being swept, ΔE_a is the amplitude of the square wave, f is the frequency of the wave, t is the time of the experiment, and sgn is the sign function. The current response is also proportional to the bulk concentration of reactant. The power of SWV is that it can be more sensitive to trace impurities in a system because the oscillating potential reduces the effect of the double layer capacitance at an electrode surface. The defining current response of SWV is,

$$i_{SWV} = i_f - i_r \tag{3.11}$$

Where i_{SWV} is the differential current density, i_f is the forward sweep current density, and i_r is the reverse sweep current density. While this technique boasts finer limits of detection than CV, it is not as widely used as CV yet and doesn't often serve as a satisfactory benchmarking tool on its own.

Table 17. Electroanalytical Techniques

Technique	Controlled Variable	Measured Variable	Primary Information
OCP	None (i=0)	Potential	Equilibrium redox state
Chronopotentiometry	Current Step	Potential vs. time	Diffusion, concentration, DRE formation
Cyclic Voltammetry	Potential sweep	Current	Redox behavior, kinetics, diffusion
Square-Wave Voltammetry	Pulsed potential	Differential current	Trace species quantification

Table 17 summarizes the defining features and utilities of the electroanalytical techniques. OCP measures thermodynamics, chronopotentiometry measures transient transport behavior, cyclic voltammetry measure's reaction mechanisms and kinetics, and square-wave voltammetry provides highly sensitive analytical detection. Together, these techniques enable comprehensive electrochemical monitoring of molten salt chemistry using a single probe platform.

3.2 ELECTROCHEMICAL LOOP PROBE DESIGN - METHODS

As discussed in Section 2.2, the prototypical molten salt system for nuclear applications will be a flowing system which may not ever reach thermodynamic equilibrium during operation. This development makes it challenging to interpret electrochemical data. There are two major dependencies that a designer must analyze prior to designing an electrochemical probe. Consider the following:

1. Redox species activity dependence with temperature
2. Current-potential response with flow

For material health monitoring, we aim to measure the concentration of corrosion products in the melt over time. Therefore, we care about a species activity dependence on temperature as the system will exist in a thermal gradient and the concentration of corrosion products will change throughout our system.

Electrochemical measurements involving a reaction are governed by Faraday's law,

$$r = \frac{I}{zF} \tag{3.12}$$

where r is the reaction rate, I is the total current, z is the number of electrons exchanged, and F is Faraday's constant. Flow around electrodes changes the transport of ions in the electrolyte which changes the current response of our sensor. Therefore, we care about the flow profile and how our sensor responds to flow.

This section highlights design calculations and considerations that were performed to fabricate our electrochemical loop probe which we will refer to as the "Echem probe."

3.2.1 FUNCTIONAL REQUIREMENTS OF ECHEM PROBE

The list of functional requirements for the Echem Probe are provided in Table 18. Some requirements were created for electrochemical analysis, such as measuring concentration of corrosion products, while others were created for mechanical fabrication, such as requiring gas seals and pressure communication.

Table 18. Functional Requirements of Echem Probe

Requirement	Specific Detail	Justification	Comments
Measure concentration of corrosion products in molten salt loop	Quantify the concentration of corrosion products in the hot and cold legs of a salt loop	This data is required to perform in real-time corrosion studies in a salt loop and relate the corrosion rate to the redox potential difference from the hot and cold leg	
Measure redox potential in molten salt loop	Potential window for measurements must access from beryllium reduction in FLiBe to oxygen evolution in FLiBe	These two redox reactions are used as a benchmark for internal references when measuring redox potential	
Thermodynamic reference electrode	The electrochemical probe must include a thermodynamic reference electrode for redox potential measurements	Including a thermodynamic reference reaction will allow for comparable redox potential measurements across different systems in literature, and it enables continuous redox monitoring	There will be backup plans in the event of the reference electrode failing mid operation

Gas sealed system	Holds a hermetic seal between the salt-facing side and the lab-atmosphere side		
Equalizes pressure	“Burps” overpressure and underpressure in the salt-facing vapor space that arises from temperature transients		
Measures temperature	The local temperature of the salt around the electrodes must be measured	Thermal gradients will be present in the system, and accurate temperature data will improve the accuracy of the interpretation of electrochemical data	In practice, it is possible to include a thermocouple in the Echem probe, but if this data is available without the inclusion of a thermocouple, we will use that instead to alleviate space constraint in probe
Minimum of two identical electrodes	The probe has at least two electrodes that are composed of the same material		
Conditions fluid flow around the electrodes	Condition the salt flowing around the electrodes to assume a flow profile which is replicable in multiple flow regimes		
Stable at operating temperatures	Operate the Echem probe at 700°C for the duration of the experiment, or until the end-life of the probe		

Salt pre-loading compatibility	The probe must have the ability to be pre-loaded with salt	Pre-loading the probe electroactive area with salt gas help with the system startup and avoiding gas bubbles being trapped around the electrodes	This requirement is somewhat dependent on whether the salt loop startup is tolerant to have some trapped gases
Calibrated surface area	Electroactive area on the probe must be measurable and can be calibrated during operation if needed	Without exact electroactive area measurement, the redox kinetics are not obtainable	

3.2.1.1 ACTIVITY DEPENDENCE WITH TEMPERATURE

When designing our Echem probe for detecting corrosion products in a recirculating salt system, we need to determine how sensitive our probe must be to detect a difference from the concentration of species in the hot and cold leg. From Section 2.6, we have shown the natural circulation loop operating temperatures in the hot and cold leg. Using these operating parameters, we'll estimate the concentration change of chromium in the melt with temperature. This section develops an order-of-magnitude estimate for chromium removal from the hot leg and chromium return or deposition in the cold leg of a non-isothermal NaF-BeF_2 molten salt loop. The calculation is intended to show effects of three separate cases:

(i) A global constant redox potential calculation
(ii) Instantaneous local equilibrium with non-constant redox potential
(iii) Thermal gradient mass transfer with finite wall response to bulk salt equilibrium

Case (i) is an internally consistent framework but may not represent the physical phenomena that occur in non-isothermal molten salt systems. Case (ii) follows a framework developed in [48] and intuits a graphical way to determine equilibrium concentration differences in chromium in a thermal gradient flow loop. Case (iii) explores the effect of including finite kinetics between the Cr in the metal phase and the Cr in the salt phase. The framework was originally developed in [22] and appears more consistent with the experimentally observed behavior of hot-leg chromium depletion and cold-leg corrosion-product deposition with respect to order of magnitude of the change. The numerical values below should be interpreted as a first-pass upper-bound estimate, not as a validated corrosion-rate model. The most important simplifying assumptions are that chromium activity in the alloy is approximated by the alloy chromium mole fraction, chromium diffusion in the alloy is approximated using a Cr-in-Ni diffusion correlation, the hot-leg surface chromium concentration can be driven toward a depleted boundary condition, and the salt-side mass-transfer resistance is not rate limiting. The input used in the calculations are given in Table 19.

Table 19. Inputs used in the chromium depletion calculation

Quantity	Symbol	Value used
Salt inventory	m_{salt}	7 kg
Salt recirculation rate	$\dot{m}_{salt}$	0.00416 kg/s
Hot-leg temperature	T_{hot}	621°C = 894.15 K
Cold-leg temperature	T_{cold}	454°C = 727.15 K
Initial dissolved chromium mole fraction	$x_{Cr,salt,0}$	5.24×10^{-4}
Chromium activity in metal phase	$a_{Cr,metal}$	$\approx x_{Cr,metal} = 0.185$
Hot-leg wetted surface area	A_{hot}	0.13 m^2
Cold-leg wetted surface area	A_{cold}	0.14 m^2
Approximate salt composition	–	57-43 mol% NaF-BeF_2
Approximate average salt formula mass	$\bar{M}_{salt}$	44.15 g/mol
Approximate alloy atomic density	C_{atoms}	1.45×10^5 mol atoms/m^3
Chromium molar mass	M_{Cr}	52.00 g/mol

Starting with a stainless steel loop, there is a passivating chromium oxide layer present on the material, usually on the order of 1-3 nm thick [49]. The Cr_2O_3 is passivating in aqueous systems where oxides have very low solubility and inhibit metal dissolution [50], but in fluoride salts, oxides generally have a less negative Gibb's free energy than their oxide counterpart and thus will readily dissolve by a dissociation reaction. Using the natural circulation salt loop dimensions, the assumed thickness of the Cr_2O_3 layer, we have between 0.0377 and 0.113 mol of Cr^{2+} in the melt, or approximately $x_{Cr,salt,0} \approx 5.24 \times 10^{-4}$. The inventory turnover time is calculated from the salt inventory and recirculation rate:

$$t_{cycle} = \frac{m_{salt}}{\dot{m}_{salt}} \frac{7 \text{ kg}}{0.00416 \text{ kg s}^{-1}} = 1.68 \times 10^3 \text{ s} \approx 28 \text{ min} \tag{3.13}$$

where t_{cycle} is the recirculation period of the coolant inventory, m_{salt} is the total mass of the salt inventory, and $\dot{m}_{salt}$ is the mass flow rate of the salt inventory. For the 57-43 mol% NaF-BeF_2 approximation,

$$\bar{M}_{salt} = 0.57 M_{NaF} + 0.43 M_{BeF_2} = 44.15 \text{ g mol}^{-1} \tag{3.14}$$

where $\bar{M}_{salt}$ is the average molar mass of the salt inventory and $\mathcal{M}_i$ is the molar mass of component i. The total moles of salt are,

$$n_{salt} = \frac{7000 \text{ g}}{44.15 \text{ g mol}^{-1}} = 1.59 \times 10^2 \text{ mol} \tag{3.15}$$

The chromium comproportionation reaction used to connect dissolved Cr^{3+}, dissolved Cr^{2+}, and metallic chromium is,

$$\frac{2}{3}\,Cr^{3+} + \frac{1}{3}\,Cr(s) \;\rightleftharpoons\; Cr^{2+} \tag{3.16}$$

The corresponding equilibrium constant is,

$$K_{Cr}(T) = \frac{a_{Cr^{2+}}}{(a_{Cr^{3+}})^{\frac{2}{3}}(a_{Cr})^{\frac{1}{3}}} \tag{3.17}$$

The sign convention used below is,

$$\Delta x_{Cr} = x_{Cr,h} - x_{Cr,c} \tag{3.18}$$

A positive value means the hot-leg equilibrium or outlet concentration is larger than the cold-leg value. This sign corresponds to the usual thermal-gradient direction of hot-leg chromium dissolution and cold-leg chromium deposition, provided the salt approaches local equilibrium with the wall.

The numerical values below use the Baes Cr^{2+}/Cr equilibrium [51] used in the accompanying graphical calculation,

$$\begin{aligned} x_{Cr,c} &= 5.24 \times 10^{-4}, \quad E_c = -3.637 \text{ V vs. } F_2/F^- \\ x_{Cr,h} &= 2.19 \times 10^{-3}, \quad E_h = -3.551 \text{ V vs. } F_2/F^- \end{aligned} \tag{3.19}$$

These values should be replaced if the final thermodynamic fit for the Cr^{2+}/Cr or Cr^{3+}/Cr^{2+} couple is revised.

(i) Constant Redox Potential Calculation

The first calculation imposes the same electrochemical potential in the hot and cold legs. This is a strong constraint and is not the same as assuming that the bulk salt composition is well mixed. The Nernst equation for a metal/metal-fluoride redox couple can be written as,

$$E(T) = E^{\circ}(T) + \frac{RT}{nF}\ln(a_{Cr^{2+}}) \tag{3.20}$$

with n = 2 for the Cr^{2+}/Cr couple. If the redox potential is artificially fixed at the cold-leg value,

$$E_{set} = -3.637 \text{ V vs. } F_2/F^- \tag{3.21}$$

then the cold-leg concentration remains,

$$x_{Cr,c} = \frac{5.24\times10^{-4}}{\gamma_{Cr^{2+}(T_c)}} \tag{3.22}$$

Using the hot-leg Nernst line at the same imposed potential gives,

$$x_{Cr,h}(E_{set}) = \frac{2.35\times10^{-4}}{\gamma_{Cr^{2+}(T_h)}} \tag{3.23}$$

Thus,

$$\Delta x_{Cr} = x_{Cr,h} - x_{Cr,c} = \frac{2.35\times10^{-4}}{\gamma_{Cr^{2+}(T_h)}} - \frac{5.24\times10^{-4}}{\gamma_{Cr^{2+}(T_c)}} = \frac{5.24\times10^{-4}}{\gamma_{Cr^{2+}(T_c)}}\left[0.448\frac{\gamma_c}{\gamma_h} - 1\right] \tag{3.24}$$

Suppose $\gamma \approx 1$ for all temperatures, then we would have,

$$\Delta x_{Cr} = -2.89 \times 10^{-4} \text{ or } \Delta m_{Cr} \approx -340 \text{ wppm Cr} \tag{3.25}$$

For a constant activity coefficient, Eq.(3.24) predicts that the Cr transport in the constant redox potential example will actually deposit in the hot leg and deplete in the cold leg. If the salt were forced to remain at a global constant potential while circulating through the temperature gradient, the sign of the calculated equilibrium driving force would favor chromium deposition or return to the metal in the hot leg and chromium dissolution in the cold leg. We can solve for a set potential at which the Cr^{2+} activity in the hot leg would equal the Cr^{2+} activity in the cold. Let E_{switch} be that potential, then we calculate it by,

$$E_{switch} = E_0 - \frac{\ln\left(\frac{x_{Cr,h}}{x_{Cr,c}}\right)}{\frac{2F}{R}\left(\frac{1}{T_h}-\frac{1}{T_c}\right)} \approx -3.772 \text{ V vs. } F_2/F^- \tag{3.26}$$

Therefore, only for imposed potentials more reducing than about -3.77 V vs. F_2/F^-would the constant potential calculation predict a larger dissolved chromium concentration in the hot leg than in the cold leg.

(ii) Instantaneous local equilibrium with non-constant redox potential

This case assumes salt is allowed to have a temperature dependent redox potential. The redox potential is then a dependent variable determined by the local temperature of local equilibrium conditions rather than a globally imposed constant. In the MSRE, the local equilibrium was set by the ratio of activities $a_{U^{4+}}/a_{U^{3+}}$ [52]which acts as a redox "buffer." Delpech et al. shows how one can use this redox buffer to calculate chromium depletion in the hot leg of a thermal gradient loop[48]. Following this method, let's assume we set a redox buffer of $a_{U^{4+}}/a_{U^{3+}}$,

$$Cr(s) + 2UF_4(l) \leftrightarrow CrF_2(l) + UF_3(l) \tag{3.27}$$

The equilibrium constant, K, is defined as a function of temperature,

$$K_{Eq.(3.27)}(T) = \frac{a_{CrF_2}a_{UF_3}^2}{a_{Cr}a_{UF^4}^2} \tag{3.28}$$

where a_i is the activity of component i. Therefore, we can write the activity of CrF_2 (the chromium in solution) as,

$$a_{CrF_2}(T) = K_{Eq.(3.27)}(T) a_{Cr} R^2_{\frac{U^{4+}}{U^{3+}}} \tag{3.29}$$

where $R_{\frac{U^{4+}}{U^{3+}}}$ is the ratio of activities of UF_4 and UF_3. Assuming ideal CrF_2 activity in the salt, the difference in equilibrium concentration of the hot and cold leg is,

$$\Delta x_{\mathrm{CrF_2}} = x^{eq}_{\mathrm{CrF_2},h} - x^{eq}_{\mathrm{CrF_2},c} = a_{\mathrm{Cr}}\left[K_{Eq.(3.27)}(T_h) - K_{Eq.(3.27)}(T_c)\right] R^2_{\frac{U^{4+}}{U^{3+}}} \tag{3.30}$$

Using Baes thermodynamic data[53], we set $K_{Eq.(3.27)}(T_h) = 2.65 \times 10^{-8}$, $K_{Eq.(3.27)}(T_c) = 4.94 \times 10^{-8}$. Let $a_{Cr} \approx x_{Cr} \approx 0.185$ in SS316, $R^2_{\frac{U^{4+}}{U^{3+}}}$ can vary from 10 to 100 as these ratios were identified as the limit of operations for MSRE. The resulting equilibrium concentration of Δx_{CrF_2} is plotted in Figure 19. The first pass of salt through the natural circulation loop predicts a mass loss range between 0.004 to 0.349 mg Cr. Depending on the depth of attack and the diffusion profile of Cr in the solid state alloy, this could significantly change the activity a_{Cr} which means the second pass of salt through the loop could predict a different mass loss calculation.

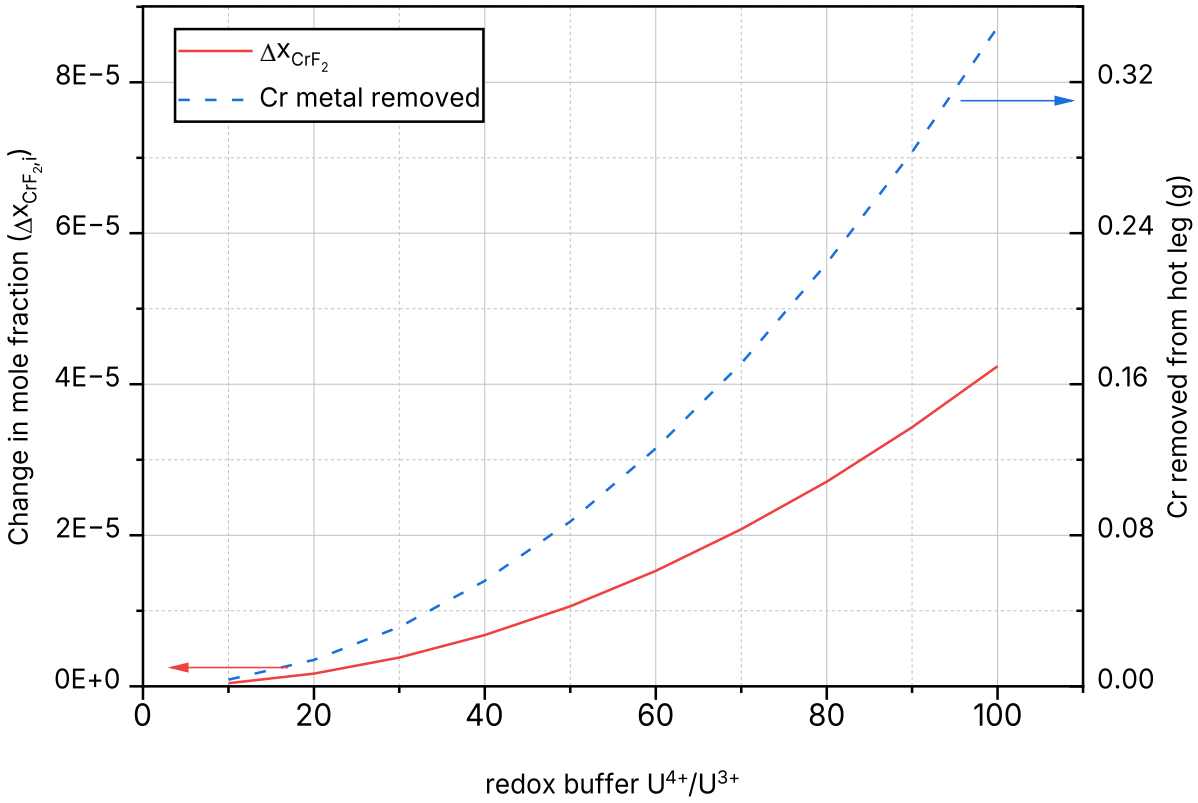


Figure 19. Chromium depletion from the hot leg in a thermal gradient loop operating at T_c = 454°C, T_h = 621°C, where redox buffer is set by the equilibrium defined in Eq.(3.27). Parameters used in the mass loss calculation are given in Table 6.

In our natural circulation loop, however, we do not have the ability to set a redox buffer with U^{4+}/U^{3+}, so we consider the case where the redox buffer is set by the Cr metal in the alloy. The disproportionation reaction, Eq.(3.31), sets the equilibrium concentration of Cr^{3+} in the melt. Its equilibrium constant is given in Eq.(3.32)

$$CrF_2(l) \leftrightarrow \frac{2}{3}CrF_3(l) + \frac{1}{3}Cr(s) \tag{3.31}$$

$$K_{Eq.(3.31)}(T) = \frac{a_{\mathrm{CrF_3}}^{2/3} a_{\mathrm{Cr}}^{1/3}}{a_{\mathrm{CrF_2}}} \tag{3.32}$$

Solving for the equilibrium CrF2 mole fraction, including a possible CrF2 activity coefficient, gives,

$$x_{\mathrm{CrF_2}}^{eq} = \frac{a_{\mathrm{CrF_3}}^{2/3} a_{\mathrm{Cr}}^{1/3}}{K_D(T)\gamma_{\mathrm{CrF_2}}(T)} \tag{3.33}$$

The hot-to-cold equilibrium ratio is therefore,

$$\frac{x_{CrF_2,h}^{eq}}{x_{CrF_2,c}^{eq}} = \frac{K_{Eq.(3.31)}(T_c)}{K_{Eq.(3.31)}(T_h)} \left(\frac{a_{CrF_3,h}}{a_{CrF_3,c}}\right)^{2/3} \left(\frac{a_{Cr,h}}{a_{Cr,c}}\right)^{1/3} \left(\frac{\gamma_{CrF_2,c}}{\gamma_{CrF_2,h}}\right) \tag{3.34}$$

The chromium thermodynamic data used in this calculation comes from HSC Chemistry 10,

$$\begin{gathered} K_{Eq.(3.31)}(454°\mathrm{C}) = 4.718 \times 10^{-3} \\ K_{Eq.(3.31)}(621°\mathrm{C}) = 6.886 \times 10^{-3} \\ \frac{K_{Eq.(3.31)}(T_c)}{K_{Eq.(3.31)}(T_h)} = 0.685 \end{gathered} \tag{3.35}$$

We can define a new parameter, Ψ, which is the grouped activity factor for this equilibrium.

$$\Psi = \left(\frac{a_{CrF_3,h}}{a_{CrF_3,c}}\right)^{2/3} \left(\frac{a_{Cr,h}}{a_{Cr,c}}\right)^{1/3} \left(\frac{\gamma_{CrF_2,c}}{\gamma_{CrF_2,h}}\right) \tag{3.36}$$

Now rewrite Eq.(3.34) with Ψ,

$$\frac{x_{CrF_2,h}^{eq}}{x_{CrF_2,c}^{eq}} = 0.685\Psi \tag{3.37}$$

We can now see that hot leg Cr dissolution will only occur when the left hand side of Eq.(3.37) is greater than 1, or when,

$$\Psi > \frac{1}{0.685} \approx 1.46 \tag{3.38}$$

While this result shows we cannot set a clear relationship between the Cr depletion in the hot leg with the equilibrium constant alone, it does give us insight into the underlying driving mass transport of Cr in the

loop. For Cr depletion in the hot leg, we can reason $\left(\frac{a_{Cr,h}}{a_{Cr,c}}\right)^{1/3} \leq 1$. So we can now reason that Cr depletion in the hot leg is constrained to,

$$\left(\frac{a_{CrF_3,h}}{a_{CrF_3,c}}\right)^{2/3} > 1.46\left(\frac{\gamma_{CrF_2,h}}{\gamma_{CrF_2,c}}\right) \tag{3.39}$$

This result shows that the equilibrium constant alone does not determine whether chromium is depleted from the hot leg. Because $K_{Eq.(3.31)}(T_h) > K_{Eq.(3.31)}(T_c)$, the chromium-only equilibrium predicts a lower hot-leg equilibrium CrF_2 concentration unless the combined activity term $\Psi > 1.46$. For hot-leg chromium depletion, $a_{\mathrm{Cr},h} \leq a_{\mathrm{Cr},c}$, so the required increase must come primarily from an increase in $a_{\mathrm{CrF_3}}$, a decrease in $\gamma_{\mathrm{CrF_2}}$, or an additional redox boundary condition. Therefore, the isolated $Cr/CrF_2/CrF_3$ equilibrium is insufficient to predict hot-leg dissolution and cold-leg deposition without further information about chromium speciation, activity coefficients, or an external redox buffer.

(iii) Thermal-gradient mass-transfer framework

The ORNL molten-fluoride corrosion literature describes thermal-gradient mass transfer as a coupled salt/alloy process. In a non-isothermal loop, the flowing salt is not in contact with a single equilibrium surface. Instead, it encounters metal surfaces at different temperatures. Because the chemical equilibrium for chromium dissolution depends on temperature, chromium can be selectively removed from hotter alloy surfaces and returned to or deposited on colder surfaces. DeVan and Evans explicitly formulated corrosion in fluoride salts in terms of thermodynamic driving forces and local equilibrium at salt-wetted metal surfaces, and they used a diffusion-controlled chromium migration model to interpret corrosion and mass transfer in INOR-8/Hastelloy-N systems[54]. Koger reported corrosion-product deposition in molten fluoride salt systems and described material removal in hot portions of loops and deposition in colder portions under temperature-gradient conditions[55], [56]. Modern summaries of the ORNL data similarly state that, in thermal-convection-loop tests, hot-side samples typically lost mass by chromium dissolution, while cold-side samples gained mass due to chromium deposition from the hot side[57]. The physical model can be described by calculating Cr activity in the following processes:

hot leg wall → chromium dissolution → flowing salt transport → cold leg deposition/return to hot leg

The ORNL-style first-pass estimate treats the hot-leg wall as a semi-infinite alloy in which chromium is initially uniform and then depleted at the salt-wetted surface. For one-dimensional diffusion with an initially uniform chromium concentration C_0 and a constant surface concentration C_s, the solution to Fick's second law is,

$$C(x,t) = C_s + (C_0 - C_s)\mathrm{erf}\left(\frac{x}{2\sqrt{Dt}}\right) \tag{3.40}$$

where $\mathrm{erf}(x)$ is the error function evaluated at x. The amount of chromium removed per unit surface area is obtained by integrating the concentration deficit:

$$\frac{n_{Cr}}{A} = \int_0^{\infty} [C_0 - C(x,t)]\, dx = 2(C_0 - C_s)\sqrt{\frac{Dt}{\pi}} \tag{3.41}$$

For an upper-bound hot-leg estimate, take the chromium surface concentration to be strongly depleted:

$$C_s \approx 0 \tag{3.42}$$

Then Eq.(3.41) becomes,

$$\frac{n_{Cr}}{A} \approx 2C_0\sqrt{\frac{Dt}{\pi}} \tag{3.43}$$

The initial chromium concentration in the alloy is approximated from the alloy chromium mole fraction and the total atomic density of the alloy:

$$C_0 = x_{Cr,metal} C_{atoms} = 2.68 \times 10^4 \text{ mol Cr m}^{-3} \tag{3.44}$$

For the chromium diffusivity, this estimate uses the Cr-in-Ni tracer diffusion correlation reported by Murarka for 600-900°C [58]:

$$D_{Cr/Ni} = 0.03\exp\left(-\frac{40800}{RT}\right) \text{ cm}^2 \text{ s}^{-1} \tag{3.45}$$

where $R = 1.987$ cal mol^{-1} K^{-1}. At 621°C,

$$D_{Cr/Ni}(621°\text{C}) = 3.19 \times 10^{-12} \text{ cm}^2 \text{ s}^{-1} = 3.19 \times 10^{-16} \text{ m}^2 \text{ s}^{-1} \tag{3.46}$$

Substituting into the semi-infinite diffusion expression, Eq.(3.43), for one inventory turnover, $t = 1683$ s, gives,

$$\frac{n_{Cr}}{A} = 2.22 \times 10^{-2} \text{ mol m}^{-2} \rightarrow \frac{m_{Cr,hot}}{A} 0.115 \text{ mg cm}^{-2} \tag{3.47}$$

For the hot-leg wetted area approximated by $A_{hot} \approx 0.14$, the total Cr lost from the metal and into the salt is approximately,

$$m_{Cr,hot} \approx 0.15 \text{ g or equivalently } x_{Cr,hot} \approx 5.42 \times 10^{-4} \tag{3.48}$$

Under the solid diffusion-limited framework, the rate of chromium removed from the hot leg is,

$$\dot{m}_{Cr} \approx 0.15 \text{ g } t_{cycle}^{-1} = 8.9 \times 10^{-5} \text{ g s}^{-1} \text{ or } 7.7 \text{ g per day} \tag{3.49}$$

We for this simplified case, we will assume the Cr added to the melt in the hot leg deposits in the cold leg and the final inventory of Cr is equal to the initial inventory at the beginning of the cycle. The Cr depletion estimate is intentionally conservative in the sense that it assumes a strongly depleted surface boundary condition. If the surface chromium concentration is not driven to zero, the result should be multiplied by the depletion factor,

$$f_{dep} = \frac{C_0 - C_s}{C_0} \tag{3.50}$$

so that,

$$m_{Cr,hot} = 0.15 f_{dep}\ \text{g} \tag{3.51}$$

This result should be interpreted as an order-of-magnitude estimate. It is most appropriate for explaining why thermal-gradient loops can sustain hot-leg material removal and cold-leg return/deposition even when the bulk salt is rapidly mixed. It should not be interpreted as a validated corrosion-rate prediction until the chromium activity coefficient in NaFBe, the actual chromium-containing dissolved species, the alloy-specific chromium diffusion coefficient, the salt-side mass-transfer coefficient, and the experimentally measured chromium concentration profile around the loop are well defined. We can still use this framework to explore what expected Cr mass transport behavior may look like in our experimental facility.

(iv) Plot of expected activity of Cr in non-isothermal loop

Using the case where we set an external redox buffer, U^{4+}/U^{3+}, we calculate the equilibrium concentration in the salt at every point in the loop. Our simplified model can assume $\gamma_{Cr}(T) = 1$, and x_{Cr} can be easily computed over the hot, cold, and isothermal regions. Assuming the solid phase Cr diffusion lags behind the equilibrium composition of the salt, we include a first order "lag model" for the true activity of Cr in the flowing salt. Let ξ be the normalized loop location parameter, where ξ varies from 0 to 1, the regions $[0,25)$, $[0.25, 0.50)$, $[0.50, 0.75)$, and $[0.75, 1.00]$ correspond to the heating, isothermal hot, cooling, and isothermal cold regions, respectively. The lag is modeled,

$$\frac{da_{Cr,bulk}}{d\xi} = k_{lag}\left(a_{Cr}^{eq} - a_{Cr}^{bulk}\right) \tag{3.52}$$

where k_{lag} is a lag constant which functions as an empirically fit parameter capturing the kinetics of Cr solid-state transport to the surface of the metal and Cr dissolution kinetics. The plot of equilibrium Cr mole fraction and actual salt Cr bulk composition is shown in Figure 20. The normalized position around the loop is broken into four equal regions of heating, isothermal hot, cooling, and isothermal cold. The local equilibrium curve describes the instantaneous salt equilibrium. The k_{lag} curves show bulk dissolved chromium mole-fraction profiles produced by an empirical lag equation. Larger k_{lag} values approach the local-equilibrium curve more closely, while smaller k_{lag} values produce greater lag through the heating and cooling regions. Regions where the bulk concentration is below the local equilibrium concentration favor chromium dissolution from the metal, whereas regions where the bulk concentration exceeds the local equilibrium concentration favor chromium deposition or return to the metal surface. Graphically, this implies the k_{lag} traces will always "approach" the local salt equilibrium line. From a control theory perspective, k_{lag} is a proportional gain which can be tuned to match the kinetics of the experimental data. We can determine the viability of this model using electrochemical quantification of Cr *in-situ* during natural circulation loop operations.

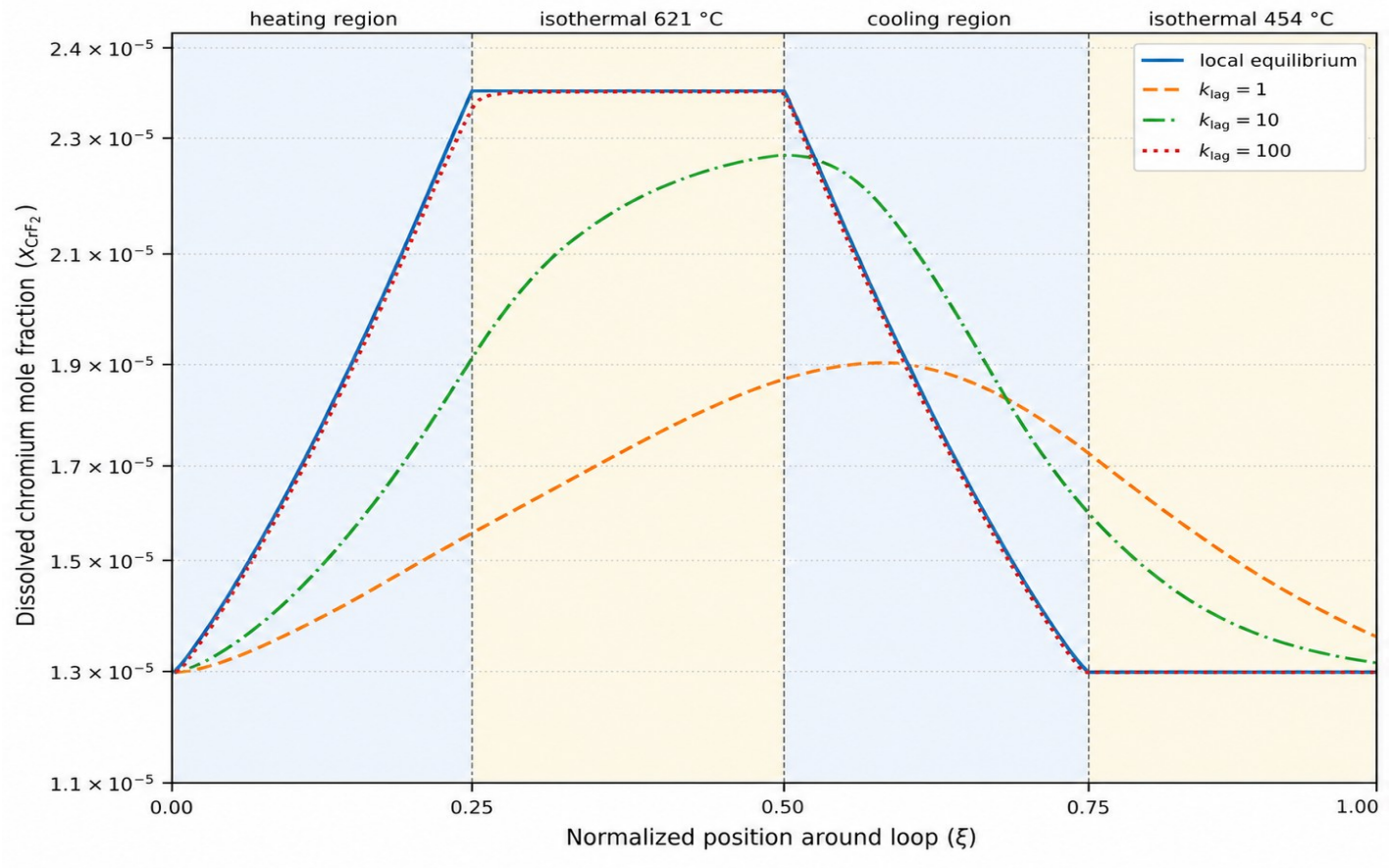


Figure 20. Cr concentration profile across non-isothermal loop with instantaneous local salt equilibrium and solid diffusion lag model assuming $a_{U^{4+}}/a_{U^{3+}} = 50$ redox buffer. 1-D model assumes fully mixed flow at every point in the normalized position. k_{lag} is an empirical parameter that describes the lumped effect of Cr solid state diffusion to the wall surface and Cr dissolution/deposition kinetics (assuming the kinetics of deposition are faster than dissolution).

3.2.1.2 Current-potential Response with Flow

With flowing systems, the electrochemical response is dependent on the velocity profile of the flow simply because the concentration profile of the fluid is also dependent on the velocity profile. All convective transport problems begin first with the assumption that ionic migration is negligible, and the continuity equation of the system becomes,

$$\boldsymbol{N}_i = -D_i \nabla c_i + \boldsymbol{v} c_i \tag{3.53}$$

$\boldsymbol{N}_i$ is the net flux density of species i, D_i is the diffusivity of species i, c_i is the concentration of species i, $\boldsymbol{v}$ is the velocity vector in 3-space, and ∇ takes is canonical definition of the gradient operator. We now write our material balance,

$$\frac{\partial c_i}{\partial t} = -\nabla \cdot \boldsymbol{N}_i + R_i \tag{3.54}$$

R_i is the bulk reaction rate of species i, usually contributing to homogenous reactions in the solution. In most of our applications this term can be ignored. Combining the two equations and assuming D is not a strong function of concentration we have,

$$\frac{\partial c_i}{\partial t} = D_i \nabla^2 c_i - \boldsymbol{v} \cdot \nabla c_i \tag{3.55}$$

Simplified *convective-transport problems* have been studied for rotating disk systems [59], [60], Poiseuille flow in tubes [61], annular regions [62], [63], [64], force convection of diffusion layers [65], [66], and natural convection of diffusion layers [67], [68]. In our design, we have a particular interest in understanding the dominating effect between forced convection and natural convection. It is well documented that molten salt electrochemical systems experience natural convection due to the thermal gradient in cells [69]. However, in a molten salt loop with flow driven by a pump, force circulation of the salt is going to contribute to the velocity profile across the electrode surface. Hence, conditioning the flow around the electrodes is a functional requirement.

For example, consider chronopotentiometry without and with the presence of mixing. Kontturi et al. [70] show the concentration profile of a cation being reduced by a constant current without the presence of mixing will take the value:

$$c(0,t) = c^b \left[1 - \sqrt{\frac{t}{\tau}}\right] \tag{3.56}$$

$c(0,t)$ is the concentration of cation at the surface of the electrode, c^b is the bulk concentration of the cation, t is the time of imposed current, and τ is the transition time defined in Eq.(3.6). This is compared to the same system with the presence of mixing which Kontturi et al. [70] have also solved analytically:

$$c(0,t) = c^b \left(1 - \sqrt{\frac{t}{\tau}} \left[1 + 2\sqrt{\pi} \sum_{n=1}^{\infty} (-1)^n \text{ierfc}\left(\frac{n\delta}{\sqrt{Dt}}\right)\right]\right) \tag{3.57}$$

δ is the thickness of the boundary layer, ierfc is the semi-integral of the complement of the error function, and all other variables take their normal definitions. The plots of surface cation concentration are shown in Figure 21 with input parameters: imposed current, $i = -7.72 \times 10^{-5}$ A/cm^2; limiting current, calculated from $i_L = -\frac{nFDc^b}{\delta} = 9.65 \times 10^{-5}$ A/cm^2; diffusivity, $D = 10^{-5}$cm^2/s; electrons transferred, $n = 1$; bulk concentration, $c^b = 10^{-6}$mol/cm^3. The time evolution of the concentration profile in the presence of mixing develops faster than the profile without mixing because the boundary layer thickness is less than the diffusion layer thickness leading to a decreased equilibration time. In this system, the applied current is less than the limiting current which results in a potential plateau in the presence of mixing. This observation is critical for a system which relies on establishing a specific cation reduction as a reference potential, such as a beryllium dynamic reference electrode (BeDRE) or potassium dynamic reference electrode (KDRE). An even more complicated problem can arise when a system supplies current above the limiting current of a reaction. As the boundary layer around the electrodes refreshes with cations less high redox potentials, i.e. are easier to reduce the analyzed cation, the apparent reduction potential of the analyzed cation will

shift anodically proportionally to the activity. This situation would occur in a molten salt system with recirculation and a constant inventory of corrosion products. Importantly, without prior knowledge of the concentration of corrosion products, the anodic shift in reduction potential of the reference cation, say beryllium in FLiBe or potassium in FLiNaK, could not be quantified. Therefore even with a perfect model for a system with mixing present, the measured equilibrium potential cannot be directly attributed to one specific redox couple using a constant current step.

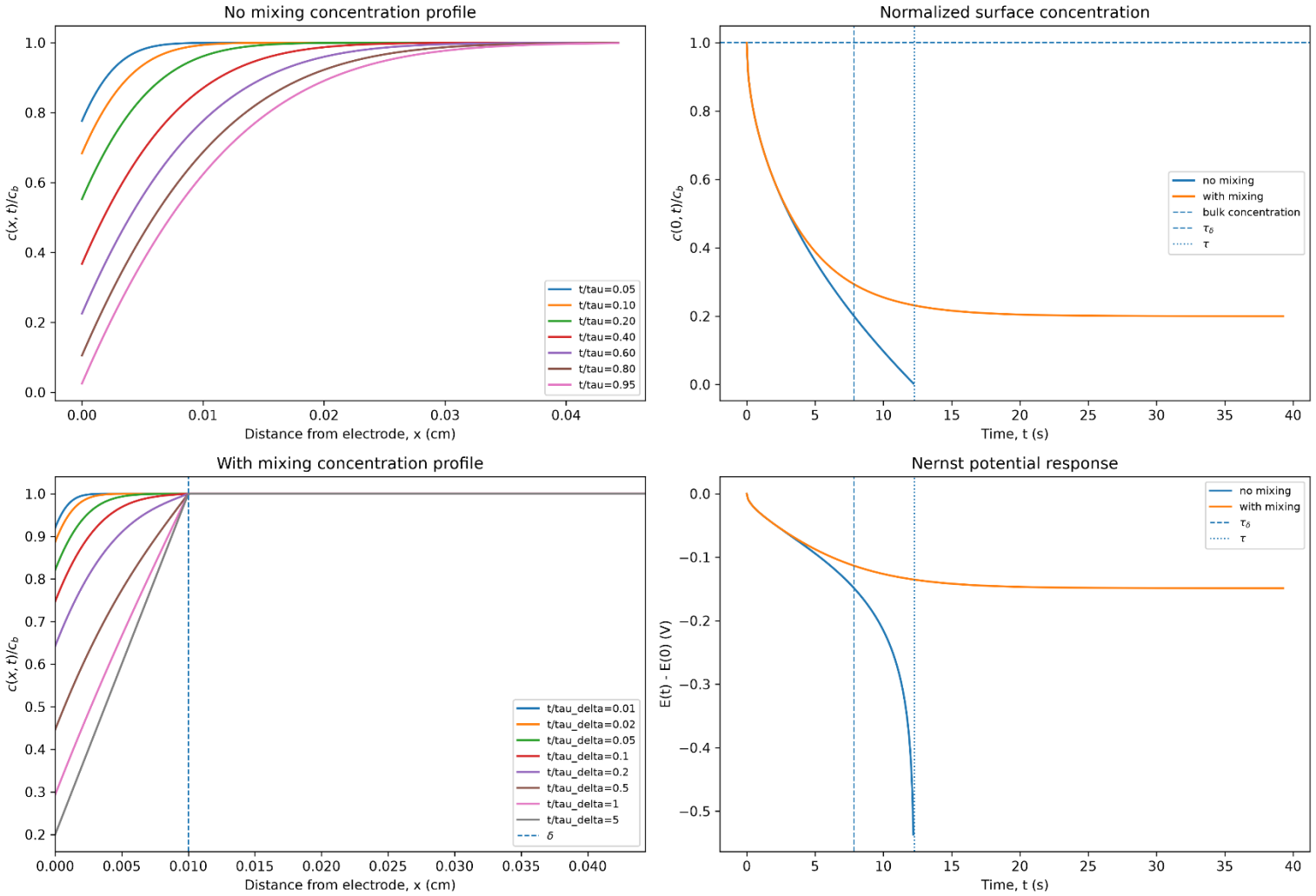


Figure 21. Concentration and potential dependence with and without boundary layer mixing. input parameters: imposed current, $i = -7.72 \times 10^{-5}$ A/cm²; limiting current, calculated from $i_L = -\frac{nFDc^b}{\delta} = 9.65 \times 10^{-5}$ A/cm²; diffusivity, $D = 10^{-5}$cm²/s; electrons transferred, $n = 1$; bulk concentration, $c^b = 10^{-6}$mol/cm³.

Another insight we can gain from Figure 21 is that there exists a timescale where the potential response in the presence of mixing nearly matches that of a system without mixing. Letting τ_δ be the time it takes for a cation to reach the electrode from the surface of the diffusion layer, for experiments where $t \ll \tau_\delta$, there is virtually no difference between the potential response in with and without mixing. Therefore, we can design sensors to operate in the regime where the reaction time occurs faster than the diffusion layer can be

replenished by mixing. With this heuristic, we branch into two separate design philosophies: (i) design a sensor which is robust enough to handle large current density to increase the reaction kinetics, or (ii) design a sensor which limits the total electroactive surface area to effectively shorten the diffusion layer to never be affected by the boundary layer mixing. We pursue both designs independently, discuss the validation of each design, and review the lessons learned from each design.

3.2.2 MECHANICAL DESIGN OF THE ECHEM PROBE

The electrochemical probe (henceforth referred to as the "Echem probe") developed for the neutron-irradiated FLiBe loop underwent multiple design iterations between 2022 and 2024, progressing from conceptual probe layouts and laboratory-scale electrochemical cells toward a fully fabricated engineering-scale probe suitable for integration with the MIT molten salt loop. Early design efforts focused on identifying the electrochemical techniques, electrode configurations, and materials required to support redox monitoring, corrosion studies, and tritium transport measurements in flowing molten fluoride salts. Initial conceptual studies considered both three-electrode and four-electrode probe configurations utilizing combinations of graphite, platinum, gold, molybdenum, glassy carbon, and thermodynamic reference electrodes (TREs) based on fluoride-compatible ionic couples. These studies also established the need for electrically insulated feedthroughs, high-temperature sealing methods, and stable reference electrode architectures capable of operation in chemically aggressive fluoride salts.

The first engineering concepts emphasized the integration of the probe within a forced-circulation molten salt loop while minimizing disturbances to the local hydrodynamic environment surrounding the electrodes. Early CAD concepts positioned the probe within the junction of a horizontal tee-section of the loop to promote relatively laminar local flow conditions. To further isolate the electrochemical measurements from large-scale loop turbulence, the electrodes were enclosed within a small sampling cavity supplied through a bypass flow arrangement. This geometry was intended to expose the electrodes to a quasi-static salt volume while still maintaining chemical communication with the primary circulating salt inventory. The design also accounted for the comparatively large dimensions of the thermodynamic reference electrode, which required enlargement of the vertical probe tube relative to the surrounding loop tubing.

In parallel with the mechanical probe development, substantial effort was directed toward development of stable thermodynamic reference electrodes for molten fluoride salts. Initial reference electrode concepts were derived from prior Ni/Ni(II)-based fluoride salt reference electrodes utilizing boron nitride (BN) housings and LaF_3 ionic membranes. Subsequent iterations explored Ag/Ag^+-based thermodynamic reference electrodes (AgTRE) in order to improve stability and reduce potential drift associated with changing salt composition within the reference compartment. Some challenges with the AgTRE design are discussed here, and more electrochemical analysis is presented in Chapter 4.

As the probe matured toward its final engineering configuration, the design increasingly incorporated features intended specifically for long-duration loop operation. A stainless-steel flow conditioning "shield" was added near the probe tip to redirect salt flow and attempt to regulate convective disturbances near the electrode surfaces. The thermodynamic reference electrode housing was refined using BN spacer stacks containing five wire-routing channels, one of which incorporated a reduced-diameter LaF_3-coated channel

filled with NiF_2-saturated FLiBe and a Ni wire electrode. This configuration allowed simultaneous electrical isolation, ionic conductivity, and structural support within a compact high-temperature assembly.

3.2.2.1 FABRICATING BN CAP WITH LaF_3 MEMBRANE

When using LaF_3 as an ionic membrane for a TRE, it must be considered that some of the membrane will dissolve in the FLiBe. These calculations are performed to determine the maximum mass of lanthanum fluoride that will be solvated in FLiBe so we may determine a lower limit of material required to fabricate the design. Additionally, we calculate the dimension change expected from the maximum loss of lanthanum in order to ensure the wall of the lanthanum fluoride layer is thick enough to maintain an ionic membrane at a maximum operating temperature of 700°C.

Key metric(s) to be computed:

1. Mass of lanthanum solvated in the reference electrode salt bath. $\left(m_{LaF_3(d)}\right)$
2. Minimum wall thickness to withstand long term exposure to a specified quantity of molten FLiBe. (y_{min})

Previous reference electrode designs would use a LaF_3 single crystal disk which has dimensions diameter, $d = 6$ mm, and height, $h = 5$ mm. This LaF_3 single crystal would be far too large for this design. Mass of lanthanum solvated in FLiBe at equilibrium can be calculated if an equilibrium solubility of lanthanum in FLiBe is known for a range of given temperatures. The formula used for this calculation is given by Eq.(3.58),

$$m_{LaF_3(d)}(T) = s_{LaF_3,FLiBe}(T) \cdot m_{FLiBe}(T) \tag{3.58}$$

The mass of FLiBe used in the reference electrode cup is calculated using the dimensions of the cup *without* LaF_3 in the cup. We don't consider the volume of the cup with LaF_3 because this would be a smaller volume of salt and thereby a smaller amount of LaF_3 could dissolve in the reduced salt volume. We are performing a conservative calculation erring on the side of more LaF_3 dissolving in the salt.

$$m_{FLiBe}(T) = \rho_{FLiBe}(T) \cdot V_{RE} \tag{3.59}$$

$$V_{RE} = \pi r_{RE}^2 h_{RE} \tag{3.60}$$

The mass of solvated lanthanum is assumed to be consumed uniformly across the inner surface of the reference electrode cup and assume the thickness of the cup decreases uniformly across the inner surface. We can calculate the thickness of material removed from the inner surface of the reference electrode cup by first computing the volume loss and then solving for the wall thickness which corresponds to this volume.

$$m_{LaF_3(d)} = \rho_{LaF_3}(T) V_{LaF_3}(y) \tag{3.61}$$

First calculations assume the density of LaF_3 is constant from the given properties data. A second pass calculation will account for a density as a function of temperature. We can simplify the calculation by assuming all the deposited LaF_3 grows from the bottom of the BN cup vertically, as depicted in Figure 22. This would lead to a conservative estimate of the minimum LaF_3 wall thickness required to prevent the

reference electrode salt from dissolving the LaF_3 wall and exiting the reference electrode. The volume of the disk of LaF_3 which would be dissolved is given below.

$$V_{LaF_3}(y) = \pi r_{RE}^2 y \tag{3.62}$$

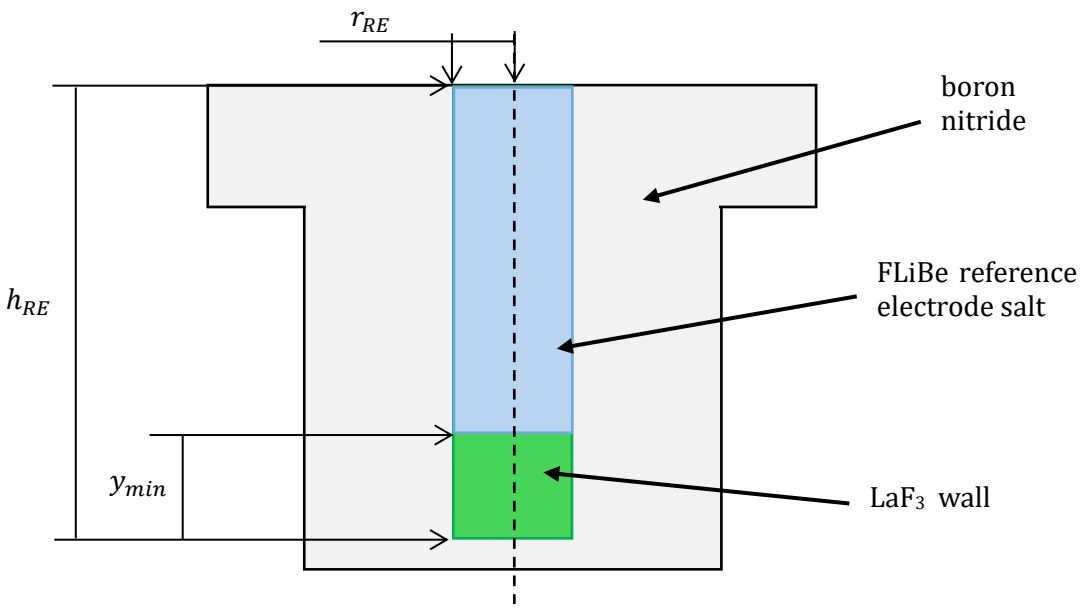


Figure 22. Schematic of the reference electrode with boron nitride body, lanthanum fluoride wall, and FLiBe reference electrode salt. Key dimensions for the calculation are labeled as they appear in the MATLAB calculations script.

The calculations written above are scripted and are performed in MATLAB R2023b. The file which contains the script for the calculations is UCBS40EG0003A. The list of constants used in the calculations are present in UCBS40EG0003A. The data which came from external references are listed below:

1. Solubility of lanthanum fluoride in FLiBe[71]
2. Density of FLiBe as a function of temperature.[72]
3. Density of LaF_3.[73]
4. Dimensions of the reference electrode boron nitride housing.

The first key result from the calculations is the total mass of LaF_3 which is dissolved in the FLiBe reference electrode salt is 11.3 mg. This number is the upper limit of LaF_3 which could dissolve in the FLiBe reference electrode salt because it was calculated using data from 700°C.

$$m_{LaF_3(d)} = 11.3 \text{ mg} \tag{3.63}$$

The second key result after running the calculations in MATLAB is that the minimum wall thickness of the LaF_3 cup is 0.247 mm. A thinner wall runs the chance of possibly dissolving in the FLiBe reference electrode salt.

$$y_{min} = 0.247 \text{ mm} \tag{3.64}$$

This calculation means that any LaF_3 coating which has more mass than 11.3 mg will reach an equilibrium with salt in the BN reference electrode cup. If the coating is thicker than 0.247 mm on the bottom of the reference electrode cup, then the coating will still be present on the bottom of the cup, and the ionic membrane will be intact. The MATLAB script that was created to solve this design calculation is given in Appendix D.9.

3.2.2.2 Component Assembly and Drawings

The first concept of the Echem probe was a simple wire electrode system which introduced electrodes into the salt loop by a feedthrough welded onto a flange. The Echem probe would be coupled with the flange lid, and the flange lid would seal hermetically to the salt loop. This design focused foremost on the simplicity of the electrochemical connections. It fails to consider how a TRE could be installed in this probe, how the thermal strain would affect the probe and flange connection, and how the pressure inside of the probe would communicate with the atmosphere in a controlled manner. The conceptual illustration of the design is given in Figure 23 and the CAD drawing of the assembly is given in Figure 24.

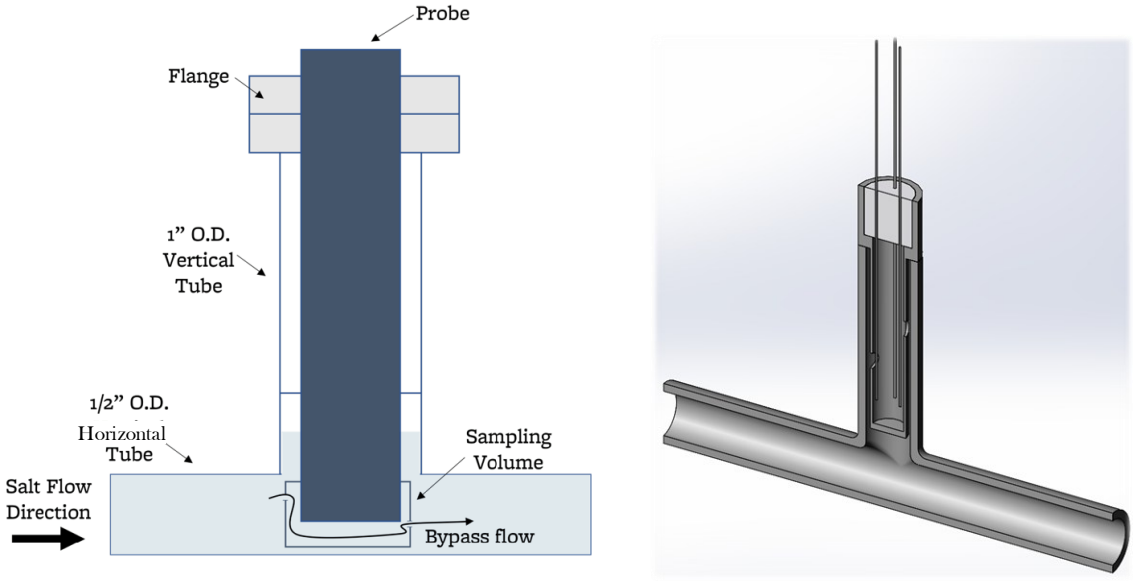


Figure 23. (left) Illustration of the probe placed in flowing loop system. Estimated physical dimensions are noted on the illustration. (right) CAD assembly of the first probe design.

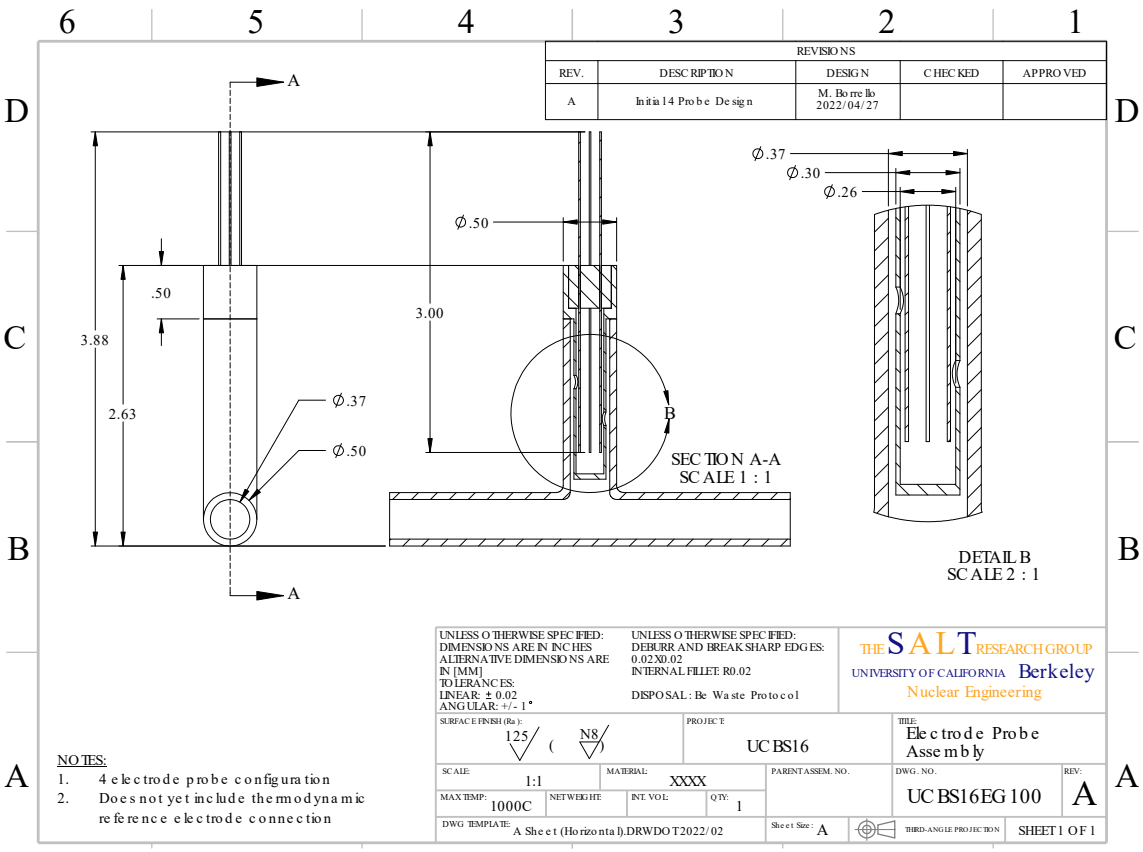


Figure 24. CAD drawing of the probe with initial 4-electrode concept and flow conditioning shield. Dimensions are given in inches.

In designing the probe assembly, it quickly became apparent that incorporating a TRE in the probe would increase the minimum diameter of the probe to be ¾" (19mm). The tubing on the salt loop which would eventually have to house the Echem probe was only ½" (12.7mm) diameter, and a design decision was made to include an in-line section of the loop which featured a 1" (25.4mm) diameter tube with a "tee" to allow for the Echem probe to be installed.

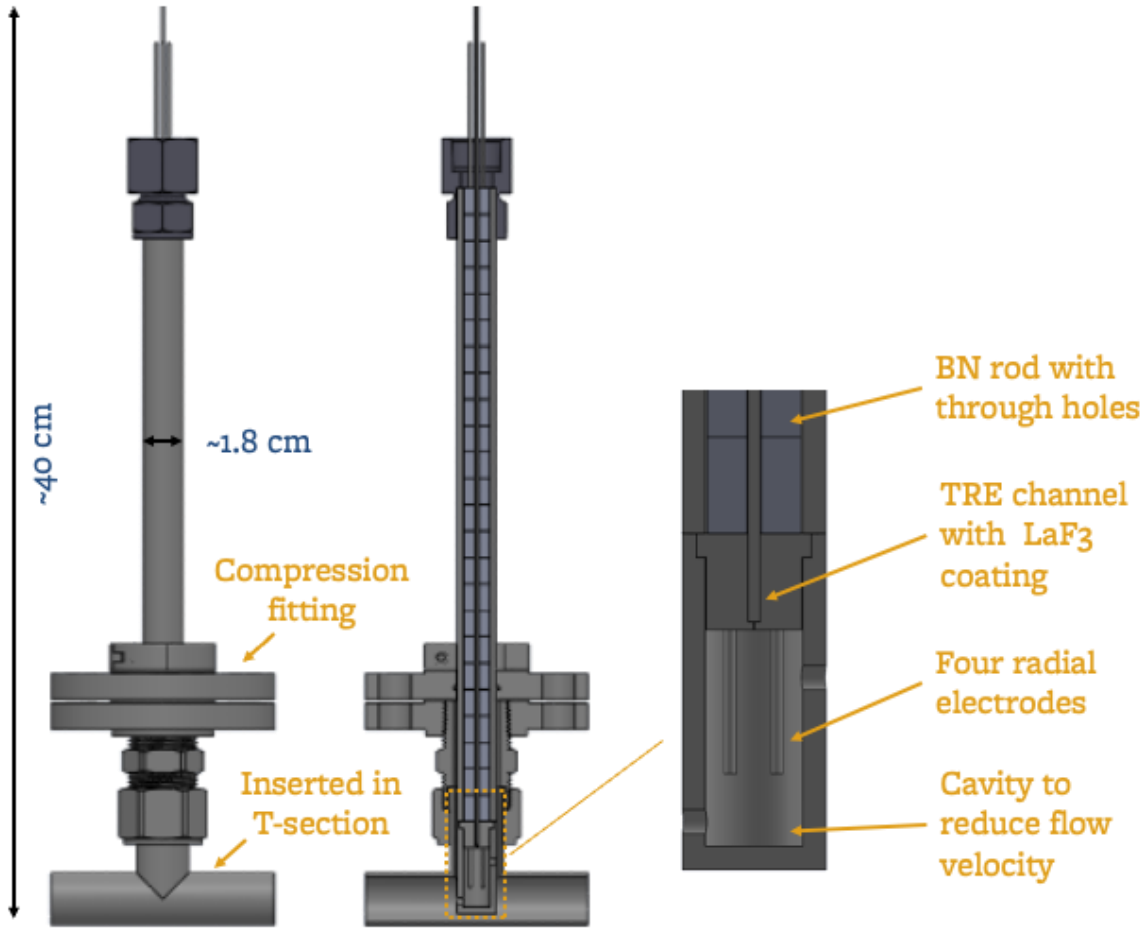


Figure 25. CAD assembly of the second iteration of the Echem probe.

The final iteration of the Echem probe assembly featured greater focus on the physical coupling of the probe to the loop as well as consideration of the thermal effects on the electrode connections. To allow for vertical positioning of the electrodes in the loop, the probe would be hermetically sealed using a Viton O-ring which sits on a groove around the bore of the top flange lid. This gas seal was tested under vacuum and mimicked the behavior of Swagelok Ultra-torr vacuum fittings. The length of the probe was extended, and BN insulating spacers are included throughout the length of the probe shaft to provide a thermal "stand-off" between the salt facing side of the electrodes and the atmosphere facing side of the electrodes. This thermal stand-off ensures the seal around the electrodes on the atmosphere facing side would not degrade from high temperature exposure.

The CAD assembly of the Echem probe shown in Figure 25 highlights the interface with the loop and the position of the electrodes in the flow shield. In this assembly, a Conax tube fitting is used to hermetically seal the top of the probe while allowing 1/16" tube conduits to pass through. Four of the tube conduits are used for passing conductive copper wire down the probe to be coupled with the electrode. One of the tube conduits is used to pass a thermocouple down into the probe. The final tube conduit is used to pass a 1/16" stainless steel tube into the probe and allow for pressure communication between the probe and ambient

environment. This tube is fitted with compression fittings that allow for manual control of pressure communication.

This design also introduces the TRE in the probe tip. The probe tip is composed of a BN end spacer with four radially symmetric bored through holes and one blind hold in the center. The blind hole is not completely closed on the salt facing side as it includes a 0.3mm diameter hole which provides salt contact to the LaF_3 ionic membrane. The design of the BN end spacer is shown in Figure 22 with the LaF_3 deposit as an ionic membrane, and the probe assembly with the BN probe tip is seen in Figure 26.

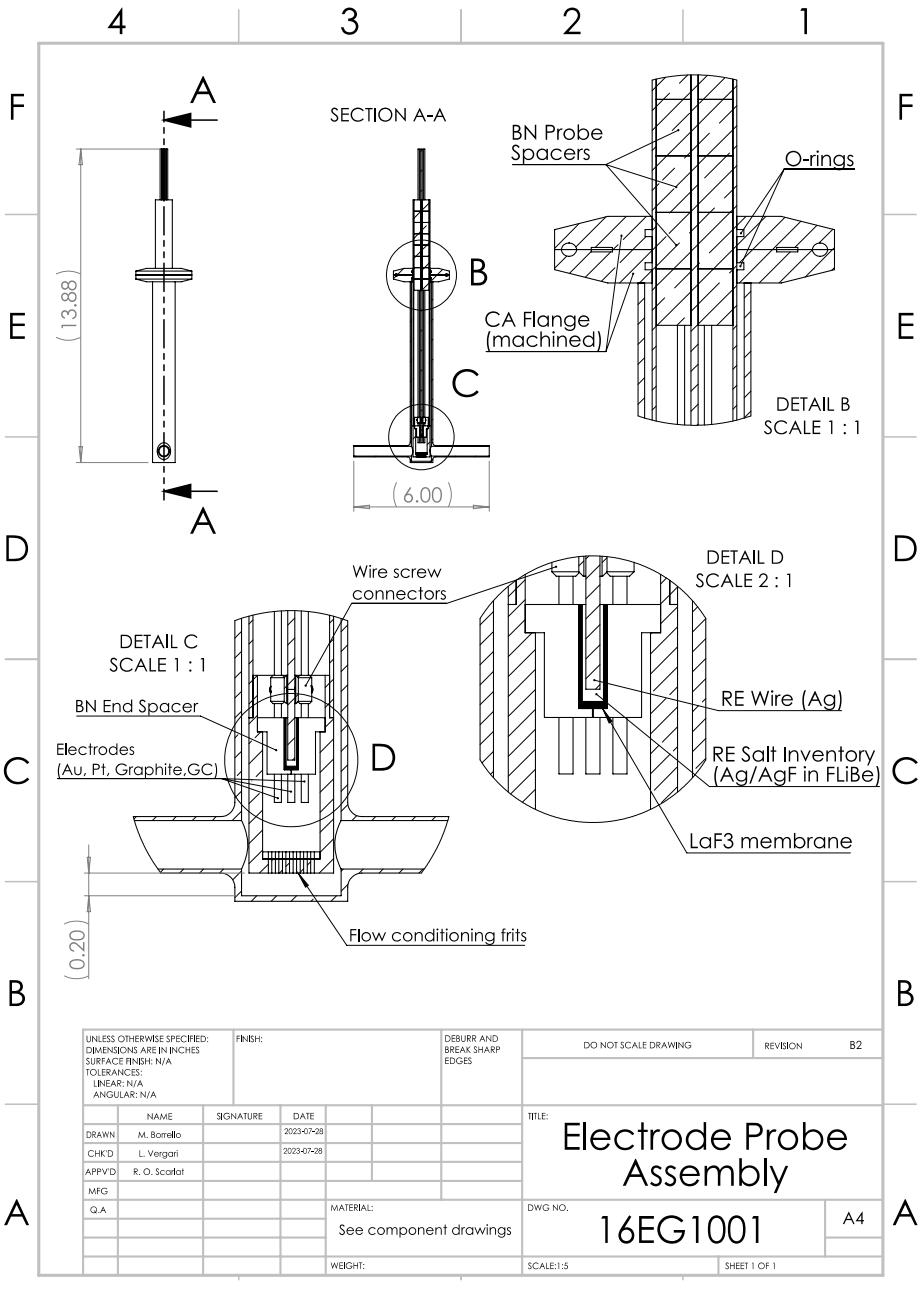


Figure 26. Final drawing of the Echem probe being installed on the salt loop. Full size drawing in Appendix A.

The coupling of electrodes to the conductive wire was solved by designing a part to connect two rods with a linked shaft held together by set screws. The part is linked in Appendix E for data archiving.

3.2.3 FABRICATION OF ECHEM PROBE

The fabricated Echem Probe, shown in Figure 27, has dimensions of approximately 40cm (15.7in) height by 1.9cm (0.75in) diameter. The conductive copper wires are fitted to extend well beyond the top of the probe so when the wires need to be replaced at the bottom, they can be fed through and clipped near the electrodes instead of passing new wires through every time. The flow shield attaches to the probe shaft with screws passing through the walls acting as pins. The center bore in the BN spacers connects directly down to the BN reference electrode cup with LaF_3 ionic membrane.



Figure 27. (left) Electrochemical probe in hand; 19mm (0.75in) diameter tube. (center) Connection between the probe shaft and the flow shield with holes to allow for salt recirculation. (right) Top of the probe with four copper wire leads entering the boron nitride spacers and connecting to the electrodes at the bottom. Conax gas sealing fitting not shown.

Figure 28 shows the function of the shaft collar clamp for vertical positioning of the electrodes. The shaft collar clamp prevents the probe shaft from dropping below the flange cap. The shaft collar clamp can be loosened and positioned along the probe shaft axis to set a maximum depth of submersion of the electrodes.

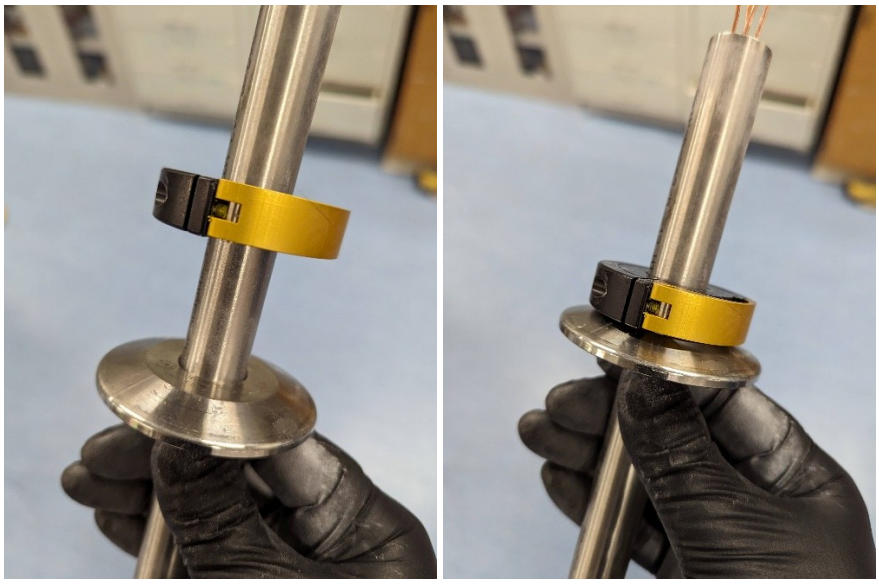


Figure 28. The shaft collar latched around the electrochemical probe shaft controls the vertical position of the probe.

The prototype coupling between the electrodes and the conductive copper wire is shown in Figure 29. This coupling mechanism uses copper crimp connectors which was suitable for aqueous testing. The copper crimp connectors were sprayed with BN aerosol to prevent shorting between the connectors. The electrode set screw connectors were not imaged before assembly, but the final assembly uses these connectors as the coupling device.

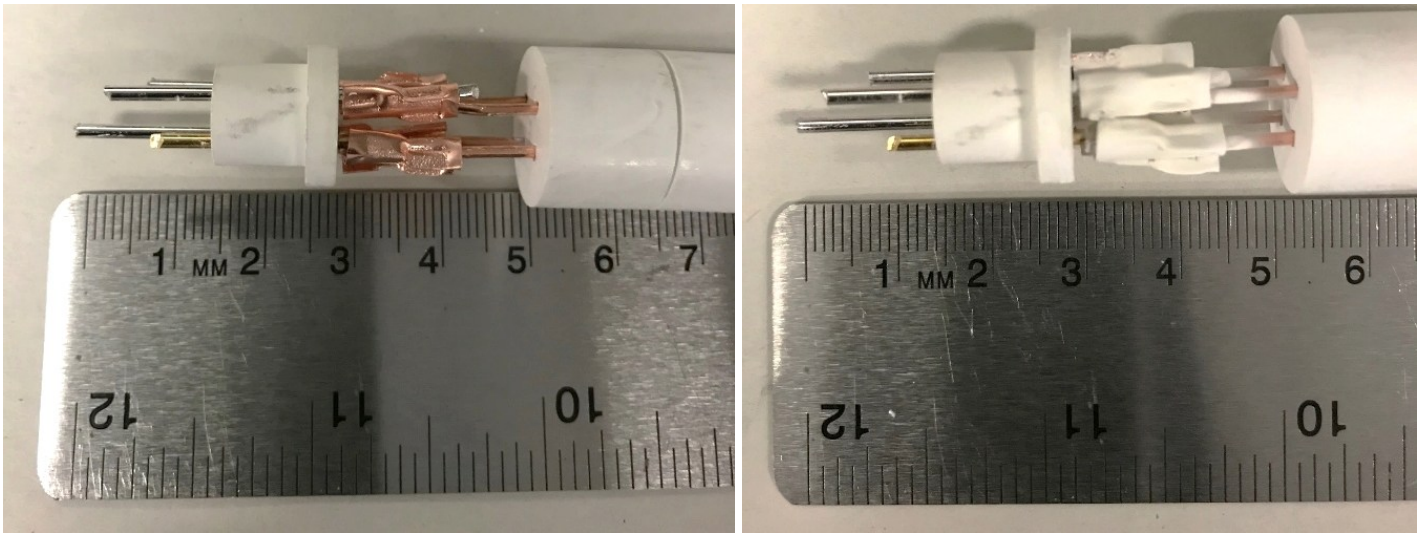


Figure 29. (left) Copper crimp connectors holding electrodes to conductive wire. (right) copper crimp connections are sprayed with electrically insulating boron nitride spray.

The geometric surface area, A_g, of the Pt WE is approximately 0.34cm^2. We define the geometric surface area of the electrodes as the exposed surface area assuming the wire is a cylinder. This is different from the electroactive surface area in that the electroactive surface area must also include the roughness of the wire and the imperfect geometry along cut surfaces and angled bends. Having an accurate measurement of the electroactive area is critical for quantitative measurements using electrochemical sensors. In our tests of the

Echem probe, we quantify electroactive area by measuring the peak current response in cyclic voltammetry with scan rate using a redox species with well characterized diffusivity.

3.3 TESTING OF ECHEM PROBE - RESULTS

Experimental validation of the evolving probe architecture was conducted throughout the design process using well defined aqueous redox chemistry and high-temperature molten salt electrochemical cells. This probe is designed for running OCP, CP, CV, and SWV measurements (can refer back to Table 17) for redox monitoring, corrosion-product detection, and oxide quantification. Electrochemical sensitivity to changing salt chemistry was demonstrated through additions of Cr_2O_3 to FLiBe, where measurable shifts in open circuit potential and chromium-associated redox peaks were observed during cyclic voltammetry measurements.

3.3.1 AQUEOUS TESTING

We characterize the probe electrochemical response by conducting open circuit potentiometry OCP and CV measurements in a solution of potassium ferricyanide (III) (99% purity, Sigma-Aldrich) and potassium chloride (ACS reagent grade, Sigma-Aldrich). The concentration in the solution consists of 0.01 M $K_3[Fe(CN)_6]$ and 0.1 M KCl. We conducted a suite of electrochemical tests with the ferricyanide including measuring OCP for approximately 100 minutes, collecting CVs of the solution with varying scan rates and conducting electrochemical impedance spectroscopy (EIS) with the Echem Probe.

Figure 30 shows the OCP of the ferricyanide solution over a 100 minute window. The data show the potential drifts towards zero volts which is to be expected of an open circuit potential in a symmetric cell (one which has identical WE and RE). We note that the potential plateaus between 5 and 10 mV in this experiment. This is likely due to the fact that OCP measurements will tend towards the thermodynamic equilibrium, but any concentration gradient that exists in the solution or impurities on the surface of the electrodes will cause a deviation from the theoretical 0 V. Considering the trend in the potential is asymptotic toward zero, we are confident the Echem Probe is collecting OCP data accurately.

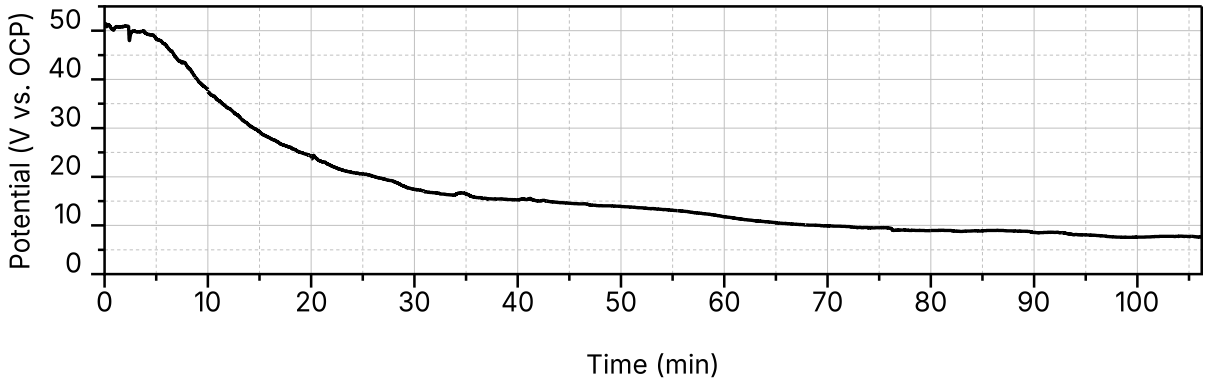


Figure 30. OCP data collected by the Echem probe in 0.01M $K_3[Fe(CN)_6]$ and 0.1 M KCl at 25°C. Pt WE, Pt CE, Pt qRE, Au AuxE.

The CV data shown in Figure 31 covers the potential window of the ferricyanide redox reaction at multiple scan rates. The ferricyanide reaction serves as a benchmark in aqueous electrochemistry[74] as it is reversible with both reduced and oxidized species soluble, so it forms characteristically clean current waves in voltammograms. The classic "duck" shaped CVs in Figure 31 is an indication that the Echem Probe is producing voltammograms that appear to match literature values of the ferricyanide reaction. To validate the data, the anodic and cathodic peaks are detected from the first derivative of the current waves and plotted against the square root of the scan rate in Figure 32. The linear trend in peak current density versus square root of scan rate is expected from analyzing the ferricyanide redox reaction on a macroelectrode system like the Echem Probe.

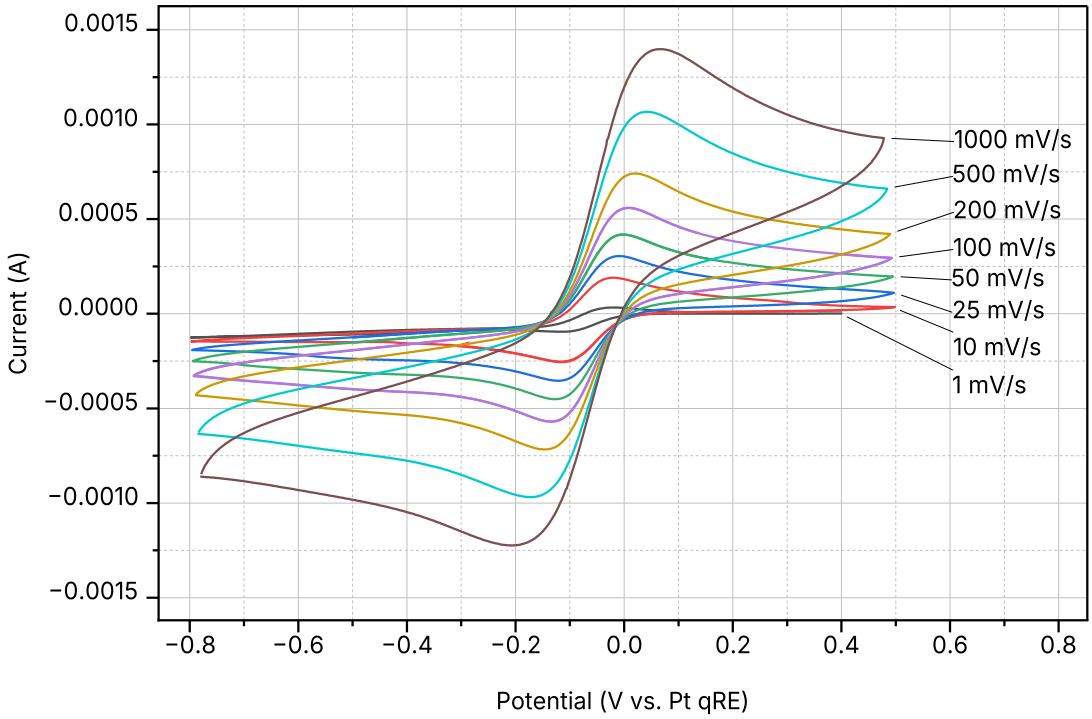


Figure 31. CV data collected by the Echem probe in 0.01M $K_3[Fe(CN)_6]$ and 0.1 M KCl at 25°C. Pt WE, Pt CE, Pt qRE, Au AuxE.

The ferricyanide redox reaction is understood to follow the Randles-Sevcik equation given by Eq.(3.9).

$$i_p = 0.4465CA_e\sqrt{\frac{n^3F^3D\nu}{RT}} \tag{3.65}$$

i_p is the peak current in the scan, C is the bulk concentration of oxidized species, A_e is the electroactive surface area, n is the number of electrons transferred, F is Faraday's constant, D is the diffusivity of the oxidized species, ν is the scan rate, R is the gas constant, and T is the absolute temperature. The slope of the linear fit in Figure 32 is:

$$\text{slope} = 0.4465CA_e\sqrt{\frac{n^3F^3D}{RT}} \tag{3.66}$$

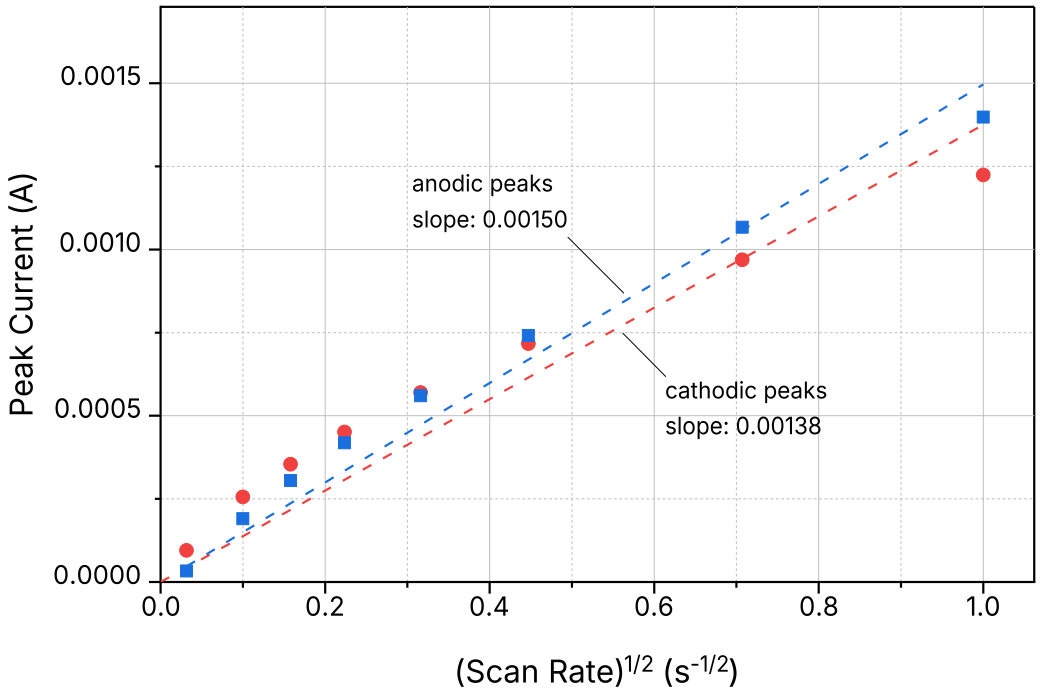


Figure 32. Peak current versus square root of scan rate data from Figure 31.

We have constant C, A_e, n, F, R, and T, therefore we have an expression for D given by:

$$D = \left[\frac{(\text{slope})}{0.4465CA}\right]^2 \frac{RT}{(nF)^3} \tag{3.67}$$

The diffusivity of the species $[Fe(CN)_6]^{3-}$ is given by Konopka and McDuffie[75]:

$$D = 7.2(2) \times 10^{-6} \frac{\text{cm}^2}{\text{s}} \tag{3.68}$$

The two distinct slopes of the ferri- ($[Fe(CN)_6^{3-}]$) and ferro- ($[Fe(CN)_6^{4-}]$) cyanide are within 8% of the average between them in Figure 32. This discrepancy in slope may be from inaccurate peak current data being selected from the cyclic voltammograms due to a shifting baseline current on the forward and reverse sweeps. Using the average slope, we calculate the electroactive surface area of the Echem Probe Pt WE.

$$A_e = \left[\frac{0.00144}{0.4465(1\times10^{-5})}\right]\left(\frac{(8.314)(298)}{(96485)^3(7.2\times10^{-6})}\right)^{1/2} = 0.20\ \text{cm}^2 \tag{3.69}$$

At first, this result was shocking in that a smaller electroactive area was measured compared to the geometric area. Upon examination of the probe after aqueous testing, it was clear that only a portion of the electrode area was wetted by the solution. The BN piece near the electrode tips was completely dry and a small mark was visible on the Pt WE. We measured the height of that mark to be approximately 3.5mm from the tip of the electrode. This corresponds to a geometric area of $A_g = 0.19\ \text{cm}^2$, which is within 5%

of the electroactive area. This result confirms the Echem probe electroactive area is approximately 5% greater than the calculated geometric area.

The EIS data are presented in Appendix B.5. EIS was conducted to measure the uncompensated resistance of the Echem Probe in the ferricyanide solution. The uncompensated resistance was calculated by fitting the EIS data to a constant phase element (CPE) model circuit and selecting the resistance value at the horizontal intercept in the Nyquist plot. The value of uncompensated resistance was approximately $R_u = 20\Omega$. This value was used to correct for ohmic drop in the CV data.

3.3.2 SALT TESTING

We tested the Echem probe in a variety of molten salt environments to show it meet its functional specifications listed in Table 18. These tests focused on evaluating the Echem Probes ability to sense redox potential over time and quantify corrosion products in FLiNaK and FLiBe. The majority of the methods, results, and discussion of this data are present in Chapter 4 and Chapter 5. Preliminary tests and results to verify the functionality of the Echem Probe are discussed here.

Electrochemical verification experiments were conducted in molten FLiBe to evaluate the performance of a multi-electrode probe assembly intended for deployment in circulating molten-salt systems. The objectives of the testing campaign were to (1) verify electrical connectivity and stability of the probe components, (2) evaluate operation of an Ag/AgF thermodynamic reference electrode (TRE) in FLiBe, (3) assess probe sensitivity to changes in melt redox chemistry, and (4) demonstrate implementation of the Be dynamic reference electrode (BeDRE) method using the probe architecture. We present test data from (1) in this section, but data from (2), (3), and (4) are presented in Sections 4.6.2, 4.4, and 4.6.3, respectively.

The probe consists of platinum working electrodes, a glassy carbon counter electrode, a gold auxiliary electrode, and an Ag/AgF thermodynamic reference electrode housed within a boron nitride (BN) body. The platinum electrodes were fabricated from 0.06 in. diameter wire with an exposed length of approximately 50 mm. The glassy carbon electrode was 0.125 in. in diameter with an exposed length of 40.5 mm and was cleaned with acetone prior to use. The gold electrode consisted of a 0.04 in. diameter wire with an exposed length of approximately 15 mm. The thermodynamic reference electrode contained a 0.10 in. diameter silver rod immersed in AgF contained within a BN housing incorporating a LaF_3 fluoride-ion conducting membrane. Prior to testing, the silver rod was mechanically polished using 300-grit SiC paper and cleaned with acetone before assembly into the reference electrode compartment.

Experiments were conducted in molten FLiBe contained within a glassy carbon crucible. Approximately 76 g of FLiBe was loaded into the crucible and heated to 600 °C. The electrodes were lowered into the molten salt once thermal equilibrium was established. Open-circuit potential (OCP), chronopotentiometry (CP), and cyclic voltammetry (CV) were performed using a Gamry Ref1000 potentiostat connected to the probe assembly.

The sensitivity of the probe to changes in salt redox chemistry was evaluated through incremental additions of Cr_2O_3 to the melt, shown in Figure 33. Following stabilization of the OCP signal, small quantities of Cr_2O_3 were introduced into the salt and mixed using a stainless-steel spatula. OCP was monitored

continuously before, during, and after each addition to observing changes in equilibrium potential associated with introduction of oxide and chromium species. Several additions were performed over the course of the experiment, including additions below the estimated solubility limit of Cr_2O_3 in FLiBe. Samples of the FLiBe–Cr_2O_3 mixture were periodically withdrawn using a sampling straw and archived for subsequent chemical characterization and correlation with electrochemical measurements. The observed OCP response was used as a qualitative indicator of probe sensitivity to changes in salt chemistry and redox state.

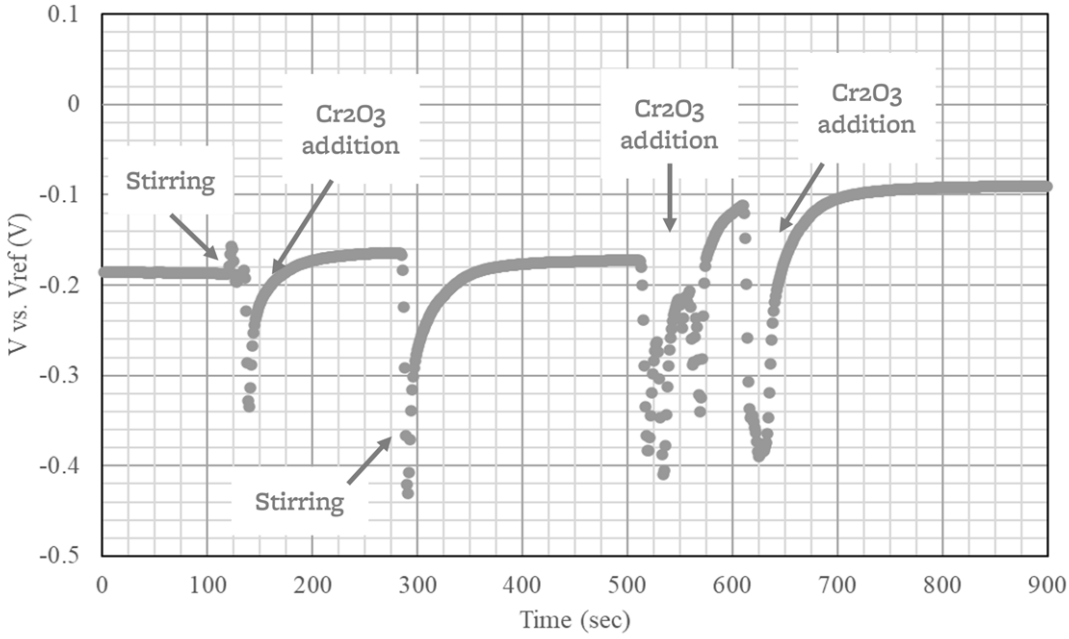


Figure 33. Changes to OCP of FLiBe at 600ºC measured with Echem Probe upon addition of Cr_2O_3 and stirring (Pt WE, GC CE, Ag/Ag^+ RE).

Throughout the testing campaign, several engineering modifications were made to improve probe reliability. These included replacement of the glassy carbon counter electrode with a longer electrode to prevent disconnection during thermal expansion, reinforcement of the BN reference electrode support wire, tightening of electrical connections to the Ag electrode, and increasing the AgF inventory within the reference electrode housing. These modifications were implemented to improve mechanical stability, maintain electrical continuity, and ensure consistent operation of the thermodynamic reference electrode during extended high-temperature testing.

3.4 ECHEM PROBE DESIGN REVIEW - DISCUSSION

The Echem probe was functional in aqueous and molten salt solutions. Aqueous testing with and without the flow shield revealed no differences in the performance of the probe in static solutions. The probe electrochemical response in molten FLiBe and FLiNaK was identical to analogous wire electrode assemblies. The probe gas seal was effective at holding 10psi with flowing argon gas passing through the high temperature cell. The suite of electrode materials—Pt, Au, Ag, W, graphite, and glassy carbon—all performed acceptably while coupled with Cu wire.

Connecting the electrode materials proved to be challenging in its own right. Graphite and glassy carbon electrodes were by far the most difficult to actually couple with the Cu wire. Using crimp Cu connectors would break the brittle graphite and glassy carbon electrodes. Additionally, copper crimp connectors would sometimes fail under repeated thermal cycling. The copper would become soft and lose its grip on the electrodes resulting in decoupling and ending the test. The design and implementation of the stainless-steel connectors made the coupling of electrodes to the conductive wire more robust and resistant to thermal cycling. However, the stainless-steel connectors were prone to some degradation around the set screw threads and would sometimes seize in position after exposure to the vapor space above the molten salt. We considered removing the electrode connectors entirely and utilizing longer electrode wire material through the probe, but this introduced the issue of not allowing replacement of the electrodes without replacing the entire probe wire. Ultimately, this design problem is a fruitful and frustrating problem that would benefit from more rapid prototyping and experimentation of wire coupling mechanisms.

It was quickly discovered that using pure AgF reference salt for the TRE would not function as simply as was originally hoped. The decomposition of AgF into a hard, semiporous, white material made it impossible to melt in a BN crucible. Instead of pursuing the AgF design, it was decided to use the Ni/NiF_2 redox couple in FLiBe for the TRE which is already well studied in literature.

Unfortunately, the Echem probe with NiTRE was never tested in a flowing salt system. A research plan was devised to test the probe in flowing salt mixed with a motorized impeller. The plan is archived in the SALT Research Group internal group folders titled "UCBS44QA04A Loop Probe Flow Shield Test Plan."

3.5 PRINTED ELECTROCHEMICAL SENSORS -INTRODUCTION

Printed electrode chip sensors offer key advantages over traditional wire electrode sensors. Printed electrode chips allow for precise control over wetted electrode geometry and surface area. Transport properties, such as diffusion coefficients, and thermodynamic properties, such as chemical compositions, of electrochemical cells can be measured by directly varying the geometry and surface area of the wetted electrodes.[76] Additionally, printed chip electrodes can be produced with wetted areas on the order of micro- and nanoscales allowing for diffusion limited electrochemical models to be applied in convective systems [76], [77].

The signal from a microelectrode is unique from macroelectrodes. The scale of the electroactive area is comparable to the scale of the diffusion layer that forms during voltammetry. This means that voltammograms produced from a microelectrode always give the appearance of a system with a well-defined diffusion layer similar to what would be seen in hydrodynamic voltammetry [78]. For online redox potential measurements, corrosion product quantification, and material health monitoring in prototypical molten salt systems, microelectrodes offer a design which eliminates the complexity of interpreting the electrochemical response to flow.

Heinze[79] studied the oxidation of ferrocene in CH_2Cl_2, $[TBA]PF_6$ (TBA=tetra-n-butylammonium) at different scan rates on a Pt microdisk electrode (r_0 = 6 μm) and noted the change in the current as the potential scan rate decreased. The slower scan rate allows for a stationary current profile to be developed which removes the peak current dependency on scan rate. This can be observed in Figure 34 as the peaks

that are present in the 10 V/s scan rate disappear in the 10 mV/s scan rate. The stationary current behavior, the 10 mV/s scan, is characteristic microelectrode behavior. Eq.(3.70)[79] characterizes the extent of nonplanar diffusion:

$$\eta = \frac{\sqrt{Dt}}{r} \tag{3.70}$$

When the nonplanar diffusion factor, η, is greater than 6, the current becomes stationary.

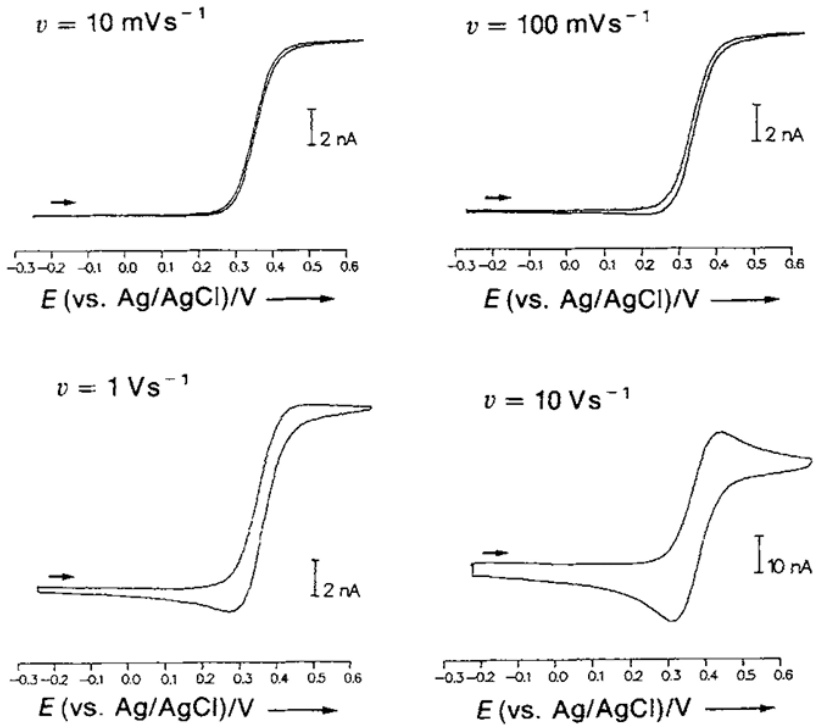


Figure 34. Reproduction of figure from Heinze[76]. Experimental cyclic voltammograms taken on microelectrodes.

Nano- and microfabrication techniques lends themselves nicely to producing microelectrode geometry on printed electrodes. Printed electrodes can be fabricated on a number of materials and geometries which aid to the deployment of sensors in areas where a probe cannot normally be inserted [80]. Recently, printed electrode chips were deployed in a LiCl-KCl eutectic (LKE) chloride salt [81] which demonstrated the design concept was robust enough to survive a high temperature molten chloride environment. It is known that silicon is incompatible with molten salts (fluorides and chlorides), but insulating the silicon wafer with Si_3N_4 is a molten halide compatible solution [77]. The printed electrodes fabricated at UC Berkeley feature platinum metal electrodes for the working electrode (WE), counter electrode (CE), reference electrode (RE), and auxiliary electrode (AuxE). Platinum was chosen as the electrode metal due to its inertness in molten fluorides. Figure 35 shows a schematic of a printed electrode with concentric electrode geometry. The stationary current profile of this electrode would be achieved when the experiment time satisfies Eq.(3.70), which is on the order of $t = 10^6$ seconds. Therefore, the electrode in Figure 35 does not meet the criteria for microelectrode geometry. The purpose of designing multiple geometries of printed electrode,

including non-microelectrodes, is to test the short term and long term response as well as determine which configurations are more robust to surviving high temperature environments.

3.6 DESIGN OF PRINTED ELECTRODES - METHODS

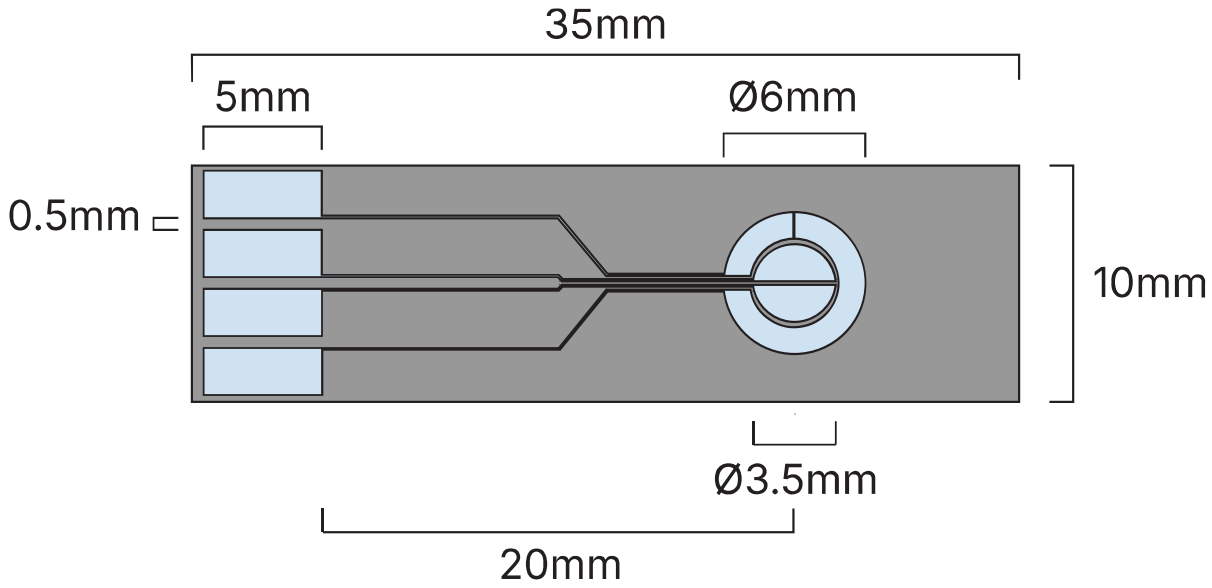


Figure 35. Schematic of a printed electrode chip featuring a four-electrode system with conductive microchannel routed toward contact pads. Configuration 1 from Table 20 is shown.

Eleven geometries of the printed electrode were previously [80] fabricated for the chip sensor, seen in Table 20. All of the configurations in Table 20 were printed in a macroelectrode and microelectrode configuration. The microelectrode configuration was created by placing a mask of microelectrode dots of diameter 50µm in an array across the defined WE area. The full details of the fabrication of the electrode configurations are given by Consiglio[80].

Figure 36 shows the layer configuration of all the printed electrode chip sensors fabricated at UC Berkeley. The assembly of the electrode layers gives us insight into possible modes of failure prone to this design. Thin metal films on Si_3N_4 must adhere over a temperature change of 600ºC. The thermal stresses that accumulate between two distinct layers can result in delamination of the layers. Additionally, while Si_3N_4 is inert to molten halides, Si and SiO_2 are prone to chemical attack. Therefore, any manufacturing defects that expose those materials will be a potential failure mechanism.

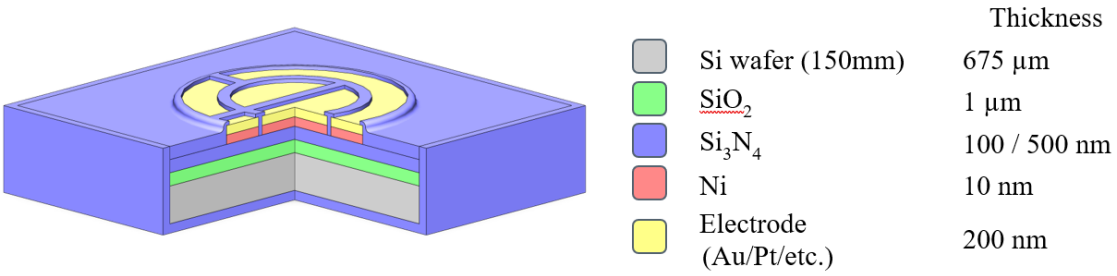


Figure 36. Printed electrode chip layer configuration schematic. The designed layer thickness and material chosen is presented in this schematic. The chosen electrode material for the electrodes fabricated at UC Berkeley was platinum. Figure reproduced from A. Consiglio.[80]

Beyond the material compatibility challenges, there is a lack of experience in using printed electrochemical sensors. There is no standard test apparatus which is suited to connect the contact pads on the chip back to a potentiostat at high temperature. Most off-the-shelf components which are designed to bridge this connection are not able to withstand the temperatures required to conduct molten salt electrochemistry. This led to the development of two separate types of test apparatus for printed electrode testing, seen in Figure 37. The salt exposure test apparatus is designed to fully immerse the sensor chip in molten fluoride salts. The salt droplet test apparatus is designed to only allow salt to wet the electroactive area of the sensor chip. The salt droplet test apparatus notably exposes the printed electrodes to a large thermal gradient along the length of the chip. The two tests examined the printed electrode's ability to survive in high temperature environments in two separate extremes.

Table 20. Printed Electrode Chip Sensor Electroactive Area Configurations[80]

Electrode Geometry		(1)	(2)	(3)	(4)	(5)	(6)
Area (mm²)	WE / Aux-WE	4.16	2.36	4.01	2.32	2.16	4.02
	RE	3.46	0.60	3.56	0.64	0.29	3.33
	CE	11.31	17.27	10.84	17.37	17.32	10.90
# of microelectrodes		70	42	71	42	35	69

Electrode Geometry		(7)	(8)	(9)	(10)	(11)
Area (mm²)	WE / Aux-WE	4.16	4.16	2.32	4.13	2.16
	RE	1.18	1.18	0.64	0.64	0.29
	CE	16.15	10.67	16.53	11.01	16.00
# of microelectrodes		70	70	42	71	N/A

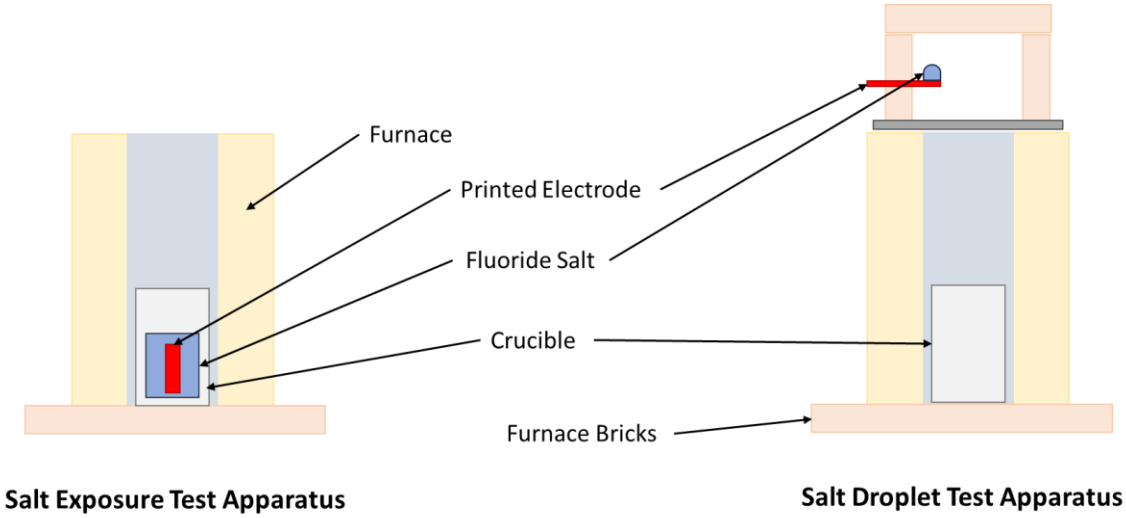


Figure 37. Schematics of two separate printed electrode test apparatuses used in argon gloveboxes. Furnace dimensions have approximate height and inner diameter of 15.24cm (6.0in) and 7.62cm (3.0in), respectively.

3.7 TESTING PRINTED ELECTRODES - RESULTS

3.7.1 AQUEOUS TESTING

Similar to the Echem Probe testing in Section 3.3, we characterized the printed electrodes in aqueous solution before high temperature testing. Two separate printed electrode designs were tested, one macroelectrode (Configuration 1 from Table 20) and one microelectrode (Configuration 3 from Table 20). The printed electrode chips were tested in aqueous solution using a solution potassium ferricyanide (III) (99% purity, Sigma-Aldrich) and potassium chloride (ACS reagent grade, Sigma-Aldrich). The concentration in the solution consists of 0.01 M $K_3[Fe(CN)_6]$ and 0.1 M KCl. The $[Fe(CN)_6]^{4-}/[Fe(CN)_6]^{3-}$ redox reaction being probed is previously characterized on printed electrodes[82]. The electrochemical reaction was studied using CV. Scans were taken from -0.8V to 0.5V vs the Pt qRE at rates of 10mV/s, 25mV/s, 50mV/s, and 200mV/s, seen in Figure 38. The position of the peak current may shift in potential due to the drift of the quasi-reference Pt electrode.

Analysis was performed on the voltammograms to calculate the diffusion coefficient of $[Fe(CN)_6]^{4-}$ and compare this value with the value accepted in literature. This also would serve as proof of the concept that diffusion coefficients from species in molten salts can be calculated using the electrode chip sensors.

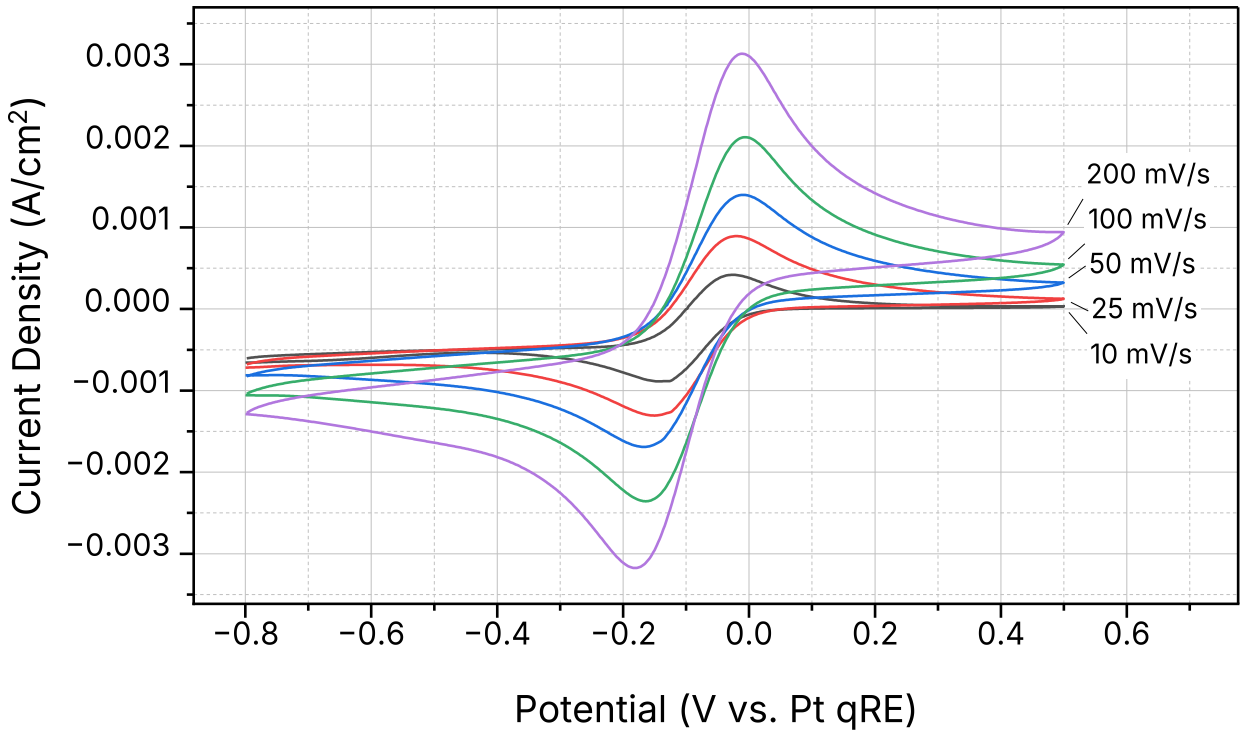


Figure 38. CVs in 0.01 M $K_3[Fe(CN)_6]$ and 0.1 M KCl measured by a printed macroelectrode configuration 4 from Table 20.

The CVs collected from the printed macroelectrode, Figure 38, have the characteristic "duck" shaped waves at all scan rates. This is to be expected as we calculated the time scale for stationary current profiles would be on the order of 10^6 seconds. The longest of these tests is on the order of 10^2 seconds long and no microelectrode behavior will occur. We can validate the current response from the printed macroelectrode by using Eq.(3.9). The peak current density data is plotted against the square root of the scan rate in Figure 39. Evaluating the diffusivity from the anodic and cathodic slopes, we have values of $D = 6.2(6) \times 10^{-6}$cm^2/s and $7.6(4) \times 10^{-6}$cm^2/s, respectively. Taking the average of the two values, we have a diffusivity $D = 7.1(3) \times 10^{-6}$cm^2/s which is the same value within the error reported by Konopka and McDuffie[75].

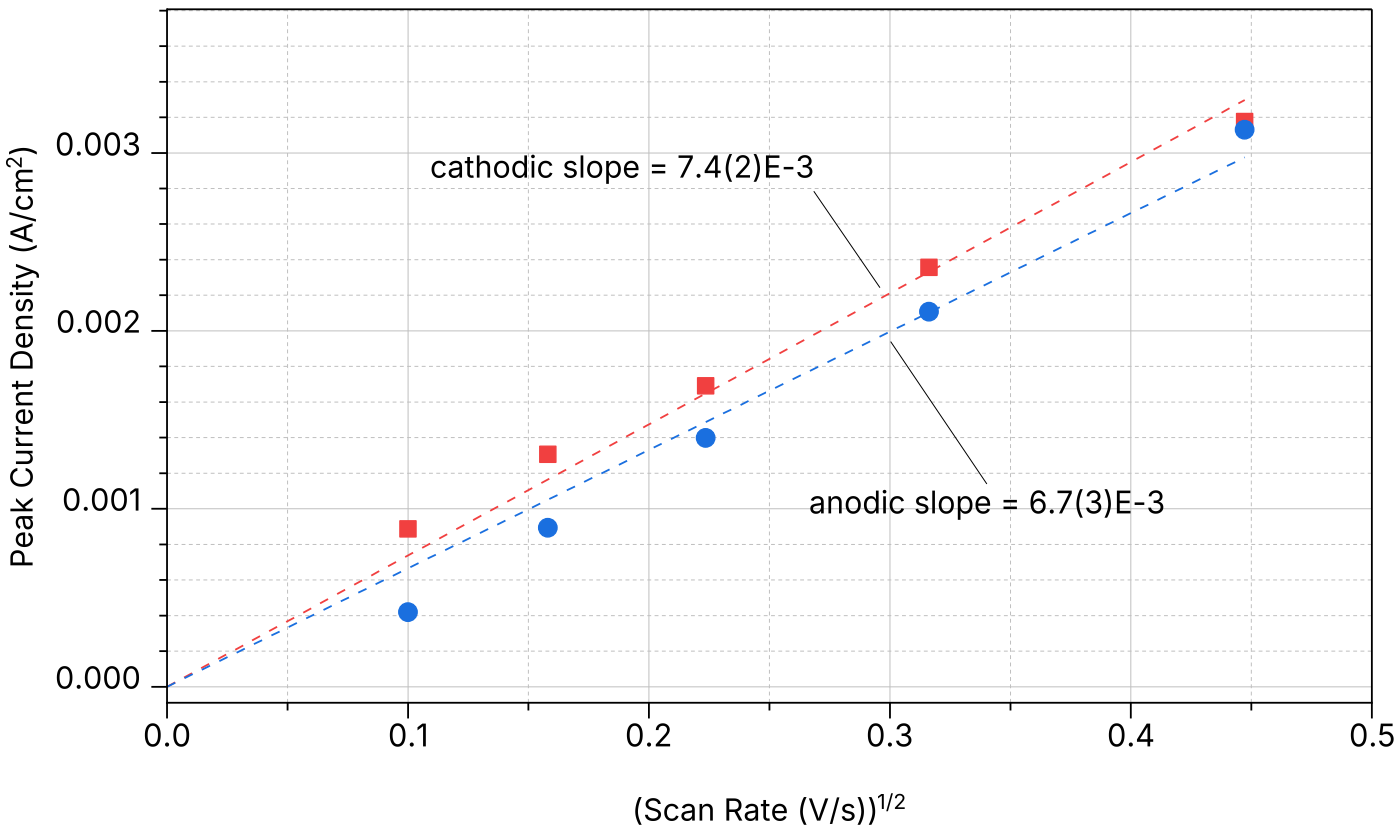


Figure 39. Peak current versus square root of scan rate data from Figure 38.

The CVs collected from the printed microelectrode, Figure 40, show a transition from "duck" shaped waves to stationary current waves around 10 mV/s. Using the diffusivity from Eq.(3.68), the calculation from Eq.(3.70) shows the maximum reaction time of the printed microelectrode that produce stationary current waves is approximately $t = 3.5$ seconds. Notably, the voltammograms in exhibit an asymmetric anodic and cathodic response, with the cathodic current magnitude exceeding the anodic return current. This asymmetry is consistent with an experiment in which only one member of the redox couple is initially present in the bulk solution. The cathodic sweep is supported by diffusion of bulk oxidized species to the microdisk array, whereas the anodic sweep is limited by the amount of reduced product generated near the microelectrode during the preceding scan.

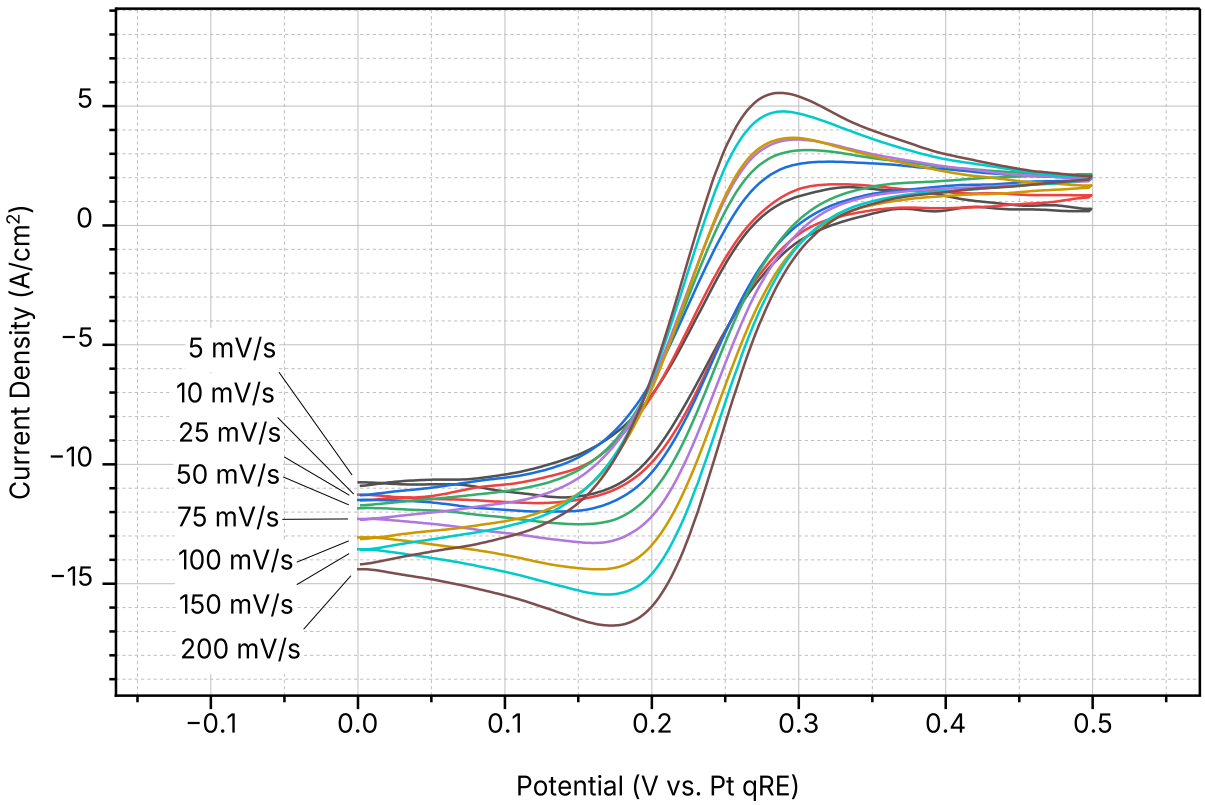


Figure 40. CVs in 0.01 M $K_3[Fe(CN)_6]$ and 0.1 M KCl measured by a printed microelectrode

The reaction in Figure 40 spans approximately 110 mV from anodic to cathodic peak, so the forward and backward reaction complete after spanning 55 mV. Therefore, scanning at a rate of 10 mV/s would result in a total reaction time of 5.5 seconds, proving the printed microelectrode should be capable of producing stationary current waves. Under keen observation, the sigmoid responses from 10 and 5 mV/s do not produce clean current plateaus. This is likely due to a small linear diffusion effect caused by the microelectrodes being spaced on an array. As polarization time increases, the radial diffusion profile becomes linear as microdisks begin to affect the concentration of solution around neighboring microdisks. This phenomenon is visualized in Figure 41, reproduced from Davies and Compton[83] which shows the stages of diffusion profile evolution from (1) to (4). This transition to linear diffusion is predicted for regular spacing of microelectrodes separated by less than 560µm[83].

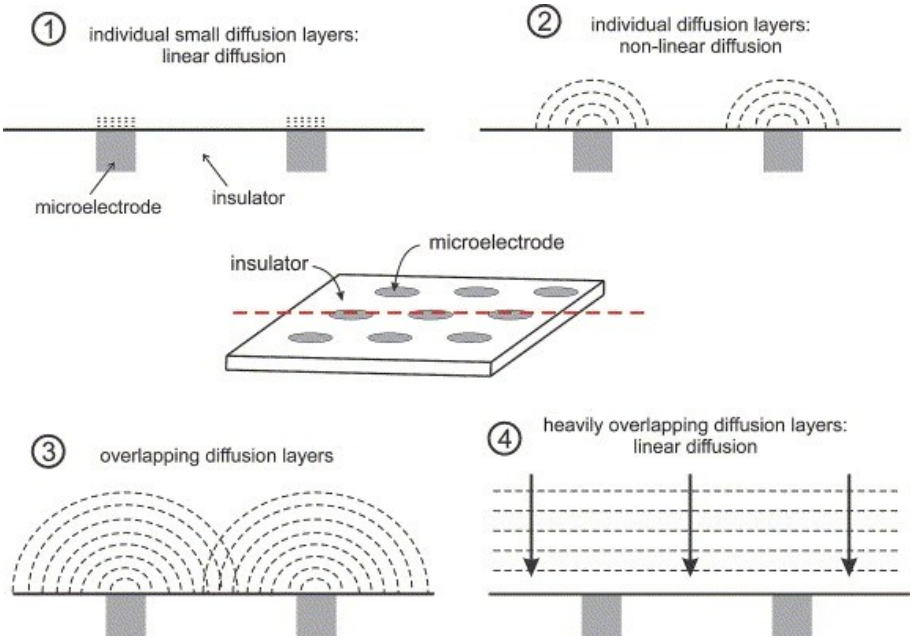


Figure 41. Reproduced from [83] showing the transition on microelectrode array from radial diffusion to linear diffusion as time evolves.

To analyze the ferricyanide diffusivity measured by the microelectrode, we cannot rely on Eq.(3.9) as that only holds for linear diffusion profiles and not profiles that are a combination of linear and radial. Instead we observe the limiting current of the microelectrode, in this case the cathodic limiting current since $[Fe(CN)_6]^{3-}$ is present in solution and must be converted to $[Fe(CN)_6]^{4-}$. The microelectrode consisted of an array of 71 microdisks, each 50 µm in diameter and uniformly, hexagonally separated by a pitch of 250 µm, giving a total active electrode area of $A_{WE} = 1.39 \times 10^{-7}$ cm^2. The limiting current was measured directly from the current plateau observed in the 5mV/s cathodic scan. The diffusivity is calculated from the equation:

$$i_L = 4nFDC_b \tag{3.71}$$

The value of the diffusivity from this experiment was $2.9(5) \times 10^{-6}$ cm^2/s. This value is less than the accepted ferricyanide diffusivity. The discrepancy is likely due to the formatting of linear diffusion profiles along the microdisk array resulting in a drop in limiting current density measured from the CV. This behavior is discussed by Davies and Compton particularly for microelectrode arrays that utilize scan rates in the 1s to 10s of millivolts per second. While we were able to confirm the microelectrode disk was sufficiently small to experience radial diffusion, the scan rates at which it could read the response of radial diffusion exclusively resulted in the establishment of a linear diffusion profile from the neighboring microdisks.

3.7.2 THERMAL STRESS TESTING

The printed electrode sensors were exposed to high temperature after successful aqueous electrochemical tests. Two printed electrodes were placed in a furnace in an argon glovebox and brought to 600°C and held at temperature for thirty minutes. The printed electrodes were allowed to cool for several hours back to

room temperature and examined on a Keyence VHX-7000N Optical Microscope with Laser-Induce Breakdown Spectroscopy (LIBS). Images of the printed electrode electroactive area, conductive channels, and connector pads were taken before and after the high temperature exposure.



Figure 42. Images of two printed electrodes fabricated with microelectrode arrays after high temperature testing. (left) Microelectrode with breakage across the conductive channels. Clean material degradation along the edges of the chip. (right) Microelectrode with conductive channels still intact. Visible damage on the edge of the chip, but the damage does not interfere with the conductive channels.

Both electrodes showed signs of delamination between the printed layers. One of the electrodes broke in half between the contact pads and the electroactive area which can be seen in Figure 42. It was unclear if the conducting channels between the electroactive area and the contact pads remained intact. Figure 43 shows the extent of the degradation of the electrode layer. Several scratches on the surface can be attributed to handling the printed electrode with tweezers in the glovebox. Discoloration and delamination are attributed to the high temperature exposure. The survival of one electrode after high temperature exposure was sufficient justification to perform a molten salt exposure test.

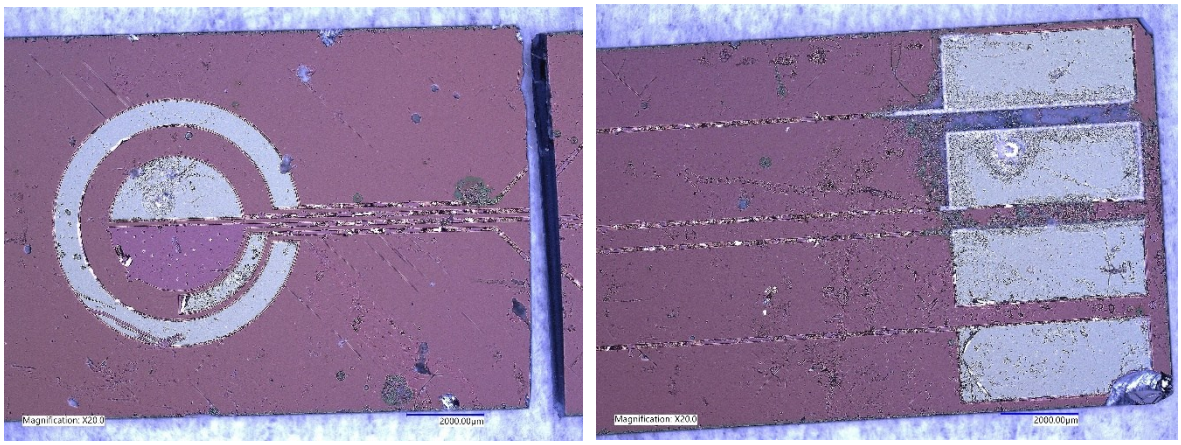


Figure 43. Images of printed electrode with brakeage across conducting channels. (left) Electroactive area on printed electrode. (right) Printed electrode contact pads leading to conductive channels.

The printed electrode in Figure 43 was ramped to 600ºC and soaked at temperature for 30 minutes. Metal layer is a platinum deposition. Small metal dots in the magenta semi-circle of the left image form a microelectrode array. The top layer of the electrode is marred with small linear defects and delamination becoming visible in wrinkling and buckling around the metal electrode areas. The conductive channels appear to have suffered from delamination, but it is unclear if they are still functional. On the right image of Figure 43, the contact pads have small visible amounts of delamination and buckling near the corners.

The electrodes were tested for electrical continuity between the contact pads and electroactive area with a multimeter. The extent of the damage to the electrode in Figure 43 prevent any further testing of the electrical continuity. In the electrode that survived the thermal stress test, there was sporadic electrical continuity depending on where the multimeter probes were touching the electrode surface. Ultimately, it was clear the some of the conductive channels were damaged beyond functionality while others managed to survive the thermal exposure. While we can clearly see the extent of the damage from thermal exposure, it is unclear what causes the material failure at high temperatures. However, it is possible for the electrode to survive the thermal exposure and maintain electrical continuity. Therefore, we continued with the testing campaign and attempted to expose the printed electrodes to molten salts.

3.7.3 FLiBe Testing

The printed electrodes were exposed to molten FLiBe with oxidants present. Testing the printed electrode material compatibility in molten fluorides with the presence of oxidants is critical to characterizing their ability to perform in prototypical reactor conditions. Determining their capability to withstand oxidizing salts is important to determine their viability.

The first printed electrode molten salt exposure was performed using the "Salt Exposure Test Apparatus" shown in Figure 37. The test was conducted in an argon glovebox in molten FLiBe with 1.0wt% Cr_2O_3 at 650^{o}C for 1 hour. After recovering the electrode from the FLiBe, delamination of the electroactive area and contact pads was noted. The metal layer of the chip appeared wetted by the salt, and frozen salt chunks stuck onto the electrode seen in Figure 44. Green, frozen salt chunks are present on the contact pads. Dark patches are areas where the Si3N4 layer is damaged. A thin layer of salt covers the entire surface.

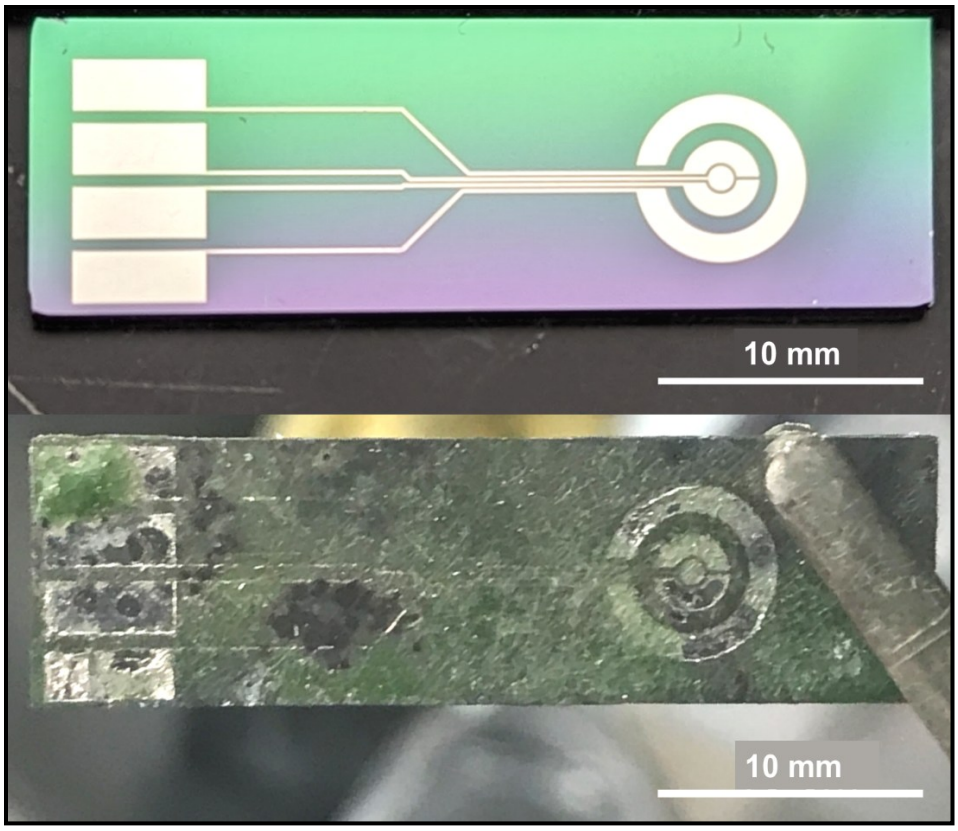


Figure 44. (top) Printed electrode before exposure to molten FLiBe. (bottom) Printed electrode after exposure to FLiBe with 1.0wt% Cr_2O_3 at 650°C for 1 hour. Delamination of the metal layer is visible.

Images of the printed electrode immediately after the FLiBe exposure were taken on an optical microscope with a Nikon Eclipse 150NL camera. The images are taken with a polarized filter to differentiate the printed electrode material from the frozen salt on the electrode surface. The frozen salt appears somewhat iridescent on the surface of the printed electrode due to the variable thickness of the layer. The clean electrode material is a single solid color for each distinct material readily observable. The image of the clean printed electrode and the salt-exposed electrode are given in Appendix B.11.



Figure 45. Printed electrode immediately after FLiBe exposure. Colored boxes are examined under magnification in Figure 46, Figure 47, and Figure 48.

Figure 46 (red box in Figure 45), Figure 47 (blue box in Figure 45), and Figure 48 (green box in Figure 45) show the extent of the damage on the printed electrode materials after the 1-hour exposure test. The iridescent colors in these figures are frozen salt of varying thickness under a polarized light filter on the microscope. Clean metal surfaces appear bright white with the polarized light filter allowing for clear distinction where salt has deposited or metal delamination occurred.

The Pt contact pads in Figure 46 shows signs of delamination similar to the thermal exposure test. The dark deposit on the contact pad is likely a salt chunk and not metal damage. This figure shows us that the damaged faced by the electrode may be largely due to the thermal exposure rather than the salt compatibility.

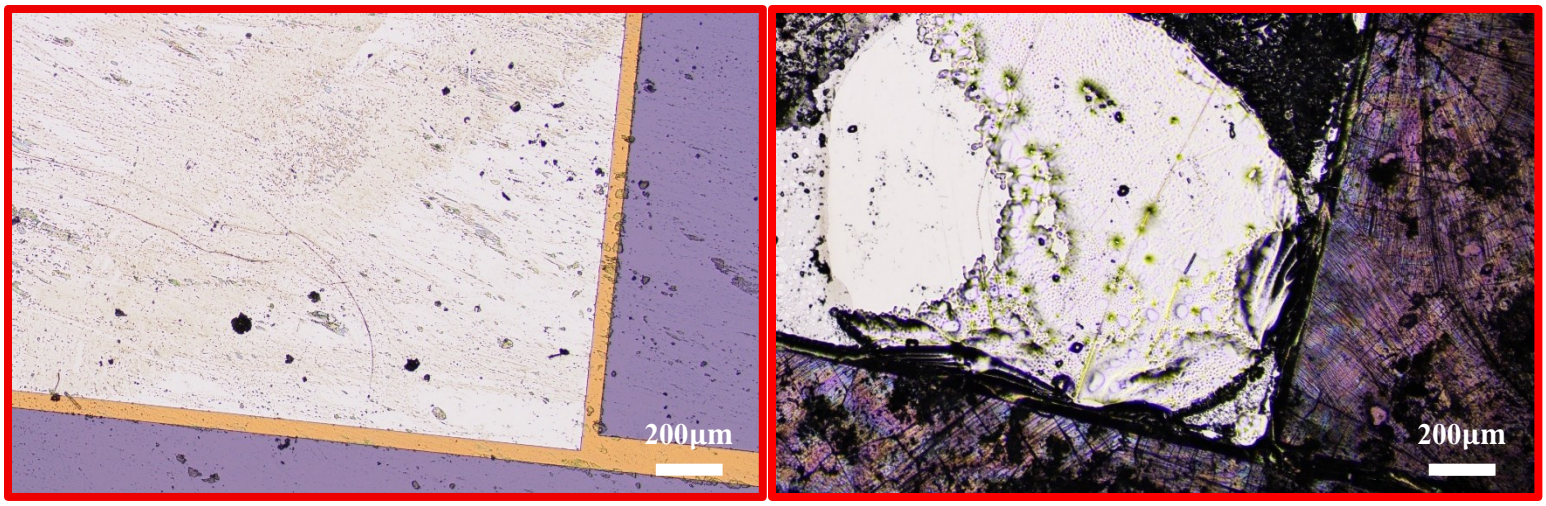


Figure 46. Optical image of microelectrode contact pad showing the difference between before and after FLiBe exposure. This image is the red box enlarged from Figure 45. (left) electrode pre-FLiBe exposure. (right) electrode post-FLiBe exposure.

Figure 47 shows the electroactive Pt layer with frozen salt covering the surface. Small signs of delamination are visible at the center electroactive surface, but largely the electroactive surface remains intact. There are linear defects going through the translucent salt layer but no visible scratching of the electrode as was visible in the thermal exposure.

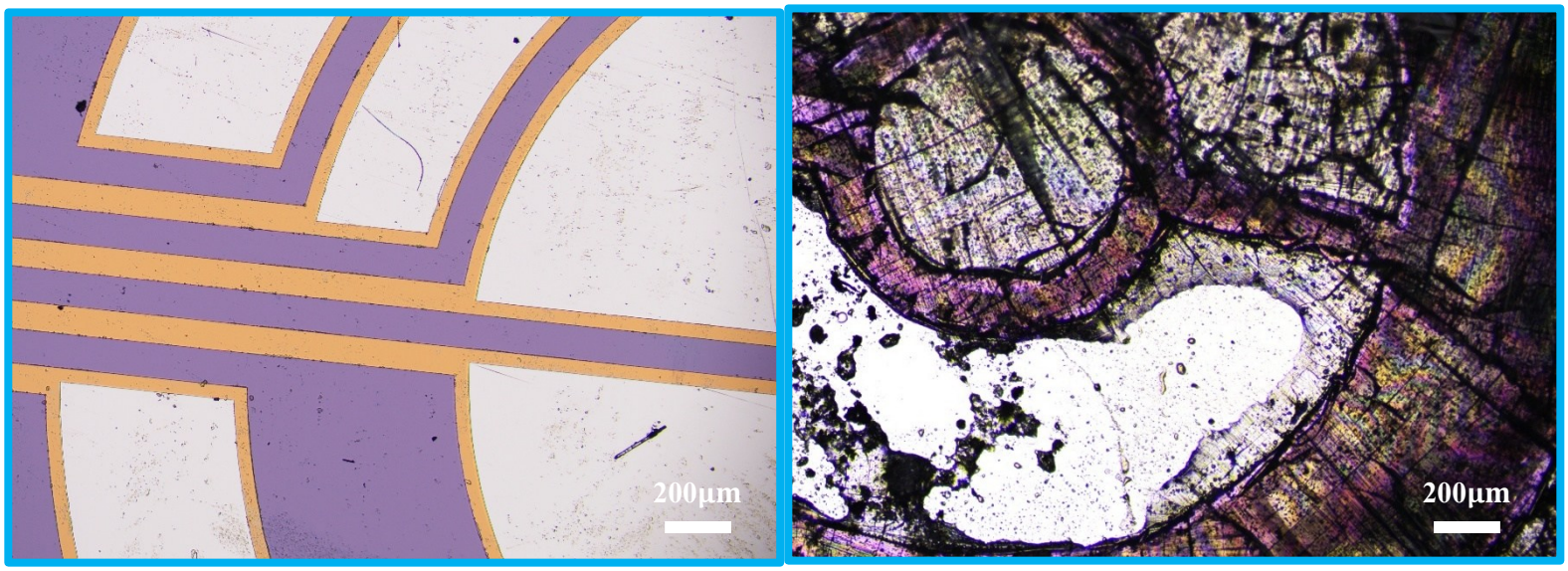


Figure 47. Optical image of microelectrode contact pad showing the difference between before and after FLiBe exposure. This image is the blue box enlarged from Figure 45. (left) Sample electrode pre-FLiBe exposure, but not the same electrode used in the FLiBe exposure. (right) Electrode post-FLiBe exposure. Frozen salt covers the electroactive surface area.

Figure 48 highlights the damage to the conductive channels between Pt contact pads and electroactive surface. The conductive channel is covered with frozen salt, but visible delamination has occurred where the channel appears darker. The darkened area is indicative of the Si_3N_4 insulating layer buckling and

allowing the metal channel to delamination in the buckled regions. This is possibly why the damage is not uniform along the channel but rather occurs at semi-regular buckling intervals.

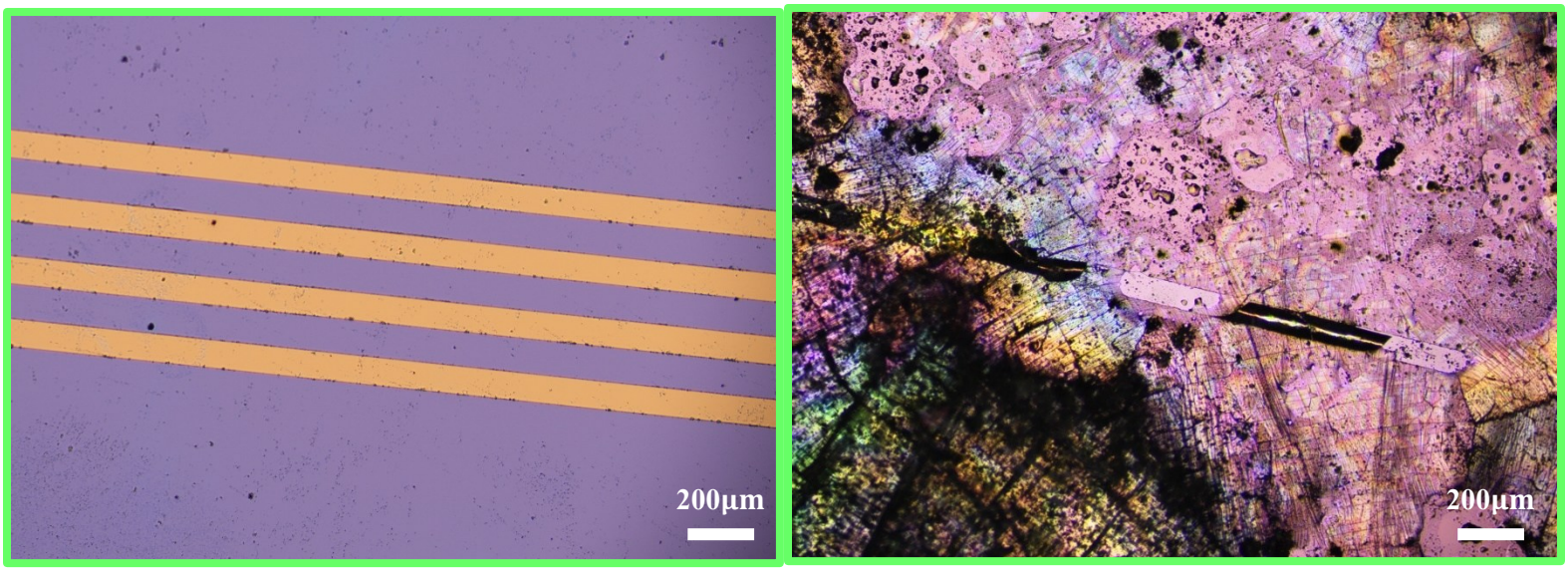


Figure 48. Optical image of microelectrode contact pad showing the difference between before and after FLiBe exposure. This image is the green box enlarged from Figure 45. (left) Electrode pre-FLiBe exposure. (right) Electrode post-FLiBe exposure. There is discontinuous contact along the conductive channels.

As we performed with the thermal stress test, a multimeter was used to determine if there was electrical continuity between the Pt contact pads and the electroactive area. We were unable to find any electrical continuity using this method. Figure 48 confirms there is damage to the conductive channels and thus the sensor lost electrical continuity between the contact pads and the electroactive area.

3.7.4 FLiNaK Testing

The FLiNaK printed electrode molten salt exposure was performed using the "Salt Droplet Test Apparatus" shown in Figure 37. This test was conducted in an argon glovebox (LC Technology, LC-150) with an atmosphere of < 0.1 ppm oxygen and moisture. We connected the printed electrode (configuration 1, see Table 20) with alligator clips and inserted it through the cutout in the wall of calcium silicate insulation (McMaster, Part# 9353K31). A 1.0226(8) g chunk of FLiNaK (46.5LiF-11.5NaF-42KF mol%) was placed on the electroactive area at room temperature. The furnace was turned on and set to hold 550°C using feedback temperature from a K type thermocouple (DwyreOmega, Part# TJ36-CAIN-116G-18-SMPW-M). The temperature held at 550°C with temperature swings of about 10°C for approximately 2 hours during which OCP and CV were performed. The details of each test are in their figure captions.

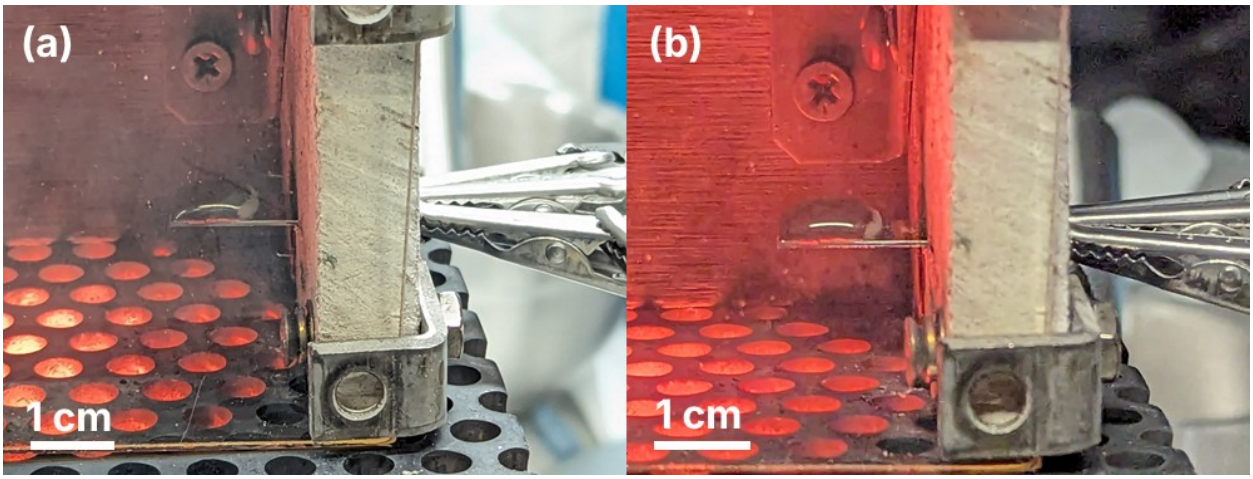


Figure 49. Printed electrode configuration 1 in Table 20. (a) Image of the droplet beginning to melt. (b) Image of the droplet at 550°C.

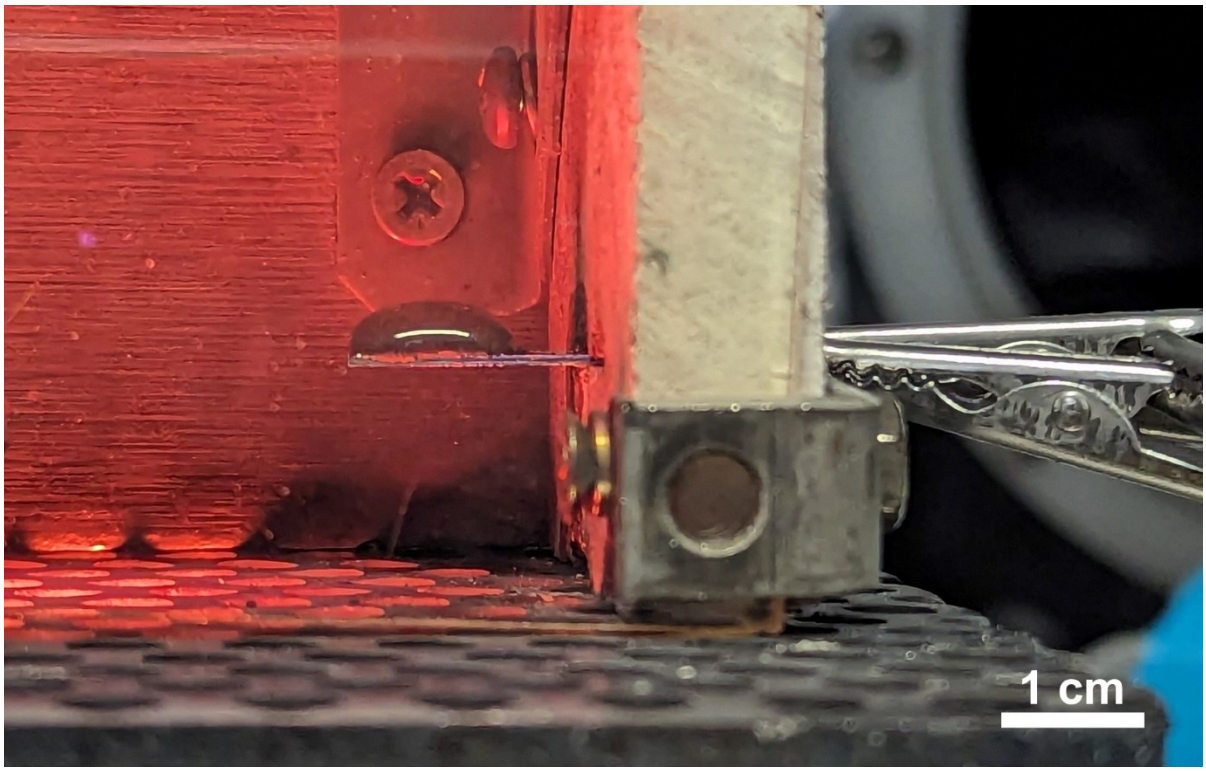


Figure 50. FLiNaK droplet (~690 mg) with 5.0wt% FeF2 added in furnace at 550°C on printed electrode sensor chip.

3.7.5 OCP ON PRINTED ELECTRODE

It was noted that the OCP measurement tended towards zero but did not reach 0V vs the open circuit which can be seen in Figure 51. This could be due to several possibilities. One possibility is that the system needed more time to equilibrate between the salt and the wetted surface. Another possibility is the droplet was not fully molten as it appears there is a salt crystal present on the right side of the droplet in Figure 50b. Finally,

it is possible that the electrode metal began to delaminate during these tests and also could cause a deviation from the expected 0V vs open circuit.

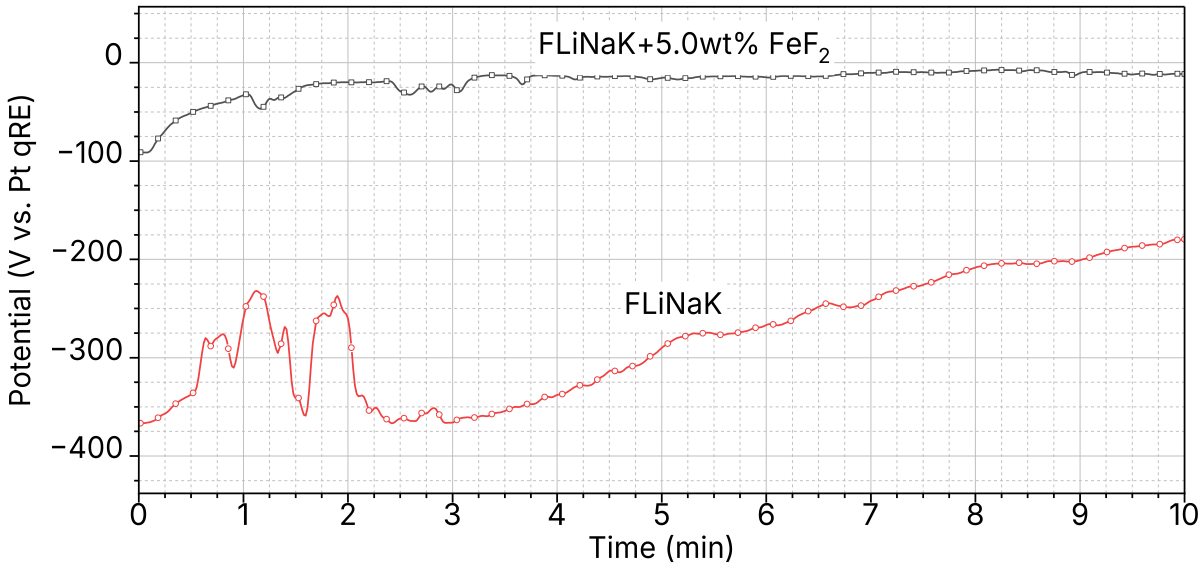


Figure 51. OCP measurement of printed electrode wetted by FLiNaK at 550°C. FLiNaK data taken on configuration 3 and FLiNaK-FeF_2 taken on configuration 1 (see Table 20 for details). Time t=0 occurs approximately 10 minutes after signs of salt melting are visible for each curve.

3.7.6 CV ON PRINTED ELECTRODE

The data from CVs performed on the printed electrodes with pure FLiNaK are presented in Figure 52. The CV parameters include a potential window -1V to 1V vs. Pt qRE, scan rate of 200 mV/s, potential step of 2 mV, and number of repeated scans of 3. Temporal evolution is shown by darkening successive points in the trace. The response did not evolve toward a reproducible cyclic voltammogram. Instead, the traces became increasingly irregular, with discontinuous “zig-zag” features and incomplete traversal of the programmed potential limits. This behavior indicates a progressive loss of electrochemical control, likely associated with instability in the working/reference/counter electrode configuration, intermittent electrical contact, reference-electrode drift, or changes in the molten-salt/electrode interface. The initial cathodic sweep may contain the onset of alkali-metal reduction, consistent with the intended observation of potassium deposition from the FLiNaK melt. However, no well-defined cathodic plating peak or corresponding anodic stripping feature was sustained over successive scans.

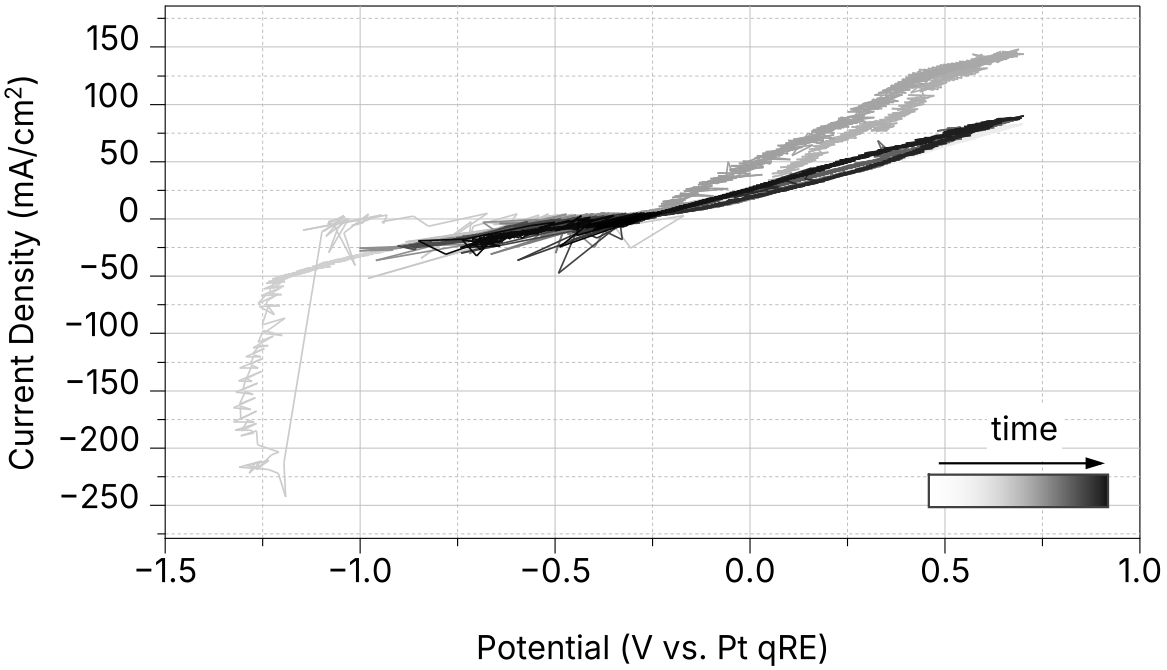


Figure 52. CV on printed electrode configuration 3 (see Table 20 for details) in FLiNaK droplet at 550°C.

The data from CVs performed on the printed electrode with FLiNaK + 5.0wt% FeF_2 is presented in Figure 53 and Figure 54. In both figures, the temporal progression of the experiment is indicated by the darkening of the trace. The CV parameters in Figure 53 include a potential window -0.1V to 0.1V vs. Pt qRE, a scan rate of 200 mV/s, a potential step of 2 mV, and five potential cycles. Unlike the prior test, we first limited the current density output to 30 mA/cm^2 with the intention not to damage the electrode. Additionally, we limited the potential window potentiostat to determine the polarization behavior over a smaller potential window to avoid reaching the potassium reduction potential. We can see that the current waves in Figure 53 are aligning

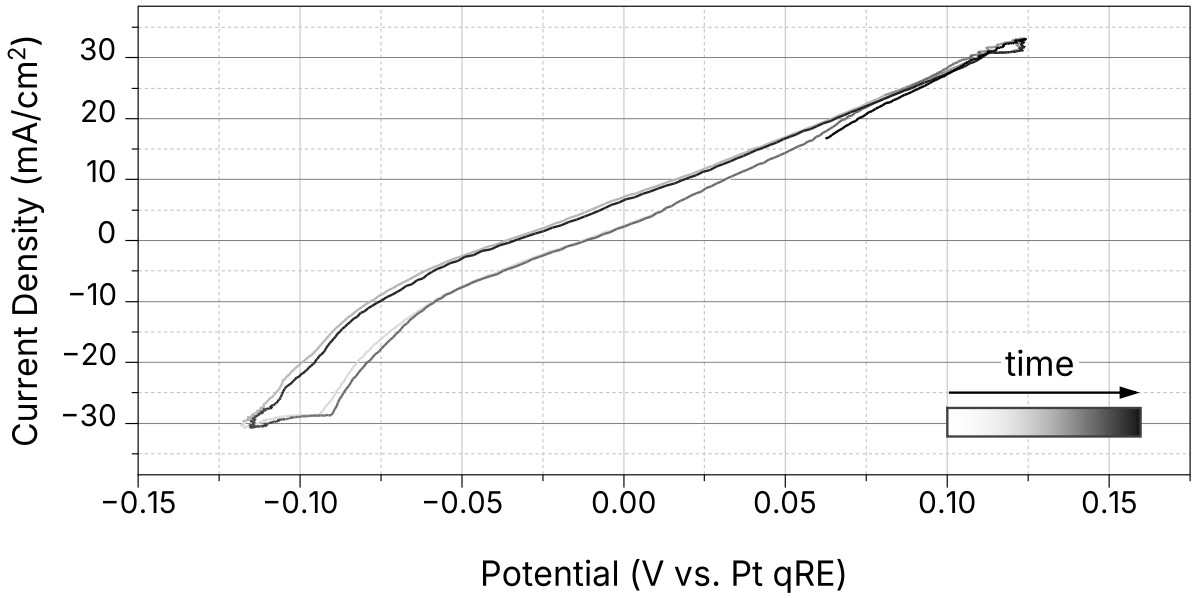


Figure 53. CV on printed electrode configuration 1 (see Table 20 for details) in FLiNaK+FeF_2 at 550°C.

The FeF_2-containing FLiNaK droplet did not produce voltametric data suitable for extracting an Fe(II) diffusion coefficient. In the aqueous validation experiments, the $[Fe(CN)_6]^{3-/4-}$ couple produced coherent current waves that could be analyzed using standard cyclic voltammetry relationships between peak current, scan rate, concentration, and diffusivity. In contrast, the FLiNaK + FeF_2 voltammograms in Figure 54 became unstable after the third sweep. The initially defined current response degraded into irregular, non-reproducible features near the cathodic portion of the scan, indicating that the measured current was no longer governed by a stable electrode/electrolyte interface.

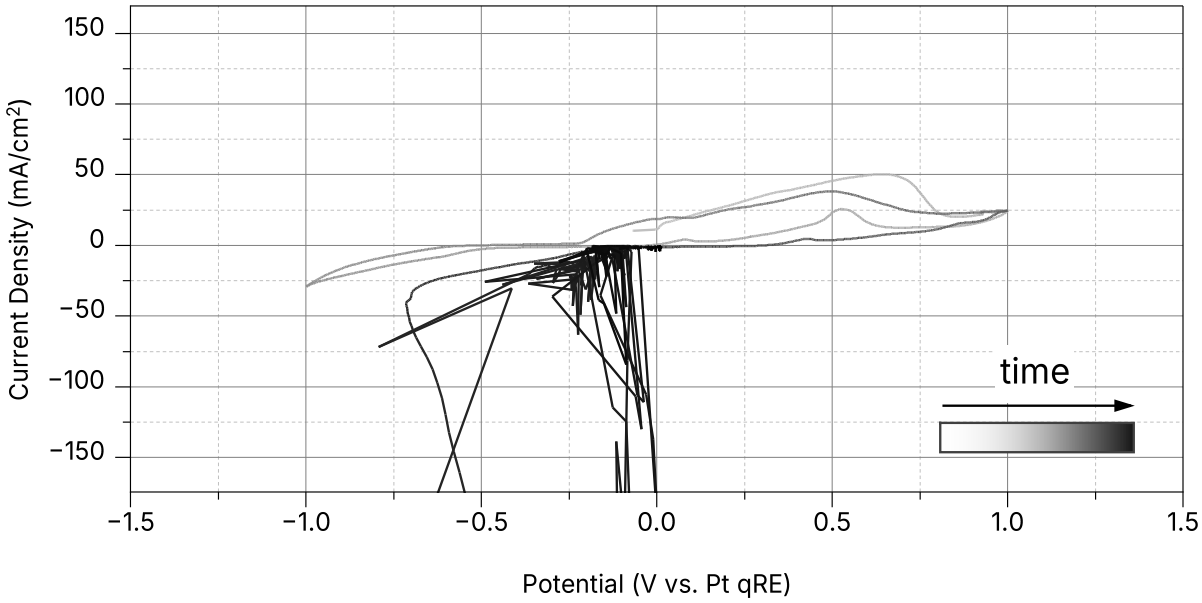


Figure 54. CV on printed electrode configuration 1 (see Table 20 for details) in FLiNaK+FeF_2 at 550°C.

Post-test inspection confirmed that the loss of electrochemical coherence was associated with physical failure of the printed electrode. After cooling, the electroactive layer had delaminated from the substrate, and the metallic electrode features remained embedded in the solidified FLiNaK droplet, as shown in Figure 55. Notably, the failure did not occur along the conductive channels but was localized in the electroactive region. This suggests that the limiting failure mode was not electrical continuity through the printed channels, but mechanical or interfacial instability at the molten salt/electrode contact area.

3.8 PRINTED ELECTRODE DESIGN REVIEW - DISCUSSION

The post-test condition of the printed electrode demonstrates a terminal failure mode for the sensor architecture under molten FLiNaK exposure. As shown in Figure 55 testing in FLiNaK containing 5.0 wt% FeF2 at 550 °C resulted in complete delamination of the electroactive metal layer from the chip substrate. The detached electrode layer remained adhered to the solidified salt droplet, while the underlying substrate showed a clearly exposed delaminated region.

The observed damage is consistent with a coupled thermal and mechanical degradation process. Molten salt wetting of the electrode surface may have promoted strong adhesion between the salt and exposed metal layer; upon cooling and solidification, contraction of the salt droplet and thermal-expansion mismatch between the metal film and substrate could have generated stresses sufficient to remove the electroactive layer. Visual inspection alone cannot isolate the dominant mechanism, but the result demonstrates that printed electrodes for molten-salt electroanalysis require further development of adhesion layers, corrosion-resistant electroactive materials, and post-test salt-removal strategies before reliable electroanalytical measurements can be performed in oxidizing molten fluoride environments.

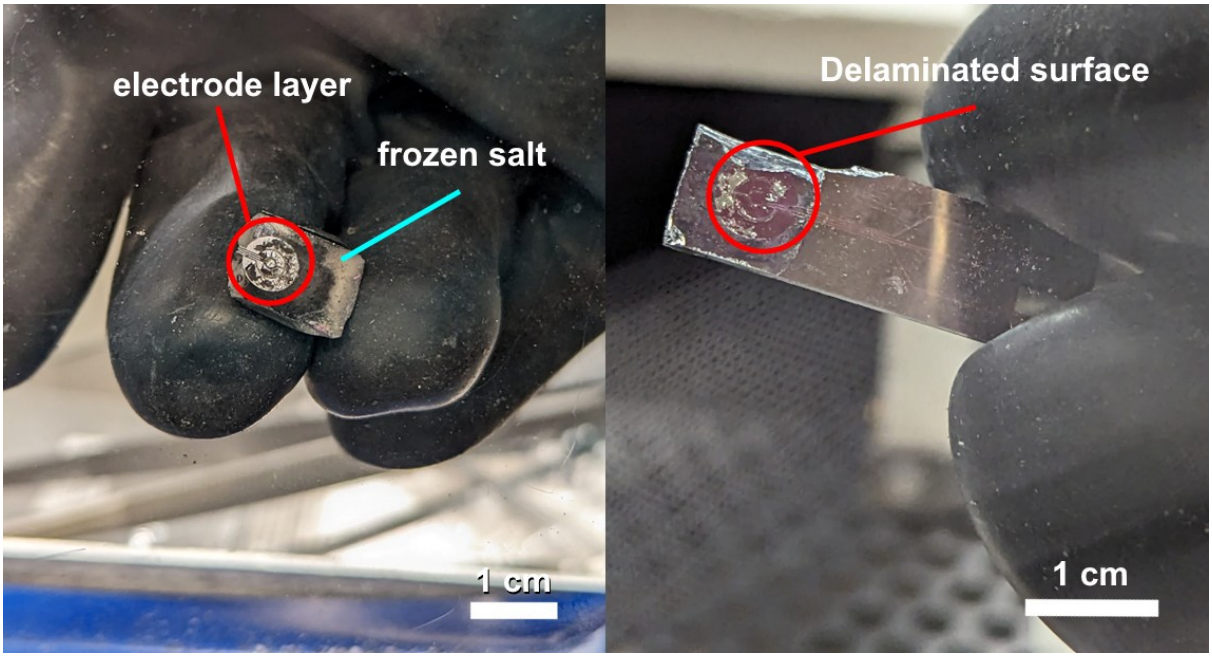


Figure 55. Printed electrode sensor chip after tests with FLiNaK with 5.0wt% FeF_2 added at 550°C for approximately 2 hours. (left) The electrode metal layer completely delaminated from the surface of the chip and stuck to the frozen salt. (right) The delaminated surface of the chip substrate showing a mark where the electroactive surface was removed from the chip.

3.8.1 OPERATIONAL CHALLENGES

Use of printed electrodes in molten-salt electrochemical experiments revealed several apparatus-level limitations that must be addressed before this platform can produce reproducible measurements. First, the droplet test configuration did not provide active control over the molten salt inventory after heating. Once the FLiNaK melted, small disturbances to the fixture could cause the droplet to shift, detach from the printed electrode, or run off the chip into the furnace catch crucible. In one test, partial loss of the molten droplet occurred during melting; therefore, the actual mass of FLiNaK in contact with the printed electrode during the experiment could not be reported with confidence.

A second limitation was mechanical loading of the printed electrode chip. The alligator clips applied localized force at the contact pads, a region that had already shown fragility during aqueous testing through chipping of the Si_3N_4 passivation layer. In the droplet apparatus, the chip was additionally loaded by the mass of the salt droplet near the electroactive region while being constrained by the clips at the opposite end. This geometry effectively caused the silicon wafer to behave as a small, cantilevered specimen, increasing the likelihood of longitudinal fracture during handling, heating, or salt melting. Future designs should therefore support the full chip length or use a dedicated chip carrier that decouples electrical connection from mechanical loading.

Unreliable electrical contact at the chip pads remained a persistent limitation. Alligator clips provided inconsistent contact with the electrode contact pads introducing a failure point that was both electrical and mechanical. Although this may reflect an inherent limitation of the current printed-electrode layout, it is likely addressable through a purpose-built potentiostat connector, such as a spring-loaded contact fixture, clamping chip carrier, or other strain-relieved interface. While the molten-salt tests indicate that the present printed electrodes are not yet robust enough for prolonged FLiNaK exposure, they also define clear design requirements for future devices: controlled salt containment, improved chip support, mechanically isolated electrical contacts, and more durable electrode/substrate adhesion.

3.9 MOLTEN SALT ELECTROCHEMICAL CELL DESIGN LESSONS - CONCLUSION

This section establishes the design basis for molten salt electrochemical sensors by separating their intended functions into redox potential control, chemical quantification, and material health monitoring. Open-circuit potentiometry, chronopotentiometry, cyclic voltammetry, and square-wave voltammetry are complementary rather than interchangeable: OCP provides equilibrium or mixed-potential information, CP probes transient deposition and diffusion behavior, CV maps redox reactions and transport-limited currents, and SWV improves sensitivity to small or overlapping peaks. The important design conclusion is that the electrochemical method must be selected before the probe configuration and assembly is finalized. A sensor intended to monitor redox potential in a low-current regime should prioritize stable reference potential and ohmic-drop control, while a sensor intended to quantify dilute corrosion products should prioritize mass-transport interpretation, surface-area calibration, and flow conditioning.

The Echem probe design shows that a molten salt loop sensor is not simply a set of electrodes inserted into a pipe; it is a coupled mechanical, thermal, electrochemical, and flow-conditioning assembly. The design requirements were driven by two major dependencies: the temperature dependence of species activity and

the current-potential response under flow. The reference-electrode design calculation further showed that approximately 11.3 mg of LaF_3 could dissolve into the reference salt at 700 C and that a minimum LaF_3 wall thickness of 0.247 mm was required to preserve the ionic membrane. These calculations led to a fabricated probe approximately 40 cm tall and 1.9 cm in diameter with replaceable electrodes, BN insulation, pressure communication, and a flow shield. The broader conclusion is that electrochemical probe design should be performed from functional requirements downward, with explicit calculations for reference-electrode lifetime, surface-area calibration, flow effects, and mechanical serviceability. Testing confirmed that the Echem probe produced interpretable electrochemical data in both aqueous benchmark solution and molten fluoride salt. In 0.01 M K3[Fe(CN)6] and 0.1 M KCl at 25 C, the OCP drifted toward a small 5-10 mV offset, and the cyclic voltammograms showed the expected reversible ferricyanide response with a peak current that is proportional to the square root of scan rate. Using the known ferricyanide diffusivity of 7.2(2)e-6 cm2/s, the measured response gave an electroactive Pt working-electrode area of approximately 0.20 cm2, which agreed within about 5% with the wetted geometric area of approximately 0.19 cm2 observed after testing. EIS gave an uncompensated resistance of approximately 20 ohms in the aqueous cell, demonstrating the ability to quantify and correct ohmic drop. Molten FLiBe testing further showed that the probe could detect changes in salt redox chemistry after Cr2O3 addition through OCP shifts and chromium-associated CV features. These results validate the probe as a functional electrochemical platform, while also showing that quantitative molten-salt interpretation will depend on careful surface-area, reference-potential, and resistance calibration in each cell configuration.

The design review indicates that the wire-electrode Echem probe is the most mature sensor architecture tested in this work, but its reliability is limited by mechanical connection details and reference-electrode integration. The probe functioned in static aqueous and molten salt cells, the gas seal held 10 psi with argon flow through the high-temperature cell, and Pt, Au, Ag, W, graphite, and glassy carbon electrodes all produced usable electrical connections when coupled to copper leads. However, brittle graphite and glassy carbon were difficult to attach without fracture, copper crimps softened and loosened after thermal cycling, and stainless-steel set-screw connectors improved robustness but introduced seizure and degradation risks in the hot vapor space. The Ag/AgF reference-electrode concept was abandoned because AgF decomposition and compatibility issues prevented reliable operation, leading the design back toward the better-established Ni/NiF2 couple. The main conclusion is that future loop probes should preserve the replaceable-wire architecture but improve electrode-to-lead coupling, avoid mechanically fragile crimped connections, and complete the planned flow-shield validation before using the probe response to interpret loop-scale transport phenomena.

Printed electrode sensors offer a potential path toward molten salt electroanalysis with better-defined geometry, lower total current, and reduced sensitivity to bulk flow than conventional wire electrodes. Their main advantage is the ability to fabricate micro- and nano-scale electroactive features whose diffusion length can become comparable to the electrode radius, allowing stationary or radial-diffusion behavior to emerge even in systems where macroelectrode interpretation would be complicated by convection. However, this section also identifies the design caveat: not every printed electrode is a microelectrode in the electrochemical sense. For the selected printed geometry, the stationary-current criterion can require impractically long times depending on radius, spacing, and diffusivity, and microelectrode arrays can transition back toward linear diffusion when neighboring diffusion fields overlap. Therefore, the conclusion

is that printed electrodes are promising for future flowing molten salt systems, but their usefulness depends on matching electrode dimensions, spacing, scan rate, and expected diffusivity to the measurement time scale.

The printed-electrode design work identifies both the opportunity and the fragility of chip-based molten salt sensors. Eleven electrode geometries were fabricated in macroelectrode and microelectrode configurations, with 50 um microdisk arrays patterned over the working-electrode regions. The Pt/Si3N4/Si multilayer structure provided chemically resistant electrode and passivation materials, but it also introduced thermal-expansion mismatch, adhesion-layer sensitivity, and vulnerability to any defect that exposed Si or SiO2 to molten halide salt. Because no standard high-temperature chip connector was available, two test apparatuses were developed: a full salt-exposure fixture and a droplet fixture that wetted only the electroactive region. This design section should close by emphasizing that printed molten-salt sensors require packaging as much as electrode fabrication. The next generation should be designed with integrated chip support, strain-relieved electrical contact, controlled salt containment, and post-test salt removal in mind, because these apparatus-level requirements determine whether the lithographically defined electrode geometry remains meaningful during high-temperature operation. [Anchor: Section 3.6; Figures 36-38; Table 18]

The printed-electrode tests demonstrate that the electrochemical concept works at room temperature, but the present chip architecture is not yet robust enough for reliable molten fluoride salt exposure. In aqueous ferricyanide testing, the printed macroelectrode produced diffusion-controlled CVs and an average diffusivity of 7.1(3)e-6 cm2/s, matching the accepted ferricyanide value of 7.2(2)e-6 cm2/s. The printed microelectrode produced more stationary current behavior at slow scan rates, but the diffusivity estimated from the limiting current was only 2.9(5)e-6 cm2/s, likely because diffusion fields from the 71 microdisks, each 50 um in diameter with 250 um pitch, overlapped and reduced the measured limiting current. High-temperature tests then exposed the dominant failure modes. After 600 C argon exposure for 30 minutes, both chips showed delamination and one fractured across the conductive channels. FLiBe exposure at 650 C with 1.0 wt% Cr2O3 for 1 hour and FLiNaK exposure at 550 C with 5.0 wt% FeF2 for approximately 2 hours produced severe metal-layer delamination, including complete removal of the electroactive layer into the frozen salt. These results show that printed electrodes can produce valid electrochemical signals, but future work must solve adhesion, thermal-stress, chip-support, and salt-wetting problems before using them for quantitative molten fluoride salt measurements. [Anchor: Section 3.7; Figures 39-56; Appendix B.7-B.12]

The electrochemical sensor development in this chapter establishes a clear hierarchy of readiness. Wire-electrode probes are presently the most practical platform for molten fluoride salt electrochemistry because they can be fabricated, repaired, recalibrated, and adapted to multiple electrode materials. Their limitations are mechanical and interpretive: electrode coupling, reference-electrode integration, surface-area calibration, and flow sensitivity must be controlled before loop data can be treated quantitatively. Printed electrodes, by contrast, offer the long-term promise of defined geometry, low total current, and microelectrode transport behavior, but the current devices failed under thermal and molten-salt exposure because the chip packaging was not yet compatible with the environment. The main conclusion is that molten salt electrochemical cell design must treat the sensor, reference electrode, electrical feedthrough,

salt containment, and local hydrodynamic environment as one system. A sensor that is electrochemically ideal but mechanically fragile is not a deployable sensor, and a mechanically robust probe that lacks reference stability or surface-area traceability cannot produce quantitative chemistry data.

4. REDOX MEASUREMENTS IN MOLTEN SALTS FOR SYSTEM HEALTH MONITORING

Electrochemical measurements have become a practical method of system health monitoring in nuclear power plants. In light-water reactors (LWRs), electrochemical sensors are routinely employed to quantify coolant chemistry, monitor corrosion-driving forces, and assess the susceptibility of structural materials to degradation mechanisms[35], [36], [37], [38], [39]. Measurements of electrochemical corrosion potential (ECP), dissolved oxidants and reductants, conductivity, and polarization resistance provide real-time indicators of the thermodynamic and kinetic conditions that govern material performance. As a result, electrochemical monitoring has positioned itself as a critical element of plant chemistry programs and safety management strategies.

The deployment of electrochemical monitoring in LWRs was driven by the need to predict and mitigate corrosion-related failures. Electrochemical corrosion potential emerged as a particularly important parameter because it provides a mechanistic connection between reactor water chemistry and environmentally assisted cracking[35]. The development of robust high-temperature reference electrodes and electrochemical probes[37], [39] enabled continuous measurements in reactor environments, allowing electrochemical data to be incorporated into predictive models of corrosion and component lifetime.

Molten salt reactors and other molten-salt-based nuclear technologies face many of the same challenges that motivate electrochemical monitoring in water-cooled reactors. MSR instrumentation frameworks emphasize (i) tracking evolving fuel salt composition for process history and control, (ii) monitoring dissolved structural alloy constituents as corrosion indicators, and (iii) measuring salt redox state because it is directly linked to corrosion risk and can evolve over time[40]. The thermodynamic equilibrium of the melt governs corrosion behavior and the stability of dissolved species. However, unlike aqueous systems, molten salts presently lack a mature suite of operational monitoring tools capable of continuously quantifying these parameters during reactor operation. As a result, many important system health indicators—including redox potential and corrosion product concentration—are often inferred indirectly or measured only through periodic sampling of the melt.

This chapter examines electrochemical measurements of redox potential in fluoride salts. Redox potential serves as a measurable representation of the oxidizing or reducing condition of the salt and directly influences corrosion thermodynamics, impurity behavior, and electrochemical transport processes[43]. By drawing parallels to the role of electrochemical monitoring in water-cooled reactors, this chapter establishes a framework for evaluating how electrochemical measurements can be used to assess, control, and ultimately maintain the health of molten salt systems.

4.1 UNDERSTANDING MOLTEN SALT REDOX POTENTIAL - BACKGROUND

Baes[51] definition of redox potential is the overall state of oxidation in the system when present in at equilibrium. That is to say, the redox potential of a salt itself is determined by the equilibrium concentration of each ion solvated in the melt. If the system deviates from equilibrium, the redox potential of the melt will change until the new equilibrium concentrations are met. This definition is similar to the equilibrium constant of a system which is defined as the ratio of the activities of products to reactants at thermodynamic equilibrium. The equilibrium constant is thought as a parameter that quantifies the tendency of a chemical

or electrochemical reaction to proceed. Olander[84] gave a related definition called the "fluorine potential," which is the free energy associated with the formation of the partial pressure of fluoride gas (F_2) in a system. The algebraic derivation of this parameter are outlined in Section 4.3. Importantly, the fluorine potential, the equilibrium constant, and the redox potential are recognized as three equivalent viewpoints of the same equilibrium behavior[85].

With known thermodynamic data and a quantified accuracy of redox potential measurements, one could measure the redox potential of a melt and calculate the activities of the solvated ions. And conversely, with known measurement of the activities of a solvated redox couple in the melt, one could calculate the redox potential and equilibrium compositions of all other species in the melt. The accuracy of using redox potential measurements for corrosion product quantification is briefly discussed in Section 5.1. For a system diagnostic, redox potential measurements can be used as ECP measurements are used to determine when system materials are prone to oxidation.

4.2 METHODS OF PROBING REDOX POTENTIAL - INTRODUCTION

One of the key functions asked of electrochemical sensor in molten salt systems is the ability to monitor redox potential. Redox potential is a measurement of the propensity for a chemical species or system to undergo a redox reaction, and it is directly proportional to the Gibbs free energy of a chemical system at equilibrium. With this information, it is possible to predict chemical speciation in the melt, concentration of chemical species in the melt, and the corrosion of materials that interface with the melt. For molten salt systems, redox potential is a highly desirable variable to measure continuously and in real time. Electrochemical sensors directly measure redox potential, yet the measured potential is only as accurate, stable, and reliable as the reference potential. We designed redox sensors to operate in molten fluoride salts each utilizing a different method of measuring a reference potential. As noted in Chapter 3, the method of measuring redox potential considerably changes the design requirements of the sensor. For example, if a system design prioritizes having a sensor with a long operating lifetime and can tolerate periodic measurements instead of continuous measurements, then the redox sensor would utilize a dynamic reference electrode for measuring reference potential. If continuous, precise measurements were necessary and the sensor lifetime was secondary, then the redox sensor would utilize a thermodynamic reference electrode for measuring reference potential.

The MSRE researchers knew the importance of measuring redox potential and devised multiple ways to measure the property. The MSRE fuel salt was set by the U^{3+}/U^{4+} ratio. This ratio was determined electrochemically and verified by spectrophotometrically. Jenkins and Mamantov[86] constructed a galvanic cell utilizing a saturated nickel reference electrode to take emf measurements. The cell diagram is shown in Figure 56.

Pt | U(IV) | U(III) ‖ Ni(II) | Ni

Figure 56. Cell diagram of U^{3+}/U^{4+} reaction studied in ORNL-4396

The chemical equilibria for the cell in Figure 56 are defined by the following half-cell and overall reactions,

$$U^{4+} + e^- \rightarrow U^{3+} \tag{4.1}$$

$$UF_4(l) = UF_3(l) + \frac{1}{2}F_2(g) \tag{4.2}$$

$$Ni^{2+} + 2e^- \rightarrow Ni(s) \tag{4.3}$$

$$NiF_2(l) = Ni(s) + F_2(g) \tag{4.4}$$

With the inclusion of the Ni/NiF_2 thermodynamic reference reaction, Jenkins and Mamantov were able to measure formal potentials of U^{3+}/U^{4+} in fluoride salts on a thermodynamic scale. This experiment shows the power of having a well-defined thermodynamic reference potential. Specifically, with a well-characterized thermodynamic reference electrode, the chemical equilibrium of the melt is known, and the activities of all the constituents can be determined. However, this is not the only method that Jenkins and Mamantov explored for quantifying redox potential. They also devised another method to determine the U^{3+}/U^{4+} ratio. Using sweep voltammetry, they measured the potential difference between an inert Pt electrode and the half-wave potential of the U^{3+}/U^{4+} reaction.

$$\Delta E_{cell} = \Delta E_{Pt} - \Delta E_{(4.1)} = \frac{RT}{nF} ln(K) \tag{4.5}$$

where K is equal to,

$$K = \frac{a_{U^{4+}}}{a_{U^{3}+}} \approx \frac{x_{U^{4+}}}{x_{U^{3}+}} \tag{4.6}$$

This method of quantifying the redox potential offers distinct advantages to that of an emf cell devised in the first example. First, and possibly the most attractive advantage to this method, is that no reference electrode is required. This is expanded on in the latter paragraphs. Second, no standard electrode potentials need to be known prior to the measurement. The measurement assumes that the response of the U^{3+}/U^{4+} is dominant in the potential window being measured. Finally, the wetted surface area of the electrodes is superfluous to the redox potential measurement. This is because the measured U^{3+}/U^{4+} redox potential is not dependent on current density.

While we say this is a measurement of "redox potential," this is somewhat of a misnomer. Measuring the change in system potential versus a quasi-reference electrode doesn't create a potential measurement on an absolute scale. However, their electrochemical measurement was *indicative* of the change in redox potential. Measuring changes in redox potential may have equivalent utility as measuring absolute redox potentials for system health monitoring.

When absolute redox potential measurements are required, it is necessary to use a well-characterized reference electrode leveraging a thermodynamic reaction equilibrium. The development of a thermodynamic reference electrode (TRE) in molten fluoride salts has been something of a "holy grail" in designing electrochemical sensors for molten salt reactors. While there is great allure in developing a

commercially available reference electrode for fluoride salt systems, there are significant obstacles which make the development of such an electrode particularly difficult. Any individual obstacles are not insurmountable. However, when all design constraints must be met concurrently, designing a TRE for fluoride salts proves to still be a challenge after decades of development.

Molten salt redox potential can be measured either as an absolute thermodynamic quantity or as a relative diagnostic of changing salt chemistry. Thermodynamic reference electrodes, such as Ni/NiF_2 systems, provide the clearest route to formal potentials and species activities because the reference reaction is fixed by a defined chemical equilibrium. Dynamic reference electrodes, such as K/K^+ in FLiNaK or Be/Be^{2+} in FLiBe, are more practical for periodic measurements and avoid maintaining a sealed reference compartment, but their validity depends on successfully depositing and stripping the reference metal under conditions where competing redox reactions do not dominate the imposed current. The important conclusion for system health monitoring is that relative redox changes may be sufficient for operational control, but absolute redox limits require a reference scale whose thermodynamic or dynamic basis is explicitly verified under the same salt composition, temperature, and transport conditions as the measurement.

4.3 PROBING REDOX IN FLINAK - METHODS

Probing redox in FLiNaK is commonly performed by referencing the potassium redox potential. This is because potassium is the first of the major constituents in FLiNaK to reduce in the electrochemical series. Therefore, by holding a cathodic current which is greater than the limiting current of the non-constituent ions of FLiNaK, the reduction potential of potassium can be obtained. Table 21 shows the recent literature which employs methods of electrochemically measuring the potassium reduction potential in FLiNaK.

Table 21. Studies identified that used potassium redox potential as reference in FLiNaK

Study (Author, Year)	Purpose	Temperatures (°C)	Compositions	Key Findings for KDRE
Ema et al., 1987 [87]	Establish the relationship between the potential of a dynamically deposited alkali-metal reference electrode and the HF/H_2 gas reference scale in molten fluorides	500-700	LiF-KF eutectic (58 mol% LiF–42 mol% KF)	Measured the potential of a KDRE an HF/H_2 gas electrode at several hydrogen partial pressures. Demonstrated that an alkali-metal dynamic reference electrode can provide a reproducible electrochemical reference in molten fluoride salts.

Durán-Klie et al., 2016 [88]	Development of a KDRE in FLiNaK for redox-potential measurement	500	FLiNaK eutectic: 46.5 mol% LiF – 11.5 mol% NaF – 42.0 mol% KF. Validation experiments included additions of NiF_2.	Developed the FLiNaK KDRE by depositing potassium on a tungsten electrode via current pulse; a stable potential plateau formed after sufficiently large pulses (4x limiting current of solvated species); validated against Ni/Ni2+ behavior in NiF2-containing FLiNaK with agreement to Nernst expectations
Shay, 2017 [89]	Replication/extension of the KDRE method in FLiNaK + 1 wt% EuF_3; calibration of quasi-reference measurements and Eu redox	650-750	FLiNaK eutectic + 1 wt% EuF_3	Reproduced the potassium dynamic reference by chronopotentiometry with 5 s pulses; showed a threshold current is needed to fully establish the K deposit; measured stable K/K^+ equilibrium plateaus after the pulse.
Guo et al., 2017 [90]	Measurement of the Eu(III)/Eu(II) couple in FLiNaK using KDRE	650-750	FLiNaK eutectic + EuF_3 additions	Used a Pt quasi-reference calibrated by the potassium dynamic reference method; applied a 5 s pulse to form a thin K layer on W and determine the potassium potential; used this calibration to characterize the Eu3+/Eu2+ couple and support Eu-based redox buffering
Chesser et al., 2018 [91]	Electrochemical behavior of dysprosium and lanthanum in FLiNaK	600-750	FLiNaK eutectic + DyF_3 and LaF_3 additions	Reported Dy and La electrochemical potentials on a K^+/K scale in FLiNaK; used a Pt quasi-reference but expressed extracted thermodynamic quantities versus K^+/K, showing the potassium-referenced scale was part of the FLiNaK electrochemistry workflow

Doniger et al., 2022 [92]	Potentiodynamic polarization/corrosion study of pure metals and alloys in FLiNaK using KDRE	700	FLiNaK eutectic	Used a Mo wire to create the K/K^+ dynamic reference and convert Pt quasi-reference data to the K/K^+ scale; measured apparent redox potentials and polarization behavior of Ni, Fe, Cr, Ni-20Cr, and 316L.
Qiao et al., 2003 [93]	Electrochemical formation of Pd–La alloy films in LiF–NaF–KF–LaF_3 melt		LiF–NaF–KF + LaF_3 (0.5 mol.% added)	FLiNaK-related dissolved-species voltametric study that used a CV-produced KDRE in FLiNaK
Peng et al., 2016 [94]	Electrochemical detection of uranium-containing precipitates in molten fluorides			Electrochemical study associated with the K/K^+ dynamic-reference literature context
Wilson, 2024 [95]	Discussion of reference electrodes for oxide monitoring in FLiNaK		FLiNaK eutectic	Reviewed the FLiNaK potassium dynamic reference electrode as a KF/K system formed by reducing K^+ onto tungsten; emphasized that potentials should be measured during post-deposition relaxation to avoid ohmic-drop distortion; presented the K/K^+ dynamic reference as a useful calibration approach for quasi-reference electrodes in FLiNaK

4.3.1 POTASSIUM DYNAMIC REFERENCE ELECTRODE (KDRE)

The change in redox potential of molten FLiNaK can be measured using a reference reaction, in this case the K/K^+ redox couple. Following Olander's definition of fluorine potential [84], given the reaction,

$$\mathrm{K(s)} + \frac{1}{2}\mathrm{F_2} \leftrightarrow \mathrm{KF(soln)} \tag{4.7}$$

and by the law of mass action,

$$K_{eq,2} = \frac{a_{KF}}{\sqrt{p_{F_2}}} = \exp\left(-\frac{\Delta G^0_{KF}}{RT}\right) \tag{4.8}$$

Then the fluorine potential in this system is calculated by,

$$\Delta\bar{G}_{F_2} = RT\ln\left(p_{F_2}\right) = RT\ln(a_{KF}) + \Delta G^0_{KF} \tag{4.9}$$

We do not calculate the exact activity of KF in the melt. We choose our standard state of formation to be pure KF liquid (The data for KF(l) spans the range of temperatures of 1100K to 2300K (827°C to 2027°C), so we are extrapolating the data from the liquid state beyond its defined range). a_{KF} is the activity of KF in FLiNaK of the specified composition.

Our cell consisted of a W WE, W CE, and W qRE. E_{OCP} of a symmetric cell is 0V in a system with uniform concentration. When we probe for this reaction in the FLiNaK melt, we perform a two-step chronopotentiometric process. First, we polarize the electrode and reduce the K^+ cation in solution to K metal. Then, we open the circuit and allow the K metal to oxidize back into K^+ cation. It is during the second step in the process that we measure the open circuit potential (E_{cell}) between the working electrode (WE) and the quasi-reference electrode (qRE). We calibrate the potential measured on our qRE by E_{cell}. Similar methods have been performed in literature[88], [96], [97].

The difference between the EMF measured on the surface of the WE during the K dissolution and the EMF measured on the surface of the WE after the melt returns to equilibrium is related to the redox potential. This is similar to the methods used by Jenkins and Mamantov reporting U^{3+}/U^{4+} redox potentials versus their Ni/Ni^{2+} reference electrode[86]. By comparing the OCP of the W WE and W qRE and the OCP of the K-plated W WE and the W CE, we can determine the potential of the K oxidation reaction relative to the OCP of our system, E_{K/K^+}.

$$E_{cell} = E_{OCP,ss} - E_{KDRE} \tag{4.10}$$

We are assuming the value $E_{OCP,ss}$ will not drift over the course of the experiment as it should be equal to 0V in a symmetrical cell and W electrodes are inert to the melt composition.

4.4 CHRONOPOTENTIOMETRY OF FLiNaK-CrF_3 - RESULTS

Chronopotentiometry was performed on the salt melt at 800°C, after additions of different amounts of CrF_3; approximately 30 minutes at 800°C was allowed between addition of CrF_3 and subsequent electrochemical measurements. Solute concentrations calculated based on complete CrF_3 dissolution before performing the electrochemical measurements and chronopotentiometry results are given in Table 22.

We observe different potential responses in the FLiNaK-CrF_3 system across the range of added CrF_3 concentrations. The blank salt unsurprisingly does not show signs of any reduction reactions until we reach a stable plateau which is attributed to K reduction. This is observable from the red trace in Figure 57.

Table 22. Summary of CP results in FLiNaK-CrF_3 @ 800°C

Run (Addition) #	Notes	Added CrF_3 Concentration [wt%] [(a)]	Added CrF_3 Concentration [mol/mol] [(a)]	Observed Ecell (vs KDRE) [V]	Observed $E_{1/4}$cr, from chronopotentiometry [V vs. qRE]	Observed τ_{rxn} from CP [sec]
0	blank	<5.1e-6 [(b)]	<1.91e-6[(b)]	1.474(8)	n/a	n/a
1		0.22	0	1.288(4)	-0.448	tau_2=0.125
2		0.45	0.000824(9)	n/a		tau_2=0.274
3	CE failed during CP	0.90	0.00171(1)	n/a		tau_1=0.140 tau_2=0.929
4		2.60	0.00345(2)	n/a		tau_1=0.865
5		5.56	0.01013(4)	n/a	n/a	n/a
6		9.05	0.02232(5)	n/a	n/a	n/a
7	Complete cell failure prevents further runs	10.9	0.03774(5)	n/a	n/a	n/a

(a) Assume all added CrF3 dissolved within 30 minutes at 800 oC. Error is calculated in Appendix A.8.

(b) LOD for ICP-OES.

(c) Measured value, for the blank, to establish Eo for the chromium redox couple. All other calculated values are based on this Eo.

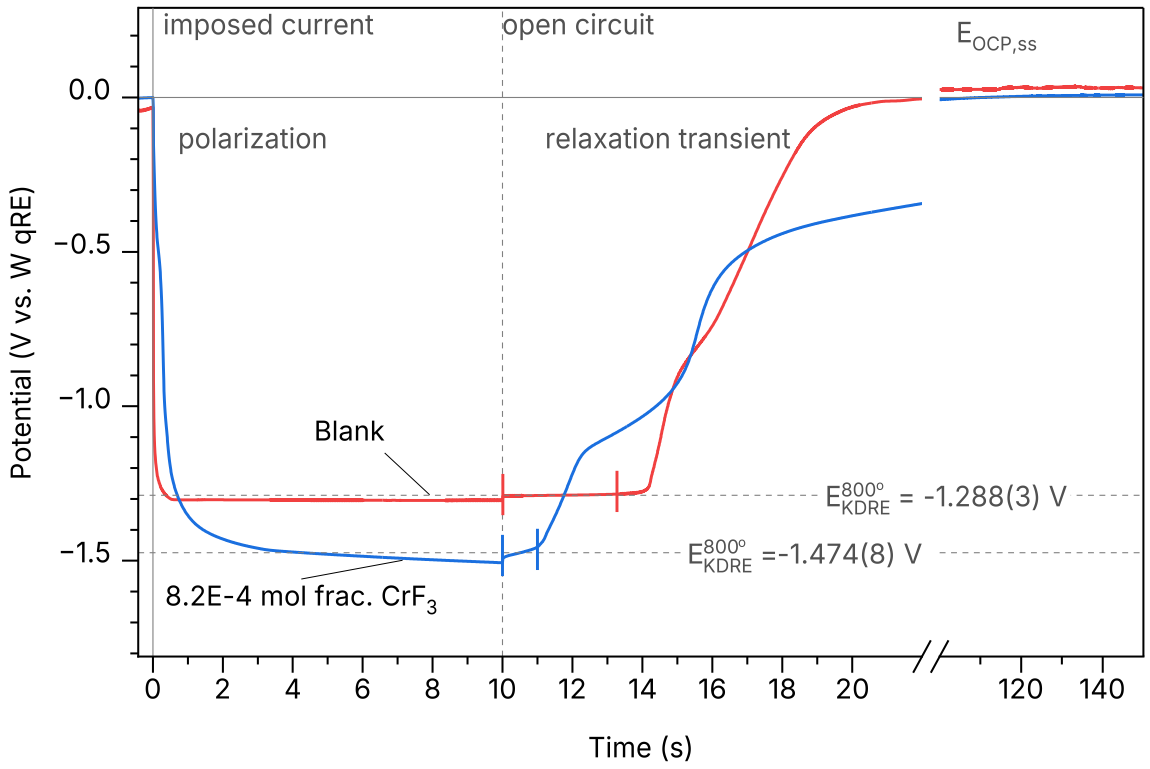


Figure 57. Chronopotentiometry of FLiNaK with and without CrF3 addition at 800oC. The K/K$^+$ oxidation potential is measured from determining the transition time on the potentiogram. W WE; W CE; W qRE; polarized with 100mA for 10 second followed by open circuit relaxation transient.

Upon adding CrF_3 to the melt, one of two scenarios are possible. Either a) E_{cell} changes upon addition of CrF_3, reflecting the $Cr(s) = Cr^{3+} + 3e^-$ equilibrium that is achieved if Cr metal is present in the salt, or b) there is no change in E_{cell} because there are no species present in the melt that can be oxidized by CrF_3. Notably, Cr metal can be produced in the salt if CrF_3 acts as an oxidant on other metal species that are lower in the electrochemical series than Cr in contact with the salt. In this cell, the only salt-facing metals were Mo and W, neither of which would be oxidized by CrF3. For example:

$$\frac{1}{4}W(s) + \frac{1}{3}CrF_3(l) = \frac{1}{4}WF_4(l) + \frac{1}{3}Cr(s); \quad \Delta G_{rx}\ (800\ oC) = 74.5\frac{kJ}{mol} \gg 0 \qquad (4.11)$$

However, the W and Mo rods have purity specs of 99.9% and 99.7% respectively. Therefore, there may have been less inert metallic elements in the impurities that could be oxidized by CrF_3, including Cr metal. Thus, if the redox potential of the salt shifts in response to CrF3 additions, that indicates presence of Cr metal or more reactive metal impurities such as Mn or Ti.

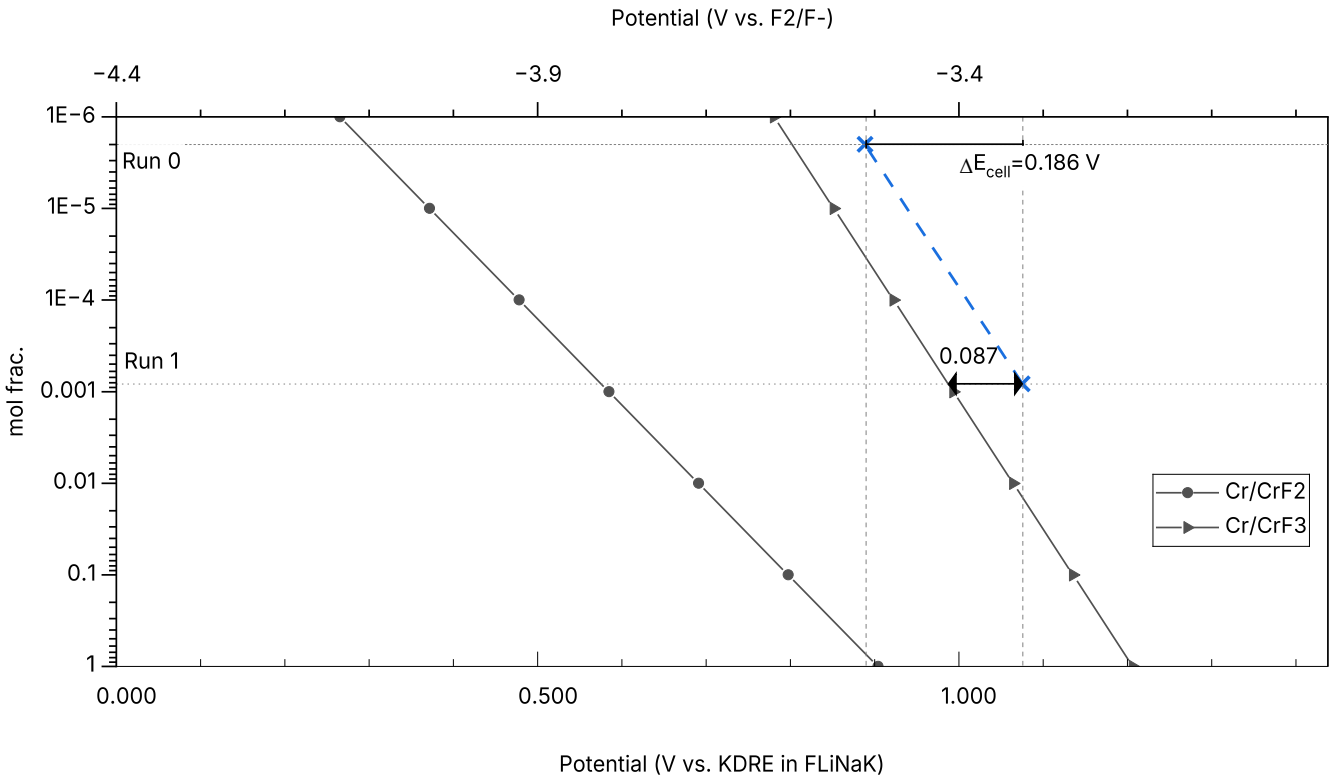


Figure 58. Ellingham diagram of Cr/Cr^{2+} and Cr/Cr^{3+} on a KDRE potential scale in FLiNaK as functions of concentration. Blue "X"s are collected data points from CP.

Based on the results in Figure 57, we are in scenario I. Therefore, the expected change in E_{cell} with addition of known amount of CrF3 can be calculated, if we assume the activity coefficient of Cr^{3+} is constant in the concentration range of the measurement:

$$\Delta E_{cell} = E_{cell,2} - E_{cell,1} = \frac{RT}{nF} \ln\left(\frac{x_{Cr^{3+},f}}{x_{Cr^{3+},i}}\right) \tag{4.12}$$

where ΔE_{cell} reflects the change in redox potential of the melt, R is the gas constant, T is the absolute temperature, n is the number of electrons exchanged in the reaction, F is Faraday's constant, $x_{Cr^{3+},f}$ is the final mole fraction of Cr^{3+} in solution, and $x_{Cr^{3+},i}$ is the initial mole fraction of Cr^{3+} in solution. Between Run 0 and Run 1 (see Table 22), a change of -0.187(3)V would be expected. The measured E_{cell} change was -0.186(6)V. Subsequent runs of CP, shown as Addition 4, Addition 5, and Addition 6 in Figure 59, were unable to achieve the KDRE. This is discussed in Section 4.4.1 and is categorized as an operational failure due to inadequate methods development.

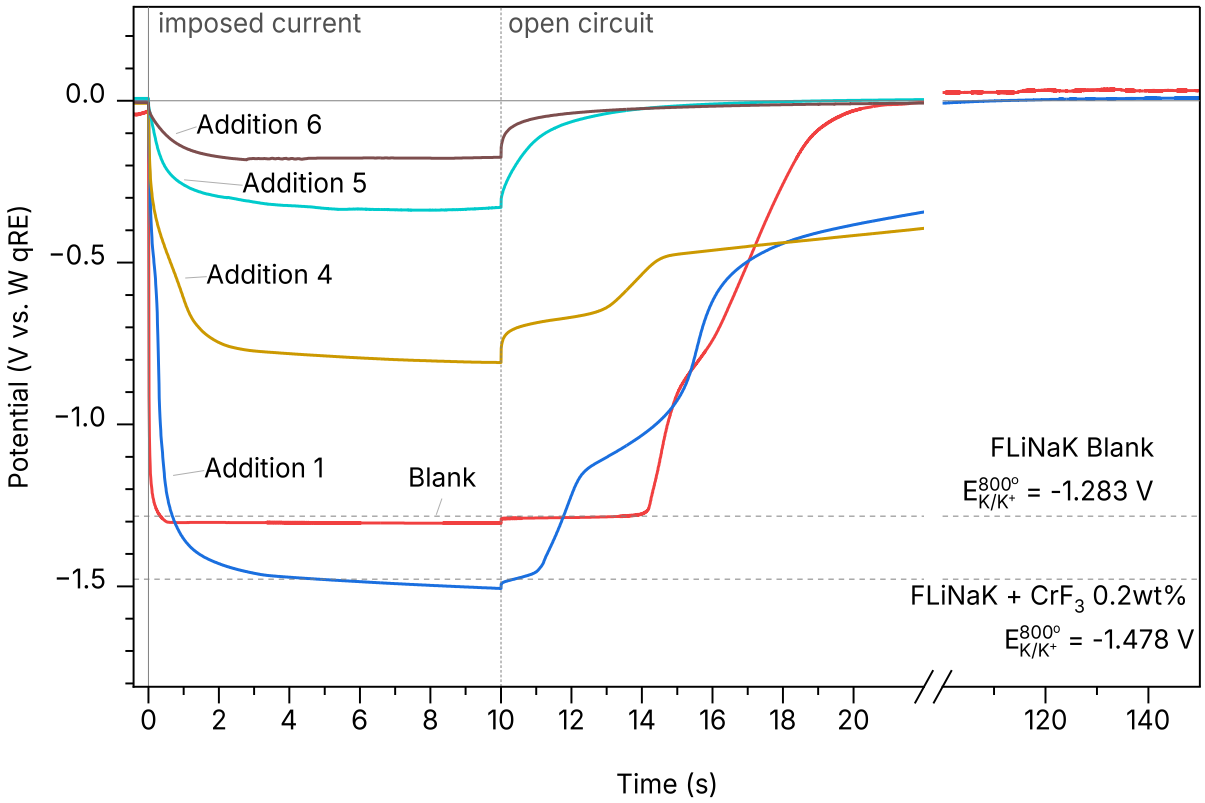


Figure 59. Chronopotentiometry of FLiNaK at 800oC with W WE, W CE, W qRE. See Table 22 for run details.

In performing CP, we were able to measure the uncompensated resistance of the cell[87], [98]. Using Ohm's law, we can determine the change in potential of the cell after a change in imposed current.

$$\Delta V = \Delta I \cdot R \tag{4.13}$$

It is clear from Figure 60 that the solution resistance causes a potential drop of 14mV with a current drop of 0.1A. This gives us a solution resistance of 0.14Ω at Addition 1. The solution resistance does not appear to scale with concentration of added CrF_3. The average solution resistance measured by CP was $0.26(1)\Omega$.

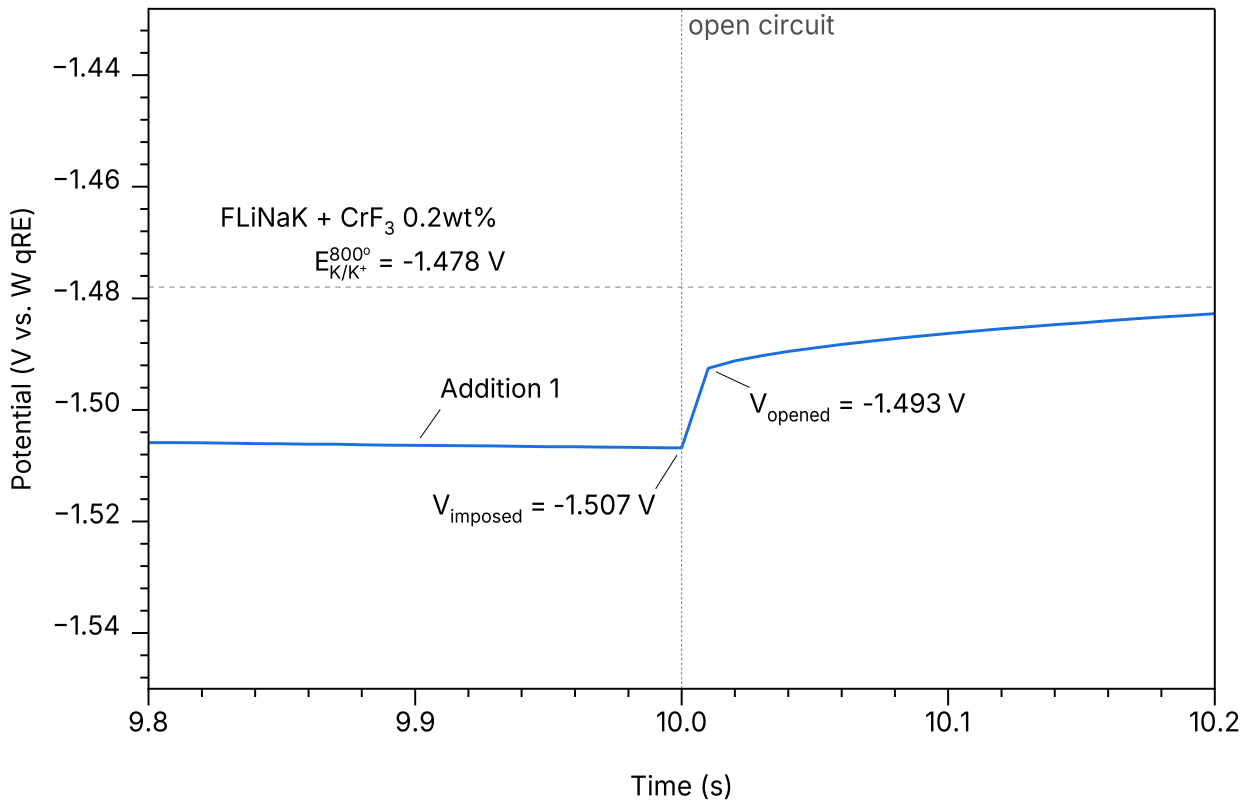


Figure 60. Zoomed in region at the transition from imposed current to open circuit in Figure 59. Showing the effect present in Addition 1 (see Table 22 for details) as an example.

For CP runs after Addition 1, the shift in reaction plateau potentials increased after each addition of CrF_3. The predicted KDRE potential plateau decreases after each addition, and therefore we can be confident that we are not reaching potassium reduction after Addition 1. The shift in potential plateau is, however, increasing with each addition of CrF_3, and this is indicative of any Cr redox reactions. We know that we are observing Cr redox reactions at the potential plateaus in Addition 4, 5, and 6 because the reduction of Cr^{3+} and Cr^{2+} occur at a less reducing potential after each addition and thus will appear to shift positive. It cannot be immediately determined if the potential plateaus observed in Addition 4, 5, and 6 are the Cr^{3+}/Cr^{2+} or the Cr^{2+}/Cr^{0} reactions.

During cell operation, it is possible to determine signatures of failure or off-normal behavior of the electrochemical sensor from the data without optically examining the cell. Being able to determine failure signatures is important for molten salt electrochemical sensing as optical examination of the electrodes and sensors is not always readily available. This is especially true when deploying a sensor in a prototypical molten salt system which will not always have an accessible free liquid surface or a viewport.

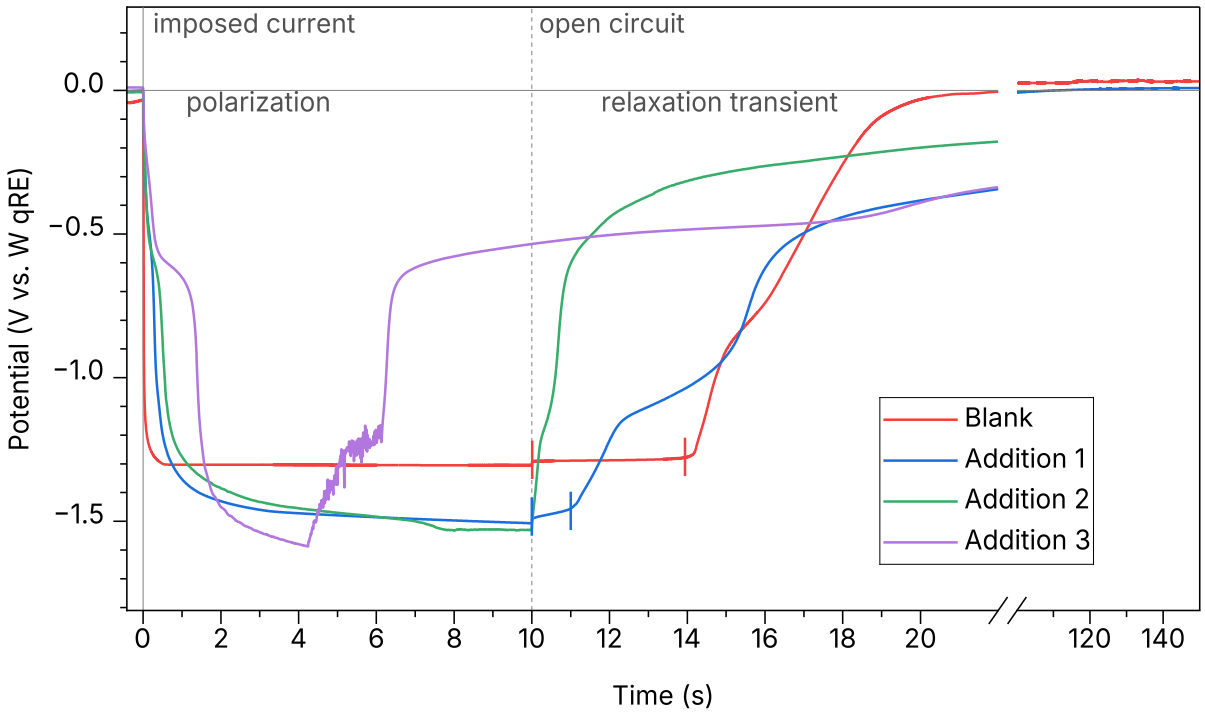


Figure 61. Chronopotentiometry data of FLiNaK-CrF_3 system; Addition 2 and Addition 3 details present in Table 22.

4.4.1 Operational Failure in Chronopotentiometry

Addition 2 was operating with a polarization step of 0.1A for 10 seconds followed by a relaxation step of 0A (open circuit) for 600 seconds. We see a plateau occur during the polarization step, but unlike the Blank and Addition 1 polarization plateaus, there is no plateau that occurs immediately afterward in the open circuit step. The lack of a plateau in the open circuit region is evidence that we did not deposit K metal on the electrode surface. The operation was to perform a KDRE measurement which relies on the plating and stripping of K metal from the FLiNaK electrolyte. Therefore, this qualifies as operational failure in the electrochemical cell and led to the inability to collect a data point in the study.

This type of operational failure can be prevented in the future by troubleshooting the control variables of chronopotentiometry in the cell. Chronopotentiometry as a technique allows for two fundamental control variables – current step setpoint and polarization time. While modern potentiostats can also allow for variable sample rates, preconditioning, and multi-current-step programs, these parameters are really most sophisticated versions of the same two fundamental control parameters. We can see this clearly by arranging Faraday's Law as follows,

$$it = znF \tag{4.14}$$

where i is the total current, t is the time of imposed current, z is the number of electrons exchanged, n is the moles of electroactive species, and F is Faraday's constant. By changing the value of i or t, we will

change the total number of electrons exchanged and thereby moving the reaction coordinate being probed by the potentiostat. In our cell, we wanted to observe K/K^+ for our KDRE measurement, but we did not reach the potassium reduction plateau. We can troubleshoot this by increasing the current step or by extending the time of polarization. By increasing the current step and/or polarization time, we are increasing the total charge transferred within the polarization period and are able to reduce more cations in the melt within the same duration of time.

During Addition 2, the potentiostat polarized the WE with 0.1A of cathodic current and did not reach the K/K^+ reaction within 10 second of polarization. This is related to the increased concentration of CrF_3 added to the system. By increasing the concentration of Cr^{3+} in the system, more total current needs to pass through the cell before we reach the K/K^+ redox reaction. We can explicitly write the total current needed to reduce all of the electroactive Cr^{3+} to Cr^0 for our 10 second polarization step.

$$i_{Cr^{3+}} = \frac{z_{Cr^{3+}} n_{Cr^{3+}} F}{t_p} \tag{4.15}$$

Letting $z_{Cr^{3+}} = 3$ for the oxidation state of Cr^{3+}, $n_{Cr^{3+}} = 8.62 \times 10^{-4}$ moles of Cr^{3+} active in the melt, $t_p = 10$ seconds for the duration of polarization, we require a total current of $i_{Cr^{3+}} = 24.95$ A. However, this is an overestimate of the necessary total current since we are only interested in the total Cr^{3+} available within the diffusion layer of the electrode. The length of the mean-free path of one-dimensional diffusion is approximated by Eq.(4.16):

$$\delta_{dl} = \sqrt{2Dt} \tag{4.16}$$

where δ_{dl} is the diffusion layer thickness and D is the diffusivity of the redox active species. Therefore, the total moles of Cr^{3+} in the diffusion layer can be calculated by multiplying the molar concentration of Cr^{3+} and the volume of the diffusion layer. Assuming the diffusion layer around the wire electrode is approximately cylindrical we can now calculate the total current required for polarization.

$$V_{dl} = \pi \delta_{dl}^2 h_w \tag{4.17}$$

$$n_{Cr^{3+}} = V_{dl} C_{Cr^{3+}} \tag{4.18}$$

The closer estimate of the number of Cr^{3+} moles in the diffusion layer is 4.69×10^{-7} mol. Therefore, the actual total current required to completely reduce the Cr^{3+} to Cr^0 is approximately 0.0136 A. This is a significant result because it is a contradiction. The total current in the cell was 0.1 A, nearly an order of magnitude greater than the calculated required current. This means there are other effects at play in the cell. Specifically, two effects that contribute to total current for complete reduction of Cr^{3+} are the charging of the electrochemical double-layer and natural convection mixing the electrolyte. The charging of the double layer can be estimated to require on the order of magnitude 10-100μC to polarize the working electrode, assuming the capacitance is approximately constant over the range of polarizing potentials[28] and assuming a typical double layer capacitance range around 10-100μF/cm^2. This effect is still over three orders of magnitude below the total charge transfer we see.

Natural convection can occur within the high temperature cell leading to the formation of a convection-diffusion layer (CDL)[69]. The CDL increased mass transfer rates to the electrode surface and increases the magnitude of the limiting current of a redox reaction compared to the limiting current in a system with just a diffusion layer. Therefore, we can conclude the operational failure in the cell was due to increased limiting currents of the cations in solution. Future experimental design and methods must account for the effect of natural convection when performing chronopotentiometry since it will affect the limiting current of constituent cations in the melt and prevent us from using the dynamic reference electrode technique.

4.4.2 Material failure in Chronopotentiometry

A different mode of failure we can see in Figure 61 is functional failure where the electrochemical cell is no longer able to meet the functional requirements specified by its design. Unlike the Blank and Addition 1, Addition 3 shows an increase in potential during the polarization step. Seeing this increase in potential during the cathodic polarization step during chronopotentiometry could indicate failure for several independent components – the potentiostat, the conductive cable, and the power supply are all possible sources of failure in this system – but the most likely cause for failure in this cell was determined to be the electrodes themselves. In Addition 3, the specific component that failed was the counter electrode in the cell. This was discovered after post-mortem examination of the electrodes. It would have been difficult to diagnose prior to removing the electrodes from the melt, but several methods are developed here to help troubleshoot this issue in the future.

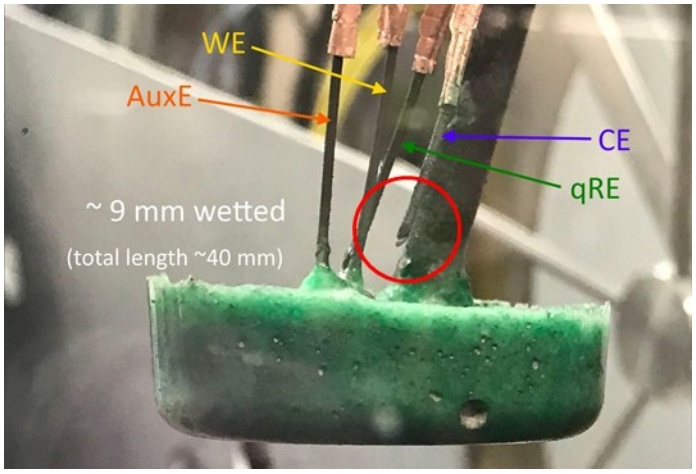


Figure 62. Image of frozen FLiNaK with 10.9wt% CrF_3 added. The red circle shows the tip of the W counter electrode consumed and sticking out of the melt.

We can see from Figure 62 the counter electrode is frozen out of the FLiNaK salt puck. From this image alone we can confidently say the behavior seen for Addition 3 in Figure 61 is caused by an open circuit error. When the potentiostat is polarizing the working electrode with cathodic current, the counter electrode must hold the equivalent anodic current for the duration of the experiment. In this scenario, the counter electrode was consumed by the anodic current and was no longer immersed in the melt resulting in a break in the circuit and stopping the flow of cathodic current into the working electrode.

During the experiment, we were unable to troubleshoot by visually observing the electrodes in the melt. However, we were able to troubleshoot the problem by running multiple open circuit potential measurements. By systematically taking open circuit potential measurements between every electrode in the cell (WE vs CE, WE vs qRE, WE vs AuxE, CE vs qRE, CE vs AuxE, and qRE vs AuxE), we found that every electrode produced an unrealistic open circuit potential versus the counter electrode. This was indicating that the counter electrode failed in the cell, though it was unclear how exactly it failed until post-mortem examination.

It is notable that the W counter electrode does not have a spontaneous reaction with any of the fluoride salts added to the melt. For example:

$$\frac{1}{4}\mathrm{W(s)} + \frac{1}{3}\mathrm{CrF_3(l)} = \frac{1}{4}\mathrm{WF_4(l)} + \frac{1}{3}\mathrm{Cr(s)}; \quad \Delta G_{rx}\ (800^{o}C) = 74.5\,\frac{kJ}{mol} \gg 0 \qquad (4.19)$$

Tungsten may not be electrochemically inert under strongly oxidizing fluoride-salt conditions. Eklund et al. showed that multiple tungsten fluoride complexes are electroactive in molten FLiNaK between 475 and 800 °C, including species assigned to W(V) and W(III) [99]. Gao et al. showed that W^{4+} and W^{6+} are electroactive in FLiNaK after solvating from WC[100]. In addition, Hildenbrand directly measured gaseous tungsten fluorides, including WF4(g), at 1000–2200 K by equilibrium mass spectrometry, demonstrating that volatile tungsten fluoride species in FLiNaK are thermochemically plausible[101]. The results of the elemental analysis indicate W did end up in the melt and likely entered the melt through the oxidation of the counter electrode in the electrochemical tests.

4.5 PROBING REDOX IN FLINAK - DISCUSSION

Chronopotentiometry in FLiNaK-CrF3 showed that KDRE-based redox measurements can be accurate at low chromium concentration but fail predictably as competing chromium reduction consumes the imposed current. The first CrF_3 addition provides a quantitative KDRE-based measurement of redox shift in this experiment. Before CrF_3 additions, the blank FLiNaK salt produced a well-defined K/K^+ dynamic reference plateau. After addition 1, the KDRE was again successfully established, and the measured change in E_{cell} was 186(6) mV, in close agreement with the Nernst-predicted shift of -0.187(3) mV. This agreement indicates that the shift in redox potential can be captured accurately when the potassium deposition and stripping steps are achieved. The same CP traces also gave an uncompensated resistance measurement, with a 14 mV potential drop for a 0.1 A current change in Addition 1 and an average measured resistance of 0.26(1) ohms.

Subsequent CrF_3 additions with current step of 100 mA for 10 second did not achieve a valid KDRE response. Instead, the cathodic polarization plateau shifted progressively to more position potentials with increasing CrF_3 additions. This behavior indicates that chromium redox reactions increasingly dominated the cathodic current before the electrode reached the K/K^+ reduction plateau. The disappearance of the KDRE plateau should not be considered simply as sensor failure; rather, it identifies an operational limit of the KDRE method under the selected current-step conditions. Once the limiting current associated with chromium reduction became sufficiently large, the imposed cathodic current was consumed by chromium reduction. The operational-failure analysis is instructive: a diffusion-layer estimate suggested that only

0.0136 A would be needed to reduce available Cr3+ near the electrode during a 10 s pulse, yet the 0.1 A pulse still did not reach the potassium plateau, implicating natural convection and enhanced mass transfer as controlling effects. This result is consistent with the convection-diffusion behavior calculated in Section 3.2.1.2. Natural convection increases the limiting current of dissolved redox-active species, thereby expanding the current required to bypass chromium reduction and reach the reference-cation deposition reaction. In this experiment, that effect limited KDRE formation at higher CrF_3 concentrations. Consequently, the later additions provide evidence of chromium-dependent changes in cathodic electrochemistry, but they do not provide addition quantitative KDRE measurements of the redox potential shift.

A separate material failure occurred when the W counter electrode was consumed and effectively opened the circuit, which was later diagnosed by pairwise OCP checks and confirmed by post-test inspection. The conclusion is that CP provides powerful redox and resistance diagnostics, but dynamic reference measurements in molten salts must be designed around convection, competing reactions, and counter-electrode lifetime. We should conclude that KDREs can quantify redox potential changes in FLiNaK, but only when the imposed deposition step exceeds the competing mass-transfer-limited currents of reaction actives species in the salt inventory.

4.6 PROBING REDOX IN FLIBE – METHODS & RESULTS

We examine the change in redox potential of FLiBe using three separate reference electrodes in this section. The design and functionality of a TRE which utilizes the Ni/NiF_2 redox couple is the focus of Section 4.6.1. Unique to this design, the TRE features a graphitic foam body with a BN coating fabricated by chemical vapor deposition (CVD) and a LaF_3 crystal cast. The measurement of the Ag/AgF redox couple in FLiBe is the focus of 4.6.2. The work outlines the design pitfalls and experimental challenges with using the Ag/AgF redox couple. Finally, we discuss the theory and application of a beryllium dynamic reference electrode (BeDRE) in Section 4.6.3. It is the aim to show that probing redox potential in FLiBe is achievable by several types of electrodes, and it is up to the designer to choose which type of electrode is best suited to the function of the sensor they wish to implement on a FLiBe system.

4.6.1 NI-NiF_2 THERMODYNAMIC REFERENCE ELECTRODE (NITRE)

The Ni/NiF_2 redox reaction has been studied in molten fluorides since Grjotheim[102] first published his work in 1957, and then a deep dive in Ni/NiF_2 redox in FLiBe and FLiNaK was led by Jenkins and Mamantov[103] in 1968. There have been several major studies on Ni/NiF_2 redox as a thermodynamic reference electrode[104], [105], [106], [107], [108], [109], [110], all of which confirming the application of a Ni/NiF_2 reference electrode for potentiometry and voltammetry in a fluoride salt system.

UC Berkeley worked with Ultramet, an advanced materials fabrication company, to develop a novel reference electrode design which is resilient to degradation after long term FLiBe exposure, produces repeatable electrochemical data, and can be incorporated into molten salt systems modularly. This material is based upon work supported by the U.S. Department of Energy, Office of Science, Office of Nuclear Energy, under Award Number DE-SC0021952.

The goal of the project was to assist in design and testing of thermodynamic reference electrode to be used in FLiBe. A porous graphite cell was to serve as the main body of the electrode, electrically insulated using chemical vapor deposition (CVD) of boron nitride (BN). Designing the NiTRE in this way intended to test the hypothesis that the porosity of graphitic foam would provide faster response time due to increased ionic membrane surface area compared to NiTRE designs[103], [104], [106], [107], [111] in literature.

Testing various porosities investigates the wettability of the BN coated graphitic foam. Without ionic contact, the NiTRE will not function as intended. Previous[103], [106] TRE designs require hours to days of preconditioning before showing signs of ionic contact. The addition of porosity to the NiTRE body is hypothesized to also reduce the required wetting time before signs of ionic contact are seen.

There was a concern about the chemical stability of the CVD-deposited BN on the porous graphite electrode. It had been previously demonstrated that NiF_2 reacts with BN at 700 ^oC, consuming the NiF_2 and degrading the BN[107], [108]. Since the CVD BN layer is thin (~ 50 um), this potential chemical degradation was of concern. We first aimed to determine the extent of degradation of the BN coated graphitic foam after a FLiBe exposure.

This first testing campaign consisted of two main experimental thrusts which characterized the materials degradation and the electrochemical response of the TRE. The first experimental thrust concerns the degradation of a boron-nitride (BN) chemical vapor deposited (CVD) layer on porous graphite under long term exposure to FLiBe at high temperatures. Six (6) unique BN coated graphite foam coupons were exposed to FLiBe held at 700C for 96 hours. The cross sections of each coupon were imaged by macro lens photography for initial qualitative results, which indicate the presence and efficacy of the BN layer after the FLiBe exposure.

The second experimental thrust characterizes the electrochemical response of the novel electrode in FLiBe. Ultramet provided UC Berkeley with open-ended cylindrical TRE bodies for electrochemical characterization. Each TRE body consists of graphite foam with CVD BN and contained lanthanum-fluoride (LaF_3) on the inside diameter which acts as an ionic membrane and a mass barrier. Ultramet's TRE was loaded with NiF2 and assembled with a Ni wire electrode. Open circuit potential (OCP) and polarizability of the TRE were measured using a Gamry Ref 600 potentiostat where the novel TRE was connected to the working lead, a second Ni wire was connected to the counter lead, and a third Ni wire was connected to the reference lead. Initial polarizability testing confirmed there was ionic contact between the interior TRE body and the exterior bulk salt. These results indicate the novel TRE shows promise for accurately monitoring salt chemistry under high temperature environments for timescales of at least 96 hours.

4.6.1.1 BN Coated Graphitic Foam Exposure

Graphitic foam disks were fabricated and covered with CVD BN. The fabrication specification for each graphitic foam disk varied the porosity, in pores per inch (ppi), and in BN coating thickness (in μm). Figure 63 shows the graphite foam disk being measured by calipers, where the scale of the image is given by the 10.00 mm gap between the two jaws of the calipers. Six BN coated graphitic foam disks were exposed to molten FLiBe at 700^{o}C for 96-hours. The exposure was performed by immersing the six disks in

hydrofluorinated FLiBe from UW-Madison. The low-density graphitic foam caused the disks to float on the FLiBe, so the disks weighed down by inserting a metal lid on the crucible to ensure they would stay immersed in the salt. After the exposure completed, the disks were removed from the salt, cross-sectioned with a low-speed saw, and set in epoxy molds for optical microscopy. The six BN coated disks exposed to FLiBe were compared to six identically manufactured disks that were brought up to 700°C for 96-hours and not exposed to FLiBe, serving as the control group. The control group disks are shown in Figure 64. The sample legend for all specimen tested is given in Table 23.

Table 23. Graphitic foam disk sample test matrix

Sample Name	Foam Porosity (ppi)	BN Coating Thickness (μm)	Salt Exposed?
40S01	100	60	No
40S02	100	60	Yes
40S03	100	154	No
40S04	100	154	Yes
40S05	65	60	No
40S06	65	60	Yes
40S07	65	154	No
40S08	65	154	Yes
40S09	0	45	No
40S10	0	45	Yes
40S11	0	135	No
40S12	0	135	Yes

Figure 63 shows graphite foam disk sample 40S01 after BN coating, with calipers included to document the disk diameter before high-temperature exposure providing pre-test geometry of the coated control specimen for comparison with post-exposure changes. Figure 64 shows a stack of graphitic foam disks mounted between metallic supports before high-temperature furnace exposure, with each disk labeled to maintain sample traceability. The control sample configuration before testing and provides a visual reference for comparing post-exposure changes in morphology, mass, or chemical condition.

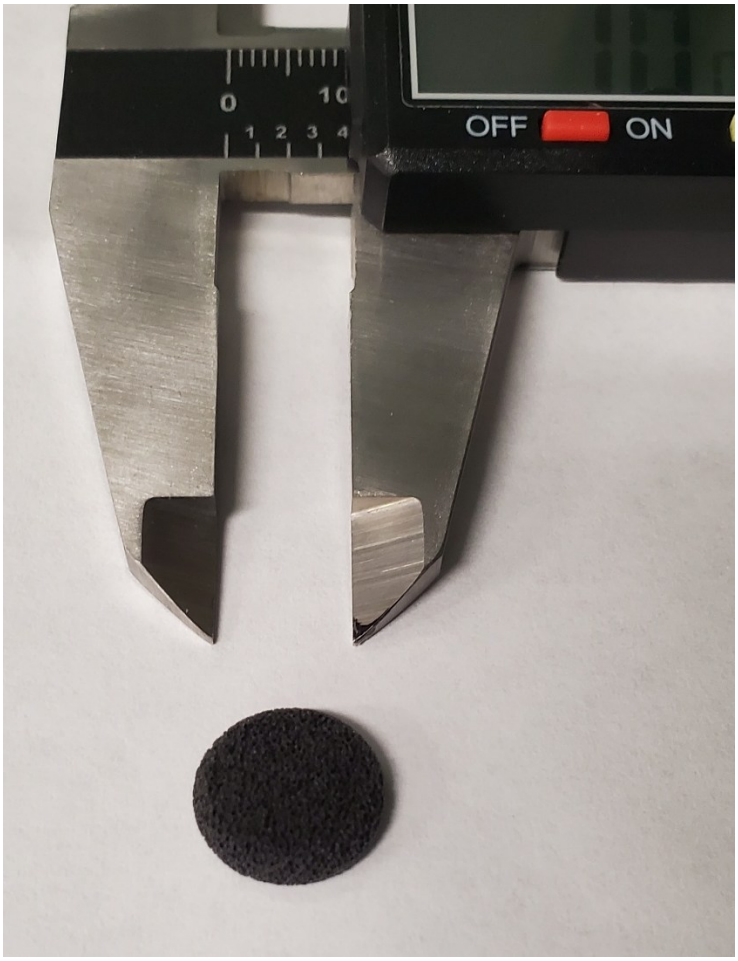


Figure 63. Graphite foam disk (Sample# 40S01, see Table 23 for details) with BN coating added via CVD. The graphite disk measures 12.97 mm (0.51 in) in diameter. The caliper jaws are open to a gap of 10.00mm.

Figure 65 shows the cross-sectional images of BN-coated graphitic foam samples after FLiBe exposure. This provides a visual comparison for the extent of salt infiltration into the foam structure versus the BN degradation. Sample 40S06 shows localized FLiBe infiltration into an open pore while adjacent pores remain preserved, whereas Sample 40S05 shows little to no visible salt infiltration, indicating that BN coating and pore morphology strongly influence salt penetration behavior under the exposure conditions. The graphite foam disks show little to no signs of degradation after exposure to FLiBe for 96+ hours. The BN coating appears to be present on the microscopy images and shows signs of FLiBe wetting. The outer pores of the graphite foam show salt infiltration while the interior pores of the foam are free of FLiBe. Salt infiltration is necessary for successful ionic contact. The successful penetration of FLiBe at least in some region of the porous coupon indicates that this can be made into a RE body.

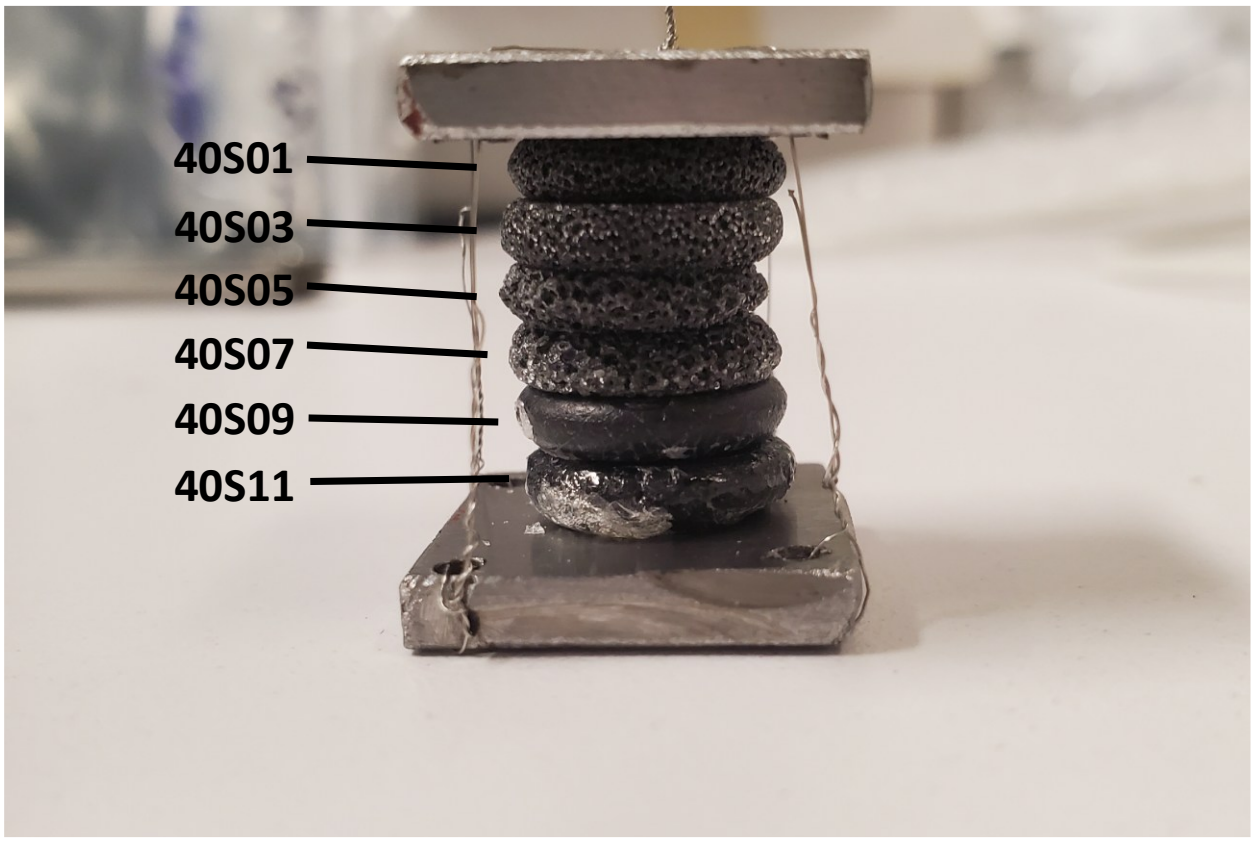


Figure 64. Stacked graphitic foam disks for control experiments. Sample names annotated in the image (see Table 23 for details) Image taken prior to inserting them in furnace for high exposure.

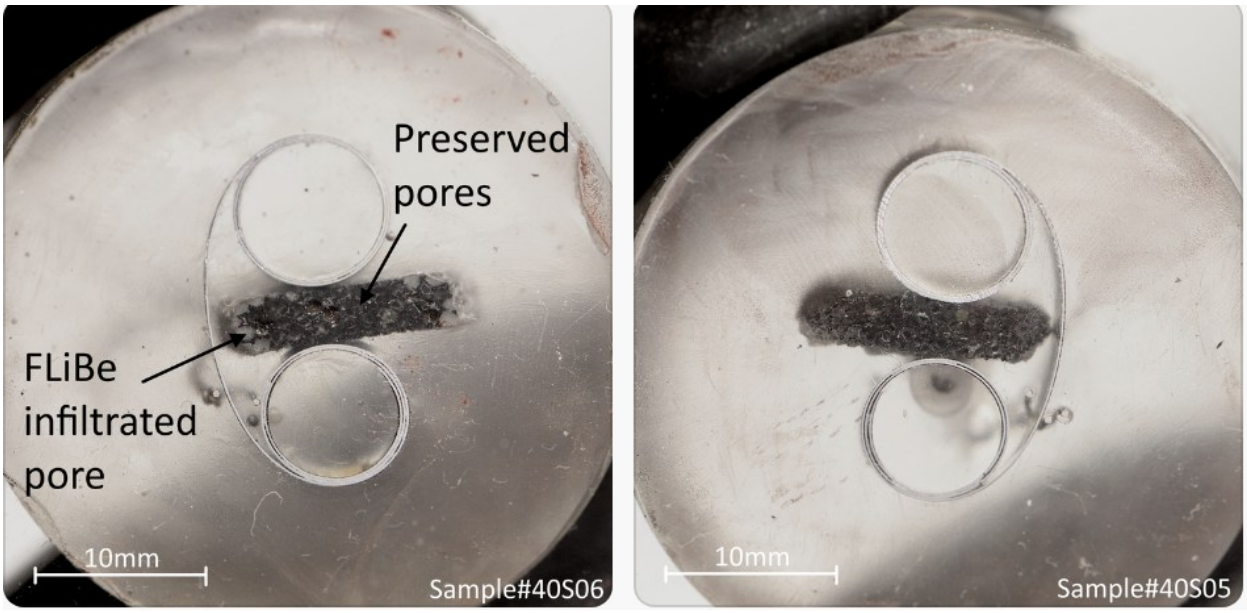


Figure 65. Cross section of BN coated graphitic foam samples. (left) Sample#40S06 (see Table 23 for details) showing signs of salt infiltration of the pores. (right) Sample#40S05 (see Table 23 for details) showing little to no salt infiltration.

Figure 66 provides an optical microscopy map of BN-coated graphitic foam sample 40S05 after high temperature exposure, showing the locations selected for higher-magnification imaging and surface evaluation. The mapped regions show no obvious macroscopic degradation of the graphitic foam structure or BN coating, supporting the interpretation that this sample experienced thermally driven degradation and no visible coating failure under the exposure conditions.

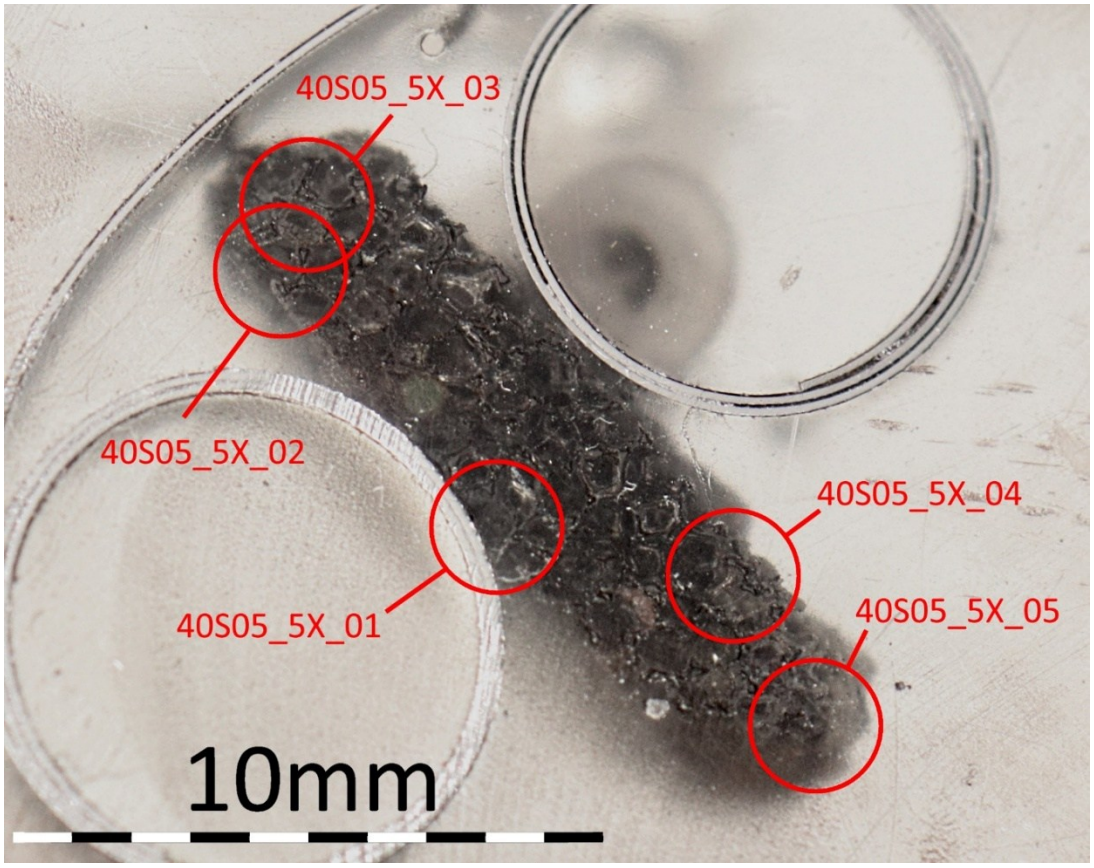


Figure 66. Sample#40S05 (see Table 23 for details) map of microscopy images. No obvious signs of graphitic foam or BN coating degradation.

Figure 67 provides an optical microscopy map of BN-coated graphitic foam sample 40S06 after FLiBe exposure, showing the locations selected for higher-magnification imaging and comparison across the exposed foam cross section. The mapped regions include areas near visible salt-infiltrated pores and preserved foam features, with no obvious macroscopic degradation of the graphitic foam or BN coating observed at this magnification.

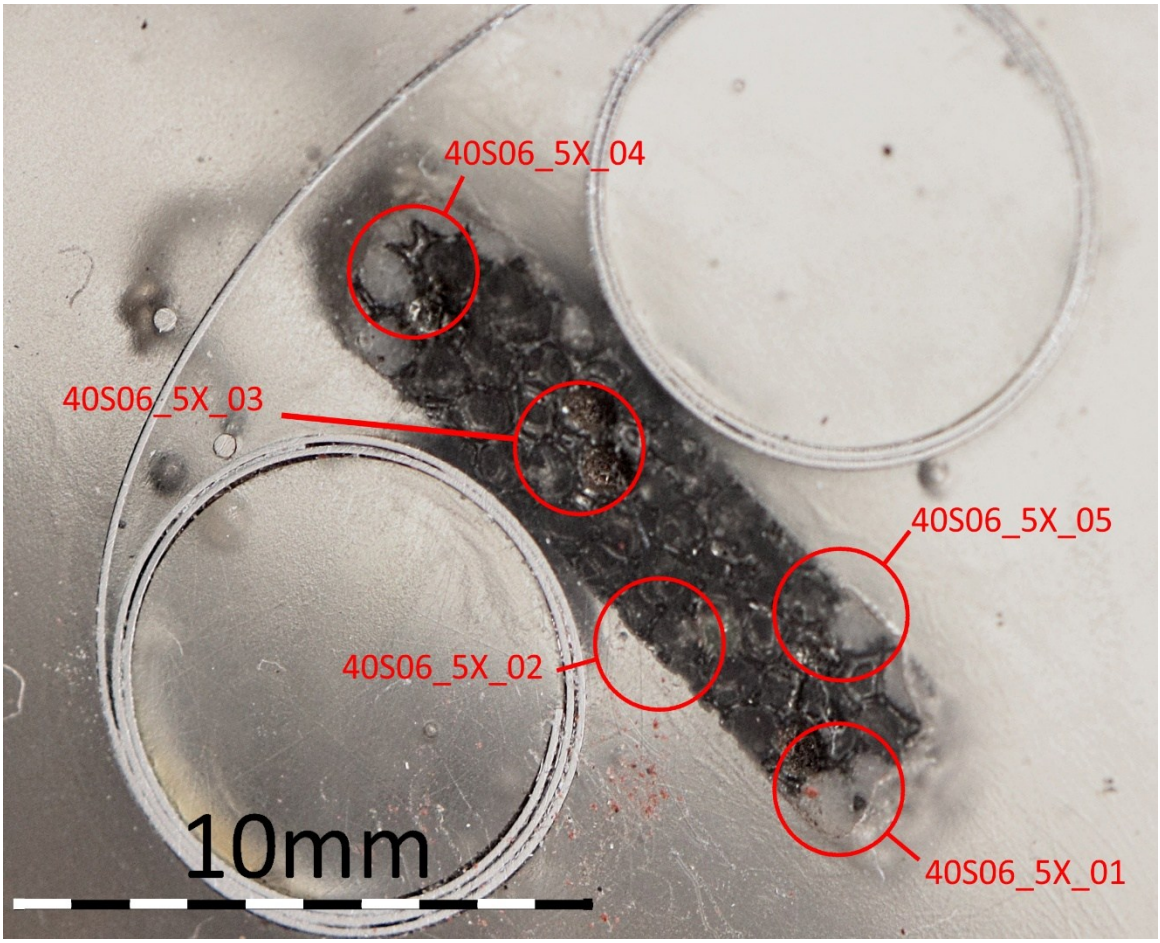


Figure 67. Sample#40S06 (see Table 23 for details) map of microscopy images. No obvious signs of graphitic foam or BN coating degradation.

Figure 68 shows an optical micrograph of BN-coated graphitic foam sample 40S05 after high-temperature exposure without FLiBe contact, corresponding to location 40S05_5X_02 in Figure 66. The dark interconnected network is the graphitic foam substrate, the gray-white crystalline layer is the BN coating, and the red-brown residue is polishing compound. The thickness of the BN coating appears to be between 10µm and 100µm with most regions appearing between 30µm and 80µm. This is only an order of magnitude because the optical image does not provide a sharply defined coating/substrate interface across all regions, and apparent thickness may be affected by polishing angle, surface roughness, and local coating accumulation within the foam structure.

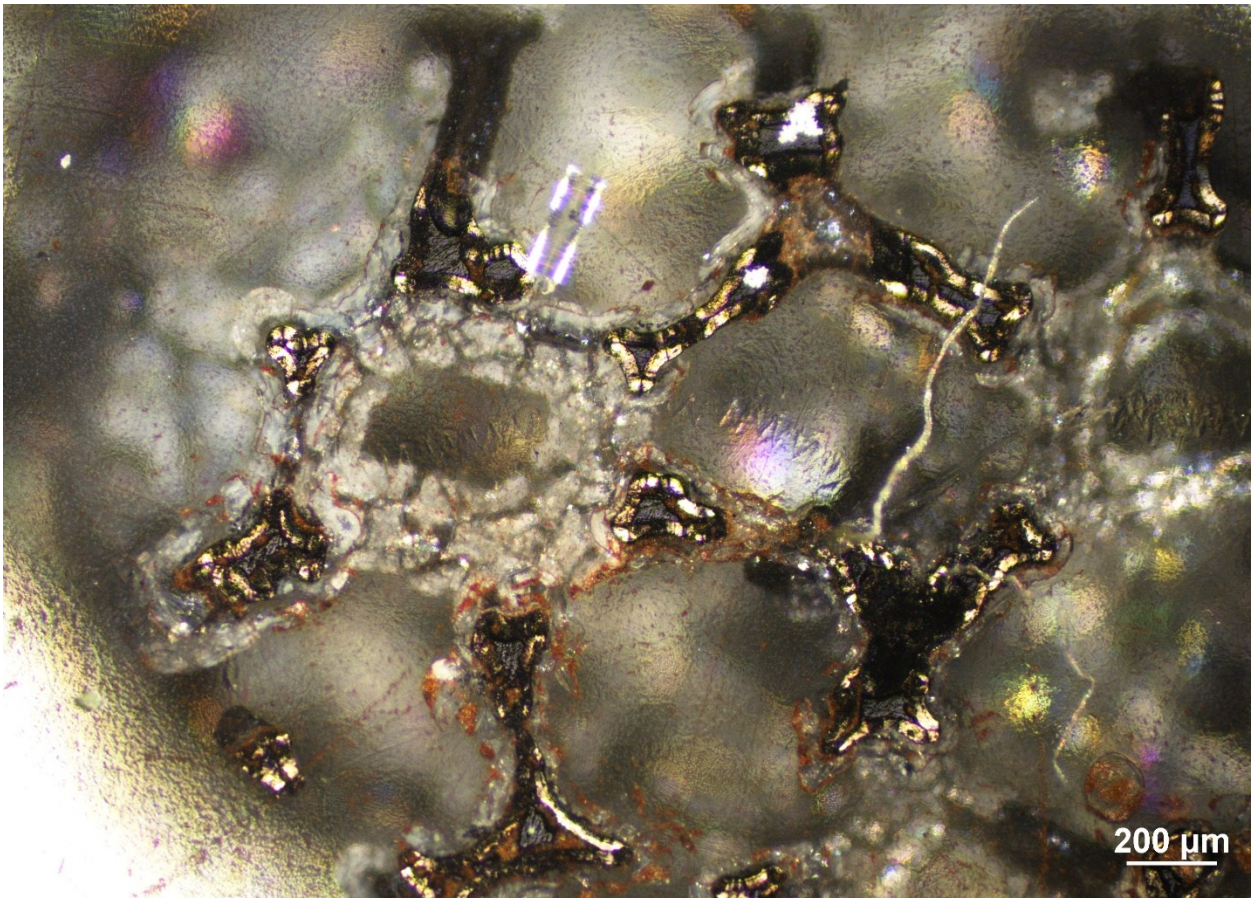


Figure 68. Microscopy at 5X magnification of Sample#40S05 (see Table 23 for details). Image location at 40S05_5x_02 shown in Figure 66. Graphitic foam seen in this image is dark network. BN coating is grey-white crystal layer on dark network. Red-brown dust is polishing compound.

Figure 69 shows an optical micrograph of BN-coated graphitic foam after high-temperature FLiBe exposure. The dark interconnected network is the graphitic foam substrate, the shiny yellow-white layer along the ligaments is the BN coating, and the large white regions are interpreted as frozen FLiBe within or adjacent to BN-covered pores. The BN coating remains visible along the foam ligaments and appears to be on the order of 10µm to 100µm thick, although the apparent thickness varies with local coating accumulation, polishing angle, and pore geometry. The image indicates that the graphitic foam structure remains visually intact at this magnification, while localized salt infiltration is observed in open or partially coated pore regions.

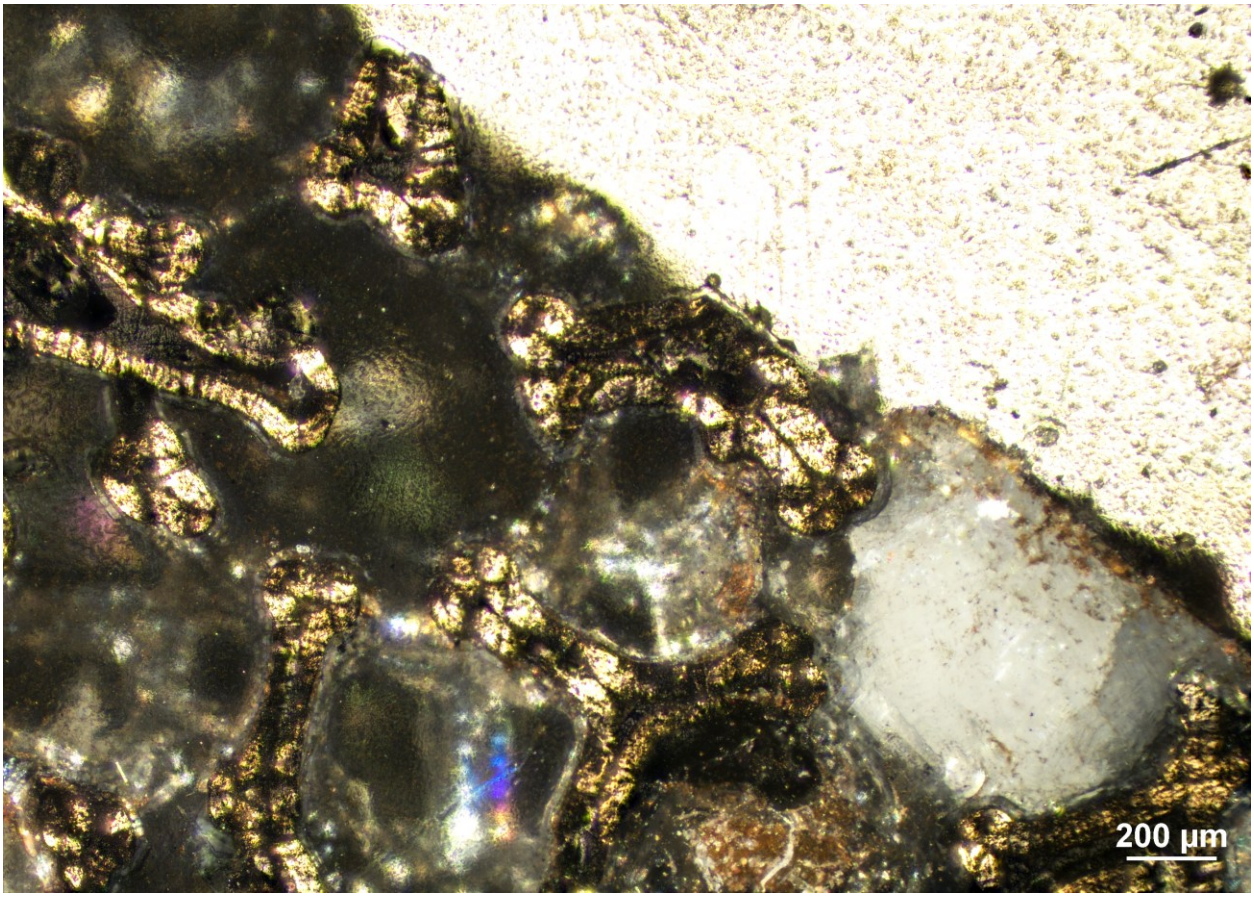


Figure 69. Microscopy at 5X magnification of Sample#40S06. Image location at 40S06_5x_05 shown in Figure 67. Graphitic foam seen in this image is dark network. BN coating is shiny-yellow crystal layer on dark network. Large white region is frozen FLiBe salt in the BN covered pores. Red-brown dust is polishing compound.

A higher magnification optical micrograph is shown in Figure 70 revealing a higher resolution of the BN coated graphitic foam microstructure after polishing. The dark regions correspond to the graphitic foam substrate, while the lighter gray-white regions along the ligament boundaries and within pore spaces are attributed to the BN coating and/or retained material within coated pores. The coating appears nonuniform at this scale, with local thicknesses on the order of several micrometers to several tens of micrometers, and no obvious large-scale cracking or delamination of the graphitic foam network is observed in this field of view. The average BN coating thickness is approximately 30µm in this image, which is on the order of magnitude seen in the sample which was not exposed to FLiBe. The orange-red residue is interpreted as polishing compound and is not treated as evidence of chemical degradation without further compositional analysis.

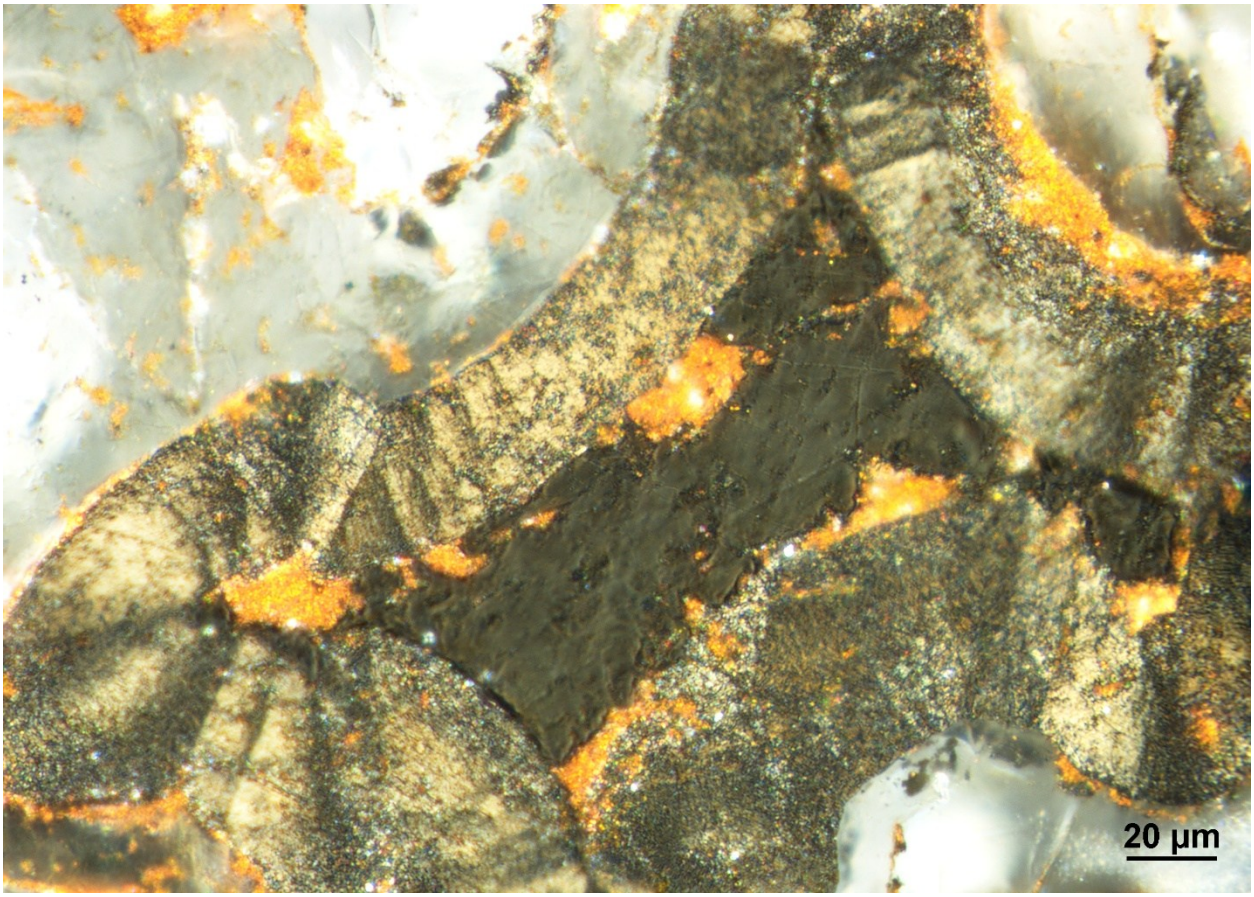


Figure 70. Microscopy of Sample#40S06 at 50X magnification. Image location at 40S06_5X_04 shown on Figure 67.

The BN coated samples demonstrate successful infiltration of FLiBe salt. The microscopy of the test versus the control group showed the FLiBe did not have noticeable effects on the degradation of the BN coating. From this preliminary test data, the variable which effect BN coating degradation was the porosity of the graphitic foam. For sample 40S09, 40S10, 40S11, and 40S12, the BN coating peeled off the samples when they reached temperature and were signs of thermal failure rather than salt induced failure. This is likely due to poor adhesion between the BN and graphite disks, and thermal expansion strained the materials to rip apart.

The disks which seemed to perform best in both the control and FLiBe exposed batch were samples 40S05 and 40S06. These samples were fabricated with 65ppi and ~60µm BN coating thickness, but the actual thickness may have varied between 30µm to 80µm. These samples sustained little to no damage from the heat treatment and FLiBe exposure. This may be due to the fact that the lower pore density improved the strength of the BN deposition onto the graphitic foam while the thinner coating relieved the thermal strain between the BN deposition and graphitic foam.

4.6.1.2 BN Coated Graphitic Foam NiTRE Testing

After successful testing of the BN coated graphitic foam disks, Ultramet produced six (6) BN coated graphitic foam reference electrode bodies. These bodies used the formulation with a porosity of 65ppi and

60µm BN thickness. The fabrication of the TRE bodies differed from the graphitic foam disks in that a LaF_3 crystal membrane was deposited on the graphitic foam TRE bodies. This membrane was to act as an ion-selective membrane in fluoride salts. The image of the cast LaF_3 membrane is shown in Figure 71. A visible and uniform dark deposit surrounded the LaF_3 cast and was examined on scanning electron microscopy (SEM) and energy dispersive x-ray spectroscopy (EDS). The data from those tests are provided in Figure 72 and Figure 73. The exterior of the cast appears to have been contaminated with carbon from the casting process. However, this is not expected to change the functionality of the LaF_3 membrane.



Figure 71. LaF_3 crystal cast for BN coated graphitic foam TRE bodies.

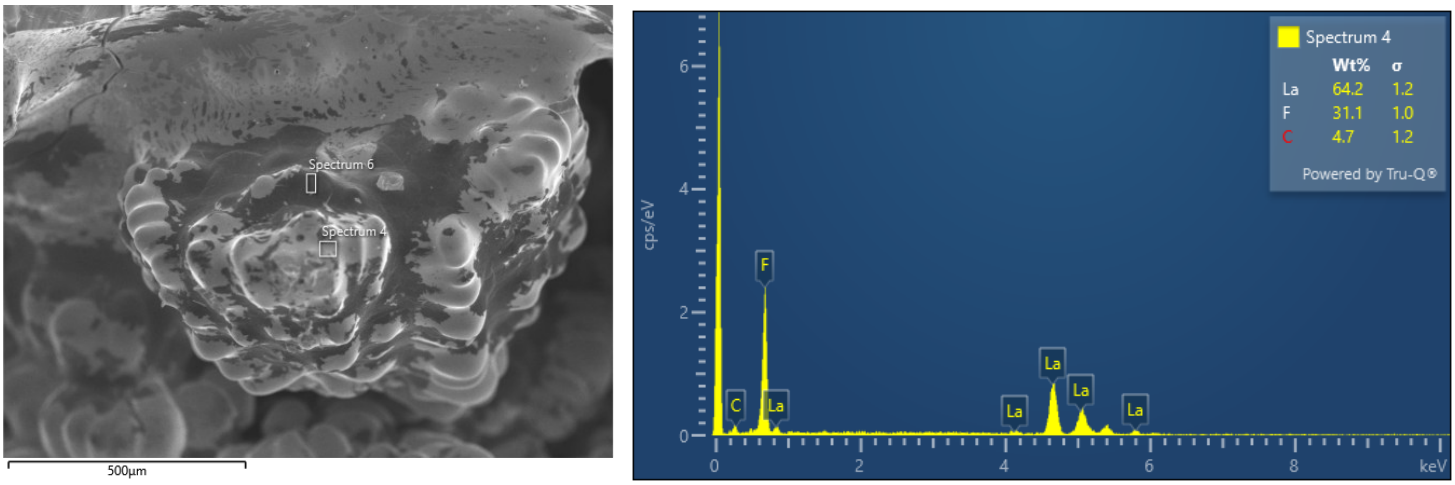


Figure 72. (left) SEM image of LaF_3 crystal cast exterior. (right) EDS of "spectrum 4" from the SEM image. Data provided by Ultramet.

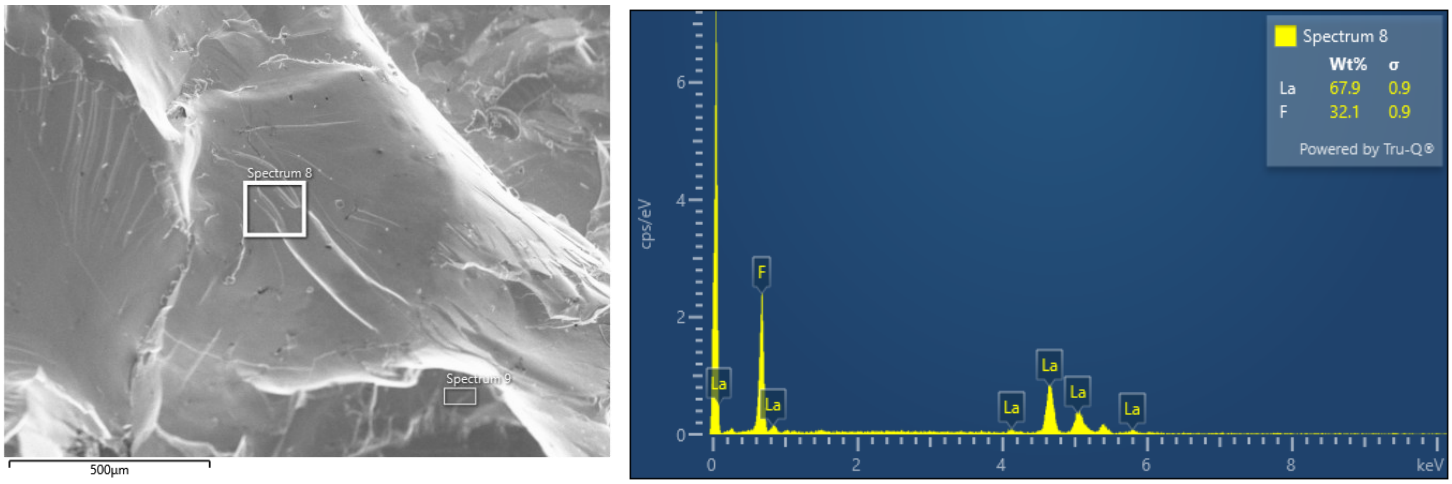


Figure 73. (left) SEM image of LaF_3 cast interior. (right) EDS of "spectrum 8" from the SEM image. Data provided by Ultramet.

The TRE bodies were planned to be tested using the Ni/NiF_2 redox couple as a reference reaction. We will continue to refer to this specific redox couple in fluoride salts as the Nickel-fluoride Thermodynamic Reference Electrode, or NiTRE. The electrochemical cell that was used to test the NiTRE was a standard 4-electrode cell connected to a Gamry Ref1000 Potentiostat. The cell consisted of a glassy carbon crucible containing FLiBe salt. The glovebox atmosphere was held around 10ppm oxygen and <1ppm moisture.

The OCP measurement for an ideal TRE should have no drift in potential when the composition of the system is constant. In practically measuring OCP, there will be an initial shift towards the system steady state OCP characteristic of wetting and thermal transients within the NiTRE body. We measured OCP by inserting a Ni wire into the graphitic foam body and added FLiBe with approximately 1mol% NiF_2 into the TRE body. The NiTRE was connected to the potentiostat working electrode connector, and two nickel wires were added to the cell as the counter electrode and quasi reference electrode. This assembly functions like a concentration cell where the working and reference electrode are comprised of the same material and the concentration of NiF_2 varies from the inside of the graphitic foam body and the salt in the crucible. With this cell, we would determine if ionic contact was being made from inside the NiTRE body to the salt in the crucible by comparing the potential measured in the open circuit to the predicted potential of Ni/Ni^{2+} at the specified concentration of NiF_2 in FLiBe.

The NiTRE was placed in the glassy carbon crucible with already molten FLiBe around 650°C and allowed to equilibrate thermally equilibrate. An initial period of drift and noise was recorded during the melting of the NiTRE salt. Spikes in the recorded potential are attributed to the Ni wire shorting with the graphitic foam crucible wall and the glassy carbon crucible. As the inner salt of the NiTRE melts, the potential stabilizes. This is seen on Figure 74.

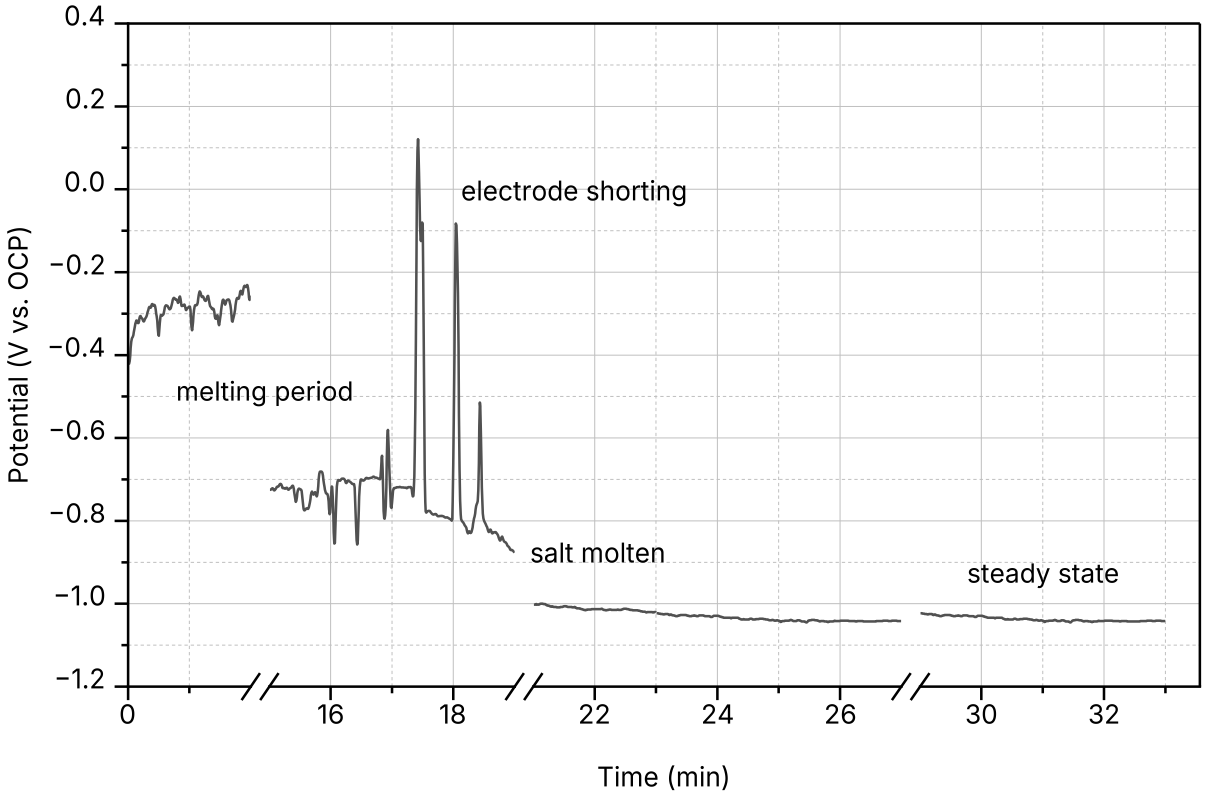


Figure 74. OCP of BN coated graphitic foam NiTRE in FLiBe with 1mol% NiF_2 in the reference salt. Steady state potential was approximately −1. 0V vs. OCP. Cell configuration; Ni WE in FLiBe+1mol% NiF_2, Ni CE, Ni qRE.

After the initial test to measure the steady state OCP, the system was allowed to freeze overnight and rest for 72-hours. After the resting period we turned the furnace, set the temperature to 650°C, and allowed the salt in the crucible and the NiTRE to melt. This time, it took approximately 90 minutes before we saw signs of melting in the NiTRE due to the thermal inertia of melting the entire system instead of solely the NiTRE. Sign of complete melting were not obvious until around 100 minutes when the OCP value settled near a steady value. This is seen in Figure 75.

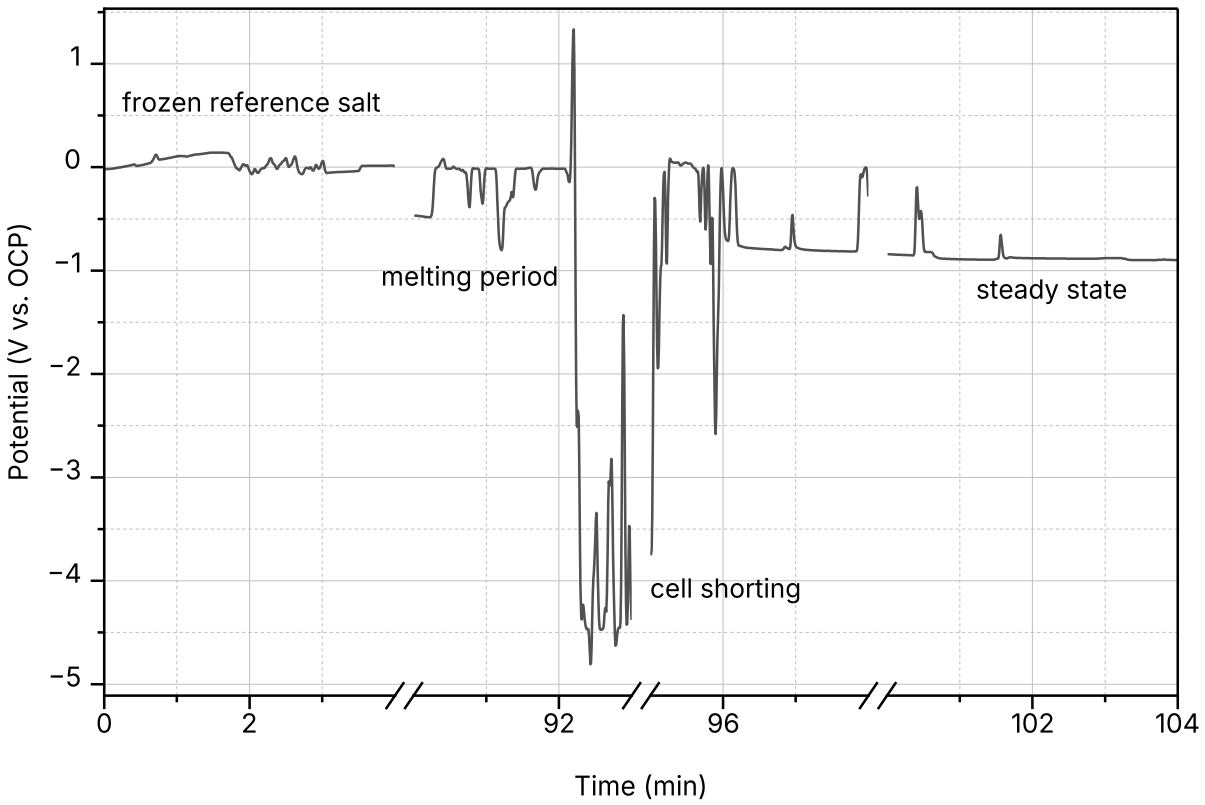


Figure 75. OCP of BN coated graphitic foam NiTRE in FLiBe with 1mol% NiF_2 in the reference salt. t=0 starts with completely frozen FLiBe in crucible. Steady state potential was approximately -0.9V vs. OCP. Cell configuration; Ni WE in FLiBe+1mol% NiF_2, Ni CE, Ni qRE.

While it appears steady state OCP was achieved in the second day of testing, it was clear the potential had drifted approximately 100mV from the first day steady state value. Post examination of the graphitic foam body showed some cracking steaming from the top of the body. In some graphitic foam NiTRE bodies, full cracks developed and broke the graphitic foam. It was determined this happened due to the tight fit of the BN cap which was used to hold the Ni wire in place in the graphitic foam body. This can be seen in Figure 76.

Attempts were made to collect cyclic polarization data from the NiTRE without the presence of the BN cap to prevent cracking the graphitic foam bodies. However, this proved to be difficult as the graphitic foam would float on the FLiBe and without the structure of the BN cap to hold the Ni wire in position, the entire NiTRE capsized and spilled the concentration of NiF_2 into the melt. The data is presented in Appendix B.13 for the curious reader. As this point, it was impossible to determine the exact composition of NiF_2 in the NiTRE and in the glassy carbon crucible. An image of the graphitic foam body suspended in FLiBe is shown in Figure 77. After spilling, open circuit potential (OCP) between NiTRE and outer salt bath dropped to nearly 0V. This does correctly reflecting a change in the redox potential of the outer salt bath considering a concentration cell with identical inner and outer concentration will read 0V vs OCP.



Figure 76. BN coated Graphitic foam NiTRE body with BN cap. (left) NiTRE with the BN cap covering reference FLiBe+1mol% NiF_2 salt bath prior to thermal exposure. (right) Same NiTRE after thermal exposure with chunk of graphitic foam body broken off.

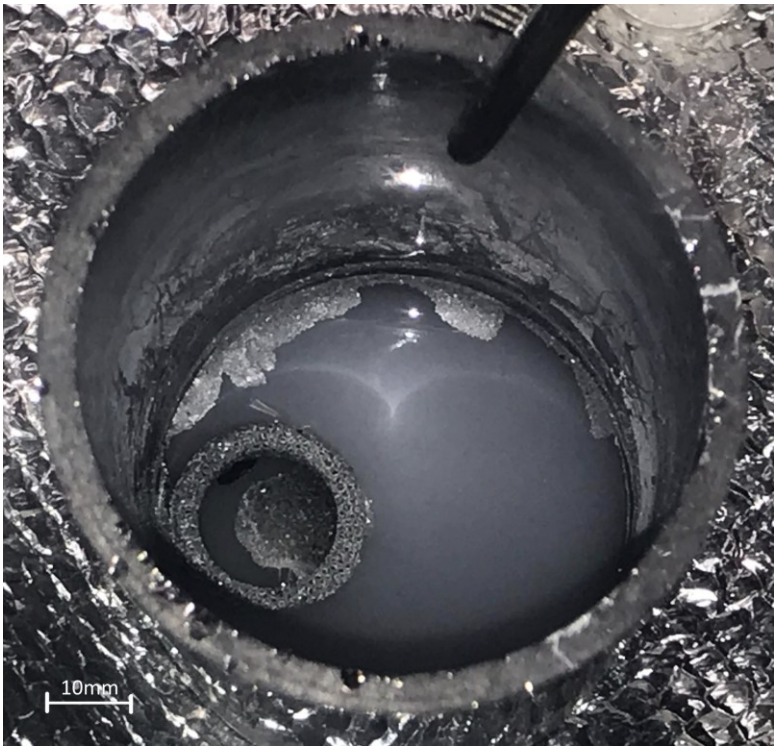


Figure 77. BN coated graphitic foam NiTRE body submerged in FLiBe. Frozen FLiBe is forming on the surface of the salt near the crucible walls and on the inside of the graphitic form body. The salt in the crucible appears slightly cloudy.

The design of the NiTRE with a BN coated graphitic foam shows potential as a mass manufacturable reference electrode. The shortcomings with this design were mainly mechanical in nature, such as the tight fit of the BN cap breaking the graphitic foam body. We saw ionic contact through the graphitic foam membrane. It is recommended that thermal cycling studies and long-term exposure studies are conducted for future work. Initial OCP measurements after a freeze-thaw of the NiTRE suggest that the measured potential will drift after repeated freeze-thaw cycles. Long-term exposure without a freeze-thaw process will probe if there is any leeching of NiF_2 from the inner bath to the outer bath. It is important to characterize both the long-term behavior and the freeze-thaw effect on the NiTRE as the life of the electrodes must be known if they are to serve as sensors to monitor molten salt system health. All images and electrochemical data relevant to the design of the BN coated graphitic foam NiTRE's not discussed in this section are present in Appendix B.

4.6.2 Silver-Silver Fluoride Thermodynamic Reference Electrode (AgTRE)

Explorations of the FLiBe system have pursued the development of a TRE which can hold a thermodynamically stable reference potential for an extended time. Current designs using the H_2/HF or Ni/Ni^{2+} couples suffer from either difficult handling of gas electrodes at high temperatures or long equilibration times. In this study, the performance of a reference electrode using the Ag/Ag^+ redox couple was assessed for long-term electrochemical stability. The Ag/AgF system was chosen to address the limitations of the Ni/Ni^{2+} TRE, as the low melting point of AgF (T_{melt} = 435°C) allows for the direct use of the pure salt in the electrode, eliminating the time-consuming dissolution step required for NiF_2.

A first attempt at an Ag/AgF TRE was constructed by melting AgF salt into a boron-nitride crucible fitted with a LaF_3 fluoride membrane and inserting a silver wire into the salt reservoir, similar to the design outlined by Carotti et al and shown in Figure 1. The TRE was immersed alongside a beryllium metal rod to measure the potential across the cell. No stable reference potential was observed, analysis of the TRE after operation revealed a layer of Ag metal coating the inner wall of the BN crucible confirmed using laser induced breakdown spectroscopy (LIBS). Two possible reactions that could explain the chemical reduction of Ag metal in the reference electrode compartment are shown in Figure 1; reactions with both moisture contamination and the BN crucible are thermodynamically favorable at the operating temperature of the TRE.

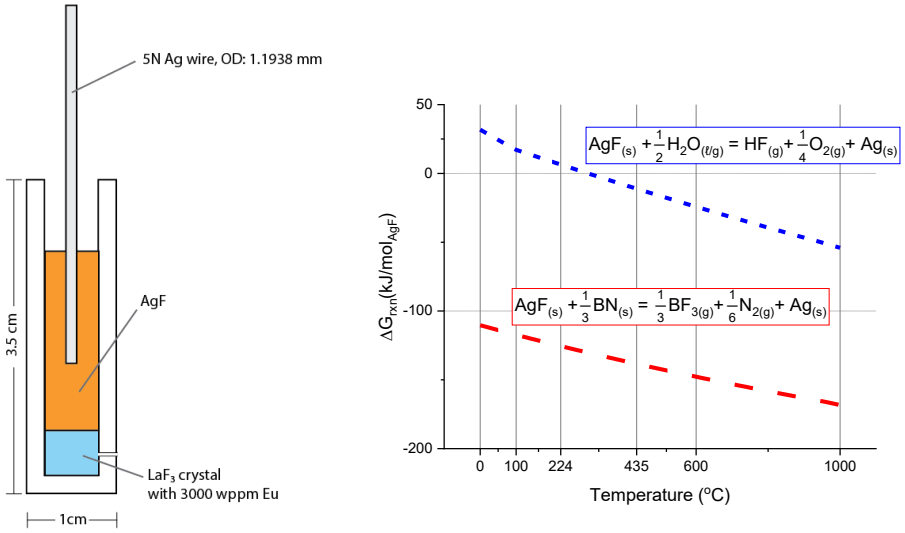


Figure 78. Schematic of the first AgF TRE construction (left) and AgF reactions with Residual Moisture (blue, short dashes) and Boron Nitride (red, long dashes) in Salt (AgF(s) used in lieu of AgF(l) HSC Data) (right)

To evaluate this, 876.7 mg of moisture contaminated AgF salt was added to a glassy carbon crucible alongside a small sample of AX05 BN and heated to 600C for 3.75 hours. After heating, a white mass on the BN was observed and confirmed as Ag metal using LIBS and a mass loss of 226.3 mg was observed after reweighing. Assuming that any residual moisture in the AgF did not significantly contribute to the initial measured mass of AgF, all lost mass was from gaseous evolution of one of the gas phase reaction products above, and all the AgF reacted to form Ag metal, ~20% of the salt would have reacted with moisture (glovebox contamination, residual) and the other ~80% reacted with the BN. This could explain both the presence of Ag metal seemingly bonded to the BN as well as the Ag metal that was not in contact with the sample shown in Figure 79.



Figure 79. (top left) AgF + BN before heating (top right) AgF + BN after heating (bottom) White deposit stuck on BN surface while being held with tweezers

Subsequent reevaluations of the TRE design resulted in a final test using a porous graphite crucible with a BN coating on the outside only, a supporting salt of FLiBe that ~13mol% of AgF could be dissolved into instead of reacting with moisture, and an Ag metal wire immersed in the FLiBe-AgF melt was performed; again tested against a Be rod. A schematic of the electrochemical cell, images of the electrode samples, and the result of ~18 hours of OCP monitoring of the cell are shown in Figure 3.

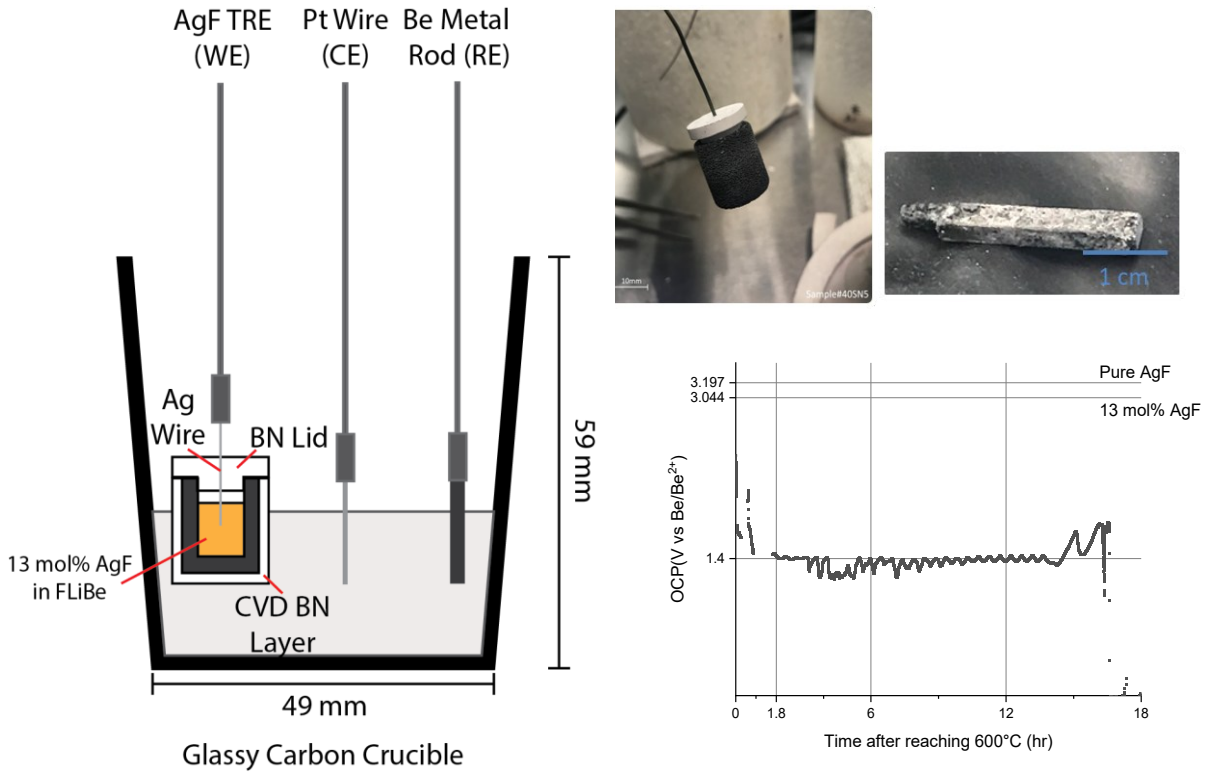


Figure 80: (left) Schematic of electrochemical cell (top right) Images of AgF TRE and Be rod (bottom right) OCP vs Be^{2+}/Be of the constructed TRE over ~18 hours.

The investigation of Ag/AgF as a reference electrode system in FLiBe revealed significant chemical compatibility challenges. While achieving a faster equilibration time (2 hours) compared to traditional Ni/NiF2 electrodes (approximately 20 hours[107]), the Ag/AgF system demonstrated unexpected reactivity with both boron nitride containment materials and moisture contaminants, resulting in the reduction of silver ions and deviation from expected potentials. The observed equilibrium potential of 1.4 V vs. Be^{2+}/Be, corresponding to parts per trillion Ag+ concentration, suggests substantial loss of silver ions. These compatibility issues ultimately shifted the design focus away from developing an AgTRE for the Echem Probe.

4.6.3 Beryllium Dynamic Reference Electrode (BeDRE)

The Beryllium Dynamic Reference Electrode (BeDRE) is a commonly utilized internal reference electrode for electrochemical measurements in molten FLiBe salts. Unlike thermodynamic reference electrodes, which maintain a fixed chemical equilibrium through a dedicated redox environment, the BeDRE is formed dynamically through the electrochemical deposition of metallic beryllium onto the surface of a metallic working electrode. Once deposited, the electrode potential is governed by the Be/Be(II) redox couple:

$$Be^{2+} + 2e^{-} \rightarrow Be^{0} \tag{4.20}$$

The standard potential of the Be/Be(II) couple in FLiBe relative to the HF/H_2 reference scale is reported by Hitch and Baes[112] as:

$$E^{0}_{\mathrm{Be^{2+}/Be}} = (-2.4430 + 0.0007962\,T)\ \mathrm{V\ vs\ HF/H_2};\ (T\ \mathrm{in}\ K) \tag{4.21}$$

Assuming thermodynamic equilibrium between deposited Be metal and dissolved BeF_2, the equilibrium half-cell potential of the BeDRE is described by the Nernst equation:

$$E_{Be^{2+}/Be} = E^{0}_{Be^{2+}/Be} - \frac{RT}{nF}\ln\left(\frac{1}{x_{BeF_2}\gamma_{BeF_2}}\right)\ \mathrm{V\ vs\ HF/H_2} \tag{4.22}$$

where $x_{\mathrm{BeF_2}}$is the mole fraction of BeF_2 in FLiBe and $\gamma_{\mathrm{BeF_2}}$is its activity coefficient. In this work, values of $x_{\mathrm{BeF_2}} = 0.34 \pm 0.01$and $\gamma_{\mathrm{BeF_2}} = 0.30 \pm 0.05$were taken from Hitch and Baes. Applying Eq. (4.22) at $600 \pm 5°\mathrm{C}$ results in an expected BeDRE potential of:

$$\mathrm{E}^{600^{o}\mathrm{C}}_{Be^{2+}/Be} = -1.834 \pm 0.008\ \mathrm{V\ vs\ HF/H2} \tag{4.23}$$

The effect of BeF_2 activity on the measured redox potential is shown in Figure 81. This plot accounts for the BeF_2 activity coefficient as a function of composition using data from Hitch and Baes[112].

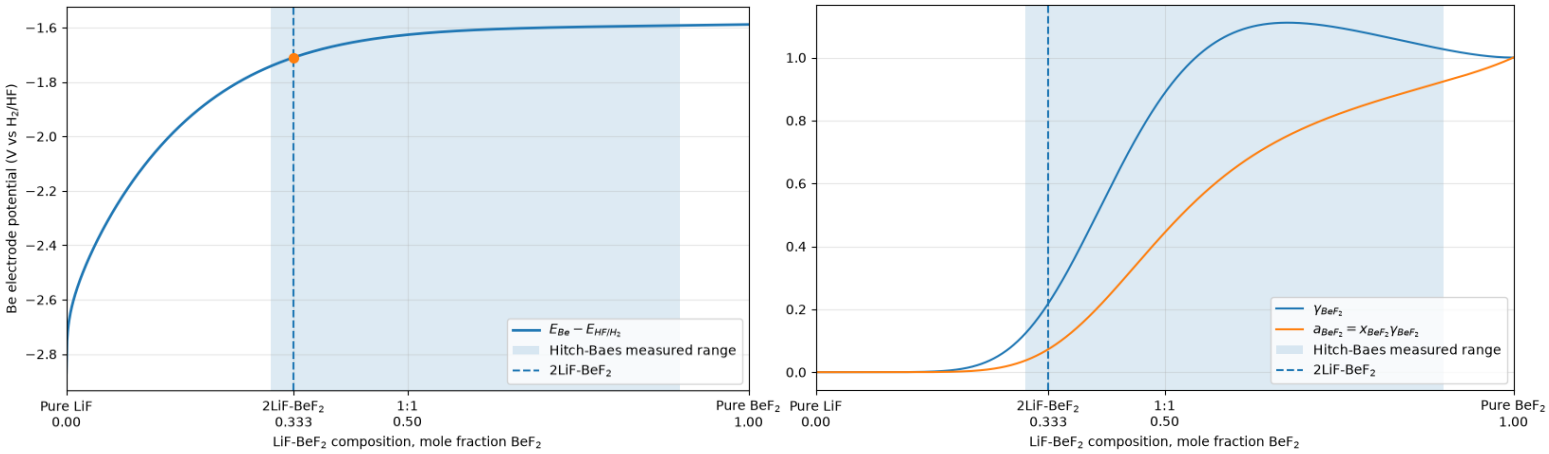


Figure 81. BeF_2 redox potential (left) and activity (right) as a function of composition in LiF-BeF_2 at 800ºC. Blue shaded region indicates the composition range of Hitch and Baes[112] data.

The BeDRE method was used by Afonichkin et al. to perform redox sensing over time in at a single point on a thermal convection loop showing sensitivity of salt redox to lab air ingress events[97]. Duran-Klie et al. developed a heuristic for setting the parameters of a chronopotentiometric wave when charging the surface of the BeDRE[88]. Kelleher et al. who showed that electrochemical deposition of Be can reproducibly establish a reference potential with variations of approximately 5 mV enabling redox potentials measured in separate experiments or salt compositions to be reported on a common BeDRE potential scale[113]. Carotti later used the BeDRE to characterize the potential of a Ni/NiF_2 thermodynamic reference electrode in FLiBe[114]. Vallet et al. demonstrated that polarization of Be electrodes in LiF-BeF_2 melts can produce significant near-electrode composition gradients, meaning that the open-circuit relaxation transient does not necessarily reflect equilibrium with the bulk salt composition [115]. This distinction is critical because the BeDRE potential is typically measured during this open-circuit relaxation period, after Be has been electrochemically deposited. Therefore, the measured plateau potential may

represent a locally modified Be/BeF_2 interfacial environment rather than the thermodynamic potential expected from the bulk FLiBe composition alone. The distinction between the BeDRE plateau potential and the thermodynamic Be/Be^{2+} equilibrium potential is important for defining corrosion-control and redox operating limits. The BeDRE provides a practical internal reference scale, but its measured potential may reflect the local interfacial salt composition produced during Be deposition rather than the bulk FLiBe composition. Therefore potentials measured versus the BeDRE should not be assumed to correspond directly to thermodynamic Be/Be^{2+}-referenced limits unless the relationship between the BeDRE plateau and the bulk equilibrium potential has been established.

In this section, BeDRE measurements are re-examined through this transport-aware framework. First, the raw BeDRE responses from Carotti's Ni/NiF_2 reference electrode measurements are analyzed to evaluate how the BeDRE plateau develops during open-circuit relaxation. Second, BeDRE measurements collected in FLiBe containing dissolved corrosion products are examined to assess how competing redox reactions influence the formation and interpretation of the dynamic reference potential.

4.6.3.1 BeDRE Concentration Gradients in FLiBe

We first examine BeDRE data collected by Carotti[116]. An electrochemical cell was assembled consisting of a molybdenum rod as a WE, a 3mm diameter glassy carbon rod as a CE, and a NiTRE as a RE. The cell measured open circuit potentials in a pot of FLiBe at 550°C for approximately 100 hours. A Gamry Reference 600 potentiostat was used to make OCP measurements. The BeDRE was measured following the methods described by Kelleher et al.[113]. Because the NiTRE reference electrode contains Ni metal in equilibrium with FLiBe saturated in NiF_2, the reference potential is fixed by the NiF_2 solubility at 550 °C. The measured BeDRE potential versus Ni/NiF_2 can therefore be interpreted as the difference between the Be/BeF_2 and Ni/NiF_2 Nernst potentials. This converts the BeDRE open-circuit transient into an apparent surface BeF_2 activity, $x_{\mathrm{BeF_2},s}\gamma_{\mathrm{BeF_2},s}$, rather than a direct measurement of the bulk FLiBe composition. Eq.(4.24) solves for the BeF_2 surface concentration as a function of time.

$$x_{BeF_2}(t) = \frac{x_{NiF_2}}{\gamma BeF_2}\exp\left[\frac{2F}{RT}\left(E_{meas}(t) - E^{o}_{Be^{2+}|Be}(T) + E^{o}_{Ni^{2+}|Ni}(T)\right)\right] \tag{4.24}$$

x_{BeF_2} is the mole fraction of BeF_2 at the surface of the BeDRE, x_{NiF_2} is the mole fraction of NiF_2 in the NiTRE, γ_{BeF_2} is the BeF_2 activity coefficient at the given surface concentration, E_{meas} is the measured OCP between the BeDRE and NiTRE, $E^{o}_{Be^{2+}|Be}$ is the standard potential of the Be redox reaction in FLiBe, and $E^{o}_{Ni^{2+}|Ni}$ is the standard potential of the Ni redox reaction in FLiBe. Notice that this function is implicit with x_{BeF_2} because γ_{BeF_2} is itself a function of x_{BeF_2}. Therefore, we must iteratively solve the equation by selecting an x_{BeF_2} values, computing the γ_{BeF_2} value, plug that activity coefficient value into Eq.(4.24), and determine if both sides are equal.

Chronopotentiometry data from a BeDRE measurement is presented Figure 82. The imposed current was held at 0.15A for 2 seconds, and the open circuit transient was held for 600 seconds. The plateau in the polarization transient corresponds to Be^{2+} reduction to Be, while the plateau in the open circuit transient

corresponds to Be oxidation to Be^{2+}. The potential plateaus vary with time indicating the changing activity of Be^{2+} in the melt at the surface of the electrode.

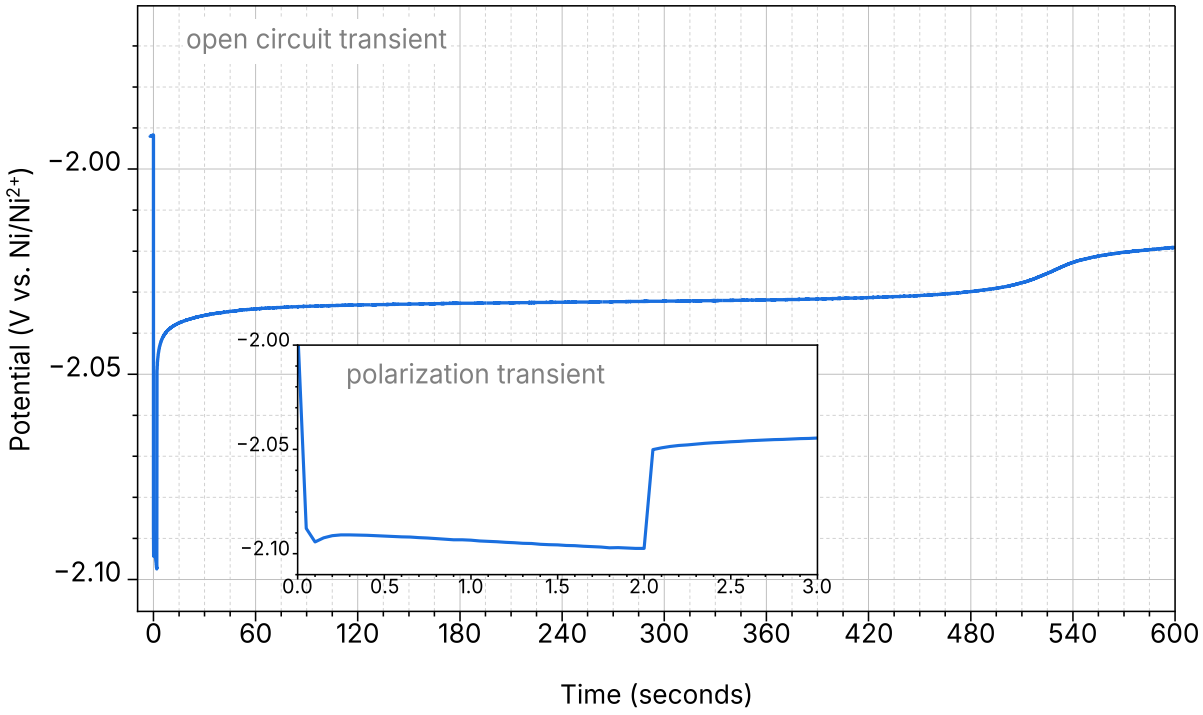


Figure 82. Chronopotentiometry data from a BeDRE measurement in FLiBe at 550°C. Electrochemical cell configuration: molybdenum WE, glassy carbon CE, Ni/NiF_2 RE.

We aim to show the apparent concentration profile of Be^{2+} at the surface of the BeDRE using a stable NiTRE reference potential. Knowing how the surface concentration of Be^{2+} evolves during Be/BeF_2 oxidation in FLiBe, we can measure more accurate measure reference potentials using the BeDRE across all FLiBe systems. While Kelleher et al. show the precision of the BeDRE measurement[113], it is our aim to improve the accuracy of the BeDRE reference potential for absolute thermodynamic measurements. The apparent Be^{2+} surface concentration on the BeDRE is shown in Figure 83 which uses the assumption that the Ni/NiF_2 potential is not drifting and is well defined by the concentration of Ni^{2+} in FLiBe at the solubility limit. This is a reasonable assumption as Carotti shows the NiTRE potential against a separate NiTRE are < 1mV apart in OCP[116].

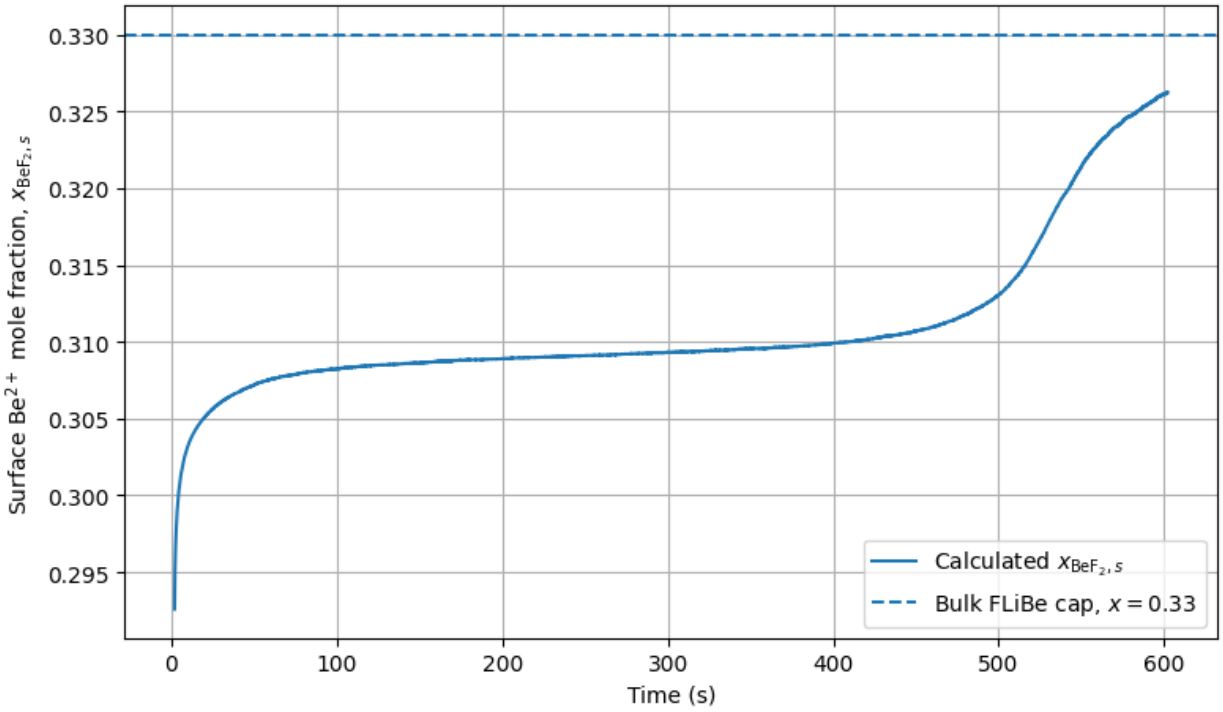


Figure 83. Apparent surface concentration on BeDRE during open circuit transient. $t = 0$ starts at the beginning of the relaxation transient on Figure 82.

Table 24. x_{BeF_2} are surface concentration values calculated from Figure 82 and Eq.(4.24)

Time (s)	E_{meas} (V vs Ni/NiF2)	x_{BeF2}
2	-2.050	0.2927
3	-2.045	0.2973
5	-2.041	0.3011
10	-2.039	0.3029
30	-2.036	0.3057
60	-2.034	0.3076
120	-2.033	0.3086
300	-2.032	0.3095
360	-2.032	0.3095
420	-2.031	0.3105
480	-2.030	0.3116
540	-2.023	0.3194
600	-2.019	0.3263

Using the surface concentration profile over time, we can calculate a mean diffusion coefficient of Be^{2+}. With an active electrode area of approximately 1.0–1.15 cm^2, we calculate the mean diffusion coefficient in FLiBe during the BeDRE transient by the formula:

$$\overline{D} = \frac{1}{\pi}\left[\frac{2i\sqrt{t_p}}{nF(C_b - C_s)}\right]^2 \tag{4.25}$$

$\overline{D}$ is the interdiffusion coefficient, i is the current density of the polarization step, t_p is the hold time of the current step, C_b is the bulk concentration of BeF_2, and C_s is the surface concentration of BeF_2. The calculation yields an apparent LiF–BeF_2 interdiffusion coefficient of $D_{app} \approx 2.0 \times 10^{-7}$to $2.7 \times 10^{-7}\ cm^2/s$. This value is about two orders of magnitude larger than Vallet's low-temperature measurements in 95 mol% BeF_2, but it overlaps the upper end of Vallet's measured range at higher temperature. The difference is expected because the BeDRE-derived surface composition is near 2LiF–BeF_2, not 95 mol% BeF_2, and LiF–BeF_2 transport properties change strongly with composition. Therefore, the calculated value is reasonable in order of magnitude but should be interpreted as an apparent interdiffusion coefficient rather than a directly measured BeF_2 self-diffusion coefficient.

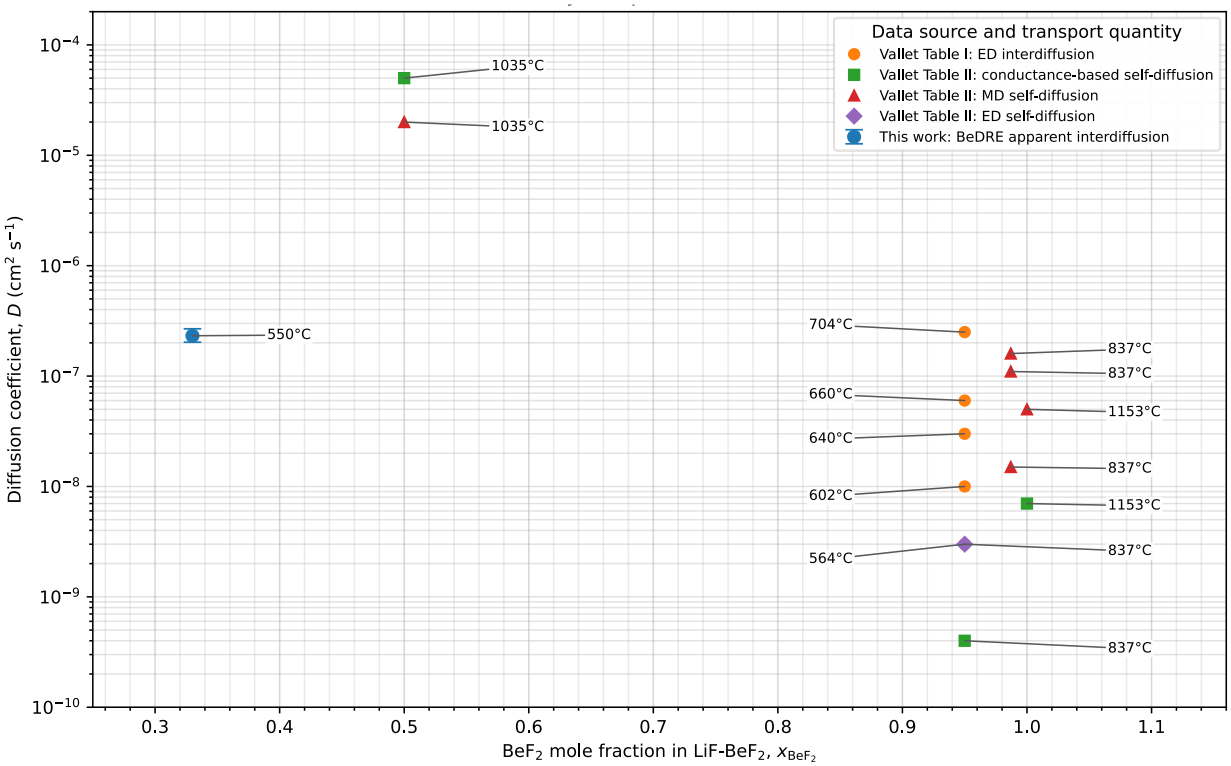


Figure 84. Apparent interdiffusion coefficient derived from the BeDRE relaxation at x_{BeF2}= 0.33 and 550 °C, compared with diffusion coefficients reported by Vallet et al. for LiF–BeF_2 mixtures. The measurement type is given by ED (electromigrational depletion), MD (molecular dynamics), or conductance.

One point of particular interest in Figure 83 is that the Be^{2+} surface concentration never returns to the assumed $x_{BeF_2} = 0.33$ value. This leaves us with two possible results. We describe each case:

(i) The surface concentration of Be^{2+} does not reach the initial bulk concentration in this oxidation step, therefore there is no oxidation potential that was measured which equals the Be/Be^{2+} oxidation potential in 2LiF-BeF_2

(ii) The initial bulk concentration of Be^{2+} was incorrect, so measuring the oxidation potential of the BeDRE using thermodynamic data for Be/Be^{2+} in 2LiF-BeF_2 will produce inaccurate potentials.

In either case, the result is that direct comparison to thermodynamic tabulated values of the Be/Be^{2+} oxidation potential in 2LiF-BeF_2 will be incorrect. If we were to assume case (i) was the correct scenario, then we would expect the potential of Be/Be^{2+} oxidation in 2LiF-BeF_2 to exist further in the time series data as the measured potential versus Ni/NiF_2 drifts upward. However, from Figure 85 we can see the reaction transient shifts from Be/Be^{2+} oxidation to a different phenomenon entirely. By performing a time axis transformation, plotting potential, E, against $\frac{\tau^{1/2}-t^{1/2}}{t^{1/2}}$, where τ is the transition time of the apparent Be/Be^{2+} reaction on the chronopotentiograms, the potential of the oxidation reaction becomes linear, and we can observe when rate of reaction no longer limits the potential based on where linearity breaks. Since the limiting reaction changes, then the surface of the electrode is not measuring the Be/Be^{2+} equilibrium. Therefore, we can conclude the BeDRE in this experiment never measured Be/Be^{2+} dissolution in 2LiF-BeF_2.

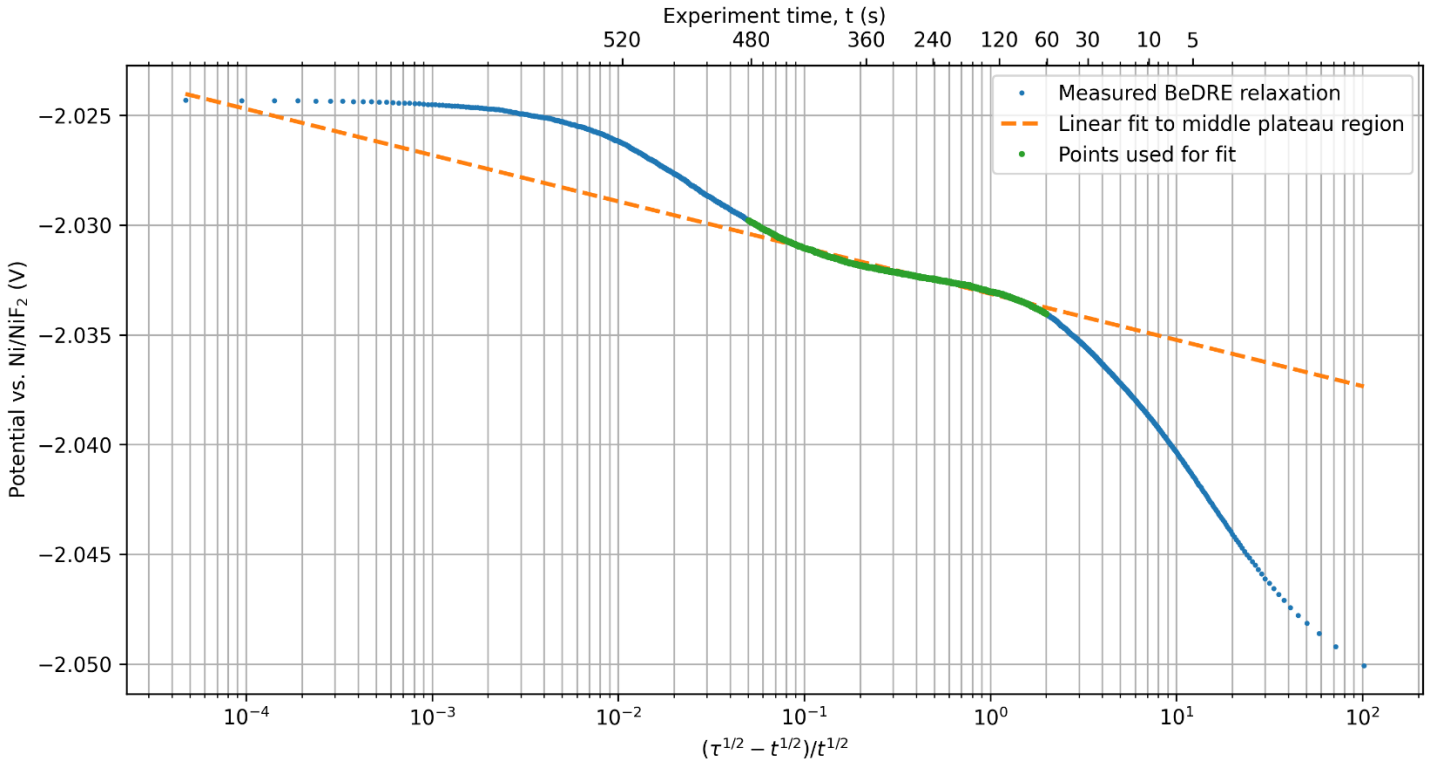


Figure 85. Chronopotentiogram of the BeDRE relaxation transient using transformed time axis, where $\tau = 529\ s$, measured from the point of inflection on Figure 82.

4.6.3.2 Open Circuit BeDRE compared to Cyclic Voltammetry

Figure 86 shows cyclic voltammograms used to estimate the Be/Be^{2+} potential from the anodic oxidation of deposited Be. During the cathodic sweep, Be is deposited onto the working electrode near the negative potential limit. On the subsequent anodic sweep, this deposited Be is oxidized back into the melt, producing

a large anodic stripping wave. The zero-current crossing of this anodic wave was used as an apparent Be/Be^{2+} potential versus the Mo quasi-reference electrode. Across repeated cycles, the zero-current crossing shifted from approximately −1.799 to −1.696V vs Mo qRE, corresponding to a 103 mV variation. This spread indicates that the Be/Be^{2+} potential measured by CV is not a single fixed value but a scan-history-dependent apparent reference potential. The variation likely reflects changes in deposited Be coverage, local BeF_2 activity, electrode surface condition, quasi-reference drift, and uncompensated resistance.

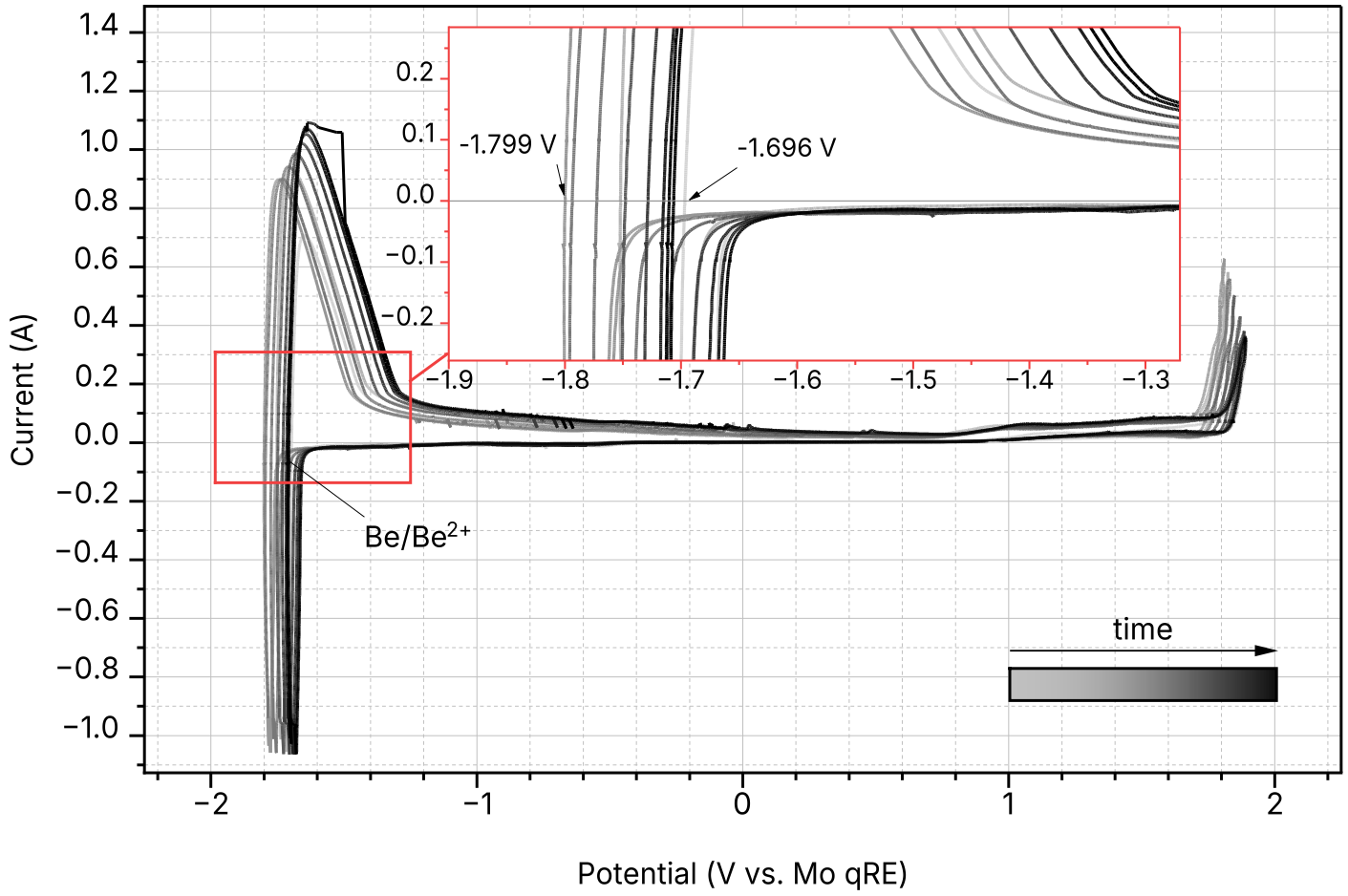


Figure 86. Cyclic voltammetry of FLiBe with trace oxidants at 600°C using a gold WE, gold CE, and silver qRE. Zoomed window shows the variation of zero-current crossing potential on anodic sweep after beryllium deposition. Temporal evolution of the data is depicted by darkening of the trace. The data has been iR corrected for a resistance of 0.3Ω.

Figure 87 shows exactly how the zero-current crossing potential evolves with scan number. The average value of the apparent Be oxidation potential is −1.742V with a standard deviation of approximately 37 mV. Clearly the Be oxidation potential measured during a voltametric sweep is not a single invariant value, rather it depends on scan history and electrode condition.

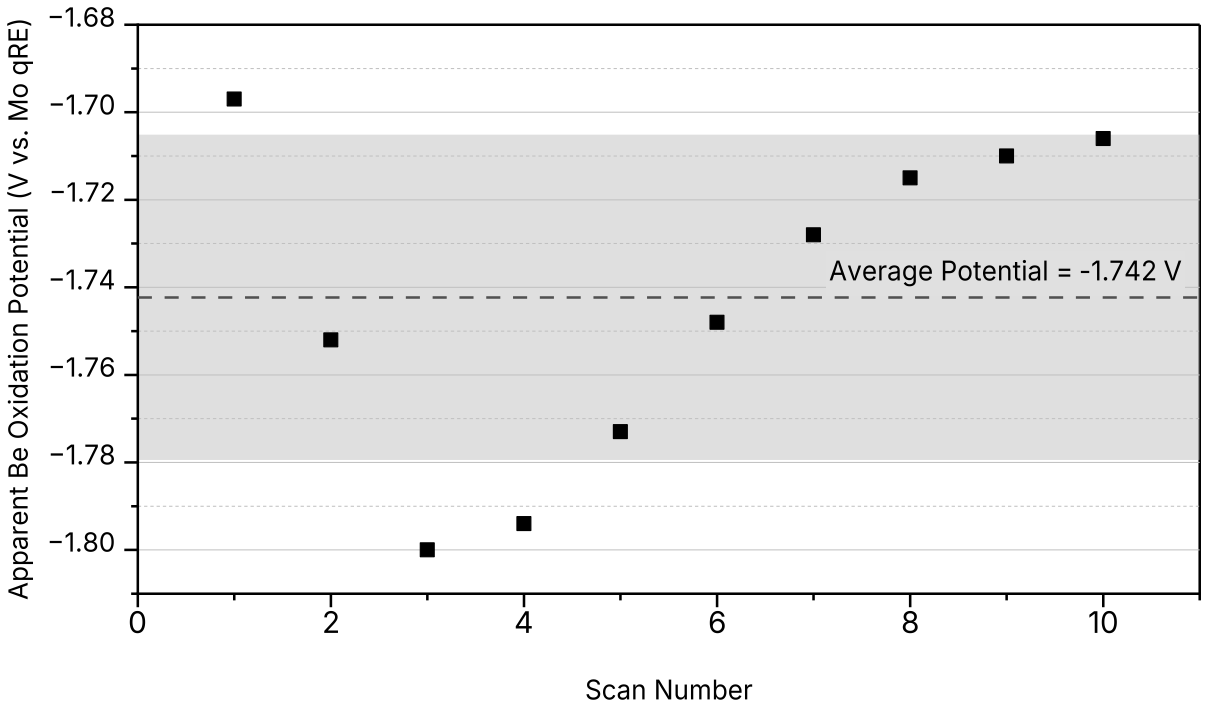


Figure 87. Apparent Be oxidation potential measured in FLiBe at 600°C using CVs. Potentials chosen at zero-current crossing potential on anodic sweep after beryllium deposition. The grey region indicate +/-1σ of the total measured values.

The same FLiBe was analyzed with CP to perform a true zero-current BeDRE measurement. The test parameters for each scan are given in Table 25.

Table 25. CP test parameters for scans depicted in Figure 88

Run #	Step 1 Current (A)	Step 1 Time (s)	Step 2 Current (A)	Step 2 Time (s)
1	-0.1	5	0	600
2	-0.15	10	0	600
3	-0.5	10	0	600
4	-0.5	30	0	600

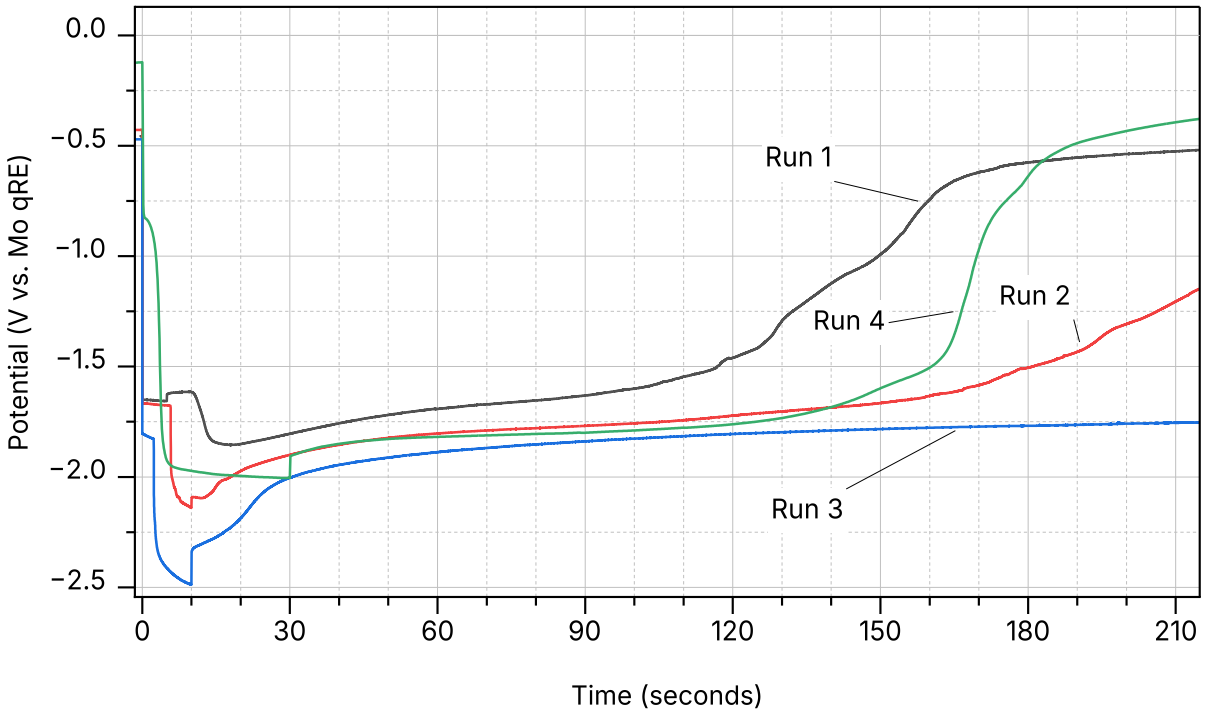


Figure 88. CP data taken in FLiBe with trace oxidants at 600°C. Consecutive runs are plotted together (see Table 25 for run details) showing the behavior of the Be oxidation plateau with different test parameters.

4.7 PROBING REDOX IN FLIBE - CONCLUSION

The FLiBe redox measurements show that several reference-electrode strategies can produce useful information, but none should be treated as a universal reference without qualification. The BN coated graphitic foam NiTRE demonstrated ionic contact and produced steady OCP values near -1.0 V and -0.9 V in repeated tests, but the approximately 100 mV drift after freeze-thaw and mechanical cracking from the BN cap indicate that mechanical design and thermal cycling currently limit reliability. The Ag/AgF approach equilibrated faster, on the order of 2 hours rather than the approximately 20 hours reported for some Ni/NiF2 systems, but AgF reacted with moisture and BN, producing Ag metal, a 226.3 mg mass loss in the AgF/BN exposure test, and an observed potential near 1.4 V vs Be^{2+}/Be consistent with severe depletion of Ag^{+} rather than a stable Ag/AgF reference. The BeDRE analysis provided the most important mechanistic insight: although the expected Be/Be^{2+} potential at 600°C is -1.834(8) V vs HF/H_2, the apparent BeF_2 surface composition during relaxation evolved from x_{BeF2} = 0.2927 at 2s to 0.3263 at 600s and did not return to the assumed bulk value of 0.33. The derived apparent interdiffusion coefficient of 2.0×10^{-7} to 2.7×10^{-7} cm^2 s^{-1} supports the interpretation that the BeDRE relaxation reflects a locally modified LiF-BeF_2 interfacial composition. Therefore, FLiBe redox potentials reported versus BeDRE should be treated as measurements on a practical internal scale unless the relationship between the BeDRE plateau and the bulk Be/Be^{2+} thermodynamic potential has been independently established.

5. ELECTROANALYTICAL CORROSION PRODUCT QUANTIFICATION IN MOLTEN SALT SYSTEMS

The study of corrosion products in molten salt is of particular importance for the development of molten salt reactors. Design engineers care about the dynamic corrosion rates of structural materials in the reactor system to determine when components need scheduled maintenance. For monitoring MSR chemistry and system health, electrochemical sensing provides a convenient solution for measuring salt chemistry *in-situ* without requiring operator intervention. This was known during operation of the Molten Salt Reactor Experiment (MSRE), but efforts to begin online electroanalytical measurements did not occur within the lifetime of the experiment. Now as MSRs continue their development, the utility of online electrochemical sensing is evident.

Electrochemical sensors are particularly well suited for measuring the concentration of soluble electroactive species in a molten salt. Numerous analytical measurements have been developed for electrochemical sensors[33], [34], [117], [118]. Tylka et al.[119] framed prior molten-salt electroanalytical quantification as a methods problem: discrepancies in actinide concentration measurements were attributed not just to voltametric theory, but to practical issues such as technique selection, verification of model assumptions, reproducibility of the electrode/electrolyte interface, and uncertainty in electrode surface area. Their work is useful precedent for this thesis because it shows that accurate *in situ* quantification in molten salts requires a validated measurement protocol rather than simple peak-current analysis, and that improved area-normalization/standard-addition strategies can bring electrochemical measurements of U and Pu in LiCl–KCl close to destructive analytical methods. In molten salt reactors, chromium is an element of particular interest for quantification in the melt. The vector by which chromium enters the melt is through corrosion of structural materials containing metallic chromium or by dissociation reactions of Cr_2O_3 [120]. Depending on the molten salt, chromium will predominantly species in the Cr(II) or Cr(III) oxidation state. For example, in 41.5LiF-11.5NaF-42KF mol% (FLiNaK) chromium will prefer to speciate as Cr(III) while in 67LiF-33BeF_2 mol% (FLiBe) chromium will prefer to speciate as Cr(II). Electrochemical quantification of chromium is that concentration measurements can be made regardless of the preferential oxidation state, so analytical methods validated in one salt can be transferred to a system with a different salt composition.

There is a fundamental problem with relying on electroanalytical measurements quantifying corrosion products in molten salts, namely that the standardized procedure for taking analytical measurements have not been devised and standardized. Studies of chromium quantification in molten salts have been published as early as the 1950s that used polarographic methods for the concentration determination[121] where more current literature use modern potentiostats and digital programs to conduct voltammetry at solid electrodes. Several voltametric techniques which have been used for quantification of transition metals in molten salts are anodic stripping voltammetry (ASV), chronopotentiometry (CP), cyclic voltammetry (CV), and square wave voltammetry (SWV). Each technique comes with its own “quirks” of operation and can be used for quantitative analysis at varying scales.

5.1 ELECTROANALYTICAL METHODS OF QUANTIFICATION - INTRODUCTION

Modern electrochemical equipment and methods have expanded the possible strategies of measuring the characteristics of molten salt systems. There is an ever-growing list of methods that probe the current-

potential (*i-E*) phase space, but we can generally categorize these methods into potentiometry, voltammetry, and coulometry. Potentiometry measured the difference in electrode potentials in an electrochemical cell. Voltammetry measures the current response to an applied potential. Coulometry measures the total charge passed through the electrochemical cell over varying applied potentials. The electrochemical response for potentiometry, voltammetry, and coulometry are sensitive to the concentration of redox active species. For each technique, given the solution to the governing differential equation of mass transport we can find an expression for the bulk concentration of the electroactive species in the melt. Multiple electroanalytical methods are applicable to dissolved corrosion product quantification in molten fluoride salts. Their governing principles, sensitivity, and practical trade-offs are summarized in Table 26.

Table 26. Electroanalytical quantification techniques

Technique	**Principle/Equation**	**Detection Limit[+]**	**Advantages**	**Limitations**
Cyclic Voltammetry (CV)	Diffusion-controlled peak current used for quantification via Randles-Sevcik-type relations; Berzins-Delahay treatment used for peak-current-based concentration extraction after baseline subtraction	10^{-5} M[122]	Identifies redox couples and speciation; enables extraction of diffusion coefficients	Broad/overlapping peaks, double-layer charging, underpotential deposition, activity-coefficient effects, and reference electrode instability can bias quantification, especially at low concentration
Square Wave Voltammetry (SWV)	Pulsed voltammetry that suppresses capacitive background and measures concentration from peak current/height; commonly used when CV peaks are too broad or masked	10^{-7}-10^{-8} M[122]	Higher sensitivity than CV; clearer peak separation; can monitor O_2/O^{2-} reaction	Requires careful control of immersed electrode area and pulse parameters[89], [95]

Anodic Stripping Voltammetry (ASV)	Preconcentrate trace metals by cathodic deposition, then anodically strip and quantify from stripping charge/peak	10^{-10}-10^{-11} M[122]	Highest sensitivity among discussed methods; effective for trace corrosion-product monitoring and calibration at very low concentrations	Requires deposition efficiency control, reproducible electrode renewal, and care to avoid alloying/plating artifacts[123]
Chronopotentiometry (CP)	Constant-current method; concentration and diffusion inferred from transition time using Sand's equation	No limit reported, typically less sensitive than stripping methods	Direct route to diffusion coefficients and transport properties; complementary to CV for validating diffusion-controlled behavior	Transition-time interpretation can be complicated by convection, multiple species, and disagreement with CV-derived diffusion coefficients[89]

While exploring the *i-E* phase space, the uncompensated resistance of the cell will start to impact our analysis. As concentration increases and the current density increases, the effect of uncompensated resistance also increases as shown by Eq.(5.1):

$$\eta_s = E_{measured} - IR_U \tag{5.1}$$

η_s is the surface overpotential of the working electrode, $E_{measured}$ is the recorded potential compared against the reference electrode, I is the total current, and R_U is the uncompensated resistance. This relationship shows that as current passing through our cell grows, so does the surface overpotential. Therefore, it is critical to correct for the uncompensated resistance of the cell when performing quantitative measurements. We apply the electrode potential correction in Eq.(5.1) to our plotted data in this chapter.

5.1.1 CP IN MOLTEN FLiNaK

Chronopotentiometry is a technique that has been used in literature to study FLiNaK with the addition of Cr in various forms[124], [125]. When reporting redox potentials in fluoride salts, chronopotentiometry is a technique of particular interest because it is used to make dynamic reference electrode measurements in the melt. Understanding how the dynamic reference electrode measurement changes with the addition of metal fluorides, like CrF_3, is particularly important for systems that propose to use electrochemical sensors for redox measurements and control. Yoko and Bailey[124] studied chromium redox chemistry in FLiNaK

using CP. Their results identified that CrF_3 added to FLiNaK showed two stepwise reductions. Yoko and Bailey applied Delahay and Mamantov's analysis[126] to show the number of electrons transferred in each respective reduction was one electron in the first reduction and two electrons in the second reduction. This lead them to hypothesize chromium reduction in FLiNaK must follow Cr^{3+}/Cr^{2+} and Cr^{2+}/Cr^{0} reactions. Wang and Zhang[125] conducted CP to study the FLiNaK-CrF_2 system which led to the derivation of a more robust formula to model the current response of stepwise reduction of $Cr^{3+}/Cr^{2+}/Cr^{0}$. A key assumption in this model is that there is some Cr^{2+} present in FLiNaK which could be present due to the disproportionation of Cr^{3+} given by Eq.(3.31).

$$2Cr^{3+} + Cr = 3Cr^{2+} \tag{5.2}$$

5.1.2 CV IN MOLTEN FLiNaK

Previous electrochemical investigations of chromium-bearing fluoride salts have established characteristic voltametric behavior for chromium redox couples in molten fluoride media. Cyclic voltammograms of the FLiNaK–CrF_3 system generally exhibit well-defined anodic stripping peaks associated with the Cr^{0}/Cr^{2+} reaction. At temperatures below approximately 850 °C, the voltametric response corresponding to the Cr^{2+}/Cr^{3+} couple becomes diminished, whereas distinct Cr^{2+}/Cr^{3+} peaks emerge at temperatures above approximately 870 °C. Yoko and Bailey[127] performed cyclic voltammetry studies of the FLiNaK–CrF_3 system over a temperature range of 612–983 °C and identified the strong temperature dependence of chromium electrochemical behavior. In subsequent work, Bailey and Yoko[128] demonstrated that reduction of Cr^{3+} to Cr^{2+} produces extensive dendritic deposits of insoluble electroactive material, providing an explanation for the observed quasi-reversible behavior of the Cr^{2+}/Cr^{3+} redox couple. Peng et al.[129] further investigated chromium electrochemistry in FLiNaK through cyclic voltammetry following additions of both CrF_2 and CrF_3 at 600 °C, Wu et al.[130] examined the FLiNaK–CrF_3 system at 700 °C, and Wang and Zhang[125] investigated the FLiNaK–CrF_2 system and experimentally verified the disproportionation behavior of Cr^{2+} in FLiNaK. Chromium electrochemical quantification is also studied in FLiBe[131] using cyclic voltammetry reinforcing the applicability of using this technique for chromium quantification in fluoride melts. Quantification by cyclic voltammetry is performed by exploiting the relationship between the peak current density and species concentration. The Randles-Sevcik equation, shown in Eq.(3.9), and the Berzins-Delahay equation, shown below in Eq.(5.3), describe the dependence of peak current of a redox reaction in a cyclic voltammogram with concentration of electroactive redox species.

$$i_p = 0.6105AC\sqrt{\frac{n^3F^3D\nu}{RT}} \tag{5.3}$$

Randles-Sevcik equation takes the assumption that the redox reaction in consideration is reversible, there are no homogenous kinetics in the diffusion layer, the system is diffusion limited (i.e. with the absence of mixing), and both reduced and oxidized species are soluble. The assumptions to derive Berzins-Delahay equation differs only in that the reduced species is assumed to not be soluble and instead deposits on the electrode surface. In the FLiNaK-CrF_3 system Cr^{3+}/Cr^{2+} is generally fit to Randles-Sevcik equation where Cr^{2+}/Cr^{0} is generally fit to Berzins-Delahay equation, though the applicability of this model is debated[132].

5.1.3 SWV IN MOLTEN FLiNaK

Square wave voltammetry (SWV) has been applied in molten-salt systems as a sensitive electroanalytical method for quantifying dissolved electroactive species when cyclic voltammetry is limited by broad peaks, background current, or overlapping redox processes. Because SWV measures the difference between forward and reverse pulse currents, the capacitive contribution is reduced and faradaic peaks are often more distinct than in conventional CV, making peak height or peak area useful for concentration dependent analysis. Prior studies have demonstrated this approach for oxide-ion quantification in molten fluorides, where SWV produced well-defined oxidation peaks proportional to oxide concentration, while CV was less suitable because gas evolution and background current obscured the analytical signal [98], [133], [134]. SWV has also been developed for quantifying metal ions in molten chloride salts relevant to pyroprocessing and molten-salt reactor fuel chemistry, including actinides, lanthanides, and minor metal ions [119], [135], [136], [137]. These studies show that SWV can provide lower detection limits and improved peak resolution compared with CV, but they also emphasize that quantitative use requires careful control of electrode area, pulse parameters, baseline correction, reference stability, and validation against independent concentration measurements or standard additions.

In the present work, SWV is treated as a high-sensitivity concentration-dependent method for detecting corrosion products in molten fluoride salts, while quantitative interpretation is limited by peak assignment uncertainty, possible surface deposition/alloying, nonideal activity effects, ohmic distortions, and pseudo reference electrode drift. As the data from the FLiNaK-CrF_3 experiment spans a range identified by a non-linear response in peak current with concentration, we do not explore the analysis of SWV in this section. We do use SWV analysis in Section 5.6 where we examine trace impurities in FLiBe.

5.2 APPLICATION OF ELECTROANALYTICAL METHODS IN FLiNaK-CrF_3 - METHODS

Understanding redox thermodynamics and mass transport of chromium in high-temperature molten salts is central to predicting corrosion and controlling chemistry in fluoride-salt systems. Voltametric methods such as cyclic voltammetry and square-wave voltammetry can, in principle, resolve the formal potential and activity effects of the Cr^{3+}/Cr^{2+} couple and quantify diffusion coefficients, enabling concentration-dependent maps needed for process control and modeling. Achieving quantitative accuracy, however, requires stable potential referencing, well-defined electrode geometry, and consistent potential windows so that small, theoretically constrained dependences (for example, Nernstian shifts of tens of millivolts and diffusion coefficients that are approximately concentration independent) can be reliably separated from instrumental and background artifacts.

Having a comparable benchmark in literature for our analysis is critical and quantifying the uncertainty within the benchmark help make our reported uncertainties credible. Our CP and CV results are benchmarked against Yoko and Bailey[127]. Our SWV results are benchmarked against Wu et al.[130]. The uncertainty analysis for each of these benchmarks is provided in Appendix A. By showing our uncertainties are within the order of magnitude of our benchmarks or lower, we will have confidence in our methods of electrochemical quantitative analysis.

5.2.1 *Preparation of FLiNaK-CrF_3 salt*

A FLiNaK eutectic salt was prepared for correlating electrochemical measurements with the elemental analysis of FLiNaK with CrF_3 additions. The eutectic FLiNaK was prepared in an argon glovebox (LC Technology; LC-150) combining 12.5701g of LiF (Sigma-Aldrich; >99.9% trace metals), 5.0623g of NaF (Sigma-Aldrich; >99% ACS Reagent), and 25.556g KF (Sigma-Aldrich; >99% ACS Reagent) in a mortar and grinding the salt for 5 minutes until it reached a uniform powder (LiF-NaF-KF: 46.36-11.53-42.10 mol%). The powdered salt was added to a glassy carbon crucible and brought to a cylindrical tube furnace (Watlow; 650W Cylindrical Furnace) and held at 400°C for 3 hours to dry the salt. No noticeable change in cover-gas moisture or oxygen was observed, so the furnace was ramped to 800°C and allowed to soak at temperature for 5 hours before continuing with the CrF_3 additions. The CrF_3 salt (Sigma-Aldrich; >99.99% trace metals) was added into the molten FLiNaK in 7 additions which were 0.094g, 0.101g, 0.198, 0.761g, 1.388g, 1.756g, and 0.982g. The final concentration of CrF_3 in the FLiNaK was 10.9wt% (0.0443 mol. frac. CrF_3). Electroanalytical tests were run at each addition, but at Addition 6 (1.756g) and Addition 7 (0.982g) the electrochemical cell failed due to current overloads and consumed electrodes.

5.2.2 *Chronopotentiometry of FLiNaK-CrF_3*

Chronopotentiometry was performed on the salt melt at 800 oC, after additions of different amounts of CrF3; approximately 30 minutes at 800 oC was allowed between addition of CrF3 and subsequent electrochemical measurements. Solute concentrations calculated based on complete CrF_3 dissolution before performing the electrochemical measurements and chronopotentiometry results are given in Table 22. The details of the potentiometric results were previously discussed in Section 4.4. We expanded the discussion on the use of CP as a method of quantifying chromium in this chapter.

5.2.3 *Cyclic Voltammetry of FLiNaK-CrF_3*

A series of cyclic voltammograms were taken of the FLiNaK-CrF_3 system at each addition of CrF_3 reported in Table 27. Key parameters from the voltammograms that are used for further analysis include the half-wave potential, $E_{1/2}$, the peak potential separation, ΔE_p, and the peak current density, i_p. These values are reported in **Error! Reference source not found.** for each identifiable reaction in the voltammograms.

Table 27. Cyclic Voltammetry Test Matrix

Addition #	Total CrF_3 added [g]	CrF_3 Concentration [wt%]	CrF_3 Concentration [mol/mol]	Temperature [°C]	Scan Rate [mV/s]
Blank	0	0	0	800(20)	1000, 500, 100, 50, 10
1	0.094(1)	0.217(2)	0.000825(9)	800(20)	1000, 500, 100
2	0.195(1)	0.449(3)	0.00171(1)	800(20)	1000, 500, 100
3	0.393(2)	0.902(6)	0.00345(2)	800(20)	1000, 500, 100
4	1.154(3)	2.602(7)	0.01013(4)	800(20)	1000, 500, 100
5	2.543(4)	5.557(9)	0.02232(5)	800(20)	1000, 500, 100
6	4.298(5)	9.05(1)	0.03774(5)	800(20)	1000, 500, 100, 50
7	5.280(6)	10.89(1)	0.04636(6)	800(20)	N/A

5.2.4 Square Wave Voltammetry of FLiNaK-CrF_3

A series of square wave voltammograms were taken of the FLiNaK-CrF_3 system at each addition of CrF_3 reported in Table 28. The data from these runs have been plotted in Appendix B for the reader. No further analysis is performed here.

Table 28. Square Wave Voltammetry Test Matrix

Addition #	Total CrF_3 added [g]	CrF_3 Concentration [wt%]	CrF_3 Concentration [mol/mol]	Temperature [°C]	Frequency [mV/s]	Potential Step [mV]	Amplitude [mV]
Blank	0	0	0	800(20)	100, 50, 25, 10	2	25
1	0.094(1)	0.217(2)	0.000825(9)	800(20)	100, 50, 25, 10	2	25
2	0.195(1)	0.449(3)	0.00171(1)	800(20)	100, 50, 25, 10	2	25
3	0.393(2)	0.902(6)	0.00345(2)	800(20)	100, 50, 25, 10	2	25
4	1.154(3)	2.602(7)	0.01013(4)	800(20)	100, 50, 25, 10	2	25
5	2.543(4)	5.557(9)	0.02232(5)	800(20)	100, 50, 25, 10	2	25
6	4.298(5)	9.05(1)	0.03774(5)	800(20)	100, 50, 25, 10	2	25
7	5.280(6)	10.89(1)	0.04636(6)	800(20)	N/A	N/A	N/A

5.3 ELECTROANALYTICAL DATA FROM FLiNaK-CrF_3 SYSTEM – RESULTS & DISCUSSION

5.3.1 CHRONOPOTENTIOMETRY RESULTS

The CP data are plotted in Figure 59 (see Section 4.4) showing representative chronopotentiograms collected during a 10 s imposed-current step followed by open-circuit relaxation. The concentrations reported in Table 20 are nominal values calculated from the mass of CrF_3 added to the melt and assume complete dissolution within 30 min at 800 °C.

The blank FLiNaK experiment produced the most negative potential during the imposed-current step. After the current was applied, the WE potential rapidly decreased and approached approximately -1.474 V versus the W qRE. This response indicates that, in the absence of added chromium, the imposed cathodic current was not supported by a significant concentration of reducible chromium species. Instead, the electrode rapidly polarized to a more negative potential region associated with background electrolyte, impurity, or alkali-metal reduction processes. After the current was removed, the blank experiment relaxed slowly toward the open-circuit potential.

The transition time of chromium reactions was measured by Kuwana's method[138], shown in Figure 89. The measured transition times also increased with chromium addition where transition times could be identified. Unlike reported values by Wang and Zhang[132], only one clear redox reaction was present in the system after Addition 1 and Addition 2. In Addition 3, there are two identifiable transition times. In Addition 4, there is only one transition time again. Subsequent additions did not produce data which could be used to measure a transition time.

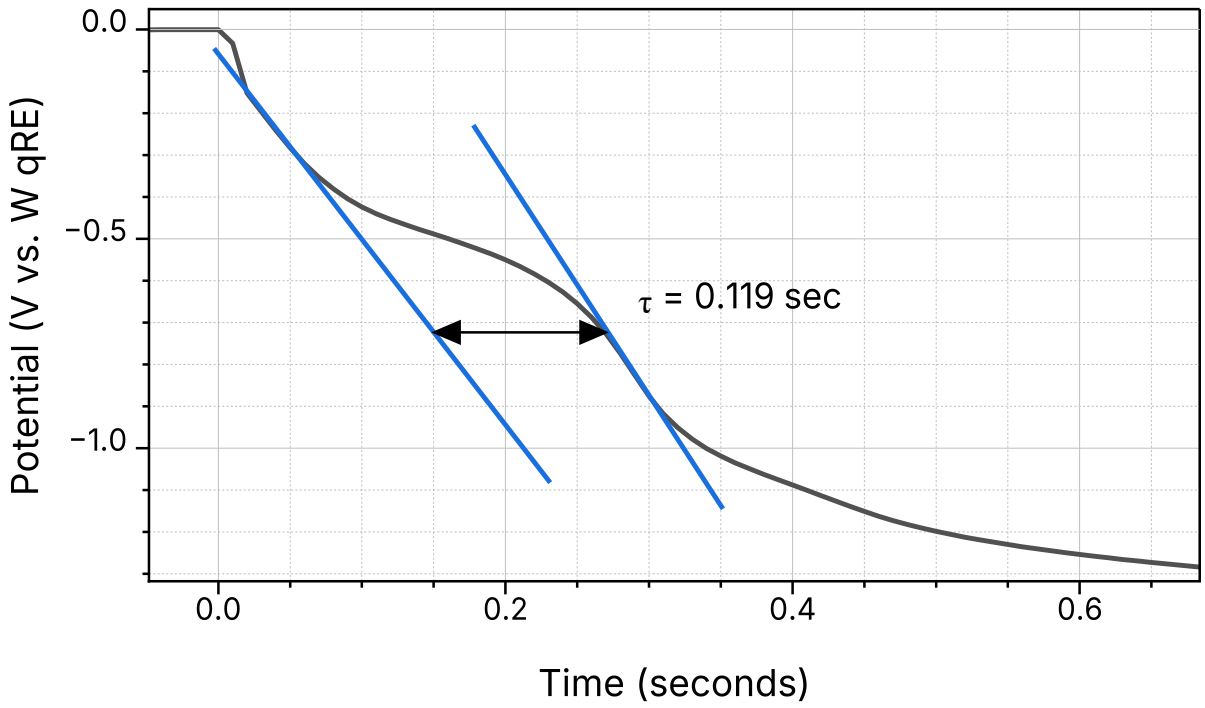


Figure 89. Chronopotentiometry data in FLiNaK-CrF_3 system from Addition 1 (see Table 22) showing how τ is measured using Kuwana's method[139].

Yoko and Bailey identify a way to determine the number of electrons transferred in successive reduction steps from a chronopotentiogram by comparing the transition times of the successive reactions[127]. The cases considered are reactions that involve a total of 3 electrons transferred, and each reaction transferred one or two electrons.

$$\text{Case I: } n_1 = 1,\ n_2 = 2; \text{ then } \frac{\tau_2}{\tau_1} = 8 \tag{5.4}$$

$$\text{Case II: } n_1 = 2, n_2 = 1; \text{ then } \frac{\tau_2}{\tau_1} = 1.25 \tag{5.5}$$

n_1 is the number of electrons transferred from the reaction at less cathodic potentials, n_2 is the number of electrons transferred from the reaction at more cathodic potentials, τ_1 is the transition time from the n_1 reaction, and τ_2 is the transition time from the n_2 reaction. The only data which we can use for this analysis is from Addition 3, where the two successive redox reactions produce measurable tau values.

$$\frac{\tau_2}{\tau_1} = \frac{0.929}{0.140} = 6.635 \approx 8 \quad (5.6)$$

The transition time ratio is close to a value of 8, indicating our data shows Cr^{3+}/Cr^{2+} followed by Cr^{2+}/Cr^{0}, and this is expected from prior literature.

From the available CP data, we calculate the diffusivity of Cr^{2+} and Cr^{3+} from the measured transition times. This calculation is performed using the Sand equation which assumes a semi-infinite diffusion layer. We compare this value with diffusivities calculated from a fixed boundary layer which is defined by the natural convection of the system. This data is shown in Table 29. These values can be interpreted as apparent diffusivities unless the natural-convection boundary-layer thickness is independently constrained.

Table 29. Calculated diffusivities of Cr^{2+} and Cr^{3+} from

				Diffusivity, D ($cm^2\ s^{-1}$)			
Run	**Cr species measured**	**Transition**	**Number of electrons, n**	**Sand Equation**	**Fixed boundary layer ($\delta = 10\mu m$)**	**Fixed boundary layer ($\delta = 25\mu m$)**	**Fixed boundary layer ($\delta = 25\mu m$)**
1	Cr^{2+}	$\tau_2 = 0.125$	2	$2.9(6) \times 10^{-4}$	$4(1) \times 10^{-5}$	$1.1(4) \times 10^{-4}$	$2.0(4) \times 10^{-4}$
2	Cr^{2+}	$\tau_2 = 0.274$	2	$1.5(3) \times 10^{-4}$	$2.0(5) \times 10^{-5}$	$5(1) \times 10^{-5}$	$1.0(3) \times 10^{-4}$
3	Cr^{3+}	$\tau_1 = 0.140$	1	$9(1) \times 10^{-5}$	$2.1(5) \times 10^{-5}$	$5.0(9) \times 10^{-5}$	$7(1) \times 10^{-5}$
3	Cr^{2+}	$\tau_2 = 0.929$	2	$1.3(3) \times 10^{-4}$	$1.1(3) \times 10^{-5}$	$2.6(8) \times 10^{-5}$	$5.2(9) \times 10^{-5}$
4	Cr^{3+}	$\tau_1 = 0.865$	1	$6(1) \times 10^{-5}$	$7(2) \times 10^{-6}$	$1.8(5) \times 10^{-5}$	$3.5(8) \times 10^{-5}$

We measured a temperature gradient of approximately 50°C from the bottom of the cell to the surface of the melt. The velocity derived from natural convection in the cell with this thermal gradient and variation in FLiNaK density is calculated by:

$$v_{nc} = \sqrt{g \frac{\Delta\rho}{\rho_{avg}} L_{nc}} \quad (5.7)$$

$$\delta \sim \sqrt{\frac{DL_{nc}}{v_{nc}}} \quad (5.8)$$

where v_{nc} is the velocity of the natural convection profile, g is the gravitational constant at sea level, $\Delta\rho$ is the density different from the hot fluid and cold fluid, ρ_{avg} is the average density of the hot and cold fluids, and L_{nc} is the length scale at which natural convection is occurring (in our cell approximately 5cm). The velocities of our system are approximately 8.9 cm s^{-1} which predicted a boundary layer on the order of 25µm. Therefore, we believe the calculated diffusivities using a boundary layer of $\delta = 25\mu m$. The full details of this calculation are given in Appendix A.13.

We must reconcile the discrepancy in our calculated Cr^{3+} diffusivity with literature. The value of Cr^{3+} diffusivity measured by Yoko and Bailey via CP is $D_{Cr^{3+}} = 1.2(3) \times 10^{-6}$ $cm^2\ s^{-1}$ [127]. Our closest value is approximately one order of magnitude greater ($D_{Cr^{3+},avg} = 1.8(5) \times 10^{-5}$ $cm^{-2}\ s^{-1}$). The cause for this discrepancy cannot be attributed to one variable alone. Underestimating the electroactive area of the W WE

would result in overpredicted diffusivity. Any kinetically limiting steps in the production of Cr^{2+} from Cr^{3+} would also result in an artificially large diffusivity to account for lower effective concentration of Cr^{3+} compared to the known addition value. This kinetically limiting effect may decrease at greater CrF^3 weight loadings which could explain why the later additions approach reported values in literature. A combination of these two effects is obfuscating the interpretation of the relatively high Cr^{3+} diffusivity.

The Cr^{2+} diffusivity decreased after each addition of Cr^{3+}. The value of Cr^{2+} diffusivity at Addition 4 ($D_{Cr^{2+}} = 3.5(8) \times 10^{-5}$) is approximately 3 to 4 times greater than diffusivities reported in lower temperature FLiNaK solutions. There are no reported Cr^{2+} diffusivities in FLiNaK at 800ºC, therefore we can only compare against values reported by Massot et al.[140] and Wu et al.[130], and ab initio prediction by Nam[141]. The same discrepancies in our Cr^{3+} measured diffusivity apply to these values which could suggest we have overpredicted the value of Cr^{2+} diffusivity in FLiNaK at 800ºC.

5.3.2 CYCLIC VOLTAMMETRY RESULTS

Several voltammograms generated by CVs in the FLiNaK-CrF3 from this work are shown. The characteristics of these voltammograms differ from prior literature. Where most voltammograms show a single, clear anodic stripping peak corresponding to the Cr^0/Cr^{2+} reaction, the CVs in this work do not all exhibit that same shape. In the voltammogram of our blank FLiNaK, we see a redox reaction which does not appear reversible, and attribute it to an oxygen evolution reaction in the melt. Additionally, there are peaks which appear in the far anodic regions of our voltammograms but are difficult to attribute to any redox reaction discussed in prior literature.

The lack of a clear anodic stripping peak may be due to the alloying of Cr with the W electrode upon deposition. Bailey and Yoko[128] show temperatures greater than 870oC, a relatively uniform deposition of Cr metal plated on stainless steel (SUH304). If Cr metal plated on the W electrode, Cr-W forms a solid solution [142] and would require a different potential to oxidize the chromium from the alloyed material. The Cr anodic stripping peak we see in our voltammograms, labeled as A1, is differentiated from what may be the Cr de-alloying oxidation peak, labeled A1'. This is visible in Figure 93.

Upon complete Cr reduction, a cathodic peak, labeled C1, appears in all of our scans. With the addition of CrF_3, a reduction "shoulder," labeled C1', was observed on the Cr^{2+}/Cr^0 peak at higher concentrations. The appearance of this should at higher concentrations may also be related to the formation of a Cr-W alloy. For the remaining section, we use A1/C1 and A2/C2 interchangeably for Cr^{2+}/Cr^0 and Cr^{2+}/Cr^{3+}, respectively.

Figure 90 shows CVs in FLiNaK at 500 mV/s scan rate with increasing concentration of CrF_3 while also indicated the theoretical reaction potentials of Cr^0/Cr^{2+} (blue vertical line) and Cr^{2+}/Cr^{3+} (red vertical line). The potential scale uses the KDRE measured in the blank as a reference potential. There are two clear anodic peaks and two clear cathodic peaks in Addition 1 and Addition 2. The theoretical chromium redox potentials are approximately at peak half wave potentials, but the theoretical potentials do not overlap the half wave potentials for all additions given. The measured chromium redox potentials deviating from theoretical potentials could be caused by several factors. Three likely reasons for the deviation are:

(i) The W qRE potential drifts with chemical composition of the melt.

(ii) The chromium redox reactions in FLiNaK are non-Nernstian.
(iii) The electroactive surface area of the CE is limiting the kinetics at the WE.

These deviations indicate that the measured peak positions should be interpreted as apparent redox potentials rather than direct thermodynamic values. First (i), because the potential scale is referenced to the KDRE measured in the blank salt, any change in the W quasi-reference potential with CrF_3 addition, melt redox state, or local surface chemistry would shift all measured peak positions relative to the theoretical chromium potentials. Second (ii), the chromium reactions may not behave ideally with concentration. Changes in Cr(III)/Cr(II) speciation, nonideal activity coefficients, metal deposition, and possible Cr-W alloy formation can shift the formal potential away from the value predicted using dilute-solution Nernstian assumptions. Third (iii), the measured response may be influenced by the finite electroactive surface area and kinetics of the counter electrode. If the counter electrode cannot sustain the complementary reaction without significant polarization, the working electrode potential includes additional cell-polarization contributions, causing the apparent peak positions and peak separations to differ from their expected values. These effects are consistent with the observation that the theoretical Cr^{2+}/Cr^0 and Cr^{3+}/Cr^{2+} potentials approximate the peak locations for the lower additions but do not remain fixed at the half-wave potentials as CrF_3 concentration increases.

In Figure 90, we also see the evolution of an anodic stripping peak. (A1; representation of Cr^0/Cr^{2+}) This provides strong evidence that added CrF_3 produces reducible chromium species that deposit during the cathodic sweep and are subsequently oxidized during the anodic sweep. This feature is weak or absent in the blank FLiNaK scan but grows with CrF_3 concentration, while the corresponding cathodic feature, C1, also increases, supporting assignment of the A1/C1 pair to the Cr^{2+}/Cr^0 deposition-stripping process. At higher CrF_3 additions, A1 broadens and separates into A1 and A1′-type features, suggesting that deposited chromium is not stripped from a single uniform surface state but instead may exist as weakly bound Cr, multilayer/rough deposits, or Cr alloyed with the working electrode. The A2/C2 features, assigned to the Cr^{3+}/Cr^{2+} couple, also become more apparent with CrF_3 addition, but their interpretation is less direct because their peak positions shift relative to the theoretical Cr^{3+}/Cr^{2+} potentials and increasingly overlap with the deposition-stripping envelope. There is systematic chromium-sensitive behavior, but the peak positions and shapes should be interpreted as apparent electrochemical responses rather than ideal reversible redox couples because qRE drift, incomplete KDRE referencing after Addition 1, chromium speciation, surface-mediated deposition, and possible alloying all contribute to the measured response.

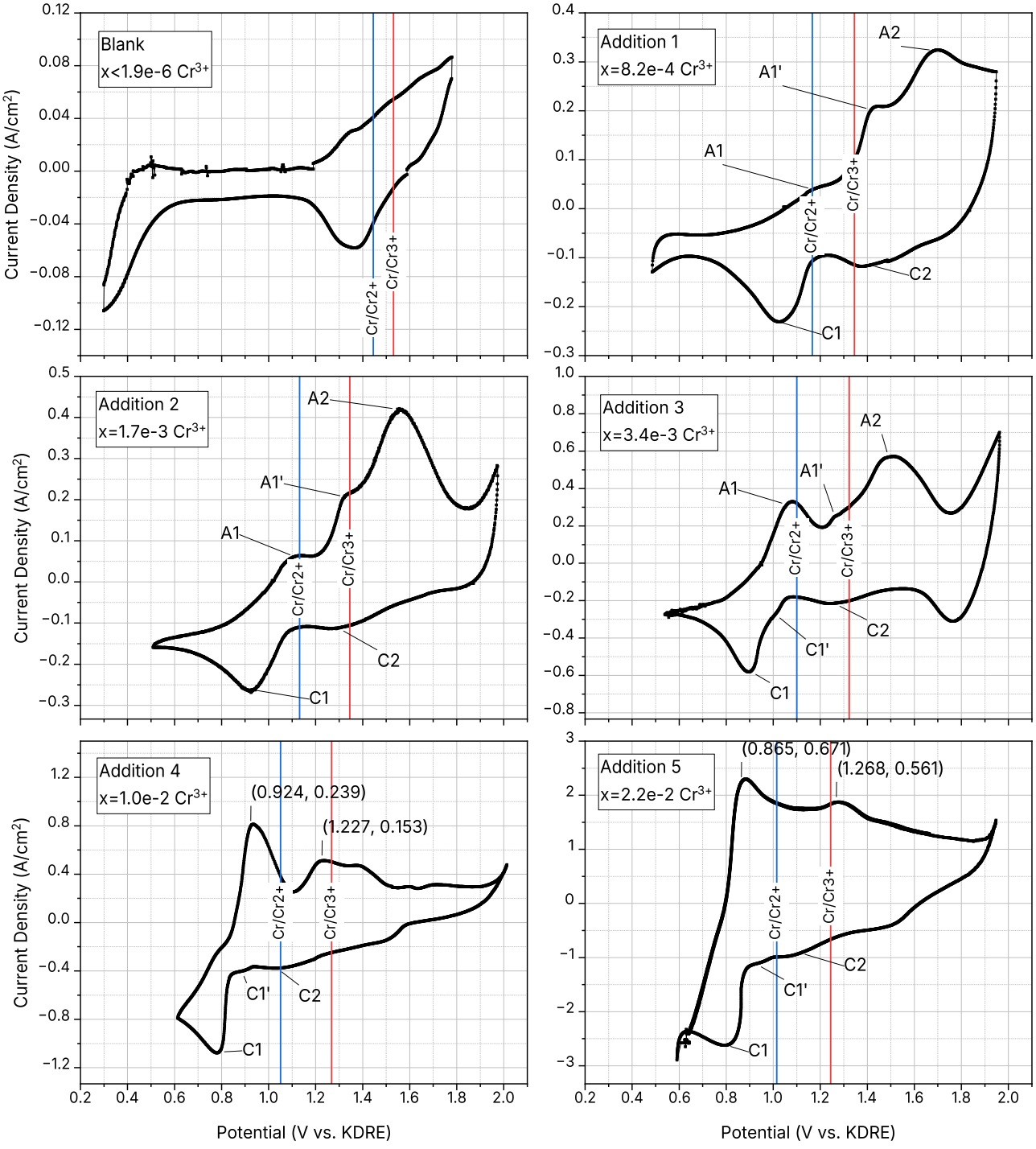


Figure 90. CVs on FLiNaK-CrF_3 system at 800°C with varying concentrations of CrF_3 added. Theoretical Cr/Cr^{2+} (blue vertical line) and Cr/Cr^{3+} (red vertical line) reaction potentials are shown. Potential scale is shifted to versus the KDRE, but only Blank and Addition 1 were able to measure the KDRE potential. Discrepancy in theoretical potentials versus the measured potential is attributed to qRE drift with added CrF_3 concentration and inability to measure the KDRE after Addition 1.

5.3.2.1 PEAKS IN THE BLANK SCANS

The blank FLiNaK was analyzed prior to CrF_3 additions to establish a baseline. The CV of the blank is shown in Figure 91 which clearly indicates there is a reaction occurring between 1.3 and 1.5 V vs. KDRE. This feature in blank FLiNaK scan is most consistently assigned to oxidation of oxygen-containing impurities[143]. The anodic peak decreases with every subsequent scan which is characteristic of holding oxide at anodic potentials above its redox potential. We can verify the anodic potential coincides with the thermodynamic value for oxygen reduction. Consider the reaction:

$$K(s) + LiF(l) + \frac{1}{4}O_2(g) = KF(l) + \frac{1}{2}Li_2O(s)$$
$$\Delta G^o_{(5.9)}(800^oC) = -143.708\ kJ \tag{5.9}$$

The redox potential at the 800°C reference state is:

$$E^o(800^oC) = -\frac{\Delta G^o_{(5.9)}(800^oC)}{nF} \approx 1.49\ V\ vs. K/K^+ \tag{5.10}$$

Then the correction for the composition of the FLiNaK and the partial pressure of the oxygen can be considered:

$$E(800^oC) = E^o(800^oC) - \frac{RT}{nF}\ln\left(\frac{a_{KF}}{a_{LiF}\cdot p_{O_2}^{1/4}}\right) \tag{5.11}$$

Assuming $a_{KF} \approx x_{KF} = 0.42$, $a_{LiF} \approx x_{LiF} = 0.465$, and $p_{O_2} = 10^{-3} - 10^{-2}$ atm, then the range of potentials we would expect to see oxygen redox in FLiNaK is:

$$E\left(800^oC, p_{O_2}\right) = 1.33\ V \text{ to } 1.39\ V \text{ vs. KDRE} \tag{5.12}$$

Therefore, the anodic feature observed in in Figure 91 is assigned to an oxide-associated background process, most likely oxidation of dissolved oxide impurities to oxygen. The thermodynamic estimate based on the Li_2O/O_2 equilibrium place this reaction near 1.3–1.4 V vs KDRE for effective oxygen pressures of 10^{-3}–10^{-2} atm, consistent with the observed anodic feature. However, the broad peak shape and associated cathodic return feature suggest that the measured response may include tungsten surface oxidation or oxyfluoride formation in addition to oxide-ion oxidation.

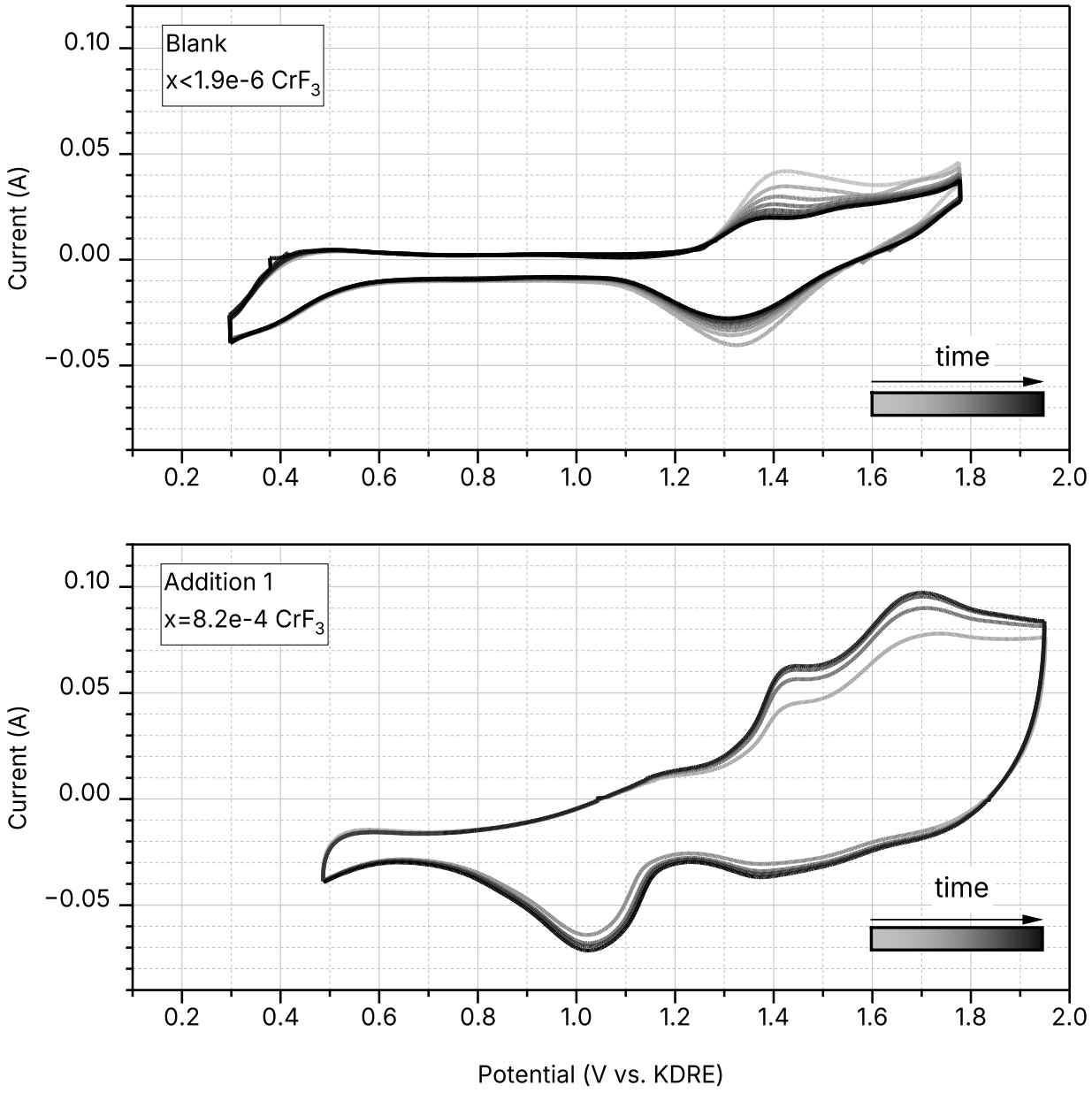


Figure 91. CV of FLiNaK Blank (top) and Addition 1 (bottom) at 800°C and 1000 mV/s scan rate, 10 consecutive scans. For features in the blank which are insensitive to Cr redox chemistry, their potential versus the KDRE should be constant through subsequent additions. The presence of redox active species in the blank cause inaccuracies in peak current and peak separation measurements.

5.3.2.2 CALIBRATION WITH PEAK CURRENTS

The chromium concentration in FLiNaK was quantified empirically by plotting the scan-rate-normalized peak current density, $i_p \nu^{-1/2}$, against the nominal added CrF_3 concentration. This approach does not require assigning a diffusion coefficient before calibration. Instead, each voltametric feature is treated as an analytical response whose magnitude is compared directly with the known chromium addition. The scan

rate-normalized peak current densities are plotted in Figure 92. Linear fits were applied to the four assigned peak labels: A1 ≡ Cr^0/Cr^{2+}; C1 ≡ Cr^{2+}/Cr^0; A2 ≡ Cr^{2+}/Cr^{3+}; C2 ≡ Cr^{3+}/Cr^{2+}.

All four peak families showed positive calibration slopes, indicating that the electrochemical response increased with added CrF_3. The strongest sensitivity was observed for C1, assigned to the Cr^{2+}/Cr reduction process, with a slope of 5.582 ± 1.066. However, this response also showed the greatest scatter, with $R^2 = 0.688$. This suggests that while C_1 is highly sensitive to chromium concentration, it is also strongly affected by nonideal effects such as metal deposition, nucleation, electrode surface history, or peak overlap. These nonidealities complicate the reaction mechanism and break the expected linearity of peak current with bulk concentration of electroactive species.

The most linear calibration was obtained for C2, assigned to the Cr^{3+}/Cr^{2+} reduction process, with $R^2 = 0.964$. Its slope, 1.837 ± 0.098, was smaller than the Cr^{2+}/Cr^0 peak slope, but the improved linearity suggests that C2 may provide the most reproducible empirical calibration feature over the concentration range studied. This result makes sense when considering the literature finds this peak to be reversible at the range of temperatures and concentrations tested in this experiment. Reversibility here implies the peak current will scale linearly with the concentration of electroactive species in the bulk which is a key requirement for designing a sensor that quantifies species in the melt. A1 and A2 also produced reasonable linear responses, with $R^2 = 0.833$and 0.862, respectively. Their slopes were similar, $2.952 \pm 0.395$for A1 and 2.620 ± 0.289 for A2, indicating comparable concentration sensitivity for the Cr^0/Cr^{2+} and Cr^{2+}/Cr^{3+} features.

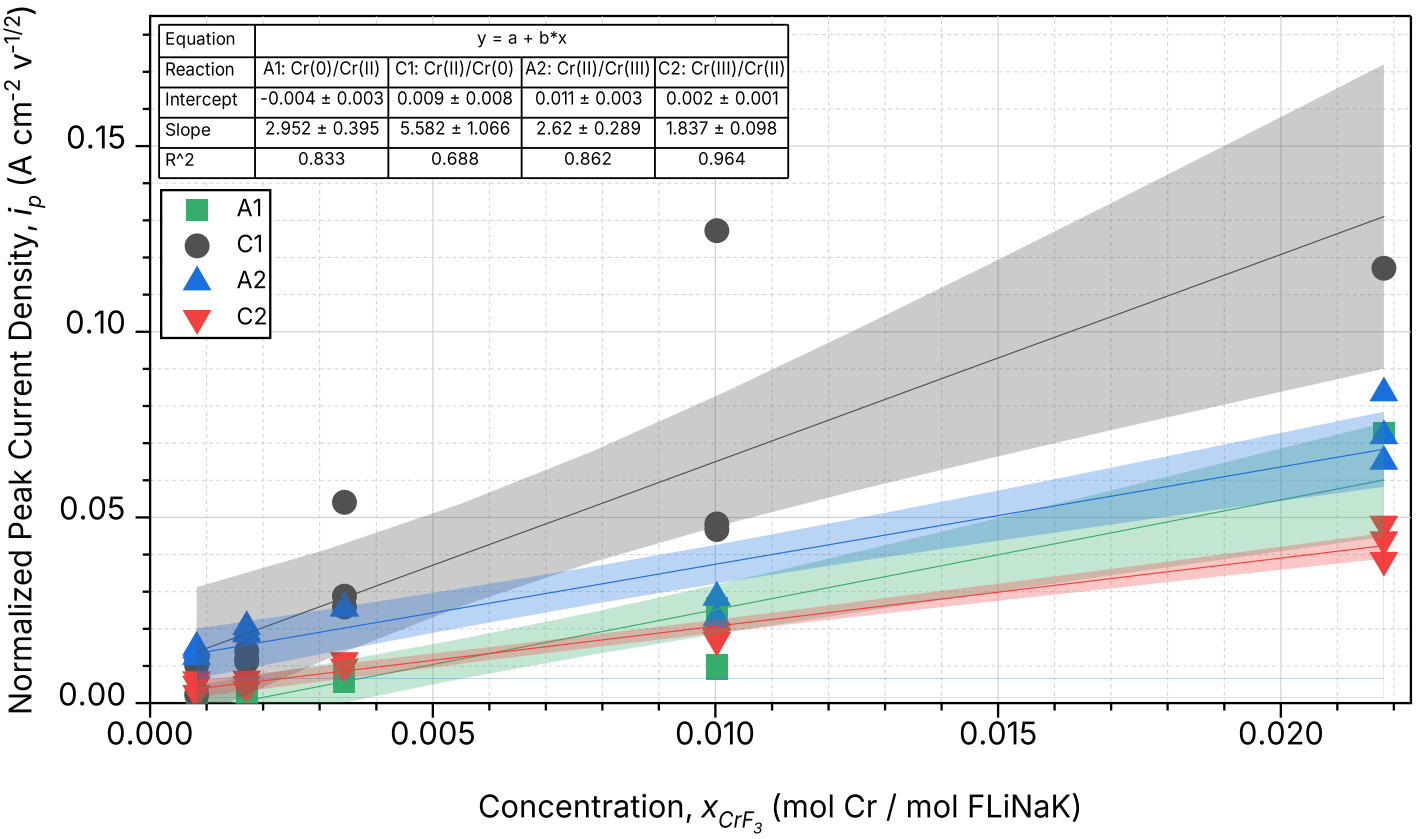


Figure 92. Peak current densities of each addition of CrF_3 (see Table 27 for details) in FLiNaK at 800°C. The peak current density is normalized by the square root of the scan rate, $v^{1/2}$. The reaction with the more linear fit is Cr^{3+}/Cr^{2+} while the reaction with the least linear fit is Cr^0/Cr^{2+}.

The intercepts for all four fits were small relative to the response at the highest CrF_3 additions. This supports the interpretation that the measured peak currents primarily arise from added chromium species rather than from a large fixed background signal. However, the nonzero intercepts and scatter among the low-concentration data indicate that background current, residual impurities, electrode conditioning, and uncertainty in peak selection still affect the calibration.

For practical quantification, C2 provides the most linear calibration, while C1 provides the highest sensitivity but lower reproducibility. Therefore, C2 is the preferred calibration feature when linearity is prioritized, whereas C1 may be useful as a sensitive qualitative indicator of chromium accumulation. Improvements for this method of quantitative analysis can be made by including peak current response with immerse depth, as discussed in [119]. Investigations for repeatability over the expected range of chromium concentrations in MSRs should be considered for industrial development of electroanalytical methods.

5.3.2.3 Calculating Diffusivities

The diffusivities, also referred to as diffusion coefficient D, of Cr^{2+} and Cr^{3+} are calculated for each CrF_3 addition by assuming the diffusivity is not dependent on scan rate. In most literature of FLiNaK-Cr systems, the diffusivity of Cr species are not assumed to vary with concentration. However, over two orders of

magnitude of added CrF_3, Cr diffusivities may not remain constant with concentration. Diffusivity dependence with concentration is a relationship that must be understood when using electroanalytical techniques for chromium quantification. Diffusivity can be used as a benchmark parameter for comparing two experimental studies because it should reflect the transport behavior of the same electroactive species under similar salt composition and temperature conditions. If the calculated diffusivities differ substantially between studies, the disagreement can indicate differences in peak assignment, concentration assumptions, electrode area, convection, uncompensated resistance, or whether the measured current is truly diffusion controlled.

The effect of scan rate on peak current density is clearly seen in Figure 93. The peak current density appears to vary proportionally to the square root of the scan rate. The peak potential separation of the A1/C1 and A2/C2 reactions vary with scan rate which indicates both reactions are quasi-reversible.

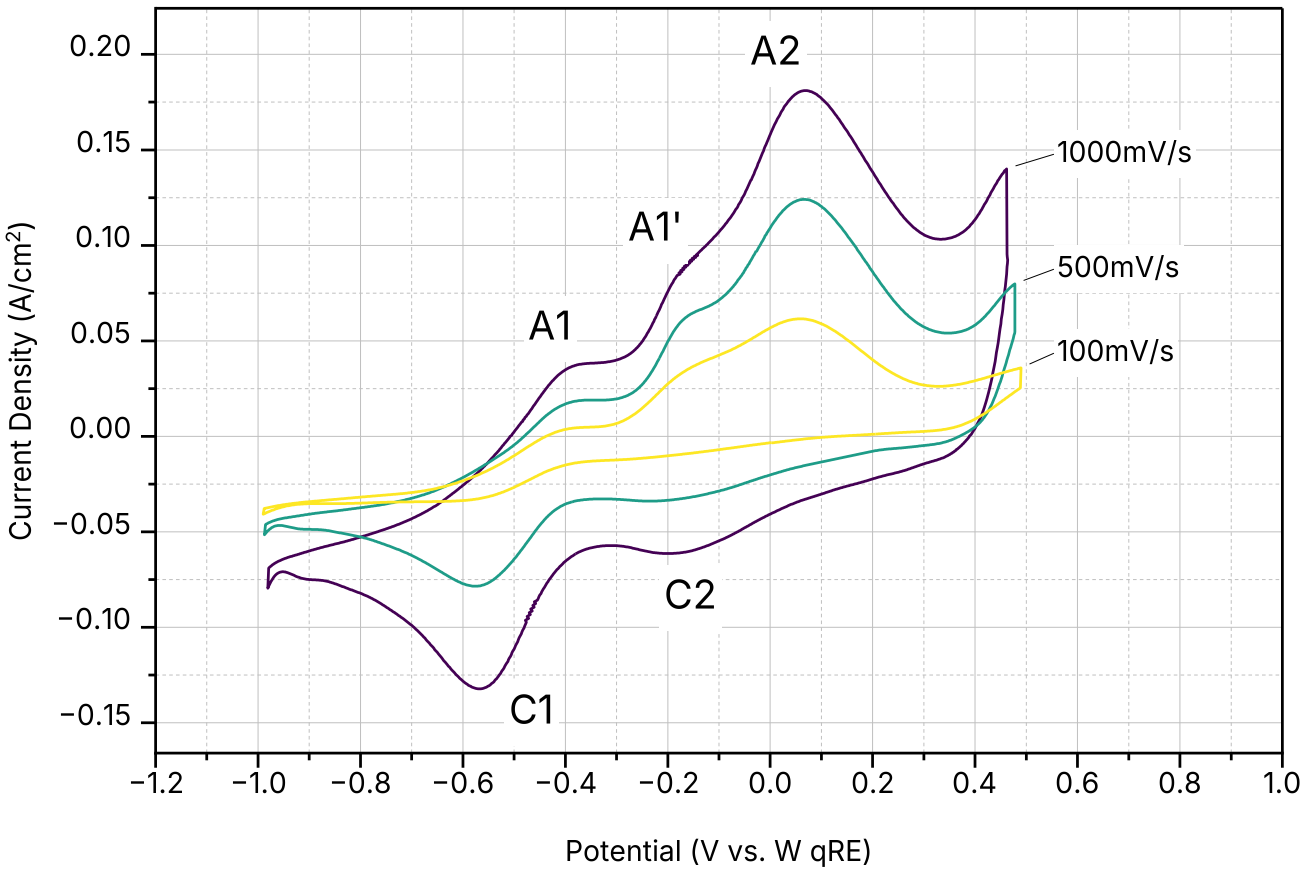


Figure 93. CV in FLiNaK-CrF_3 at 800°C at with x_{CrF3} = 1.7e-3 at varying scan rates.

We use linear diffusion approximation in this analysis. Berzin and Delahay show the approximation introduces less than 5% error in the result when cylindrical or spherical electrodes satisfy the following condition in the system:

$$\frac{D\tau}{r^2} \leq 3 \times 10^{-3} \tag{5.13}$$

where D is the diffusivity of the reacting species, τ is the time elapsed since electrolysis begins, and r is the radius of the cylindrical or spherical electrode. In our study of $D_{Cr^{3+}}$, we simplify the time since electrolysis begins by overestimating the time to always be $\tau = 1$ second, and use the diffusivity 8.3×10^{-7} cm^2/s reported by Yoko and Bailey[127]. The dimensionless parameter given in Eq.(5.13) results in 3.3×10^{-4} which gives us confidence we can use the linear diffusion analysis provided here. The diffusivity of Cr^{2+} and Cr^{3+} in FLiNaK are calculated and reported in Table 30 and plotted over concentration of added CrF_3 in Figure 1Figure 94. Diffusivities measured at different scan rates for the reactions in Table 30 vary between 14% to 68% relative standard deviation, shown in Table 31. Therefore, the diffusivity in not scan rate independent and this implies there are more complex kinetics in the diffusion layer or surface interactions that are not considered in Eq.(3.9) and Eq.(5.3). The error bars are representative of the standard deviation of the measured diffusivities over different scan rates.

Table 30. Calculated diffusivities for Addition 2 (see Table 27 for details)

Peak Name	ν (mV/s)	i (A/cm^2)	$D_{R\text{-}S}$ (cm^2/s)	$D_{R\text{-}S,avg}$ (cm^2/s)	$D_{B\text{-}D}$ (cm^2/s)	$D_{B\text{-}D,avg}$ (cm^2/s)
A1	1000	0.127	1.136E-7	6.558E-8	6.072E-8	3.505E-8
	500	0.064	5.77E-8		3.084E-8	
	100	0.019	2.543E-8		1.359E-8	
A1’	1000	0.293	6.047E-7	7.584E-7	3.232E-7	4.053E-7
	500	0.213	6.391E-7		3.416E-7	
	100	0.121	1.031E-6		5.511E-7	
C1	1000	-0.444	1.389E-6	1.069E-6	7.421E-7	5.713E-7
	500	-0.266	9.968E-7		5.327E-7	
	100	-0.108	8.216E-7		4.391E-7	
A2	1000	0.607	2.076E-5	2.198E-5	1.110E-5	1.174E-5
	500	0.417	1.96E-5		1.047E-5	
	100	0.213	2.557E-5		1.366E-5	
C2	1000	-0.205	2.368E-6	1.461E-6	1.266E-6	7.81E-7
	500	-0.113	1.439E-6		7.691E-7	
	100	-0.032	5.77E-7		3.084E-7	

Table 31. Relative standard deviation of Diffusivities across scan rates and constant concentrations

Peak	RSD of D across scan rate
A1 ($Cr^0 \rightarrow Cr^{2+}$ stripping)	68.00%
A1′	31.20%
C1 ($Cr^{2+} \rightarrow Cr^0$)	27.20%
A2 ($Cr^{2+} \rightarrow Cr^{3+}$)	14.40%
C2 ($Cr^{3+} \rightarrow Cr^{2+}$)	61.30%

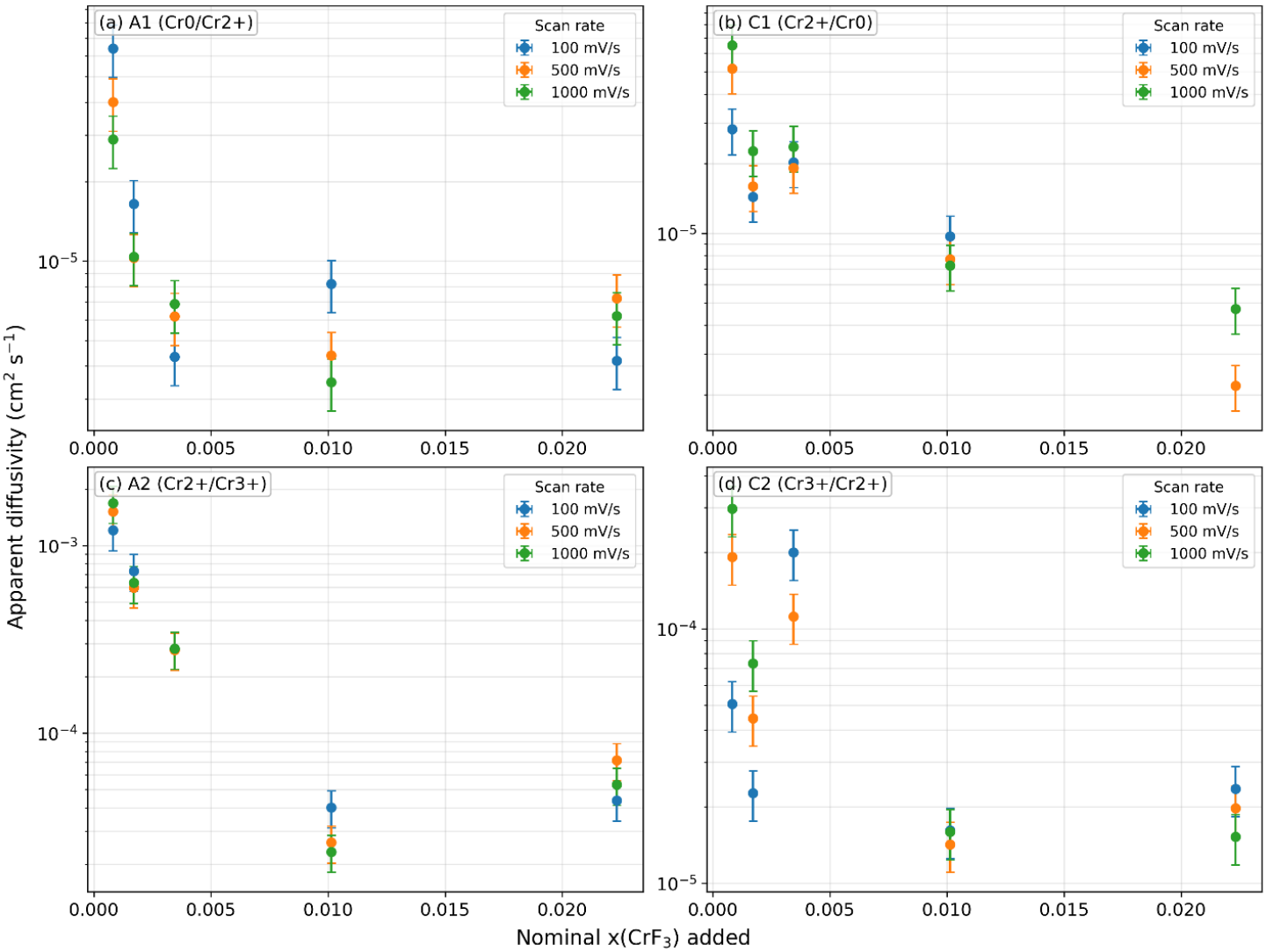


Figure 94. Apparent diffusivity as a function of added CrF_3 mole fraction in FLiNaK at 800°C (see Table 27 for details). Data are shown for scan rates of 100, 500, and 1000 mV s^{-1}. Error bars in x reflect the uncertainty in added CrF_3 mole fraction, while error bars in y reflect propagated uncertainty in apparent diffusivity including contributions from concentration, assumed electrode surface area, and temperature.

5.3.2.4 Calculating Activity Coefficients

The half wave potentials for the Cr^0/Cr^{2+} and Cr^{2+}/Cr^{3+} reaction were extracted from the CVs. The redox potential of the reaction is observed to shift with the log of the concentration of added Cr^{3+} to the melt. Peak-potential uncertainty was estimated from the standard deviation of the A2 and C2 peak positions measured across scan rates for each CrF_3 loading which reflects both peak-picking uncertainty and scan-rate-dependent peak shifts associated with quasi-reversible and nonideal electrochemical behavior. The peak location variability increases with chromium concentration which suggests increasing kinetic and interfacial complexity at elevated chromium loadings.

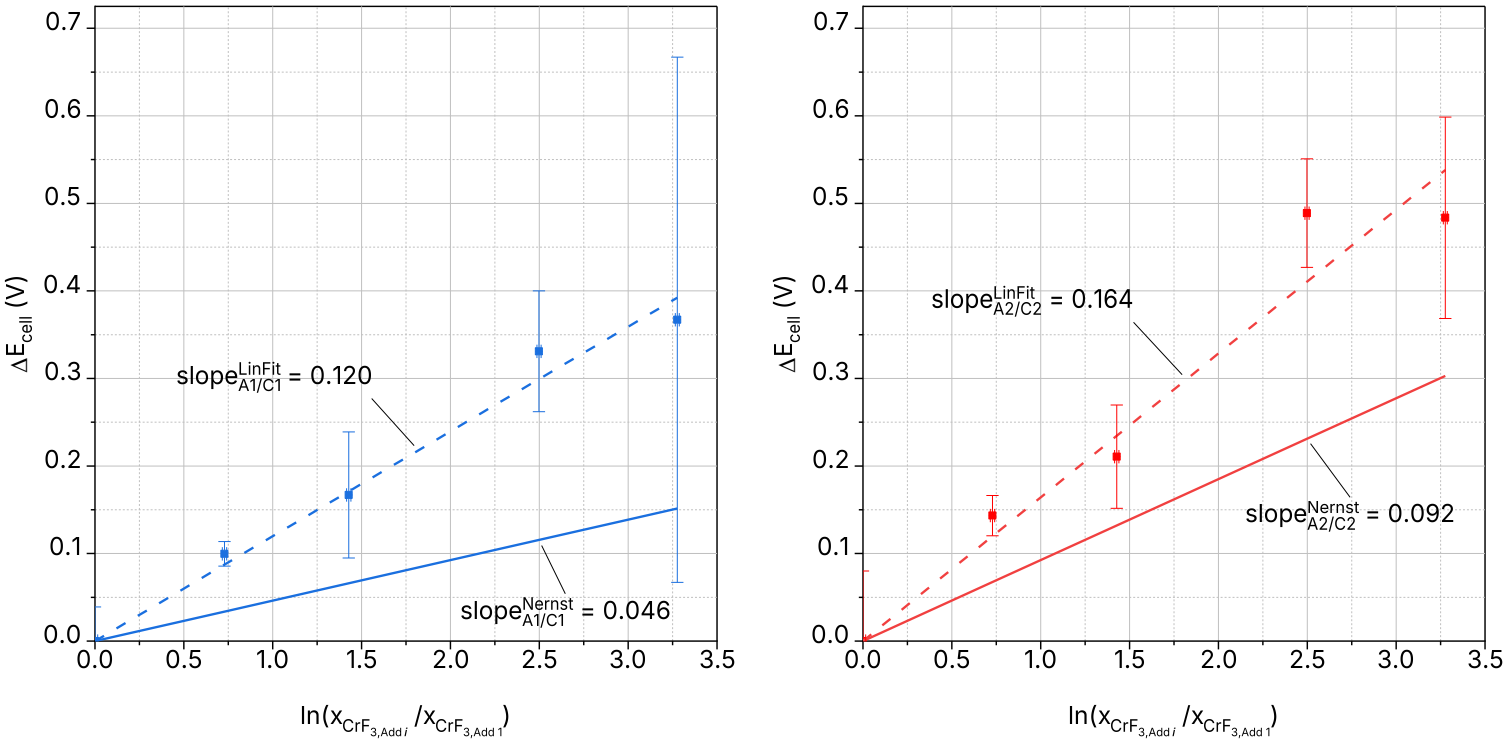


Figure 95. Half wave potential of the Cr^0/Cr^{2+} reaction (left, blue) and Cr^{2+}/Cr^{3+} reaction (right, red) in CVs measured at 500 mV/s. Y-error bars are from the uncertainty in peak locations identified in the CVs due to ohmic drop and poor peak resolution. X-error bars are calculated from uncertainty in CrF_3 titration mass.

The predicted change in cell potential (Nernst slopes in Figure 95) is calculated using the HSC Chemistry database for the free energy of formation of CrF_2(l) and CrF_3(l). This result shows the activity of Cr in the melt is concentration dependent, and this data is in a regime where we cannot apply the Nernst equation without also including activity coefficients for Cr. Massot et. al[140] measured the CrF_2 activity coefficient in 60LiF-40NaF mol% at 750C and found it to be unity over a range of 0.050 to 0.113 mol CrF_2/kg LiF-NaF. Our results from shift in half-wave potential of Cr^0/Cr^{2+} show that the Nernst equation is not sufficient for modeling the shift in the reaction's redox potential. However, this is known to be a quasi-reversible reaction, and the shift in half-wave potential for a quasi-reversible reaction is not conclusive to elucidate the activity coefficient of CrF_2 in FLiNaK. Redman and Weaver[144] measured CrF_2 and CrF_3 solubility in FLiNaK at 800°C and found through their measurements the activity coefficient of CrF_3 must be less than 10^{-3}, assuming the activity coefficient of CrF_2 is unity.

We must update our model for the predicted change in cell potential. This time, we include the activity coefficient, $\gamma_{Cr^{3+}}$:

$$\Delta E_{cell} = \frac{RT}{nF}\ln\left(\frac{x_{Cr^{3+},f}}{x_{Cr^{3+},1}}\right) + \frac{RT}{nF}\ln\left(\frac{\gamma_{Cr^{3+},f}}{\gamma_{Cr^{3+},1}}\right) \quad (5.14)$$

The equation of the linear fit in Figure 95 is given:

$$\Delta E_{cell} = 0.164 \ln\left(\frac{x_{Cr^{3+},f}}{x_{Cr^{3+},1}}\right) \tag{5.15}$$

The variables have the same identity as in Eq.(4.12) with the addition of $\gamma_{Cr^{3+},1}$ and $\gamma_{Cr^{3+},f}$ being the activity coefficient of Cr^{3+} at the first and final state respectively. Then from the linear fit of the half-wave potentials in Figure 95, we rewrite Eq.(5.14) as an expression for the ratio of activity coefficients:

$$\ln\left(\frac{\gamma_{Cr^{3+},f}}{\gamma_{Cr^{3+},1}}\right) = \ln\left(\frac{x_{Cr^{3+},f}}{x_{Cr^{3+},1}}\right) \cdot \left[\left(\frac{nF}{RT}\right)(0.164) - 1\right] \tag{5.16}$$

Eq.(5.16) gives us an equation for the ratio of activity coefficients in our cell. We can scale our data with Redman and Weaver's data for Cr^{3+} activity coefficient using their reported CrF_3 at equilibrium. The CrF_3 activity coefficient in ORNL-1816 is $\gamma_{CrF_3} = 9(1) \times 10^{-4}$ which was measured at $x_{CrF_3} = 2.7(1) \times 10^{-2}$. Fixing this point, we can calculate the activity coefficient for our data as a function of concentration. This data is reported in Table 32. We note that this calculation has assumed that the Cr^{2+} activity coefficient is unity. This assumption comes from the observation of Blander[145] that fluoride salt components will negatively deviate from ideality, (i.e. $\gamma_i < 1$). By assuming Cr^{2+} also deviates from ideality, this would only lower the calculated activity coefficient of Cr^{3+} in FLiNaK, thus the activity coefficients we calculate can be viewed as maximum theoretical values that satisfy Eq.(5.14).

Table 32. Calculated Activity Coefficients for Cr^{3+} in FLiNaK

Loaded CrF_3 (mol/mol)	Activity Coefficient
$8.24(9) \times 10^{-4}$	$7(3) \times 10^{-7}$
$1.71(1) \times 10^{-3}$	$2(1) \times 10^{-6}$
$3.43(2) \times 10^{-3}$	$8(3) \times 10^{-6}$
$1.01(4) \times 10^{-2}$	$6(2) \times 10^{-5}$
$2.21(5) \times 10^{-2}$	$2(1) \times 10^{-4}$
$2.7(1) \times 10^{-2}$*	$9(1) \times 10^{-4}$

*Calculation from ORNL-1816

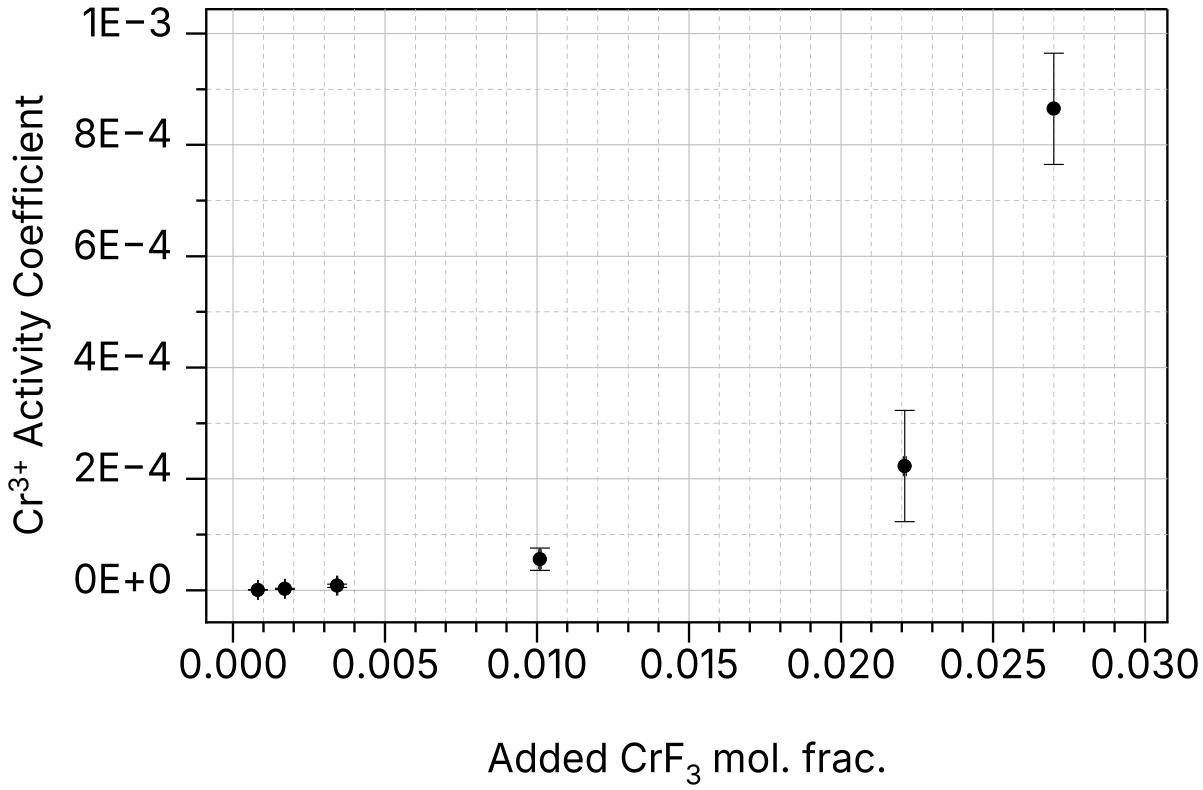


Figure 96. Calculated activity coefficient of Cr^{3+} using ORNL-1816 data as baseline.

Table 32 data is plotted in Figure 96 showing the dependence of activity coefficient on concentration of Cr^{3+} added to FLiNaK. At the dilute limit, the activity coefficient appears to vanish. This is reflective of the functional form we used to fit the activity coefficient and does not reflect the physical reality of the activity coefficient. This is a limitation of calculating the activity coefficient based on the concentration without having a known reference state where the activity coefficient is approximately equal to unity.

5.4 QUANTIFICATION IN FLINAK-CrF_3 SYSTEM - CONCLUSIONS

Both CP and CV present unique challenges for quantitative analysis. Each method's successes and shortcomings are briefly discussed. CP of FLiNaK-CrF_3 melts was able to use a KDRE technique as an internal reference in low concentrations of added CrF_3. CP is useful for making quick measurement of the uncompensated resistance of the cell. This is obvious from the At concentrations above 0.22wt% CrF_3 was unable to reach potassium reduction potentials due to the failures discussed in Section 5.2.2 and thus made potentiometric analysis difficult when no known internal reference was available. Additionally, the chronopotentiometry data interpretation for quantitative analysis is unreliable when natural convection is present in the cell and alters the transition time of the reaction.

Cyclic voltammetry is robust for clearly identifying the locations of redox reaction across the potential window. As the concentration of CrF_3 added to the FLiNaK increased, the effect of ohmic drop also increased to the point of shifting peaks by as much as 240mV. It was possible to correct ohmic drop using CP data, but CV data alone would not permit this correction to be made. At higher concentrations also

would overload the maximum current in the potentiostat. The proposed solution to this challenge is to utilize electrodes with smaller surface area for this system. This would help reduce both the effective iR drop in the system by lowering the surface area as well as gain access to sensing higher concentration ranges of electroactive species. Electrochemical quantification of chromium in molten FLiNaK is feasible, but the measured response deviates strongly from ideal electroanalytical behavior due to concentration-dependent thermodynamics, multi-step chromium reduction, and dynamically evolving interfacial processes including deposition, alloying, and surface accumulation.

5.5 Application of Electroanalytical Methods in FLiBe with Impurities – Methods

The objective of the electrochemical detection experiment was to determine whether degradation products from a NiWC3b cermet tribology specimen could be detected in molten FLiBe using *in situ* electrochemical methods. The experiment was designed as a composition-perturbation study in which the electrochemical response of the melt was measured first for FLiBe containing trace oxidants, then after addition of a known oxidant spike, and finally after exposure to the NiWC3b specimen. Changes in open-circuit potential, cyclic voltammetry, and square-wave voltammetry were interpreted as evidence of changes in the redox state and dissolved metal inventory of the salt.

Three melt conditions were examined at 600 °C: FLiBe containing trace oxidants, FLiBe after addition of 0.05 mol% EuF3, and FLiBe after addition of the NiWC3b tribology specimen. EuF3 was used as a known oxidizing addition to provide an intentional perturbation of salt chemistry before the cermet specimen was introduced. The NiWC3b specimen was then contacted with the oxidizing salt so that soluble corrosion products, including possible cobalt and tungsten species, could enter the melt and modify the voltametric response.

Electrochemical tests were performed in an argon-atmosphere glovebox using a wire-electrode cell immersed in molten FLiBe. The cell used a gold working electrode, gold counter electrode, silver quasi-reference electrode, and gold auxiliary electrode shown in Figure 97. A type K thermocouple in a stainless-steel sheath was positioned in the salt for temperature control. Between experimental steps, the electrodes were allowed to equilibrate with the melt while the furnace was held at constant temperature. The glovebox atmosphere was maintained at less than 0.1 ppm moisture and less than 1 ppm oxygen during operation.



Figure 97. Wire-electrode electrochemical cell used for high-temperature FLiBe measurements. Electrochemical cell: Au WE, Ag qRE, Au CE, Au AuxE. The top image shows clean wire electrodes prior to salt exposure; the bottom image shows the electrodes frozen into the FLiBe puck after testing.

The use of gold and silver electrodes was selected to provide inert metal surfaces for exploratory high-temperature fluoride-salt electrochemistry. However, later observations indicated that the electrode materials and electrical connections were not fully inert under all operating conditions. These observations were treated as an important limitation of the measurement and are discussed as part of the data-quality considerations below.

Before conducting voltametric measurements intended to detect corrosion products, the salt redox potential was snapshot using the BeDRE and the potential scale was references against the assumed Be/Be^{2+} oxidation potential in FLiBe. The open-circuit potential, plotted in Figure 98, was then shifted relative to this Be/Be^{2+} reference point to express the melt redox potential on a common scale. Redox-potential measurements were collected before and after the NiWC3b specimen was contacted with the melt. The measurements were continued until the potential approached a quasi-steady value. The long relaxation time was interpreted as evidence that deposited beryllium and the electrode/salt interface required tens of minutes to equilibrate after polarization. The shift in OCP relative them to BeDRE shows that there was a

chemical effect after added the NiWC3b specimen in FLiBe possible due to leeching of W or Ni from the specimen.

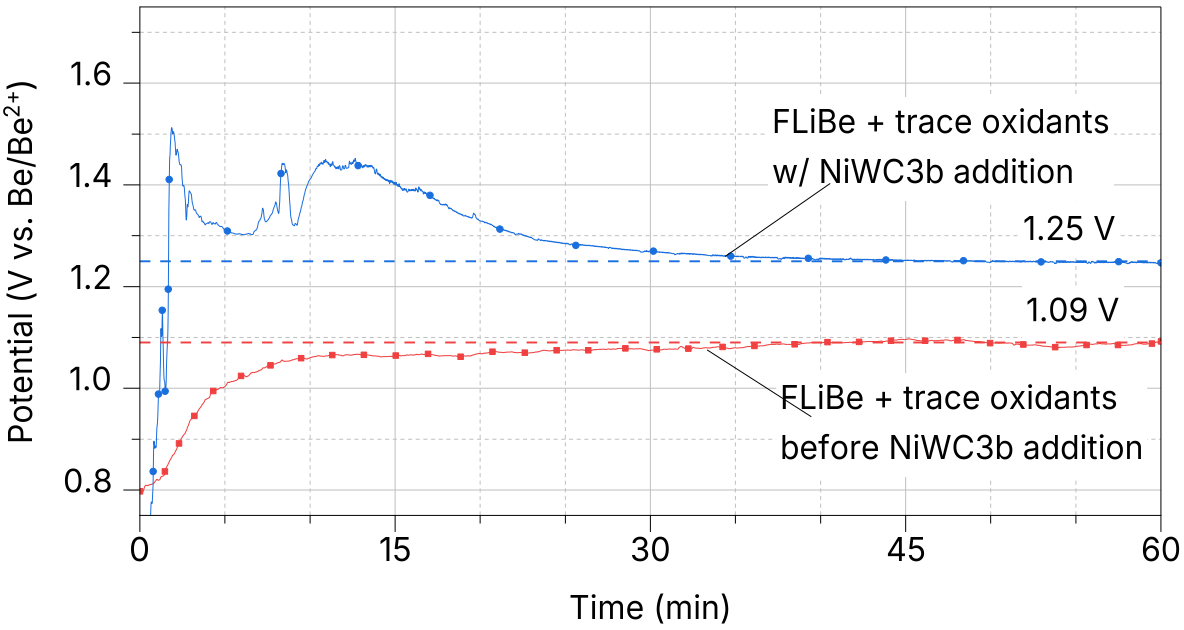


Figure 98. Redox-potential measurements of FLiBe at 600 °C before and after the NiWC3b tribology specimen was contacted with the melt.

Cyclic voltammetry was used to survey the accessible potential window of the FLiBe melt and to identify electrochemical features that might correspond to dissolved corrosion products. The entire potential window reaching beryllium reduction is shown in [figure]. CVs were collected for FLiBe containing trace oxidants, after EuF3 addition, and after NiWC3b addition. The scans were intended to identify reduction and oxidation features associated with soluble metal species, but the interpretation was complicated by overlapping redox processes, low expected corrosion-product concentrations, and capacitive/background current associated with the high-temperature electrode interface.

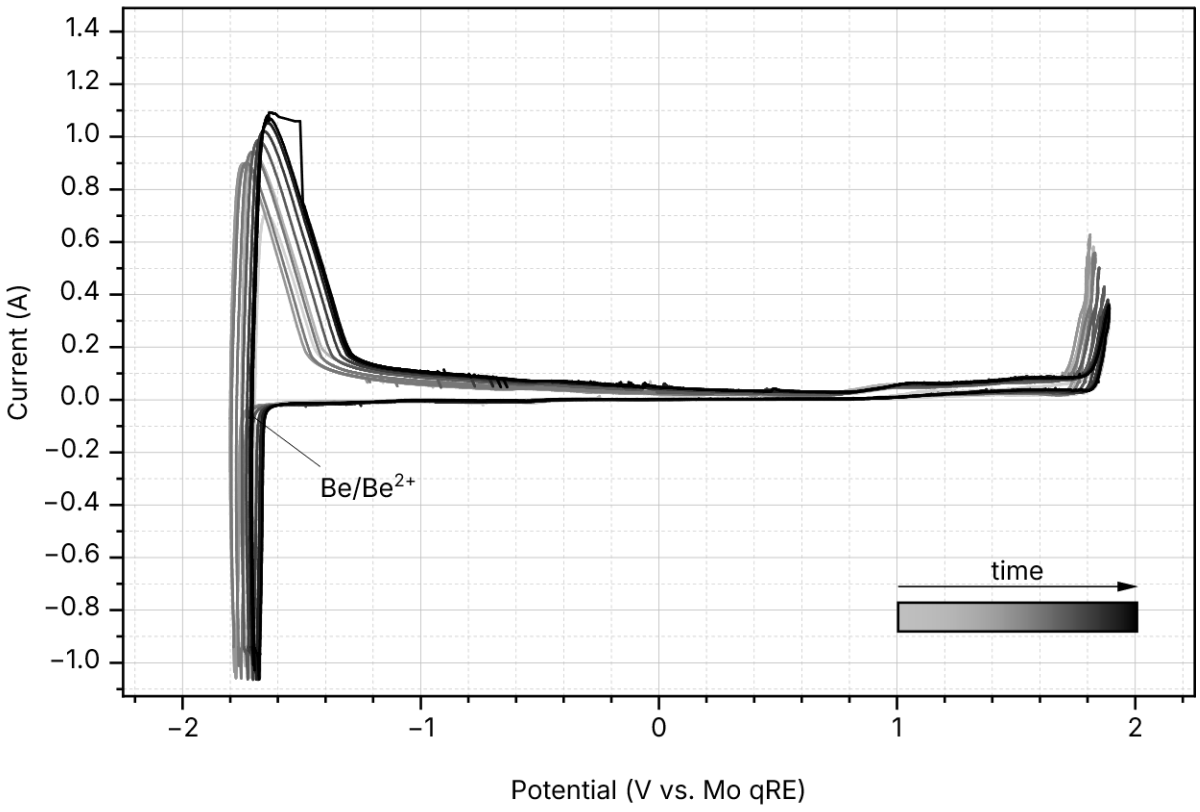


Figure 99. CV of FLiBe blank at 600°C showing potential window down to beryllium reduction. The upper limit may be gold fluorination or oxyfluoride formation.

Repeated CV scans were also used to evaluate the variability of the Be/Be^{2+} reference response (see Figure 86, Section 4.6.3.2). The zero-current crossing associated with Be oxidation was used to estimate the Be/Be^{2+} reference potential, and the observed cycle-to-cycle range was approximately 103 mV. This variability was treated as a practical lower bound on the uncertainty of peak assignments made relative to the Be/Be^{2+} scale.

Square-wave voltammetry was used as the primary electroanalytical method for detecting changes in dissolved corrosion-product inventory because SWV provides higher sensitivity to faradaic features than conventional CV under the present experimental conditions. SWV scans were collected at 600 °C using a gold working electrode, gold counter electrode, and silver quasi-reference electrode. After post examination of the cell, the SS616 electrode connector on the gold counter electrode was contacting the salt during the voltammetry experiments. Therefore, we assume the SS316 was also contributing to the counter electrode current. The square-wave parameters were a frequency of 100 Hz, potential pulse size of 25 mV, potential step size of 2 mV, and stepping in the oxidizing direction.

The SWV traces were compared across the three salt conditions. New peaks appearing after EuF3 addition and changes in peak amplitude or prominence after NiWC3b addition were interpreted as evidence that the electrochemical response was sensitive to changes in salt composition. Figure 100 shows the SWV data for all three melt compositions plotted on the same axis. Because immersion depth, wetted area, and surface

roughness were not precisely controlled, the analysis emphasized peak positions and relative peak intensities within a single sweep rather than absolute comparisons of peak height between separate sweeps.

5.6 ELECTROANALYTICAL DATA FROM FLIBE SYSTEM – RESULTS & DISCUSSION

Figure 100 shows the square wave voltammogram of FLiBe after EuF_3 and NiWC3b additions, at 600ºC, using Au WE, SS316 CE, Ag qRE. Scans were taken with the parameters: frequency, 100 Hz; potential pulse size, 25 mV; potential step size, 2 mV; potential stepping toward the oxidizing direction. Vertical grid lines denote reaction potentials detected with plausible ionic species being detected in the redox reaction. The concentration of the plausible reactants detected are annotated to suggest how much dissolved species would need to be in the melt to product a peak at the given potential, assuming a Nernstian behavior. Peak currents are annotated where the trace crosses the vertical grid lines. The width of the second half of the deposition peak at half-max was calculated and annotated below the horizontal arrows.

Peak-width analysis was used as a diagnostic method to estimate apparent electron-transfer numbers from the SWV response. Using the Barker reversible SWV relation at 600 °C, interpreted widths of approximately 0.132 V correspond to two-electron behavior, while widths of approximately 0.265 V correspond to one-electron behavior. Because several features may involve metal deposition on a foreign substrate, the Fatouros-Krulic model was also evaluated as a sensitivity analysis. In this framework, χ represents the ratio of diffusion-layer dissolved inventory to deposited surface inventory, and ρ represents the magnitude of uncompensated-resistance distortion relative to the thermal electrochemical voltage scale. The calculations show that the inferred electron number is sensitive to the assumed deposition regime, especially when χ and ρ increase. Therefore, the reported values are best interpreted as apparent electron-transfer numbers rather than definitive reaction stoichiometries. Final mechanistic assignments require corroboration from thermodynamic potentials, additive response, and independent compositional analysis.

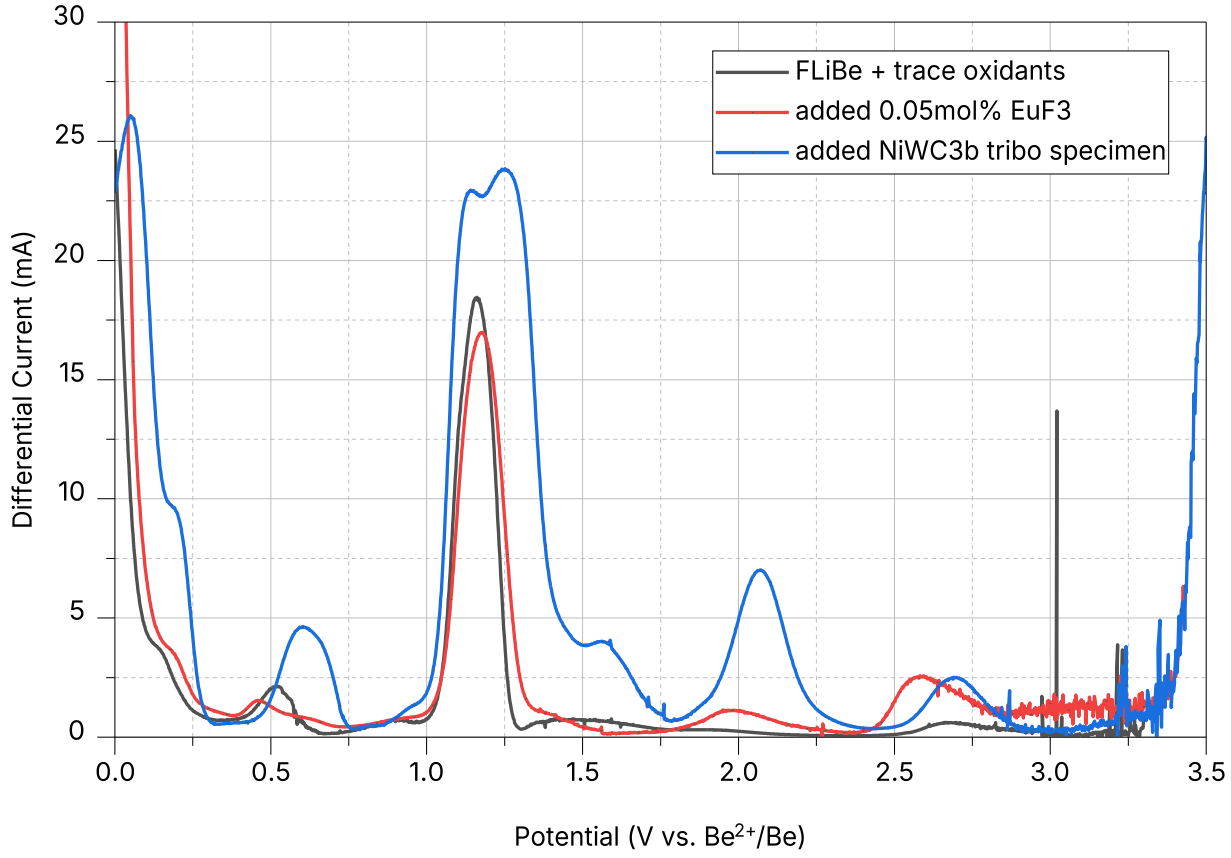


Figure 100. Square wave voltammogram of FLiBe after EuF_3 and NiWC3b additions, at 600°C with plausible peak assignments given in Table 33.

Table 33. Figure 100 Peak Assignment Summary

Potential vs Be^{2+}/Be	Observed behavior	Recommended interpretation	Confidence
~0.05–0.08 V	Large feature appears after EuF_3 addition, near the cathodic edge.	Be/Au surface process.	Low to medium
~0.56–0.60 V	Small feature exists in baseline and Eu scans and becomes clearer after NiWC3b exposure.	Au/surface-associated or minor impurity process.	Low
~1.20–1.30 V	Strong peak already present in trace-oxidant FLiBe and persists after EuF3 addition; broadens or overlaps after NiWC3b exposure.	Likely Cr-related baseline response	High

~1.56 V	Shoulder or feature appears most clearly after NiWC3b exposure.	Possible Fe or other transition-metal impurity/degradation-product process.	Low to Medium
~2.07 V	New or enhanced feature after NiWC3b exposure.	Best treated as NiWC3b-associated. The broader report favors Ni2+/Ni0 in this region; W remains possible but less proven.	High
~2.7 V	Small high-potential feature near the anodic window.	Oxide, oxygen, anion, or electrode oxidation; not a reliable quantitative degradation-product peak at this stage.	Low to Medium

The widths at half-max are used for calculating number of electrons transferred in each reaction using the Barker model, given by Eq.(5.17)[146], and the Fatouros & Krulic model, given by Eq.(5.18)[147]. Barker's model calculates the number of electrons transferred assuming reversible reactions are occurring, the reactions follow Nernstian behavior, and both reduced and oxidized species are soluble in the electrolyte solution. The equation is,

$$W_{\frac{1}{2}} = 3.52\frac{RT}{nF} \tag{5.17}$$

where $W_{\frac{1}{2}}$ is the width of the peak at half max, R is the gas constant, T is the temperature, n is the number of electrons, and F is Faraday's constant. Fatouros & Krulic derive a model for calculating the number of electrons transferred with the assumption that the reduced species is plated on the electrode surface. This equation is,

$$\mathcal{W}_2 = \frac{nFw_2}{RT} \tag{5.18}$$

where w_2 is the width of the second half of the peak height when scanning to a reducing potential. $\mathcal{W}_2$ is approximated by,

$$\mathcal{W}_2 = 0.37\chi^{-0.5} + 0.45\chi^{0.11} + (0.26 + 0.01\chi)\rho \tag{5.19}$$

and,

$$\chi = \frac{C_{ox}^{*}\sqrt{D_{ox}\Delta t}}{\Gamma_1} \tag{5.20}$$

$$\rho = \frac{n^2F^2AR_uC_{ox}^{*}\sqrt{D_{ox}}}{RT\sqrt{\Delta t}} \tag{5.21}$$

where C_{ox}^{*} is the concentration of the oxidized metal ion in the bulk electrolyte, D_{ox} is the diffusivity of the oxidized species, Δt is the pulse period (which is equal to half the inverse frequency), Γ_1 is the surface concentration of the reduced species, A is the electrode area, and R_u is the uncompensated resistance of the cell. χ is a dimensionless number relating the concentration of charged species in the electrolyte to the

concentration of charged species on the electrode surface, and it generally lies between 0.14 and 9.6.[147] ρ is a variable that considers the uncompensated resistance of the cell but transforms the value to a dimensionless number.

For the present data, we make assumptions for the diffusivities and surface concentrations of the reduced and oxidized species in the melt. This data is not readily available in literature and would require future property measurements to accurately calculate the number of electrons transferred using the given models. We calculated the number of electrons transferred by assuming the order of magnitude for each parameter and used these values as inputs to the equations. Using the peak potentials and full width at half-max values from Figure 100, the apparent number of electrons transferred in each reaction are reported in Table 34.

Table 34. Number of Electrons Transferred in SWV with comparing Barker and Fatouros & Krulic model predictions

Peak Potential (V vs. Be/Be^{2+})	**0.057 V**	**0.600 V**	**1.257 V**	**1.562 V**	**2.070 V**	**2.700 V**
Barker	2	2	1	1	1	1
F&K ($\chi = 0.1, \rho = 1$)	2	2	1	1	1	1
F&K ($\chi = 0.1, \rho = 5$)	3.2	3.2	1.6	1.6	1.6	1.6
F&K ($\chi = 0.1, \rho = 9$)	4.4	4.4	2.2	2.2	2.2	2.2
F&K ($\chi = 1, \rho = 1$)	1.2	1.2	0.6	0.6	0.6	0.6
F&K ($\chi = 1, \rho = 5$)	2.5	2.5	1.2	1.2	1.2	1.2
F&K ($\chi = 1, \rho = 9$)	3.7	3.7	1.8	1.8	1.8	1.8
F&K ($\chi > 4, \rho = 1$)	1.1	1.1	0.6	0.6	0.6	0.6
F&K ($\chi > 4, \rho = 5$)	2.5	2.5	1.3	1.3	1.3	1.3
F&K ($\chi > 4, \rho = 9$)	3.9	3.9	1.9	1.9	1.9	1.9

*Fatouros & Krulic is abbreviated F&K

Without knowledge of the specific reaction and mechanism being studied in Figure 100, we perform sensitivity analysis on χ and ρ in the Fatouros and Krulic model. The Fatouros–Krulic parameter χ compares the amount of oxidized species available in the diffusion layer during a square-wave half-period to the surface concentration of deposited reduced species.

$$\chi = \frac{\text{diffusion layer dissolved inventory}}{\text{surface deposited inventory}} \tag{5.22}$$

Therefore, sensitivity in the calculation for number of electrons transferred is described by one of three regimes,

i. $\chi = 0.1$; formation of a sub-monolayer of reduced species (small inventory of dissolved oxidized species)
ii. $\chi = 1$; formation of a monolayer with equivalent diffusion-layer oxidized species inventory
iii. $\chi \geq 4$; diffusion-layer oxidized species inventory exceeds monolayer coverage of reduced species (formation of multilayers is possible)

The Fatouros–Krulic parameter ρ represents the magnitude of uncompensated-resistance distortion relative to the thermal electrochemical potential scale RT/nF.

$$\rho = \frac{\text{characteristic uncompensated resistance potential drop}}{\text{Nernstian potential shift}} \tag{5.23}$$

Therefore, sensitivity in the calculation for number of electrons transferred is described by one of three regimes,

i. $\rho \leq 0.1$; reaction potential is dominated by Nernstian equilibrium
ii. $\rho = 1$; reaction potential is measurably distorted from Nernstian equilibrium
iii. $\rho \geq 4$; ohmic drop distortion changes apparent electron transfer

The most physically reasonable rows from Table 34 are the rows where $\rho \approx 1$. Using $R_u = 0.5\ \Omega$, a representative electrode area of 0.3 cm^2, $D \sim 10^{-5}\ \text{cm}^2/\text{s}$, $f = 100$ Hz, and monolayer-scale reduced-species surface coverages of order $10^{-9}\ \text{mol/cm}^2$, most of the expected ρ values are less than or nearly 1. The $\rho = 5$and $\rho = 9$ rows should be treated as high-ohmic-distortion sensitivity cases. The Barker and Fatouros–Krulic analyses give apparent electron-transfer numbers of approximately two for the low-potential features at 0.057 and 0.600 V and approximately one for the higher-potential features. However, because the Fatouros–Krulic model shows strong sensitivity to $\chi$and ρ, these values should be interpreted as diagnostic peak-shape indicators rather than definitive reaction stoichiometries.

Elemental analysis was conducted on FLiBe that had been used in the degradation product detection tests. Each of the sampled salts was digested in a CEM SP-Discover 80 Microwave Digester System. Digestion was performed by adding a measured mass of salt to a solution made of 6 mL of 14 M nitric acid and 3 mL DI water, placing the solution in a Teflon-lined quartz tube, inserting the tube into the CEM Digester System, ramping to 210°C, holding for 10 minutes at 250 psig, and then settling to ambient conditions. Due to the presence of beryllium in the digests, sample dilutions were made to the salt digests in order to allow the samples to be analyzed in the ICP systems and stay below the limits of airborne beryllium concentration specified by Cal/OSHA Section §5205. The digestion efficiency of the FLiBe before NiWC3b addition and the FLiBe after NiWC3b addition was 60% and 85%, respectively. The reason for differences in digestion efficiency is unclear.

Table 35. In-salt Element Concentrations from ICP-OES

Sample	Li (g/g)	Be (g/g)	Cr (wppm)	Fe (wppm)	Ni (wppm)	W (wppm)	Co (wppm)	Ag (wppm)	Eu (wppm)
FLiBe before NiWC3b exposure	0.0830(5)	0.060(1)	21(1)	399(7)	34(6)	607(32)	<18.7	207(3)	<0.45
FLiBe after NiWC3b exposure	0.1180(4)	0.0826(5)	3.2(3)	89(2)	<2.4	161(15)	<11.3	<2.24	1.0(1)

*Values in parenthesis represent one standard deviation from the reported value.

The values from elemental analysis were used to calculate reaction potentials using formal potentials given in Baes thermodynamic data in FLiBe. It is assumed each reaction follows Nernstian behavior in FLiBe at dilute concentrations.

Table 36. Reaction Potentials in FLiBe

Sample	Cr2+/Cr	Cr3+/Cr2+	Fe2+/Fe	Fe3+/Fe2+	Ni2+/Ni	W4+/W	Co2+/Co	Ag+/Ag
FLiBe before NiWC3b exposure	1.075	0.932*	1.564	1.964*	1.915	2.091*	1.540*	2.559*
FLiBe after NiWC3b exposure	1.005	0.79*	1.508	1.852*	1.816	2.066*	1.540*	2.210*

*formal potentials calculated from HSC half-cell reactions

The calculated reaction potentials using the elemental analysis results differ from the annotated peaks in the SWV polarogram (Figure 100). It is possible that the calculated reaction potentials are inaccurate due to a misrepresentation in the elemental analysis results. More work is required to develop the method of detecting and identifying peaks from corrosion products from NiWC3b in FLiBe. The gold electrodes that were used in this study continued to degrade in the FLiBe during tests and may have changed salt chemistry more than the NiWC3b tribology specimen making it difficult to demonstrate the ability for electrochemical sensors to detect the degradation products. We were able to show the signal of SWV polarograms change with the addition of the NiWC3b plate, but we are not able to match the peak potentials to calculated potentials from elemental analysis data. It is recommended that future work focuses on correlating the peak potentials in FLiBe with corrosion products to elemental analysis of the FLiBe and understanding ensuring the elemental analysis results are representative of the melt.

5.7 Quantification and Redox Peak Assignments - Conclusions

This section shows that corrosion-product quantification in molten fluoride salts is method-dependent, and that no single electroanalytical technique is sufficient across all concentration regimes. CV is useful for identifying redox couples and estimating concentrations from diffusion-controlled peak currents, but its practical detection limit is on the order of 1e-5 M, and its accuracy is degraded by broad peaks, alloying, double-layer charging, and reference drift. SWV improves sensitivity to approximately 1e-7 to 1e-8 M by suppressing capacitive background, but it requires careful control of pulse parameters and electrode area. ASV offers the lowest detection range, approximately 1e-10 to 1e-11 M, but depends on reproducible deposition, stripping, and electrode renewal. CP provides direct access to transition times and dynamic reference behavior, but convection and multiple reactions complicate quantitative interpretation. The common requirement across all methods is correction for uncompensated resistance because the measured potential differs from the surface potential by I*Ru, and the error grows with current. Thus, electrochemical quantification should be presented as a calibrated measurement framework, not as a direct reading of concentration from a single peak.

The FLiNaK-CrF3 dataset demonstrates both the promise and the nonideality of electroanalytical chromium quantification. The CP data gave a transition-time ratio of 0.929/0.140 = 6.635 in Addition 3, close to the expected value of 8 for sequential Cr^{3+}/Cr^{2+} followed by Cr^{2+}/Cr^{0} reduction, supporting the expected stepwise chromium mechanism. The most linear calibration was obtained for C2, assigned to the Cr^{3+}/Cr^{2+} reduction process, with $R^2 = 0.964$. Its slope, 1.837 ± 0.098, was smaller than the Cr^{2+}/Cr^{0} peak slope, but the improved linearity suggests that C2 may provide the most reproducible empirical calibration feature over the concentration range studied. This result makes sense when considering the literature finds this peak to be reversible at the range of temperatures and concentrations tested in this experiment. Reversibility here implies the peak current will scale linearly with the concentration of electroactive species in the bulk which is a key requirement for designing a sensor that quantifies species in the melt.

The CV data identified chromium-associated peaks, an oxide-associated background feature near 1.3-1.5 V vs KDRE in the blank, and concentration-dependent shifts in half-wave potential, but the peak shapes differed from ideal reversible behavior and from some literature voltammograms. Diffusivities calculated from Addition 2 varied substantially with scan rate, with relative standard deviations from 14.4% for A2 to 68.0% for A1, indicating that the assumptions behind simple Randles-Sevcik or Berzins-Delahay analysis are not fully satisfied. Peak-potential shifts were also used to estimate an apparent concentration dependence of the Cr3+ activity coefficient, giving values from approximately 7e-7 at x_CrF3 = 8.24e-4 to 2e-4 at x_CrF3 = 2.21e-2 when scaled to the ORNL-1816 reference value of 9e-4 at x_CrF3 = 2.7e-2. These results support chromium quantification by electrochemistry, but only with explicit treatment of activity coefficients, ohmic drop, quasi-reversibility, surface accumulation, and alloying or dealloying of chromium on tungsten electrodes. [Anchor: Section 5.3; Figures 88-95; Tables 26-29]

The FLiBe impurity-detection experiment shows that SWV is sensitive to changes in salt chemistry after additive and material exposure, but the present dataset does not yet provide defensible quantitative peak assignments. SWV after EuF3 and NiWC3b additions at 600 C produced features near 0.057, 0.600, 1.257, 1.562, 2.070, and 2.700 V vs BeDRE. Peak-width analysis using the Barker relation and Fatouros-Krulic sensitivity cases suggested apparent two-electron behavior for the low-potential features and apparent one-electron behavior for higher-potential features when ohmic distortion is modest, but the inferred electron number depends strongly on the assumed deposition regime and uncompensated-resistance parameter. ICP-OES showed large differences between the FLiBe before and after NiWC3b exposure, including Cr decreasing from 21(1) to 3.2(3) wppm, Fe decreasing from 399(7) to 89(2) wppm, W decreasing from 607(32) to 161(15) wppm, and digestion efficiency changing from 60% to 85%. Reaction potentials calculated from the elemental-analysis concentrations did not align with the annotated SWV peak potentials, and degradation of the Au electrodes may have changed the salt chemistry more than the NiWC3b specimen itself. The conclusion is that SWV can detect changes in FLiBe impurity chemistry, but future quantification requires better controlled electrode materials, representative elemental analysis, repeated additive controls, and post-test electrode characterization before peak assignments can be used as corrosion-product concentrations.

6. CONCLUSION

The central objective of this dissertation is therefore to develop and evaluate electrochemical sensing methodologies and deployment strategies capable of monitoring molten fluoride salt chemistry under increasingly representative operating conditions. Rather than focusing on a single electrochemical technique or sensor design, this work examines the broader problem of integrating electrochemical diagnostics into realistic molten salt systems. To address these questions, this dissertation combines system design, electrochemical sensor design, sensor viability and characterization testing, and electroanalytical studies. Experimental platforms ranging from static crucible experiments to natural circulation and recirculating molten salt loops were designed and constructed to investigate electrochemical sensor performance under progressively more realistic operating conditions. Electrochemical measurements included open-circuit potential (OCP) measurements, chronopotentiometry (CP), cyclic voltammetry (CV) , and square-wave voltammetry (SWV) techniques performed in molten fluoride salts including 2LiF-BeF_2 (FLiBe), 46.5LiF-11.5NaF-42KF (FLiNaK), and 57NaF-43BeF_2 (NaFBe)-based systems. Complementary analytical techniques, including inductively coupled plasma mass spectroscopy/optical emission spectroscopy (ICP-MS/OES), were used to quantify dissolved metal concentrations and validate electrochemical measurements where appropriate.

We present a framework for the design of molten salt systems based on functional requirements, operational constraints, and the dominant physical phenomena under investigation. Molten salt systems were categorized as static, flowing, recirculating, and complex systems to provide a basis for relating experimental objectives to system architecture. The framework was applied to the design of a FLiBe salt transfer system and a natural circulation molten salt loop intended for corrosion, chemistry, and electrochemical sensing experiments. As discussed in Section 2.4, the salt-transfer data show that inexpensive process measurements can provide both operational control and system diagnostics when they are interpreted together. Thermocouple data identified heater failures during shakedown, forecasted thermal response within 1% of the eventual steady temperature depending on location, and captured transfer-specific signatures. The TT11 temperature spike marked salt entering the transfer line, while the TT04 temperature drop indicated cooling from the incoming argon cover gas. A 20 kg transfer into TK02A was measured gravimetrically with a slope of 2.088 kg/min, while the predicted transfer rate from argon volumetric displacement was 2.034 kg/min using FI01 and a 10% flow-meter uncertainty. The approximately 2.7% difference between the measured and predicted rates is smaller than the flow-indicator uncertainty, supporting the assumption that, under leak-tight and low-compressibility conditions, inlet gas volume can be used as a practical estimate of displaced molten salt volume.

The final loop design represents a compromise between reactor-relevant corrosion conditions and the practical constraints of glovebox operation. The selected configuration uses a 26 kg dry SS316H/SS316L loop assembly, 1 NPS Schedule 40 loop piping, a 1/2 NPS Schedule 40 drain straw, approximately 7.1 kg of salt inventory, 3 kW thermal input, and a predicted steady-state flow velocity of approximately 0.4 cm/s. These parameters make the loop suitable for low-flow, thermally driven corrosion and redox-sensing studies, but they also identify the operating risks that must be managed before long-duration testing: low circulation velocity may complicate startup, heat rejection must be actively adjustable, and the system must remain recoverable during filling, draining, and off-normal cooling. Because natural circulation has not yet

been demonstrated in this loop, the design outcome should be presented as a validated engineering design basis rather than as an experimentally proven operating envelope.

The investigation of chromium activity dependence with temperature showed that electrochemical response in flowing molten salt systems must be interpreted through both local redox chemistry and loop transport. Chromium transport could not be predicted from temperature dependence alone. The isolated $Cr/CrF_2/CrF_3$ equilibrium predicted a lower equilibrium CrF_2 concentration at the hot temperature and therefore did not independently explain hot-leg chromium depletion. Instead, hot-leg dissolution and cold-leg deposition require an additional redox boundary condition or activity constraint. For example, an MSRE-style U^{4+}/U^{3+}buffer and setting $U^{4+}/U^{3+} \approx 50$ predicts an increase in equilibrium CrF_2 mole fraction from 1.23×10^{-5}at $454°$Cto 2.28×10^{-5}at $621°$C, corresponding to a driving concentration difference of 1.06×10^{-5}, or approximately 12.5 wppm Cr in the salt. This result supports the broader conclusion that electrochemical measurements in flowing thermal-gradient systems are sensitive to local wall equilibrium, alloy chromium activity, redox buffering, and the degree to which the flowing salt approaches equilibrium during circulation. The design basis for molten salt electrochemical sensors on prototypical reactor systems necessitates measuring redox potential shifts, corrosion product changes, and material health evolution on the order of the predicted swings from the thermal-gradient Cr mass transfer calculation.

Open-circuit potentiometry, chronopotentiometry, cyclic voltammetry, and square-wave voltammetry are complementary rather than interchangeable: OCP provides equilibrium or mixed-potential information, CP probes transient deposition and diffusion behavior, CV maps redox reactions and transport-limited currents, and SWV improves sensitivity to small or overlapping peaks. The important design conclusion is that the electrochemical method must be selected before the probe configuration and assembly are finalized. The Echem probe design shows that a molten salt loop sensor is not simply a set of electrodes inserted into a pipe; it is a coupled mechanical, thermal, electrochemical, and flow-conditioning assembly. Testing confirmed that the Echem probe produced interpretable electrochemical data in both aqueous benchmark solution and molten fluoride salt. EIS gave an uncompensated resistance of approximately 20 ohms in the aqueous cell, demonstrating the ability to quantify and correct ohmic drop. Molten FLiBe testing further showed that the probe could detect changes in salt redox chemistry after Cr_2O_3 addition through OCP shifts and chromium-associated CV features. These results validate the probe as a functional electrochemical platform, while also showing that quantitative molten-salt interpretation depends on careful calibration of surface area, reference potential, resistance, flow effects, and the redox boundary condition that defines local equilibrium chemistry in each cell or loop configuration.

Printed electrode sensors offer a potential path toward molten salt electroanalysis with better-defined geometry, lower total current, and reduced sensitivity to bulk flow than conventional wire electrodes. Their main advantage is the ability to fabricate micro- and nano-scale electroactive features whose diffusion length can become comparable to the electrode radius, allowing stationary or radial-diffusion behavior to emerge even in systems where macroelectrode interpretation would be complicated by convection. Therefore, the conclusion is that printed electrodes are promising for future flowing molten salt systems, but their usefulness depends on matching electrode dimensions, spacing, scan rate, and expected diffusivity to the measurement time scale. The printed-electrode tests demonstrate that the electrochemical concept works at room temperature, but the present chip architecture is not yet robust enough for reliable molten

fluoride salt exposure. After 600ºC argon exposure for 30 minutes, both chips showed delamination and one fractured across the conductive channels. FLiBe exposure at 650 C with 1.0 wt% Cr_2O_3 for 1 hour and FLiNaK exposure at 550 C with 5.0 wt% FeF_2 for approximately 2 hours produced severe metal-layer delamination, including complete removal of the electroactive layer into the frozen salt. These results show that printed electrodes can produce valid electrochemical signals, but future work must solve adhesion, thermal-stress, chip-support, and salt-wetting problems before using them for quantitative molten fluoride salt measurements.

Molten salt redox potential can be measured either as an absolute thermodynamic quantity or as a relative diagnostic of changing salt chemistry. Thermodynamic reference electrodes, such as Ni/NiF_2 systems, provide the clearest route to formal potentials and species activities because the reference reaction is fixed by a defined chemical equilibrium. Dynamic reference electrodes, such as K/K^+ in FLiNaK or Be/Be^{2+} in FLiBe, are more practical for periodic measurements and avoid maintaining a sealed reference compartment, but their validity depends on successfully depositing and stripping the reference metal under conditions where competing redox reactions do not dominate the imposed current. Chronopotentiometry in FLiNaK-CrF_3 showed that KDRE-based redox measurements can be accurate at low chromium concentration but fail predictably as competing chromium reduction consumes the imposed current. After addition 1, the KDRE was again successfully established, and the measured change in Ecell was 186(6) mV, in close agreement with the Nernst-predicted shift of -0.187(3) mV. The conclusion is that CP provides powerful redox and resistance diagnostics, but dynamic reference measurements in molten salts must be designed around convection, competing reactions, and counter-electrode lifetime.

The FLiBe redox measurements show that several reference-electrode strategies can produce useful information, but none should be treated as a universal reference without qualification. The BN-coated graphitic-foam NiTRE demonstrated ionic contact and produced steady OCP values near -1.0 V and -0.9 V in repeated tests, but the approximately 100 mV drift after freeze-thaw and mechanical cracking from the BN cap indicate that mechanical design and thermal cycling currently limit reliability. The Ag/AgF approach equilibrated faster, on the order of 2 hours rather than the approximately 20 hours reported for some Ni/NiF_2 systems, but AgF reacted with moisture and BN, producing Ag metal, a 226.3 mg mass loss in the AgF/BN exposure test, and an observed potential near 1.4 V vs Be^{2+}/Be consistent with severe depletion of Ag^+ rather than a stable Ag/AgF reference. The BeDRE analysis provided the most important mechanistic insight: although the expected Be/Be^{2+} potential at 600ºC is -1.834(8) V vs HF/H_2, the apparent BeF_2 surface composition during relaxation evolved from x_{BeF2} = 0.2927 at 2s to 0.3263 at 600s and did not return to the assumed bulk value of 0.33. The derived apparent interdiffusion coefficient of 2.0 × 10−7 to 2.7 × 10−7 cm2 s-1 supports the interpretation that the BeDRE relaxation reflects a locally modified LiF-BeF_2 interfacial composition. Therefore, FLiBe redox potentials reported versus BeDRE should be treated as measurements on a practical internal scale unless the relationship between the BeDRE plateau and the bulk Be/Be^{2+} thermodynamic potential has been independently established.

Corrosion-product quantification in molten fluoride salts is method-dependent, and that no single electroanalytical technique is sufficient across all concentration regimes. CV is useful for identifying redox couples and estimating concentrations from diffusion-controlled peak currents, but its practical detection limit is on the order of 1e-5 M, and its accuracy is degraded by broad peaks, alloying, double-layer charging,

and reference drift. SWV improves sensitivity to approximately 1e-7 to 1e-8 M by suppressing capacitive background, but it requires careful control of pulse parameters and electrode area. ASV offers the lowest detection range, approximately 1e-10 to 1e-11 M, but depends on reproducible deposition, stripping, and electrode renewal.. CP provides direct access to transition times and dynamic reference behavior, but convection and multiple reactions complicate quantitative interpretation. Thus, electrochemical quantification should be presented as a calibrated measurement framework, not as a direct reading of concentration from a single peak. Additionally, having a well defined boundary layer, or diffusion layer thickness, is critical to interpreting electrochemical data in flowing systems for quantitative transient electrochemical measurements.

The FLiNaK-CrF_3 dataset demonstrates both the promise and the nonideality of electroanalytical chromium quantification. The CP data gave a transition-time ratio of 0.929/0.140 = 6.635 in Addition 3, close to the expected value of 8 for sequential Cr^{3+}/Cr^{2+} followed by Cr^{2+}/Cr^{0} reduction, supporting the expected stepwise chromium mechanism. The CV data identified chromium-associated peaks, an oxide-associated background feature near 1.3-1.5 V vs KDRE in the blank, and concentration-dependent shifts in half-wave potential, but the peak shapes differed from ideal reversible behavior and from some literature voltammograms. The FLiNaK-CrF_3 dataset demonstrates both the promise and the nonideality of electroanalytical chromium quantification. The CP data gave a transition-time ratio of 0.929/0.140 = 6.635 in Addition 3, close to the expected value of 8 for sequential Cr^{3+}/Cr^{2+} followed by Cr^{2+}/Cr^{0} reduction, supporting the expected stepwise chromium mechanism. The most linear calibration was obtained for C2, assigned to the Cr^{3+}/Cr^{2+} reduction process, with $R^2 = 0.964$. Its slope, 1.837 ± 0.098, was smaller than the Cr^{2+}/Cr^{0} peak slope, but the improved linearity suggests that C2 may provide the most reproducible empirical calibration feature over the concentration range studied. This result makes sense when considering the literature finds this peak to be reversible at the range of temperatures and concentrations tested in this experiment. Reversibility here implies the peak current will scale linearly with the concentration of electroactive species in the bulk which is a key requirement for designing a sensor that quantifies species in the melt. Diffusivities calculated from Addition 2 varied substantially with scan rate, with relative standard deviations from 14.4% for A2 to 68.0% for A1, indicating that the assumptions behind simple Randles-Sevcik or Berzins-Delahay analysis are not fully satisfied. These results support chromium quantification by electrochemistry, but only with explicit treatment of activity coefficients, ohmic drop, quasi-reversibility, surface accumulation, and alloying or dealloying of chromium on tungsten electrodes.

The FLiBe impurity-detection experiment shows that SWV is sensitive to changes in salt chemistry after additive and material exposure, but the present dataset does not yet provide defensible quantitative peak assignments. SWV after EuF3 and NiWC3b additions at 600 C produced features near 0.057, 0.600, 1.257, 1.562, 2.070, and 2.700 V vs BeDRE. ICP-OES showed large differences between the FLiBe before and after NiWC3b exposure, including Cr decreasing from 21(1) to 3.2(3) wppm, Fe decreasing from 399(7) to 89(2) wppm, W decreasing from 607(32) to 161(15) wppm, and digestion efficiency changing from 60% to 85%. Reaction potentials calculated from the elemental-analysis concentrations did not align with the annotated SWV peak potentials, and degradation of the Au electrodes may have changed the salt chemistry more than the NiWC3b specimen itself. The conclusion is that SWV can detect changes in FLiBe impurity chemistry, but future quantification requires better controlled electrode materials, representative elemental

analysis, repeated additive controls, and post-test electrode characterization before peak assignments can be used as corrosion-product concentrations.

The results demonstrate that electrochemical sensing can provide quantitative and reproducible information regarding molten salt chemistry when measurements are interpreted within the context of the coupled thermodynamic and transport processes governing the system. The work establishes methods for monitoring dissolved corrosion products, evaluates the performance and limitations of several high-temperature reference electrode concepts, and provides new insight into the dynamic behavior of beryllium-based reference electrodes in fluoride salts. Furthermore, the research demonstrates that successful deployment of electrochemical sensors requires consideration of system-level phenomena—including salt flow, thermal gradients, electrical resistance, and experimental architecture—in addition to traditional electrochemical theory. Beyond individual sensor development, the dissertation presents experimental platforms and operational methodologies that enable future long-duration studies of corrosion, redox chemistry, and molten salt process monitoring. Collectively, this work advances the development of electrochemical diagnostics for molten fluoride salts by integrating sensor development, experimental infrastructure, and fundamental electrochemical analysis into a unified framework for *in situ* chemical monitoring. The results contribute to the broader goal of enabling continuous characterization and control of molten salt chemistry in advanced reactor systems and other high-temperature molten salt technologies, where reliable knowledge of the chemical state is essential for safe, efficient, and predictable operation.

Research Funding Acknowledgements

This work was supported by the U.S. Department of Energy, Office of Nuclear Energy, through the Nuclear Energy University Program Award No. IRP-20-22026, IRP-22-28329, NEUP-21-24102, and the U.S. Department of Energy Award No. DE-SC0021952.

Statement on AI Usage

During preparation of this work, the author used ChatGPT-5.5 to assist with grammatical revision, sentence clarity, and organization of methods and results descriptions. After using this tool, the author reviewed and edited the content to reflect his original analysis and takes full responsibility for the content of the published work.

References

[1] L. Vergari, M. Nelson, A. Droster, C. Contescu, N. Gallego, and R. O. Scarlat, "Infiltration of molten fluoride salts in graphite: Phenomenology and engineering considerations for reactor operations and waste disposal," *J. Nucl. Mater.*, vol. 572, p. 154058, Dec. 2022, doi: 10.1016/j.jnucmat.2022.154058.

[2] N. Winner, H. Williams, R. O. Scarlat, and M. Asta, "Ab-initio simulation studies of chromium solvation in molten fluoride salts," *J. Mol. Liq.*, vol. 335, p. 116351, Aug. 2021, doi: 10.1016/j.molliq.2021.116351.

[3] G. L. Yoder, D. Heatherly, D. Wilson, and M. Caja, "FLiNaK compatibility studies with Inconel 600 and silicon carbide," *Nucl. Eng. Des.*, vol. 307, pp. 172–180, Oct. 2016, doi: 10.1016/j.nucengdes.2016.06.037.

[4] C. L. Dym, A. M. Agogino, O. Eris, D. D. Frey, and L. J. Leifer, "Engineering Design Thinking, Teaching, and Learning," *J. Eng. Educ.*, vol. 94, no. 1, pp. 103–120, 2005, doi: 10.1002/j.2168-9830.2005.tb00832.x.

[5] C. L. Dym and D. C. Brown, *Engineering design: representation and reasoning*, 2nd ed. Cambridge: Cambridge university press, 2012.

[6] J. T. Dillon, "The Classification of Research Questions," *Rev. Educ. Res.*, vol. 54, no. 3, p. 35, 1984, doi: 10.3102/00346543054003327.

[7] H. Davy, "XXIII. Electro-chemical researches, on the decomposition of the earths; with observations on the metals obtained from the alkaline earths, and on the amalgam procured from ammonia," *Philos. Trans. R. Soc. Lond.*, vol. 98, pp. 333–370, 1807, doi: 10.1098/rstl.1808.0023.

[8] W. D. Manly *et al.*, "AIRCRAFT REACTOR EXPERIMENT--METALLURGICAL ASPECTS," ORNL-2349, 4227617, Jan. 1958. doi: 10.2172/4227617.

[9] H. G. MacPherson, "Molten-Salt Reactor Program Quarterly Progress Report for Period Ending October 31, 1959," ORNL-2890, 1960.

[10] G. M. Adamson, R. S. Crouse, and W. D. Manly, "INTERIM REPORT ON CORROSION BY ZIRCONIUM-BASE FLUORIDES," ORNL-2338, 4107813, Jan. 1961. doi: 10.2172/4107813.

[11] B. Cai *et al.*, "Natural convection effects in molten LiF-NaF-KF," *Electrochimica Acta*, vol. 509, p. 145274, Jan. 2025, doi: 10.1016/j.electacta.2024.145274.

[12] R. C. Robertson, "MSRE DESIGN AND OPERATIONS REPORT PART I DESCRIPTION OF REACTOR DESIGN".

[13] O. Levenspiel, *Engineering Flow and Heat Exchange*. Boston, MA: Springer US, 2014. doi: 10.1007/978-1-4899-7454-9.

[14] C. A. Depew and R. C. Zenter, "Laminar flow heat transfer and pressure drop with freezing at the wall," *Int. J. Heat Mass Transf.*, vol. 12, no. 12, pp. 1710–1714, Dec. 1969, doi: 10.1016/0017-9310(69)90104-5.

[15] A. Redkin *et al.*, "Thermal Properties of Li2BeF4 near Melting Point," *Thermo*, vol. 2, no. 3, pp. 107–115, Sep. 2022, doi: 10.3390/thermo2030010.

[16] D. E. Holcomb and S. M. Cetiner, "An Overview of Liquid Fluoride Salt Heat Transport Systems," ORNL/TM-2010/156, 990239, Sep. 2010. doi: 10.2172/990239.

[17] Manohar S. Sohal, Piyush Sabharwall, Pattrick Calderoni, Alan K. Wertsching, and S. Brandon Grover, "Conceptual Design of Forced Convection Molten Salt Heat Transfer Testing Loop," INL/EXT-10-19908, 1000546, Sep. 2010. doi: 10.2172/1000546.

[18] D. Kearney *et al.*, "Engineering aspects of a molten salt heat transfer fluid in a trough solar field," *Energy*, vol. 29, no. 5, pp. 861–870, Apr. 2004, doi: 10.1016/S0360-5442(03)00191-9.

[19] K. Robb, "Simplified High-Temperature Molten Salt CSP Plant Preconceptual Design," ORNL/TM-2022/2377, 1856690, Mar. 2022. doi: 10.2172/1856690.

[20] G. Yoder Jr., K. Robb, E. Dominguez-Ontiveros, D. Felde, D. Fugate, and D. Holcomb, "Start-up Operation Experience with a Liquid Fluoride Salt Forced Convection Loop," ORNL/TM--2023/2978, 1995677, Aug. 2023. doi: 10.2172/1995677.

[21] B. C. Kelleher, S. F. Gagnon, and I. G. Mitchell, “Thermal gradient mass transport corrosion in NaCl-MgCl 2 and MgCl 2 -NaCl-KCl molten salts,” *Mater. Today Commun.*, vol. 33, p. 104358, Dec. 2022, doi: 10.1016/j.mtcomm.2022.104358.
[22] J. W. Koger, “Mass transfer between Hastelloy N and a molten sodium fluoroborate mixture in a thermal convection loop,” ORNL-TM--4271, 4442416, Dec. 1972. doi: 10.2172/4442416.
[23] A. Burak *et al.*, “Root cause analysis of a molten salt pump in FLUSTFA,” *Nucl. Eng. Des.*, vol. 444, p. 114365, Dec. 2025, doi: 10.1016/j.nucengdes.2025.114365.
[24] R. O. Scarlat, “Design of Complex Systems to Achieve Passive Safety: Natural Circulation Cooling of Liquid Salt Pebble Bed Reactors”.
[25] C. M. Sclafani, “Design and fabrication of a natural circulation loop for characterization of molten salt corrosion effects on stainless steel over time.”
[26] “Understanding GFCI Nuisances,” Henderson Engineers. Accessed: May 08, 2026. [Online]. Available: https://www.hendersonengineers.com/insight_article/understanding-gfci-nuisances/
[27] “UL 514B Ed. 6-2012 - Conduit, Tubing, and Cable Fittings - Published Date: March 28, 2024.” Accessed: May 08, 2026. [Online]. Available: https://webstore.ansi.org/standards/ul/ul514bed2012?srsltid=AfmBOorVHDEE8QRI2nZbPrP5k7hD57QGdwHoSpaW7SYnDgfVO2SFpcwZ
[28] J. Newman and N. P. Balsara, *Electrochemical systems*, Fourth edition. in The electrochemical society series. Hoboken, NJ: Wiley, 2021.
[29] “Handbook of aluminium. 2: Alloy production and materials manufacturing,” New York , NY: Marcel Dekker, 2003.
[30] “Recycling Used Nuclear Fuel Brochure.pdf.” Accessed: May 07, 2026. [Online]. Available: https://www.anl.gov/sites/www/files/2023-09/Recycling%20Used%20Nuclear%20Fuel%20Brochure.pdf
[31] J. J. Laidler, J. E. Battles, W. E. Miller, J. P. Ackerman, and E. L. Carls, “Development of pyroprocessing technology,” *Prog. Nucl. Energy*, vol. 31, no. 1–2, pp. 131–140, 1997.
[32] R. W. Benedict *et al.*, “Pyroprocessing Progress at Idaho National Laboratory”.
[33] A. J. Bard and L. R. Faulkner, *Electrochemical methods: fundamentals and applications*, 2. edition. New York Weinheim: Wiley, 2001.
[34] D. D. Macdonald, *Transient Techniques in Electrochemistry*. Boston, MA: Springer US, 1977. doi: 10.1007/978-1-4613-4145-1.
[35] D. D. Macdonald and G. R. Engelhardt, “A Critical Review of Radiolysis Issues in Water-Cooled Fission and Fusion Reactors: Part II, Prediction of Corrosion Damage in Operating Reactors,” *Corros. Mater. Degrad.*, vol. 3, no. 4, pp. 694–758, Dec. 2022, doi: 10.3390/cmd3040038.
[36] J. de D. Sánchez, “Key Emerging Issues and Recent Progress Related to Plant Chemistry/Corrosion (PWR, CANDU, and BWR Nuclear Power Plants)”.
[37] A. Molander, S. Eriksson, K. Pein, and S. (Sweden) Swedish Nuclear Power Inspectorate, “A survey of reference electrodes for high temperature waters,” Swedish Nuclear Power Inspectorate, Stockholm (Sweden), SKI-R--00-52, Nov. 2000. Accessed: Jun. 03, 2026. [Online]. Available: https://inis.iaea.org/records/tp5va-wby67
[38] G. Nagy, Z. Kerner, J. Balog, R. Schiller, and 28 Rue Saint Dominique Societe de Chimie Industrielle (SCI), “High temperature electrochemistry related to light water reactor corrosion,” Societe de Chimie Industrielle (SCI), 28 Rue Saint Dominique, F-75007 Paris (France), INIS-FR--3899, 2004. Accessed: Jun. 03, 2026. [Online]. Available: https://inis.iaea.org/records/7fc51-zft03
[39] A. Khan, A. Qurashi, W. Badeghaish, M. N. Noui-Mehidi, and M. A. Aziz, “Frontiers and Challenges in Electrochemical Corrosion Monitoring; Surface and Downhole Applications,” *Sensors*, vol. 20, no. 22, p. 6583, Jan. 2020, doi: 10.3390/s20226583.
[40] D. Holcomb, R. Kisner, and S. Cetiner, “Instrumentation Framework for Molten Salt Reactors,” ORNL/TM-2018/868, 1462848, Jun. 2018. doi: 10.2172/1462848.
[41] J. Newman, “ENGINEERING DESIGN OF ELECTROCHEMICAL SYSTEMS,” *Ind. Eng. Chem.*, vol. 60, no. 4, pp. 12–27, Apr. 1968, doi: 10.1021/ie50700a005.

[42] “High temperature on-line monitoring of water chemistry and corrosion control in water cooled power reactors,” IAEA, IAEA-TECDOC-1303, Jul. 2002. Accessed: Nov. 15, 2024. [Online]. Available: https://www-pub.iaea.org/MTCD/Publications/PDF/te_1303_web.pdf
[43] J. Zhang *et al.*, “Redox potential control in molten salt systems for corrosion mitigation,” *Corros. Sci.*, vol. 144, pp. 44–53, Nov. 2018, doi: 10.1016/j.corsci.2018.08.035.
[44] S. A. Walker, M. E. Tano, A. Abou-Jaoude, and O. Calvin, “Depletion-driven thermochemistry of molten salt reactors: review, method, and analysis,” *Front. Nucl. Eng.*, vol. 2, Jun. 2023, doi: 10.3389/fnuen.2023.1214727.
[45] K. Sridharan and T. R. Allen, “12 - Corrosion in Molten Salts,” in *Molten Salts Chemistry*, F. Lantelme and H. Groult, Eds., Oxford: Elsevier, 2013, pp. 241–267. doi: 10.1016/B978-0-12-398538-5.00012-3.
[46] H. J. S. Sand, “III. On the concentration at the electrodes in a solution, with special reference to the liberation of hydrogen by electrolysis of a mixture of copper sulphate and sulphuric acid,” *Lond. Edinb. Dublin Philos. Mag. J. Sci.*, vol. 1, no. 1, pp. 45–79, Jan. 1901, doi: 10.1080/14786440109462590.
[47] A. Ševčík, “Oscillographic polarography with periodical triangular voltage,” *Collect. Czechoslov. Chem. Commun.*, vol. 13, pp. 349–377, 1948, doi: 10.1135/cccc19480349.
[48] S. Delpech, E. Merle-Lucotte, T. Auger, X. Doligez, D. Heuer, and G. Picard, “MSFR: Material issues and the effect of chemistry control,” 2009.
[49] C.-O. A. Olsson and D. Landolt, “Passive films on stainless steels—chemistry, structure and growth,” *Electrochimica Acta*, vol. 48, no. 9, pp. 1093–1104, Apr. 2003, doi: 10.1016/S0013-4686(02)00841-1.
[50] R. W. Revie, *Uhlig’s Corrosion Handbook*, 3rd ed. Hoboken, NJ: John Wiley & Sons, 2011. doi: 10.1002/9780470872864.
[51] C. F. Jr. Baes, “The Chemistry and Thermodynamics of Molten Salt Reactor Fuels,” *Nucl Met Met Soc AIME*, vol. 15, pp. 617–644, Jan. 1969.
[52] R. E. Thoma, “CHEMICAL ASPECTS OF MSRE OPERATIONS.,” Oak Ridge National Lab., Tenn., ORNL--4658, Jan. 1971. doi: 10.2172/4675946.
[53] C. F. Jr. Baes, “The Chemistry and Thermodynamics of Molten Salt Reactor Fuels,” *Nucl Met Met Soc AIME*, vol. 15, pp. 617–644, Jan. 1969.
[54] J. H. DeVan and R. B. Evans, Iii, “CORROSION BEHAVIOR OF REACTOR MATERIALS IN FLUORIDE SALT MIXTURES,” ORNL-TM-328, 4774669, Sep. 1962. doi: 10.2172/4774669.
[55] J. W. Koger, “Mass transfer between Hastelloy N and a molten sodium fluoroborate mixture in a thermal convection loop,” ORNL-TM--4271, 4442416, Dec. 1972. doi: 10.2172/4442416.
[56] J. W. Koger, “CORROSION PRODUCT DEPOSITION IN MOLTEN FLUORIDE SALT SYSTEMS”.
[57] S. S. Raiman and S. Lee, “Aggregation and data analysis of corrosion studies in molten chloride and fluoride salts,” *J. Nucl. Mater.*, vol. 511, pp. 523–535, Dec. 2018, doi: 10.1016/j.jnucmat.2018.07.036.
[58] S. P. Murarka, M. S. Anand, and R. P. Agarwala, “Diffusion of Chromium in Nickel,” *J. Appl. Phys.*, vol. 35, no. 4, pp. 1339–1341, Apr. 1964, doi: 10.1063/1.1713615.
[59] B. Levich, “The theory of concentration polarisation,” *Discuss. Faraday Soc.*, vol. 1, p. 37, 1947, doi: 10.1039/df9470100037.
[60] D. P. Gregory and A. C. Riddiford, “Transport to the surface of a rotating disc,” *J. Chem. Soc. Resumed*, no. 0, pp. 3756–3764, Jan. 1956, doi: 10.1039/JR9560003756.
[61] L. Graetz, “Ueber die Wärmeleitungsfähigkeit von Flüssigkeiten,” *Ann. Phys.*, vol. 261, no. 7, pp. 337–357, Jan. 1885, doi: 10.1002/andp.18852610702.
[62] C. S. Lin, E. B. Denton, H. S. Gaskill, and G. L. Putnam, “Diffusion-Controlled Electrode Reactions,” *Ind. Eng. Chem.*, vol. 43, no. 9, pp. 2136–2143, Sep. 1951, doi: 10.1021/ie50501a045.

[63] W. L. Friend and A. B. Metzner, “Turbulent heat transfer inside tubes and the analogy among heat, mass, and momentum transfer,” *AIChE J.*, vol. 4, no. 4, pp. 393–402, 1958, doi: 10.1002/aic.690040404.
[64] T. K. Ross and A. A. Wragg, “Electrochemical mass transfer studies in annuli,” *Electrochimica Acta*, vol. 10, no. 11, pp. 1093–1106, Nov. 1965, doi: 10.1016/0013-4686(65)80034-2.
[65] A. Acrivos, “Solution of the Laminar Boundary Layer Energy Equation at High Prandtl Numbers,” *Phys. Fluids*, vol. 3, no. 4, pp. 657–658, Jul. 1960, doi: 10.1063/1.1706102.
[66] M. J. Lighthill, “Contributions to the theory of heat transfer through a laminar boundary layer,” *Proc. R. Soc. Lond. Math. Phys. Sci.*, vol. 202, no. 1070, pp. 359–377, Aug. 1950, doi: 10.1098/rspa.1950.0106.
[67] M. G. Fouad and N. Ibl, “Natural convection mass transfer at vertical electrodes under turbulent flow conditions,” *Electrochimica Acta*, vol. 3, no. 3, pp. 233–243, Oct. 1960, doi: 10.1016/0013-4686(60)85007-4.
[68] N. Ibl, “The use of dimensionless groups in electrochemistry,” *Electrochimica Acta*, vol. 1, no. 2, pp. 117–129, Jul. 1959, doi: 10.1016/0013-4686(59)85001-5.
[69] Y. Gao *et al.*, “Attenuated Natural Convection in Molten Salt Electrochemical Systems with Minimal Heat Dissipation,” *J. Phys. Chem. Lett.*, vol. 15, no. 44, pp. 11022–11026, Nov. 2024, doi: 10.1021/acs.jpclett.4c02680.
[70] K. Kontturi, L. Murtomäki, and J. A. Manzanares, *Ionic Transport Processes: in Electrochemistry and Membrane Science*. Oxford, UK: Oxford University Press, 2008.
[71] W. T. Ward, R. A. Strehlow, W. R. Grimes, and G. M. Watson, “SOLUBILITY RELATIONS AMONG RARE-EARTH FLUORIDES IN SELECTED MOLTEN FLUORIDE SOLVENTS,” ORNL-2749, 4220883, Nov. 1959. doi: 10.2172/4220883.
[72] R. Vidrio, S. Mastromarino, E. Still, L. Chapdelaine, and R. O. Scarlat, “Density and Thermal Expansivity of Molten 2LiF-BeF2 (FLiBe): Measurements and Uncertainty Quantification,” *J. Chem. Eng. Data*, vol. 67, no. 12, pp. 3517–3531, Dec. 2022, doi: 10.1021/acs.jced.2c00212.
[73] “Lanthanum Fluoride (LaF3) Materials Data.”
[74] N. Elgrishi, K. J. Rountree, B. D. McCarthy, E. S. Rountree, T. T. Eisenhart, and J. L. Dempsey, “A Practical Beginner’s Guide to Cyclic Voltammetry,” *J. Chem. Educ.*, vol. 95, no. 2, pp. 197–206, Feb. 2018, doi: 10.1021/acs.jchemed.7b00361.
[75] S. J. Konopka and Bruce. McDuffie, “Diffusion coefficients of ferri- and ferrocyanide ions in aqueous media, using twin-electrode thin-layer electrochemistry,” *Anal. Chem.*, vol. 42, no. 14, pp. 1741–1746, Dec. 1970, doi: 10.1021/ac50160a042.
[76] J. Heinze, “Ultramicroelectrodes in Electrochemistry,” *Angew. Chem. Int. Ed. Engl.*, vol. 32, no. 9, pp. 1268–1288, 1993, doi: 10.1002/anie.199312681.
[77] E. O. Blair, D. K. Corrigan, J. G. Terry, A. R. Mount, and A. J. Walton, “Development and Optimization of Durable Microelectrodes for Quantitative Electroanalysis in Molten Salt,” *J. Microelectromechanical Syst.*, vol. 24, no. 5, pp. 1346–1354, Oct. 2015, doi: 10.1109/JMEMS.2015.2399106.
[78] K. Kontturi, L. Murtomäki, and J. A. Manzanares, *Ionic Transport Processes: in Electrochemistry and Membrane Science*. Oxford University Press, 2008. doi: 10.1093/acprof:oso/9780199533817.001.0001.
[79] J. Heinze, “Ultramicroelectrodes in Electrochemistry,” *Angew. Chem. Int. Ed. Engl.*, vol. 32, no. 9, pp. 1268–1288, 1993, doi: 10.1002/anie.199312681.
[80] A. Consiglio, “Electrochemical cell and microfabricated chip sensors for electroanalysis of molten salt,” University of California, Berkeley, 2020.
[81] H. J. Levene, “Production and optimisation of molten salt compatible micro- and nanoelectrodes for enhanced electroanalysis in LiCl-KCl Eutectic,” Nov. 2019, Accessed: Aug. 29, 2023. [Online]. Available: https://era.ed.ac.uk/handle/1842/36650

[82] S. D. Branch, A. M. Lines, J. Lynch, J. M. Bello, W. R. Heineman, and S. A. Bryan, "Optically Transparent Thin-Film Electrode Chip for Spectroelectrochemical Sensing," *Anal. Chem.*, vol. 89, no. 14, pp. 7324–7332, Jul. 2017, doi: 10.1021/acs.analchem.7b00258.

[83] T. J. Davies and R. G. Compton, "The cyclic and linear sweep voltammetry of regular and random arrays of microdisc electrodes: Theory," *J. Electroanal. Chem.*, vol. 585, no. 1, pp. 63–82, Nov. 2005, doi: 10.1016/j.jelechem.2005.07.022.

[84] D. Olander, "Redox condition in molten fluoride salts," *J. Nucl. Mater.*, vol. 300, no. 2–3, pp. 270–272, Feb. 2002, doi: 10.1016/S0022-3115(01)00742-5.

[85] M. Anderson *et al.*, "Heat Transfer Salts for Nuclear Reactor Systems - Chemistry Control, Corrosion Mitigation, and Modeling," Jan. 2015.

[86] "Molten-Salt Reactor Program [Disc 3]." Accessed: Oct. 23, 2025. [Online]. Available: https://moltensalt.org/references/static/downloads/pdf/ORNL-4396.pdf

[87] K. Ema, Y. Ito, T. Takenaka, and J. Oishi, "Relation between potentials of Li,K/Li+,K+ dynamic reference electrode and HF/H2 gas electrode in a molten LiF-KF system," *Electrochimica Acta*, vol. 32, no. 10, pp. 1537–1540, Oct. 1987, doi: 10.1016/0013-4686(87)85099-5.

[88] G. Durán-Klie, D. Rodrigues, and S. Delpech, "Dynamic Reference Electrode development for redox potential measurements in fluoride molten salt at high temperature," *Electrochimica Acta*, vol. 195, pp. 19–26, Mar. 2016, doi: 10.1016/j.electacta.2016.02.042.

[89] N. Shay, S. Guo, and J. Zhang, "Electrochemical Sensor Development for Fluoride Molten Salt Redox Control," *Trans. Am. Nucl. Soc.*, vol. 116, pp. 176–177, 2017.

[90] S. Guo, N. Shay, Y. Wang, W. Zhou, and J. Zhang, "Measurement of europium (III)/europium (II) couple in fluoride molten salt for redox control in a molten salt reactor concept," *J. Nucl. Mater.*, vol. 496, pp. 197–206, Dec. 2017, doi: 10.1016/j.jnucmat.2017.09.027.

[91] R. Chesser, S. Guo, and J. Zhang, "Electrochemical behavior of dysprosium and lanthanum in molten LiF-NaF-KF (Flinak) salt," *Ann. Nucl. Energy*, vol. 120, pp. 246–252, Oct. 2018, doi: 10.1016/j.anucene.2018.05.045.

[92] W. H. Doniger, A. Couet, and K. Sridharan, "Potentiodynamic Polarization of Pure Metals and Alloys in Molten LiF-NaF-KF (FLiNaK) Using the K/K+ Dynamic Reference Electrode," *J. Electrochem. Soc.*, vol. 169, no. 7, p. 071502, Jul. 2022, doi: 10.1149/1945-7111/ac7a66.

[93] H. Qiao, T. Nohira, and Y. Ito, "Electrochemical formation of Pd–La alloy films in a LiF–NaF–KF–LaF3 melt," *J. Alloys Compd.*, vol. 359, no. 1, pp. 230–235, Sep. 2003, doi: 10.1016/S0925-8388(03)00203-2.

[94] H. Peng, M. Shen, Y. Zuo, X. Tang, R. Tang, and L. Xie, "Electrochemical technique for detecting the formation of uranium-containing precipitates in molten fluorides," *Electrochimica Acta*, vol. 222, pp. 1528–1537, Dec. 2016, doi: 10.1016/j.electacta.2016.11.135.

[95] P. M. F. Wilson, J. P. Ferguson, and W. G. Cook, "Electrochemical monitoring of oxide in molten salts," *Proc. Can. Nucl. Soc.*, Jun. 2022, Accessed: Jun. 04, 2026. [Online]. Available: https://proceedings.cns-snc.ca/index.php/pcns/article/view/7251

[96] B. Kelleher, K. Dolan, M. Anderson, and K. Sridharan, "Observed Redox Potential Range of Li_2BeF_4 Using a Dynamic Reference Electrode," *Nucl. Technol.*, vol. 195, no. 3, pp. 239–252, Sep. 2016, doi: 10.13182/NT15-140.

[97] V. K. Afonichkin *et al.*, "Dynamic reference electrode for investigation of fluoride melts containing beryllium difluoride," *J. Fluor. Chem.*, vol. 130, no. 1, pp. 83–88, Jan. 2009, doi: 10.1016/j.jfluchem.2008.07.017.

[98] L. Massot, L. Cassayre, P. Chamelot, and P. Taxil, "On the use of electrochemical techniques to monitor free oxide content in molten fluoride media," *J. Electroanal. Chem.*, vol. 606, no. 1, pp. 17–23, Aug. 2007, doi: 10.1016/j.jelechem.2007.04.005.

[99] S. E. Eklund, J. Q. Chambers, G. Mamantov, J. Diminnie, and C. E. Barnes, "Tungsten Fluorides: Syntheses and Electrochemical Characterization in the FLINAK Molten Salt Eutectic," *Inorg. Chem.*, vol. 40, no. 4, pp. 715–722, Feb. 2001, doi: 10.1021/ic000491o.

[100] J. Gao, L. Zhang, G. Li, Y. Gao, and X. Xi, “Electrochemical separation of tungsten from scrap cemented carbide WC in FLiNaK melt,” *Int. J. Refract. Met. Hard Mater.*, vol. 121, p. 106671, Jun. 2024, doi: 10.1016/j.ijrmhm.2024.106671.
[101] D. L. Hildenbrand, “Thermochemistry of the gaseous tungsten fluorides,” *J. Chem. Phys.*, vol. 62, no. 8, pp. 3074–3079, Apr. 1975, doi: 10.1063/1.430907.
[102] K. Grjotheim, “On the Electrochemical Series of Metals in the Eutectic Melt of Sodium- and Potassium-Fluorides,” *Z. Für Phys. Chem.*, vol. 11, no. 3_4, pp. 150–164, May 1957, doi: 10.1524/zpch.1957.11.3_4.150.
[103] H. W. Jenkins, G. Mamantov, and D. L. Manning, “E.M.F. measurements on the nickel-nickel(II) couple in molten fluorides,” *J. Electroanal. Chem. Interfacial Electrochem.*, vol. 19, no. 4, pp. 385–389, Dec. 1968, doi: 10.1016/S0022-0728(68)80101-9.
[104] H. R. Bronstein and D. L. Manning, “Lanthanum Trifluoride as a Membrane in a Reference Electrode for Use in Certain Molten Fluorides,” *J. Electrochem. Soc.*, vol. 119, no. 2, p. 125, 1972, doi: 10.1149/1.2404146.
[105] B. F. Hitch and C. F. Baes, “A NiNiO reference electrode of the third kind for molten fluorides,” *J. Inorg. Nucl. Chem.*, vol. 34, no. 1, pp. 163–169, Jan. 1972, doi: 10.1016/0022-1902(72)80374-9.
[106] C. G. Kontoyannis, “Pyrolytic boron nitride coated graphite as a container of reference electrodes for molten fluorides,” *Electrochimica Acta*, vol. 40, no. 15, pp. 2547–2551, 1995, doi: https://doi.org/10.1016/0013-4686(94)00364-7.
[107] F. Carotti, H. Wu, and R. O. Scarlat, “Characterization of a Thermodynamic Reference Electrode for Molten LiF-BeF2 (FLiBe),” *J. Electrochem. Soc.*, vol. 164, no. 12, p. H854, Sep. 2017, doi: 10.1149/2.1591712jes.
[108] F. Carotti, A. Laudenbach, H. Wu, M. Straka, and R. O. Scarlat, “Characterization of a Thermodynamic Reference Electrode for Molten LiF-BeF2 (FLiBe): Part II. Materials Analysis,” *J. Electrochem. Soc.*, vol. 166, no. 15, pp. H835–H841, 2019, doi: 10.1149/2.1161914jes.
[109] S. A. Dowben *et al.*, “Comparison of Ni/NiF2 and Ag/AgF for a Stable Redox Couple for Molten Fluoride Salt Reference Electrodes,” presented at the Transactions of the American Nuclear Society, 2023, pp. 315–318. doi: 10.13182/T128-42071.
[110] S. A. Dowben *et al.*, “Electrochemical Analysis of Metal Stability in Candidate Reference Electrode Fluoride Salts (FLiNaK + 1 wt% AgF, MnF2, or NiF2),” *J. Electrochem. Soc.*, vol. 171, no. 2, p. 027501, Feb. 2024, doi: 10.1149/1945-7111/ad2151.
[111] C. G. Kontoyannis, “Graphite as Membrane in a Reference Electrode for Molten Fluorides Between 650 and 800 °C,” *ECS Proc. Vol.*, vol. 1994–13, no. 1, pp. 371–378, Jan. 1994, doi: 10.1149/199413.0371PV.
[112] B. F. Hitch and C. F. Baes, “Electromotive force study of molten lithium fluoride-beryllium fluoride solutions,” *Inorg. Chem.*, vol. 8, no. 2, pp. 201–207, Feb. 1969, doi: 10.1021/ic50072a004.
[113] B. Kelleher, K. Dolan, M. Anderson, and K. Sridharan, “Observed Redox Potential Range of Li_2BeF_4 Using a Dynamic Reference Electrode,” *Nucl. Technol.*, vol. 195, no. 3, pp. 239–252, Sep. 2016, doi: 10.13182/NT15-140.
[114] F. Carotti, “Electrochemical Studies for Tritium Transport in Graphite and Molten FLiBe,” 2019.
[115] C. E. Vallet, H. R. Bronstein, and J. Braunstein, “Electromigrational Depletion (ED) Chronopotentiometry Temperature Dependence of Diffusion in Molten BeF2-LiF,” *J. Electrochem. Soc.*, vol. 121, no. 11, p. 1429, Nov. 1974, doi: 10.1149/1.2401702.
[116] F. Carotti, “Electrochemical Studies for Tritium Transport in Graphite and Molten FLiBe,” University of Wisconsin - Madison, 2019. [Online]. Available: https://search.library.wisc.edu/digital/AWFETNY7WAJA428G
[117] D. Harvey, *Modern analytical chemistry*. Boston: McGraw-Hill, 2000.
[118] J. Newman, “Electrochemical Systems”.
[119] M. M. Tylka, J. L. Willit, J. Prakash, and M. A. Williamson, “Method Development for Quantitative Analysis of Actinides in Molten Salts,” *J. Electrochem. Soc.*, vol. 162, no. 9, pp. H625–H633, 2015, doi: 10.1149/2.0401509jes.

[120] Y. L. Wang, Q. Wang, H. J. Liu, and C. L. Zeng, “Effects of the oxidants H2O and CrF3 on the corrosion of pure metals in molten (Li,Na,K)F,” *Corros. Sci.*, vol. 103, pp. 268–282, Feb. 2016, doi: 10.1016/j.corsci.2015.11.032.
[121] Iu. K. Delimarskii and B. F. Markov, *Electrochemistry of Fused Salts*. Washington, D.C.: The Sigma Press, 1961.
[122] Pattrick Calderoni, “An experimental test plan for the characterization of molten salt thermochemical properties in heat transport systems,” INL/EXT-10-19921, 1000534, Sep. 2010. doi: 10.2172/1000534.
[123] Dr. Kumar Sridharan *et al.*, “Molten Salt Heat Transport Loop: Materials Corrosion and Heat Transfer Phenomena,” DOE/ID/14675, 934785, Jul. 2008. doi: 10.2172/934785.
[124] T. Yoko and R. A. Bailey, “Electrochemical Studies of Chromium in Molten LiF - NaF - KF (FLINAK),” *J. Electrochem. Soc.*, vol. 131, no. 11, pp. 2590–2595, Nov. 1984, doi: 10.1149/1.2115363.
[125] Y. Wang and J. Zhang, “Electrochemical Properties of CrF2 in FLiNaK Molten Salt and the New Analytical Methods for their Determination,” *J. Electrochem. Soc.*, vol. 167, no. 8, 2020, doi: 10.1149/1945-7111/ab8923.
[126] P. Delahay and G. Mamantov, “Voltammetry at Constant Current: Review of Theoretical Principles,” *Anal. Chem.*, vol. 27, no. 4, pp. 478–483, Apr. 1955, doi: 10.1021/ac60100a001.
[127] T. Yoko and R. A. Bailey, “Electrochemical Studies of Chromium in Molten LiF - NaF - KF (FLINAK),” *J. Electrochem. Soc.*, vol. 131, no. 11, p. 2590, Nov. 1984, doi: 10.1149/1.2115363.
[128] R. A. Bailey and T. Yoko, “High-temperature electroplating of chromium from molten FLINAK,” *J. Appl. Electrochem.*, vol. 16, no. 5, pp. 737–744, Sep. 1986, doi: 10.1007/BF01006927.
[129] H. Peng, M. Shen, C. Wang, T. Su, Y. Zuo, and L. Xie, “Electrochemical investigation of the stable chromium species in molten FLINAK,” *RSC Adv.*, vol. 5, no. 94, pp. 76689–76695, Sep. 2015, doi: 10.1039/C5RA09919F.
[130] W. Wu, S. Guo, and J. Zhang, “Electrochemical Behaviors of Cr(III) in Molten LiF-NaF-KF Eutectic,” *Int. J. Electrochem. Sci.*, pp. 225–234, Jan. 2018, doi: 10.20964/2018.01.21.
[131] W. H. Doniger and K. Sridharan, “Application of voltammetry for quantitative analysis of chromium in molten 2LiF-BeF2 (FLiBe) salt,” *J. Electroanal. Chem.*, vol. 838, pp. 73–81, Apr. 2019, doi: 10.1016/j.jelechem.2019.02.048.
[132] Y. Wang and J. Zhang, “Electrochemical Properties of CrF2 in FLiNaK Molten Salt and the New Analytical Methods for their Determination,” *J. Electrochem. Soc.*, vol. 167, no. 8, 2020, doi: 10.1149/1945-7111/ab8923.
[133] A. A. Maslennikova *et al.*, “Determination of the Oxygen Content in the LiF–NaF–KF Melt,” *Materials*, vol. 16, no. 11, p. 4197, Jan. 2023, doi: 10.3390/ma16114197.
[134] M. Shen, H. Peng, M. Ge, Y. Zuo, and L. Xie, “Use of square wave voltammeter for online monitoring of O2− concentration in molten fluorides at 600 °C,” *J. Electroanal. Chem.*, vol. 748, pp. 34–39, Jul. 2015, doi: 10.1016/j.jelechem.2015.04.023.
[135] Yanmei C., Hu Z., Guoan Y. E., Huakui Z., and Huayi Y. I. N., “Quantitative Analysis of Sm^{3+} in LiCl-KCl Eutectic Melt by Square Wave Voltammetry,” *J. Nucl. Radiochem.*, vol. 48, no. 2, pp. 206–216, Apr. 2026, doi: 10.7538/hhx.2026.48.02.0206.
[136] H. Zhang *et al.*, “Square wave voltammetry for real time analysis of minor metal ion concentrations in molten salt reactor fuel,” *J. Nucl. Mater.*, vol. 527, p. 151791, Dec. 2019, doi: 10.1016/j.jnucmat.2019.151791.
[137] W. Wu, S. Guo, and J. Zhang, “Electrochemical Behaviors of Cr(III) in Molten LiF-NaF-KF Eutectic,” *Int. J. Electrochem. Sci.*, vol. 13, no. 1, pp. 225–234, Jan. 2018, doi: 10.20964/2018.01.21.
[138] D. Hawley and R. N. Adams, “Homogeneous chemical reactions in electrode processes: Measurement of rates of follow-up chemical reactions,” *J. Electroanal. Chem. 1959*, vol. 10, no. 5, pp. 376–386, Nov. 1965, doi: 10.1016/0022-0728(65)80040-7.

[139] T. Kuwana, D. E. Bublitz, and G. Hoh, "Chronopotentiometric Studies on the Oxidation of Ferrocene, Ruthenocene, Osmocene and Some of their Derivatives[1]," *J. Am. Chem. Soc.*, vol. 82, no. 22, pp. 5811–5817, Nov. 1960, doi: 10.1021/ja01507a011.
[140] L. Massot, M. Gibilaro, D. Quaranta, and P. Chamelot, "Corrosion Products Electrochemical Behaviour into Molten LiF-NaF: Investigation of Cr(II) System," *J. Electrochem. Soc.*, vol. 168, no. 2, p. 026510, Feb. 2021, doi: 10.1149/1945-7111/abe088.
[141] H. O. Nam, A. Bengtson, K. Vörtler, S. Saha, R. Sakidja, and D. Morgan, "First-principles molecular dynamics modeling of the molten fluoride salt with Cr solute," *J. Nucl. Mater.*, vol. 449, no. 1–3, pp. 148–157, Jun. 2014, doi: 10.1016/j.jnucmat.2014.03.014.
[142] S. V. N. Naidu, A. M. Sriramamurthy, and P. R. Rao, "The Cr−W (Chromium−Tungsten) system," *Bull. Alloy Phase Diagr.*, vol. 5, no. 3, pp. 289–292, Jun. 1984, doi: 10.1007/BF02868555.
[143] A. A. Maslennikova *et al.*, "Determination of the Oxygen Content in the LiF–NaF–KF Melt," *Materials*, vol. 16, no. 11, p. 4197, Jan. 2023, doi: 10.3390/ma16114197.
[144] J. D. Redman and C. F. Weaver, "Stability of Chromium and Iron Fluorides in Various Molten Fluorides," ORNL-1947.
[145] W. H. Jordan, S. J. Cramer, and A. J. Miller, "Aircraft Nuclear Propulsion Program: Quarterly Progress Report for Period Ending December 31, 1956, Part 1 - 5," Oak Ridge National Laboratory (ORNL), Oak Ridge, TN (United States), Mar. 1957. doi: 10.2172/1373535.
[146] G. C. Barker, R. L. Faircloth, and A. W. Gardner, "SQUARE WAVE POLAROGRAPHY. PART IV. AN INTRODUCTION TO THE THEORETICAL ASPECTS OF SQUARE WAVE POLAROGRAPHY," Great Britain Atomic Energy Research Establishment, Harwell, Berks, England (United Kingdom), AERE-C/R-1786, Feb. 1956. Accessed: Oct. 03, 2024. [Online]. Available: https://www.osti.gov/biblio/4317989
[147] N. Fatouros and D. Krulic, "Analysis of the square wave voltammetry for reversible metal deposition on a foreign substrate – Experimental study of silver deposition on gold," *J. Electroanal. Chem.*, vol. 706, pp. 76–85, Oct. 2013, doi: 10.1016/j.jelechem.2013.07.019.
[148] G. J. Janz, "Thermodynamic and Transport Properties for Molten Salts: Correlation Equations for Critically Evaluated Density, Surface Tension, Electrical Conductance, and Viscosity Data," *J. Phys. Chem. Ref. Data*, vol. 17, 1988.
[149] D. F. Williams, "Assessment of Candidate Molten Salt Coolants for the NGNP/NHI Heat-Transfer Loop," ORNL/TM--2006/69, 1360677, Jun. 2006. doi: 10.2172/1360677.
[150] T. Lichtenstein, M. A. Rose, J. Krueger, E. Wu, and M. A. Williamson, "Thermochemical Property Measurements of FLiNaK and FLiBe in FY 2020," p. 34, 2020, doi: 10.2172/1734856.
[151] J. Schorne-Pinto, A. Birri, and T. M. Besmann, "Thermophysical Properties for 2lif-Bef2 (Flibe) with Uncertainty Quantification," Mar. 21, 2024, *Social Science Research Network, Rochester, NY*: 4767341. doi: 10.2139/ssrn.4767341.
[152] R. B. Bird, W. E. Stewart, and E. N. Lightfoot, *Transport phenomena*, Revised ed. New York: Wiley, 2007.
[153] E. I. Khrushcheva and M. R. Tarasevich, "Electrochemical Determination of Surface Area of Metals," *Russ. Chem. Rev.*, vol. 47, no. 5, pp. 416–424, May 1978, doi: 10.1070/RC1978v047n05ABEH002227.
[154] D. Ohm and K. F. Domke, "Controlled deposition of 2D-confined Pd or Ir nano-islands on Au(1 1 1) following Cu UPD, and their HER activity," *J. Electroanal. Chem.*, vol. 896, p. 115285, Sep. 2021, doi: 10.1016/j.jelechem.2021.115285.

Appendix A. General Calculations

A.1 Salt Transfer Operating Pressures

A conservative calculation for the minimum required pressure to perform the salt transfer is given. The calculations are performed by the mechanical energy balance described in Eq.(2.2). Begin by calculating the pressure required to overcome the head of the system. Our system will operate near 600°C and needs to overcome 1m of head. Using the density of FLiBe provided by Janz[148],

$$\rho = 2413 - 0.488T \left[\frac{kg}{m^3}\right] \tag{A.1-1}$$

$$g\Delta z = \left(9.81\frac{m}{s^2}\right)(1m)\left(1990\frac{kg}{m^3}\right) \approx 19{,}522\ Pa \tag{A.1-2}$$

Therefore, we need to apply slightly greater pressure to the fluid to overcome the frictional losses in the transfer line. Assume we apply 20,000 Pa, then the remaining pressure will be converted into kinetic energy

$$\Delta P = 20{,}000 - 19{,}522 = 478\ Pa \tag{A.1-3}$$

$$\Delta v = \sqrt{2\frac{\left(478\frac{kg}{s^2 m}\right)}{\left(2.0\frac{kg}{m^3}\right)}} \approx 0.693\frac{m}{s} \tag{A.1-4}$$

Using this velocity, we calculate the Reynolds number of the flow through our ¼" tube with inner diameter of 0.0109m (0.43"). Using a correlation for viscosity developed by Williams et al. [149],

$$\mu = 0.000116\, exp\left(\frac{3755}{T}\right)\ [Pa \cdot s] \tag{A.1-5}$$

$$Re = \frac{\left(1990\frac{kg}{m^3}\right)\left(0.693\frac{m}{s}\right)(0.0109\ m)}{(0.0086\ Pa{\cdot}s)} \approx 1{,}750 < 4{,}000 \tag{A.1-6}$$

Therefore, our flow will be laminar. However, in an attempt to prevent freezing in the tube we want the flow to be turbulent to prevent temperature stratification (this is an operating heuristic, but it has proven important in a previous salt transfer procedure). Let Re > 4000, then the fluid velocity must be

$$v > \frac{4000(0.0086\ Pa{\cdot}s)}{\left(1990\frac{kg}{m^3}\right)(0.0109\ m)} = 1.59\frac{m}{s} \tag{A.1-7}$$

We can now calculate the frictional losses of the system assuming the flow stays above the turbulent velocity throughout the transfer line. For turbulent flows, we use the Blasius correlation,

$$f_F = 0.079Re^{-\frac{1}{4}} \approx 0.00993 \tag{A.1-8}$$

Our transfer line is approximate 1.5m (60") long which corresponds to a frictional loss of,

$$\Sigma F = \frac{2(0.00993)(1.5\ m)\left(4.5\frac{m}{s}\right)^2}{(0.0109\ m)} \approx 6.91\frac{J}{kg} \quad \text{(A.1-9)}$$

This frictional loss will change the fluid velocity and also the flow regime. To combat this, we want to iteratively solve this problem such that for a given system pressure, we can push fluid through the transfer line without losing turbulent flow throughout the operation. Using a nonlinear solver, we find the velocity which yields a head loss equal to the head loss of the tubing. Table 37 shows the final velocity in the transfer line after with a steady state frictional loss calculation. The yellow highlighted cells show the objective condition of the nonlinear solver was met, i.e. height equals head loss in the tube. The blue highlighted cell shows the final velocity of the fluid exiting the line.

The result of this calculation gives us a required operating pressure of P = 33.5 kPa or approximately 48.5 psi. This operating pressure is within the range of safe pressures in the glovebox and the vessels being pressurized.

Table 37. Initial and Final calculations for velocity of fluid in transfer line

Step #	Description	Equation	Calculation
1.	Start from the simplified mechanical energy balance for velocity	$\Delta P = \frac{2f_F L\rho v^2}{d} + \rho g\Delta z$	
		$v = \sqrt{\frac{\Delta P - \rho g\Delta z}{\frac{2f_F L\rho}{d}}}$	
2.	Guess an initial v	$v = 1.59\frac{m}{s}$	
3.	Compute the Reynolds number	$Re = \frac{\rho v d}{\mu}$	$Re_{init} = 4010$
			$Re_{final} = 347$
4.	If Re > 4000, use Blasius correlation	$f_F = 0.079Re^{-\frac{1}{4}}$	$f_{F,init} = 0.00993$
	Else, use laminar correlation	$f_F = \frac{16}{Re}$	$f_{F,final} = 0.0461$
5.	Update the velocity	$v_i = \sqrt{\frac{\Delta P - \rho g\Delta z}{\frac{2f_F L\rho}{d}}}$	$v_{init} = 1.59\frac{m}{s}$
6.	Repeat steps 3-5 until velocity has converge	$v_i \approx v_{i+1}$	$v_{final} = 0.138\frac{m}{s}$
			Need a new ΔP

7.	If the flow is laminar or unstable, increase the pressure drop in step 1, use old velocity in step 2, and repeat step 6. Minimize the required pressure to stay turbulent.	$\Delta P_{new} = \Delta P + P_{guess}$	$\Delta P_{new} = 30{,}000\ Pa$ $v_{final} = [1.4 - 2.1]\frac{m}{s}$ v is in a boundary regime
8.	When flow in step 6 is turbulent, the operating pressure is determined	$\Delta P_i \approx \Delta P_{i+1} \approx \Delta P_{min}$	$\Delta P \approx \Delta P_{min} = 33{,}500\ Pa$ $v_{final} = 1.65\frac{m}{s}$ $Re_{final} = 4050$

A.2 Transfer Line salt "Bleed-Off" Mass

To stop the transfer of salt from the supply vessel to the transfer vessel, the pressure supply is bypassed from the transfer line causing the salt to drain from the high points above the free liquid surface. This will empty the volume of the salt in the transfer line into the supply and transfer tanks. In order to complete the salt transfer procedure with accurate masses being transferred, we want to ensure the salt being drained from the line is accounted in the total mass transferred.

$V_t \equiv$ volume of the transfer line

$d_t \equiv$ inner diameter of transfer line

$l_t \equiv$ length of transfer line

$m_s \equiv$ mass of salt

$\rho_s \equiv$ density of salt at operating temperature

The length and diameter of the transfer line are known, and the density of the salt is known. From these values, we can calculate the total mass of the salt in the transfer line. Then knowing what fraction of the length of the transfer line is pointing toward the transfer vessel after the apex in the line, we can easily calculate the mass of salt that will drain into the transfer vessel after the pressure bypass is actuated.

$$l_t \approx 60 \text{ in} = 152.4 \text{ cm} \quad \text{(A.2-1)}$$

$$d_t \approx 0.18 \text{ in} = 0.4572 \text{ cm} \quad \text{(A.2-2)}$$

$$V_t = l_t\left(\frac{\pi d_t^2}{4}\right) = (152.4 \text{ cm})\left(\frac{\pi(0.4572 \text{ cm})^2}{4}\right) \approx 25.02 \text{ cm}^3 \quad \text{(A.2-3)}$$

$$m_s = V_t \rho_t = (25.02\ \text{cm}^3)\left(1.99 \frac{\text{g}}{\text{cm}^3}\right) \approx 49.8\ \text{g} = 0.0498\ \text{kg} \quad \text{(A.2-4)}$$

This mass of salt is negligibly small compared to the 20kg and 5kg being transferred to TK02 and TK03. However, when transferring to TK04, we will want to consider this volume of salt draining after the pressure bypass is actuated.

A.3 Heating Time vs Power Input for TK01

Melting the FLiBe in TK01 is the first step to performing the salt transfer procedure. Melting approximately 50kg of salt is not an easy task to be performed inside of a glovebox mainly due to the heat required for melting must be below the maximum heat rejection capacity of the glovebox heat exchangers. At the time of the salt transfer operation, the glovebox had approximately 2kW of remaining heat rejection budget (this is defined by the total heat rejection load minus the occupied heat rejection load). This means the maximum heating load we could include on the entire salt transfer system was 2kW.

The length of time it would take to melt all 50kg of FLiBe can be calculated from the total sensible heat and latent heat required to bring the room temperature system up to 600°C divided by the power input to the system. The heat capacity of solid and liquid FLiBe is taken from Lichtenstein[150],

$$c_{p,solid} \approx c_{p,liquid} \approx 1900 \frac{J}{kgK} \quad \text{(A.3-1)}$$

We know the melting point and operating temperature to be,

$$T_{melt} = 459^o C \qquad T_{op} = 600^o C \quad \text{(A.3-2)}$$

The mass of the FLiBe is weighed,

$$m_{salt} \approx 50\ kg \quad \text{(A.3-3)}$$

The heat of fusion value is taken from Schorne-Pinto et al.[151]

$$\Delta H_f = 0.431 \frac{J}{kg} \quad \text{(A.3-4)}$$

Then the total heat required to bring the system to operating temperature is,

$$Q_{sens,1} = c_{p,solid} m_{salt} (T_{melt} - 25^o C) = 41{,}230\ kJ \quad \text{(A.3-5)}$$

$$Q_{lat} = \Delta H_f m_{salt} = 21{,}565\ kJ \quad \text{(A.3-6)}$$

$$Q_{sens,2} = c_{p,liquid} m_{salt} (T_{op} - T_{melt}) = 13{,}395\ kJ \quad \text{(A.3-7)}$$

$$Q_{tot} = Q_{sens,1} + Q_{lat} + Q_{sens,2} = 76{,}190\ kJ \quad \text{(A.3-8)}$$

As TK01 increases in temperature, the efficiency of the system will drop due to the increase in heat loss through the insulation at higher temperatures. This is visualized as jumping between efficiency lines in Figure 101 as the operation continues. In principle, we can determine the efficiency of the system at each power level by setting a power and calculating the theoretical time it takes to reach a set temperature versus the actual time it takes to reach the temperature. This process would take several more days of shakedown testing and wasn't required for the salt transfer system to function as intended.

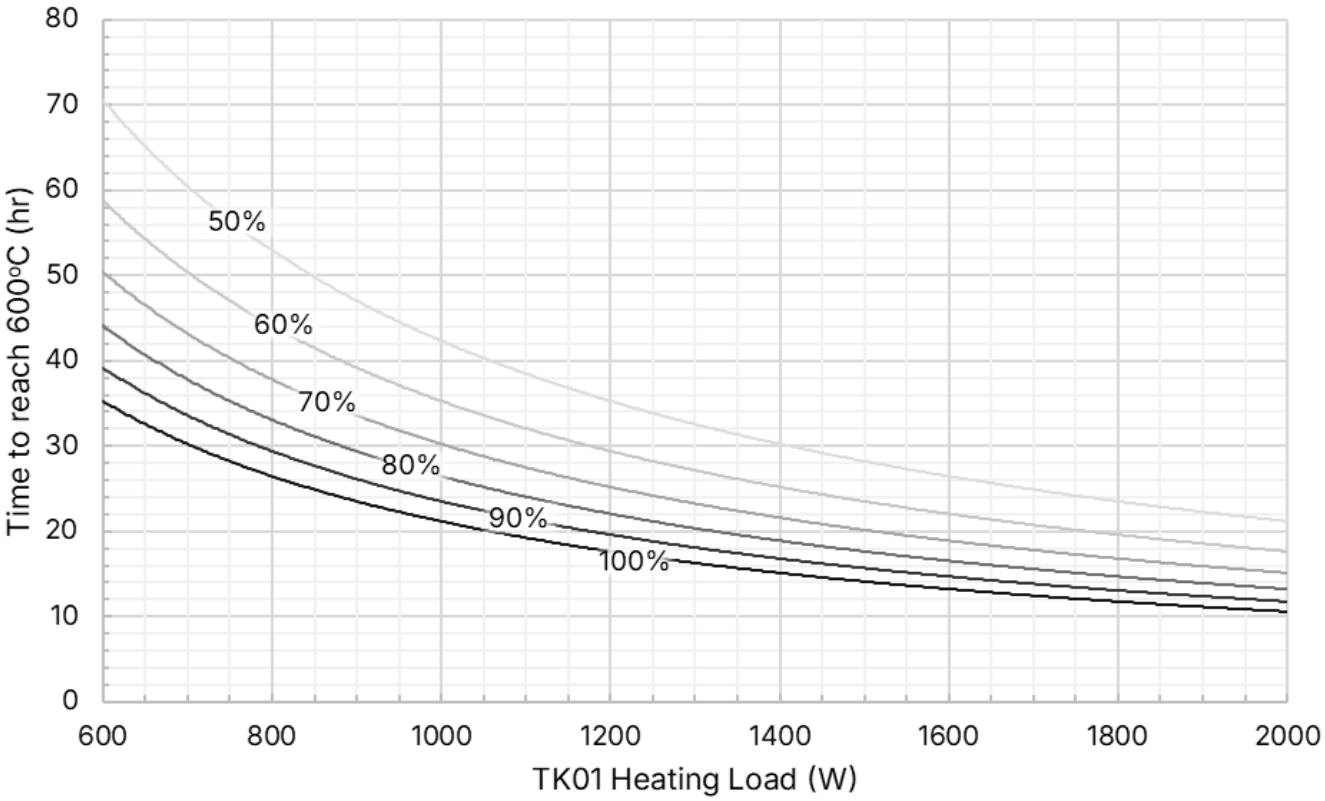


Figure 101. Time for TK01 to reach operating temperature as a function of heater load

During the first and second attempt of the salt transfer, we decided to err on the side of less heating load (Q=1200W) on TK01, unaware that our theoretical insulation value of around 80-90% efficiency was a gross overestimate. In actuality, the insulation was likely closer to 20-30% efficient based on the time it took to reach 500°C. For the third attempt, we choose to work with the higher end of heating load (Q=1800W) aware that TK01 heating efficiency would shift towards the 50% efficiency curve shown on Figure 101.

A.4 Heat Loss from Transfer Line During Operation

The salt transfer operation is preceded by isothermal operation of the system. The procedure calls to bring the system to 500°C and hold isothermal conditions for 24-hours. However, it is not possible to probe the entire system temperature and ensure all walls are at 500°C before beginning the salt transfer operation. We estimate the heat loss from the system during the salt transfer operation and calculate the temperature drop

in the flowing salt as a function of position in the transfer line. If we suspect the salt in the line will freeze before exiting into the transfer tank, then we will need to hold the system at higher temperatures to combat this obstacle.

An explicit formula for the heat loss in an insulated pipe is given by Bird et al., in *Introductory Transport Phenomena*[152]. The formula calculates a given heat loss through a specified length of pipe assuming a constant temperature fluid traveling through the pipe.

$$Q = h(2\pi R_i L)\left(T_f - T_a\right)\frac{1}{1-\mathrm{Bi}_i\left[\left(\frac{k_i}{k}\right)\ln\kappa - \ln\left(\frac{R_i}{R}\right)\right]} \tag{A.4-1}$$

Q is the total heat lost, h is the heat transfer coefficient at the surface of the pipe insulation-cover gas interface, R_i is the radius of the insulation from the pipe centerline, L is the length of the total pipe section that is isothermal, T_f is the temperature of the isothermal fluid traveling in the length of pipe, T_a is the ambient temperature of the cover gas, Bi_i is the Biot number of the pipe insulation, k_i is the thermal conductivity of the pipe insulation, k is the thermal conductivity of the pipe material, κ is the ratio of the pipe inner radius to the pipe outer radius, and R is the radius of the pipe from the fluid centerline. The heat transfer coefficient that models the system can be replaced by the R-value, $\mathcal{R}$, given by the insulation specification. For our ceramic fiber blanket with a thickness of 3in, we have an R-value of $\mathcal{R} = 3\frac{m^2K}{W}$. This relates to h by the formula,

$$h = \frac{1}{\mathcal{R}} = 0.33\frac{W}{m^2K} \tag{A.4-2}$$

The constants for our system are given,

$$R = 0.125in\left(0.0254\frac{m}{in}\right) = 0.003175\,m \tag{A.4-3}$$

$$R_{inner} = 0.09in\left(0.0254\frac{m}{in}\right) = 0.002286\,m \tag{A.4-4}$$

$$R_i = 3in\left(0.0254\frac{m}{in}\right) = 0.0762\,m \tag{A.4-5}$$

$$L \approx 150in\left(0.254\frac{m}{in}\right) = 3.81\,m \tag{A.4-6}$$

$$T_f = 500^oC \tag{A.4-7}$$

$$T_a = 30^oC \tag{A.4-8}$$

$$k = 16.3\frac{W}{mK} \tag{A.4-9}$$

$$k_i = 0.05\frac{W}{mK} \tag{A.4-10}$$

$$\kappa = \frac{R_{inner}}{R} = \frac{0.09}{0.125} = 0.72 \quad \text{(A.4-11)}$$

Assuming the transfer line is well described by this system model, we can now calculate total heat losses assuming there is constant temperature fluid traveling through the system. Then, we will improve our calculation and assume the fluid has n separate equilibrium stages along the pipe where $n = \frac{L}{\Delta L}$, and in each equilibrium stage the fluid temperature drops from a heat low in the pipe section of length ΔL. The heat loss in the pipe segment can be calculated as ΔQ, which is related to the drop in fluid temperature by the first law of thermodynamics.

$$\Delta Q = mc_p \Delta T$$

$$\Delta T = T_f - T_{f,new}$$

We can rationalize that the heat loss in a subsequent tube segment must be less than the heat loss of the previous segment because the fluid will be at a colder temperature and the driving force for cooling decreases. Therefore, a conservative calculation for determining the heat loss in the transfer line can be given directly by Eq.(A.4-1) and plugging in all the constants set above. The heat loss in the transfer line at the steady state temperature is approximately,

$$\Delta Q \approx 130\ W \quad \text{(A.4-12)}$$

Therefore, we must provide this much heating load to the transfer line to prevent the temperature from dropping during the operation.

A.5 Pressure stability with large volumes

When considering the compressibility of a gas to drive salt flow from TK01 to TK02, we consider the sensitivity of the pressure in TK01 gas space to the volume change. If we assume two different starting volumes of gas space, one much smaller than the other, then we can see the sensitivity of the change in volume on the pressure in the cover gas. This is a glorified application of the ideal gas law, but its utility cannot be understated when trying to design salt transfer systems driven by a pressurized gas.

Case I: Initial volume of cover gas 1cm^3 increases by 100cm^3

$$\frac{P_f}{P_i} = \frac{V_i}{V_f} = \frac{1}{101} \quad \text{(A.5-1)}$$

$$P_f = 0.0099 P_i \quad \text{(A.5-2)}$$

Case II: Initial volume of cover gas 100cm^3 increases by 100cm^2

$$\frac{P_f}{P_i} = \frac{V_i}{V_f} = \frac{100}{200} \quad \text{(A.5-3)}$$

$$P_f = 0.5 P_i \quad \text{(A.5-4)}$$

This is to reiterate that the relative change in volume of gas space is the contributing factor to pressure change during volume transfer out of TK01. If we also consider that the pressure during the operation stays constant, then the "difference" in pressure we calculated from initial to final states is compensated by the increase in moles of gas in the gas space. Consider the moles required to add to the final gas space in Case I to bring the final pressure back to the initial pressure,

$$\frac{1}{0.0099} P_f = P_i \tag{A.5-5}$$

$$\frac{1}{0.0099} n \tag{A.5-6}$$

A.6 Echem Probe Sensitivity to Cr^{2+} Temperature Dependence

For a fluoride salt system that uses chromium as the redox buffer, the potential is set by the ratio of Cr^{2+}/Cr^{3+} derived from the disproportionation reaction,

$$Cr^{2+} \leftrightarrow \frac{2}{3} Cr^{3+} + \frac{1}{3} Cr \tag{A.6-1}$$

We assume the starting redox potential is set by the amount of Cr_2O_3 which dissolves in the fluoride melt from the oxide layer on the stainless steel. Assuming chromium enters the melt at first by the dissociation reaction,

$$\mathrm{Cr}_2O_3(s) = 2Cr^{3+} + 3O^{2-} \tag{A.6-2}$$

We assume the chromium exists in the Cr^{2+} oxidation state in FLiBe, so we have the reaction,

$$2Cr^{3+} + Cr = 3Cr^{2+} \tag{A.6-3}$$

This reaction strips Cr^0 from the stainless steel walls. The amount stripped depends on the amount of Cr^{3+} present in the system. For thickness δ = 1nm (the calculation for up to 3nm thickness will result in a final answer multiplied by 3), with the total inner surface area of the natural circulation loop $A \approx 0.27 m^2$, the volume of the passivation layer is,

$$V = A\delta = (0.27m^2)(1 \times 10^{-9}m) = 2.7 \times 10^{-10}m^3 \tag{A.6-4}$$

the density of Cr_2O_3 is approximately $\rho = 5.22 g/cm^3$,

$$m_{Cr_2O_3} = \rho V = (2.7 \times 10^{-10}m^3)\left(5.22 \frac{g}{cm^3}\right)\left(1 \times 10^2 \frac{cm}{m}\right)^3 = 0.00141\ g \tag{A.6-5}$$

$$n_{Cr_2O_3} = \frac{m_{Cr_2O_3}}{\mathcal{M}_{Cr_2O_3}} = \frac{0.00141\ g}{151.99 \frac{g}{mol}} = 9.27 \times 10^{-6}\ mol \tag{A.6-6}$$

A.7 Coulometry of the Diffusion Layer

It is significant that the diffusion layer is well understood in electrochemical experiments as the reactions at the surface of the electrode see a concentration profile over time and space, characteristic of heterogeneous reactions. Coulometry of the diffusion layer allows us to leverage Faraday's law and perform logic checks to infer the total amount of species that are reacting inside the diffusion layer. This analysis is important if we wish to understand what reaction we are observing at the electrode surface when we are relying on the KDRE. Using the data from Run 4 on Table 22, we see that there was a potential plateau above where we would expect the KDRE potential to be. We want to determine if that plateau was the result of chromium reduction, so we will analyze the total charge transferred during the experiment and compare it to the total charge required to reduce Cr^{3+} to Cr^{0}.

We first calculate the total amount of charge passed through the potentiostat over a duration of time. For our chronopotentiograms, that number is

$$Q = I \cdot t = (1\ C \cdot s^{-1})(10\ s) = 10\ C \tag{A.7-1}$$

Then we calculate the approximate diffusion layer thickness and volume. Using the correlation provided by Bard and Faulkner[33],

$$\delta_D = (2D_{Cr^{3+}}t)^{\frac{1}{2}} \tag{A.7-2}$$

The approximate volume of the cylinder around our wire electrodes would then be,

$$\mathrm{V_{D,cyl}} = \pi\delta_{\mathrm{D}}^2 \mathrm{h_w} = \pi(0.0132\ \mathrm{cm})^2(0.9\ \mathrm{cm}) = 0.000493\ \mathrm{cm^3} \tag{A.7-3}$$

The density of FLiNaK is given by Lichtenstein[150],

$$\rho = 2.45 - 6.85 \times 10^{-4}\mathrm{T} = 2.45 - 0.548 = 1.902\ \mathrm{g/cm^3} \tag{A.7-4}$$

We calculate the mass of FLiNaK in the diffusion volume and then the mass of Cr^{3+} that is in the diffusion volume,

$$\mathrm{m_{D,cyl}} = \rho \mathrm{V_{D,cyl}} = \left(1.902 \frac{\mathrm{g}}{\mathrm{cm^3}}\right)(0.000493\ \mathrm{cm^3}) = 0.000937\ \mathrm{g} \tag{A.7-5}$$

$$\mathrm{m_{Cr^{3+}}} = \frac{(\mathrm{wt\%_{Cr^{3+}}})}{100}\left(\mathrm{m_{D,cyl}}\right) = \frac{2.6}{100}(0.000937\ \mathrm{g}) = 0.00002436\ \mathrm{g} \tag{A.7-6}$$

$$\mathrm{n_{Cr^{3+}}} = \frac{\mathrm{m_{Cr^{3+}}}}{\mathcal{M}_{\mathrm{Cr}}} = \frac{2.436\times10^{-5}\ \mathrm{g}}{51.996\frac{\mathrm{g}}{\mathrm{mol}}} = 4.69 \times 10^{-7}\ \mathrm{mol} \tag{A.7-7}$$

Assuming we reach the terminal reduction step of chromium, the total charge to bring Cr^{3+} to Cr^{0} in the diffusion layer would be,

$$Q_{Cr} = n_{Cr^{3+}} zF = (4.69 \times 10^{-7}\ \text{mol}\ Cr^{3+}) \left(3 \frac{\text{mol}\ e^-}{\text{mol}\ Cr^{3+}}\right) \left(96485 \frac{C}{\text{mol}\ e^-}\right) = 0.1356\ C \quad \text{(A.7-8)}$$

This appears to be a contradiction! Somehow, the potentiostat pushed 10C of charge through the cell but only 0.1356C of charge were needed to completely reduce the chromium leaving ~9.86C of charge for high energy reductions. We can reconcile this contradiction by realizing our diffusion limited assumption was wrong. In molten salt systems, thermal gradients will arise from the nature of how difficult it is to keep a cell well insulated while also inserting metal electrodes and crucibles which act like heat transfer fins. The thermal gradient gives rise to natural circulation and mixes the diffusion layer of the salt, making a convection-diffusion layer (CDL). This effect is seen in molten salt electrochemistry[69]. Therefore we must be aware that the diffusion-limit potentiometry and voltammetry analysis is not sufficient for analyzing our data.

A.8 Error Propagation of CrF_3 concentration in FLiNaK

Quantitatively determining CrF_3 concentration by electrochemical methods requires rigorous error analysis of the standard additions of CrF_3 in the molten FLiNaK. We present the error analysis calculations for determining the concentration of CrF_3 added to FLiNaK, including the error from the preparation of the FLiNaK itself.

The FLiNaK was prepared from LiF (Materion, >99.9%), NaF (Materion, >99.9%), and KF (Materion, >99%) salts. The measured mass of each component is given below,

$$m_{LiF} = 12.570(2)\ g \qquad n_{LiF} = 0.48460(8)\ mol \quad \text{(A.8-1)}$$

$$m_{NaF} = 5.062(1)\ g \qquad n_{NaF} = 0.12056(2)\ mol \quad \text{(A.8-2)}$$

$$m_{KF} = 25.566(1)\ g \qquad n_{KF} = 0.43989(2)\ mol \quad \text{(A.8-3)}$$

$$m_{FLiNaK} = 43.198(2)\ g \qquad n_{FLiNaK} = 1.0451(1)\ mol \quad \text{(A.8-4)}$$

The standard additions of CrF_3 were measured prior to each addition i as $CrF_{3,i}$,

$$m_{CrF_3,1} = 0.094(1)\ g \qquad n_{CrF_3,1} = 0.000862(9)\ mol \quad \text{(A.8-5)}$$

$$m_{CrF_3,2} = 0.101(1)\ g \qquad n_{CrF_3,2} = 0.000927(9)\ mol \quad \text{(A.8-6)}$$

$$m_{CrF_3,3} = 0.198(2)\ g \qquad n_{CrF_3,3} = 0.00182(2)\ mol \quad \text{(A.8-7)}$$

$$m_{CrF_3,4} = 0.761(2)\ g \qquad n_{CrF_3,4} = 0.006982(2)\ mol \quad \text{(A.8-8)}$$

$$m_{CrF_3,5} = 1.388(3)\ g \qquad n_{CrF_3,5} = 0.01274(3)\ mol \quad \text{(A.8-9)}$$

$$m_{CrF_3,6} = 1.756(3)\ g \qquad n_{CrF_3,6} = 0.01611(3)\ mol \tag{A.8-10}$$

$$m_{CrF_3,7} = 0.982(2)\ g \qquad n_{CrF_3,7} = 0.00901(2)\ mol \tag{A.8-11}$$

Then the concentration of the salt after each standard addition increases in CrF_3. The total concentration of the melt are given in mole fraction, $x_{CrF_3,i}$, not molarity. Molarity is volume dependent and the volume of FLiNaK is temperature dependent and does not lend itself well to studying molten salts across varying temperatures.

$$x_{CrF_3,1} = 0.000825(9)\ mol \tag{A.8-12}$$

$$x_{CrF_3,2} = 0.00171(1)\ mol \tag{A.8-13}$$

$$x_{CrF_3,3} = 0.00345(2)\ mol \tag{A.8-14}$$

$$x_{CrF_3,4} = 0.01013(4)\ mol \tag{A.8-15}$$

$$x_{CrF_3,5} = 0.02232(5)\ mol \tag{A.8-16}$$

$$x_{CrF_3,6} = 0.03774(5)\ mol \tag{A.8-17}$$

$$x_{CrF_3,7} = 0.04636(6)\ mol \tag{A.8-18}$$

A.9 Uncertainty of CrF3 concentration in Yoko and Bailey (1984)

Yoko and Bailey report a single concentration of Cr^{3+} in FLiNaK throughout their report. However, concentration defined as mol/L is a temperature dependent variable. We can see this from the following,

$$C_{CrF_3}(T) = \frac{n_{CrF_3}}{V_{salt}(T)} = \frac{n_{CrF_3}}{m_{salt}\rho_{salt}(T)} = \left(\frac{n_{CrF_3}}{m_{salt}}\right)\frac{1}{\rho_{salt}(T)} \tag{A.9-1}$$

Mole fraction, on the other hand, is invariant with temperature.

$$x_{CrF_3} = \frac{n_{CrF_3}}{\left(\frac{m_{salt}}{\mathcal{M}_{salt}}\right)} = \frac{n_{CrF_3}}{n_{salt}} \tag{A.9-2}$$

To find the uncertainty in their analysis of diffusivity, we show that for a range of temperatures, the error in the actual mole fraction of the system is mainly determined by the error in the uncertainty of the concentration as the density of the salt changes.

$$\mathcal{M}_{salt}\left(\frac{n_{CrF_3}}{m_{salt}}\right) = \mathcal{M}_{salt}\left(C_{CrF_3}(T)\rho_{salt}(T)\right) \tag{A.9-3}$$

$$x_{CrF_3} = \mathcal{M}_{salt}\left(C_{CrF_3}(T)\rho_{salt}(T)\right) \quad \text{(A.9-4)}$$

For example, from table 3, the concentration of the melt is reported to have 0.09 mol/L CrF_3. This means at one of the reported temperatures between 612C-983C, one of these concentrations is "correct" while the others will be off by a factor inversely proportional to density of FLiNaK. If we assume that the reported concentration at 612C was correct, then the actual concentrations at each temperature would be calculated,

$$C_{CrF_3}(983C) = C_{CrF_3}(612C)\left(\frac{\rho_{salt}(612C)}{\rho_{salt}(983C)}\right) \quad \text{(A.9-5)}$$

$$C_{CrF_3}(893C) = C_{CrF_3}(612C)\left(\frac{\rho_{salt}(612C)}{\rho_{salt}(893C)}\right) \quad \text{(A.9-6)}$$

$$C_{CrF_3}(804C) = C_{CrF_3}(612C)\left(\frac{\rho_{salt}(612C)}{\rho_{salt}(804C)}\right) \quad \text{(A.9-7)}$$

$$C_{CrF_3}(716C) = C_{CrF_3}(612C)\left(\frac{\rho_{salt}(612C)}{\rho_{salt}(716C)}\right) \quad \text{(A.9-8)}$$

The greatest discrepancy of reported concentrations would be if the concentration was measured at 612C and the values was used without being corrected at 983C. This gives an error of,

$$err\% = \frac{\left(C_{CrF_3}(612C) - C_{CrF_3}(983C)\right)}{C_{CrF_3}(612C)} \cdot 100\% = 12.5\% \quad \text{(A.9-9)}$$

A.10 Uncertainty of electrode surface area in Yoko and Bailey (1984)

There are two reported working electrodes for the Yoko and Bailey paper. One is a Pt wire and the other is a Pt microdisk. The critical dimensions of each electrode are given in the paper, but no error is reported with the measurements. We can assume there is some error in the measurement from the rounding error on each number.

For the Pt wire electrode, we calculate the surface area,

$$A_{cyl} = 2\pi rh + \pi r^2 \quad \text{(A.10-1)}$$

$$A_1 = 2\pi\left(\frac{0.23\text{cm}}{2}\right)(1.13\text{cm}) + \pi\left(\frac{0.23\text{cm}}{2}\right)^2 = 0.85805\text{cm}^2 \quad \text{(A.10-2)}$$

There is rounding error in this calculation because the reported diameter (2.3mm) and the reported height (11.3mm) can both vary as much as +/- 0.05mm. So we calculate the area of the high and low rounding results,

$$A_{1,min} = 2\pi\left(\frac{0.225\text{cm}}{2}\right)(1.125\text{cm}) + \pi(0.225\text{cm})^2 = 0.83498\text{cm}^2 \quad \text{(A.10-3)}$$

$$A_{1,max} = 2\pi\left(\frac{0.235\text{cm}}{2}\right)(1.135\text{cm}) + \pi\left(\frac{0.235\text{cm}}{2}\right)^2 = 0.88131\text{cm}^2 \quad \text{(A.10-4)}$$

Then the relative uncertainty of the surface area from rounding errors on the critical dimensions is calculated,

$$err\% = \frac{(0.88131 - 0.83498)}{0.85805} \cdot 100\% = 5.4\% \quad \text{(A.10-5)}$$

A.11 Uncertainty in peak current density data in Yoko at Bailey (1984)

The peak current is proportional to the surface area of the working electrode and the concentration of the electroactive species. Therefore, the error in both measurements will propagate to the current density,

$$i_p \propto A \cdot C_{CrF_3} \quad \text{(A.11-1)}$$

Then error propagates as,

$$\Delta i_p = \sqrt{\left(\left(\frac{\partial i_p}{\partial A}\right)\Delta A\right)^2 + \left(\frac{\partial i_p}{\partial C_{CrF_3}}\Delta C_{CrF_3}\right)^2} \quad \text{(A.11-2)}$$

where Δ corresponds to the relative error on the measured variable. Thus, the actual uncertainty on the measured peak current is,

$$\Delta i_p = \sqrt{(0.054)^2 + (0.125)^2} \cdot 100\% = 13.7\% \quad \text{(A.11-3)}$$

This matches closely with Yoko and Bailey's comment in their discussion, noting that their measured diffusivities have an uncertainty of 20%. To obtain this uncertainty in diffusivity, the peak current uncertainty must have larger contributions from either the concentration, the surface area, or both. Assuming the remaining uncertainty is all from the electrode surface area, we calculate,

$$\Delta A = \sqrt{\Delta i_p^2 - \Delta C_{CrF_3}^2} \cdot 100\% \approx 15.6\% \quad \textit{(A.11-4)}$$

It is believable that there would be on the order of 10% uncertainty in reporting the electroactive surface area of an electrode as there is roughness in the real object that makes the geometric area deviate from the actual area. Yoko and Bailey do not mention that temperature uncertainties are in their results, but we can assume there is some temperature uncertainty as well.

A.12 Surface concentration in Fatouros and Krulic Model

In the Fatouros–Krulic model, the metal-deposition response is described using dimensionless quantities for reversible deposition on a dissimilar substrate, and the model explicitly accounts for underpotential

adsorption and iR effects. One parameter of importance is the surface concentration of reduced species, Γ_1 which has been calculated electrochemically by two independent methods. Khrushcheva and Tarasevich [153] determined a compact monolayer of hydrogen on a Pt electrode had a charge density of approximately 210 and μC/cm^2. This charge density corresponds to a total number of adsorbed H atoms,

$$N_H = \frac{Q_H}{F} = 2.18 \times 10^{-9} \text{ mol H cm}^{-2} \quad \text{(A.12-1)}$$

Because hydrogen adsorption is a 1 to 1 process on Pt, this corresponds to a Pt monolayer of approximately

$$\Gamma_{ML} = 2 \times 10^{-9} \text{ mol cm}^{-2} \quad \text{(A.12-2)}$$

Ohm and Domke [154] show the charge density of Cu on Au(111) corresponds to,

$$Q_{Cu,ML} = 0.35 \; to \; 0.46 \; mC \; cm^{-2} \quad \text{(A.12-3)}$$

So the lower and upper monolayer densities are,

$$N_{Cu} = \frac{Q_{Cu}}{2F} = 1.81 \; to \; 2.38 \times 10^{-9} \; mol \; cm^{-2} \quad \text{(A.12-4)}$$

Both methods agree the order of magnitude for a monolayer formatting on inert electrodes is 2×10^{-9} mol cm^{-2}. Therefore, estimating the surface concentration for the Fatouros and Krulic analysis of SWV data, we can use 1×10^{-9}mol cm^{-2} as the surface concentration for the formation of a sub-monolayer. Sensitivity analysis spanning two orders of magnitude, 10^{-8} to 10^{-10} mol cm^{-2} will sufficiently cover the regimes of when metal deposition reactions are in the range of $\chi < 1$, $\chi = 1$, and $\chi > 1$.

A.13 Natural-Convection Velocity and Boundary-Layer Estimate

The goal of this analysis is to estimate whether natural convection around an electrode in molten salt can plausibly establish a thin concentration boundary layer on the order of 10 to 50 μm. This estimate is useful for interpreting chronopotentiometric transition times using a finite diffusion-layer model rather than the semi-infinite Sand equation.

The following values were used:

Quantity	Symbol	Value
Bulk salt temperature	T_{bulk}	800 deg C
Hot local salt temperature	T_{hot}	850 deg C

Quantity	Symbol	Value
Characteristic wall/electrode length	L	3 cm = 0.03 m
Gravitational acceleration	g	9.81 m/s^2
Representative chromium-species diffusivity	D	1×10^{-9} m^2/s

The FLiBe density was estimated using the linear density correlation reported by Vidrio et al. for molten FLiNaK:

$$\rho_{FLiNaK} = 2579.3 - 0.624T_C \tag{A.13-1}$$

where ρ is in kg/m^3 and T is in ºC. At 800ºC and 750ºC, the density is respectively,

$$\rho(800) = 1909.7\frac{kg}{m^3} \tag{A.13-2}$$

$$\rho(750) = 1940.9\frac{kg}{m^3} \tag{A.13-3}$$

Therefore, the density difference and average value is respectively,

$$\Delta\rho = 31.2\frac{kg}{m^3} \tag{A.13-4}$$

$$\rho_{avg} = 1925.3\frac{kg}{m^3} \tag{A.13-5}$$

The reduced gravity associated with the density difference is:

$$g' = \frac{g\Delta\rho}{\rho_{avg}} = 0.159\frac{m}{s^2} \tag{A.13-6}$$

A characteristic buoyancy velocity scale over a wall or electrode length L is:

$$U_{nc} = \sqrt{g'L} = 0.069\frac{m}{s} \approx 7\frac{cm}{s} \tag{A.13-7}$$

Therefore, the natural-convection velocity scale around a 3 cm electrode or wall section is expected to be on the order of 1 to 10 cm/s, with this simple buoyancy estimate giving approximately 7 cm/s. For mass transfer near the electrode, a simple convective-diffusive estimate of the concentration boundary-layer thickness is:

$$\delta_c \sim \sqrt{\frac{DL}{U_{nc}}} \tag{A.13-8}$$

Using a diffusivity in the range of,

$$D = 1 \times 10^{-9} \text{ to } 1 \times 10^{-8} \text{ m}^2 \text{ s}^{-1} \quad \text{(A.13-9)}$$

With a length scale around $L = 0.03$ m and velocity area $U_{nc} = 0.07$ m s^{-1}, we calculate a boundary layer thickness:

$$\delta_c \sim \sqrt{\frac{(1\times10^{-9})(0.03)}{0.057}} = 2.1 \times 10^{-4}\, m \approx 21\mu m \quad \text{(A.13-10)}$$

$$\delta_c \sim \sqrt{\frac{(1\times10^{-8})(0.03)}{0.057}} = 6.5 \times 10^{-4}\, m \approx 65\mu m \quad \text{(A.13-11)}$$

This estimate falls directly around the assumed 25 to 50 μm concentration boundary-layer range used in the finite diffusion-layer chronopotentiometry analysis.

Appendix B. Supplementary Data & Figures

B.1 Measured Current and Power Curves for Variac Controllers

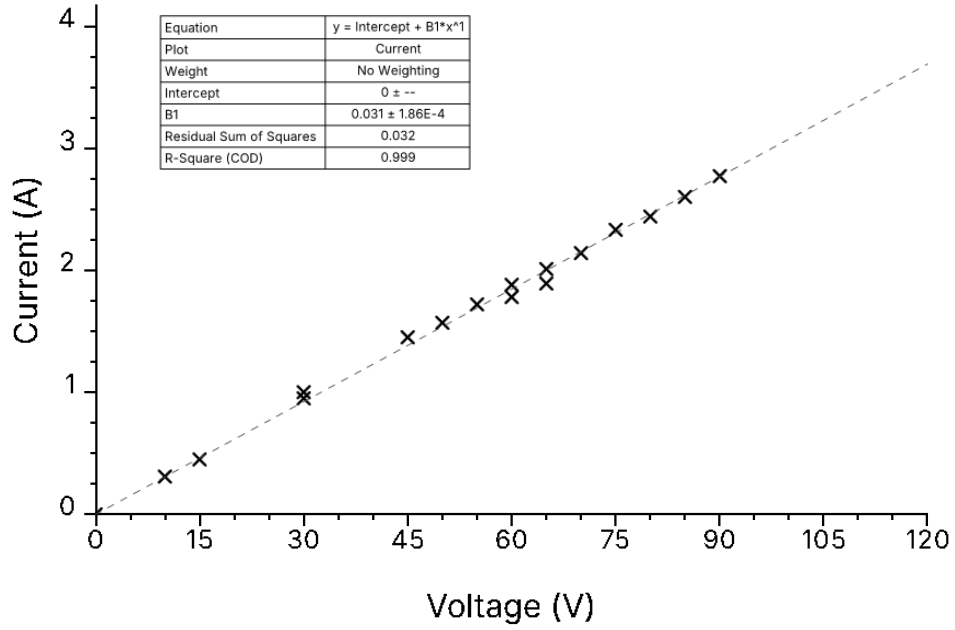


Figure 102. Current curve as a function of voltage on variable power controller. The controller output follows Ohm's law within the range of tested outputs.

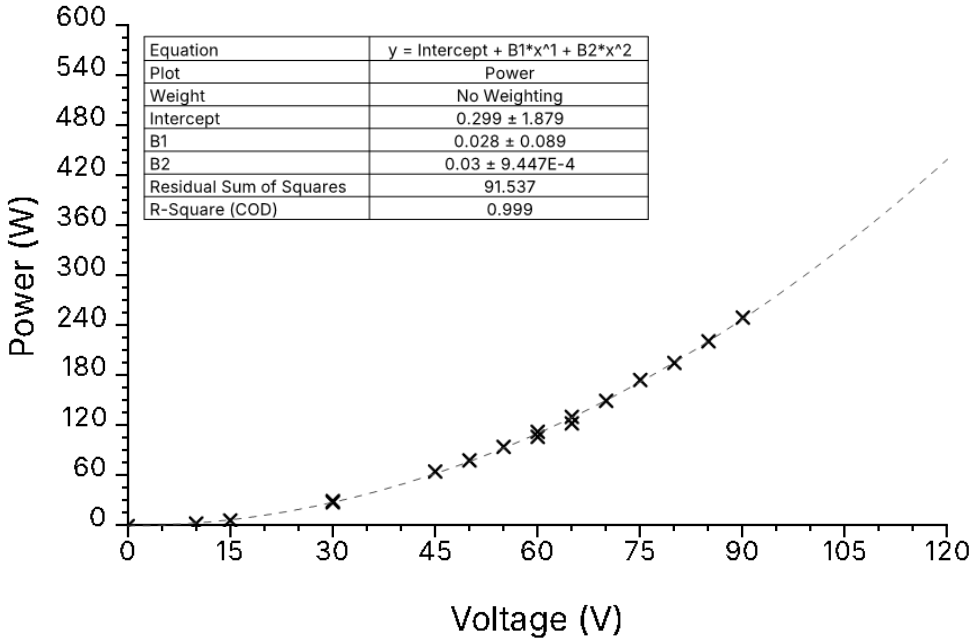


Figure 103. Power curve as a function of voltage on variable power controller. The controller output follows $P = V^2/R$ within the range of tested outputs.

B.2 Wiring Diagram for PID Controllers

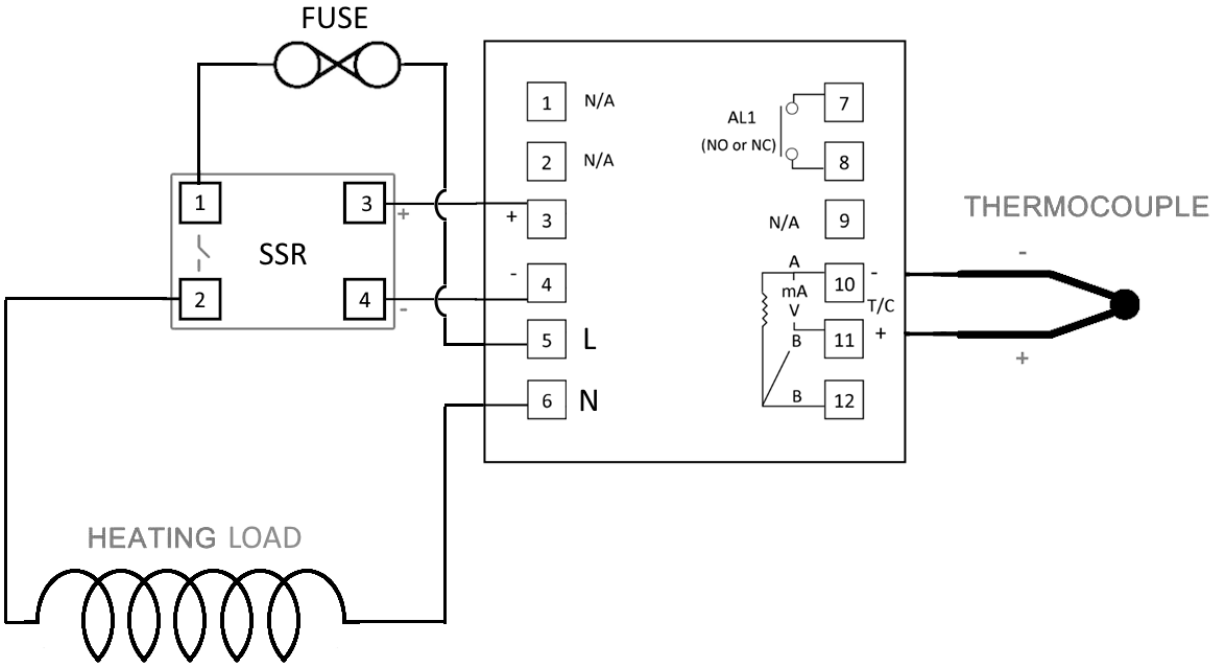


Figure 104. Wiring diagram of HTS Amptek PID Module installed in lab assembled controllers.

B.3 Dynamic Pressure Losses through Fittings

When sizing pipe for fluid flow, the dynamic pressure drop across a region of pipe fittings can be modeled as an equivalent "length over diameter" of straight pipe. The L/D factors in this work were calculated using the table below. Values from this table were taken from Levenspiel[13].

FITTING IDENTIFICATION			**L/D Factors**							**K Factors**	
ColRow	Description	Name	Water	Glycol	Brine	Diesel	Petrol	Steam	Gas	Coeff C	Expon E
A8	90 deg Elbow: Regular Screwed	EL90-RG-SC	45	53	61	45	36	30	35	1.5	-0.6092
A9	90 deg Elbow: Long Radius Screwed	EL90-LR-SC	25	29	34	25	20	15	20	0.75	-0.8787
A10	90 deg Elbow: Regular Flanged	EL90-RG-Fl	45	53	61	45	36	30	35	0.45	-0.253
A11	90 deg Elbow: Long Radius Flanged	EL90-LR-FL	25	29	34	25	20	15	20	0.4	-0.463
A12	45 deg Elbow: Regular Screwed	EL45-RG-SC	25	29	34	25	20	20	25	0.35	-0.1365
A13	45 deg Elbow: Regular Flanged	El45-RG-FL	15	18	20	15	12	15	20	0.22	-0.1414
A14	Return U-Bend: Regular Screwed	BEND-RG-SC	90	105	123	90	72	70	75	1.35	-0.5
A15	Return U-Bend: Regular Flanged	BEND-RG-FL	90	105	123	90	72	70	75	0.425	-0.255

A16	Return U-Bend: Long Radius	BEND-LR-SC	50	59	68	50	40	45	45	0.426	-0.5182
A17	Tee: Line Flow Screwed	TEE-LF-SC	20	24	27	20	16	20	25	0.9	0
A18	Tee: Branch Flow Screwed	TEE-BF-SC	65	76	89	65	52	65	70	1.85	-0.3747
A19	Tee: Line Flow Flanged	TEE-LF-FL	20	24	27	20	16	20	25	0.265	-0.4695
A20	Tee: Branch Flow Flanged	TEE-BF-FL	65	76	89	65	52	65	70	1	-0.2851
A21	Strainer: Basket	STRAINER	90	105	123	90	72	70	75	2.4	-0.5609
A22	Union / Coupling	UNION	45	53	61	45	36	30	35	0.083	-0.6644
A23	Inlet: Bell-Mouthed	INLET-BM	20	24	27	20	16	20	25	0.05	0
A24	Inlet: Square-Edged	INLET-SE	45	53	61	45	36	30	35	0.5	0
A25	Outlet: All Types	OUTLET	65	76	89	65	52	65	70	1	0

B.4 Pseudo Code for Calculating the mass flow rate and inventory of the salt loop

We began by selecting the salt inventory and determining salt properties. This information came from the design specifications from ThorCon's secondary heat exchanger system which used NaF-BeF_2 (43mol% - 57mol%). Flow rate in a natural circulation loop circuit is a strong function of the fluid density, thermal conductivity, heat capacity, viscosity, and thermal expansion coefficient. Using Eq.(2.27) and Eq.(2.28), we selected a temperature rise across the loop and a heater power input to solve each equation independently. We restricted the overall dimensions and geometry of the loop in order to further constraint the mass flow rate equations. In a glove box, the overall size of the loop is severely constrained and cannot exceed the space designated for the loop and its instrumentation. The maximal dimensions in our glove box are 72.0cm x 38.1cm x 152cm (34in x 18in x 60in). We proposed a set difference in elevation of the heat reservoir and the heat sink, Δz_{NC} to be anywhere between 45.7cm to 91.4cm (18in to 36in).

At this stage of the design, we considered several options for the nominal diameter of the main loop circuit. The primary tradeoff was that larger-diameter piping would allow for greater integration of corrosion coupons and instrumentation. However, increasing the pipe diameter also raises the required salt inventory and the heater power needed to operate the loop. To evaluate these competing factors, we incorporated a range of standard pipe and tube dimensions into our mass flow calculations. We then constrained the design space by applying limits on the maximum allowable heater power and the minimum allowable tube diameter.

The process of iterating a design can become complicated without the use of a designed calculator which the parameters can be tweaked easily without needing to repeat every calculation from scratch. For the purposes of our design, an Excel workbook was sufficient for our calculations. After choosing the final

design parameters, a Python script was created to make the design process more practical in the future both internally in the research group and externally if other groups want to use the same method of calculations.

Original designs consisted of larger diameter pipe to mimic more closely the ORNL MSRE loop designs. After iterating calculations with 2NPS pipe dimensions, we concluded very quickly that the power requirements would be outside of our ability to cool in a glovebox. An example calculation is shown below using the 2NPS pipe dimensions. The results are shown to show the rationale for making certain finale decisions. Materials properties are withheld from this summary as they are provided by a ThorCon materials correlation report not yet available for public disclosure. The resulting mass flow rate, heater power, and total loop volume are available for disclosure because they are the result of the design process.

ID = 5.25 cm [2.067 in.]
L_1 = 61.0 cm [24 in.]
L_2 = 45.7 cm [18 in.]
L_3 = 81.3 cm [32 in.]
L_4 = 48.3 cm [19 in.]
$m_{(n+1)} = 2\rho_0^2 g\beta (\Delta z_{NC} \Delta T_h)/(F' (Re(m_n,T)))$
$F' (Re(m_n,T)) = C_i f(Re)$
$C_i = (1/A^2)(L_i/D)$
$f = 64/Re$
$Q = m_n C_{p,h} \Delta T_h = 3$ kW

The maximum allowable heater power in the glovebox is 3 kW due to overheating concern. We calculate ΔT_h using this procedure.

The calculation converges when $m_n \approx m_{n+1}$

initial guess,
$m_0 = 0.01$ kg/s
$\Delta T_h = 78$ K

This temperature rise is lower than the necessary design specifications. After converging, the temperature rise will not increase.

final flow rate,
$m_{NC} = 0.023$ kg/s
$\Delta T_h = 60$ K

total salt inventory,
m = 15.5 kg

These parameters result in a system that does not meet the functional requirements. Therefore, the next iteration will isolate one of the parameters, for example the inner diameter of the piping, and then rerun the

computation. This process will be continued until the operating parameters meet the functional requirements.

B.5 EIS of Echem Probe in Aqueous Solution

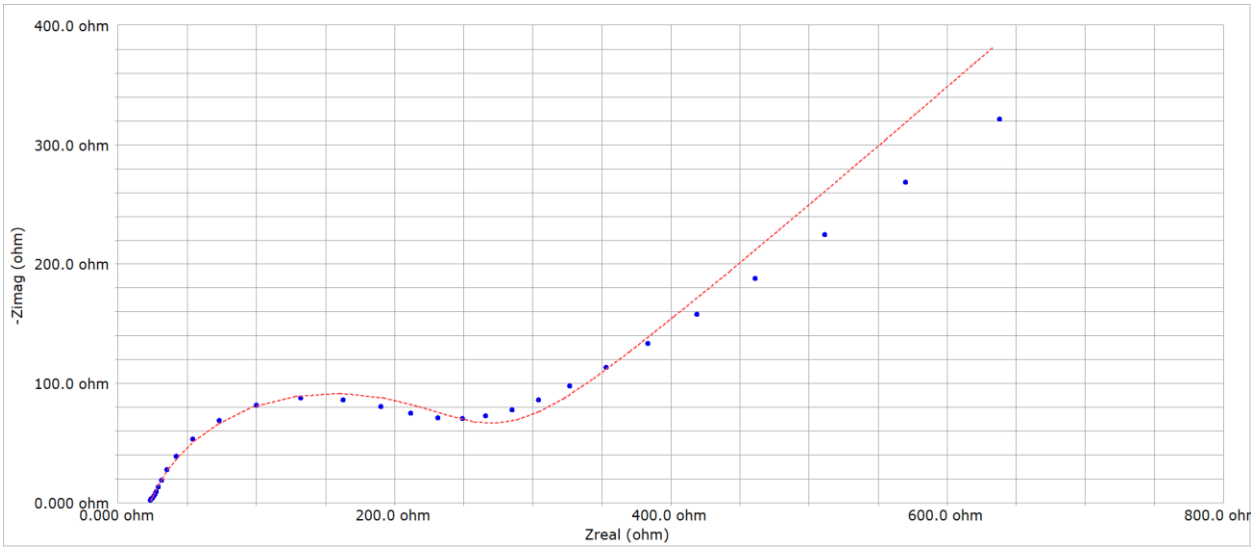


Figure 105. EIS data of Echem probe in 0.01M $K_3[Fe(CN)_6]$ and 0.1 M KCl at 25°C. Pt WE, Pt CE, Pt qRE, Au AuxE. R_u is approximately 20Ω from the CPE with diffusion model fit (red dashed line).

B.6 Images of Echem Probe in Experiments

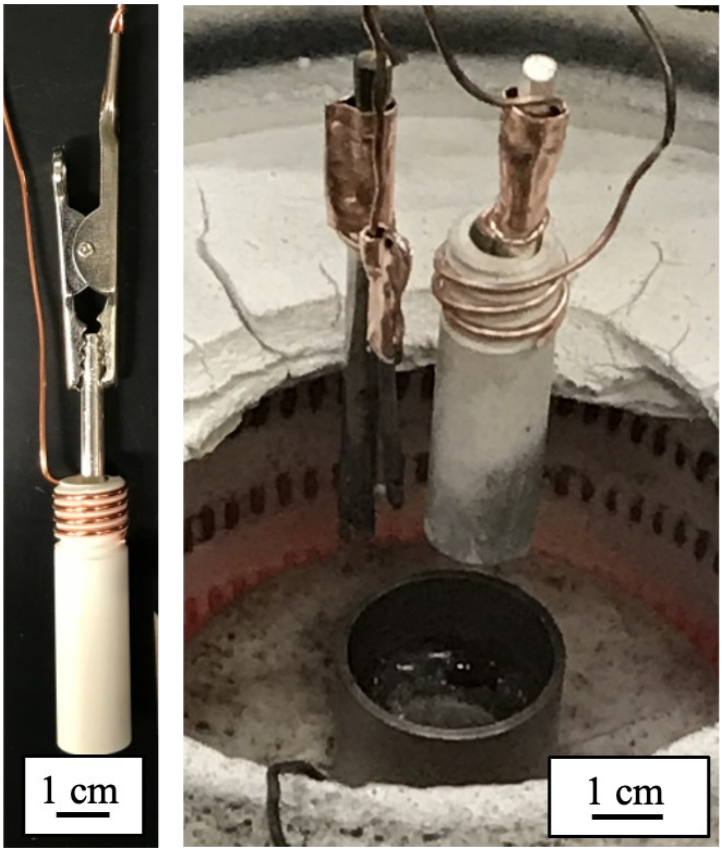


Figure 106. (left) Ag^+/Ag TRE in BN crucible. (right) Ag^+/Ag TRE, Ni CE, and Pt WE tested in FLiNaK at 600°C in a Ni crucible

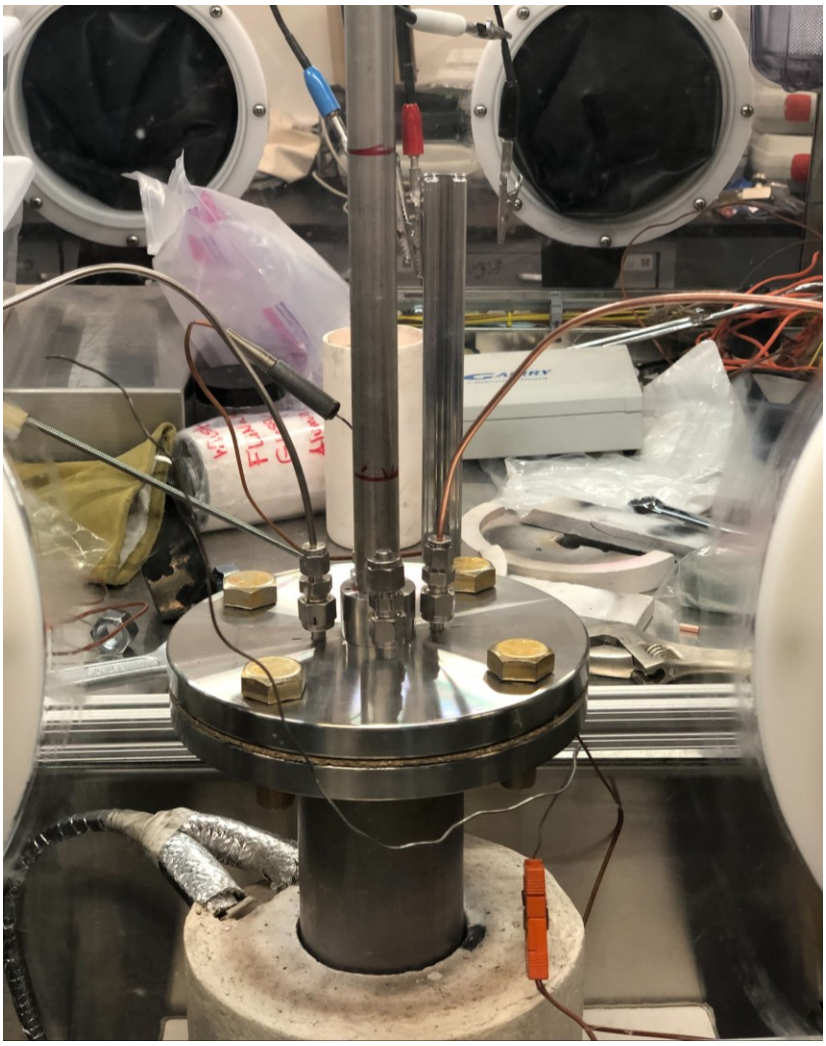


Figure 107. Electrochemical probe for FLiBe experiments installed in gas-tight cell in the beryllium glovebox-train. Echem probe is the central tube in the flange lid.

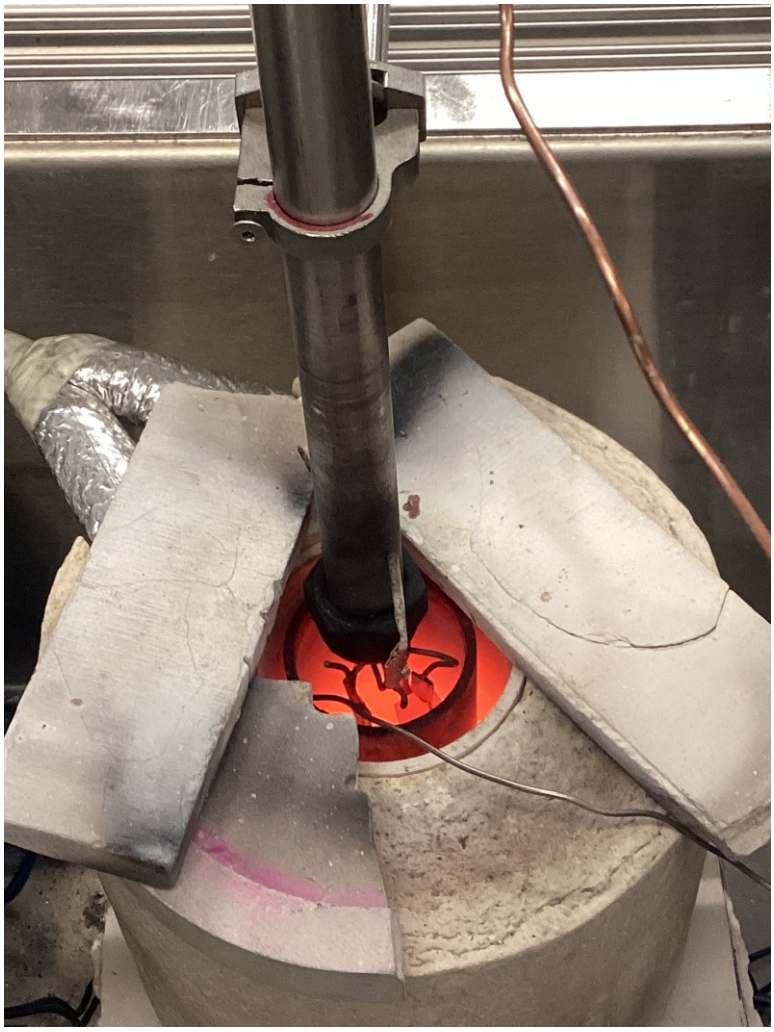


Figure 108. Electrochemical probe used for E-TDS experiments. Electrodes (graphite WE, GC CE, Ag, RE) are immersed in FLiBe at approximately 900°C.

B.7 Wire Electrode vs Printed Electrode Cyclic Voltammogram

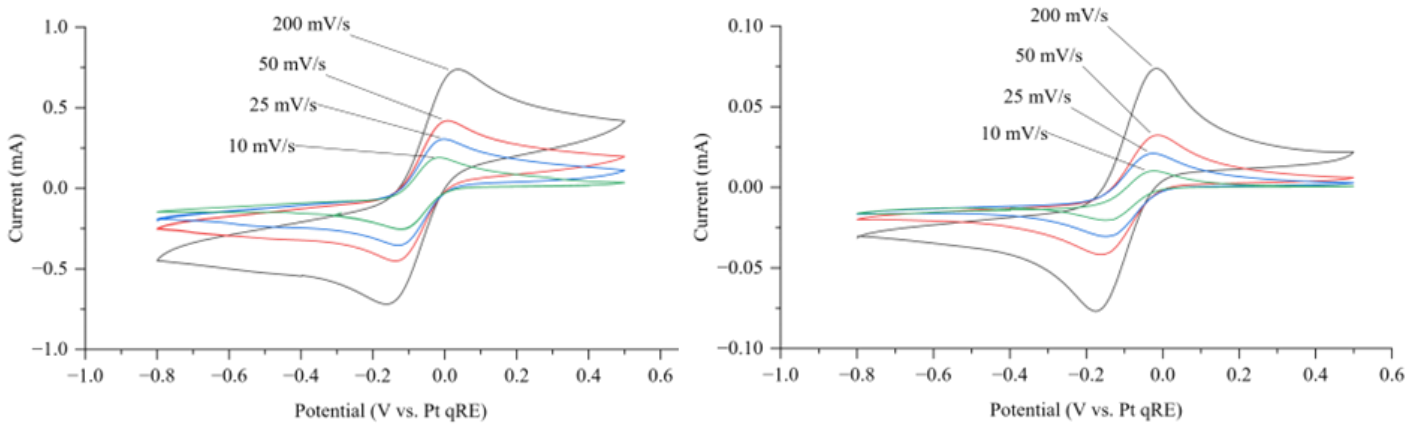
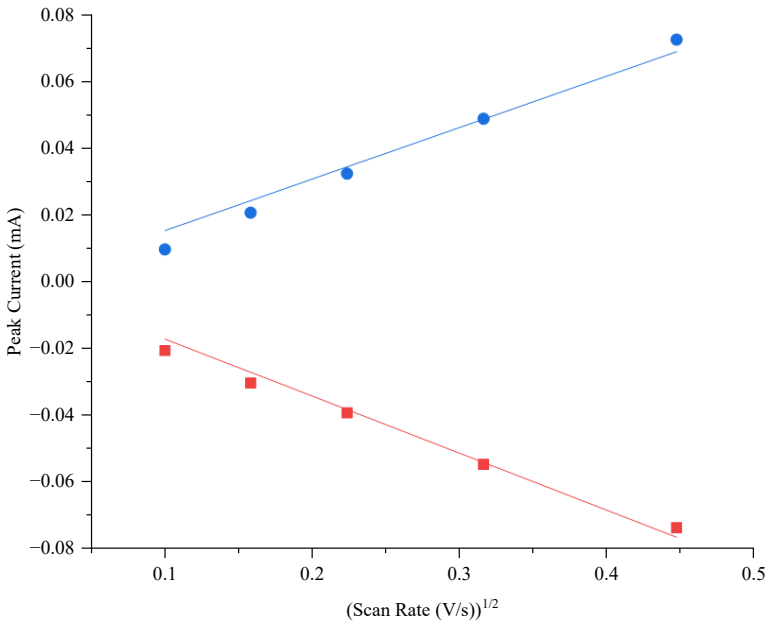


Figure 109. Cyclic Voltammograms from two separate electrochemical sensors in an aqueous solution of 0.01 M K3[Fe(CN)6] and 0.1 M KCl. The [Fe(CN)6]4-/[Fe(CN)6]3- redox reaction being probed is previously characterized on printed electrodes by prior literature [3]. The position of the peak potential may shift due to the drift of the quasi-reference Pt electrode. Current is reported because effective surface area and surface roughness of the electrodes was not determined, since surface roughness of the electrodes was not measured. (a) CV polarogram measured by the tradition wire electrodes. (b) CV polarogram measured by the printed electrodes. See Table 20 for printed electrode surface areas.



Equation	y = a + b*x	
Plot	Peak Reducing Current	Peak Oxidizing Current
Weight	No Weighting	
Intercept	0 ± --	0 ± --
Slope	-1.711E-4 ± 4.556E-6	1.544E-4 ± 6.407E-6
Residual Sum of Squares	3.197E-11	6.323E-11
Pearson's r	-0.999	0.997
R-Square (COD)	0.997	0.993
Adj. R-Square	0.996	0.991

Figure 110. Peak oxidizing and reducing currents from CV scans with the printed electrode chip in in an aqueous solution of 0.01 M $K_3[Fe(CN)_6]$ and 0.1 M KCl. The slope of the line is proportional to the square root of the diffusivity of the ionic species given by the Randels-Sevcik equation.[33]

B.8 Printed Electrode CV in FLiNaK

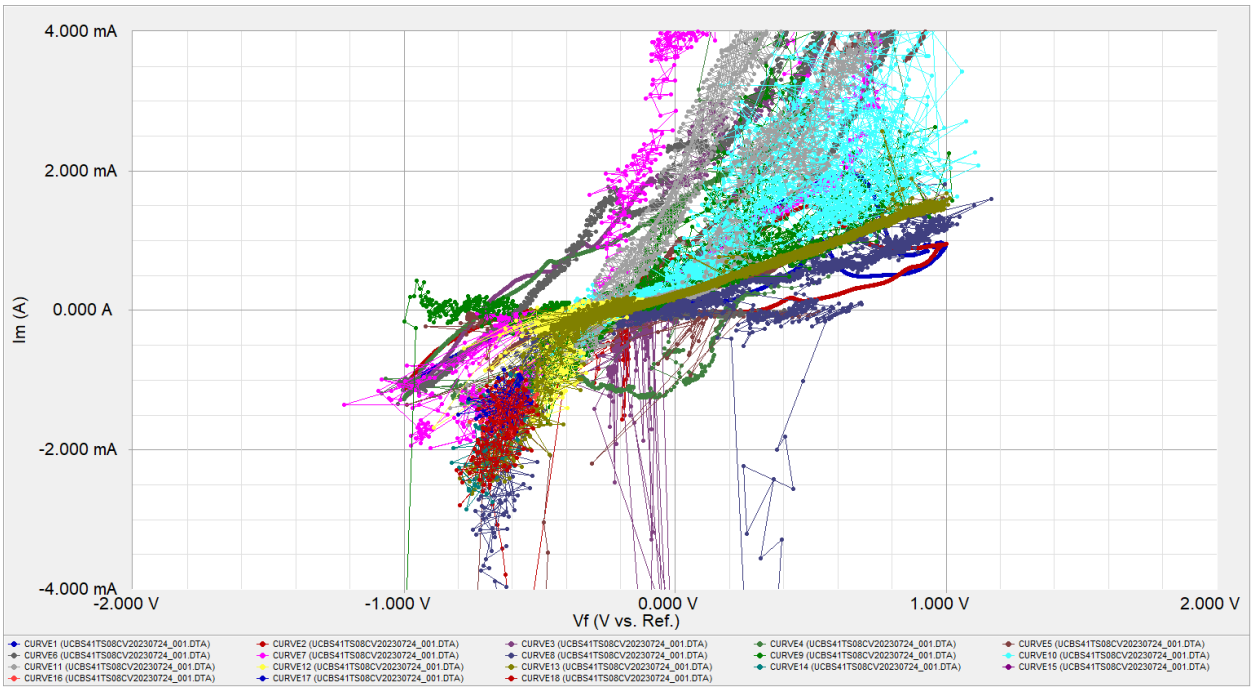


Figure 111. Cyclic voltammogram of FLiNaK droplet (~700 mg) at 550ºC on printed electrode sensor, configuration 6 in Table 20. Repeated cycles were conducted at 100 mV/s, and after each cycle the noise of the scan would increase. After 12 cycles, the scans failed in the window around -0.7V vs Ref and -2mA. Examining this electrode post experiment it became clear it was badly damaged and the electroactive area was not functioning properly.

B.9 CV of FLiBe with Impurities at Varying Potential Window

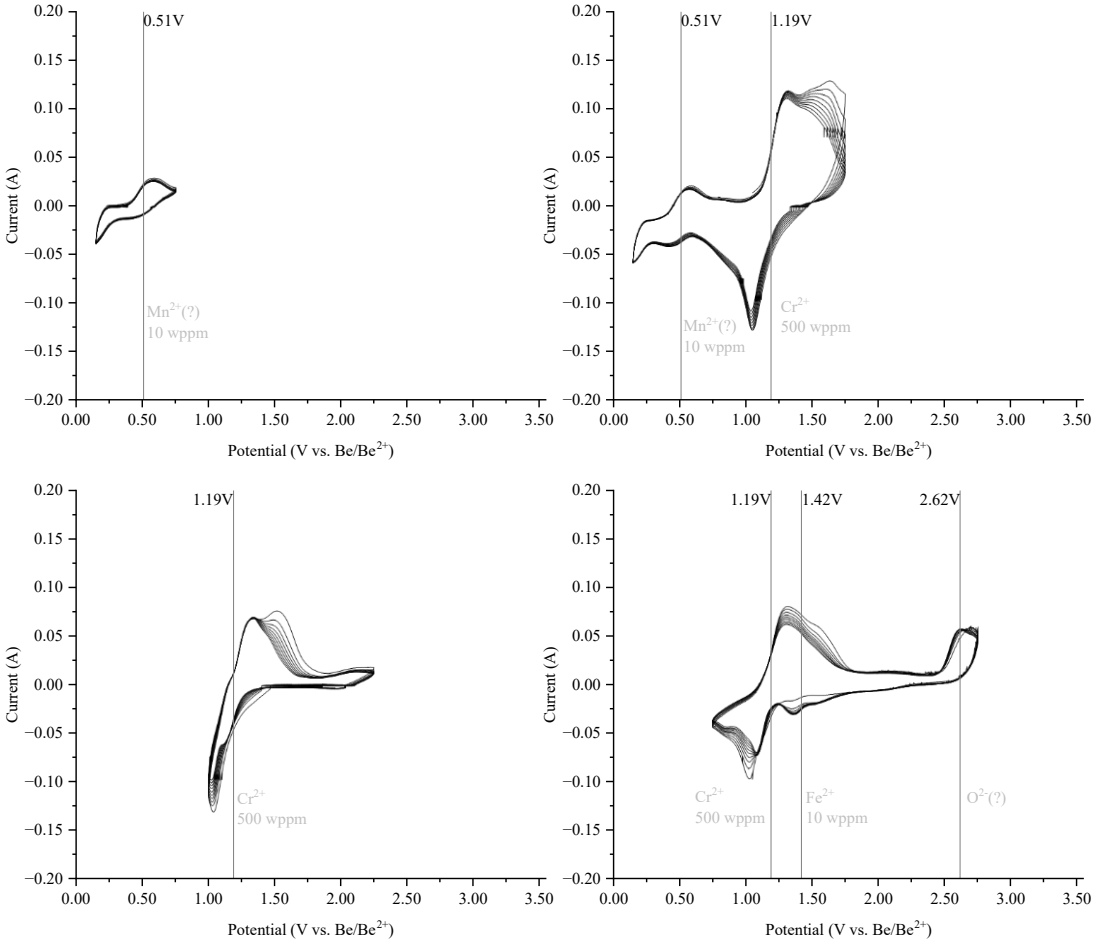


Figure 112. Cyclic voltammograms of FLiBe with trace oxidants at 600ºC. The electrode used in this cell were Au WE, Au CE, Ag qRE. Scan rate for all four scans was 1 V/s. Each scan covers slightly different potential windows attempting to sandwich particular reactions. The text next to each vertical line indicated a proposed concentration of cation which would correspond to a given half-cell reaction in FLiBe.

B.10 CV of FLiBe with Impurities at varying scan rate

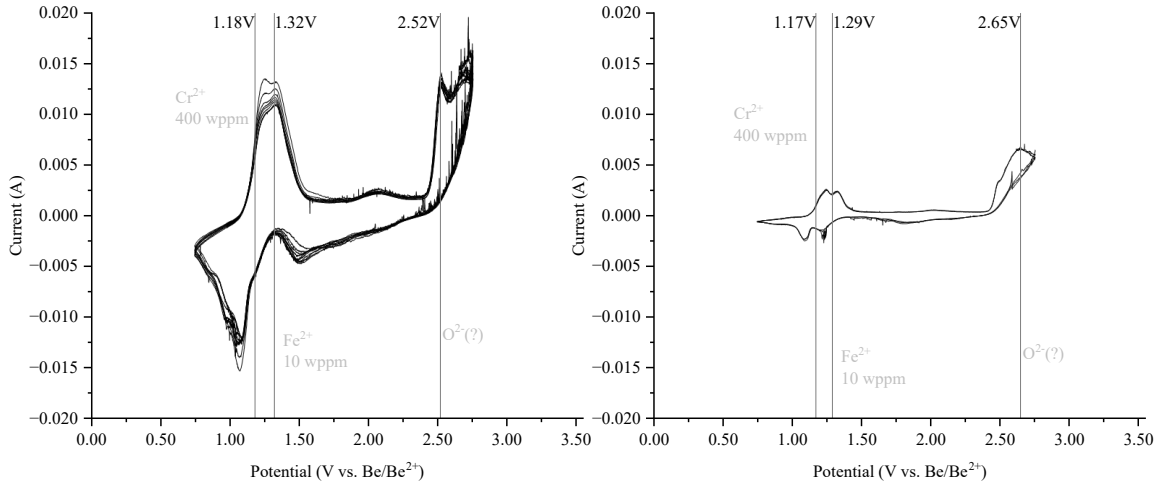


Figure 113. Cyclic voltammograms of FLiBe with trace oxidants at 600ºC. The electrode used in this cell were Au WE, Au CE, Ag qRE. Scan rate for the plot of the left was 100 V/s. The scan rate for the plot on the right was 10 mV/s. The text next to each vertical line indicated a proposed concentration of cation which would correspond to a given half-cell reaction in FLiBe.

B.11 Microscopy and LIBS of Printed Electrodes

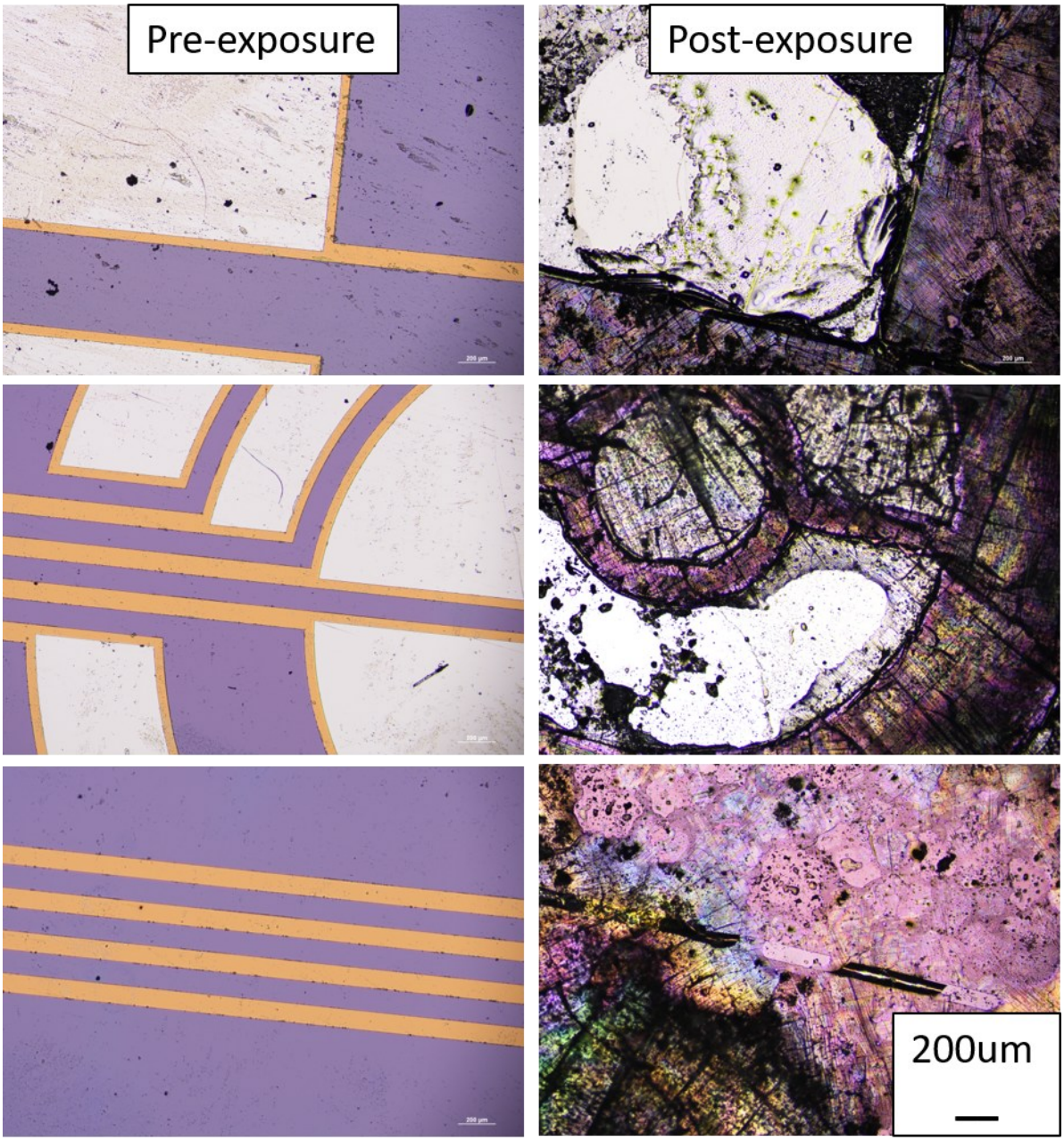


Figure 114. Pre- and post-exposure images of printed electrodes from FLiBe exposure test at 650°C.

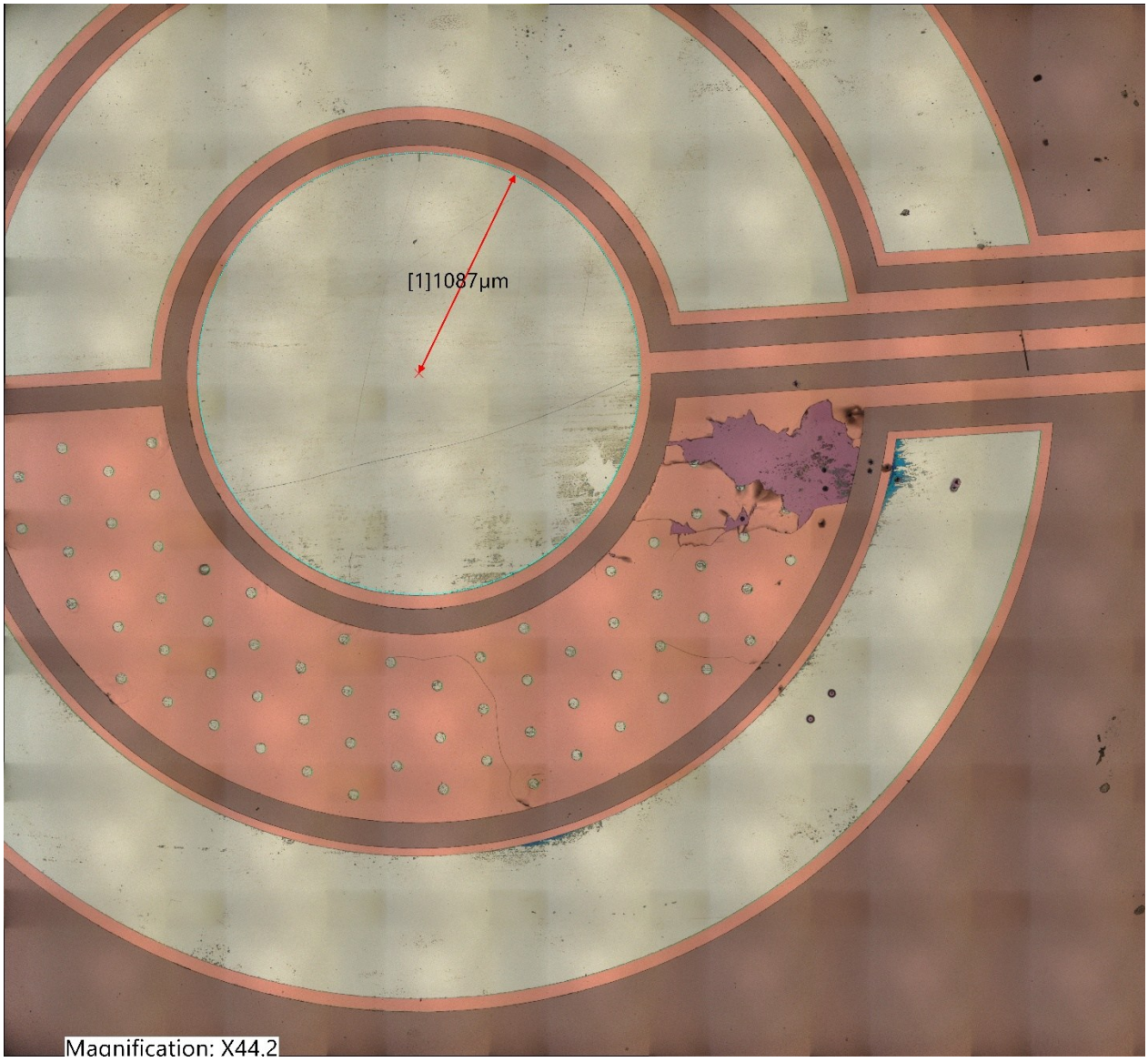


Figure 115. Printed electrode configuration 3 from Table 20. Evidence of a manufacturing defect in the printed electrode. The electrically insulating surface deposit of Si_3N_4 is removed, revealing a subsurface layer of possible SiO_2 or Ni.

Multi-point analysis

No.	Presumed material	Pt	Si	O	N	K
1	Platinum	25.8%	45.0%	29.2%	0.0%	
2	Platinum	64.3%	13.9%	21.8%	0.0%	
3	Silicon compound	6.0%	64.0%	30.0%	0.0%	
4	Platinum	61.7%	15.9%	22.4%	0.0%	
5	Platinum	58.9%	10.4%	19.5%	0.0%	11.2%
6	Silicon compound	5.8%	62.8%	31.4%	0.0%	
7	Silicon compound	7.0%	51.8%	38.1%	0.0%	3.1%
8	Platinum	24.3%	48.9%	25.7%	0.0%	1.1%
9	Silicon compound	5.1%	61.9%	33.0%	0.0%	
10	Platinum compound	18.2%	54.9%	26.9%	0.0%	
11	Silicon compound	6.5%	61.5%	32.0%	0.0%	

*** Nitrogen is not readily detectable with this instrument**

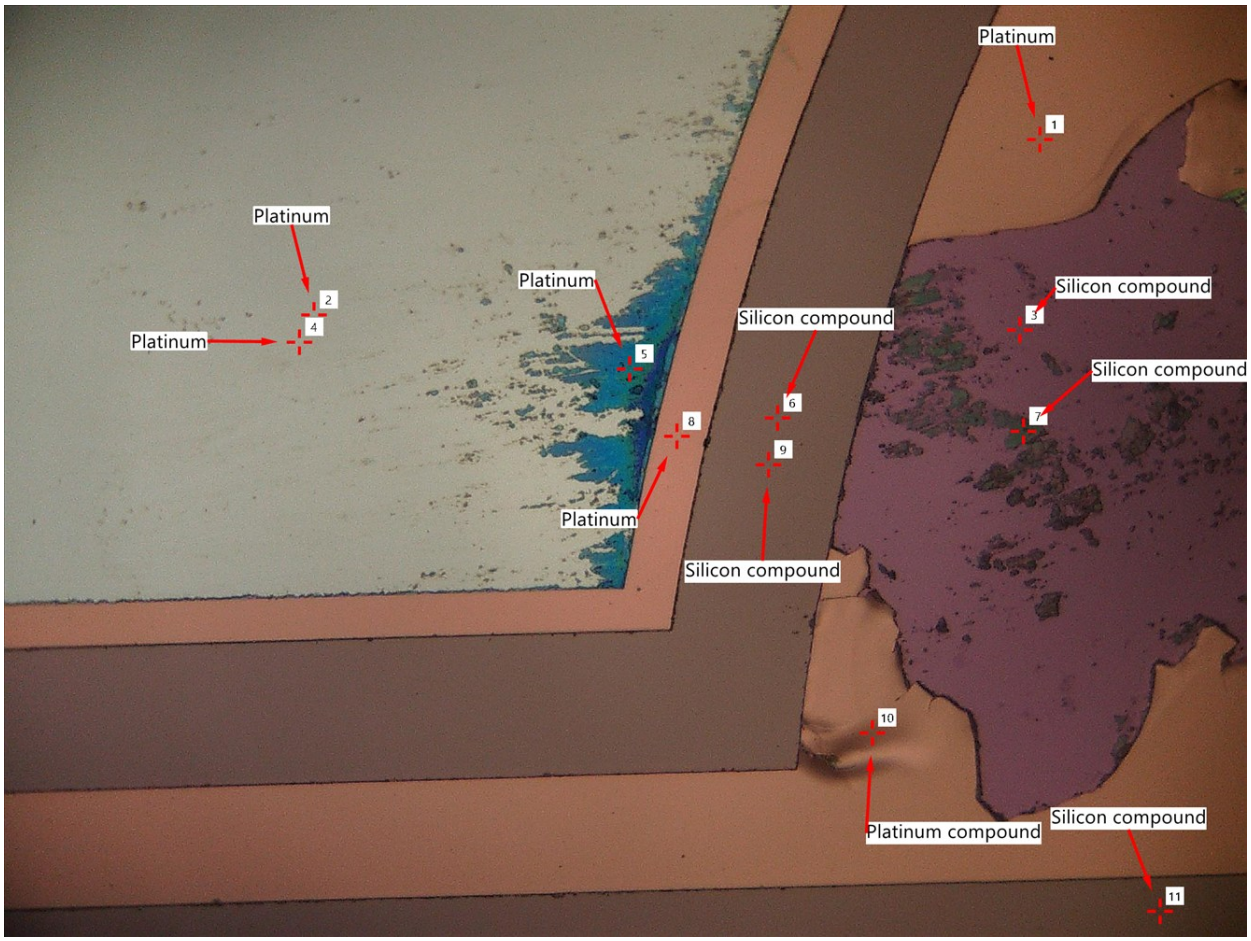


Figure 116. Printed electrode configuration 3 from Table 20. LIBS analysis of different colored regions in the image is provided in the table above.

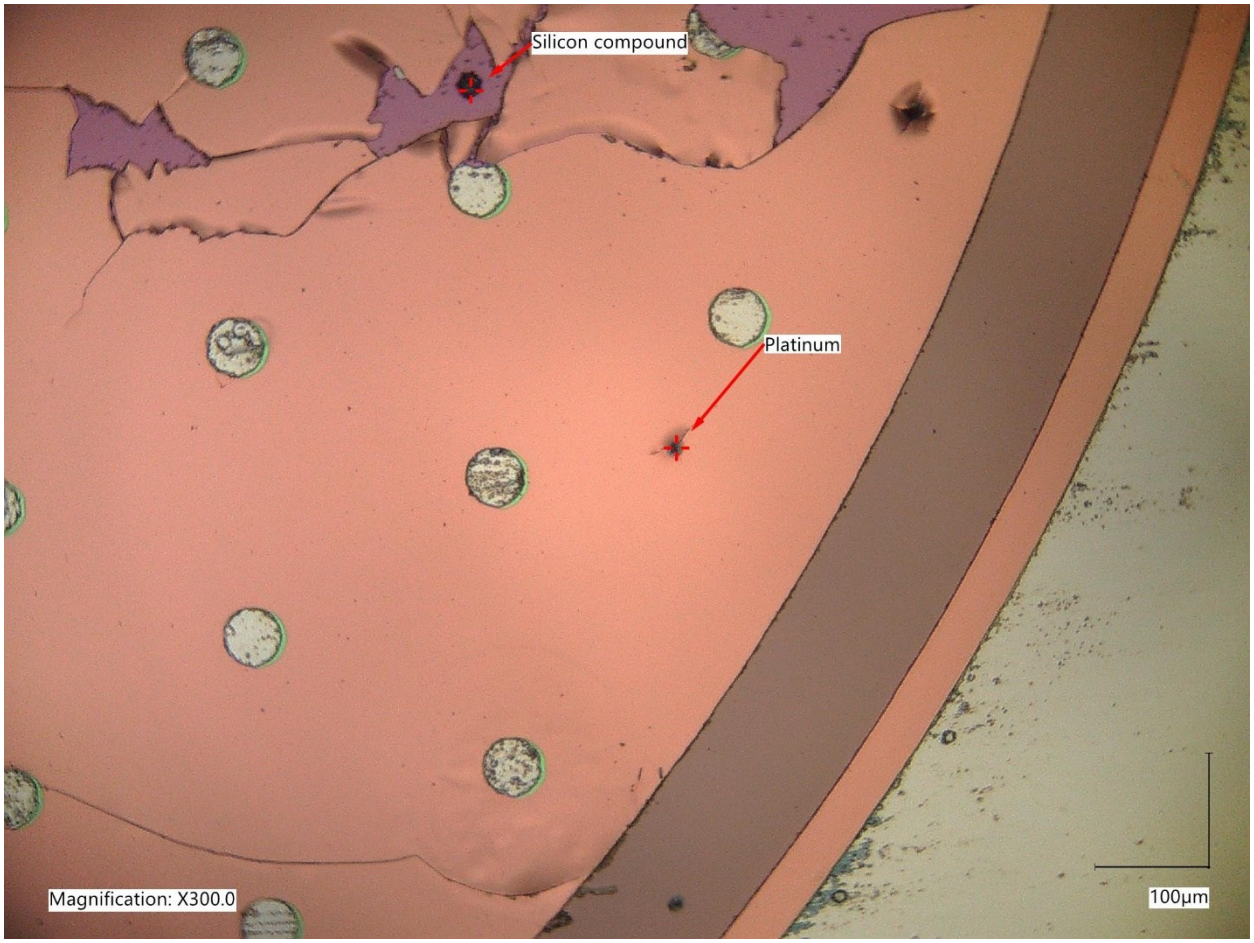


Figure 117. Printed electrode configuration 3 from Table 20. Elemental analysis bulk composition reported from LIBS. The "silicon" compound is likely SiO_2 from the subsurface adhesion layer. The "platinum" indicated by the arrow is surprising because Consiglio[80] did not indicate Pt would be present at that location.

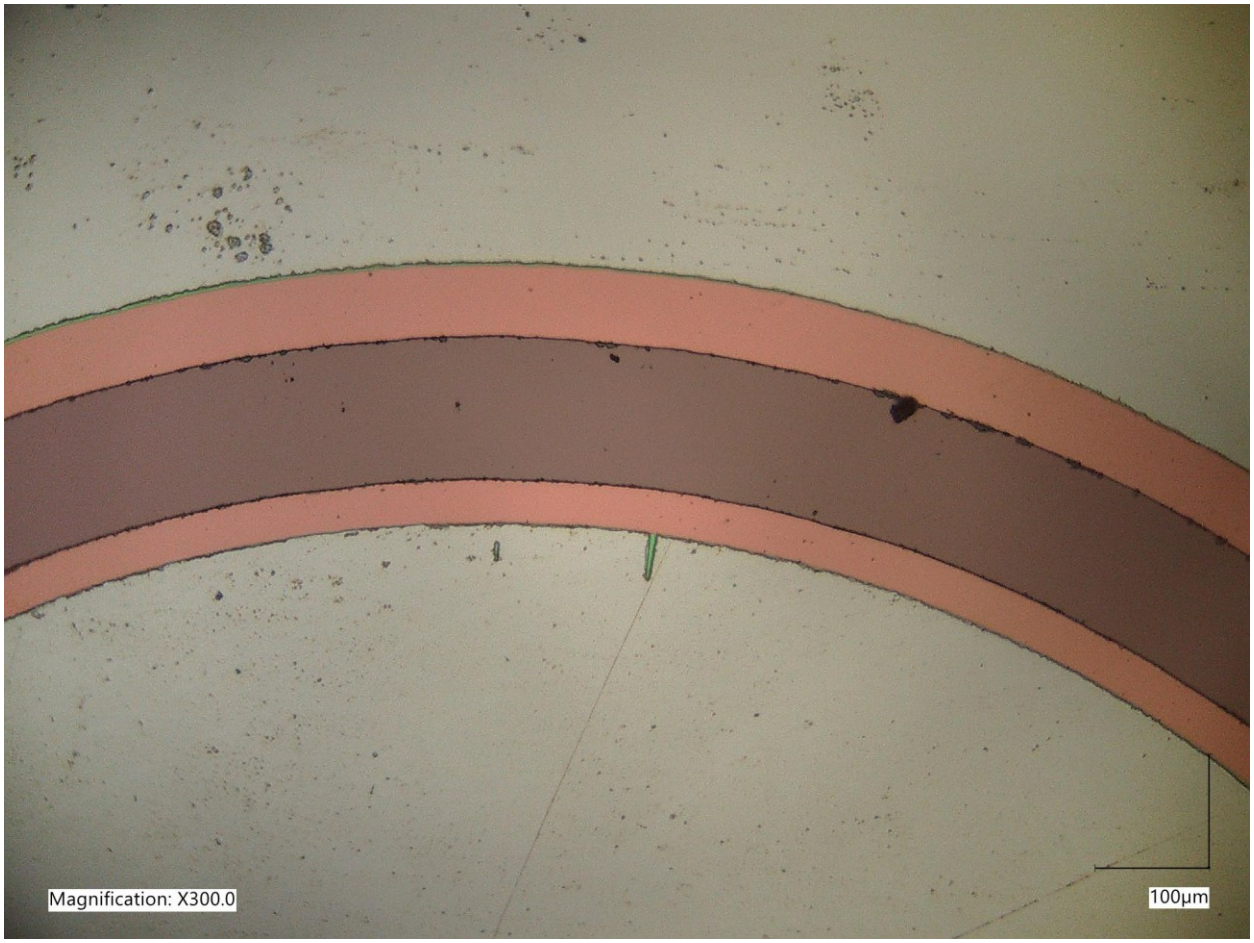


Figure 118. Printed electrode configuration 3 from Table 20. Green "crack" shape in the electroactive layer shows excess deposit of Si_3N_4 bleeding into the electrode region. Green layers are indicative of Si_3N_4 overlapping with Pt. Dark regions are of unknown composition.

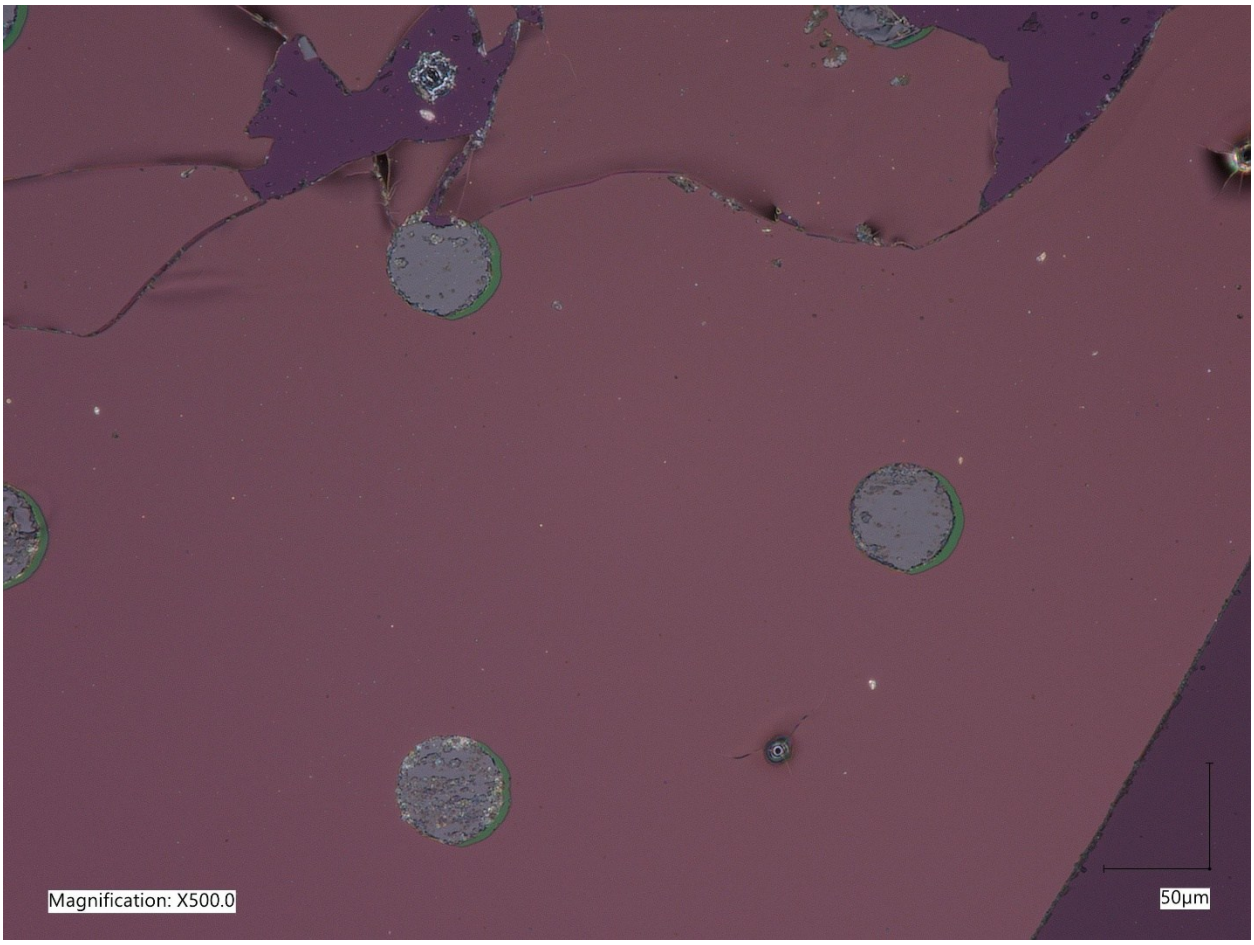


Figure 119. Printed electrode configuration 3 from Table 20. Close up of electroactive surfaces on the WE array. Cracks and delamination of the Si_3N_4 layer are visible. Small black dot near the bottom-right of the image is where the laser from LIBS analysis ablated material. Green layers are indicative of Si_3N_4 overlapping with Pt.

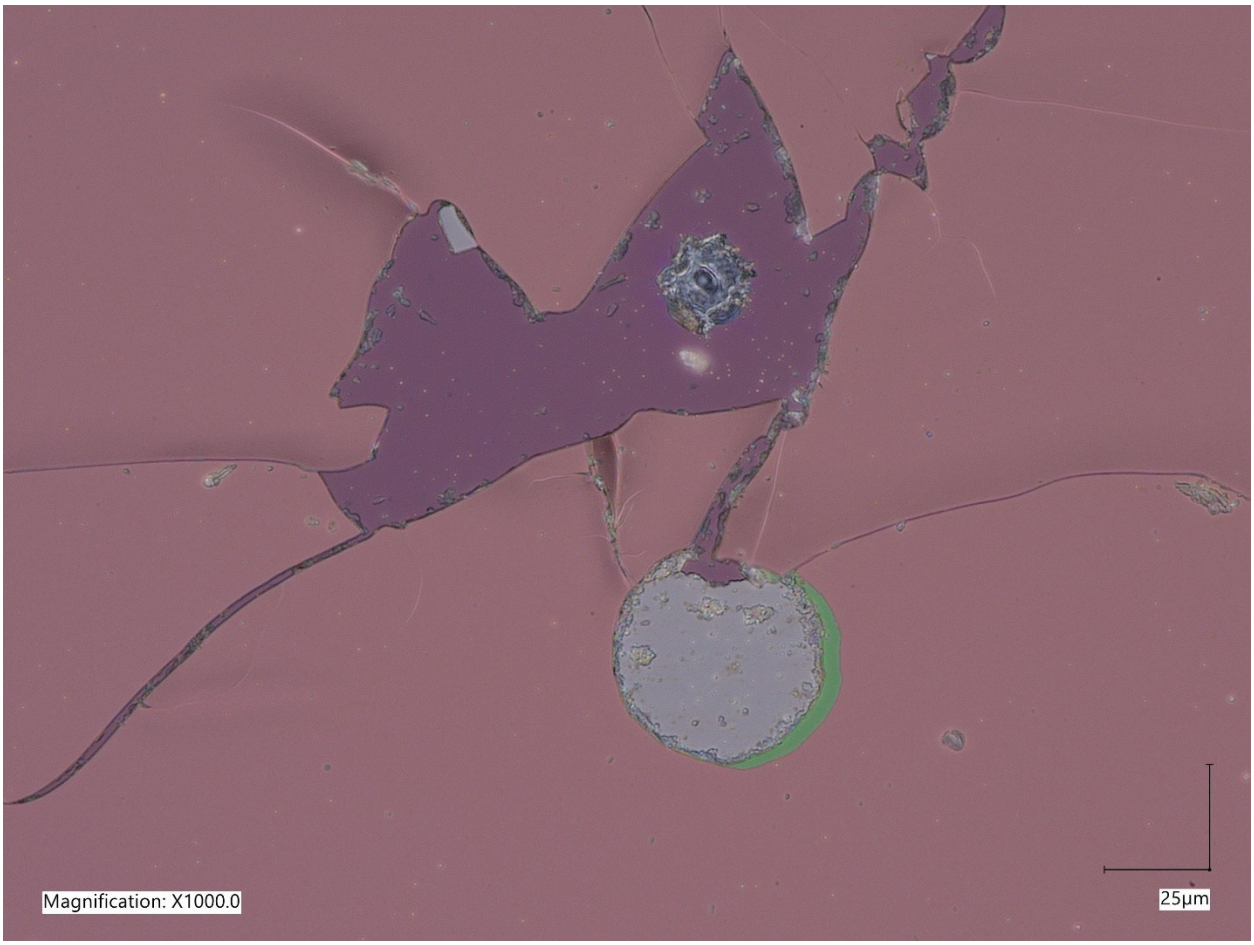


Figure 120. Printed electrode configuration 3 from Table 20Table 20. Close up of individual microelectrode on the WE array. Clear signs of delamination and cracking of the Si_3N_4 layer (pink) are present. Possible signs of Pt surface roughness is seen (grey aberrations in grey disk). Green layers are indicative of Si_3N_4 overlapping with Pt.

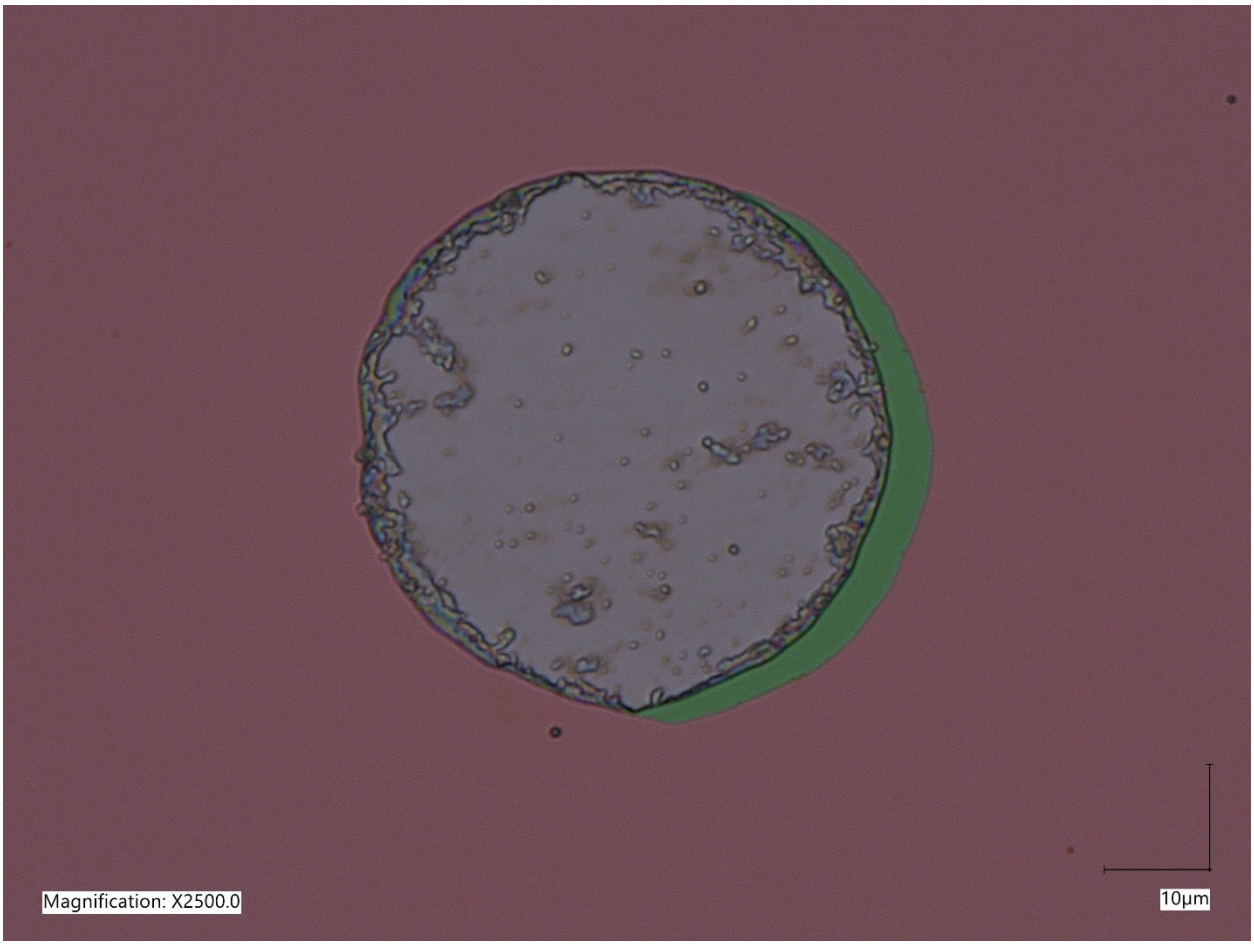


Figure 121. Printed electrode configuration 3 from Table 20. Green layers are indicative of Si_3N_4 overlapping with Pt. Grey disk is the Pt electroactive area. Small translucent bits in the grey disk may be remaining photoresist from fabrication and not indicative of Pt surface roughness.

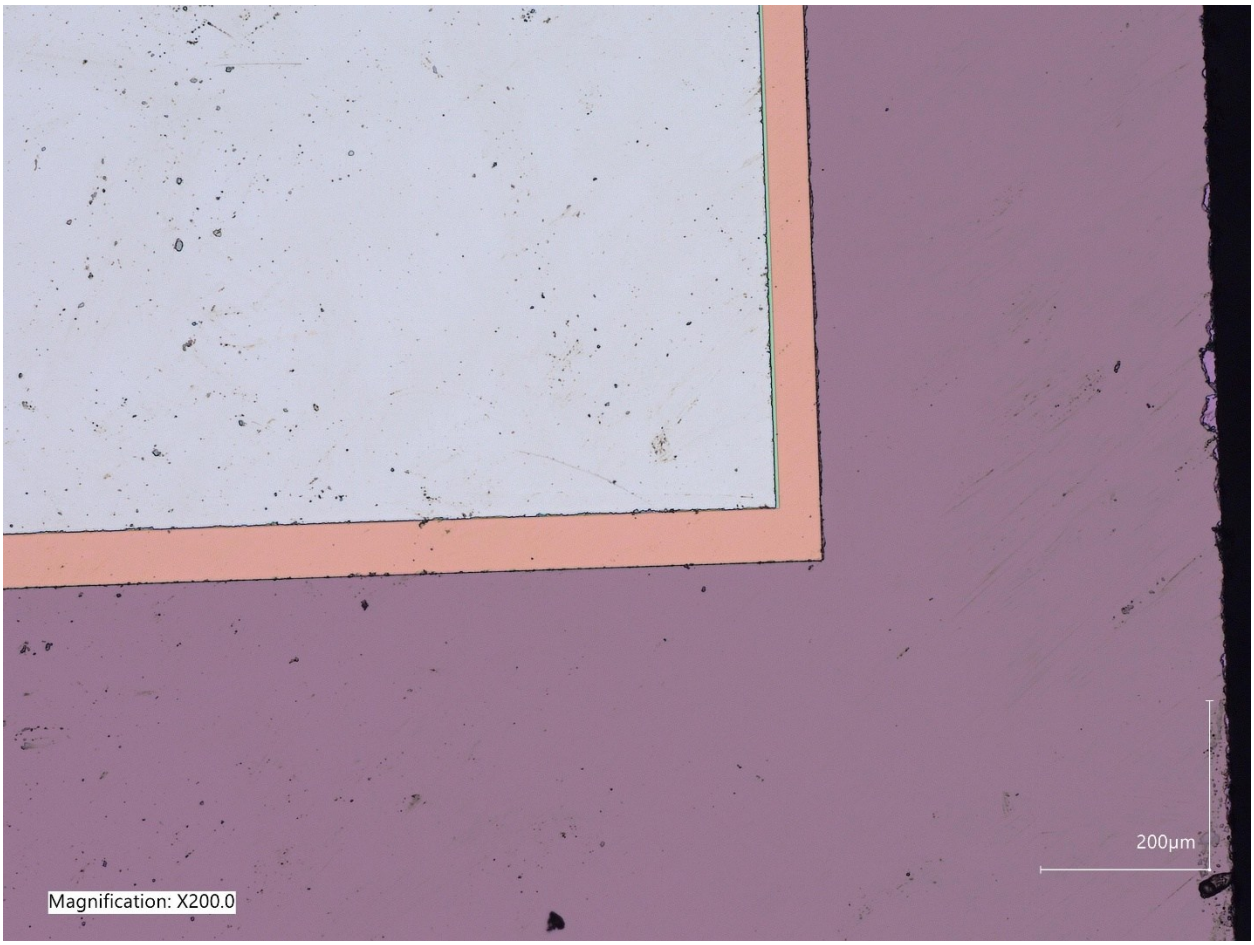


Figure 122. Printed electrode configuration 3 from Table 20. Close up of a Pt contact pad which gets connected to an alligator clip in the test apparatus. The grey region is Pt. It is unclear what the difference is between the peach region and the purple region while they appear to have the same LIBS spectrum.

B.12 Microscopy and LIBS of Wire Electrodes after FLiBe Testing

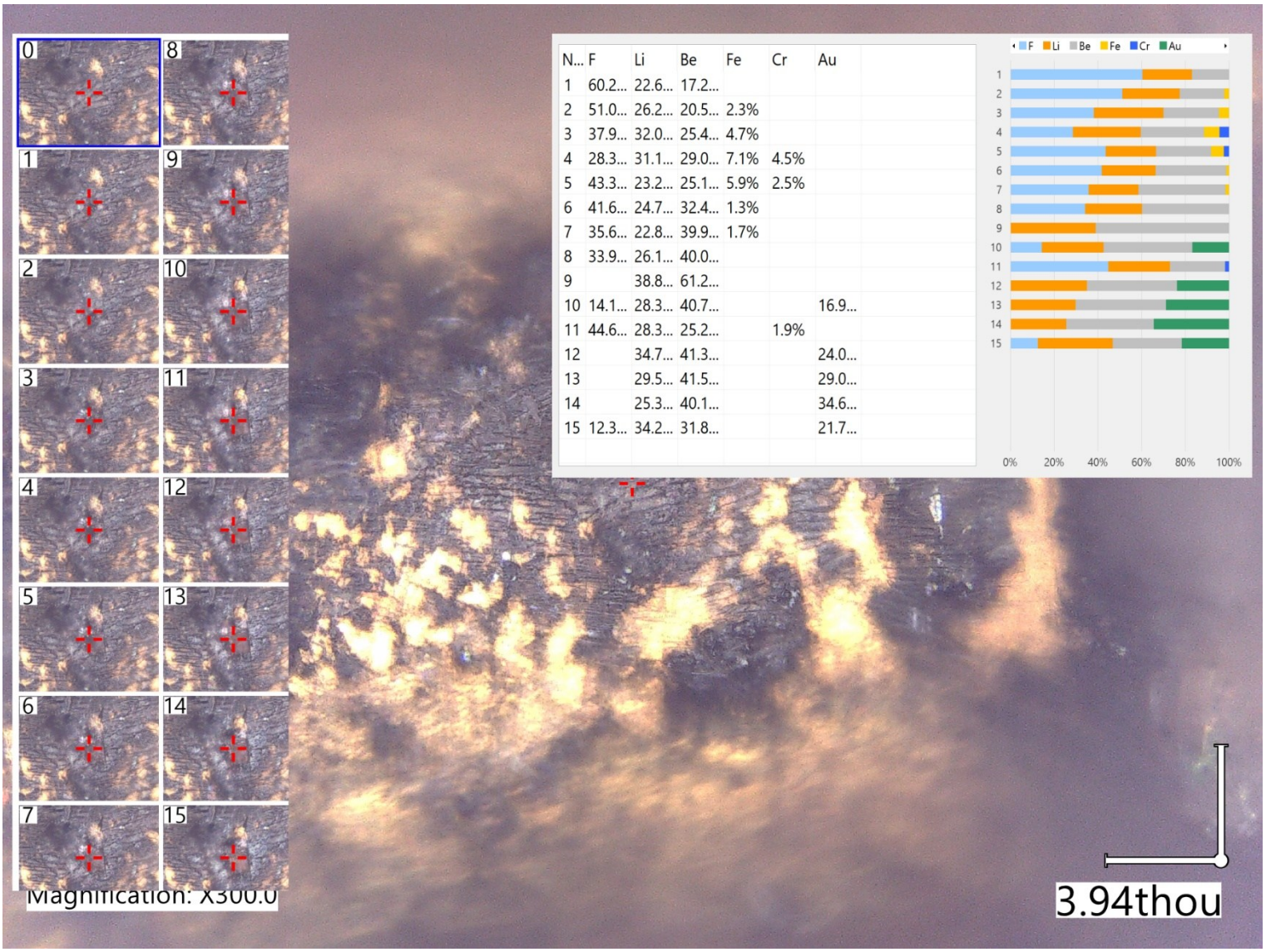


Figure 123. Zone 1 of the Au WE from FLiBe electrochemical test for corrosion product detection. Zone 1 was wetted by the FLiBe and participated in electrochemical reactions. Large image showing the view at 0 drilling steps. Small figures to left of image show the surface after each ablation step. Subplot to the right shows approximate atomic composition of the surface after ablation steps 1 to 15.

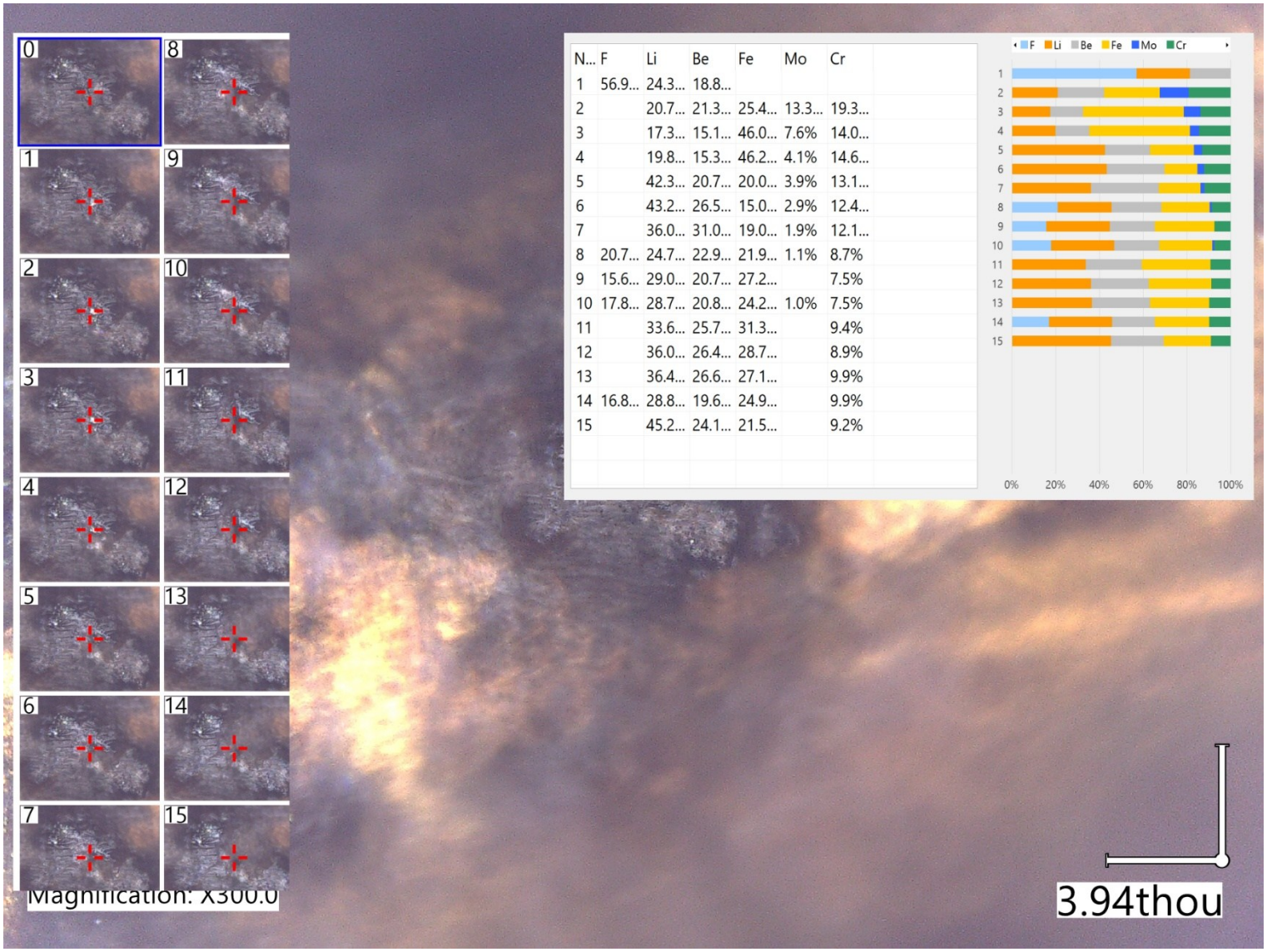


Figure 124. Zone 1 of the Au WE from FLiBe electrochemical test for corrosion product detection. Zone 1 was wetted by the FLiBe and participated in electrochemical reactions. Large image showing the view at 15 drilling steps. Small figures to left of image show the surface after each ablation step. Subplot to the right shows approximate atomic composition of the surface after ablation steps 16 to 30.

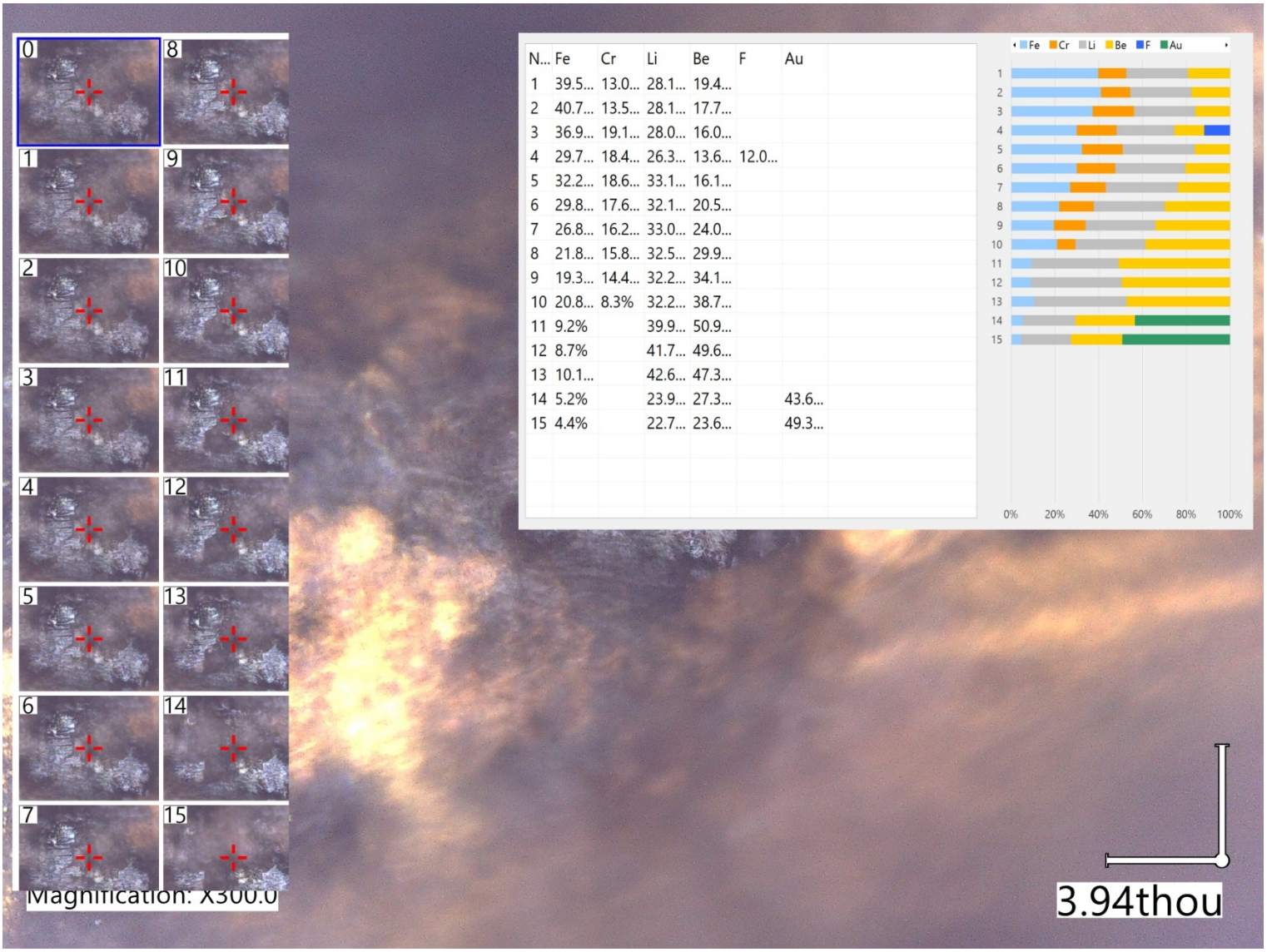


Figure 125. Zone 1 of the Au WE from FLiBe electrochemical test for corrosion product detection. Zone 1 was wetted by the FLiBe and participated in electrochemical reactions. Large image showing the view at 30 drilling steps. Small figures to left of image show the surface after each ablation step. Subplot to the right shows approximate atomic composition of the surface after ablation steps 31 to 45.

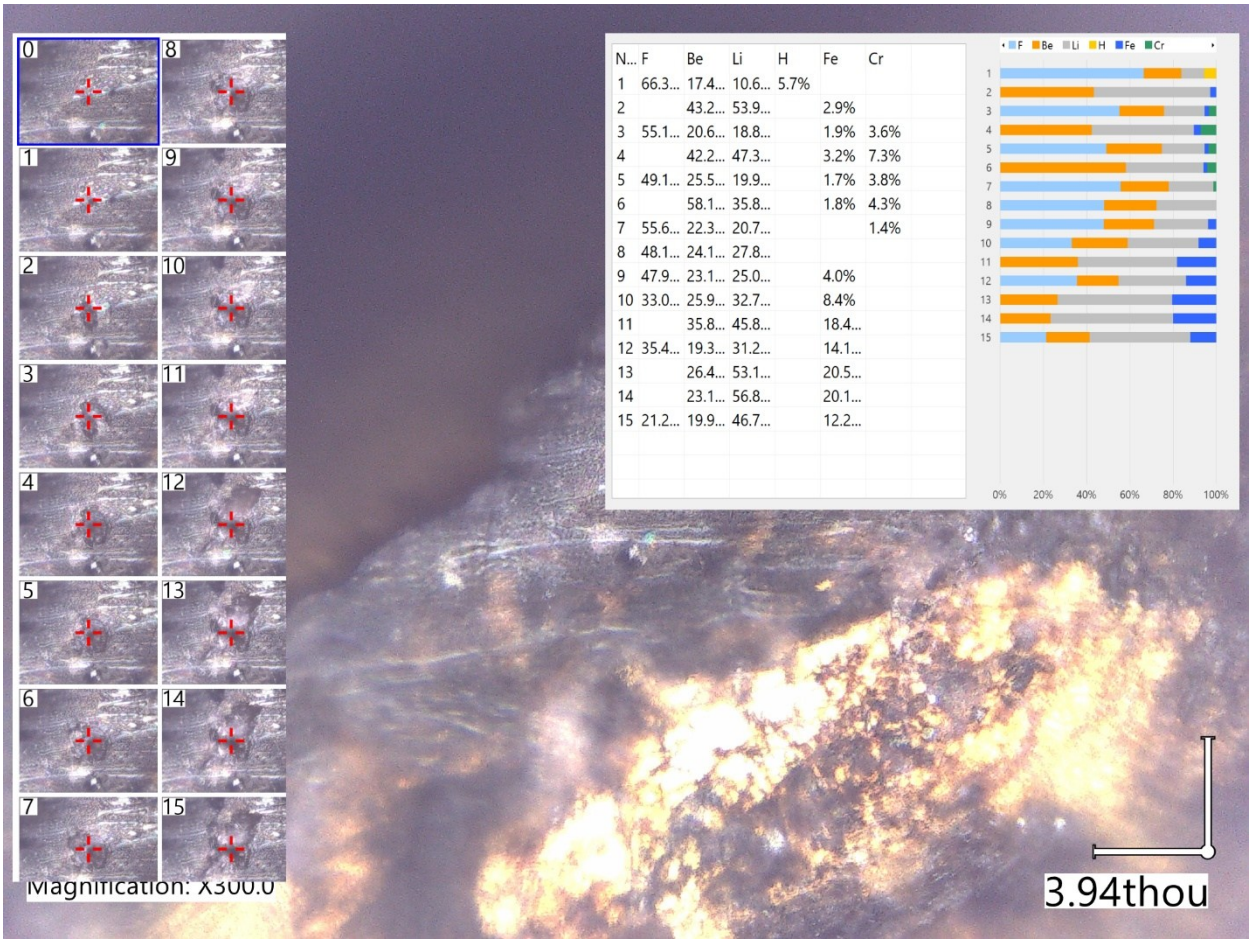


Figure 126. Zone 2 of the Au WE from FLiBe electrochemical test for corrosion product detection. Zone 2 was wetted by the FLiBe and participated in electrochemical reactions. Large image showing the view at 0 drilling steps. Small figures to left of image show the surface after each ablation step. Subplot to the right shows approximate atomic composition of the surface after ablation steps 0 to 15.

B.13 Cyclic Polarization of Ultramet NiTRE

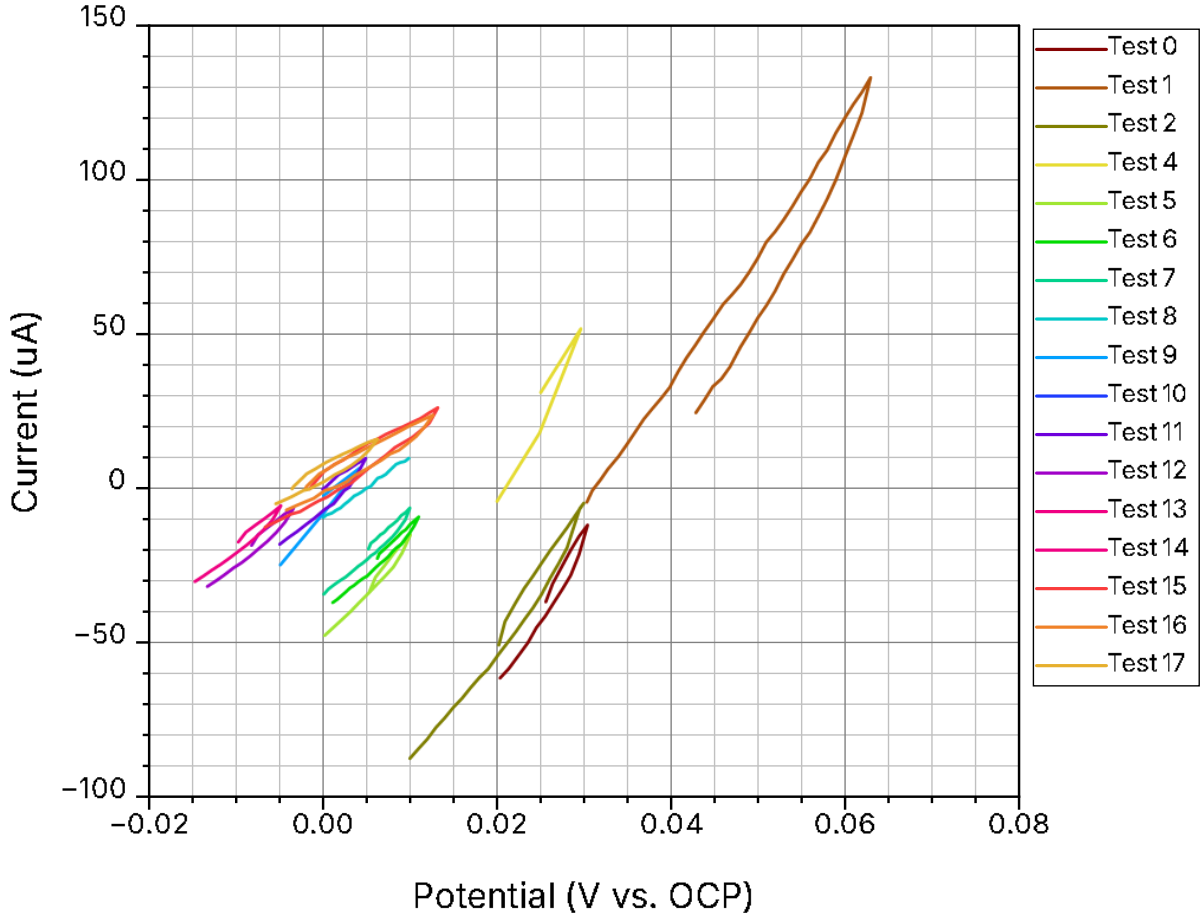


Figure 127. Cyclic polarization curves of BN coated graphitic foam body NiTRE. Data was recorded after NiTRE body capsized in the melt and the melt concentration inside matched the melt concentration outside.

B.14 Cyclic Voltammograms of FLiNaK-CrF_3

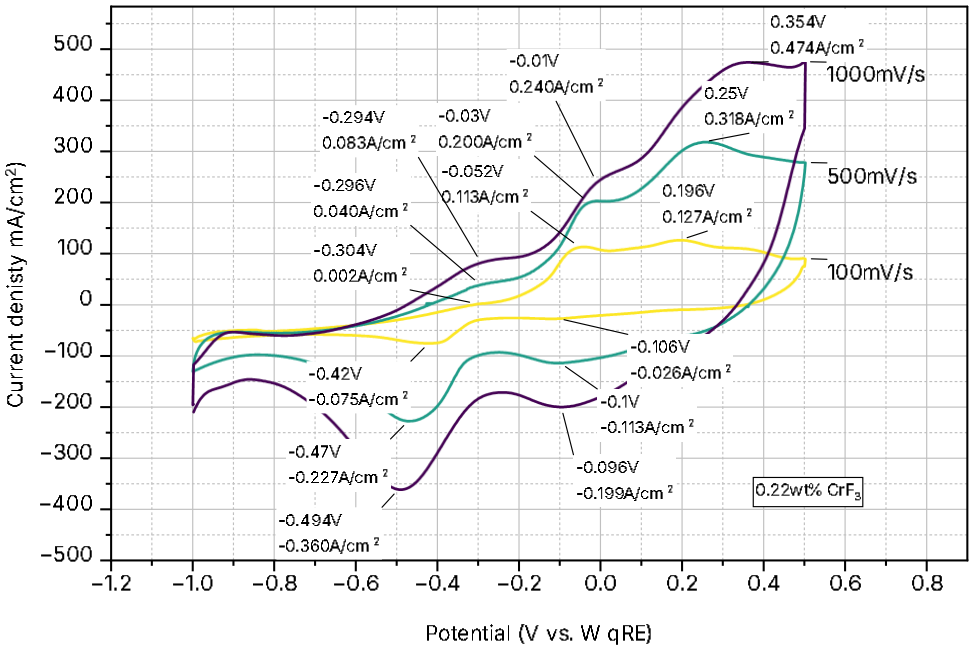


Figure 128. CV of FLiNaK-CrF_3 at 800ºC and x_{CrF3} = 8.2e-4. W WE, W CE, W qRE. Peak locations and currents are identified.

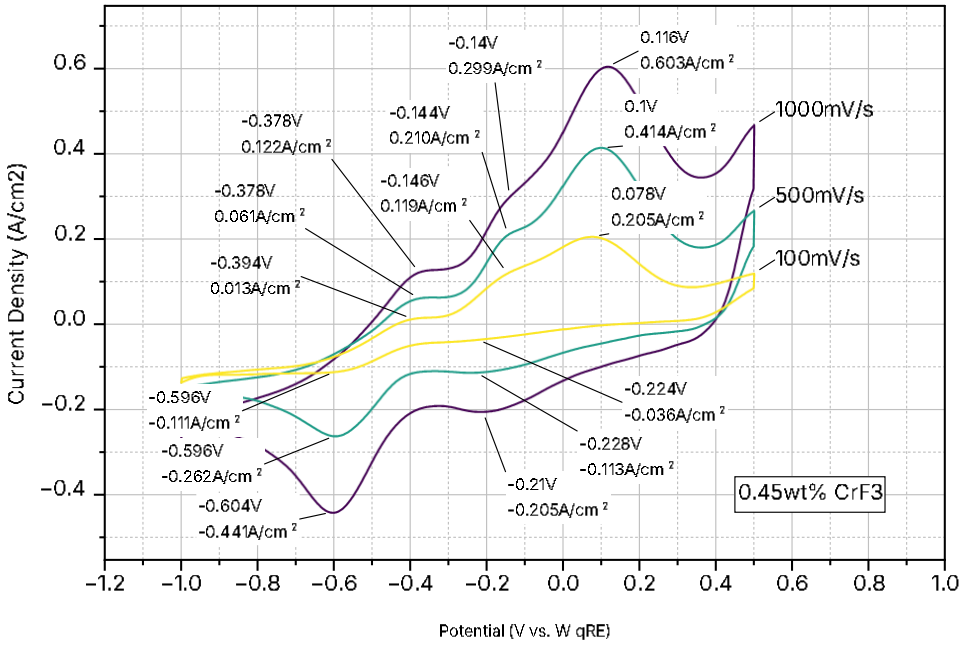


Figure 129. CV of FLiNaK-CrF_3 at 800ºC and x_{CrF3} = 1.7e-3. W WE, W CE, W qRE. Peak locations and currents are identified.

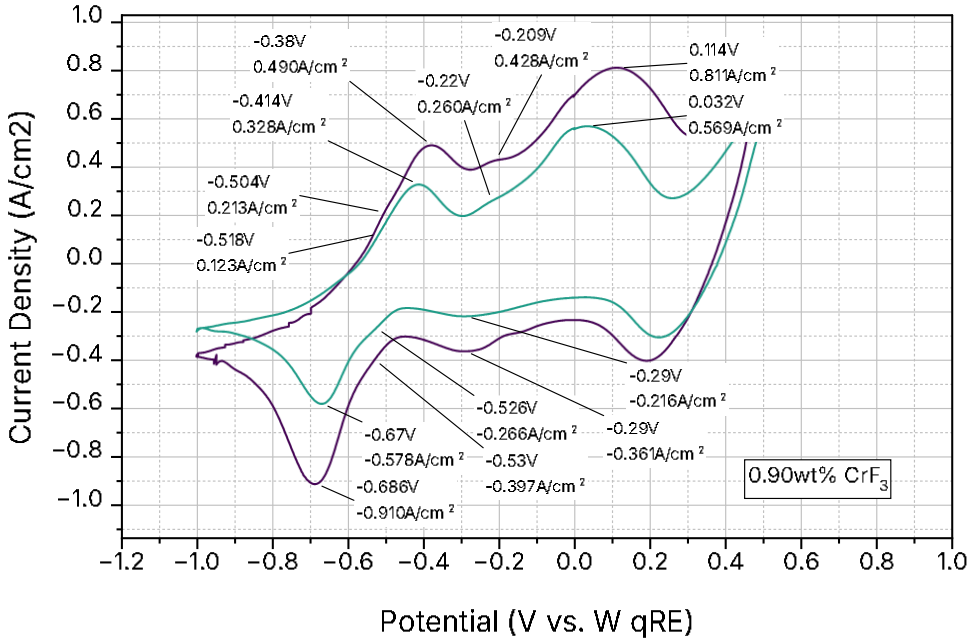


Figure 130. CV of FLiNaK-CrF_3 at 800°C and x_{CrF3} = 3.4e-3. W WE, W CE, W qRE. Peak locations and currents are identified.

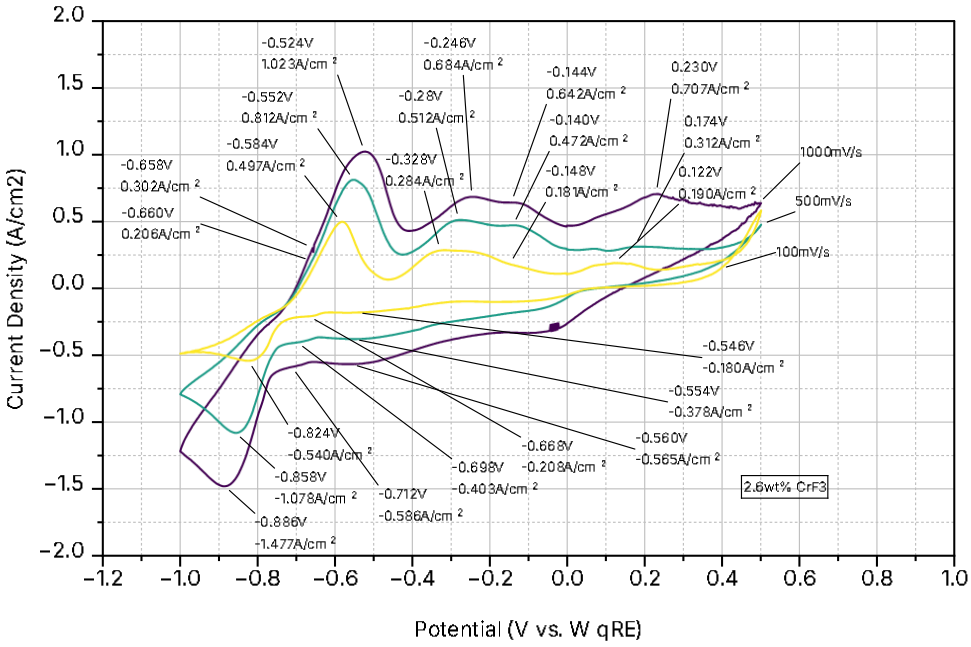


Figure 131. CV of FLiNaK-CrF_3 at 800°C and x_{CrF3} = 1.0e-2. W WE, W CE, W qRE. Peak locations and currents are identified.

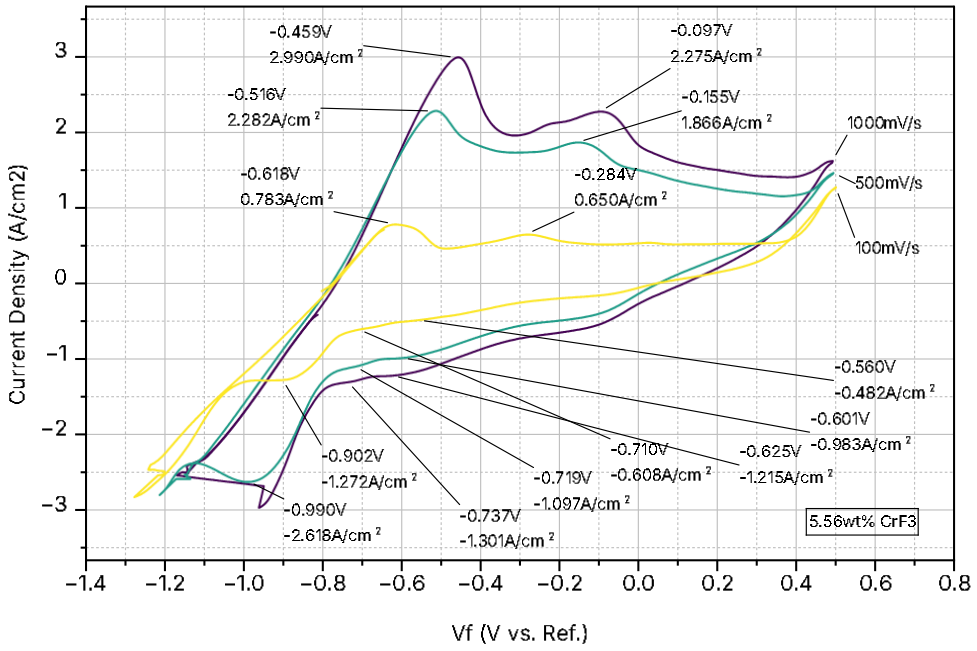


Figure 132. CV of FLiNaK-CrF_3 at 800°C and x_{CrF3} = 2.2e-2. W WE, W CE, W qRE. Peak locations and currents are identified.

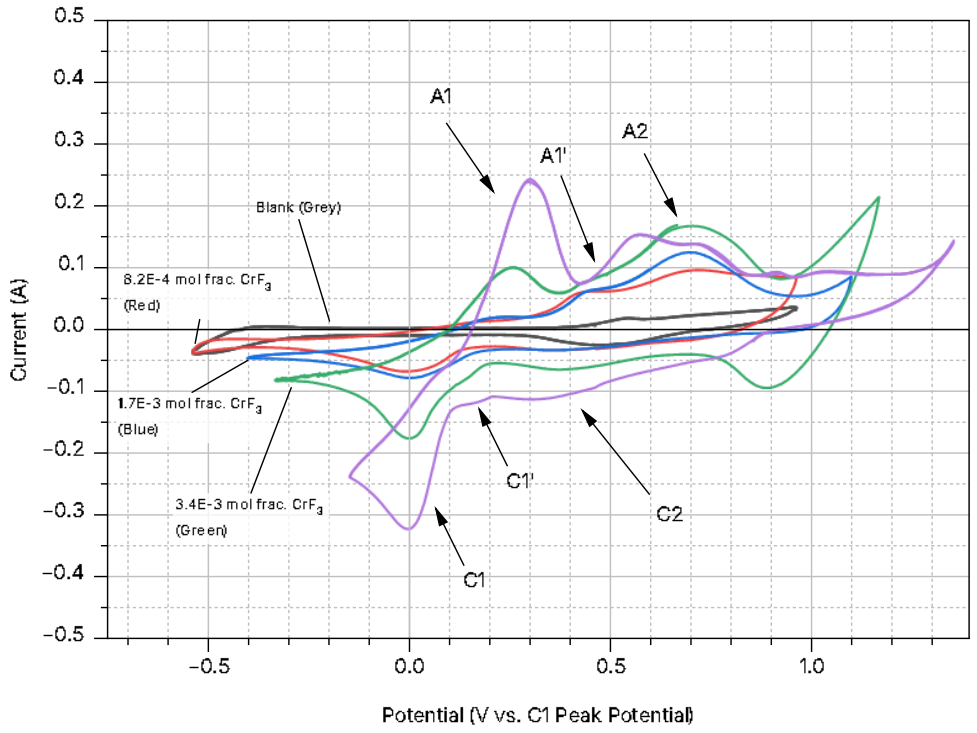


Figure 133. CVs of FLiNaK-CrF_3 at 800°C with varying concentration of CrF_3. Potentials have been shifted such that the C1 (Cr^{2+}/Cr^0) peak potential is 0V.

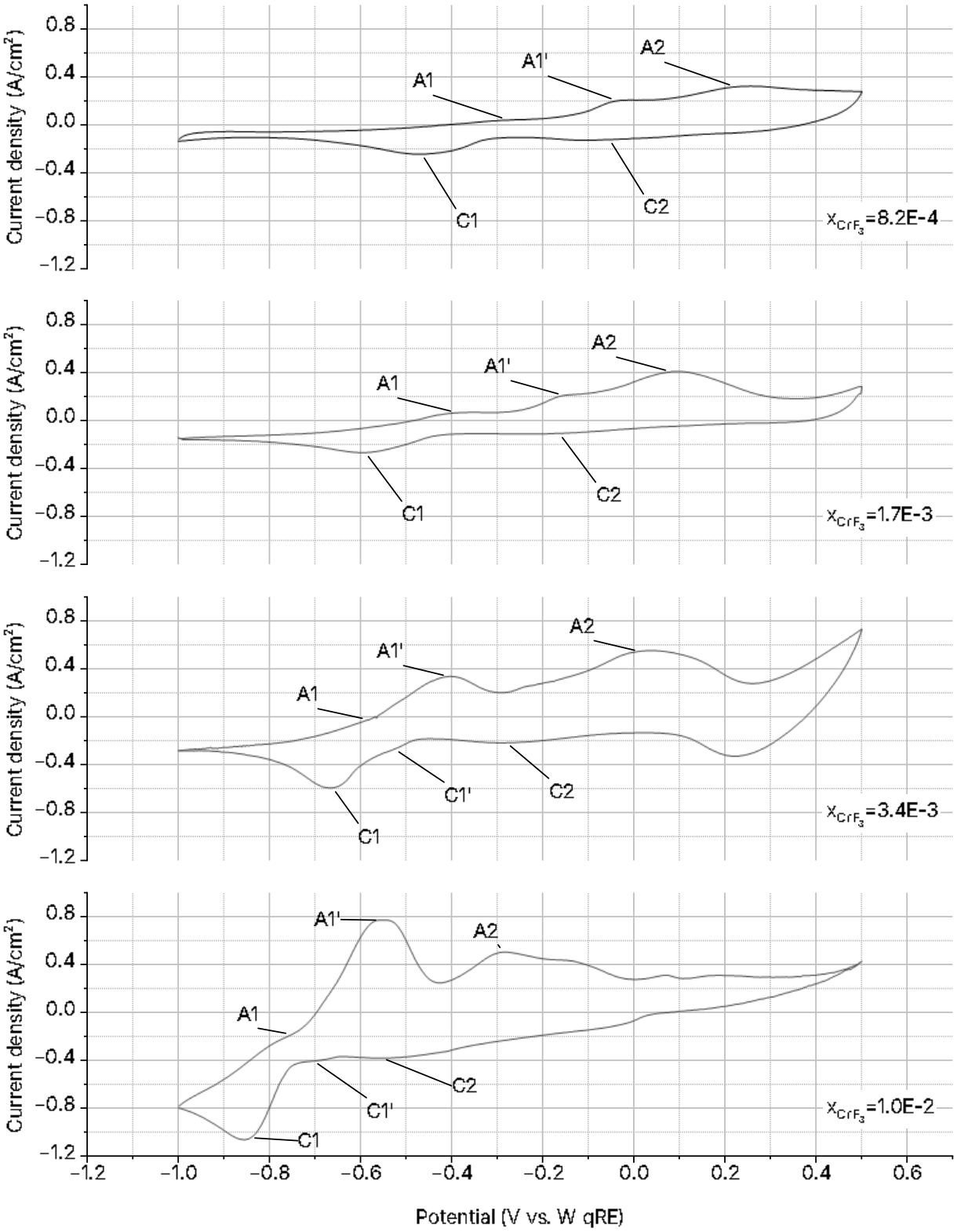


Figure 134. CVs of FLiNaK-CrF_3 at 800°C at 500mV/s. C1/A1' correspond to Cr^0/Cr^{2+}; C2/A2 correspond to Cr^{2+}/Cr^{3+}. A1 peak may be characteristic of Cr-W dealloying. C1' peak appears to be characteristic of underpotential deposition (UPD) of Cr metal.

B.15 Temperature profile during FLiNaK-CrF_3 Additions

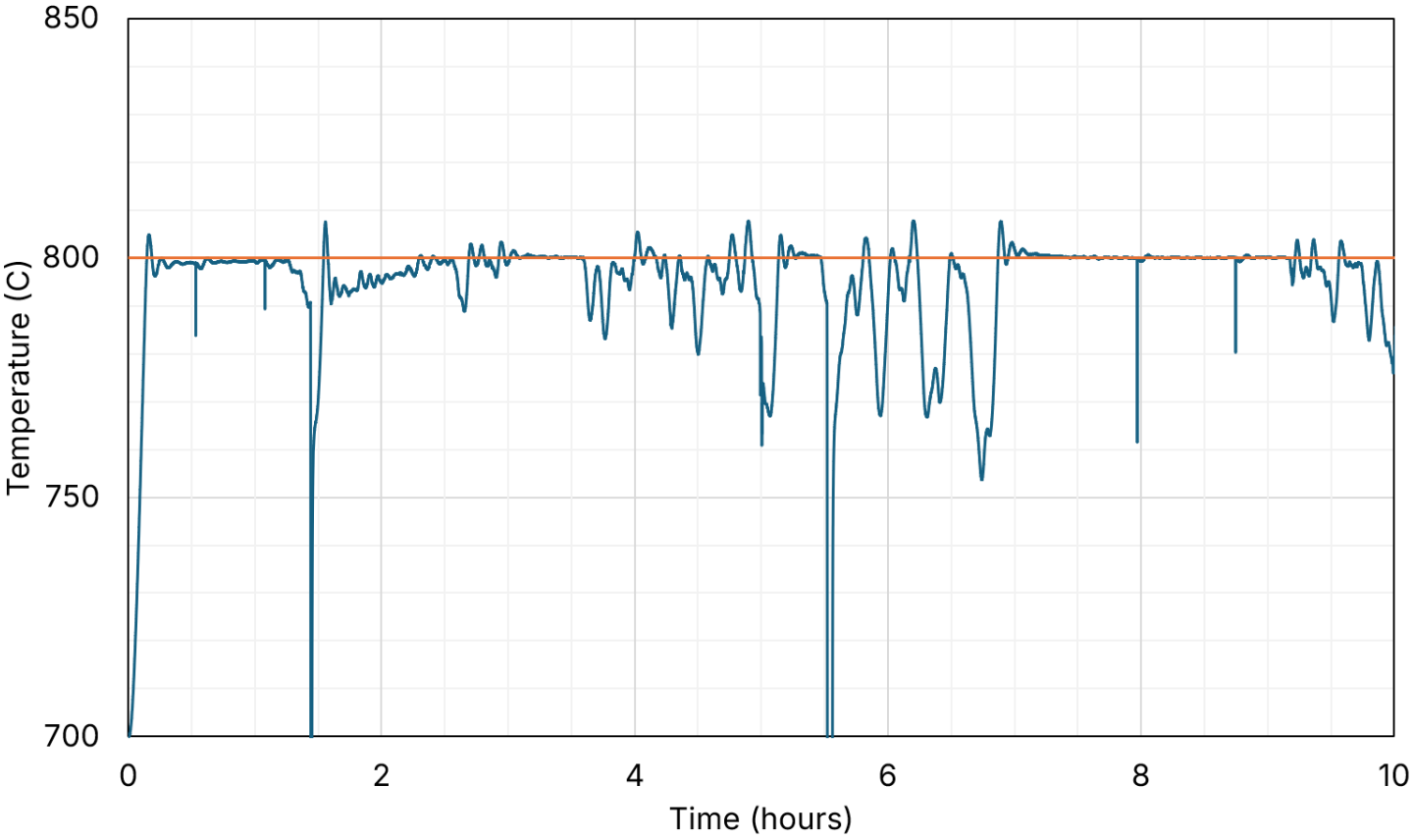


Figure 135. Temperature of the FLiNaK-CrF_3 system during electroanalytical testing. Temperature was measured by a K Type thermocouple in a Mo sheath placed in the salt. Dips and oscillations on the temperature trace are caused by opening and closing the furnace lid.

Appendix C. Supplementary Photos & Images

C.1 Images of Salt Transfer Equipment and Assembly



Figure 136. Image of TK01 Li-7 enriched FLiBe salt vessel (front) and natural enrichment FLiBe salt vessel (back) at UW-Madison.



Figure 137. TK01 salt vessel containing Li-7 enriched FLiBe. (left) Vessel wrapped with ceramic fiber insulation. (right) Vessel wrapped with insulation tape and loaded in the glovebox on top of furnace brick insulation.



Figure 138. (left) Assembled TK02A transfer vessel with Swagelok fittings, salt-facing thermocouple, and pressure gauge. (middle) Vessel with wrapped heating tape around the bottom half of the vessel. (right) Vessel with ceramic fiber insulation and insulation tape on the walls.

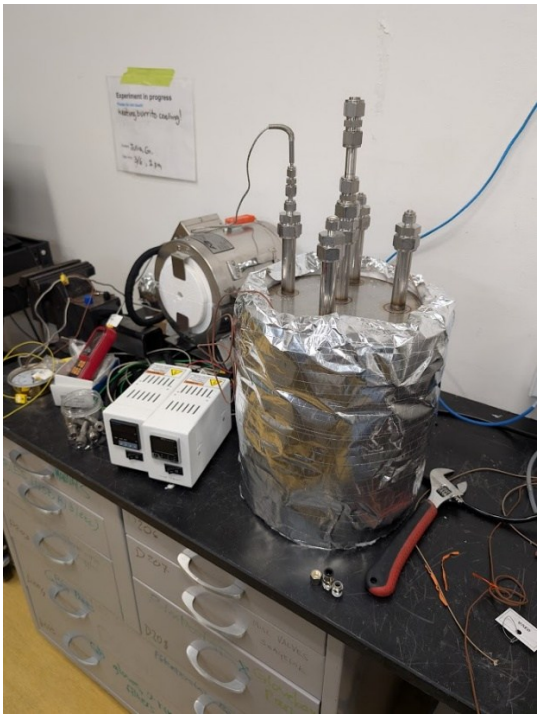


Figure 139. TK02B salt vessel assembled for heating tape preliminary testing.



Figure 140. Singed insulation caused by a thermocouple-induced short of a heating tape. (Left) Transfer line with heating tape and insulation replacement. (Right)

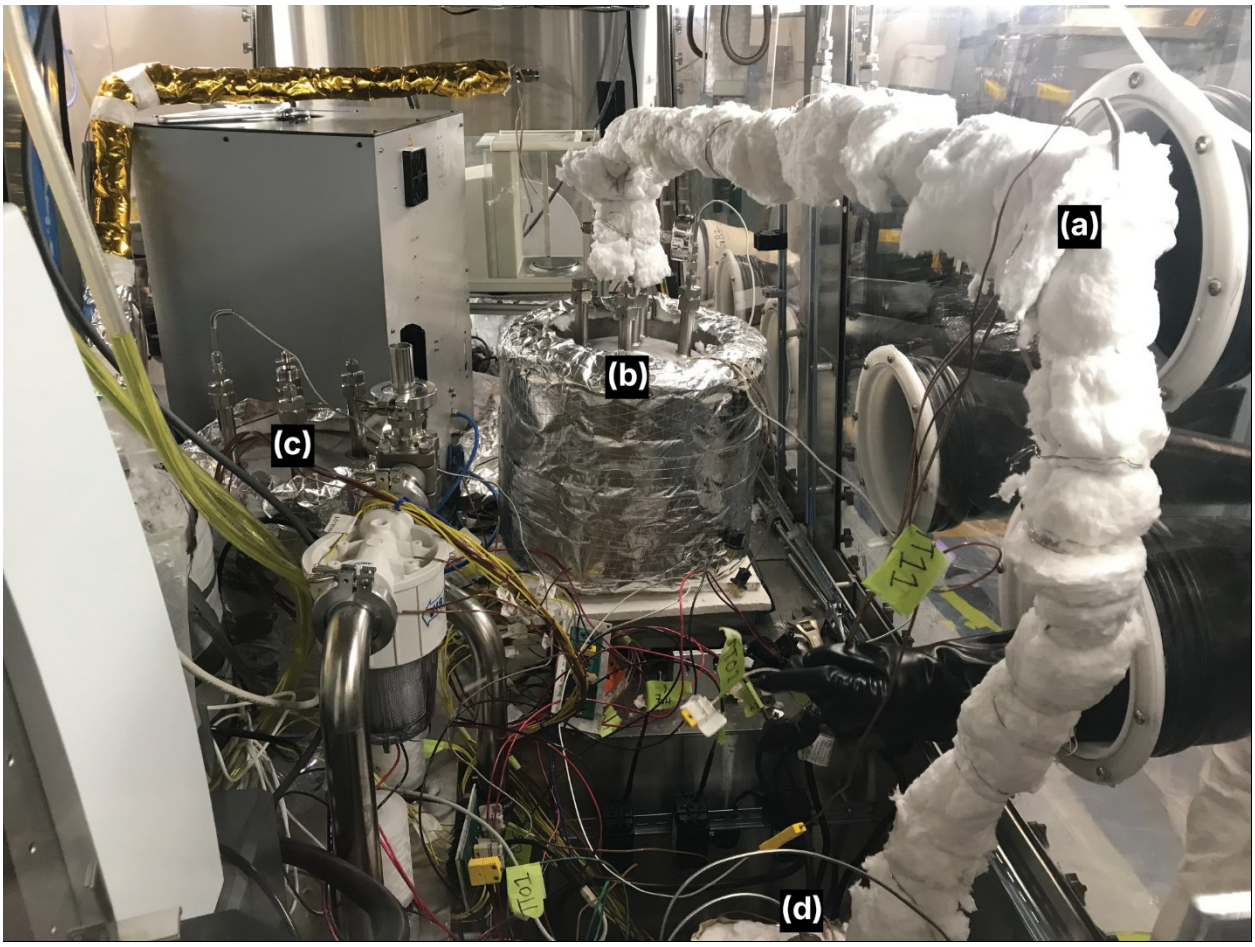


Figure 141. Salt transfer system side-view with redesigned salt transfer line. (a) new salt transfer line, (b) TK02, (c) TK03, and (d) TK01.



Figure 142. heat damage to the plexiglass window on the bottom-west panel of glovebox 4.

Damage to the glovebox during salt transfer attempt 2 is observed in Figure 142. The prolonged extreme heat from the vessel had affected the plexiglass window of the glovebox. Minor delamination and considerable bubble formation was observed. A thermometer gun recorded the temperature of this damaged area at around 82°C. For the safety of maintaining a barrier between the inside and outside of the glovebox, the second salt transfer attempt was halted until the failure could be identified and rectified. However, inspection of the glovebox led to the discovery of more damage to the plexiglass window of the glovebox. While previous insulation appeared to be effective at preventing direct damage from heat exposure, it did not prevent the metal portion of the glovebox from heating up substantially. Through conduction, this transferred heat to plexiglass components, resulting in damage on the border between the two materials. Once this issue was noticed, we immediately stopped heating as it was clear the current transfer apparatus could not safely reach its required temperature.

Appendix D. Supplementary Tables & Documents

D.1 Salt Transfer Operation Timeline

A rough timeline summarizing the events of this specific project is provided in Table 38. The successful salt transfer attempt timeline is given in Table 39.

Table 38. Timeline of Major Events for the Salt Transfer Procedure

Event Date	Notes
2024-11	UCB and MIT have a meeting to discuss the Li-7 enriched FLiBe transfer. Salt transfer planning begins.
2025-01	UCB receives Li-7 enriched FLiBe vessel. Dimensions are taken and system assembly is drafted in CAD.
2025-02	Salt transfer procedure is written, and glovebox opening is scheduled for the following month.
2025-03	First salt transfer attempt. Unsuccessful in performing the transfer due to failing heating tapes making it not possible to melt the salt.
2025-04	Troubleshooting heating bands on salt transfer system, but the cause of failure is still unclear.
2025-06	New heating bands arrive for Li-7 FLiBe tank. Glovebox is opened and system is reconfigured with new heating
2025-07	Second salt transfer attempt. Unsuccessful in performing the transfer due to damage of the glovebox plexiglass from radiative heat escaping the system.
2025-08	Glovebox opening to add more insulation and trace heating to the system. Added radiative heat shield around the glovebox interfaces.
2025-09	Glovebox recirculation blower broke. Procedure was postponed until the blower was replaced.
2025-10	Onboarding new researchers and operators for salt transfer procedure. Safety review conducted with new researchers prior to beginning system shakedown.
2025-11	Salt transfer system shakedown testing verified controllers and heaters function appropriately. Installed electrical protections on controller power supplies.
2025-12	Third salt transfer attempt. Successfully performed the salt transfer procedure. Report on salt transfer procedure begins.
2026-01	System breakdown and lab decontamination efforts in accordance with the beryllium hygiene plan.

Table 39. Salt Transfer Attempt 3 Timeline

Event Date	**Event Time**	**Details**
2025-09-18		UCB/MIT meeting to discuss the plan moving forward with GB pump repairs, GB opening, and salt transfer procedure
2025-10-01		GB pump replaced and cover gas restored to low oxygen and moisture
2025-10-11		Heating zones reconnected to controllers and thermocouples reconnected to data loggers

2025-10-20		Completed writing of shakedown testing and transfer operation checklist
2025-10-24		Electrical safety systems, remote monitoring systems, and HF safety systems installed on and around the system assembly
2025-11-07		Safety review of the system and procedure completed and procedure approved
2025-11-14		System shakedown procedure begins
2025-11-21		System shakedown complete
2025-11-24	2:00pm	HZ1, 2, 3 each stepped from 25% to 50% power (150W to 300W)
2025-11-25	1:00pm	HZ1, 2, 3 each stepped from 50% to 60% power (300W to 360W)
	3:00pm	HZ1, 2, 3 each stepped from 60% to 80% power (360W to 480W)
	4:40pm	HZ2 failed, unknown cause of failure but will not turn back on. Salt melting procedure continues with only HZ1 and HZ3 heating TK01.
2025-11-26	10:00am	HZ1, 3 each stepped from 80% to 90% power (480W to 540W)
	10:30am	HZ3 tripped GFCI on power supply. Breaker flipped back on as soon as it was noticed.
	12:00pm	HZ1, 3 each stepped from 90% to 100% power (540W to 600W). TK01 surface thermocouples surpass the FLiBe melting point.
	5:00pm	HZ1, 3 each stepped from 100% to 0% power (600W to 0W). The system was left to cool for the holiday weekend.
2025-12-01	9:00am	HZ1, 3 stepped from 0% to 50% power (0W to 300W)
	10:30am	HZ4 stepped from 0% to 20% power (0W to 92W)
	2:30pm	HZ4 stepped from 20% to 50% power (92W to 234W)
	3:00pm	All heating zones tripped the GFCI breakers. Data logging and controller power dropped for a brief window.
	3:30pm	GFCI breakers reset and power restored, but HZ4 power continues to trip the GFCI breaker. Melting process continues without heat applied to HZ4. HZ1, 3 stepped from 50% to 100% power (300W to 600W).

	6:00pm	GFCI breaker tripped on HZ3
2025-12-02	12:00am	GFCI breaker reset on HZ3. Temperatures continued to rise.
	7:00am	GFCI breaker tripped on HZ3.
	3:00pm	GFCI breaker reset. HZ3 switched to manual variac power control. HZ3 output power set to 100% (600W).
	6:00pm	GFCI breaker tripped on HZ3. Attempt to reset breaker only to have it trip again.
2025-12-03	9:00am	GFCI breaker reset on HZ3. Power set to 80% (480W). Successfully did not trip the breaker.
	12:00pm	Surface thermocouples all reading above salt melting point. Melting procedure complete.
	2:00pm	Salt transfer operation begins. 20.2kg of salt transferred from TK01 to TK02.
	3:00pm	TK02 set aside to allow salt to freeze. Transfer line was unwrapped and heating tapes in HZ4 were inspected. We found damage to the tapes and rewrapped the line with two 4ft section of heating tape (2x 312W heating load; total of 628W heating load; max current 2.6A).
	5:00pm	GFCI breaker tripped on HZ3. System was left alone for overnight and temperatures stayed constant.
2025-12-04	12:00pm	GFCI breaker reset on HZ3. Power set to 50% (300W). Successfully did not trip the breaker. HZ4 power stepped from 0% to 10% (63W).
	3:00pm	GFCI breaker tripped on HZ4. Breaker reset and HZ4 power set to 20% (124W).
	6:00pm	HZ4 power stepped from 20% to 30% (124W to 189W). GFCI on HZ4 tripped within a few minutes. Multiple attempts to reset the GFCI breaker, but HZ4 power would no longer stay on.
2025-12-05		Continue to troubleshoot HZ4 heating tapes. Replaced heating tapes again with two 4ft sections (2x 312W; total of 628W heating load; max current 2.6A).
2025-12-06		Another salt transfer attempt was made, but the system did not push any salt through the transfer line. It was concluded that the transfer line developed a salt plug somewhere and would need to be melted.

2025-12-09		Heating tapes were replaced on HZ4 multiple times without success. Attempts at continuing the salt transfer procedure were tabled until a new idea could be formulated.

D.2 Salt Transfer System Functional Requirements

Table 40. Salt Transfer System Functional Requirements

Requirement	Specific Detail	Justification	Comments
Maintain operating temperature	$T_{salt} \geq 500^{o}C$	The system must hold above the melting temperature of FLiBe plus some margin of sensible heat	This requirement must also comply the process heat limit
Heat delivered by conduction heaters	Heat must be conducted to the system, not through radiation or convection	The glovebox interfaces cannot handle excess radiative and convective heat transfer, so we avoid using this type of equipment. We do not have the infrastructure for induction furnaces.	It will be more principled to use the existing infrastructure for this project
Move molten salt through transfer line	Salt must be transferred under liquid conditions between the supply vessel and the receiving vessel	Moving liquid salt avoids having to cut open vessels and create a crushed powder	
Fail safe under freezing conditions	If salt freezes, the system must be able to fail safe without causing damage to itself or glovebox interfaces	When salt freezes, it forms solid plugs. In the event of freezing, we want to ensure the formation of plugs does not create new hazards, such as pressure build up	We can expect salt to freeze during power trips of the system
Melting operations are locally controlled	The system must be designated into heating zones which can independently be controller for melting	Salt expands when melting, and controlling the location of the melting mitigates salt expansion damage to pipes/fittings/instruments	
Temperature measurements throughout system	The system temperature needs to be measured during the operation with sensors than can operate up to 700°C	Temperature data is required to know when the system is at/above the salt melting point, and local temperature spikes need to be noticed for the system and operator safety	Temperature data will be most available on the surface of the system, but gas-facing temperature probes and salt-facing temperature probes are

			recommended for more precise measurements
Remote temperature monitoring	The system must be able to remotely communicate temperature data	The system will need to be monitored at any point in the day, and remote monitoring will improve the safety of the operation	This capability is routine for lab experiment that need to maintain high temperature overnight
Pressure vent control	Pressure that accumulates in the system can be vented either manually or automatically	Temperature transients in a closed system will produce pressure swings	Manual operation is satisfactory for most operations, but a mechanical relief valve should be considered when overnight operations begin
Chemistry control of the gas phase	Moisture and oxygen control of the cover gas is required to maintain the purity of the FLiBe	Moisture and oxygen ingress will produce side reactions with FLiBe at molten temperatures, and these reactions can cause the salt to become oxidizing and introduce more impurities to the system	This is also to prevent the salt from becoming more oxidizing when it is delivered to MIT
Mass accountancy	The system must directly measure the transferred mass of salt between the supply vessel and the receiving vessel	We need to be accurate with the mass transferred between vessels, and we do not want to trust an approximate volumetric measurement since the volume will be dependent on the temperature of the system, and the accuracy of the recorded temperature is unknown	Since the salt is not visible in the vessels, a direct mass measurement helps verify when the salt is flowing in the system as well
Emergency Stop Button	An emergency stop button must be readily accessible for the entire system	In the event of an accident of natural disaster, the system needs to be de-energized with the press of a single button	Using the breaker box in the lab would be a suitable “button” for this need

D.3 Salt Transfer System Design Constraints

Table 41. Salt Transfer System Design Constraints

Constraint	Specific Detail	Justification	Comments
Glovebox dimensions	The system must fit within the confined space of the glovebox train.	The procedure must occur within a purified atmosphere, and the more robust way to ensure a pure atmosphere is to conduct the procedure inside of a glovebox	A similar procedure has been performed like this in the past, so it is familiar to the research group
Maximum ambient temperature	$T_{amb} \leq 40^{o}\mathrm{C}$	The glovebox maximum cover gas temperature cannot exceed 40°C to prevent moisture from escaping the molecular sieves	This is a constraint given by the glovebox manufacturer
Maximum interface temperature	$T_{int} \leq 140^{o}\mathrm{C}$	The materials in the glovebox which interface with the salt transfer system (plexiglass, n-butyl gloves) begin to degrade at 140°C	If a glovebox interface fails, the procedure will need to be stopped and restarted
Salt facing materials control	All salt-wetted interfacing materials must be made of stainless steel (SS316)	Aim to avoid corrosion of salt-facing materials by using the same materials that the salt already sees at its solid-liquid interface	Small surface area interactions are permissible, such as through fittings which may have slightly dissimilar materials
Feedthrough interfaces	All power wires, sensor wires, pressure lines, and operator interfaces need to meet the glovebox feedthrough requirements	The glovebox feedthrough requirements make operation of certain equipment more difficult than considering the equivalent operation on the lab floor	This is not a new constraint for equipment operation in our lab

D.4 Thermocouple Legend for Salt Transfer Operation

All thermocouple shown in Figure 4 were monitored using an eight-channel Dwyer Omega 8-channel TC data acquisition system (DAQ) equipped with digital logging software. Temperature data were recorded continuously throughout system operation and stored for subsequent analysis. The recorded measurements were used to monitor heater performance, track thermal transients during melting and transfer operations, and reconstruct the thermal history of the system. This data also provided diagnostic information for interpreting system behavior during both nominal operation and off-normal conditions.

Table 42. Thermocouple Legend for Figure 4

Thermocouple ID	Thermocouple Type	Justification
TT01	K	Salt-facing temperature measurement in the supply vessel, TK01. Installed in a vacant feedthrough on TK01.
TT02	K	Salt-facing temperature measurement in the MIT transfer vessel, TK02. Installed in a vacant feedthrough on TK02 as by design.
TT03^{+}	K	Salt-facing temperature measurement in the UCB transfer vessel, TK03. Installed in a vacant feedthrough on TK03 as by design.
TT04	N	Surface temperature measurement of TK01 bottom. Defines the vertical temperature profile and confirms where melting is occurring.
TT05	K	Surface temperature measurement of TK01 middle. Defines the vertical temperature profile and confirms where melting is occurring.
TT06	K	Surface temperature measurement of TK01 top. Defines the vertical temperature profile and confirms where melting is occurring
TT07	K	Surface temperature measurement of TK02 bottom. Defines the vertical temperature profile and is used to determine when TK02 is safe to handle without thermal protection.
TT08	K	Surface temperature measurement of TK02 top. Defines the vertical temperature profile and is used to determine when TK02 is safe to handle without thermal protection.

TT09[+]	K	Surface temperature measurement of TK03 bottom. Defines the vertical temperature profile and is used to determine when TK02 is safe to handle without thermal protection.
TT10[+]	K	Surface temperature measurement of TK03 top. Defines the vertical temperature profile and is used to determine when TK02 is safe to handle without thermal protection.
TT11	K	Surface temperature measurement of salt transfer line in heating zone 4 (HZ4). Confirms when transfer line region is above the melting point of FLiBe.

[+]Not pictured in Figure 4. A different configuration of the system exists where TK02A is replaced with TK02B.

D.5 Power Controller Legend for Salt Transfer Operation

Each heating zones shown in Figure 4 was supplied by a dedicated power controller operating under proportional-integral-derivative (PID) feedback control. Temperature measurements from the corresponding thermocouples were used as process variables for closed-loop temperature regulation. Several commercially available and in-house assembled controllers were used throughout the system. The heating zones, power controllers, and associated control schemes are summarized in Table 43.

Table 43. Heating Zone and Power Controller Legend

Heating Zone	Location	Power Controller	Control Scheme	Justification
HZ1	TK01	Omega Benchtop PID Controller	PID Feedback	OTS controller for more assurance TK01 will be supplied process heat without possible chance of equipment fault. Provides temperature feedback control with max power output limit control. Ability to monitor real-time process variable-control variable curves. Ability to be used with lab remote monitoring capabilities.
HZ2	TK01	Amptek PID Controller	PID Feedback	OTS controller for more assurance TK02 will be supplied process heat without possible chance of equipment fault. Provides temperature feedback control with max power output limit control.
HZ3	TK02 TK03[+]	Inkbird PID Controller	PID Feedback	IHA controller for training researchers how to build a power controller with PID logic.
HZ4	transfer line	Amptek PID Controller	PID Feedback	IHA controller for training researchers how to build a power controller with PID logic.

+Not pictured in Figure 4. A different configuration of the system exists where TK02A is replaced with TK02B.

Table 44. Heating Zone and Power Controller Legend for Second Attempt

Heating Zone (Location)	Power Controller	Control Scheme	Justification
HZ1 (TK01)	Amptek BBA300-SSR PID Controller	PID Feedback	These controllers were functioning with minimal errors during the first attempt. It was preferred by the operators to use these controllers over the Omega and Inkbird controllers
HZ2 (TK01)	Amptek BBA300-SSR PID Controller	PID Feedback	

HZ3 (TK02A) (TK02B)[+]	VEVOR TDGC2-2000VA Variable Transformer	Manual power control	For more precise power control on the transfer line, it was decided to rely on manual power control instead of tuning PIDs to perform temperature control.
HZ4 (transfer line)	VEVOR TDGC2-2000VA Variable Transformer	Manual power control	

[+]Not pictured in Figure 4. A different configuration of the system exists where TK02A is replaced with TK02B.

Table 45. PID Controller Component Table

Component Name	**Component Function**
HTS Amptek PID Module, 1/16 DIN, 85V to 270V, SSR output	Control the power output based on input temperature, interfaces with SSR
Omega Solid State Relay, SSRL660AC100	Regulate the amount of supply power to the heating load, interfaces with PID and mains power
Inkbird SSR 40DA Heat Sink	Provides cooling to SSR block during operation
Digi-Sense Panel-Mount Thermocouple Jack	Panel mount interface for thermocouple input, interfaces with PID terminal block
Eaton Fuse Holder panel mount, ¼” 10A SLDR	Panel mount interface fuse, interfaces with mains power
Qualtek Power Cord, 18AWG 5-15P-CBL	Power cord connecting mains power to SSR, interfaces with SSR and fuse holder

D.6 Pressure Indicator Legend for Salt Transfer Operation

The pressure indicators in Figure 4 were pressure gauges installed in-line with the gas used to push the FLiBe from TK01 or installed on a vessel which would read the cover gas pressure directly. The in-line pressure gauges were used by operators to fine tune the pressure of the argon gas being used to push salt through the transfer lines. Accounting for the frictional losses and the change in height of the salt from TK01 to TK02, the calculated pressure required to push the salt while staying turbulent in the transfer line was 48.5 psi. The pressure indicator distinctions are included in Table 46.

Table 46. Pressure Indicator Legend

Pressure Indicator ID	Pressure Range (Graduation Marks)	Justification
PI01	0-3000psig (100psi)	Upstream pressure indicator installed on the pressure control valve. Reads the remaining gas cylinder pressure, which had a maximum pressure of 2400psig.
PI02	0-100psig (2psi)	Downstream pressure indicator installed on the pressure control value. Reads the pressure immediately after the diaphragm in the regulator. Outlet pressure would be controlled by PCV01.
PI03	0-30psig (1psi)	Pressure indicator for TK01 to verify pressure was continuous inside the tank from the argon supply line.
PI04	0-30psig (1psi)	Pressure indicator installed for future utility on the receiving tanks when shipped to MIT.
PI05+	0-30psig (1psi)	Pressure indicator installed for future utility on the receiving tanks when shipped to MIT.

+ Not pictured in Figure 4. A different configuration of the system exists where TK02 is replaced with TK03.

D.7 Salt Transfer Operation Safety Review

The design philosophy adopted throughout this work emphasizes not only achieving the intended system function but also maintaining safe operation under foreseeable off-normal conditions. Consequently, the salt transfer system design was evaluated through a review of design basis accidents (DBAs) and operational failure modes that could reasonably occur during the transfer procedure.

A design basis accident is a postulated event used to evaluate system response to abnormal operating conditions and to verify that adequate mitigation strategies exist to maintain personnel safety and system integrity. Although the salt transfer system operates on a laboratory scale, many of the same engineering principles applied to larger nuclear systems remain relevant. Anticipating potential failures before operation allows mitigation strategies to be incorporated directly into the system design and operating procedures. Table shows the DBAs considered for the system, the consequences of these accidents, and the mitigation strategy employed to recover the operation.

Table 47. Design Basis Accidents (DBAs)

#	Event	Effect	Consequence	Mitigation
1	Heating tapes burn out/heating tapes provide insufficient heating	Temperature drops on transfer line.	Salt will freeze in the transfer line during the operation	Pause the transfer, de-energize the heating zone, and replace the heating tapes before proceeding.
2	Controller fuse breaks	De-energizes the heating zone powered by the controller. Temperatures begin to drop.	Salt freezing can occur in the vessel/transfer line.	Pause the transfer, de-energize the heating zone, and replace fuse before proceeding.
3	Insulation does not adequately protect glovebox from heat.	Glovebox, particularly the plexiglass window, suffers heat damage.	Window is at risk of failure, which could cause a glovebox breach.	Pause the transfer, de-energize heating, and add/improve insulation before proceeding.
4	Exposed hot apparatus causes damage to glove.	Glove seal is potentially compromised.	Potential glovebox breach.	Follow standard glove change procedure. Properly insulate any exposed parts of the apparatus before proceeding.
5	Earthquake (magnitude <5.0) loosens thermocouple and power connections.	Possible loss of temperature monitoring and/or power to heating zones.	Salt freezing can occur in the vessel/transfer line.	Pause the transfer, visually assess the connections, physically reconnect loose connections if safe to do so, and confirm total reconnection using the Omega PLATINUM software before proceeding.

6	Earthquake (magnitude >5.0) causes hot vessel to tip off of its support.	Vessel could rest on the glovebox causing heat damage to the glovebox and melting the plexiglass window. Power and monitoring connections could disconnect.	Potential glovebox breach due to window failure. Loss of remote monitoring capabilities.	Pause the transfer, de-energize heating, and check connections. Assess the position of the vessel and reposition it if possible after cooling. A meeting would likely be necessary before continuing the procedure.
7	Thermocouple short/failure.	Loss of temperature information transferred between the vessel and the temperature logging software or power control system.	Potential loss of heating to a given heating zone leading to salt freezing in the vessel/transfer line. Loss of remote monitoring capabilities.	If a heating zone loses power, pause the transfer, de-energize the heating zone, and assess redundant thermocouples as replacements before proceeding. If a non-essential thermocouple breaks, utilize a redundant or probe thermocouple in its place.
8	Argon leak at argon piping section *outside* of glovebox train during operation.	Drop in lab oxygen levels as argon is released into atmosphere. Drop in argon gas pressure to drive salt transfer, and thus less mass flow rate than intended.	Potential extreme safety hazard to those performing the operation. Potential reduction in salt mass flow rate could lead to salt freezing if the flow is too slow to avoid the heat loss necessary to solidify.	If a low-oxygen alarm is sounded, stop all work immediately and evacuate the lab. Proceed with low-oxygen hazard procedures. If oxygen levels are still suitable, pause the transfer, de-energize the heating zone, and assess the location of the leak. Repair and verify before reattempting.
9	Argon leak at argon piping section *inside* of glovebox train during operation.	Drop in argon gas pressure to drive salt transfer, and thus less mass flow rate than intended.	Potential reduction in salt mass flow rate could lead to salt freezing if the flow is too slow to avoid the heat loss necessary to solidify.	Pause the transfer, de-energize the heating zone, and assess the location of the leak. Repair and verify before reattempting.

10	Slow surface levelling of transferred liquid salt in receiving vessel (TK02 or TK03).	Transferred liquid salt begins to clog transfer line and reduces mass flow rate.	Coupled with inadequate heating in HZ05, salt could potentially freeze and block transfer line at end.	If an inadequate surface levelling rate is observed, de-energize the heating zones, allow the salt in the receiving vessel to level out, and resume operations as though restarting with a lower, allowable mass flow rate.

[+]For more details about the emergency response, see Appendix D.1.

The majority of credible failure modes are associated with loss of thermal control. Heater failures, controller failures, insulation deficiencies, and power interruptions all ultimately manifest as decreasing salt temperature and the potential formation of frozen salt plugs. Many failure modes are recoverable if detected early. The mitigation strategies therefore emphasize system observability through temperature measurements, operator intervention, and the ability to pause operations without compromising system integrity. The DBA review highlights the importance of designing for recovery rather than assuming ideal operation. Salt freezing, equipment failures, and operational interruptions are foreseeable events in molten salt systems, and robust system designs must provide a safe path to recover from these conditions.

D.8 Salt Transfer Step-by-Step Procedure

POWER AND TEMPERATURE MONITORING SETUP FOR TRANSFER FROM TK01 TO TK02

1. Connect heating tape power controllers to each respective zone for the salt transfer procedure.
    a. Heating Zone 1: TK01 Top, 600W ceramic band clamshell heater
        i. Omega PID
    b. Heating Zone 2: TK01 Middle, 600W ceramic band clamshell heater
        i. Amptek PID
    c. Heating Zone 3: TK01 Bottom, 600W ceramic band clamshell heater
        i. Amptek PID
    d. Heating Zone 4: Salt transfer line, 624W (total load) heating tapes
        i. Variac power supply
    e. Heating Zone 5: TK02/TK03, 624W (total load) heating tapes
        i. Variac power supply
2. Connect thermocouples to Omega-TC DAQ boxes and then configure data collection on Omega-TC logging software.
    a. TS01: Omega-TC DAQ
        i. Connects to TT01-TT08
    b. TS02: Omega-TC DAQ
        i. Connects to TT09-TT12

HEATING SYSTEM SHAKEDOWN

1. Set controller maximum output power limiter to 50%.
2. Run each heating zone under manual control. Set manual power output to 20%.
3. Monitor the temperatures of each zone until a steady state is reached.
4. Record the steady state temperature.
5. Repeat the above steps but at 20%, 30%, 40%, and 50% output power.

STOP

This is the end of the procedure for Day 2. Ensure all GB windows are closed before leaving the lab. Message the slack #lab channel to remind researchers the lab is still under respirator only operation, and not to enter without a Tyvek suit. The procedure will continue tomorrow.

HEATING SYSTEM SHAKEDOWN (CONTINUED)

6. Set controller maximum output power limiter to 10%.
7. Run each heating zone under PID control. Add setpoint to controller using the value of the 10% power output steady state temperature.
8. Monitor the temperatures of each zone until the setpoint is reached.
9. Record the temperatures in the OMEGA TC logging software.

10. Repeat the above steps using the setpoint temperatures from the 20%, 30%, 40%, and 50% manual output power tests from the day previously.

STOP

This is the end of the procedure for Day 3. Ensure all GB windows are closed before leaving the lab. Message the slack #lab channel to remind researchers the lab is still under respirator only operation, and not to enter without a Tyvek suit. The procedure will continue tomorrow.

TK01 SALT MELTING PROCEDURE

1. Set the controllers in each heating zone to PID control.
2. Limit the power output of each controller to 10%.
3. Use the setpoints from the previous heater shakedown test and allow the system to reach steady state.
4. Once at steady state, update the power output limit to 20%. Repeat the steps at each new steady state for 30%, 40% and 50% power output limits.
5. Once the tank has reached steady state at 50% output power under PID control, allow the system to hold in this state for the rest of the day.
6. Record observations of the glovebox condition and the system condition.
    a. It is crucial to note that the system can hold this state indefinitely so that we can allow for slow melting and heating over the course of multiple 12 hour days. This will prevent overnight monitoring from being required.

STOP

This is the end of the procedure for Day 4. Ensure all GB windows are closed before leaving the lab. Message the slack #lab channel to remind researchers the lab is still under respirator only operation, and not to enter without a Tyvek suit. The procedure will continue tomorrow.

TK01 SALT MELTING PROCEDURE (CONTINUED)

Bring the tank back to temperature at the 50% power output limit steady state. Do this by slowly ramping the power limit back to 50% if the current system temperatures are below the setpoints previously recorded.

This is important so the heating tapes don't burn out by drawing high power in one burst. This is different from using current limiting fuses, since the main concern is bursts in current in the operating conditions, not current overdraw outside of operating conditions.

Switch controllers to manual output.

Continue to raise controller output power limit until the required salt steady state temperature of 600C is being held.

When 600C is reached, allow the system to equilibrate at this temperature for a day.

If the temperature is reached at the end of the day, repeat this task the next day starting with the higher output power limits.

This will work because the system is well insulated and won't cool off in one night.

STOP

This is the end of the procedure for Day 5. Ensure all GB windows are closed before leaving the lab. Message the slack #lab channel to remind researchers the lab is still under respirator only operation, and not to enter without a Tyvek suit. The procedure will continue tomorrow.

SALT TRANSFER PROCEDURE FROM TK01 TO TK02

1. Check that the temperatures in HZ1 and HZ2 are at the operating temperature of 500ºC, or at minimum stable and above the melting point, approximately 458ºC.
2. Raise the power in HZ3 and HZ4 to allow the temperatures to reach the operating temperature of 500ºC, or at minimum stable and above the melting point, approximately 458ºC.
3. Ensure the scale is functional in GB4. Troubleshoot using the scale before attempting the salt transfer.
4. Set PCV01 to 10 psig.
5. Connect argon supply line to TK01.
6. Verify V02 (Argon supply needle valve) is closed.
7. Verify V06 (TK01 Argon supply isolation) is closed.
8. Open V07 (TK01 gas vent).
9. Open V06 (TK01 Argon supply isolation).
10. Open V02 (argon supply needle valve) to check flow rate. Set flow rate to 1.0 L/min.
    a. The volume of salt being transferred is approximately 9.8 L, so we will run the operation for 9.8 mins at 1.0 L/min.
11. Close V06 (TK01 Argon supply isolation).
12. Close V07 (TK01 gas vent).
13. When the salt is molten and TK02 and the transfer line are both preheated, begin the salt transfer as follows:
    a. Verify V08 (TK02 Vent) is open
    b. Close V07 (TK01 Argon supply isolation)
    c. Open V06 (TK01 Argon supply isolation)

    d. Monitor scale to determine how much salt has been transferred
14. When approximately 20 kg of salt has been transferred into TK02, stop the salt transfer as follows:
    e. Close V06 (TK01 Argon supply isolation)
    f. Open V07 (TK01 Argon supply isolation)
    g. Turn off power to HZ3 and HZ4. Allow both zones to cool.

STOP

This is the end of the procedure for Day 6. Ensure all GB windows are closed before leaving the lab. Message the slack #lab channel to remind researchers the lab is still under respirator only operation, and not to enter without a Tyvek suit. The procedure will continue tomorrow.

TRANSFERRING SALT FROM TK01 TO TK03

1. Detach TT02 (TK02/B Thermocouple) and V08 (TK02/B Vent) onto TK02
2. Attach TT02 (TK02/B Thermocouple) and V08 (TK02/B Vent) onto TK03 (UCB vessel)
3. Position TK03 (UCB vessel) on a scale
4. Attach transfer line between TK01 and TK03 (UCB vessel)
5. Verify V07 (TK01 Vent) is open to allow venting due to thermal expansion
6. Verify V08 (TK02/B Vent) is open to allow venting due to thermal expansion
7. Begin melting the salt in TK01
8. Begin pre-heating the transfer line
9. Begin pre-heating TK02
10. Set PCV01 to 60 psig
11. Verify V02 (Argon supply needle valve) is closed
12. Verify V06 (TK01 Argon supply isolation) is closed
13. Set PCV02 to < 10 psig
14. Open V02 (Argon supply needle valve) just off its closed seat
15. Open V06 (TK01 Argon supply isolation)
16. Observe FI-1 (Argon Supply Flow Indicator). Slowly open V02 to achieve desired salt flow rate
17. Close V06 (TK01 Argon supply isolation)
18. Connect argon supply line to TK01
19. When the salt is molten and TK02 and the transfer line are both preheated, begin the salt transfer as follows:
    a. Verify V09 (TK03 Vent) is open
    b. Close V07 (TK01 Argon supply isolation)
    c. Open V06 (TK01 Argon supply isolation)
    d. Monitor scale to determine how much salt has been transferred

20. When approximately 5kg of salt has been transferred into TK02 , stop the salt transfer as follows:
    a. Close V06 (TK01 Argon supply isolation)
    b. Open V07 (TK01 Argon supply isolation)

STOP

This is the end of the procedure for Day 7. Ensure all GB windows are closed before leaving the lab. Message the slack #lab channel to remind researchers the lab is still under respirator only operation, and not to enter without a Tyvek suit. The procedure will continue tomorrow.

TRANSFERRING SALT FROM TK01 TO TK04 (GLASSY CARBON CRUCIBLE)

1. Detach TT02 (TK02/B Thermocouple) from TK03 (13-kg vessel B)
2. Insert TT02 (TK02/B Thermocouple) into TK04 (Glassy Carbon Crucible)
3. Position TK04 (Glassy Carbon Crucible) inside furnace
4. Attach transfer line between TK01 and TK04 (Glassy Carbon Crucible)
5. Verify V07 (TK01 Vent) is open to allow venting due to thermal expansion
6. Begin melting the salt in TK01
7. Begin pre-heating the transfer line
8. Begin pre-heating furnace containing TK04 (Glassy Carbon Crucible)
9. Set PCV01 to 60 psig
10. Verify V02 (Argon supply needle valve) is closed
11. Verify V06 (TK01 Argon supply isolation) is closed
12. Set PCV02 to < 10 psig
13. Open V02 (Argon supply needle valve) just off its closed seat
14. Open V06 (TK01 Argon supply isolation)
15. Observe FI-1 (Argon Supply Flow Indicator). Slowly open V02 to achieve desired salt flow rate
16. Close V06 (TK01 Argon supply isolation)
17. Connect argon supply line to TK01
18. When the salt is molten and TK04 (Glassy Carbon Crucible) and the transfer line are both preheated, begin the salt transfer as follows:
    a. Close V07 (TK01 Argon supply isolation)
    b. Open V06 (TK01 Argon supply isolation)
19. When enough salt has been transferred into TK04 (Glassy Carbon Crucible), stop the salt transfer as follows:
    a. Close V06 (TK01 Argon supply isolation)
    b. Open V07 (TK01 Argon supply isolation)

STOP

This is the end of the procedure for Day 8. Ensure all GB windows are closed before leaving the lab. Message the slack #lab channel to remind researchers the lab is still under respirator only operation, and not to enter without a Tyvek suit. The procedure will continue tomorrow.

SALT TRANSFER PROCEDURE - END OF LIFE

GB Opening:

- Day 1 – Preparation pt 1
  1. Move the samples from GB3/4
     a. Samples removed from the GB require name, date, project number, eLab ID (scannable or item number at the least) and associated hazards on their label
  2. Inventory Tyvek suits and other PPE
  3. Prepare overpacks on vessels
     a. MIT vessel overpack
     b. UW vessel overpack
     c. UCB vessel overpack
     d. Potentially 2 more overpacks for NaFBe loop items
- Day 2 – Preparation pt 2
  1. Prepare the Be zone with tarp and sticky mats
  2. Unplug all controllers/heaters from outside
  3. Bag the controllers
  4. Unwrap the salt transfer system
  5. Cut transfer line and store in GB2
  6. Install tube fittings/cap open lines
  7. Reclaim any lost salt on GB floor
  8. Bag dusty materials
- Day 3 – Opening, Tank Removal, Closing, Clean Up, Be Swipes
  1. Set up Be air monitor
  2. Open GB3W panel
  3. Remove hose protrusion
  4. Clean hose and trash it
  5. Close GB3W panel
  6. Open GB4E panel
  7. Lift vessels out of the box
  8. Clean surface of all vessels
  9. Be swipe surfaces of all vessels

10. Double bag vessels in overpack
11. Close overpacks and post appropriate signage
12. Close GB4E panel
13. Wrap up Be zone tarp and sticky mats
14. Clean the floor/all horizontal surfaces
15. Swipe areas around the lab

- Day 4 – Purging, Be Analysis
  1. Purge GB3/4 down to usable levels
  2. Swipe lab and conduct routine Be lab report procedures
- Day 5 – Regen, restore GB operation
  1. Regen GB3/4 and restore cover gas recirculation

D.9 MATLAB Script for LaF_3 Crystal Sizing Calculation

The full MATLAB script with the sizing calculations was published to this word document. Some of the lines have not preserved their original orientation due to the format of the document. For troubleshooting and bug fixing, please open the source code itself, UCBS40EG0003A.

```
%% Definitions and Constants

Temperature = 700 + 273; % [K]
MolarMass_LiF       = 25.939; % [g/mol]
MolarMass_BeF2      = 47.01; % [g/mol]
MolarMass_FLiBe     = 2 / 3 * MolarMass_LiF + 1 / 3 * MolarMass_BeF2; % [g/mol]
MolarMass_LaF3      = 195.9; % [g/mol]

syms radius;

% inner radius of the BN reference electrode salt cup
r_RE    = 0.125 / 2 * 0.0254;   % [m]

% height of the BN reference electrode salt cup
h_RE    = 0.4606 * 0.0254;  % [m]

% volume of the reference electrode cup
V_RE    = pi * (r_RE)^2 * (h_RE); % [m^3]

% solubility of LaF3 in LiF-BeF2-UF4 (62.8 - 36.4 - 0.8 mol%)
s_LaF3_FLiBe = @(Temperature) 1e-2 * (8915.88586 .* exp(-(10000 ./ Temperature) / 1.14486) + ...
                                                                0.06596); % [mol frac LaF3/solvent]

% density of FLiBe
rho_FLiBe = @(Temperature) 2245 - 0.424 .* Temperature; % [kg/m^3]

% denisty of LaF3 @ 298K
rho_LaF3 = 5940; % [kg/m^3]

% volume of the electrode wire in reference electrode
d_wire = 1 / 32 * 0.0254; % [m]
h_wire = 0.25 * 0.0254; % [m]
V_wire = pi / 4 * d_wire^2 * h_wire; % [m^3]


% LaF3 mass loss calculations %

    % volume of reference electrode cup (will change with LaF3 thickness)
    V_FLiBe    = V_RE - V_wire; % [m^3]

    % mass of FLiBe in reference electrode cup
    m_FLiBe = 1e3 * V_FLiBe * rho_FLiBe(Temperature); % [g]

    % moles of FLiBe in reference electrode cup
    n_FLiBe = m_FLiBe / MolarMass_FLiBe; % [mol]

    % moles of LaF3 that will saturate FLiBe in reference electrode
    n_LaF3  = s_LaF3_FLiBe(Temperature) .* n_FLiBe; % [mol]

    % mass of LaF3 that will saturate FLiBe in reference electrode
    m_LaF3  = n_LaF3 * MolarMass_LaF3; % [g]


% LaF3 wall thickness loss calculations %

    % volume loss of LaF3 coating
    V_LaF3 = m_LaF3 * 1e-3 ./ rho_LaF3; % [m^3]

    % minimum thickness of LaF3 wall
    y_min = V_LaF3 / pi / r_RE^2; % [m]
```

```
formatSpec = 'Minimum thickness of LaF3 crystal in reference electrode is %4.3f mm\n';
fprintf(formatSpec, y_min)
```

```
Minimum thickness of LaF3 crystal in reference electrode is 0.247 mm
```

Appendix E. Data Archiving

Document Number/ Folder Number/ Experiment Name (with Link)	Format/ File Type	Contents of Document/Folder	Relevant Chapters Chapter 2 Chapter 3 Chapter 4 Chapter 5
UCBS28CF01 Salt Loop Design	Folder	Complete folder with all the 3D models and drawings of the natural convection molten salt loop	Chapter 2
UCBS28EG007v3 Natural Circulation Salt Loop Design Calculations	Xlsx	Calculator for estimating order of magnitude of salt flow rate in natural circulation molten salt loop. Maintenance of the calculator is to be continued on https://github.com/Michael-Borrello-PhD/natural-circulation-loop-design	Chapter 2
UCBS28EG014v2 Salt Loop HX Calculations Sheet	Xlsx	Calculator for designing heat exchanger geometry for natural circulation salt loop heat rejection	Chapter 2
UCBS28EG025 Salt Loop Flow Diagram	Visio	Block flow diagram with preliminary controls logic embedded in the diagram	Chapter 2
UCBS28EG028v1 Salt Loop Controls Design and Operating Specifications	Docx	Specifications for operation of the natural circulation molten alt loop. Operating modes are discussed, but not exhaustive.	Chapter 2
UCBS28EG03 GB4 Design	Folder	Contains design specifications, 3D models, and drawings of the glovebox with interfaces that house the natural circulation loop.	Chapter 2
UCBS28EG02 Control System 04 CA Control Box	Folder	Contains all documentation related to programming and operating the Copenhagen Atomics control system	Chapter 2
2022-09-02 Drain Vessel heating tape testing	eLab Experiment	Experiment notes for testing heating tapes from NaFBe salt transfer	Chapter 2
2022-09-12 Transfer Line Connection and Dry Run	eLab Experiment	Experiment notes for configuring NaFBe salt transfer system	Chapter 2
2022-09-15 ThorCon Supply Vessel Heating Tape test and salt heating characterization	eLab Experiment	Experiment notes for heating tape tests from NaFBe salt transfer	Chapter 2
2022-09-19 ThorCon Supply Vessel Heating Tape Removal	eLab Experiment	Experiment notes from heating tape failure on NaFBe salt transfer system	Chapter 2

2022-09-26 ThorCon Salt Preheating	eLab Experiment	Experiment notes from heating of NaFBe salt transfer vessel. Contains operator methods for manually logging temperatures and ensuring safe operation.	Chapter 2
2022-10-09 ThorCon Salt Preheating	eLab Experiment	Experiment notes from heating NaFBe salt transfer vessel. Contains temperature data over time to show heating curves of the system.	Chapter 2
2022-10-17 Salt Transfer Line Clearing	eLab Experiment	Experiment notes from removal of frozen salt from transfer line tubing. Images shown of transfer line clogged with frozen salt.	Chapter 2
2022-11-07 Crucible Transfer	eLab Experiment	Experiment notes from NaFBe salt transfer into 100mL GC crucible. Contains temperature data over time.	Chapter 2
2023-12-07 Thermocouple Placement and Insulation Wrapping	eLab Experiment	Experiment notes for installing TCs on the salt loop. Contains images of the TC locations on the loop and insulation wrapping progression.	Chapter 2
2025-03-13 Salt Transfer Remote Monitoring	eLab Experiment	Contains the operators logs from the first salt transfer attempt	Chapter 2
2025-06-20 Decontaminating lab and Be swipe analysis preparation	eLab Experiment	Contains the Be swipe and air monitoring data for lab decontamination	Chapter 2
2025-06-26 Heating System Shakedown	eLab Experiment	Contains shakedown testing methods and operating parameters from the second salt transfer attempt	Chapter 2
2025-08-13 GB Opening and System Modifications	eLab Experiment	Contains salt transfer system reconfiguration notes and swipe sample details for lab decontamination	Chapter 2
2025-09-09 Swipe Digestion and Standards Preparation	eLab Experiment	Contains full procedure used for preparing Be standard for decontamination and sample details for Be decontamination report	Chapter 2
UCBS16EG1000 Electrode Probe Assembly	Folder	All custom designs documents for the fabrication of the Echem Probe, including CAD models and specifications.	Chapter 3
UCBS16EG1001B2-Electrode-Probe-Assembly	Pdf	Current assembly drawing of the Echem Probe	Chapter 3
UCBS16EG1012A3-Electrode-Screw-Terminal-Connector	Pdf	Current drawing for electrode screw terminal connectors	Chapter 3
UCBS16EG1100 Electrode Probe OTS Components	Folder	All 3D models for the off-the-shelf components in the Echem Probe assembly	Chapter 3

UCBS40EG03 Electrochem Cell SOLIDWORKS Drawing files	Folder	Current drawings for interfacing materials with the Echem Probe, including the flow shield and BN parts	Chapter 3
UCBS40EG0211C Electrode Flow Shield	Pdf	Current drawing of the Echem Probe flow shield	Chapter 3
UCBS40QA0001 lanthanum-fluoride-laf3-data-sheet	Pdf	Data sheet for LaF_3 material properties	Chapter 3
UCBS40EG0003A LaF3 crystal sizing calculations	MATLAB script	Calculator for sizing the dimensions of LaF_3 crystal in BN end spacer for Echem Probe	Chapter 3
UCBS41TS04 Printed Electrode FLiBe exposure 20230323	Folder	Contains optical image data from printed electrode exposure in FLiBe + Cr_2O_3	Chapter 3
UCBS41TS08 Printed Electrode Tests dta files in FLiNaK	Folder	Contains electrochemical .dta files from printed electrode exposure in FLiNaK	Chapter 3
UCBS40EG0204B BN Probe Spacer	Pdf	Current drawing of the Echem Probe BN electrically and thermally insulating spacers	Chapter 4
UCBS40EG0203B BN End Spacer	Pdf	Current drawing of the Echem Probe BN terminal spacer with geometry to interface with the flow shield	Chapter 4
UCBS40RC01 Images of Ultramet Samples	Folder	Contains all images of the Ultramet samples, including porous graphitic foam discs and reference electrode bodies	Chapter 4
UCBS40RC02 Files from Ultramet	Folder	Contains all EDS spectra and relevant design documentation from Ultramet about the porous graphitic foam samples and LaF3 casting	Chapter 4
UCBS40TS01 RE Phase I Data	Folder	Contains all electrochemical data collected from the Ultramet NiTRE testing campaign	Chapter 4
01 – Cell assembling	eLab Experiment	Experiment notes from Echem Probe tests in FLiBe. Contains cell configuration details and images with dimension of the assembly.	Chapter 3
Echem experiment 230208	eLab Experiment	Experiment notes from Echem Probe tests in FLiBe. Contains cell configuration details.	Chapter 5
03 - Echem experiment 230215	eLab Experiment	Experiment notes from Echem Probe tests in FLiBe. Contains cell configuration details.	Chapter 5
Flibe electrochem 20230217	eLab Experiment	Experiment notes from Echem Probe tests in FLiBe. Contains .dta files collected on the Echem Probe in FLiBe.	Chapter 5
04/16 Assembling TRE and preliminary test	eLab Experiment	Experiment notes from AgTRE test for Echem Probe	Chapter 3, Chapter 4

BN Coated Graphite Foam Long Exposure in FLiBe	eLab Experiment	Experiment notes from NiTRE Ultramet materials testing. Includes images of materials, sample data, and procedure for testing.	Chapter 4
Electrochemical Sensor for Pump Health Monitoring	eLab Experiment	Contains all experiment notes from electrochemical studied in FLiBe for pump health monitoring.	Chapter 5
UCBS51TS09 2024-12-10 Cr solubility with Echem	Folder	Contains all electrochemical data collected from the FLiNaK-CrF_3 system investigating solubility and quantitative analysis.	Chapter 5
UCBS51SF0101 Echem Analysis of CrF3 in FLiNaK	Opj	OriginLab project file that contains the current analysis of the FLiNaK-CrF_3 data, including data and figures to be included in J-63	Chapter 5
2024-12-11 sampling FLiNaK-CrF3 for solubility studies	eLab Experiment	Experiment notes from FLiNaK-CrF_3 additions including the .dta files from the electrochemical runs	Chapter 5